

UCC

University College Cork, Ireland
Coláiste na hOllscoile Corcaigh

Challenges in the Design of Tension Moored Floating Wind Turbines

Christopher Wright

A Thesis Submitted for the
Degree of Doctor of Philosophy

In the School of Engineering

Department of Civil and Environmental Engineering

National University of Ireland, Cork

2022

Supervisors:

Dr. Jimmy Murphy & Dr. Vikram Pakrashi

Head of Department: Prof. Liam Marnane

Contents

Declaration xxx

Abstract xxxi

Acknowledgements xxxii

List of Publications xxxiii

1 Introduction **1**

1.1 Floating Offshore Wind Turbines 1

1.2 Tension Moored Floating Offshore Wind Turbines 2

1.3 Research Outline 2

1.4 Goals 3

1.5 Credit statement 4

2 Literature Review **5**

2.1 Floating Offshore Wind Energy Review 5

2.1.1 Irish FWT potential 7

2.2 Proposed Floating Concepts 7

2.2.1 Tension Moored Platform 7

2.2.2 Hybrid Platform Types 14

2.3 Combined Wind and Wave Energy Review 16

2.3.1 Co-location 16

2.3.2 Combined Platform 17

2.3.2.1 Fixed Platform 17

2.3.2.2 Floating Platform 18

2.4 Modelling Techniques and Issues 25
2.4.1 Potential Flow Theory Boundary Element Methods 25
2.4.2 Hydrodynamic Structural Coupling/ Hydroelasticity 27
2.4.3 Vortex Method 27
2.4.4 Mooring Modelling Methods 28
2.4.5 Coupled Hydro Aero Elastic Simulations 30
2.4.5.1 Models & Model Validation 30
2.4.5.2 Required Model Fidelity 33
2.4.5.3 Aerodynamic Damping and Turbulence Effects 37
2.4.5.4 Viscous Damping 38
2.4.5.5 Platform & Tower Elasticity 38
2.4.5.6 Drivetrain 39
2.4.5.7 Extreme & Survival Modelling 40
2.4.5.8 Control 40
2.4.5.9 Model Predictive Control (MPC) 41
2.4.5.10 Linear Quadratic Regulator). 42
2.4.5.11 Receding Horizon Control 43
2.4.6 Computational Fluid Dynamics 43
2.4.7 Experimental Modelling 47
2.4.7.1 Wave Basin Modelling 47
2.4.7.2 Offshore Testing 53
2.4.7.3 Wind Tunnel Testing 54
2.4.7.4 Hybrid Modelling 55
2.4.8 System Identification 55
2.4.9 Comparison of Floating Platforms 56
2.4.10 Tension Moored Platforms 58
2.4.10.1 Modelling Method Comparisons 58
2.4.10.2 VIV 59
2.4.10.3 Higher Order Forces 59
2.4.11 Non-Linearities 61

2.4.11.1 Nonlinear wave . . . 61
2.4.11.2 Variable Submergence . . . 62
2.4.11.3 Slow Drift . . . 63
2.4.12 Wind and Wave Misalignment . . . 64
2.4.13 Extreme/Survivability Modelling . . . 64
2.4.14 Fault Detection and Modelling . . . 65
2.4.15 Platform and Mooring Faults . . . 65
2.4.16 Crew Transfer . . . 66
2.4.17 Risk and Uncertainty Analysis . . . 67
2.5 Design Optimisation . . . 68
2.5.1 Deployed Environment . . . 68
2.5.2 Platform . . . 69
2.5.3 Mooring System . . . 72
2.5.4 Integrated Design . . . 73
2.6 Wave Field . . . 73
2.6.1 Near Trapping . . . 73
2.6.2 WEC Array . . . 74
2.7 HAWT vs. VAWT . . . 75
2.8 Platform Dampers . . . 76
2.8.1 Heave Plate . . . 76
2.8.2 Air Spring Vibration Absorber . . . 77
2.8.3 Wave Energy Convertors . . . 77
2.8.4 Tuned Mass Dampers . . . 77
2.8.5 Tuned Liquid Column Dampers . . . 78
2.9 Gaps in the literature . . . 78

3 Methodology **81**

3.1 Description of the Software used in the Course of This Work . . . 81
3.1.1 FAST . . . 81
3.1.1.1 HydroDyn . . . 81

3.1.1.2 MoorDyn . . . 82
3.1.1.3 AeroDyn . . . 82
3.1.1.4 BeamDyn . . . 82
3.1.1.5 ServoDyn . . . 83
3.1.1.6 BMODES . . . 83
3.1.2 Ansys AQWA . . . 83
3.1.3 NEMOH . . . 83
3.1.4 OrcaFlex . . . 84
3.2 Simulation Modelling Approach . . . 84
3.2.1 Viscous Drag . . . 85
3.2.2 Tendon Stiffness . . . 86
3.2.3 Natural Periods . . . 87
3.2.4 Methods to determine RAO . . . 87

4 Numerical Modelling of FWT **91**
4.1 HEXWIND Numerical Modelling . . . 93
4.1.1 Natural Periods . . . 93
4.1.2 Second-Order Loads . . . 94
4.2 Numerical Convergence . . . 97
4.2.1 Mesh Convergence Study . . . 97
4.2.2 OrcaFlex Mooring Convergence Study . . . 99
4.2.3 Viscous Drag Element Size Convergence Study . . . 101
4.2.4 Flexible Tower Element Size Convergence Study . . . 102
4.3 Numerical Model Validation . . . 104
4.3.1 Wave Basin . . . 105
4.3.2 Model Set Up . . . 106
4.3.2.1 False Bottom . . . 106
4.3.2.2 Fabrication . . . 107
4.3.3 Still Water . . . 108
4.3.4 Wind load . . . 110

4.3.5 Tendon pretension . . . 112
4.3.6 Regular Waves . . . 113
4.3.7 Irregular Waves . . . 121
4.3.7.1 Method 1: Theoretical JONSWAP waves . . . 123
4.3.7.2 Method 2: Measured JONSWAP waves . . . 125
4.3.7.3 Spectral Results . . . 127
4.3.8 Rogue Waves . . . 128
4.4 Conclusions . . . 149

5 Design of TWind **151**

5.1 Design Conditions . . . 152
5.1.1 Bathymetry . . . 152
5.1.2 Extreme Wave Extrapolation . . . 153
5.1.3 Curtailed Wind Energy based on Wave Height . . . 156
5.2 Design Turbine . . . 160
5.2.1 NREL 5 MW Ref Turbine . . . 160
5.3 Design of Tower . . . 160
5.4 Design of Floating Substructure . . . 162
5.4.1 Maximum size of tubular elements . . . 162
5.5 Design Optimisation . . . 163
5.6 Parameter Study . . . 165
5.6.1 Parameter Study of Hydrodynamic Parameters . . . 166
5.6.1.1 Parameter Study of Varying Draft . . . 167
5.6.1.2 Parameter Study of Column and Pontoon Radius . . . 173
5.6.1.3 Parameter Study of Column Spacing . . . 181
5.6.2 FAST Model Set-up . . . 188
5.6.3 Effect of Flexible Tower . . . 189
5.6.4 Design Result . . . 199
5.7 Installation Stability Design . . . 200
5.8 Time Domain Modelling of Tow Conditions . . . 209

5.9 Conclusions . . . 218

6 Design of Combined Wind and Wave Energy Convertor 221

6.1 Design Philosophy . . . 223

6.2 Preliminary Design . . . 223

6.2.1 Wind to Wave Ratio . . . 223

6.3 Design of standalone WEC . . . 225

6.4 WEC Parameter Study . . . 228

6.5 WEC and TLP Survivability . . . 231

6.5.1 Surge Plates . . . 231

6.5.2 Submergence Operation . . . 232

6.6 TWindWave . . . 232

6.6.1 Survival Mode . . . 233

6.7 Numerical Modelling . . . 235

6.8 Results . . . 237

6.8.1 Hydrodynamic Interaction . . . 237

6.8.2 Power Production . . . 238

6.8.3 Platform Performance . . . 245

6.8.4 Survival Modes . . . 249

6.9 Numerical Model Validation . . . 251

6.9.1 LIR National Ocean Test Facility Deepwater Basin . . . 252

6.9.2 Design and Fabrication of Physical Model . . . 252

6.9.2.1 Tower . . . 252

6.9.2.2 WEC . . . 254

6.9.2.3 Regular Waves . . . 260

6.10 Conclusions . . . 264

7 Design Sensitivity to Anchor Misposition 269

7.1 Introduction . . . 269

7.2 Anchor Misposition . . . 270

7.2.1 Anchor Type and Positional Tolerance . . . 271

7.2.2 Methods . . . 272
7.2.3 Misposition Results . . . 273
7.2.4 Mitigation Methods . . . 275
7.2.4.1 Nearest Neighbour Installation Method . . . 280
7.2.4.2 Furthest Neighbour Installation Method . . . 281
7.2.5 Mitigation Results . . . 281

8 Discussion and Conclusions 285

8.1 Discussion . . . 285
8.2 Limitations . . . 287
8.2.1 Chapter 3. Numerical Modelling of FWT . . . 287
8.2.2 Chapter 4. Design of TWind . . . 288
8.2.3 Chapter 5. Design of Combined Wind and Wave Energy Convertor 288
8.2.4 Chapter 6. Design Sensitivity to Anchor Misposition . . . 289
8.3 Future Work . . . 289
8.3.1 Chapter 3. Numerical Modelling of FWT . . . 289
8.3.2 Chapter 4. Design of TWind . . . 289
8.3.3 Chapter 5. Design of Combined Wind and Wave Energy Convertor 289
8.3.4 Chapter 6. Design Sensitivity to Anchor Misposition . . . 290
8.4 Recommendations . . . 290
8.4.1 Design Conditions . . . 290
8.4.2 Recommendations for Design Approaches . . . 292
8.4.3 Recommendations for Experimental Tank Testing . . . 293
8.4.4 Pathway to Standardization . . . 294

A HEXWIND Experimental Validation of Numerical Model 295

B Acer Method 319

C Results of TWind Time-domain Tow Simulations 321

D TWind and TWINDWAVE Scale Model Five Way Joiner Fabrication Process **333**

List of Figures

2.1 Search for Articles with keywords Floating Wind Turbine on Sciendirect . 6
2.2 Evolution of the Blue H TLP 8
2.3 MIT/NREL TLP 8
2.4 Evolution of the PelaStar TLP 9
2.5 WindStar TLP 10
2.6 EsaFloater 10
2.7 HEXWIND 11
2.8 GL Garrad Hassan TLP 11
2.9 Iberdrola's TLPWIND 12
2.10 Design History of GICON - TLP 13
2.11 SBM Offshore Inclined TLP 13
2.12 Stiesdal TLP 14
2.13 ECO TLP 15
2.14 Bachynski and Moan TLPWT 15
2.15 FPP Poisdon 18
2.16 WindFloat WECs 19
2.17 SFC 20
2.18 TLPWT with PA 22
2.19 C-HYP 23
2.20 T-HYP 24
2.21 Iturrioz OWC WT 25
2.22 Iturrioz OWC WT 26

3.1 Simulation Flow Chart 85
3.2 Comparison of RAO Calculation Method 89

4.1 Surge Difference Frequency QTF Load 95
4.2 Heave Sum Frequency QTF Load 95
4.3 Pitch Sum Frequency QTF Load 96
4.4 HEXWIND mesh with 10877 elements 98
4.5 Pitch Added Mass for Mesh Convergence Study 98
4.6 Tendon Free Decay Segment Discretization Convergence Test 100
4.7 Drag Force Segment Discretization Convergence Test 102
4.8 Tower Free Decay Segment Discretization Convergence Test 104
4.9 Photograph of HEXWIND as installed in the wave basin. In the foreground the false bottom can be seen. Copyright IFREMER with permission for reproduction granted 107
4.10 Photograph of HEXWIND from the still water level. Perspective is distorted due to the use of an underwater fish eye lens. Copyright IFREMER with permission for reproduction granted 108
4.11 Numerical & Experimental Surge free decay tests, showing the effects of varying the drag coefficient 110
4.12 Photograph of Wind Load Thruster, mounted on Bending Load Cell. . . . 111
4.13 Calibration of Thrust Load generation, PWM shown at model scale, while thrust is shown at full scale 111
4.14 Numerical Pitch RAO for Regular Waves, Individual Pretension Variation Study 113
4.15 Numerical Tendon Tension RAO for Regular Waves, Individual Pretension Variation Study 114
4.16 Numerical & Experimental Surge RAO's for Regular Waves, crosses indicates Experimental value, circles indicates simulated value 115
4.17 Numerical & Experimental Heave RAO's for Regular Waves, crosses indicates experimental value, circles indicates simulated value 116

4.18 Numerical & Experimental Pitch RAO's for Regular Waves, crosses indicates experimental value, circles indicates first order simulated value . . . 117

4.19 Numerical & Experimental Line 1 Tension RAO's for Regular Waves, crosses indicates experimental value, circles indicates first order simulated value . . . 118

4.20 Fitted drag coefficients for the Irregular Wave Cases, Method 1 and 2. Note: for the wave cases the drag coefficient in the splash zone is set to zero in order to not induce additional third order viscous drift motions . . 124

4.21 Comparison of Numerical & Experimental Surge standard deviations for Irregular Waves. Simulations with theoretical JONSWAP wave spectra . 126

4.22 Comparison of Numerical & Experimental Surge low frequency standard deviations for Irregular Waves. Simulations with theoretical JONSWAP wave spectra . . . 127

4.23 Comparison of Numerical & Experimental Surge wave frequency standard deviations for Irregular Waves. Simulations with theoretical JONSWAP wave spectra . . . 128

4.24 Comparison of Numerical & Experimental Heave standard deviations for Irregular Waves. Simulations with theoretical JONSWAP wave spectra . 129

4.25 Comparison of Numerical & Experimental Heave low frequency standard deviations for Irregular Waves. Simulations with theoretical JONSWAP wave spectra . . . 130

4.26 Comparison of Numerical & Experimental Heave wave frequency standard deviations for Irregular Waves. Simulations with theoretical JONSWAP wave spectra . . . 131

4.27 Comparison of Numerical & Experimental Pitch standard deviations for Irregular Waves. Simulations with theoretical JONSWAP wave spectra . 132

4.28 Comparison of Numerical & Experimental Pitch low frequency standard deviations for Irregular Waves. Simulations with theoretical JONSWAP wave spectra . . . 132

4.29 Comparison of Numerical & Experimental Pitch wave frequency standard deviations for Irregular Waves. Simulations with theoretical JONSWAP wave spectra 133

4.30 Comparison of Numerical & Experimental Tendon Tension standard deviations for Irregular Waves. Simulations with theoretical JONSWAP wave spectra 133

4.31 Comparison of Numerical & Experimental Tendon Tension low frequency standard deviations for Irregular Waves. Simulations with theoretical JONSWAP wave spectra 134

4.32 Comparison of Numerical & Experimental Tendon Tension wave frequency standard deviations for Irregular Waves. Simulations with theoretical JONSWAP wave spectra 135

4.33 Comparison of Numerical & Experimental total frequency Surge standard deviations for Irregular Waves. Simulations with observed wave elevation. OBS, FST, NEW, QTF and Fitted QTF, indicate the observed, first order, Newman's approximation, Full QTF and drag coefficient fitted Full QTF simulations respectively 136

4.34 Comparison of Numerical & Experimental low frequency Surge standard deviations for Irregular Waves. Simulations with observed wave elevation. OBS, FST, NEW, QTF and Fitted QTF, indicate the observed, first order, Newman's approximation, Full QTF and drag coefficient fitted Full QTF simulations respectively 137

4.35 Comparison of Numerical & Experimental wave frequency Surge standard deviations for Irregular Waves. Simulations with observed wave elevation. OBS, FST, NEW, QTF and Fitted QTF, indicate the observed, first order, Newman's approximation, Full QTF and drag coefficient fitted Full QTF simulations respectively 138

4.36 Comparison of Numerical & Experimental total frequency Heave standard deviations for Irregular Waves. Simulations with observed wave elevation. OBS, FST, NEW, QTF and Fitted QTF, indicate the observed, first order, Newman's approximation, Full QTF and drag coefficient fitted Full QTF simulations respectively 139
4.37 Comparison of Numerical & Experimental low frequency Heave standard deviations for Irregular Waves. Simulations with observed wave elevation. OBS, FST, NEW, QTF and Fitted QTF, indicate the observed, first order, Newman's approximation, Full QTF and drag coefficient fitted Full QTF simulations respectively 140
4.38 Comparison of Numerical & Experimental wave frequency Heave standard deviations for Irregular Waves. Simulations with observed wave elevation. OBS, FST, NEW, QTF and Fitted QTF, indicate the observed, first order, Newman's approximation, Full QTF and drag coefficient fitted Full QTF simulations respectively 141
4.39 Comparison of Numerical & Experimental total frequency Pitch standard deviations for Irregular Waves. Simulations with observed wave elevation. OBS, FST, NEW, QTF and Fitted QTF, indicate the observed, first order, Newman's approximation, Full QTF and drag coefficient fitted Full QTF simulations respectively 142
4.40 Comparison of Numerical & Experimental low frequency Pitch standard deviations for Irregular Waves. Simulations with observed wave elevation. OBS, FST, NEW, QTF and Fitted QTF, indicate the observed, first order, Newman's approximation, Full QTF and drag coefficient fitted Full QTF simulations respectively 143
4.41 Comparison of Numerical & Experimental wave frequency Pitch standard deviations for Irregular Waves. Simulations with observed wave elevation. OBS, FST, NEW, QTF and Fitted QTF, indicate the observed, first order, Newman's approximation, Full QTF and drag coefficient fitted Full QTF simulations respectively 144

4.42 Comparison of Numerical & Experimental total frequency Tendon Tension standard deviations for Irregular Waves. Simulations with observed wave elevation. OBS, FST, NEW, QTF and Fitted QTF, indicate the observed, first order, Newman's approximation, Full QTF and drag coefficient fitted Full QTF simulations respectively 145

4.43 Comparison of Numerical & Experimental low frequency Tendon Tension standard deviations for Irregular Waves. Simulations with observed wave elevation. OBS, FST, NEW, QTF and Fitted QTF, indicate the observed, first order, Newman's approximation, Full QTF and drag coefficient fitted Full QTF simulations respectively 146

4.44 Comparison of Numerical & Experimental wave frequency Tendon Tension standard deviations for Irregular Waves. Simulations with observed wave elevation. OBS, FST, NEW, QTF and Fitted QTF, indicate the observed, first order, Newman's approximation, Full QTF and drag coefficient fitted Full QTF simulations respectively 147

4.45 Comparison of Numerical & Experimental Minimum Tendon Tension for Rogue Waves. Black crosses and blue asterisks indicate the extreme range of the 50 random tendon tension variations at the 10% and 50% levels respectively. Black and blue error bars indicate the 50th percentile of the values at the 10% and 50% levels respectively. 148

5.1 Map of Irish Continental Shelf, including contour lines of all water depth above 500 m (excluding the far offshore Rockall Bank) and the M-buoy locations. The Lambert azimuthal equal-area projection is shown here as is used for the area calculations. 154

5.2 Sea Area at certain Depth and distance to Coast 154

5.3 Extreme Wave Analysis for Binned Significant Wave Heights: Maximum Wave Height 157

5.4 Extreme Wave Analysis for Binned Significant Wave Heights: Anomaly Index 158

5.5 Curtailed Energy dependant on wave height at which wind turbine ceases power production. Dashed lines indicate the total available energy without imposing any wave height curtailment. 159
5.6 Pitch Free Decay Test spectral density, Comparison of original tower with three novel shortened tower designs. A shortened tower with reduced, equal and increased mass as compared with the original tower design. . . . 162
5.7 Comparison Mass properties of New Tower type with OC3-Hywind tower 163
5.8 Comparison of New Tower type with OC3-Hywind tower, Stiffness properties 164
5.9 Tower Bending Mode Frequency with Water Depth 165
5.10 Three Models from the Parameter Study 166
5.11 Effect of Increasing Platform Draft on the Surge Radiation Terms 168
5.12 Effect of Increasing Platform Draft on the Surge Excitation Force 169
5.13 Effect of Increasing Platform Draft on the Heave Radiation Terms 169
5.14 Effect of Increasing Platform Draft on the Heave Excitation Force 170
5.15 Effect of Increasing Platform Draft on the Pitch Radiation Terms 170
5.16 Effect of Increasing Platform Draft on the Pitch Excitation Force 171
5.17 Effect of Increasing Platform Draft on the Yaw Radiation Terms 172
5.18 Effect of Increasing Platform Draft on the Yaw Excitation Force 173
5.19 Effect of Increasing Column and Pontoon Radius on the Surge Radiation Terms 174
5.20 Effect of Increasing Column and Pontoon Radius on the Surge Excitation Force 175
5.21 Effect of Increasing Column and Pontoon Radius on the Heave Radiation Terms 176
5.22 Effect of Increasing Column and Pontoon Radius on the Heave Excitation Force 177
5.23 Effect of Increasing Column and Pontoon Radius on the Pitch Radiation Terms 178
5.24 Effect of Increasing Column and Pontoon Radius on the Pitch Excitation Force 179

5.25 Effect of Increasing Column and Pontoon Radius on the Yaw Radiation Terms . . . 180
5.26 Effect of Increasing Column and Pontoon Radius on the Yaw Excitation Force . . . 181
5.27 Effect of Increasing Column Spacing on the Surge Radiation Terms 182
5.28 Effect of Increasing Column Spacing on the Surge Excitation Force 183
5.29 Effect of Increasing Column Spacing on the Heave Radiation Terms 183
5.30 Effect of Increasing Column Spacing on the Heave Excitation Force 184
5.31 Effect of Increasing Column Spacing on the Pitch Radiation Terms 184
5.32 Effect of Increasing Column Spacing on the Pitch Excitation Force 185
5.33 Effect of Increasing Column Spacing on the Yaw Radiation Terms 186
5.34 Effect of Increasing Column Spacing on the Yaw Excitation Force 187
5.35 Effect of Flexible Tower on Pitch RAO 192
5.36 Effect of Flexible Tower on Tendon Tension RAO 193
5.37 Effect of Flexible Tower and Tendon Pretension on Pitch Natural Frequency 194
5.38 Effect of Flexible Tower and Platform Mass to Tendon Pretension Ratio on Pitch Natural Frequency 195
5.39 Effect of Flexible Tower and Platform Mass to Pitch Standard Deviation, All Models 196
5.40 Effect Tower Modelling Technique, Model 106 197
5.41 Effect Tower Modelling Technique, Model 155 198
5.42 3D Impression of Initial Design. Components are drawn to scale 199
5.43 3D Impression of Transport and Installation Condition. Components are drawn to scale 201
5.44 Static Stability of Floats with a Draft of 5 m 202
5.45 Static Stability of Floats with a Draft of 4 m 203
5.46 Static Stability of Floats with a Draft of 3 m 204
5.47 Maximum Wind Speed which comply with the DNV Stability Requirements 205
5.48 TWind Tow Condition Surge RAO 206
5.49 TWind Tow Condition Heave RAO 207

5.50 TWind Tow Condition Pitch RAO 208

5.51 Encounter Periods for Varying Tow Speeds and Wave Directions, $T_z = 5$ s 210

5.52 Encounter Periods for Varying Tow Speeds and Wave Directions, $T_z = 7.5$ s211

5.53 Encounter Periods for Varying Tow Speeds and Wave Directions, $T_z = 10$ s212

6.1 Design Philosophy for the addition of WEC to an existing TLPWT. The pretension required for TLPWT survivability is exploited for the WECs power generation phase 224

6.2 WEC capture width ratio from literature study 226

6.3 Ratio of Annual Wind Energy to Wave Energy 227

6.4 Performance Metrics for Individual WEC 230

6.5 3D Impression of TwindWave Operational mode with WECs at the mean water level. Components are drawn to scale 235

6.6 3D Impression of TWindWave Survival mode with WEC submerged and rotated to 67.5 degrees. Components are drawn to scale 236

6.7 Mesh for mode cases analysed: (a) Operational, (b)-(j) Survival Submergence: (b) 5 m, (c) 10 m, (d) 15 m, (e) 20 m, (f) 25 m, (g) 22.5°, (h) 45.0°, (i) 67.5°, (j) 90.0° 237

6.8 View of model setup in OrcaFlex 238

6.9 WEC and tendon numbering scheme 239

6.10 Added mass for coupled platform surge and float surge 240

6.11 Radiation damping for coupled platform surge and float surge 241

6.12 Added mass for coupled float 1 surge and float 3 & 4 surge 241

6.13 Radiation damping for coupled float 1 surge and float 3 & 4 surge 242

6.14 Added mass for coupled float 1 pitch and float 3 & 4 pitch 242

6.15 Radiation damping for coupled float 1 pitch and float 3 & 4 pitch 243

6.16 Average power for WEC's, numbers indicate percentage change from the hydrodynamic interaction to no-interaction simulations 244

6.17 Tower bending moment, numbers in black indicate percentage change from hydrodynamic interaction to no interaction case, numbers in bold blue indicate percentage change from interaction case to no WEC case 246
6.18 Platform Surge, Heave Pitch and Nacelle Acceleration, numbers in black indicate percentage change from hydrodynamic interaction to no interaction case, numbers in bold blue indicate percentage change from interaction case to no WEC case 247
6.19 Platform tendon tension, numbers in black indicate percentage change from hydrodynamic interaction to no interaction case, numbers in bold blue indicate percentage change from interaction case to no WEC case . . 248
6.20 RAO's for platform surge, heave and pitch motions, nacelle acceleration, tendon 1 tension, and tower bending moment for various submergence methods 250
6.21 Tower Mass (A) and Stiffness (B) as Designed and with available materials 253
6.22 Photograph of TWindWave in Wind only mode (TWind). As installed in wave basin 255
6.23 Calibration of PTO Dampers, Results shown at full scale 256
6.24 Photograph of TWindWave in WEC Operational Mode 257
6.25 Photograph of TWindWave in WEC free mode in wave basin, showing details of the WEC - platform interface. 258
6.26 Photograph of TWindWave in WEC operational mode in wave basin , showing details of the WEC - platform, tendon and tower interfaces. . . . 259
6.27 Regular wave surge comparison between the numerical and physical modelling techniques for all TWindWave configurations tested 260
6.28 Regular wave heave comparison between the numerical and physical modelling techniques for all TWindWave configurations tested 261
6.29 Regular wave pitch comparison between the numerical and physical modelling techniques for all TWindWave configurations tested 262
6.30 Regular wave Tendon 1 tension comparison between the numerical and physical modelling techniques for all TWindWave configurations tested . . 263

6.31 Regular wave Tendon 2 and 4 tension comparison between the numerical and physical modelling techniques for all TWindWave configurations tested 264

6.32 Regular wave Tendon 3 tension comparison between the numerical and physical modelling techniques for all TWindWave configurations tested . . 265

6.33 Regular wave Bow WEC comparison between the numerical and physical modelling, with and without PTO damping 266

6.34 Regular wave Bow WEC comparison between the numerical and physical modelling, with and without PTO damping 267

6.35 Regular wave Port and Starboard WEC comparison between the numerical and physical modelling, with and without PTO damping 267

7.1 View of platform and anchor misposition. Dashed tendon line is the design case with no misposition, solid tendon line is the misposition case. Seabed circles indicate the anchor target area. Horizontal distances of the misposition length are exaggerated to retain clarity. 272

7.2 Possible Anchor Positional Locations 274

7.3 Anchor misposition worst case 276

7.4 Anchor misposition effects on Dynamics: Worst Case, where X is the platform surge, A is the nacelle acceleration and T1 is Tendon 1 277

7.5 Anchor Misposition effects on Dynamics: All Cases, where T 1-4 is Tendon 1 - 4 278

7.6 Anchor Misposition effects on Dynamics: All Cases, where X, Z, RY is the platform surge, heave, pitch, A is the nacelle acceleration 279

7.7 Examples of NNIM and FNIM positional results. Horizontal offset distance has been distorted to retain clarity. Numbers indicate installation order 281

7.8 Results of NNIM and FNIM compared to the design offset for ten worst case simulations, where X, Z, RY is the platform surge, heave, pitch, A is the nacelle acceleration. 283

7.9 Results of NNIM and FNIM compared to the design offset for ten worst case simulations, where T1-4 is Tendon 1 - 4 284

A.1 Regular Wave 1, Numerical & Experimental Spectral Density Responses . 295

A.2 Regular Wave 2, Numerical & Experimental Spectral Density Responses . 296

A.3 Regular Wave 3, Numerical & Experimental Spectral Density Responses . 296

A.4 Regular Wave 4, Numerical & Experimental Spectral Density Responses . 297

A.5 Regular Wave 5, Numerical & Experimental Spectral Density Responses . 297

A.6 Regular Wave 6, Numerical & Experimental Spectral Density Responses . 298

A.7 Regular Wave 7, Numerical & Experimental Spectral Density Responses . 298

A.8 Regular Wave 8, Numerical & Experimental Spectral Density Responses . 299

A.9 Regular Wave 9, Numerical & Experimental Spectral Density Responses . 299

A.10 Regular Wave 10, Numerical & Experimental Spectral Density Responses 300

A.11 Regular Wave 11, Numerical & Experimental Spectral Density Responses 300

A.12 Comparison Between Theoretical JONSWAP and Observed Spectral Density, Irregular Wave No. 1 - 6 301

A.13 Comparison Between Theoretical JONSWAP and Observed Spectral Density, Irregular Wave No. 7 - 12 302

A.14 Comparison Between Theoretical JONSWAP and Observed Spectral Density, Irregular Wave No. 13 - 15 303

A.15 Numerical & Experimental Surge, Heave, Pitch and line 1 Tension Spectral Response Density for Irregular Wave 1. Simulations with theoretical JONSWAP wave spectra 304

A.16 Numerical & Experimental Surge, Heave, Pitch and line 1 Tension Spectral Response Density for Irregular Wave 1. Simulations with observed wave time series 304

A.17 Numerical & Experimental Surge, Heave, Pitch and line 1 Tension Spectral Response Density for Irregular Wave 2. Simulations with theoretical JONSWAP wave spectra 305

A.18 Numerical & Experimental Surge, Heave, Pitch and line 1 Tension Spectral Response Density for Irregular Wave 2. Simulations with observed wave time series 305
A.19 Numerical & Experimental Surge, Heave, Pitch and line 1 Tension Spectral Response Density for Irregular Wave 3. Simulations with theoretical JONSWAP wave spectra 306
A.20 Numerical & Experimental Surge, Heave, Pitch and line 1 Tension Spectral Response Density for Irregular Wave 3. Simulations with observed wave time series 306
A.21 Numerical & Experimental Surge, Heave, Pitch and line 1 Tension Spectral Response Density for Irregular Wave 4. Simulations with theoretical JONSWAP wave spectra 307
A.22 Numerical & Experimental Surge, Heave, Pitch and line 1 Tension Spectral Response Density for Irregular Wave 4. Simulations with observed wave time series 307
A.23 Numerical & Experimental Surge, Heave, Pitch and line 1 Tension Spectral Response Density for Irregular Wave 5. Simulations with theoretical JONSWAP wave spectra 308
A.24 Numerical & Experimental Surge, Heave, Pitch and line 1 Tension Spectral Response Density for Irregular Wave 5. Simulations with observed wave time series 308
A.25 Numerical & Experimental Surge, Heave, Pitch and line 1 Tension Spectral Response Density for Irregular Wave 6. Simulations with theoretical JONSWAP wave spectra 309
A.26 Numerical & Experimental Surge, Heave, Pitch and line 1 Tension Spectral Response Density for Irregular Wave 6. Simulations with observed wave time series 309
A.27 Numerical & Experimental Surge, Heave, Pitch and line 1 Tension Spectral Response Density for Irregular Wave 7. Simulations with theoretical JONSWAP wave spectra 310

A.28 Numerical & Experimental Surge, Heave, Pitch and line 1 Tension Spectral Response Density for Irregular Wave 7. Simulations with observed wave time series 310
A.29 Numerical & Experimental Surge, Heave, Pitch and line 1 Tension Spectral Response Density for Irregular Wave 8. Simulations with theoretical JONSWAP wave spectra 311
A.30 Numerical & Experimental Surge, Heave, Pitch and line 1 Tension Spectral Response Density for Irregular Wave 8. Simulations with observed wave time series 311
A.31 Numerical & Experimental Surge, Heave, Pitch and line 1 Tension Spectral Response Density for Irregular Wave 9. Simulations with theoretical JONSWAP wave spectra 312
A.32 Numerical & Experimental Surge, Heave, Pitch and line 1 Tension Spectral Response Density for Irregular Wave 9. Simulations with observed wave time series 312
A.33 Numerical & Experimental Surge, Heave, Pitch and line 1 Tension Spectral Response Density for Irregular Wave 10. Simulations with theoretical JONSWAP wave spectra 313
A.34 Numerical & Experimental Surge, Heave, Pitch and line 1 Tension Spectral Response Density for Irregular Wave 10. Simulations with observed wave time series 313
A.35 Numerical & Experimental Surge, Heave, Pitch and line 1 Tension Spectral Response Density for Irregular Wave 11. Simulations with theoretical JONSWAP wave spectra 314
A.36 Numerical & Experimental Surge, Heave, Pitch and line 1 Tension Spectral Response Density for Irregular Wave 11. Simulations with observed wave time series 314
A.37 Numerical & Experimental Surge, Heave, Pitch and line 1 Tension Spectral Response Density for Irregular Wave 12. Simulations with theoretical JONSWAP wave spectra 315

A.38 Numerical & Experimental Surge, Heave, Pitch and line 1 Tension Spectral Response Density for Irregular Wave 12. Simulations with observed wave time series 315

A.39 Numerical & Experimental Surge, Heave, Pitch and line 1 Tension Spectral Response Density for Irregular Wave 13. Simulations with theoretical JONSWAP wave spectra 316

A.40 Numerical & Experimental Surge, Heave, Pitch and line 1 Tension Spectral Response Density for Irregular Wave 13. Simulations with observed wave time series 316

A.41 Numerical & Experimental Surge, Heave, Pitch and line 1 Tension Spectral Response Density for Irregular Wave 14. Simulations with theoretical JONSWAP wave spectra 317

A.42 Numerical & Experimental Surge, Heave, Pitch and line 1 Tension Spectral Response Density for Irregular Wave 14. Simulations with observed wave time series 317

A.43 Numerical & Experimental Surge, Heave, Pitch and line 1 Tension Spectral Response Density for Irregular Wave 15. Simulations with theoretical JONSWAP wave spectra 318

A.44 Numerical & Experimental Surge, Heave, Pitch and line 1 Tension Spectral Response Density for Irregular Wave 15. Simulations with observed wave time series 318

C.1 Winch Mean Tension Float Draft 3 m, Peak Wave period of 6 s. Barplot colours indicate wind speeds, blue (10 m/s), red (15 m/s), orange (20 m/s), purple (25 m/s), green (30 m/s). D_V and D_W indicate the wind and wave direction respectively. 322

C.2 Winch Mean Tension Float Draft 3 m, Peak Wave period of 10 s. Barplot colours indicate wind speeds, blue (10 m/s), red (15 m/s), orange (20 m/s), purple (25 m/s), green (30 m/s). D_V and D_W indicate the wind and wave direction respectively. 322

C.3 Winch Peak Tension Float Draft 3 m, Peak Wave period of 6 s. Barplot colours indicate wind speeds, blue (10 m/s), red (15 m/s), orange (20 m/s), purple (25 m/s), green (30 m/s). D_V and D_W indicate the wind and wave direction respectively. 323

C.4 Winch Peak Tension Float Draft 3 m, Peak Wave period of 10 s. Barplot colours indicate wind speeds, blue (10 m/s), red (15 m/s), orange (20 m/s), purple (25 m/s), green (30 m/s). D_V and D_W indicate the wind and wave direction respectively. 323

C.5 Peak Pitch Motion Float Draft 3 m, Peak Wave period of 6 s. Barplot colours indicate wind speeds, blue (10 m/s), red (15 m/s), orange (20 m/s), purple (25 m/s), green (30 m/s). D_V and D_W indicate the wind and wave direction respectively. 324

C.6 Peak Pitch Motion Float Draft 3 m, Peak Wave period of 10 s. Barplot colours indicate wind speeds, blue (10 m/s), red (15 m/s), orange (20 m/s), purple (25 m/s), green (30 m/s). D_V and D_W indicate the wind and wave direction respectively. 325

C.7 Peak Roll Motion Float Draft 3 m, Peak Wave period of 6 s. Barplot colours indicate wind speeds, blue (10 m/s), red (15 m/s), orange (20 m/s), purple (25 m/s), green (30 m/s). D_V and D_W indicate the wind and wave direction respectively. 326

C.8 Peak Roll Motion Float Draft 3 m, Peak Wave period of 10 s. Barplot colours indicate wind speeds, blue (10 m/s), red (15 m/s), orange (20 m/s), purple (25 m/s), green (30 m/s). D_V and D_W indicate the wind and wave direction respectively. 326

C.9 RNA Peak Acceleration Float Draft 3 m, Peak Wave period of 6 s. Barplot colours indicate wind speeds: blue (10 m/s), red (15 m/s), orange (20 m/s), purple (25 m/s), green (30 m/s). D_V and D_W indicate the wind and wave direction respectively. 327

C.10 RNA Peak Acceleration Float Draft 3 m, Peak Wave period of 10 s. Barplot colours indicate wind speeds: blue (10 m/s), red (15 m/s), orange (20 m/s), purple (25 m/s), green (30 m/s). D_V and D_W indicate the wind and wave direction respectively. 327

C.11 Winch Peak Tension Float Draft 5 m, Peak Wave period of 6 s. Barplot colours indicate wind speeds, blue (10 m/s), red (15 m/s), orange (20 m/s), purple (25 m/s), green (30 m/s). D_V and D_W indicate the wind and wave direction respectively. 328

C.12 Winch Peak Tension Float Draft 5 m, Peak Wave period of 10 s. Barplot colours indicate wind speeds, blue (10 m/s), red (15 m/s), orange (20 m/s), purple (25 m/s), green (30 m/s). D_V and D_W indicate the wind and wave direction respectively. 328

C.13 Winch Mean Tension Float Draft 5 m, Peak Wave period of 6 s. Barplot colours indicate wind speeds, blue (10 m/s), red (15 m/s), orange (20 m/s), purple (25 m/s), green (30 m/s). D_V and D_W indicate the wind and wave direction respectively. 329

C.14 Winch Mean Tension Float Draft 5 m, Peak Wave period of 10 s. Barplot colours indicate wind speeds, blue (10 m/s), red (15 m/s), orange (20 m/s), purple (25 m/s), green (30 m/s). D_V and D_W indicate the wind and wave direction respectively. 329

C.15 Peak Pitch Motion Float Draft 5 m, Peak Wave period of 6 s. Barplot colours indicate wind speeds, blue (10 m/s), red (15 m/s), orange (20 m/s), purple (25 m/s), green (30 m/s). D_V and D_W indicate the wind and wave direction respectively. 330

C.16 Peak Pitch Motion Float Draft 5 m, Peak Wave period of 10 s. Barplot colours indicate wind speeds, blue (10 m/s), red (15 m/s), orange (20 m/s), purple (25 m/s), green (30 m/s). D_V and D_W indicate the wind and wave direction respectively. 330

C.17 Peak Roll Motion Float Draft 5 m, Peak Wave period of 6 s. Barplot colours indicate wind speeds, blue (10 m/s), red (15 m/s), orange (20 m/s), purple (25 m/s), green (30 m/s). D_V and D_W indicate the wind and wave direction respectively. 331

C.18 Peak Roll Motion Float Draft 5 m, Peak Wave period of 10 s. Barplot colours indicate wind speeds, blue (10 m/s), red (15 m/s), orange (20 m/s), purple (25 m/s), green (30 m/s). D_V and D_W indicate the wind and wave direction respectively. 331

C.19 RNA Peak Acceleration Float Draft 5 m, Peak Wave period of 6 s. Barplot colours indicate wind speeds, blue (10 m/s), red (15 m/s), orange (20 m/s), purple (25 m/s), green (30 m/s). D_V and D_W indicate the wind and wave direction respectively. 332

C.20 RNA Peak Acceleration Float Draft 5 m, Peak Wave period of 10 s. Barplot colours indicate wind speeds, blue (10 m/s), red (15 m/s), orange (20 m/s), purple (25 m/s), green (30 m/s). D_V and D_W indicate the wind and wave direction respectively. 332

D.1 3D Model of 5 Way Joiner 333

D.2 3D Model of 5 Way Joiner in 3D Printing Software including Internal Mesh Stiffner 334

D.3 Photograph of 5 Way Joiner During the 3D Printing Process 334

D.4 Photograph of Completed 5 Way Joiner 335

Glossary

AEP Annual energy production.

BEM boundary element method.

CFD computational fluid dynamics.

DOF degree of freedom.

FEM finite element method.

FOWTs floating offshore wind turbines.

FSI fluid-structure interaction.

FWT floating wind turbine.

GA genetic algorithm.

HAWT Horizontal Axis Wind Turbine.

IEC International Electrotechnical Commission.

LQR linear quadratic regulator.

MCDA multi criteria decision analysis.

MUP multi-use offshore platforms.

NMF nacelle magnification factor.

NRHC non-linear receding horizon control.

OEM original equipment manufacturer.

ORE Offshore Renewable Energy.

OREDP Offshore Renewable Energy Development Plan.

OWC oscillating water column.

OWSC oscillating wave surge converter.

OWT offshore wind turbine.

PTO power take off.

RAO response amplitude operator.

RNA rotor nacelle assembly.

SPAR Single point anchor reservoir.

STC SPAR Torus Combination.

TLB tension leg buoy.

TLCD tuned liquid column dampers.

TLD tuned liquid dampers.

TLP tension moored platform.

TLS tension leg SPAR.

TMFWT tension moored floating wind turbines.

UCC University College Cork.

VAWT Vertical Axis Wind Turbine.

WEC wave energy convertor.

WT wind turbine.

Declaration

I the author declare that this thesis, submitted for the degree of Doctor of Philosophy in the School of Engineering, is the author's own work and has not been submitted for another degree, either at University College Cork or elsewhere. All external references and sources are clearly acknowledged and identified within the contents. I have read and understood the regulations of University College Cork concerning plagiarism and intellectual property.

_____

Christopher Wright

Abstract

In order to harness the extensive offshore wind resource, both in Ireland and in many parts of the world with deep offshore seas, the deployment of wind turbines on floating structures is required. Tension moored floating wind turbines are one type of platform with potential to be used for such deployments. These highly constrained platforms offer many benefits but also unique challenges compared against other platform stability types.

This thesis investigated the use of such platforms through a combination of numerical simulations and experimental wave basin tank testing. Design improvements in an existing platform, HEXWIND, are identified, leading to the design of a novel platform, TWind. As tension moored platforms are highly constrained in heave, pitch and roll motions, a significant coupling and design complexity is introduced between the wind turbines flexible tower and the pitch/roll motions. The effect of this tower flexibility is parametrised in this work.

As tension moored platforms rely on the tendon pretension for stability, operations such as installation and maintenance towing without tendons are statically unstable. Additional float for tow stability are designed and analysed in this work. These floats are designed to become wave energy converters once the platform is installed on site. The structural dynamic and hydrodynamic interaction effects of including these WEC are analysed in detail. Novel survival modes for the WEC floats are proposed. Design considerations related to potential tendon anchor misplacement are also analysed.

A platform parameter study has led to a greater understanding of the design effects of modifying the floating concept dimensions. The addition of active WEC on the TMFWT is seen to significantly increase the platform forces and dynamics, with the tower root bending moment doubling compared to the standalone TMFWT.

With 100's of GW's of proposed floating offshore wind capacity to be developed this century, the results from this thesis help improve the state of the art in tension moored floating wind design, installation and survivability.

Acknowledgements

This thesis is dedicated to my parents for their endless love, support and encouragement.

I would also like to acknowledge the kind and helpful guidance of my two supervisors Dr. Jimmy Murphy and Dr. Vikram Pakarashi, the support and camaraderie of my colleagues and friends at MAREI: Matthew Shanley, Pierre Benreguig, Nico Tomey Bozo, Phelim Larkin, the knowledgeable and hard working staff at the LIR NOTF; Tom Walsh, Niall O'Sullivan and Christian van Der Boch who helped greatly with the experimental test campaigns. amongst many others in the MaREI centre.

I would also like to acknowledge the Marine and Renewable Energy Ireland (MaREI), a Science Foundation Ireland (SFI) supported project, grant no. 12/RC/2302 who partly funded this research. The testing at IFREMER was funded by MARINET, a European Community research infrastructure initiative which funds periods of access to marine renewables test facilities.

List of Publications

First Author

[1] Christopher Wright, Keith O'Sullivan, Jimmy Murphy, and Vikram Pakrashi. Experimental comparison of dynamic responses of a tension moored floating wind turbine platform with and without spring dampers. In *Journal of Physics: Conference Series*, volume 628, page 012056. IOP Publishing, 2015.

[2] Christopher Wright, Vikram Pakrashi, and Jimmy Murphy. The dynamic effects of marine growth on a floating tension moored wind turbine. In *Progress in Renewable Energies Offshore. G. Guedes Soares. Proceedings of RENEW 2016, 2nd International Conference on Renewable Energies Offshore, Lisbon, Portugal*, number 1. CRC Press, 2016.

[3] Christopher Wright, Vikram Pakrashi, and Jimmy Murphy. Dynamic effects of anchor positional tolerance on tension moored floating wind turbine. In *Journal of Physics: Conference Series*, volume 753, page 092019. IOP Publishing, 2016.

[4] Christopher Wright, Vikram Pakrashi, and Jimmy Murphy. Modelling of a combined tension moored wind and wave energy convertor system. In *12th European Wave and Tidal Energy Conference (EWTEC 2017)*, volume 2017, pages 1–10, 2017.

Co-author

[1] Vesna Jaksic, Christopher Wright, Jimmy Murphy, Afeef Chanayil, Shaikh Faruque Ali, DP Mandic, and Vikram Pakrashi. Dynamic response mitigation of floating wind turbine platforms using tuned liquid column dampers. *Phil. Trans. R. Soc. A*, 373(2035):20140079, 2015.

[2] Vesna Jaksic, Christopher Wright, Afeef Chanayil, Shaikh Faruque Ali, Jimmy Murphy, and Vikram Pakrashi. Performance of a single liquid column damper for the control of dynamic responses of a tension leg platform. In *Journal of Physics: Conference Series*, volume 628, page 012058. IOP Publishing, 2015.

[3] Vesna Jaksic, Christopher Wright, DP Mandic, Jimmy Murphy, and Vikram Pakrashi. A delay vector variance based marker for an output-only assessment of structural changes in tension leg platforms. In *Journal of Physics: Conference Series*, volume 628, page 012059. IOP Publishing, 2015.

[4] Mathew Shanley, Christopher Wright, Cian Desmond, Aldert Otter, and Jimmy Murphy. Access to a floating wind turbine. In *Design and Construction of Wind Farm Support Vessels, London, UK*, number 1. Royal Institution of Naval Architects, 2017.

Chapter 1

Introduction

1.1 Floating Offshore Wind Turbines

The global installed capacity of offshore wind currently stands at 35.3 GW [1], mostly on fixed bottom foundations with less than 200 MW on floating foundations [2]. These floating projects are pre-commercial demonstration units mainly on two platform technology types, the semi-submersible Windfloat Atlantic and Kincardine(75 MW, on eight units) and the spar HyWind Scotland (30 MW, five units), with the remainder made up of single deployments by various developers. These are early days for the floating wind industry as pre-commercial scale deployments are planned for the coming years. Floating wind turbines have the potential to meet the world's total electricity demand 11 times over by 2040 [3]. A consensus has still not been established over which platform technology or even platform technology type is most optimised for deployment. Platform types are categorised by how the primary stability is achieved. Tension moored platforms are stabilised through a combination of excess buoyancy in the hull and taut mooring lines providing a high stiffness restoring force. Single point anchor reservoir (SPAR) platforms are stable through a deep ballast counterweight barge platforms are stable through a waterline area righting moment and semi-submersibles are stable through a combination of waterline area and ballast. In this thesis research will concentrate on tension moored floating wind turbines (TMFWT).

1.2 Tension Moored Floating Offshore Wind Turbines

Tension moored floating wind turbines (also known as tension moored platform wind turbines) have numerous advantages over SPAR and semi-submersible, for example, lower tower bending moments, lower rotor nacelle assembly (RNA) accelerations, lower hull mass, lower station keeping footprint, less likely to suffer from cascading failures. They also have some disadvantages, for example, not being stable without mooring lines (making tow to site costly), expensive mooring and anchor systems.

1.3 Research Outline

In Chapter 2 an in depth literature review of floating offshore wind turbines is presented. The literature review begins with an overview of the history of offshore fixed wind, current technologies for floating wind, a detailed review of the state of the art in physical and numerical modelling of such and opportunities for synergies between wind and wave energy platforms. Current challenges to the deployment of floating offshore wind turbines (FOWTs) are then summarized, this summary guides the research carried out in the course of this PhD and subsequent chapters progress from here.

In Chapter 3 the numerical modelling framework used in the course of this work is presented. Crucial to confidence in numerical modelling results, convergence studies on definable elements are presented. These convergence studies include potential flow theory mesh elements size, finite element mooring segment size, viscous drag element element size, flexible tower element size. The numerical modelling approach used is the hybrid combination of time domain potential flow theory and Morison equation viscous flow elements. An existing floating wind turbine (FWT) design from MaREI (HMRC), the HEXWIND tension moored FWT platform is used for validation purposes. The required model fidelity is described, including the use of second order wave force models. These modelling techniques are then used with confidence in subsequent chapters.

In Chapter 4 the design procedure of a TMFWT, named TLPWind, is presented in detail. The design conditions for potential sites off the South and West coast of Ireland are presented and then used in the subsequent design work. For tension moored plat-

forms high mooring stiffness, the flexible tower presents challenges to the designer, these challenges are presented and a novel solution of shortening the flexible mono structure of the tower by adding diagonal braces is introduced. Parameterised results of modelling the tower as rigid or flexible is presented in order to aid future designers. A detailed parameter study on the hydrodynamic elements is then given. As TMFWTs are not hydrostatically stable without their mooring lines, the design of temporary additional buoyancy elements allowing stability for transit conditions is carried out.

In Chapter 5 the design of a combined wind and wave energy convertor (WEC) system is described. The design of a single WEC is introduced before the detailed design of the combined system is considered. The four temporary buoyancy modules proposed in Chapter 4 are used as the floats for a point absorbing WEC system, while the FWT platform is the "stationary" reference body. As WECs suffer from large motions and loads in above rated severe sea-states, a novel survivability mode is proposed, which includes a combined ballast, submergence, rotation and locking operation. The importance of hydrodynamic coupling between the 5 floating bodies (The FWT and 4 WEC floats) is shown. A Physical model of the TLPWind (from Chapter 4) and the combined wind and wave energy converter (TWindWave) is used as a validation step.

In Chapter 6 the TMFWT's anchor positional sensitivity is studied. tension moored platform (TLP) tendons and anchors are designed and modelled as exactly vertical in-line components. This work investigates how varying anchor misposition tolerances will affect the stability, dynamic motions and line tensions of a TMFWT.

In Chapter 7 the final conclusions, recommendations, limitations and potential future work are summarized.

1.4 Goals

1. Develop and validate by physical tank testing, numerical modelling techniques for floating wind turbines.

2. Present the design conditions for a number of potential FWT sites on the West and South coasts of Ireland.

3. Design a tension moored floating wind turbine which is self-stable for tow to site and has the potential to convert both wind and wave energy into electricity.

4. Present the design decisions to aid future designers, this includes a large parameter study on the floating platform geometry.

5. Evaluate and quantify design uncertainties related to TMFWT.

1.5 Credit statement

On recommendations of the examiners a credit statement has been added here. The author has carried out all writing, simulation set up, running, post processing and analysis, experimental test campaign scheduling, experiment running, post processing and analysis. The TWind and TWindWave scale models were designed and fabricated by the author, with the exception of the aluminium sections, which the author managed the procurement off from an external supplier. Additional fabrication support came from the LIR NOTF mechanical laboratory team. For the TWind and TWindWave the author carried out pre model wave, wave gauge and load cell calibration with the exception of the air dampers which were calibrated by LIR NOTF support staff. The TWind and TWindWave concepts in all configurations were solely conceived by the author. Coupling of NEMOH and OpenFast has been coded by the author.

Chapter 2

Literature Review

2.1 Floating Offshore Wind Energy Review

In 1972 Professor William E. Heronemus [4] proposed the use of large scale offshore floating wind turbines to overcome the negatives of onshore wind turbines; these being unsightly, and consuming valuable agricultural and urban development land. Musial [5] gave a general technical description of several types of floating platforms that would be suitable for FWT's. In 1998 Tong [6] designed a SPAR buoy with heave plate, moored by 6 catenary chain lines, to support a 1.5 MW wind turbine (WT). Since these early days the research literature in the field of floating wind turbines has grown dramatically, a search for the terms floating wind turbines on ScieneDirect produces over 5,300 results, with almost half of these published in the last 5 years alone. The publication rate per year in this field is shown in Figure 2.1[7].

A report from ORE Catapult [8] in 2015 outlined the main challenges for FWTs as follows:

- To develop turbine designs specifically for use on floating structures, rather than using WT's adapted from fixed structures
- Fully optimising support structures for FWT's
- Cost of anchors and their installation is high, thus an investigation in to innovative anchor systems is required

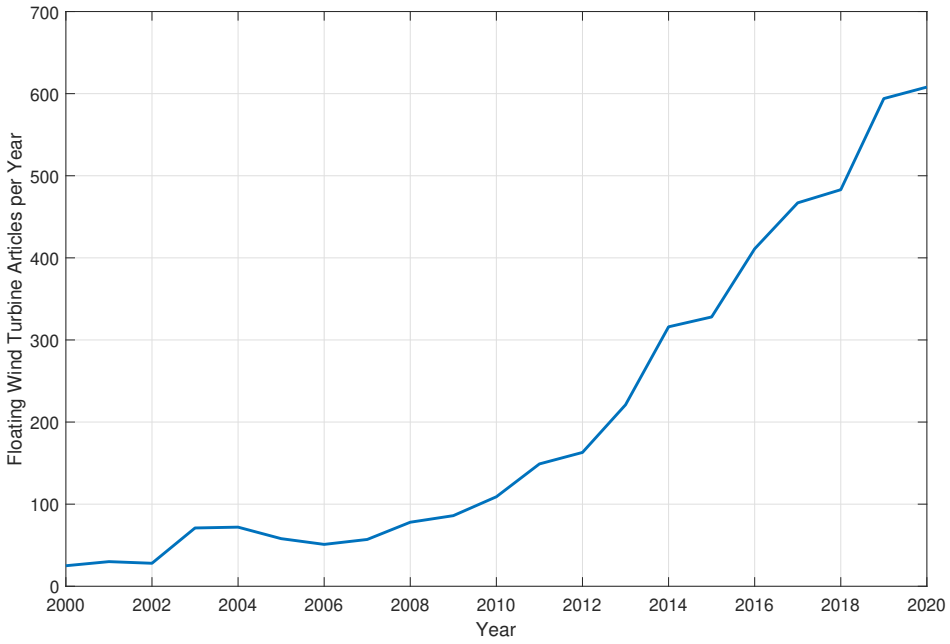


Figure 2.1: Search for Articles with keywords Floating Wind Turbine on Sciendirect

- Lack of experience with dynamic power cables leading to conservative design
- Lack of consensus on best approach to installation, e.g. use of special purpose or multi-purpose vessels
- Distance from shore and harsh environmental conditions limit availability for inspection and maintenance

Matha [9] compares the industrial design methodologies for fixed and floating WT's. The substructure design process for FWT's is not yet at a level of industrialization comparable to fixed-bottom substructure design methodologies, where standardized design and realization procedures are well established throughout the industry. Strach [10] gives recommendations for future research areas for FWT's. Castro [11] developed a methodology to determine the economic feasibility of a floating offshore wind farm. A FWT's life-cycle is divided into five components: concept and definition, design and development, manufacturing, installation, exploitation and dismantling. The FWT farm is subdivided into five components: offshore wind turbine, floating platform, mooring, anchoring and electric system. The methodology has been used to analyse an offshore

location: the Galician region (North-West of Spain). Results indicate that the best economic area in the Galician region is the area located from the Ría de Pontevedra to the Ría de Ribadeo. In addition, comparing the three floating offshore wind platforms, the semi-submersible platform and the SPAR platform are the best options in economic terms for this location.

2.1.1 Irish FWT potential

Ireland's Offshore Renewable Energy Development Plan (OREDP) was published in 2014 and sets the total development potential for Offshore Renewable Energy (ORE). Wave energy in shallow water depths of 10 to 100 m has the potential for an installed capacity of 12.5 to 13.6 GW, while the equivalent in deep water depths of 100 to 200 m is 15 to 17.5 GW. Fixed and floating offshore wind has the potential of 9.8 to 12.5 GW and 25 to 27 GW respectively. Accoriding to Henderson [12], Irish waters have a greater potential for 40 GW of FWT and are predominately suited for TLP and semi-submersible platforms because of water depths in the 50 to 300 m region.

2.2 Proposed Floating Concepts

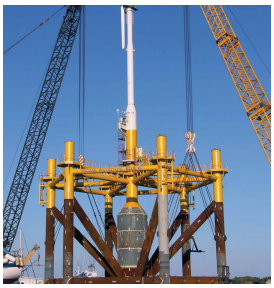
There has been a great number of FWT concepts proposed and designed by both industry and research. A methodology to classify FWT depending on its stability method is commonly used [13]. These classifications are defined according to how each platform type achieves stability. The three categories are ballast, mooring line or buoyancy stabilised. This section examines proposed tension stabilised floating wind concepts.

2.2.1 Tension Moored Platform

A review of some of the TLPWT concepts developed by industry or academia are given here.

BlueH [12], a multi-national group of companies based in the Netherlands, have developed a TLP concept consisting of a larger structure with multiple surface piercing members, with the potential advantage of improved stability, including in damaged con-

ditions, but at the detriment of greater structural size and cost. An off grid prototype with an inactive turbine for visualisation purposes was installed 21 km off Brindisi, Italy in 100 m waters during 2007/8



(a) Blue H deployed 2007



(b) New Blue H

Figure 2.2: Evolution of the Blue H TLP

A TLP platform has been developed in collaboration between MIT and NREL (See Figure 2.3). It originated from Tracy's "Parametric Design of Floating Wind Turbines" work[14]. On a re-analysis of this platform, significant deviations in motions where found. This was attributed to a miscalculation of the platform's mass matrix. A redesign of the platform spoke length was undertaken by Matha [15]

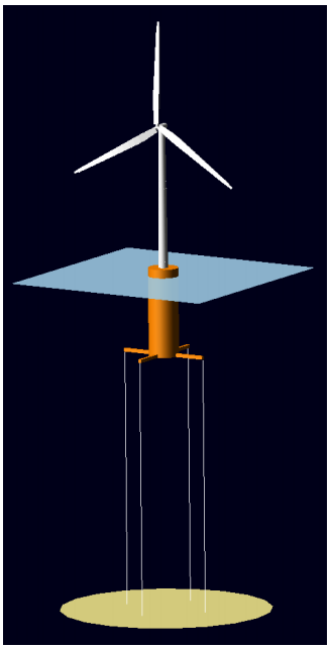
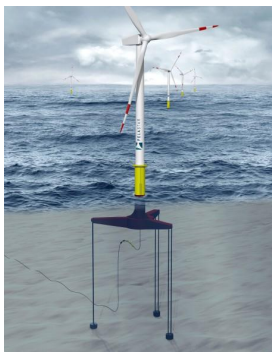


Figure 2.3: MIT/NREL TLP

PelaStar is a tension moored floating wind turbine platform conceived by Glosten engineers in 2006 (See Figure 2.4). It is composed of a narrow central cylinder extending below the tower, at the base of which a larger diameter cylinder with radial spokes is situated. Tendons are located on the extremities of the spoke legs. Like many designs It has gone through a number of design iterations since it was first publicised. It has grown from three to five spoke legs, the number of moorings on each reducing from two to one. Due to a cost of energy report [16] it is one of the few commercial floating wind platforms with detailed information publicly available.



(a) Three Leg PelaStar



(b) Five Leg PelaStar

Figure 2.4: Evolution of the PelaStar TLP

WindStar is a tension moored floating wind turbine platform proposed by Zhao et al, [17] (See Figure 2.5). from State Key Laboratory of Ocean Engineering, Shanghai Jiao Tong University in 2012. It is composed of one central column, with three radiating corner columns and pontoons. The pontoons protrude beyond the end of the columns to were the tendon moorings are located. Three tendons are located at the extremities of each pontoon. It is designed to be towed to site, stabilised by additional temporary

buoyancy units added to the outer columns.

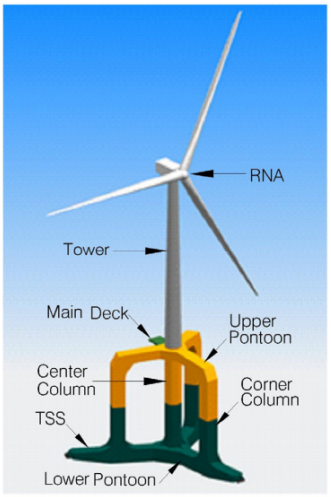


Figure 2.5: WindStar TLP

Casale et al. [18] analysed 3, 5 and 6 legged tension moored platforms in 2010 and decided that the 6 legged version, named EsaFloater was the most favourable design (See Figure 2.6). It is designed to accommodate a 6 MW WT in a water depth of 200 m.



Figure 2.6: EsaFloater

Researchers in the Hydraulics & Maritime Research Centre (HMRC) in University College Cork (UCC), took the 6 legged version of the EsaFloater above and redesigned the complete assembly to be self stable for tow to site and to be deployed at a reduced water depth of 150 m. Significant buoyancy is moved from the horizontal pontoons to the vertical columns. This platform was unpublished at the beginning of this thesis.

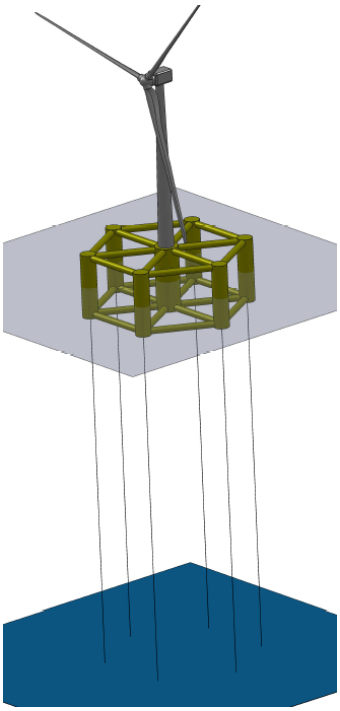


Figure 2.7: HEXWIND

In 2010 Andrew Henderson et al. [19] proposed a three legged braceless TLP for German waters(See Figure 2.8). It was argued that TLP structures are most suitable for the relatively shallow German water depths of approximately 50 m as this is too shallow for SPAR platforms and semi-submersible platform catenary moorings becoming too complex. This platform is designed to support the NREL 5 MW reference turbine.



Figure 2.8: GL Garrad Hassan TLP

Iberdrola have developed a tension moored floating wind turbine platform called

TLPWIND (See Figure 2.9). It is designed for a 5 MW WT and is composed of four legs, each with two mooring tendons. This is a redundant system allowing one line of each leg to break. It has been successfully tested in maximum wave heights of 31 m. As this platform is not self-stable for the tow and installation phase a semi-submersible barge has also been designed by Iberdrola for this purpose [20].



Figure 2.9: Iberdrola's TLPWIND

GICON - TLP is, like the name suggests, a tension moored floating wind turbine platform conceived by the GICON group in 2009 [21]. It has shown some of the most extreme design changes since first publicised(See Figure 2.10). Starting as a three legged truss structure and evolving to a four legged braceless structure.

IFPEN in collaboration with SBM Offshore [22] has designed a three legged inclined tension moored FWT (See Figure 2.11). Due to the inclined tendons the primary motion of this platform is not, as is typical for TLP's, surge, it is instead a pitch about a point just below the RNA.

Henrik Stiesdal has designed a three legged tension moored WT(See Figure 2.12). This design offers a number of innovative solutions, firstly the fact that it is an open-source design, meaning all information on design is freely shared. Secondly its buoyancy

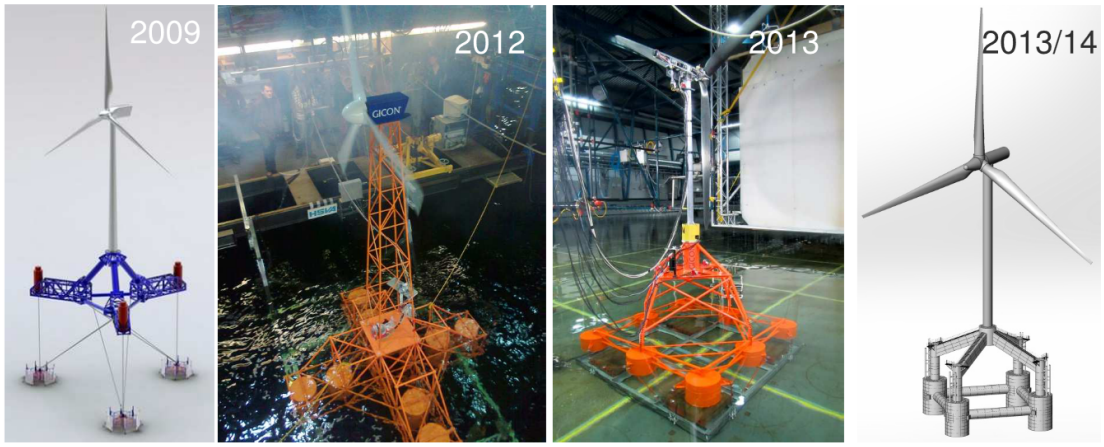


Figure 2.10: Design History of GICON - TLP



Figure 2.11: SBM Offshore Inclined TLP

system is comprised of multiple modular small buoyancy tanks rather than single large buoyancy units as is generally the case. It is designed for a 7 MW generic turbine. DBD Systems LLC have designed a concrete cylindrical TLP foundation [23] for supporting 6-7 MW WT's in water depths greater than 100 m. The concrete is pored using the "slip form" construction method. Tendons are connected to a gravity base.

In 2012, Bachynski and Moan proposed 5 TLP designs(See Figure 2.14). In the conclusions, platform numbers 3 and 4 where noted to be the most promising of these concepts.



Figure 2.12: Stiesdal TLP

2.2.2 Hybrid Platform Types

In order to lower the costs of FWT, new floater concepts have been proposed. One such concept, TetraSpar [25], involves suspending a keel structure below a floating structure which supports the tower and RNA. The keel structure is restrained by 6 lines, preventing any relative motion between the two bodies and providing low COG stability characteristics similar to a SPAR platform. the main benefit over a typical SPAR FWT are the low draft possible in transit, where the submerged keel is raised to just under the main floating body. The overall station keeping is provided by 3 catenary lines.

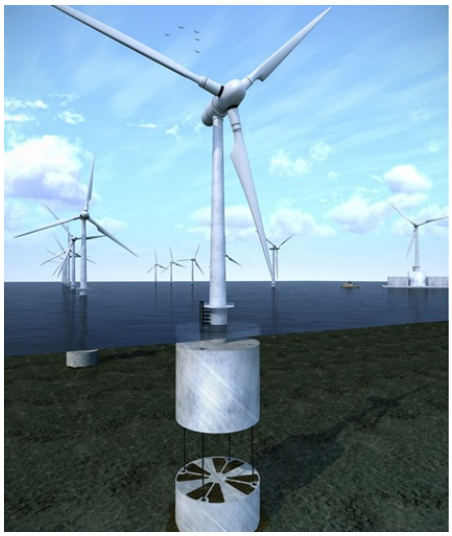


Figure 2.13: ECO TLP

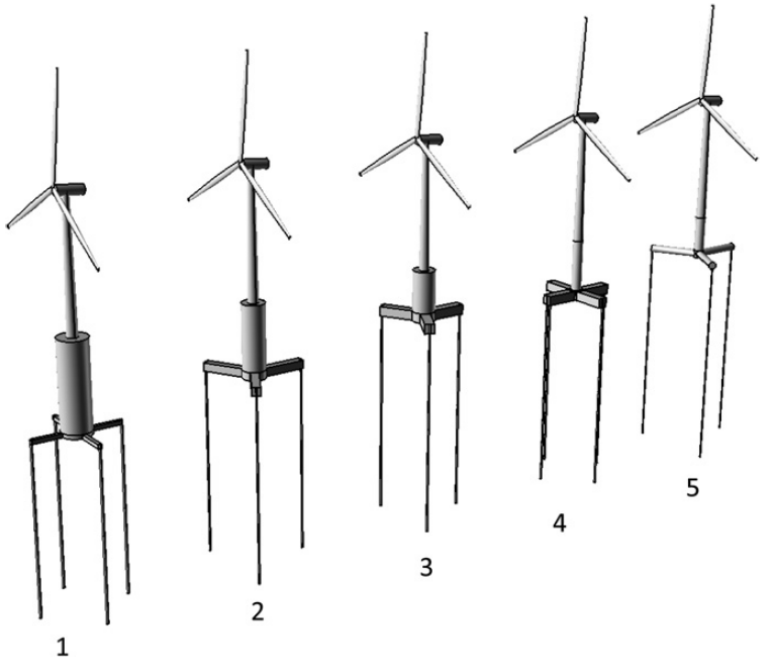


Figure 2.14: Bachynski and Moan TLPWT

2.3 Combined Wind and Wave Energy Review

Combining wind and wave energy technologies has been studied as a way to achieve more reliable and higher capacity energy production. Combined wind and wave energy farms have the ability to reduce downtime and power variability by of up to 87 % and 6 % respectively, the combination of wave and offshore wind is more effective in reducing downtime and variability at sites where both resources are only weakly correlated [28]. Co-located farms are thus an opportunity to increase the power production from renewables in a cost-competitive way.

Combined wind and wave energy may be either co-located using separate technologies or combined into a single technology.

2.3.1 Co-location

Fusco et al. [29] presents a methodology to assess the possible benefits of the combination of wind energy with wave energy for Irish sites. The two resources are significantly uncorrelated and thus the integration of wind and waves in combined farms, at these locations, allows the achievement of a more reliable, less variable and more predictable electrical power production. The resulting benefits are particularly clear in the case of a relatively small and quite isolated electrical system such as the Irish one. Here, in fact, high levels of wind penetration strongly increase the requirement of surplus capacity and cause a much lower efficiency for conventional thermal plants. Cradden [30] assessed the benefits of combining wind and wave energy harvesting for three European marine energy test sites. It was demonstrated that wave and wind power show medium to high correlation at each of the three sites, with evidence that the wave time series lags the wind by between 1 and 5 hours. Chozas [31] analysed the benefits of combining wind and wave power output for day ahead power markets. It has been demonstrated that combined power productions are more predictable than when wind and wave technologies are working individually, and hence, balancing costs reduce. Azzellino [32] used a marine spatial planning approach to investigate the co-location of wind and wave energy farms. Two key benefits were identified as follows, the variability of the produced power can be decreased,

and the power availability can be increased. The greater the correlation of the wind and wave resource the less benefit there is. Perez [33] reviewed the methods of combining wind and wave energy power in a single farm. The existence of an abundant combined resource together with the strong synergies existing between both technologies makes a compelling argument for combining wave and offshore wind energy to achieve a sustainable and rational exploitation of the offshore energy resources. However, fundamental research is highlighted as crucial to test the validly, sustainability and integration of these combined systems; and to determining to what extent these new or adapted WECs are suitable to be combined with current offshore wind farms. Zanuttigh [34] presents a methodology for multi-criteria design of multi-use offshore platforms (MUP) for marine renewable energy harvesting. The methodology consists of four steps: a pre-screening phase, to assess the feasibility of different maritime uses at the site; a preliminary design of the alternative schemes based on the identified maritime uses; a ranking phase, where the performance of the MUPs is scored by means of expert judgement of the selected criteria; a preliminary design of the selected MUP selected. An example application of this procedure to a site offshore the Western Sardinia coast, Mediterranean Sea, Italy, is provided. In this site the deployment of a MUP consisting of wave energy converters, offshore wind turbines and aquaculture is specifically investigated.

2.3.2 Combined Platform

2.3.2.1 Fixed Platform

Baudry [35] assessed the power production of a torus shaped PA WEC reacting against a monopile WT foundation. Latching control was found to significantly increase the power production by an amplification factor of 2.5. Pakrashi [36] studied the structural changes required to add a PA (Point-absorber) to a monopile offshore wind turbine (OWT). The addition of a point absorber to a monopile foundation results in a significant increase in structural loading that is dependent on water depth and site conditions. A significantly larger monopile is required to resist the environmental conditions on the west coast site than on the east. Independent of location, there is an increase in steel tonnage for design

when a point absorber is combined with the turbine.

2.3.2.2 Floating Platform

Floating Power Plant [37] is a 37 meter wide off-shore test combined wind and wave energy platform. It has 140 kW of wave energy and three 11 kW WT's, an image of it deployed can be seen in Figure 2.15. It is the only combined wind and wave energy converter to have sea trials.

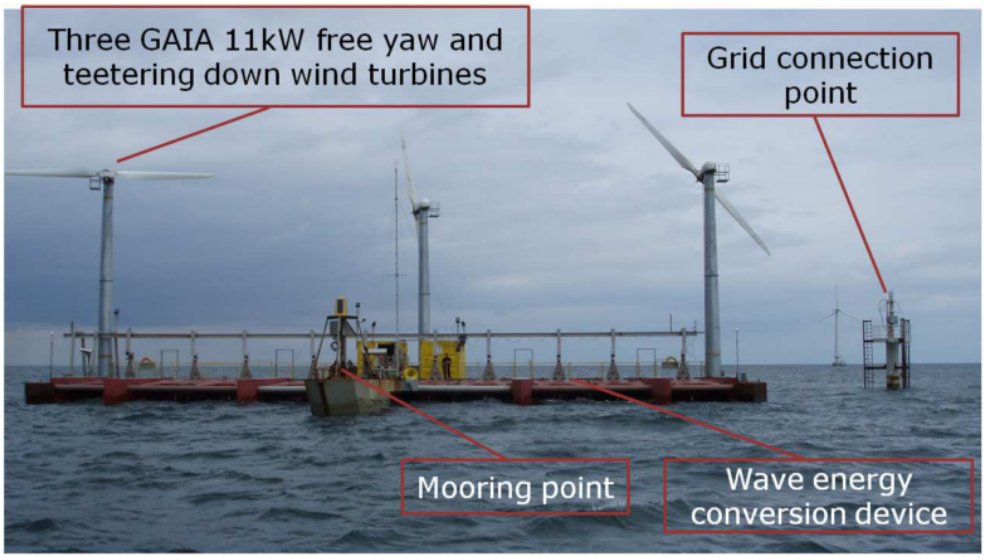


Figure 2.15: FPP Poisdon

WindFloat has been modelled numerically and physically supporting a number of different WEC technology types. These being 1) A spherical point absorber installed in the center of the WindFloat platform [38]. 2) Two oscillating water column (OWC) mounted on the platform columns [39]. 3) Three pitching flaps mounted on the platform braces [40]. Firstly analysing the pitching flap type WECs. A 1:78.5 scaled model was tested at the UC Berkeley Richmond Field Station ship testing facility. The combined system (WindWaveFloat) was numerically modelled using OracFlex. Simulation results indicated that the numerical models presented herein are also only valid for wave heights below H=6m and for a given geometry, after being validated with the supporting wave tank data. The surge motion of the WindWindFloat is marginally lower than the Wind-Float alone around the flap pitch natural period. The heave and pitch motions of the

WindWindFloat also tend to decline slightly (mostly around the flap natural period), but the numerical model results do not reflect that decline very accurately.

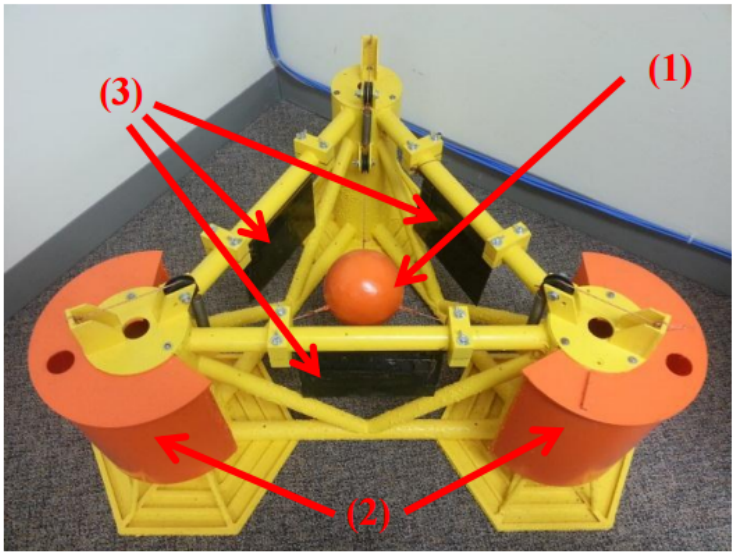


Figure 2.16: WindFloat WECs

O'Sullivan [41] studied the feasibility of combined wind and wave energy converters, highlighting the difficulties in designing such complex systems. Issues with O&M accessibility to the RNA were identified due to large numbers of motion induced interruptions.

Karimirad [42] studied a combined SPAR and pitching PA. The SPAR was inspired by the HyWind device and was designed to support a 5 MW WT. The pitching PA inspired by Wavestar was placed 20 m from the SPAR. The SIMO-RIFLEX coupled code was used to analyse the concepts power production. Results show the total displacement of the WEC buoy is just 2.2% of the total displacement of the FWT. However, it will be shown that the added power production is more than 6%. The hydrodynamic interaction between SPAR and WEC buoy is neglected in the present work. This means that the diffraction/radiation problem is solved separately for each body. This should be reasonable assumption for investigating the feasibility of combining the wind and wave energy devices.

Borg [43] proposed the idea of a combined wind and wave energy platform system. The WEC's in this system had the shared goal of reducing platform motions and generating power.

Michailides [44],[45] and Luan [46] analysed a combined system composed of three flap type WEC's on a braceless semi-submersible WT. Modelling and analysis in the time-domain of the combined concept in stochastic wind and wave environment are carried out using the coupled tool Simo/Riflex/AeroDyn. Results show the following: The natural periods of the semi-submersible platform are not much influenced by introducing the rotating flaps. The introduction of the rotating flaps results in a max increase of: (a) 5.4% of the mooring line tensions, (b) 5.6% of the tower's bending moment and (c) 0.8% of the blade's bending moment. The introduction of the rotating flaps doesn't affect the produced wind power. The total produced power is increased by 1% to 8% for the examined environmental conditions.

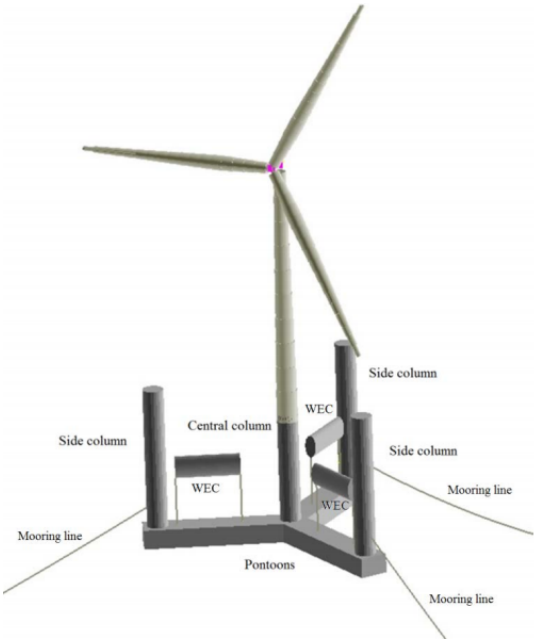


Figure 2.17: SFC

The SPAR Torus Combination (STC) concept combines a SPAR floating wind turbine and a torus-shaped heaving-body WEC [47]. Ren [48] analysed the long-term fatigue damage prediction of the mooring lines and the annual energy production estimation. Simulations using coupled analysis of wind-wave induced long-term stochastic responses has been performed using the SIMO-TDHMILL code in the time domain. Results show the annual wind power plays a dominant role in the total power production of the STC system, and exhibits smaller differences among 20 random seed results than those for

annual wave power. The annual wind power production of the floating SPAR system is slightly larger than that of the fixed bottom system. The annual fatigue damage of two selected type of mooring lines under 20 random seed conditions have been estimated and compared with each other. The estimations of annual fatigue damage among different random seeds are significantly different, and the annual fatigue damage of the Stud-chain mooring line is much larger than that of six strand wire rope mooring line. Considering that the annual fatigue damage of the Stud-chain is too large to be acceptable for practical projects, the Six-strand-wire-rope type mooring line is recommended for this selected site condition. Muliawan [49] numerically analysed the STC in operational and survival mode using the coupled SIMO/TDHMILL in the time domain. Simulations show the extreme responses are primarily governed by the wave induced response because during such extreme conditions, the wave force acting on the system is significantly higher than the aerodynamic force. It is because the thrust force on the turbine is small after the cut-out speed. Wan [50] performed experiments on the STC in survival mode with a scale factor of 1:50 in the towing tank of MARINTEK, Norway. Two survival modes were analysed; locking the WEC to the SPAR both at the mean surface elevation and in a submerged position. In the submerged position the motion and forces between SPAR and torus are decreased. Both Matheiu instability and slamming occurred for the mean surface elevation configuration.

The STC can also be used to reduce sway instabilities [51]. Results demonstrated that the buoy stabilises/reduces the pitch motion of wind turbine when its metacentric height is positive [52].

Bachynski [53] introduced a combined concept consisting of a single column TLP which supports a 5 MW WT and 3 point absorber WECs. Two variations of the WECs are considered: one that is constrained to purely heave motion relative to the TLP hull (Type A), and a hinged device which moves in coupled surge and pitch as well as heave (Type B). In operational conditions with aligned wind and waves, the combined concepts showed several benefits compared to the TLPWT: reduced surge and pitch motions, reduced tendon tension and tower base bending moment variation, and slightly reduced WT power variation. The combined concepts introduced increased yaw motion,

particularly for WEC type B, and the advantages were generally larger for TLPWT + WEC A. The base bending moment on the WEC guide, however, was significantly larger for TLPWT + WEC A compared to TLPWT + WEC B. In survival conditions, reductions in surge and yaw motions were observed, but significant increases in pitch motions and tendon tension variations were seen (compared to the TLPWT). WEC type A in survival mode 1 caused extreme tendon variations due to impact with the end stops. While the guide bending moment for WEC type A in survival mode 2 was similar to that of survival mode 1, locking the WEC to the lower end stop resulted in better overall combined platform performance. A more complex locking system (survival mode 3) would be best for either type of WEC. Wannon et al. [54] studied slamming and green water of this concept A combined TLP and torus type WEC is introduced and analysed [55] by Ren et al.

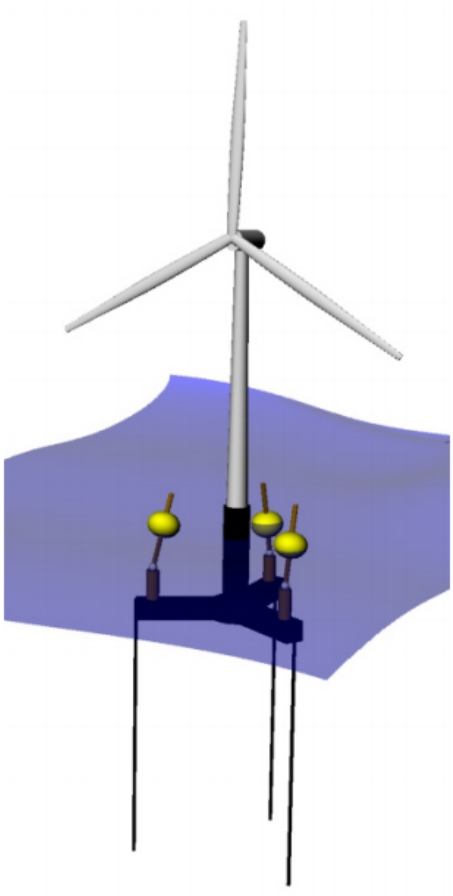


Figure 2.18: TLPWT with PA

Soulard [56] carried out a technical feasibility study for a hybrid ocean energy converter, with balanced wind and wave contributions. A 100 m diameter circular barge (C-HYP) equipped with floating oscillating wave surge converter (OWSC) supported a 5 MW WT.

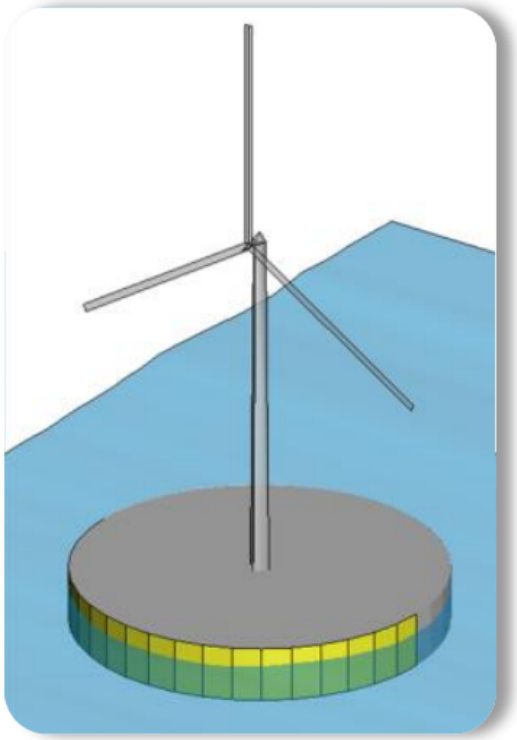


Figure 2.19: C-HYP

Soulard [57] proposed a 100 m large semi-submersible platform designed with five columns and equipped with floating pitching WECs supporting a 5 MW WT. A “Wave to Wire" model was used to compare the annual average absorbed power figures are compared with published results for existing ocean energy converters.

Iturrioz [58] design a combined wind and wave energy system composed of a semi-submersible concrete structure, supporting a 5 MW WT and three 1060 kW OWC WEC's. Physical experiments were carried out at 1:35 scale in the Cantabria Coastal and Ocean Basin. A numerical model has been developed by extending the potential flow solver Nemoh with the 3 generalized modes representing the OWCs. The physical modelling was used to tune the friction coefficient of the OWC power take off (PTO). A fully coupled model was proposed as the next step.



Figure 2.20: T-HYP

Mazarakos [59] design a combined wind and wave energy system composed of a TLP structure, supporting a 5 MW WT and three OWC WEC's. A fully coupled numerical model is outlined which operates in the frequency domain. The aerodynamic loading is calculated using Blade Element Momentum theory. Results show a surprising decrease in tendon tension for increasing wind speed and as such have been deemed untrustworthy by the current author.

Fenu et al [60] models a combined floating wind turbine and gyroscopic wave energy converter. Hull pitch motions could be reduced by up to 37%, nacelle accelerations by 10% and power production improved by 120% (in low wind speed regions) by using the gyroscopic system. Castro [61] gives a methodology to access the life cycle cost of combined floating wind and wave energy systems.



Figure 2.21: Iturrioz OWC WT

2.4 Modelling Techniques and Issues

2.4.1 Potential Flow Theory Boundary Element Methods

Linear potential flow theory is used to calculate the wave potential from the incident, diffracted, and radiated waves that effect a floating structure. The Laplace equation is applied through boundary conditions. This theory assumes that the flow is irrotional and non-viscous. A boundary element method (BEM) code is used to solve for the forces on a floating body. Bavsic [62] compared the added mass calculated through an analytical method and a BEM. The comparison for both a horizontal cylinder and a tanker vessel were shown to achieve a good agreement. Advantages for BEM were cited as avoiding uncertainties in choosing flow factors for analytical methods, while disadvantages were centred on the relatively high computational cost.

Geng [63] analyses a Truss SPAR platform using a pure BEM and BEM with an

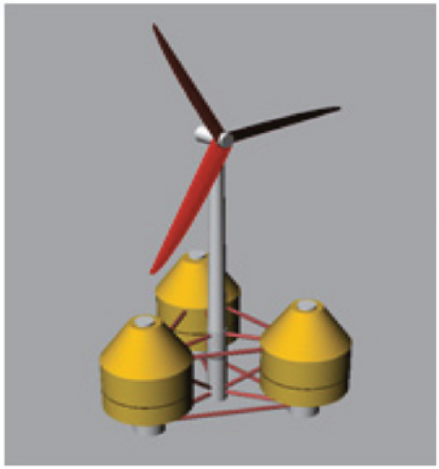


Figure 2.22: Iturrioz OWC WT

additional linearised viscous damping term. For Truss SPAR platform regarded as a rigid body in motion, its external viscous damping is the main source of damping, whose value can be approximated using the velocity force formula. When the viscous damping between the structure and water is considered, the motion produced by natural vibration can be counteracted by viscous damping, and there is only the periodic vibration left under incident wave frequency. Thus, the first-order motion response can be more intuitively represented, and the interference of natural vibration is avoided, which are very important in numerical calculation. In addition, by analysing of motion curve without damping, the natural period of different motion directions can be obtained approximately.

Sow presented two methods to overcome the lack of viscous damping in modelling floating bodies using BEM, firstly using a viscous damping correction [64] and secondly using linearised drag only Morison equation elements [65]. Results of both are compared to experimental testing at the Universiti Teknologi Malaysia towing tank. Both methods are closer to the experimental results than the BEM alone. The Morison equation method shows closer correlation while the viscous damping correction method tends to over/under predict depending on wave frequency.

Chan [66] extended the use of BEM to include calculation of the instantaneous wetted surface on the MIT/NREL tension-leg platform. The time-domain Green function is used to solve the linear and non-linear free-surface problems. A good agreement was found for the linear and second-order surge diffraction force calculated using this method and

FAST's HydroDyn module.

2.4.2 Hydrodynamic Structural Coupling/ Hydroelasticity

Borg [67] compared the traditional rigid body assumption of a FWT platform with that of a more realistic flexible body. HAWC2 was coupled to WAMIT and used to model a floating SPAR supporting the DTU 10 MW Reference Wind Turbine. The generalised modes approach was used in WAMIT. It was found that the flexible mode is significantly excited in an extreme event, indicating an increase in predicted substructure internal loads.

Luan [69] developed a time domain model in Simo/Riflex/Aerodyn that can accurately predict the structural loads on the hull of a FWT, by modelling the hull as a finite element model rather than one rigid body. Response are shown to be in good agreement with a reference model. In the operational conditions, considerable low-frequency components can be observed in the spectra of the obtained global forces and moments in the pontoons of the reference floating wind turbine. The results indicate that the low-frequency aerodynamic loads, the fluctuations of the hydrostatic pressure forces and the fluctuations of the gravity loads of floating wind turbines are important contributions to the structural responses, in particular, in the low-frequency range.

2.4.3 Vortex Method

Eliassen [70] proposed the use of cascade approach, combined with a 2D potential vortex method to analyse the AeroElastic behaviour of FWTs. Since it is a potential flow code it is limited to modelling attached flow, and dynamic stall is therefore not modelled. The aerodynamic loads at lower angles of attack are however well estimated, meaning results are limited to the range lower than the expected stall limit. Jeon [71] used a vortex lattice method to analyse the effect of a pitch motion. The unwanted aerodynamic turbulent wake state was shown to occur both when the floating wind turbine is operated at a low speed inflow condition and while the turbine is pitching into the wind. The convection of the tip vortex was seen to play an important role in governing of the behaviour of the rotor in a turbulent wake state. Manolas [72] compared simulations using BEM modelling

to those provided by the General Unsteady Vortex Particle (GENUVP) free-wake vortex aerodynamic modelling using the NREL 5 MW OC3 FWT. BEM aerodynamic modelling was found to provide higher loads and therefore is on the safe side.

2.4.4 Mooring Modelling Methods

Masciola [73][74] compared simulations of a O&G TLP platform using two tendon modelling techniques, either ideal massless spring or finite element approaches. Differences between the models are most apparent in directions sensitive to the longitudinal tether vibrations, which are the heave and roll/pitch degree of freedom (DOF). The two models show the most promise to agree when the cable dissipative capacity balances the internal energy. This, however, is often not the case. Frequently, one finds the longitudinal damping too small, and the transverse damping too large. Another crucial performance metric identified in the analysis is the buoyancy to tether stiffness ratio. This ratio must remain small for the two model to produce comparable results. Contrary to conventional wisdom, the platform mass-to-tether mass ratio does not explicitly appear as a one of the metrics. It was shown that as water depth becomes large, longitudinal vibrations become more noticeable because of frequency matching between roll/pitch and heave direction and the longitudinal tether vibration modes.

Senjanovic [75] described the use of linearised tendon modelling for TLP structures. Different methodologies were compared and the resulting motions compared. The surge response amplitude operator (RAO) was seen to be consistent no matter which method used, while the heave and pitch RAO's varied between methods. Senjanovic [76] expands on this work by analysing the fully non-linear restoring stiffness of TLP tendons. Comparison of numerical results determined for ISSC TLP with those of finite element method (FEM) analysis shows that the stiffness matrix formulation based on energy approach for large yaw is the most reliable.

Masciola [77] also compared the two mooring modelling techniques, either ideal massless spring or finite element approaches on the DeepCwind semi submersible NREL 5 MW WT. Numerical simulations were compared against a 1/50 scale Froude model tested at the MARIN wave basin facility. It was shown that the quasi-static mooring approxima-

tion can underestimate peak mooring line loads versus a model using a dynamic mooring line.

Qiao [78] estimated the damping that the mooring line of the ITI Energy Barge supporting the NREL 5 MW WT produces. The numerical estimation method is derived from the energy absorption by a mooring line resulting from the FWT motion. The numerical method is validated by a 1/80 scale model test. Simulations show that the non dimensional damping initially increases and then decreases with increasing non-dimensional pretension. The non-dimensional damping increases with increasing excitation amplitude. The peak non-dimensional damping of the horizontal motions is only approximately 10% that for the vertical motions. The mooring line damping in the wave frequency range should be considered in the vertical motion prediction of the platform. For small pretension, the non-dimensional damping increases with increasing non-dimensional pretension. For large pretension, the non-dimensional damping becomes less dependent on the non-dimensional pretension. The non-dimensional damping decreases for both the horizontal and vertical motions with increasing excitation period. When the non-dimensional period increases twice, the non-dimensional damping becomes approximately 1/4 of that for all non-dimensional pretensions. With increasing drag coefficient, the non-dimensional damping almost linearly increases.

Lin [79] modelled a non-linear taut mooring system for a taut moored FWT. It was seen that a linear spring model under estimates the mean position when the turbine is operating, but over estimates the amplitude of the platform response at low frequencies when the turbine has shut down.

Li [80] modified FAST to examine the response of a FOWT with polyester mooring lines. An enhanced stiffness model has been implemented to account for large elongations of the line in a taut moored platform. Comparison has been made against the linear spring method. Although the mooring system's static load-offset graph is linear, the linear spring method fails to consider the dynamic response of the mooring line. It under-predicts the motion of the floating body in the wave plus wind condition. This under prediction also affects the maximum mooring line tension, as its value is dependent on the instantaneous position of the floating platform.

2.4.5 Coupled Hydro Aero Elastic Simulations

2.4.5.1 Models & Model Validation

Wayman [81] analysed both the MIT/NREL Shallow Drafted Barge (SDB) and the MIT/NREL (TLP) using the fully coupled FAST software. The RAO for both combined systems demonstrate the effects of coupling the floating platform with a WT through the small, but nonzero response in yaw and sway. This is despite the fact that the excitation forces are only in the surge, heave and pitch direction.

Jonkman[82] compared three FAST models of the ITI energy barge with previous studies in the frequency domain. The first model had a rigid turbine, no control system, and a linearised form of the mooring system in surge and sway. For the second model, a quasi-static mooring system model was used. The third model had a fully flexible WT and variable-speed generator-torque and blade-pitch control systems. The rigid model was seen to match well with previous frequency domain results. The flexible nonlinear mooring model was seen to predict much greater roll and yaw displacements.

Bae [83] coupled the time domain hydrodynamic and mooring FEM software CHARM3D with FAST. The rotor-floater coupling effects for a 1.5 MW WT were seen to increase the standard deviations and maximum values of floater motions, accelerations and tether tensions. This effect was seen to increase as the tendon stiffness decreased, due to nearing of the pitch/roll and tower first bending moment frequencies.

Karimirad [84] compared the hydroelastic codes HAWC2 and USFOS/vpOne for a tension leg SPAR (TLS) supporting the NREL 5 MW WT. The analyses were limited to wave-induced responses. The code-to-code comparisons indicated that the motion and tension responses are in good agreement. A comparison of the use of a rigid and elastic formulation of the SPAR and the tower indicated that structural damping of the elastic body only slightly affects the general surge and pitch motion. However, the tension is not affected by this feature, except for the heave resonant response. This paper warned that although natural periods may be outside the wave spectrum, that non-linear hydrodynamic loading can excite the natural frequencies, which can be even worse for wind-induced motion because turbulent wind has significant energy around

these frequencies.

Zhang [85] studied the semi-submersible floating foundation of a 600 kW wind turbine in 60 m deep water considering the coupled load effects of wind turbine-tower- floating foundation and mooring lines and ocean environment. SESAM was modified to include WT thrust modelling. Wave periods which generate significant heave, roll and pitch motions were identified, which the platform should be redesigned to avoid. A WT operating limit of 4m was also identified. Wind load was identified as a significant load in the operational range.

Karimirad [86] used the fully coupled Simo-Riflex-AeroDyn codes to study the operational conditions of a braceless semi-submersible platform supporting NREL's 5 MW WT. The overall global motions of the platform, mooring line tension responses and wind turbine data show that the presented concept is suitable for offshore wind application in deep water.

Yu [87] studied the coupled dynamics of the OC3-Hywind platform using FAST. The gyroscopic effect of the rotor and the blade-pitch-controller-induced instability bring about a strong non-linearity for the system, as a consequence of which, the system responds to multiple excitation frequencies when under a regular wave condition. Meanwhile, the results of "effective RAO" indicate a coupling between the surge and the pitch of the platform. For the platform yaw motion, on the other hand, it shows excitations caused by the gyroscopic loading from the rotating rotor combined with the pitch motion. Since the wind and the wave are set to point along in x direction, a typical mooring line load shows a coincidence with the surge motion. From the results in the paper, it can be seen that the wind-induced loads mainly influence the low-frequency excitations including the resonance response in the surge and pitch natural frequencies but have little effect on the wave-frequency responses. Especially for the surge motion, the response amplitude is much larger under the wind wave conditions, which indicates that the surge motion is mainly stimulated by the wind loads. Meanwhile, the coupling of the surge and the pitch is also validated under the wind-wave conditions. The corresponding response of the system loads is a superposition of the mean value induced mainly by the wind and the fluctuation induced mainly by the wave. The result also indicates a noticeable

situation that if on the system acts a large force induced by external environmental conditions in X direction and a corresponding large drift displacement occurs, the mooring line 1 would have the risk of failure for being slack.

Karageorgopoulos [88] used FAST to compare the performance of two SPAR buoys supporting 5 MW WT. The SPARs were similar apart from varying drafts of 120 m and 100 m. There was no significant change to the operational capabilities of the platform with smaller draft, indicating that this is the better choice.

Driscoll [89] performed a validation of the FAST software against the full scale Hywind 2.3 MW demonstration FWT. The overall system performance and behaviour were validated for eight sets of field measurements that span a wide range of operating conditions. The simulated controller response accurately reproduced the measured blade pitch and power. The structural and blade loads and spectra of platform motion agree well with the measured data. Nygaard [90] gives the development, verification and validation of the fully coupled 3DFloat software.

Min [91] numerically models the OC3-HYWIND FWT using the coupled COUPLE-FAST. Results were compared to experiments conducted at the Deepwater Offshore Basin in Shanghai Jiao Tong University (SJTU) with a 1:50 Froude scale. COUPLE module calculates the potential wave loads on a moored floating structure by using either a diffraction wave theory or the Morison equation. The numerical model was calibrated carefully in the following aspects; mooring line stiffness, tower bending stiffness, added-mass and drag coefficients, moment of inertia and yaw stiffness and damping of the platform, etc. After the calibration, COUPLE-FAST reproduced the experimental system properties well. The free decay simulations showed good agreement with those of the experiment. Ten cases of different met-ocean conditions were considered in the simulations, including the wind loadings only, the wave loadings only, and the combined wind and wave loadings. Overall, the simulated dynamic responses in the wave frequency range were in satisfactory agreement with the corresponding measurements, which indicates wave loads were well predicted. For mean positions of the platform, however, the simulated results rendered smaller values than those of the experiments in the cases involving wind loads. We think these results are due to the fact that the simulated thrust

forces were significantly smaller than the measured thrust forces. To verify whether or not the large differences between predicted and measured mean positions are caused by the discrepancies between the simulated and measured thrust wind forces, alternative simulations were made by directly using the measured thrust forces as input, i.e. the FAST module was excluded in this approach. The simulated FOWT motions using this approach showed satisfactory agreement with the measurements.

Reference results of the OO-star concrete three legged semi-submersible platform using the DTU 10 MW Reference Wind Turbine and FAST are given here [92].

2.4.5.2 Required Model Fidelity

Wang [93] analysed the small angular displacement assumption used in the numerical modelling of FWT. In conventional ship dynamic analysis, superposition of the six degrees of freedom (surge, sway, heave, roll, pitch and yaw) is assumed to be valid. However, for large angular motions, the order in which the rotational motions are applied matters. For example, a specific orientation in space results if a ship is moved through a large angle of roll, then a large angle of pitch applied at that roll angle, and finally a large angle of yaw is applied to the result; if the same roll, pitch and yaw angles are applied in a different order, a different final orientation in space will result. Simulations using FAST, which implies direct superposition of angular motions are compared with a large-angle analysis tool called Loose which is based on large-angle theory in which angles are combined using sequenced Euler angles. Numerical instability is identified in FAST when large rotations beyond its intended limits are generated.

Sandner [94] developed a reduced order model for the analysis of FWT. Computational speed is 100 times faster than real-time, while FAST is of the order of 1. Steady states, resonance frequencies up to the first tower mode and a statistical analysis of International Electrotechnical Commission (IEC) load cases confirm the validity of the model.

Karimirad[95] created a simplified coupled code using Simo-Riflex and TDHMILL. Simulations were compared against the HAWC2 code for the DeepSpar and ShortSpar FWTs. The aerodynamic forces are applied as a time varying thrust force at the rotor

hub. The relative wind velocity with respect to the structure motion is considered to calculate the thrust force. A filter is used to represent the controller in this study by removing the contribution from a certain frequency band from a given signal. The agreement between the codes is seen to be good.

Lupton [96] attempted to quantify the nonlinearity of FWT's by comparing a linearised model with a full aero-hydro-control-elastic code. The study has shown that, for realistic platform pitch frequencies and amplitudes, the flapwise blade response of a floating wind turbine will depend linearly on the amplitude of the platform pitch motion. Realistic platform natural frequencies have been estimated based on the range of values found in the literature. Outside this range, the response does become non-linear.

Matha [97] used a reduced nonlinear FOWT model to identify critical and less critical IEC DLC situations. Results from the reduced model have been compared to a higher fidelity model in FAST. Results in frequency and time domain as well as extreme and fatigue load predictions demonstrate that a good agreement exists between the two models. The more critical DLC should then be modelled in higher fidelity.

Lupton [98] developed a linearised frequency domain model of the coupled structural dynamics, hydrodynamics, aerodynamics and control system dynamics of the OC3-Hywind FWT. Results from this method were compared against a fully coupled nonlinear model. The following points were noted. While strictly the structural dynamics of a floating wind turbine are nonlinear, for realistic conditions the effects were found to be small. The blade response was linear even for large platform motions as long as the rotor speed is below 20 RPM and the frequency of platform motion is below 1.2 rad s^{-1}. The tangent aerodynamic linearisation overestimates the forces when stall occurs; the harmonic linearisation can capture this better. Although the dynamics of the rotor wake are non-linear, it was demonstrated that a similar linearisation can capture the dynamic behaviour well. WT control linearisation works well when the wind speed is not close to the rated wind speed, with errors in the rotor torque and thrust loads less than 10 % of the rated torque and thrust. Close to the rated wind speed, the control behaviour is less linear and the two controllers interact, leading to larger errors. In some cases this is due to the underlying non-linear behaviour, causing the rotor torque and thrust

errors to increase up to 40 %. The linearised frequency-domain approach is suitable for fast, approximate modelling of the overall response of floating wind turbines. As implemented, the tangent linearisation approach is about 35 times faster than the non-linear simulations. The harmonic linearisation approach was more variable, running between 14 times faster and 2 times slower than the non-linear simulations.

Salehyar [99] numerically examined the aerodynamically generated added-mass and damping effects on the blades using a quasi-static blade-element method and an unsteady boundary-element method. The results based on unsteady simulation suggest that there exists a phase shift in the aerodynamic force as frequency increases, causing a switching from dissipation-dominated behaviour in low frequency to a mixture of dissipation and inertia effects in high frequency. The quasi-static method, on the other hand, cannot predict this potentially important phenomenon. We also show that compared with other dissipation effects such as the wave radiation damping and the damping from the mooring system, the aerodynamic damping is smaller in magnitude and thus negligible in the responses of the platform itself. Nevertheless, its effect on the structural vibration of the tower may still be significant.

Wang [100] used a frequency-domain identification approach to fit a state space to approximate the convolution term in the differential equation of motion for a FWT. The aim of this was to increase computational efficiency. Comparisons of simulations using a time-domain identification approach for fitting the state space model validated this approach.

Farrugia [101] used a modified open source free-wake code to improve computational efficiency for the simulation of the NREL 5 MW WT under floating conditions. Results show that the a linear relationship is obtained between aerodynamic loading response amplitude and the surge velocity amplitude. Difference between the mean power coefficient under surge conditions and the steady power coefficient increases with tip speed ratio. It was recommended to either redesign future FOWT's to not operate in the high tip speed region or to design the platform with increased surge damping.

liu [102] coupled hydro-aero solvers to model the coupled effects on the OC3 Hywind FWT. Aerodynamics are solved using the classic BEM approach with two additional

elements: Prandtl's tip loss factor and the empirical Glauert correction. Hydrodynamics are calculated using first order potential with the addition of a Morison equation viscous term. Results show the response of wind and wave can be added to compute the wind-wave induced response at the stable point of motion. Uniformly constant wind may lead to a constant surge and pitch, which determines the mean displacement of stable state. A static analysis can be performed to obtain the average position of platform where the hydrodynamic model can be established. With the presence of wind, the displacement decay at a faster rate. The linear simplification of mooring system does not work in the case of large displacement. A more detailed dynamic analysis of mooring system is required. The maximum value of displacement appears shortly after the transient loading is applied. Schemes to include the transient state remain to be developed so that difficulties in simulating wind turbine system with control strategies.

Aggarwal [103] studied a modified OC3 Hywind SPAR concept using FAST in operational ($11.5 ms^{-1}$) and survival/idling ($30.0\ ms^{-1}$) and a large sea-state (Pierson-Moskowitz (P-M) spectrum with Hs = 6 m and Tp = 10 s). Simulation results showed the survival loads are Gaussian while the operational conditions have non-Gaussian responses and are also larger than survival ones.

Lemmer [104] uses a linear time-invariant (LTI) system identification state-space model to calculate the motions of the OC3-Hywind and the OC4-DeepCwind FWTs. Simulation results are compares against the conventional convolution integral method. An advantage of this method is the fact that the wave excitation force time series do not have to be calculated prior to a simulation through an inverse Fourier transform, the wave height is a direct input to the model. The results show that with a small number of states it is possible to obtain a good agreement for realistic wave frequencies, even for a complex semi-submersible shape in surge, heave and pitch direction. The wave excitation transfer function has been used to represent the disturbance dynamics of a coupled FOWT model and the overall transfer function from wave height to the wind turbine tower-top displacement has been calculated and verified through a comparison with the non-linear FOWT model with the wave force time series as input. The fitted model is important for model-based controller design because the knowledge of the wave

excitation dynamics can be used to design controllers for optimal disturbance rejection and load reduction.

2.4.5.3 Aerodynamic Damping and Turbulence Effects

Karimirad [105] investigated the effect of aerodynamic damping of an operational and parked WT on a SPAR buoy. A land based controller for the NREL 5 MW WT was used. The aerodynamic damping of rotating rotor reduces the wave induced responses through the control of blades/ rotational speed of shaft as well as the pitch resonant response through relative motion of the platform. For below rated wind speed the damping is sufficient for reducing the resonant responses but in over rated wind speed the excitation forces are higher and the damping is not sufficient.

Gueydon [106] studied the effect of the rotor thrust on the aerodynamic damping and motions of a semi submersible FWT. Two fully coupled numerical models are used, both using aNyPHATAS but calibrated against either the OC4 or OC5 experimental results of the DeepCwind semi submersible test campaign. Simulation results show that the aerodynamic damping acts mainly on the resonance peak of surge and pitch. For this semi submersible, these resonance peaks are the direct responses to low frequent second-order wave loads. It was also observed in the model tests and the simulations that the aerodynamic damping has the strongest effect on pitch. It can thus be concluded that the wind turbine loads interact firstly with the low frequent pitch response for a rotor spinning at fixed rotation speed in steady wind. The motion responses at resonance are sensitive to variations in the amplitudes of excitations and the level of damping. For the considered semi submersible floating foundation, the heave resonant response in waves is governed by linear wave loads since the heave natural period is within the wave frequency region. Whereas, the resonance responses in surge and pitch are governed by low frequent second-order wave loads.

A detailed study on turbulent winds concluded the following points [107]. That the coherent turbulent structures affect floater loading mainly in high-wind conditions. Failing to model lateral coherence can lead to an overestimation of predicted loads. Kaimal generally performs better than Mann in high-wind, high-load scenario. Loads on

the mooring system are most sensitive to atmospheric stability in low winds. Loads on the blade root are most sensitive to atmospheric stability in high winds.

2.4.5.4 Viscous Damping

Shen [108] studied the effect of viscous damping on the DeepCwind 5 MW TLP WT. Simulations were performed using both FAST and CRAFT. Results show the viscous forces on both the column and pontoons and those on the tendons contribute to higher harmonic excitation in the pitch resonance, with the former dominating the response. The excitation effect of the viscous force on the tendons decreases with increasing wave periods, and the damping effect increases and overwhelms the excitation effect. The amplitude of the third higher harmonic resonant pitch motion increases with increasing wave heights for small waves, reaching a maximum when the wave height attains a threshold and decreasing with further increases in the wave height. These responses are mainly caused by the increasing damping effect of the viscous drag force. Aerodynamic loads provide significant damping for pitch motion, which mitigates the severity of resonant motion and also changes the dynamic response characteristics of the tendons by changing their mean tensions. An additional coupling between surge and pitch is observed, and it is caused by the presence of aerodynamic forces. This effect slightly increases the pitch response at the wave frequency.

2.4.5.5 Platform & Tower Elasticity

Bae [109] analysed the effect of tower elasticity and aerodynamic loading on a TLP supporting the 5 MW NREL reference WT. It was shown that the elasticity of the tower can dramatically affect the platform pitch motion through the shift of pitch natural frequency. It was also seen that strong aerodynamic damping is also generated from the rotating blades and weakens the pitch resonance effect. It was recommended that the conventional oil and gas rigid body hydrodynamic solvers are not used for the analysis of FWT's.

Finn [110] attempted to define when hydroelasticity (combined fluid-structure interaction for floating flexible structures in waves) is required for modelling. It was shown

that if the first wet elastic natural frequency is higher than 5 times the peak frequency of a sea spectra or roughly 2-5 times the wave frequency in regular waves, the loading condition may be assumed quasi-static, else a hydroelastic assumption must be assumed.

Wehmeyer [111] analysed the effect of including a rigid or flexible tower in the numerical modelling of TLP WT. The numerical models were verified with experimental data from a 1:80 scale model tested at the 3D wave basin at Aalborg University. numerical models were shown to have a good fit. A rigid tower was seen to significantly under predict pitch motion both numerically and physically.

Ma [112] developed a coupled floater and mooring dynamics solver and analysed a TLP and SPAR FWT. Simulation results were compared against experimental results.Rigid body motion and internal forces of structure could be simulated reasonably by the presented numerical model.The influence of the flexibility on the structure response has been investigated by the simulation. For TLP type of FOWT, smaller stiffness of lower hulls results in an increase of mooring tension and bending moment on the lower hull.

Campos [113] analysed the effects of structural flexibility in a concrete SPAR floater. The model computes a dynamic time domain non-linear FEA for FOWT's, integrating all the effects of the external forces and the structural stiffness to obtain the displacements at each point of the structure at each time step. The flexible concrete structure subjected to the combined action of wind and waves presents 2% larger peak inclination than the rigid body while the more flexible material produces a 16% larger inclination.

2.4.5.6 Drivetrain

Xing [114] studied the drivetrain dynamics of a 750 kW SPAR-type floating wind turbine. Fully coupled time-domain analyses were performed using HAWC2. The results show that there are general increases in the standard deviations of the main shaft loads and internal drivetrain responses in the FWT compared to a fixed WT. These increases are a result of the increased main shaft loads in the FWT, especially the non-torque loads. An improved four-point drive-train support (4PT) system is studied and compared against the original three-point support system for the FWT. The 4PT system significantly

reduces the tooth contact forces and bearing loads in the low-speed stage, but this result comes at the expense of increased main bearing radial loads.

2.4.5.7 Extreme & Survival Modelling

Wehmeyer [115] investigated the effect of non-linear sea state on the ULS of a TLP WT. The surface elevation and kinematics are generated by a second-order wave model including all sub- and super-harmonics, with and without an embedded Stream-function wave. Simulations show that the irregular incident wave runs over predict the measured maximum loads by 32% on average, where the non-linear irregular wave runs yield more conservative load ratios. From this, it can be concluded that the linear irregular incident wave is sufficiently conservative even though the non-linear incident wave model better resembles the surface elevation (and probably the wave kinematics). The embedded wave approach results in slightly lower overall averaged maximum loads, i.e., an over prediction of 29%. Therefore, based on the current status, it is concluded that the embedded wave approach provides a controlled and time-efficient engineering tool for the investigated FOWT.

Endegnanew [116] went a step further than the typical coupled simulation by modelling a power network in addition to the typical hydro aero elastic modelling. This was accomplished using the FEDEM Windpower software. As a case study, a SPAR floating WT's response to a symmetrical three phase grid fault, that caused a 50% voltage drop at the turbine converter's terminal, was studied. It was found that the turbine rides through voltage-dips without severe effects on electrical systems. Minor but non significant tower bending moment changes were observed due to the loss of torque.

2.4.5.8 Control

Savenije [117] developed a general control strategy and applied it in a case study to the GustoMSC Tri-Floater and the OC3 Hywind SPAR platforms. Through simulations using PHATAS-aNySIM-AQWA it is shown that not only does the floating platform have an influence on the wind turbine control, but also vice versa. The developed algorithm for floating platform damping stabilises the controlled FWT, while minimizing the impact

on the performance of the regulating pitch control loop.

Fleming [118] optimized the WT controller on the WindFloat platform in order to reduce structural loads. The fixed-bottom controller of an 8 MW OWT was modified for use on the WindFloat platform. An overall reduction of tower base bending moment DEL of about 20 % was achieved for most wind speeds. The controller used incorporated two novel features. First, both platform pitch and nacelle velocity were used simultaneously in control. Second, the controller was designed in the frequency domain both to separate the control activities of these loops and to trade off additional damping of resonant modes with the tendency of controllers to feed back wave frequency-range excitation.

Goupee [119] experimentally analysed the effect of various WT controllers on the DeepCwind semi-submersible supporting the MARIN stock WT in the MARIN Offshore Basin. The controllers used were as follows; A fixed blade pitch with constant rotor speed, an active blade pitch control with constant speed and varying controller gain and a variable speed active pitch controller. Results show that active turbine controllers reduce motions and loads, through modification of the low-frequency response and phasing.

A control strategy based on adaptive second order sliding mode approach, combining collective and individual collective blade pitch control, showed good performance for power regulation, platform pitch motion reduction and reduction of blades fatigue load [120].

2.4.5.9 Model Predictive Control (MPC)

Lindeberg [121] presented a novel wind turbine control system sing a linear Model Predictive Control approach which gives a smooth power output during transitions between different controllers. Regarding tower stability, these simulations have demonstrated that the suggested control system gives a stabilisation of tower oscillations. In the MPC approach used here, this is essentially achieved simply by using a prediction horizon that exceeds the periodicity of the tower oscillations. Since tower oscillations have a low frequency, this has the downside that it requires a relatively large prediction horizon, and therefore gives relatively high computational requirements. Regarding bumpless transfer, the simulations have clearly demonstrated that the system using the proposed algorithm

for smooth transition indeed exhibits a smooth system behaviour. In comparison to a case with sudden transition, the behaviour is significantly improved.

Raach [122] analysed a non-linear model predictive controller (NMPC) with individual pitch control for FWT. The NMPC controller is then compared to the standard baseline controller and an individual pitch control extension for the baseline controller. The NMPC controller shows promising results reducing significantly the blade loads.

Yang [123] designed and tested an individual pitch control (IPC) system integrated with disturbance accommodating control (DAC) and model prediction control (MPC) through fuzzy control. The goal of the system is to reduce fatigue loads. The new individual pitch controller is tested on the NREL offshore 5 W WT mounted on a barge with a spread-mooring system, running in FAST, operating above-rated condition. Compared to the original baseline collective pitch control, the IPC system shows a better performance in reducing fatigue loads and is robust to complex wind and wave disturbances as well, power performance is similar.

2.4.5.10 Linear Quadratic Regulator).

Christiansen [124] developed a WT control strategy based on a gain-scheduled linear quadratic regulator (LQR) controller that deals with wind and wave misalignment It requires estimates of the wind speed and wave frequency. It was compared against the existing OC3 hywind control model. The result is a wind and wave control strategy capable of actively damping structural oscillations, while fulfilling the objective of maximizing power.

Christiansen [125] added an additional control loop to a conventional onshore WT controller in order to reduce the effects of wave disturbance and negative aerodynamic damping.

Lemmer [126] investigated the effect of the control inputs on the system outputs of the triple SPAR 10 MW FWT. A multi-input multi-output (MIMO) method was used. Simulations show the blade pitch angle can most effectively control rotor speed and tower top displacement for low frequencies, whereas the generator torque has a much smaller impact. However, the generator torque, together with the blade pitch angle (multi-input),

can effectively mitigate the present right-half plane zero. A linear quadratic regulator (LQR) assuming perfect state measurements has been designed. The comparison to a previously developed SISO controller shows that the LQR can significantly reduce the system responses and attenuate various resonances. However, even the LQR, can hardly attenuate the excitations from the waves. which confirms the results of the preceding MIMO analyses of the open loop. The comparison of non-linear time-domain simulations with linear frequency-domain calculations showed good agreement, which endorses the use of these computationally efficient methods for controller tuning under realistic environmental conditions

Predicting the incident wave also shows promise in reducing WT loads by the use of a deterministic finite-horizon LQR controller [127]. The optimal controller is shown to reduce the fore-aft tower base bending moment, especially components excited by the wave force.

2.4.5.11 Receding Horizon Control

Galvani[128] proposed a new non-linear control system based on a real-time non-linear receding horizon control (NRHC) methodology. The controller is independent of the iterative solutions and constitutes the novelty of this work. Simulations are carried out in FAST v.8 and a Matlab solver on the OC3-Hywind SPAR buoy platform. Simulation results provide the optimal performance of NRHC in comparison to the classical PI controller with the additional advantage of real-time tuning properties.

2.4.6 Computational Fluid Dynamics

Nematbakhsh [130] compared simulations of a TLP WT using BEM (SIMO-RIFLEX) and computational fluid dynamics (CFD). For the wave studied (0.75 rad/s frequency and 7.7 m height) the surge shows a dominant response at the incoming wave frequency and good agreement between both approaches is observed. A higher mean surge is noted in the CFD based method. This can be due to better representation of non-linear effects in the CFD based model, namely by applying the hydrodynamic force at the TLPWT instantaneous position and by integrating the hydrodynamic loads up to exact

free surface. The higher mean surge in the CFD based model results in TLPWT mean position to be further downstream in surge and lower in heave. However, these differences do not considerably affect the TLPWT design driving parameters such as tendon forces and tower base moments, since it only affects the dynamic mean position of TLPWT. The difference between two approaches, as expected, is lower for the smaller waves and becomes larger as the wave height increases.

Viré [129] coupled the open source Navier-Stokes equation solver Fluidity-ICOM and the non-linear solid structure dynamics code Y3D. The coupled models are tested on the two case studies were analytical models exist: flow past a fixed wind turbine represented by an actuator disk, and the dynamics of a cylindrical pile floating at the interface between air and water. The modelling technique is shown to be accurate and will be used to analyse FWTs.

Tran [131] investigated how the periodic pitching motion of the WT due to the floating platform motion effects the vortex-wake-blade interaction for the aerodynamic performance of an FOWT. Unsteady CFD simulations based on the dynamic mesh technique were compared with unsteady BEMs. It is shown that the unsteady aerodynamic loads of the floating offshore wind turbine become sensitively changed due to the variation of frequency and amplitude of the platform motion. Additionally, there are strong flow interaction phenomena between the rotating blades with oscillating motions and generated blade-tip vortices. It is also importantly shown in this paper that the generated wake strength behind the rotating blades during the forward pitching motion is stronger than that during the backward pitching motion.

Tran [132] also simulated the unsteady hydrodynamics using CFD method with dynamic motion based on overset grid and potential based panel approach for the semi-submersible DeepCWind FOWT. The numerical results of the free-decay analysis have been compared with experimental data and the results show a good agreement without considering any further modifications such as additional damping which is generally required for conventional potential based approaches. The RAO of the surge, heave, and fairlead tension of mooring line were compared to experimental data when the only wave condition is considered. The results obtained by CFD and potential based panel

approach show reasonable agreement with previous studies and experiment data.

Nematbakhsh [133] modelled a FWT barge platform using a numerical wave tank. Results were compared to linear BEM analysis and experiments and showed good overall agreement. BEM was seen to over predict resonance motion due to lack of viscous damping.

Oggiano [134] compared CFD simulations of a braceless semi-submersible FWT to experimental results from the towing tank at MARINTEK in Trondheim, Norway.Good agreement in vertical and horizontal forces between CFD and experiments was found for the floating cases and vertical and horizontal motion resulted to be correctly predicted in the free hull case. The agreement between the simulations and the experiments can be considered satisfactory for the test cases studied, however the validation cases tested were limited and future work is needed in order to prove and confirm the feasibility of the VOF method as general tool for floating structures.

Leble[135] coupled a Navier-Stokes solver for the hydrodynamics and a Helicopter Multi-Block flow solver for the aerodynamics to model a 10 MW semi submersible FWT. The motion of the floating offshore wind turbine is computed using a Multi-Body Dynamic Model of rigid bodies and frictionless joints. Mooring cables are modelled as a set of springs and dampers. The partitioned coupling can be weak or strong. If the coupling scheme does not involve Jacobians relating the solutions of the two solvers, the scheme is called weak or loose. Explicit coupling schemes, as the one used in this work, are weak. On the other hand, if a Jacobian is employed, the scheme is called strong or tight, as the solution is equivalent to what would be achieved by a monolithical formulation. The results showed that the weak coupling method used here is adequate for the solution of the problem at hand.

Heilskov [136] compared CFD results of a TLP WT from OpenFOAM, with a flexible mesh approach and StarCCM+, with the overset mesh method, to physical experiments carried out in the DHI wave basin, Hoersholm. It was demonstrated with reasonable results that the model is able to capture the transfer of complicated wave impact forces on the motion of FWT, due to non-linear wave interaction including viscous effects. This includes complex interaction between the mooring system and the body. Hence, both the

motions and the forces in the mooring lines were monitored. As part of the validation, the sensitivity of the solver to body displacements has been assessed. Even for moderate body displacements and rotations, the flexible mesh method in OpenFOAM fails due to numerical instabilities as a result of distortion of the mesh degrading the quality of the mesh significantly and the two-way coupling between the fluid solver and the 6-DOF solver. Tests have shown that OpenFOAM is particularly numerically sensitive to body discontinuities coinciding with the water surface interface. The StarCCM+ results illustrated that with the overset grid method, we are able to capture effects of complicated non-linear wave interaction of complex viscous nature on the motion of a moored structure. The results obtained with StarCCM+ compare with the measured motion of and tension forces on the TLP in both regular and irregular waves.

Yan [137] proposed a computational fluid-structure interaction (FSI) framework for the simulations of the interaction between free-surface flow and floating structures, such as offshore wind turbines. The framework is based on a suitable combination of the FEM and isogeometric analysis (IGA), and has good efficiency, accuracy and robustness characteristics. The free-surface phenomena are modelled using the Navier-Stokes equations of incompressible two-fluid flow in conjunction with the level set method. The FEM-based moving-domain ALE-VMS technique is employed to discretise the fluid mechanics equations, while the IGA-based rotation-free shell and beam/cable formulation is employed to model the mechanics of floating structures. the OC3-Hywind FWT with a non-spinning rotor was modelled subject to a variety of wave conditions. For the low-amplitude Airy wave conditions, the platform displacements predicted by present work are in good agreement with the low-fidelity modelling results from NREL.

leble [138] analysed a 10 MW WT on a semi submersible platform using high fidelity methods. The aerodynamic loads on the rotor are computed using the Helicopter Multi-Block flow solver developed at the University of Liverpool. The method solves the Navier-Stokes equations in integral form using the arbitrary Lagrangian-Eulerian formulation for time-dependent domains with moving boundaries. Hydrodynamic loads on the support platform are computed using the Smoothed Particle Hydrodynamics method. The results showed that the weak coupling method put forward in the paper is adequate for the

solution of the problem at hand.

Yuanchuan [139] used OpenFOAM to analyse the effects of a the dynamical motion of a FWT platform on the WT characteristics. The surge, heave and pitch are superimposed onto the rotation of the WT. It was found that both thrust and torque are largely influenced by the prescribed platform motion, indicating that the motion response of the supporting platform for a floating wind turbine should be taken into account during the design procedure.

Differences in CFD and experimental modelling described as coming from the errors owing to mooring modelling, symmetry of the computational domain, neglected aerodynamic damping of the turbine and tower, restriction in the degrees-of-freedom, not considered electrical power cable, and uncertainties of the experiments[140] .

2.4.7 Experimental Modelling

2.4.7.1 Wave Basin Modelling

There are four main methods for modelling WT loading on a floating platform in a wave basin [141];

1. **Mechanical Pulley System:** Constant horizontal load applied through a mass hanging via a pulley from the nacelle [142].

2. **Actuator Method:**. Here the wind forces are modelled using one or more actuators, commonly either one or more ducted fan or a multiple wire actuator system. A ducted fan with high revs/min that is attached to the top of the tower. A constant or variable wind thrust can be modelled, and with the inclusion of a feed-back loop, which includes the motions of the platform, the relative (between incoming wind and platform motion) wind thrust can be applied [143] [144].

3. **Applied Wind on Disk:** Wind is generated using an array of fans and applied to a thin disk. A drag coefficient of 1.2 is used to model the thrust force [10].

4. **Applied Wind on Model Turbine:** Wind is generated using an array of fans, and applied to a model turbine. As Froude scaling and Reynolds scaling (required

for wind blade lift modelling) are not compatible (either thrust force of aerodynamic damping being incorrect) turbine blade geometry must be modified to include longer chord lengths in order to correctly model all effects [11]. Advantages of this method over the previously mentioned include correct modelling of aerodynamic torque and the gyroscopic effect of the rotor [12]. The gyroscopic effect can be compensated for in the first three modelling methods by attaching a motor and simple mass rotor that turns at the correct revolutions per minute.

Shin [146] [147] experimentally modelled an inverted conical cylinder FWT moored by a spring tensioned leg (STL) in the Ocean Engineering Wide Tank of the University of Ulsan. Four triangle plates, which are made of light plastic material, were attached to the platform for reducing surge and pitch motions of the platform. These plates were used to greatly increase the drag forces at the lower part of platform. The thrust in basin model test was scaled in Froude number. An inverted conical cylinder type FOWT shows decent motions in most of load cases compared with the OC3-Hywind SPAR model moored by a STL at 320 m deep. As the area of appendage plates grew, the peak response and the natural frequency in surge and pitch became smaller.

Tomasicchio [148] experimentally modelled the MIT/NREL TLP and OC3-Hywind platforms at 1:40 scale in the DHI Offshore Wave Basin. Wind load is simulated by computer controlled wind fans.Curbois [149] describes the wind generation system at the Ocean Engineering Wave Basin of École Centrale Nantes. It is composed of four centrifugal fans, a diffuser, a convergent form, a honeycomb and a screen. Analysis of the generated wind shows a satisfying velocity homogeneity and a low turbulence level.

Wehmeyer [150] experimentally analysed an industry inspired three armed structure TLPWT design in the 3D deep water basin of the Hydraulics and Coastal Engineering Laboratory at the University of Aalborg at a scale of 1:80. Due to the fact that the blade aerodynamic damping in the feather survival state is negligible, the RNA is modelled as a lumped mass. It was found that the inclusion of second order waves increases the ringing response and increases the number of slack events.

Le [151] physically modelled the WINFLO semi-submersible supporting a 2 bladed

1 MW WT in the IFREMER, Brest wave tank at a model scale 1/25. Wind load is generated by an array of 3 x 4 fans and combined with ducts to cover a 4.4 m x 3.3 m air flow exit area. Testing revealed that the operational WT has a stabilizing effect on pitch, indicating that aerodynamic damping is present. Motions, in particular maximum angles (roll/pitch), are acceptable for the WT to function. Accelerations in the floater and nacelle are deemed acceptable.

Adam [152] experimentally studied the GICON TLP WT in the MARIN wave basin. The platform forces due to the superposition of wind and wave loads where compared against the forces due to a coupled wind and wave loading, and were found to be comparable up to the cut-out wind speed. It should be noted that this result is specific only to this platform as unlike the typical TLP it is highly constrained by diagonal tendons and is non compliant in the surge, sway and yaw DOFs.

Huij [153] experimentally modelled the GustoMSC Tri-Floater semi-submersible FWT in wind and wave loading at the offshore basin at MARIN. The platform was 1:50 Froude scaled, while the blade geometry was modified to reproduce the correct thrust force. A comparison was made to fully coupled numerical analysis using Ansys-AQWA coupled to the aero-servo-elastic wind turbine simulation program PHATAS. Results are comparable, validating the first order numerical hydrodynamics used.

Hong [154] experimentally modelled a 1:100 scaled SPAR buoy supporting a 5 MW WT. No aerodynamic loading was modelled. The free decay test results show that the heave natural frequency is very sensitive to the waterplane area, and less sensitive to changes in the mooring line spring constant, and locations of the center of gravity and fairlead. However, the pitch natural frequency is significantly affected by the location of the center of gravity. An increase in the metacentric height results in an increase in the pitch natural frequency. Regular wave test results show that the RAO of pitch, nacelle displacement, and mooring line tensions increase as the wave frequency decreases toward the pitch and heave natural frequencies. However, the RAO of nacelle acceleration decreases as the wave frequency decreases toward the natural frequencies. The results also show that an increase in the height of the center of gravity produces a decrease in the pitch RAO. RAO patterns of pitch and nacelle surge are similar to each other. This

implies that pitch motion mainly contributes to the nacelle surge motion. Even though the nacelle displacement RAO has the smallest value with a high center of gravity, the RAO of the mooring line length change is mainly affected by the fairlead location. The RAO of the mooring line change increases as the height of the fairlead increases

Make [155] used RANS CFD modelling to quantify the scaling effects of small scale model WT's. The MARIN Stock Wind Turbine (MSWRT) was scaled to reproduce the same performance characteristics as the full scale NREL 5 MW WT. This was compared against a geometrically scaled NREL 5 MW WT. The objective of the MSWT design in generating as close as possible the same thrust as the NREL turbine in full-scale conditions, for the design condition, was been attained. The NREL WT showed highly separated flow at model-scale and less so at full scale.

Duan [156] experimentally modelled a 1:50 scale SPAR buoy supporting the NREl 5 MW WT at the Deepwater Offshore Basin in Shanghai Jiao Tong University. Wind was generated using a system of 9 axial fans(3 x 3 array). The blades were modelled using the same modified aerodynamic properties as the UMAINE testing. Results show the yaw motion resonance angular frequency is mostly excited by the angular frequency of rotor spinning both for wind only and integrate wind-wave load case. Under wind-wave load conditions, the surge and pitch motion have a strong coupling effect on each other, while heave motion is out of the coupling effect. For surge, pitch and heave, the aerodynamic effect basically does not shift the angular frequencies of resonance responses both for natural-excited and wave-excited. It basically does not change the peak amplitude of resonance response excited by wave as well. Nevertheless, the peak value excited by natural frequency, representing for the motion fluctuation in time history, had been substantially reduced due to aerodynamic effect, which benefit the fatigue maintenance of mooring system. Duan [157] extended this research to examine the on the response characteristic differences between the thrust matched blade system (TMBS) and the geometry-matched blade system (GMBS), which utilize redesigned thrust-matched and original geometry-matched blades. Gyroscopic effects of rotor rotation are found weakened in the TMBS, and yaw oscillation in the TMBS is not solely excited by rotor rotation, unlike in the GMBS. Coupling effects between surge and pitch are found in

both the TMBS and GMBS under combined wind-and-wave condition. Furthermore, restraining effects of wind loads on motions in the GMBS and TMBS are both evident at natural frequencies while show distinct behaviours at the wave frequency.

Campos[158] experimentally modelled a monolithic concrete SPAR FWT at 1:100 scale in the CIEM wave flume. Results were compared against frequency domain simulations from ANSYS AQWA. As expected, the use of both Airy and Stokes 5th order wave theories results in similar predictions for the wave kinematics. On the other hand, the rough approximation of the dynamic pressure above the mean water level for the Airy wave theory, in comparison with the non-linear Stokes 5th order theory, results in larger heave amplitudes as larger are the wave periods. It seems to be clear that for those structures with significant geometrical differences around the mean water level, the use of non-linear waves have to be considered in order to increase the accuracy of the vertical motions prediction. The numerical code is fast enough to be used as efficient and accurate pre-design tool, being capable to compute simulations up to full scale equivalent time-series of 1200s in less than 2 minutes.

Make [159] analysed the significance of scaling effects on the NREL 5 MW reference WT and the MARIN Stock Wind Turbine (MSWT) using CFD. Both model and full-scale conditions were studied for a fixed non-moving platform and rotor-only turbine. It was found that scaling effects are indeed significant and a highly three-dimensional and additionally separated flow was observed. Based on these findings two methods were proposed to expand the applicability of BEMT-based tools to off-design and model scale conditions. First, instead of using commonly used 2D XFOIL data, 2D CFD RANS data was used. The use of purely 2D data from 2D CFD RANS computations did however not result in the desired improvements when compared to XFOIL-based results. The second proposed method is based on the use of 2D airfoil data obtained by post-processing of 3D flow data coming from 3D CFD computations. This new approach was shown to be successful and can therefore be extremely useful for future model-scale FOWT testing campaigns to do preliminary performance predictions. All BEMT-based and CFD results presented in this paper were compared to model-scale experimental data of the NREL 5 MW turbine and the MSWT over the full range of TSR.

Martin [160] presented two scaling methodologies to address the dissimilitude normally experienced when attempting to measure global aerodynamic loads on a small scale wind turbine rotor from a full scale reference. The first, termed direct aerofoil replacement (DAR), redesigns the profile of the blade using a multipoint aerofoil optimisation algorithm, which couples a genetic algorithm (GA) and XFOIL, such that the local non-dimensional lift force is similar to the full scale. Correcting for the reduced Reynolds number in this manner allows for the non-dimensional chord and twist distributions to be maintained at small scale increasing the similitude of the unsteady aerodynamic response; an inherent consideration in the study of the aerodynamic response of floating wind turbine rotors. The second, the geometrically free rotor design (GFRD) methodology, which utilises the Python based multi-objective GA DEAP and blade-element momentum code CCBlade, results in a more simplistic but less accurate design. Numerical simulations of two rotors, produced using the defined scaling methodologies, show an excellent level of similarity of the thrust and reasonably good torque matching for the DAR rotor to the full scale reference. The GFRD rotor design is more simplistic, and hence more readily manufacturable, than the DAR, however the aerodynamic performance match to the full scale turbine is relatively poor.

Gueydon [161] analysed three methods to scale down WT blade design and applied each to the DeepCwind semi-submersible floating wind turbine at scale 1:50. The effects of the differences between these 3 methods on the motions of the floater in waves and wind are analyzed. In the absence of a controller for the rotor, no significant differences related to the induced aerodynamic damping was noticed, but an offset in the motion related to a thrust deficit was observed.

Pegalajar [162] experimentally modelled the DTU 10 MW TLP WT in the DHI Denmark wave basin at a scale of 1:60. Experimental data was compared with numerical modelling carried out using Flex5. Results show that even in extreme sea states, a good match in surge was obtained after calibration. The heave motion presents a certain correlation for the intermediate sea states, while for the smaller ones the measurements were too influenced by uncertainty. For the larger sea states, as well as for intermediate sea states with wind, a reasonable match with the test signal was found. The measured

pitch response was proven to be unrealistic, thus a linear recalibration of the signal was needed to compare it to the predictions. Even after recalibration, significant discrepancies between tests and simulations were found for pitch with only waves — likely due to a larger amount of energy at the pitch natural frequency. in Flex5 — while a closer match is obtained for the cases with wind and waves. The nacelle acceleration did not match as well as the motion signals did for all cases, but the aerodynamic damping was observed in both experimental and numerical setup. The line tension is generally well predicted, although in some cases the numerical model underpredicts the extreme loads.

Stewart [163] gave a review of a number of different FWT wave basin experiments.

Mcelman [164] described the development of a wind generation facility at the existing MARIN wave basin. CFD was used to aid this design. Phase 1 CFD simulations aided in the design of the wind generator system, as complex flow patterns in the basin could be identified and addressed. During phase 2 measurements, flow from the test section to the bottom and top row of fans dominated the turbulence and velocity profiles until the addition of inlet vanes. It is highly likely that a functioning turbine in a basin of this size alters the flow profile in the basin. Phase 3 simulations showed that a honeycomb simplified as a momentum source term does not sufficiently model real basin flows. It is possible to develop a wind-wave facility as a retrofit of an existing tow tank, providing a research grade wind profile, given special design and operational attention to the main phenomena present in the basin.

2.4.7.2 Offshore Testing

An alternative to connecting the FWT to the grid is using a standalone grid simulator [165] on the floating platform itself for electrical loading of the test WT. Advantages of this approach include forgoing unnecessary costs and the required environmental monitoring (i.e., an expensive and lengthy sea floor study is needed for cable routing, burial, etc). A 1:8 scale model of the VolturnUS semi-submersible FWT was tested in Maine in 2014 [166] [167].

Skaare [168] compared measurements of the full scale HyWind demonstrator against simulations generated by SIMA. Results show that it is challenging to achieve good corre-

spondence between measurements and simulations with respect to mooring line tensions for the case below the rated wind speed. The mooring line response in this case is probably dominated by wind loads since the wind thrust is high and the waves are small. The proposed method for estimation of the undisturbed wave elevation at the turbine, by separating the diffracted wave from the incident wave field, leads to good correspondence between simulations and measurements in the wave frequency range. This is observed in power spectrum plots of structural bending moments, mooring line tensions and in high-pass filtered time-domain snapshot plots of the roll and pitch motions. Conclusions suggest developing a lighter and more cost-effective floating WT solution for future developments.

2.4.7.3 Wind Tunnel Testing

A good summary of the hardware in the loop testing of WTs mounted on floating wind turbines in wind tunnels is given in [169]. Li [80] performed experiments on a two bladed downwind WT at the Mie University Fluid Engineering Laboratory's wind tunnel. By controlling the pitch angle it is suggested that the WT thrust and thus platform motions can be reduced. The thrust coefficients are decreased with the increase of pitch angle. Rockel [170] measured the wake effect of FWT by placing two freely rotating model WT's in the closed-circuit wind tunnel at Portland State University. The wake and turbulence behind these turbines was compared against the case where the WT's were fixed. The fixed turbine causes an increase in turbulent mixing by having an increased drag on the flow due to its rigidity. This effect is reduced for the floating turbine due the additional degree of freedom and hence its ability to follow fluctuations in the flow. The ability of the turbine to move with the flow absorbs turbulent fluctuations as seen in the Reynolds stresses. The downwind rotating WT experiences a greater load reduction than the fixed WT. The pitching motion of the turbine leads to the need of longer distances between floating turbines in a farm, to allow for a better recovery of the wake to achieve the same power production, as for bottom fixed turbines. But due to its ability to damp fluctuations, floating turbines are expected to benefit in terms of fatigue loads.

2.4.7.4 Hybrid Modelling

Bachynski [171] numerically analysed the effect of actuator sensitivity on real time hybrid experimental modelling. It was found that due to the large mass and small motions of the system, the relative effects of limited actuation on motions were large. Bayati [172] designed a 6 DOF system allowing a wind turbine to be modelled in a dedicated wind generation facility, while the hydrodynamics would be modelled numerically in real time. Stewart [173] describes the use of a real time actuator system to model the aerodynamics while the hydrodynamics are physically modelled in a wave basin. The paper compares the use of a real time aerodynamic solver Aerodyn and a method which bypasses this and applies a predefined force directly. Experimental results had not been released at the time of publication and therefore the set up was numerically modelled. The simulations presented showed that using a predefined aerodynamic force time series can lead to large differences in both loads and platform motions when comparing simulations to experiments. These errors are due to the lack of realistic feedback between the platform motion and the aerodynamics captured in the simulations with predefined aerodynamic loads. Oguz et al. [174] used a software in the loop approach to model a TLP WT. Only aerodynamic thrust loads are physically modelled by the use of a ducted fan. Gyroscopic and aerodynamic torque loads are neglected. a modified version of the FAST aero-hydroservo-elastic code in which the standard hydrodynamic calculations to find instantaneous values for platform position, attitude and velocities are replaced, in real time, by the values obtained from the tank measurements. A comparison of results from physical and numerical simulations show that, the numerical predictions from FAST were very close to the results obtained from the experiments in some cases, but in other cases the numerical model failed to accurately predict the platform response.

2.4.8 System Identification

Davidson [175] used CFD to generate data for a WEC system identification model. The advantages over physical tank testing are outlined, primarily being the ability to easily constrain motion to a single DOF, without imposing large friction forces.

2.4.9 Comparison of Floating Platforms

Nejad [176] numerically modelled a fully coupled simulation of FWT on one land based WT, one SPAR, one TLP and two semi submersible platforms. The study took an in depth look into the fatigue damage analysis of the WT drivetrain. The results suggest that the main bearings sustain more damage in floating wind turbines than on land-based. The highest main bearing damage is observed for the SPAR floating wind turbine. The large wave induced axial load on the main shaft is found to be the primary reason of this high damage in the SPAR wind turbine.

Matha [15] numerically compared the dynamics of the ITI Energy barge, the OC3-Hywind SPAR buoy and the MIT/NREL TLP. The comparison indicates that all floating wind turbines show increased loads on turbine components as compared to the land-based system. The investigated barge design is very susceptible to significant roll and pitch motions and, consequently, has the greatest turbine loads by far among the concepts. The SPAR buoy platform motions in roll and pitch are greater than for the TLP, but for yaw the SPAR buoy is more stable than the TLP. This yields generally greater blade and tower loads for the SPAR buoy than for the TLP, except for loads affected primarily by platform yaw. The TLP shows lower damage equivalent loads in the tower than the other two concepts.

Jonkman [177] numerically compared three platforms supporting the NREL 5 MW WT using the FAST software: the MIT/NREL TLP, the OC3-Hywind SPAR buoy and the ITI Energy barge. All of the floating wind turbines show increased loads on turbine components as compared to the land-based system, and therefore, they must be strengthened. The platform motion induced ultimate and fatigue loads for all turbine components in the ITI Energy barge are the highest found for the three concepts. The differences in the ultimate and fatigue loads between the MIT/NREL TLP system and the OC3-Hywind system are not significant, except for the loads in the tower, which are greater in the OC3-Hywind system. Robertson [178] compared the dynamics of 6 FWT concepts: a barge, a semi-submersible, two TLPs, and a SPAR buoy at two different depths. The performance of these models was compared to that of a base model

with a turbine supported by a fixed land-based tower. Performance was evaluated via a comprehensive loads and stability analysis adhering to the procedures of the International Electrotechnical Commission (IEC) 61400-3 offshore wind turbine design standard. In summary, all of the floating wind turbines show increased loads on turbine components as compared to the land-based system, and therefore must be strengthened. The platform motion-induced ultimate and fatigue loads for all turbine components in the ITI Energy barge are the highest found for these six concepts. The designs for the two TLP systems were very different, but it was found that their response was fairly similar. This shows that the method for stabilizing the floating system is more influential on the dynamics of the system than the details of the design. The differences in the ultimate and fatigue loads between the TLP systems and the SPAR and semi systems are not significant, except for the loads in the tower, which are less for the TLP systems. The modeling of the OC3-Hywind system at a shallower depth did not have a significant effect on the system dynamics.

Koo [179][180] experimentally compared three generic FWT platform concepts at MARIN: a SPAR, a semi-submersible, and a TLP. The hammer test results show that the tower structural natural frequencies are significantly influenced by the supporting floater. The stiffer foundation, such as a TLP, provides a lower bending frequency of the turbine tower than a compliant foundation such as a SPAR buoy or a semi-submersible. The free decay test results show that the steady wind substantially increases pitch damping of the SPAR buoy and semi-submersible. The white noise test results also show that the steady wind increases the surge and pitch damping for all three floating platforms. On the contrary, the wind load increases the wave frequency motion of the SPAR buoy. The results of the wave only cases indicate that the SPAR buoy tested possesses the smallest surge response in irregular seas while the TLP system tested exhibits the smallest pitch response of any of the systems. The semi-submersible response for both DOF studied is typically in between that of the TLP and SPAR buoy in the wave energy frequency range; however, the semi-submersible exhibits by far the greatest second order difference-frequency associated motion response. For a TLP floating wind turbine, the wind loading significantly increases the pitch response of the system; however, the

pitch response energy as a whole is still quite small. For the SPAR buoy and semi-submersible designs, the operating wind turbine significantly damps the response of the structures at the pitch natural frequency, and in the case of the semi-submersible, also damps the response at the surge natural frequency. The nacelle surge acceleration for the TLP at low energy sea states possesses significant response near the coupled platform pitch/tower bending frequency whereas the other two systems do not. For intermediate sea states, the unique motion characteristics of the semi-submersible platform yield a near net zero motion of the 90 m hub height wind turbine, minimizing nacelle motion and the accompanying inertial loads. The tower base bending moment for all three systems at low sea states is characterized by significant response at the platform pitch frequencies, this being above the wave energy frequency for the TLP and below it for the SPAR buoy and semi-submersible. For severe sea state conditions, the tower bending moment response for all three systems is dominated by the wave and not the platform pitch frequencies. On the topic of moorings, the TLP mooring load response in the frequency domain is approximately an order of magnitude greater than for the SPAR buoy and semi-submersible floating wind turbine designs. In addition, the SPAR buoy and semi-submersible response is primarily located at the system surge natural frequencies whereas the TLP mooring load response is substantial in the wind energy, wave energy, and coupled platform pitch/tower bending natural frequencies.

2.4.10 Tension Moored Platforms

2.4.10.1 Modelling Method Comparisons

Nematbakhsh [182] uses an in house Navier-Stokes equations CFD solver and the BEM coupled SIMO-RIFLEX-AeroDyn to compare the wave-induced response of a TLP. The two models show good overall agreement, although the CFD shows increased damping due to the simplification of drag in the potential flow model. The potential flow model also misses a high frequency heave and pitch response which the CFD model shows.

2.4.10.2 VIV

Vortex induced vibration (VIV) has been known to effect the tendons of TLP structures for some time. Chen [183] used a coupled ANSYS fluid and solid physics solver to study the VIV behaviour in TLP tendons. According to the dynamic analysis results, one can conclude that even the slight forced oscillation imposed on tethers' top leads to the VIV amplification and instability risk with given low pretension value; and the situation would be aggravated provided they are orthogonal to each other in the case of "synchronization" between forced oscillation and self-excited VIV taking place in the same plane. Wang [184] used the CFD code CFX-pro to study the VIV of a cylindrical and variable cross-section tendon on a TLPWT. The variable cross-section tendon gave lower vortex shedding frequency compared to the cylindrical tendon for the same velocity.

More recently Kim [185] numerically studied the effects of VIV and found it to be an issue when the current velocity is fast enough to induce non-negligible stresses. In cases when the tendon is sufficiently long and flexible, a reduction in fatigue life was found to occur.

2.4.10.3 Higher Order Forces

Springing and ringing are TLP representative nonlinear responses of high frequency, observed in severe sea conditions. Springing phenomena are steady state and are excited by the sum-frequency components of irregular waves. Ringing is a transient motion with a bursting peak.

Liu [186] used a higher-order boundary element method (HODEM) with free-surface Green function for the computation of the first and second order hydrodynamic loading on a TLP. It was seen that the free-surface component is the most important for the heave and pitch excitations.

Roald [187] analysed the effect of second-order forces on a SPAR and TLP WT using FAST. Simulations show the effect of the second-order hydrodynamics is relatively small for the SPAR configuration, and its motion response across the high- and low-frequency domain is largely determined by the turbine's aerodynamics. On the other hand, the

influence of second-order hydrodynamics is relatively large for the TLP configuration, with the motion response in heave being dominated by sum-frequency effects.

Cong [188] analysed the effect of TLP pontoons on the first and second order diffraction forces and the possibility of trapped waves. It was found that pontoons have an appreciable effect on the diffracted wave field for long incident regular waves and increase the largest response notably when the near-trapping phenomenon occurs at the second-order.

Gueydon [189] Second order inertial effects caused by sum and difference frequency interactions have been described as important for TLPWT's. BEM requires that the body be rigid, and as second order forces depend on motion of a body to first order forces the effect of tower stiffness on body motions cannot be accounted for. The tower stiffness is seen to significantly alter the body motions. A proposed method to deal with this effect involves modifying the pitch stiffness of the rigid platform to match the flexible tower pitch natural frequency.

Pegalajar [190] used models of various complexity to determine the effects of second order wave kinematics on a 10 MW TLP FWT. Simulations were compared against experimental data from [191] the DHI Denmark wave basin. Results show that including second-order wave kinematics was not found to have a great impact on nacelle acceleration, as the effect is negated by the large inertia of the TLP wind turbine. The deep water condition tends to diminish the superharmonics in the second-order wave kinematics, which could potentially excite the pitch motion and increase the motion of the nacelle. A greater impact of the wave kinematics is observed on the surge motion, leading to a better prediction of surge motion in most cases, as expected given the more accurate description of the wave kinematics when including the sub-harmonic and super-harmonic second-order contributions. Finally, the more advanced numerical models have been employed to enhance the simple one. Given the absence of pitch motion in the Matlab model, it originally underpredicted nacelle acceleration. The stiffness of the tower was reduced to recreate the same frequency in the nacelle motion as in the Flex5 models, and the damping was adjusted towards obtaining the same nacelle acceleration as with Flex5. These modifications resulted in a much better performance of the simple model,

which is now comparable to the more advanced models in the cases presented in this study. This research thus illustrates how models of different fidelity can be combined to allow fast load assessment with simple models in early design stages, and later more accurate design through the more advanced models.

Zoul [193] experimentally analysed the effects of sharp highly non-linear waves on the ISSC TLP platform in the MARINTEK and TAMU wave basins. It was found that the nonlinear high-frequency components of the measured wave forces play the primary role in producing large high-frequency resonant motions and tensions. Strong asymmetric wave in storm seas can produce ringing if the wave hits the TLP columns, while weak asymmetric waves produce only springing. Kim [194] analyses the effect of springing by analysing the second-order response induced by sum-frequency excitations. The maximum tendon tensions are determined by fitting a non Gaussian probability distribution to the eigenvalue analysis of the second-order response. The results of this method are seen to compare favourably to those from direct simulations. Gu [192] studied the effect of transient impact loads on a TLP structure, using sin, triangular and rectangular shaped temporal loadings. The most severe impact was found to be that which generates a large yaw moment.

2.4.11 Non-Linearities

2.4.11.1 Nonlinear wave

The wave non-linearity effect becomes significant for surge and mooring line tension for large waves while floater heave, pitch motion, tower base bending moment and pontoon axial force are less sensitive to the nonlinear wave effect. In the extreme condition, linear wave theory underestimates wave elevation, floater surge motion and mooring line tension compared with fully nonlinear wave theory [195]. Experimental study of freak waves on TLP [196].

2.4.11.2 Variable Submergence

Variable submergence is the changing of the water surface elevation on the platform due to the dynamic wave structure interaction. The BEM solves a solution for a constant submergence and comes with the limitation of small amplitude motion. Accounting for variable submergence can introduce variable hyrdostatics, added mass, wave loading and buoyancy. According to Ahmad (1996) variable submergence was found to be a major source of nonlinearity and significantly enhanced the surge and heave responses, which in turn introduced tether tension fluctuations. It should be noted here that the effect of variable submergence depends on the percentage change in submerged volume with displacement. Comparing operational conditions for a traditional semi-sub shaped large water plane area TLP, such as was used to generate the findings above against a small water plane area TLP, the former exhibits the most significant changes. BEM being a linear potential flow solver cannot take variable submergence into account. Timit, called a "Exact Equations of Motion" solver only deals with nonlinear hydrostatics, keeping hydrodynamics linear. NREL's WEC-Sim has the ability to solve for instantaneous hydrostatics and Froude-Krylov forces, while radiation damping and diffraction forces are linear.

Antonutti [197] studied the effect of modelling the instantaneous wetted surface on wind and wave induced inclination of a modified Dutch tri-floater in the frequency domain. The traditional BEM approach was found to under predict heave motions in the wave energy region by 10 to 60% Antonutti [198] also analysed the same in the time domain, adding viscous forces by means of a drag only Morison equation. A range of hydro-aero coupling effects were noted. It was noted that as platforms are designed to be smaller, in order to become more economical, the effects of inclination non-linearities will become more pronounced.

Hydrostatic non-linearity have significant effect on the heave response of floating wind turbine. [199]

2.4.11.3 Slow Drift

Lupton [200] developed a frequency-domain model of a flexible floating wind turbine structure with first- and second-order hydrodynamic loading. A simplified closed from analysis of the scaling of the second-order response with the size of the platform was developed. Limited data is available to verify the error introduced by the approximations used in this paper; in the one available case, the approximate result is conservative by, at worst, a factor of 40.

Roald [187] compared the mean-drift force and mean wind turbine thrust for the OC3-Hywind floating wind turbine. For the cases where the turbine is operating, the mean-drift force is less than 1% of the rotor thrust. In more severe environmental conditions, where the turbine is idling and the rotor thrust is significantly lower, the mean-drift force amounts to about 10%–15% of the rotor thrust. However, this is still low enough to neglect the mean-drift force in general. The significance of the mean-drift force would likely be even smaller if the direct wind drag load on the tower, which has not been considered here, would be included in the simulation. The response due to aerodynamic excitation is several orders of magnitude higher than the response due to second-order hydrodynamic effects and dominates the overall response of the turbine. This holds for all considered conditions and not only for the surge degree of freedom but also for heave and pitch. From these results, it is concluded that in the case of the OC3-Hywind SPAR, aerodynamic excitation has a much more significant effect on the motion response than the excitation from difference-frequency hydrodynamic forces. A detailed investigation on the numerical estimations of the slow-drift forces of the HiPRWind 1.5 MW floating wind turbine platform was performed by Samos [201]. Experimental work in regular, bicromatic and irregular waves was used to validate the numerical predictions. The use of Newman's approximation can lead to an under estimation of the second-forces in the frequencies that will be the most energetic ones. While the full QTF approach was seen to match well with the experimental observation. A white noise QTF approach was developed where the second order force spectrum was taken as constant and the surge motion was decoupled from other responses. In this method only those difference frequency

pairs which equal the natural surge frequency are used. Discrepancies compared to those obtained with the full QTF matrix were only minimal, justifying this approach. The use of this approach reduces the computational time substantially, requiring elements only in one diagonal of the QTF matrix.

A full QTF method was shown to greatly improve the prediction of a SPAR FWTs LF responses compared with Newman's approximation [202]

The second order sum and difference frequency loads were compared in detail by Zhao et al. on a large semi submersible 5 MW and 10 MW FWT [203].

2.4.12 Wind and Wave Misalignment

Philippe [204] modelled the MIT/NREL Shallow Drafted Barge which supports the NREL 5 MW WT using a linearised version of FAST. Varying wind and wave direction was shown to excite natural modes differently.

2.4.13 Extreme/Survivability Modelling

Johannessen [205] analysed extreme wave loading on the Snorre A O&G platform experimentally and numerically using CFD. The extreme events were seen to be highly nonlinear, and it is recommended to run a large number of extreme wave time-series in order to produce the correct extreme wave load.

Karimirad [206] studied the extreme wave behaviour of a SPAR platform supporting the 5 MW NREL turbine. Two codes were compared for the study DeepC and HAWC2. DeepC calculates hydrodynamics using BEM potential flow results from Simo/Riflex, while HAWC2 uses instantaneous vessel position Morison equation. The results are seen to be both comparable to each other and experimental testing. In harsh conditions the coupled dynamic response is dominated by wind induced response. The motion response of the rigid and elastic FWT in harsh condition is found to be almost the same.

Hsu [207] modelled the extreme tensions of a 1:50 scale FWT which is similar to the VolturnUS semi-submersible platform. The modelled mooring line snap events were compared to experimental events in both frequency and amplitude probabilities.

Jamalkia [208] used a fuzzy-based damage detection method to evaluate the consequences of damage to the mooring lines of a SPAR and TLP FWT. Numerical modelling was carried out using a combination of Morison equation for the wave loading and a relative velocity wind thrust force. Results of clean signals are compared against those with generated noise in order to determine the methods effectiveness in real world situations. Results show that damage detection is carried out successfully in all classes of damage without noise. In the presence of weak noise, a significant percentage of damage classes are diagnosed with high percent of SR. By increasing damage severity in some lines, it cannot be expected to have better damage detection, because of the switching effect incidence. In both kinds of FWTs, choosing the mean amplitude of dynamic response as an extracted features give better results than corresponding ones with dominant frequencies in different noise levels. The proposed method is more compatible for SPAR than TLP. This result is because of the stronger coupling between DOFs and more wave effects in TLP than SPAR.

Wang [210] predicts the extreme values of the NREL 5 MW OC3-Hywind FWT by using a combined Peaks over threshold (POT) and declustering algorithm. The extreme response probability plot based on an optimum threshold value has been compared with the probability plot based on an empirical threshold value, and the accuracy and efficiency of the new approach have been convincingly validated. The approach is found to be more robust than the empirical approach.

2.4.14 Fault Detection and Modelling

A mixed fault detection architecture was established by integrating a model-based and a signal-based scheme to detect and isolate a mix of critical faults for FOWTs [211]. A robust reliability analysis of FWT was presented [212].

2.4.15 Platform and Mooring Faults

Bae[216] couples CHARM3D (hydrodynamics and mooring loads) and FAST to analyse the OC4 DeepCwind semi-submersible platform with a broken mooring line and subsequent loss of power line. Simulations show the drift distance with one mooring line

broken can be over 700 m, which could be a significant risk to neighbouring FOWTs or offshore structures. Platform and turbine orientations can be significantly changed due to the loss of one mooring line. As a result, the nacelle yaw error became large, which can be a negative effect for FOWTs. However, there were no significant differences in the overall power output as a result of the active blade pitch and generator torque controllers when power cable is not disconnected during the platform drift. When horizontal offset becomes large, power-line is likely to be disconnected and its influence was also investigated. The changes in the structural responses, such as tower base shear force, after mooring line loss can be serious, so checking the relevant structural reliability is an important factor when considering risk assessment associated with FOWT. The platform and wind turbine responses after one mooring line loss can differ depending on the mooring pattern, failed mooring position, and the direction of the environmental loadings, so detailed simulations with various failure scenarios should be carried out including drift directions and distances, especially for the design of farm configurations.

2.4.16 Crew Transfer

Martini [217] used a frequency domain approach to model the behaviour of a catamaran completing a crew transfer operation to the OC4 semi-submersible FWT. Findings indicate that the response of the vessel is importantly affected by the motions of the platform, especially when the motions of the latter is expected to be large. Contact forces are larger when the relative motion of the two bodies would be larger, if they were free to move. Access is considered possible when no-slip conditions occur at the fender, and when the relative rotations of the two bodies are within a certain tolerance. For short, regular waves beam seas provide the best configuration for access. For longer waves, head seas are preferable, also taking advantage of the platform shielding effect. Accessibility has been calculated for an offshore location in Scotland, using 34 years of hindcast data with hourly resolution. On average, the chosen site resulted to be accessible for 23.7% of the time. July is the month in which access is more probable (50% of the time, on average), while January the month in which access is less probable (9% of the time). A very large uncertainty associated with those values has been calculated,

which highlights the importance of long-term reliable data to correctly design offshore maintenance strategies.

Martini [218] also numerically analyses the availability of a walk to work system for a semi-submersible FWT. A multibody constrained model has been developed in the frequency domain. Two vessels have been evaluated: a catamaran with fender and a supply vessel with motion-compensated gangway. For the catamaran, contact forces and displacement transfer functions have been calculated. For the supply vessel, transfer function for the relative motion at the gangway tip have been computed. Accessibility was calculated using hindcast data supposing that the vessels operate a semi-submersible floating platform off the coast of Portugal. With the catamaran, access is possible for 20% of the year while with the supply vessel for 76% of the year. Accessibility depends strongly on the vessel and floating platform properties, the fender friction coefficient, the gangway compensation limits and the confidence factor used for the calculation of the extreme responses.

2.4.17 Risk and Uncertainty Analysis

Raed [219] used a First Order Second Moment method (FOSM) to analyse the uncertainty in the OC4 semi-submersible platform. The maximum contribution of the total uncertainty variance comes from the wave height and the wave period for the semi-submersible floating support structure. Marine growth was ranked as a secondary level of uncertainty. Proskovics [220] provided a methodology for the risk assessment of deep water FWT substructures. Four categories of risk were identified: technology risks, manufacturing risks, health, safety and environmental (HSE) risks, and commercialisation risks. By using and adapting a standard methodology for risk assessment, early risk identification, analysis, evaluation and treatment of those risks relating to the design of floating substructure technologies can be performed. When applied as part of a holistic risk management process the procedures outlined in this paper should lead to de-risking of floating wind technology not just in terms of the technological risks associated with innovations in engineering but also in terms of the manufacturing, HSE and commercialisation risks.

2.5 Design Optimisation

2.5.1 Deployed Environment

Amundsen [221] introduced the effect that having a WT cut-out sea state, would have on power production and survival modes. Environmental data from seven offshore oil platforms in the Norwegian and North Sea were analysed. A control strategy similar to the high-wind hysteresis, where the WT would only cut back in once the sea state dropped below a cut-in limit was tested. This was introduced in order to avoid a high frequency of cut-outs/ins. Control strategy's using predicted sea-states are also tested. These were tested on a tension leg buoy (TLB). When the acceptable limit of energy loss was set to 1%, the optimal Hs,cut-out was found to be 8 or 9 metres.

Martini [222] analysed how power production varies depending on meto-ocean conditions for a sample semi-submersible FWT located off the coast of Santander, Spain. The behaviour of the wind turbine is simulated in the time domain for a subset of 500 hourly conditions, selected using a maximum dissimilarity algorithm (MDA), to reduce the computational effort. Results regarding floating platform motions are then interpolated for the whole set of data using radial basis functions (RBF). Tower inclination and hub acceleration are selected as relevant operating parameters. When one of them exceeds its safety threshold, the machine is supposed to be stopped. If no stops are considered, the capacity factor is 39%, while imposing more restrictive tolerances results in a non-linear decrease of the energy yield.

Zountouridou [223] studied FWT for the Mediterranean Sea while Hwang [224] studied FWT for Korean waters.

Onstad [225] analysed 2 years of data from a Seawatch buoy located at the HyWind demonstration site. Analysis shows that the 2 years the Seawatch buoy carried out measurements were a relatively calm period. Therefore it is reason to believe that the 50 year extreme values for wind gust and wave should be higher than 30.5 m/s and 13.3 m, respectively. As eddies are present at the west coast of Norway, the 50 year extreme value of current at 20 m depth, is expected to be higher than 1.4 m/s. In order to correct for the calm measuring period, a long term extrapolation of the buoy wind data was

conducted. Due to a low wind speed correlation of R2 speed = 0.77 between the target and reference data and a poor Gumbel fit, the calculated 50 year extreme value of 44.7 m/s at hub height is found to be inaccurate. The presented long term wind direction distribution is more plausible with a wind direction correlation of R2 dir = 0.94.

A numerical and experimental analysis of FWT water depth effects on both slack and taut moored systems was performed [226]. Results showed platform heave motion with slack mooring configurations and mooring line top tension are more sensitive to water depth.

It is recommended to perform detailed operation and maintenance modelling to adequately capture operational expenses of FWT farms [227].

2.5.2 Platform

There have been numerous studies on finding the optimal FWT platform design. The design of TLP using simplified method is presented by Uzunog in[228].

Sclavounos [229] used a pareto front optimisation technique and a fully coupled numerical model to determine the most economical FWT platform design. The parameter space included designs moored by tension and catenary lines. The optimized TLP and Slack Catenary designs lead to low nacelle acceleration RMS values in a ten meter seastate. In milder wave environments the nacelle accelerations are expected to be a lot lower. Other than cost, the water depth presents no restrictions, and for a number of the TLP designs considered in the present study the larger the water depth the lower the nacelle acceleration. Subsequent studies have shown that this work had a flawed mass moment of inertia calculation and thus results are non optimal.

Lee [230] also used a a pareto front optimisation technique and a fully coupled numerical model to determine the most economical catenary moored FWT platform design. it was concluded that as the water depth becomes shallower, the dynamic performance becomes more challenging and harder to satisfy the design requirements than it is at deep water depths.

Myhr [233] attempted to make a TLB FWT more transparent" to wave loading by minimising the structural volume of the splash zone. The vertical cylinder in the splash

zone was replaced by two different support structures, firstly a space frame and secondly three slender cylindrical columns. Numerical results indicate that the space frame may require similar pretension to a conventional TLB in order to maintain tensions during extreme events. Replacing the cylinder in the wave action zone with a space frame may reduce the wave forces by a significant amount as long as bracing is either unused or kept to a minimum.

Fredheim [234] quantified the fatigue life of the braces of a semi-submersbile FWT.

Hall [235] used a genetic algorithm approach to evaluate the best floating platform designs for SPAR, semi submersible and tension moored FWT. A pareto front based on RNA acceleration is developed from the study. Results indicate the following: At no point does a SPAR buoy design sit on the Pareto front. The presence of these relatively complex four- and seven-cylinder platforms on the Pareto front, and the absence of simpler buoyancy- or ballast-stabilized designs, would appear to challenge the conventional wisdom in support structure design for floating wind turbines. However, the complexity of these designs may carry additional costs and risks not accounted for in the framework. If accounted for, these factors could tip the balance back toward more conventional single- or three-cylinder platform designs.

Sethuraman [236] introduced the nacelle magnification factor (NMF) as a novel metric in order to understand the overall platform behaviour and help decide the hub height that ensures lowest nacelle displacement. The NMF is a ratio between the pitch RAO at the nacelle and at COG. Xun Meng [237] used a multi criteria decision analysis (MCDA) method-TOPSIS for the design optimisation of TLP to support a 4 MW WT, in comparison with a monopile and truss. It consisted of a combined economical and environmental optimisation function, considering not only commonly used parameters such as mass of steel, but also effects such as seabed disturbance and whether the support structure type has been certified for WT use previously.

Chodnekar [238] analysed a parameter study (varying the diameter, draft and ballast weight) on a TLP supporting a 5 MW WT. It is seen that by maintaining low reserve buoyancy (initial tension) and high metacentric height, the maximum force in the mooring cables can be reduced.

Meng [239] used a parameter based optimisation study to find the optimal design of a TLP to support a 5 MW WT. The maximum displacement, maximum Von Mises stress ,dynamic excitation constrains, sum-frequency effects and positive tension requirements of the TLP are selected as state constraints for the design optimization. Wang [240] investigated the effects of TLP spoke dimensions on the motion of a FWT. Five models of various spoke length were analysed using FAST. Results indicate that dynamic characteristics improve when spoke dimension is considered. The primary effect of spoke on the dynamic characteristics is that the spoke dimension effect increases the added mass matrices. This effect was most evident in the yaw-yaw direction, where the M66 value increased from zero to E5. Moreover, A42 and A15 values were not neglected. For the same spoke dimension ratio, when the total displacement increases, the added mass matrices also increase. Damping did not always increase and became constant at some point.

Leimeister [241] presented a methodology for upscaling a FWT to support WTs with larger power rating. Upscaling of the OC4-DeepCwind semi-submersible floating platform from 5 MW to 7.5 MW was performed. Two upscaled floating platforms(water and concrete ballasted) were designed with the focus on hydrodynamic performance, and compared regarding their static properties and dynamic behaviour. The resulting platforms presented some issues as follows: Extremely high stability limits, of 73.2 (water ballasted) and 92.8 (concrete ballasted). The damped natural period in heave (19.1 s) is on the lower side of the typical range for semi-submersible platforms. For an optimized upscaling procedure, it is recommended that different scaling factors should be used for each component (smaller scaling factor for the upper columns, larger one for the base columns), in order to achieve higher natural frequencies in heave. This inhomogeneous scaling would most likely also influence the amount of displaced water volume.

Power optimisation by rearranging the wind farm lay out in real time by passively repositioning of floating offshore wind turbines using existing turbine control degrees of freedom [242].

2.5.3 Mooring System

Carbono [244] used a genetic algorithm (GA) comprised of 10000 iterations to optimise the mooring system for a semi submersible O&G platform for multiple steady state environmental load cases. Hordvik [245] investigates methods for selecting and optimising the mooring system for FWT's in shallow water. Clump weights are recommended in this situation for reducing mooring tension. Goldschmidt [246] suggested sharing mooring and anchor systems for multiple FWT's. Results show that although no natural period resonance effects occur, displacements can become large and are increased when greater numbers of FOWTs are coupled. This will cause issues for the power cable. Rodrigues [247] analysed a novel FWT concept where the WT's operational steady state position would be adjustable by varying the mooring line length. The work uses an evolutionary optimization strategy in a nested configuration which simultaneously optimizes the anchoring locations and the wind turbine position within the mooring lines for each individual wind direction. up to 4.4% higher wind farm efficiencies were observed when larger manoeuvre areas were assigned to the turbines, which may be traduced to a 5% reduction of the LPC and a capital gain of 35 million euro.

Weller [248] described how synthetic ropes possess performance characteristics and economies of scale which are in many respects superior to steel components. A state of the art review of these ropes are carried out.

An innovative mooring system has been designed to reduce the pitch motions of FWT [249]. A methodology for modelling and fatigue life monitoring of mooring lines for FWTs based on the reliability approach is shown [251].

Simulations of a hydraulic based mooring system that enables a variable, non-linear line stiffness characteristic demonstrate that mean mooring line loads can be reduced in the region of 9–17% through a combination of lower static and dynamic loads, while the peak loads observed in extreme conditions were reduced by 17–18%. These load reductions, however, come at the expense of some additional platform motions [252].

2.5.4 Integrated Design

Due to the highly complex aero-hydro-elastic controller interactions it seems unwise to design each sub component of the full FWT in isolation. Integrated design techniques are gaining popularity as the following reveal.

Sandner [253] introduced a simplified single DOF (pitch) model in order to design the WT controller. This was extended to a 9-dof multibody system with simplified aerodynamics and Morison equation allowing a pre-dimensioning of the structure. Lemmer [254] presented the integrated conceptual design of FOWT on a concrete torus semi-submersible platform supporting the 10 MW INNWIND reference wind turbine. A simplified linearised coupled simulation model has been used with limited information on the aerodynamic blade characteristics. A linear model predictive controller (MPC) was compared against a PI-controller. It was used to control the pitch and generator torque to minimize structural loads and to guarantee constant power output in above rated wind speed.

2.6 Wave Field

2.6.1 Near Trapping

Arnott [255] experimentally measured the wave field and runup in and around a TLP. In addition to significant runup on the legs, the large dimensions of this platform were seen to cause large waterspouts to erupt from the surface in steep waves. This should be taken into account for the air-gap required for the deck or in the case of the FWT the WT blades. Using numerical nonlinear methods on an array of four fixed vertical cylinders Bai [256] identified the following higher order excitation phenomenon. At one specific incident wave frequency and direction one trapped mode is excited by second order wave effects, while a different trapped mode (having similar symmetries) is excited by third order wave effects. Wolgamot [257] considered aspects of wave radiation from arrays of floating truncated cylinders through observation of empirical results. A pumping mode with all cylinders heaving as a single rigid body appears to be a common feature of

cylinders arranged in a circular fashion, and with sufficiently many cylinders approaches a wave-free mode. These near-wave-free modes may be simply adapted to form near-motion-trapping structures by varying the cylinder geometry. As the pumping mode is not associated with rapid variation of the hydrodynamic coefficients this is relatively straightforward. It is remarkable that such a close approximation to a motion-trapping structure can be formed so simply, by a structure which has neither a true moonpool nor a complicated profile below the waterline

2.6.2 WEC Array

Complex interactions exist between multiple floating bodies. As such specific modelling methodologies must be used for multi body hydrodynamics. O'Cathain [261] used Newton-Euler equations with eliminated constraints to model a two-body hinged-barge system. This method results in the convenient integration of active loads (as opposed to interbody constraint forces) acting on the multibody system.

In the case of extracting power from waves, arrays of WEC should be spaced to optimise power production. Ashton [258] experimentally measured the power production in an array of 5 WEC's and found a notable power increase in some locations.

Haller [259] experimentally analysed the wave field in the nearfield of an array of five PA WEC's. Denser WEC-arrays were seen to lead to more shadowing. Frequency and directional spreading in the wave field smooths the wave height variation and reduces the shadow in the lee of the arrays.

Stratigaki [260] experimentally studied an array of 5 x 5 heaving WEC in the Shallow Water Wave Basin of DHI (Denmark). Results show the following: Wave height decrease is observed only after the third row of 5WECs for the aligned array. For the staggered array, wave height decrease starts between the second and the third row of 5 WECs for long-crested waves. The highest wave height increase is found upwave of the front row of 5 WECs for both arrays (the first ones facing the incoming waves), as a result of significant diffraction effects. Wave height increase has a "parallel" pattern to the front WEC row. This pattern becomes diagonal towards the WEC columns located at the sides of both WEC arrays, and is a result of increased wave height at the sides of the

array. The highest wave height dissipation is observed at locations, at least at distance 10D downwave of the WEC array, and within a zone of width -5D <X <+5D

2.7 HAWT vs. VAWT

Paulsen [262] compared the 5 MW DeepWind Vertical Axis Wind Turbine (VAWT) to the NREL 5 MW Horizontal Axis Wind Turbine (HAWT) SPAR. Annual energy production (AEP) values were shown to be similiar. Increasing wind speed causes power variations to increase for the DeepWind WT, which is different compared to the pitch controlled NREL 5 MW, which has less power variability. Chowdhury [263] studied the effect of inclination angle on the power production of VAWT's using CFD. The VAWT in tilted condition produces greater torque at the downwind proportion of spin in comparison to an upright one. The bottom part of tilted turbine's downwind blade gets fresh air. Whereas, in up- right condition, the entire downwind blade gets exhaust air of the blade from upwind condition. The wake is also deflected downwards, meaning farms of floating HAWT's could be placed closer together that their fixed counterparts.

Cheng [264] compared operational and survival conditions for 3 bladed 5 MW HAWTs and 2 to 4 bladed 5 MW VAWTs on the same semi submersible platform. The results show that the three- and four-bladed floating VAWTs and the three-bladed floating HAWTs considered have similar performances in the variation of generator power production, in the maximum tower base bending moment and in the fatigue damages at tower base and mooring lines. However, The annual power production of the floating VAWTs is about 17.6% less than that of the floating HAWTs, the maximum tensions in mooring line for the three- and four-bladed floating VAWTs are approximately four times higher than that of floating HAWTs, which implies a significant challenge for their mooring systems. The maximum tower base bending moment and fatigue damage in the two-bladed floating VAWT are extremely significant. Cheng [265] also compared a SPAR supporting a HAWT and VAWT.

2.8 Platform Dampers

2.8.1 Heave Plate

Tao [266] analysed heave plate parameters by a finite difference method to solve the incompressible Navier-Stokes equations in the primitive-variables formulation. The strong influence of diameter ratio was found on the vortex shedding and the viscous damping. However, the effect of changing diameter ratio was found to be dependent very strongly on KC number. Within the parameter range of KC up to 1.0 calculated in this study, it is found that the form drag due to flow separation and vortex shedding generated by the sharp edges of the disk are the dominant mechanisms of energy dissipation. Selection of the disk geometry in terms of the diameter should be considered in combining with KC number of heave oscillation since the disk geometry effect on drag is strongly influenced by KC number. A general trend of increasing damping ratio on increasing diameter ratio is found from Tao's numerical calculation. However, any increase beyond a certain diameter would not result in appreciable increases in drag. Based on the axisymmetric finite difference method, it is suggested that the disk extension be at least four times the typical heave amplitude to achieve the optimum drag effect.

Antonutti [197] analysed the effect of varying the submergence depth of heave plates on a modified Dutch Tri-floater using BEM. Lopez [267] performed large scale physical experiments and CFD modelling of heave plate effectiveness. Results indicate that damping and added mass coefficients show, on one hand, a small dependence with frequency and, on the other hand, a large dependence with the motion amplitude. A conservative damping coefficient equal to 6% of the critical damping can be considered adequate for the prototype heave plate for frequency domain analysis. A corresponding drag coefficient equal to 4.0 can be used in time domain simulations to define Morison elements. Added mass coefficient values predicted with the potential solver (WADAM) are not accurate enough. The used solver does not contemplate modelling thin plates with doublets. The relatively low accuracy of the results highlights the importance of these elements when performing potential flow simulations of offshore platforms which include thin plates. Zhu [268] proposed a novel moveable heave plate semi-submersible

(MHS) platform. The conceptual design shows the optimum connection stiffness between heave plate and platform. Critical design parameters are identified. Frequency regions were damping performance is greater than a traditional heave plate are identified. Unlike TMD's this tends to be away from the natural frequency of the platform.

A heave plate could significantly reduce the mooring tension under extreme sea conditions [269]

2.8.2 Air Spring Vibration Absorber

Bian [270] proposed a novel air spring type vibration absorber (VAB) to allow the deployment of TLP's in ultra deep water (~2400 m).The VAB consists of a vertical caisson with bottom open to the sea and top enclosing an air chamber. The mass of the water column interacts with the TLP to produce pressure variations out of phase with the heave and pitch resonant motion of the floater. Using this system the tendon axial stiffness requirement is reduced, and tendons can be designed for an ultra-deepwater TLP which essentially scale linearly with water depth, instead of quadratically, as is the case for a conventional TLP.

2.8.3 Wave Energy Convertors

Borg [43] proposed the idea of a combined wind and wave energy platform system. The WEC's in this system had the shared goal of reducing platform motions and generating power. A 5 MW VAWT was modelled on the Dutch ti-floater, using a single additional DOF in heave for the WEC. Rather than modelling a specific WEC design, trying to optimize it withinits dynamic characteristic constraints, here the optimum damping and stiffness coefficients were found that would represent the 'ideal' damping device for either the energy generation or motion reduction cases.

2.8.4 Tuned Mass Dampers

Si [271] modelled and optimised a tuned mass damper (TMD) for the OC3 Hywind FWT. The tuning is based on D'Alembert's principle. FAST-SC is used to simulate the effects of the TMD. The results demonstrate that the design of TMD with small

spring and damping coefficients will achieve much load reduction in the above rated wind speed condition. However, it will deteriorate system performance when the turbine is working in the below rated wind speed or parked situations. In contrast, the design with large spring and damping constants will produce moderate load reduction in all working conditions.

Ha [272] proposed the use of multilayer tuned liquid dampers (TLD) to reduce the pitch motion of SPAR FWTs.

2.8.5 Tuned Liquid Column Dampers

Lee [273] physically modelled a tuned liquid column dampers (TLCD) on a TLP structure. Using the TLCD a reduction in pitch motion of up to 50% could be observed. For the surge motion, the reduction can reach as high as 30% in general. In the tests of larger wave-height, mitigation effect is better and similar phenomenon is also observed for longer period of waves. A large reduction in tendon tensions was also observed. Zeng [274] proposed a novel type of TLCD which involves a number of additional horizontal bends. The effective natural frequency of the TLCD depends on its length, and thus limitations of its use is often deployable deck space. The S-shaped TLCD has the advantage over a conventional TLCD in this regard. It was tested on a TLP and is found to be effective in reducing platform surge and heave motions.

2.9 Gaps in the literature

An extensive literature review of floating wind turbine design, optimisation, simulation and experimental validation has been carried out. This review has focused on tension moored floating wind platforms, with the following gaps in the research literature identified:

- Representative metocean design values for Irish offshore sites.
- Parametrisation of a floating wind platform design with regards to tow stability, especially for tension moored type.

- Detailed effects of anchor misposition on tension moored platform response and forces.
- Detailed understanding of the effects a flexible tower has on a tension moored floating wind turbine, especially regarding how to account for such in early stage concept design.
- The design of a tension moored combined wind and wave energy converter.
- Details about the viscous behaviour of TLP platforms in varying sea-states.

This thesis will attempt to address these points.

Chapter 3

Methodology

3.1 Description of the Software used in the Course of This Work

In the course of this work, numerous software packages were used, modified or developed by the author. A description of the most often used packages are given below. Pre and post processing of simulations was carried out using author generated MATLAB scripts.

3.1.1 FAST

FAST (now renamed OpenFAST) joins aerodynamic, hydrodynamic, control, electrical system and structural dynamics models to enable coupled nonlinear simulations of offshore fixed and floating wind turbines in the time or frequency domain. It is an 18 DOF (6 FWT platform DOF and 12 WT DOF) solver written by NREL and its use is standard in the research world. It has been validated by numerous cross code and physical model comparisons [275]. The following FAST modules have been used in the course of this work:

3.1.1.1 HydroDyn

The HydroDyn module calculates the hydrodynamic forces on the FWT platform, either through Morison equation or through the use of potential flow theory forces. To use the

latter option, the hydrodynamic parameters must be input from a hydrodynamic solver such as WAMIT/NEMOH/AQWA etc.

3.1.1.2 MoorDyn

MoorDyn is a finite element mooring line force and position calculation tool. The model accounts for internal axial stiffness and damping forces, weight and buoyancy forces, hydrodynamic forces from Morison equation, and vertical spring-damper forces from contact with the seabed. A limitation of this tool is the fact that hydrodynamic forces assume still water, only taking into account the movement of the mooring line itself and not waves or current.

3.1.1.3 AeroDyn

Aerodyn is an aerodynamics module for calculating the forces of a horizontal-axis wind turbine and tower. Aerodyn can take into account the following effects, rotor wake/induction, blade airfoil aerodynamics, tower influence on the fluid local to the blade nodes and tower drag. Aerodynamic calculations are based on the principles of actuator lines, where the 3D flow around a body is approximated by local 2D flow at cross sections, and the distributed pressure and shear stresses are approximated by lift forces, drag forces, and pitching moments lumped at a node in a 2D cross section.

3.1.1.4 BeamDyn

BeamDyn is a time-domain structural-dynamics module for slender structures. The model underlying BeamDyn is the geometrically exact beam theory (GEBT) [276]. GEBT supports full geometric nonlinearity and large deflection, with bending, torsion, shear, and extensional degree-of-freedom (DOFs); anisotropic composite material couplings (using full $6*6$ mass and stiffness matrices, including bend-twist coupling); and a reference axis that permits blades that are not straight (supporting built-in curve, sweep, and sectional offsets). The GEBT beam equations are discretized in space with Legendre spectral finite elements (LSFEs). LFSEs are p-type elements that combine the accuracy

of global spectral methods with the geometric modeling flexibility of the h-type finite elements (FEs) [277]

3.1.1.5 ServoDyn

Servodyn models the WT controller, enabling control over the following elements, pitch, generator and torque. The following controller types are available; Simple variable-speed torque control, simple induction generator control, thevenin-equivalent induction generator control, high-speed shaft brake, nacelle-yaw control,

3.1.1.6 BMODES

BModes is a finite-element code that provides dynamically coupled modes for a beam. It is used to generate the mode shapes of the tower in a coupled platform, moorings, tower, RNA model. As Fast requires uncoupled modes to run the modes generated by BMODES are decoupled by selecting the most prominent DOF of each mode, before passing a best fit polynomial through that component. A Matlab script provided by NREL is used to generate these coefficients. FAST requires these polynomial coefficients to sum to unity as the mode shapes are normalized by the tip displacement.

3.1.2 Ansys AQWA

Ansys AQWA is a potential flow theory boundary element method (BEM) solver. The hydrodynamic parameters are solved for the first and second order effects. Slow drift, difference frequency effects can be solved either through the Newman's approximation or through a full calculation of the quadratic transfer functions (QTFs).

3.1.3 NEMOH

NEMOH is an open source first order potential flow theory BEM solver developed by researchers at Ecole Centrale de Nantes. NEMOH is written in python and a MATLAB interface toolbox is supplied with the download.

3.1.4 OrcaFlex

Orcina's OrcaFlex is a time domain hydrodynamic solver, floating bodies can be solved by Morison equation or by direct input of hydrodynamic parameters (from WAMIT or Ansys AQWA), mooring lines are solved by a finite element model, using Morison equation. Unlike MoorDyn, the hydrodynamic forces are calculated using the relative velocity between mooring line element and wave/current velocity. For implicit integration OrcaFlex uses the Generalised-alpha integration scheme [278]. The forces, moments, damping, mass etc. are calculated by local equations of motion for each free body and each line node. Then the system equation of motion is solved at the end of the time step. Because the position, velocity and acceleration are unknown at the end of the time step an iterative solution method is required.

In OrcaFlex rotations are defined by Euler angles. Rotations are applied in the following order, first about the global z axis (yaw), then the new localised y axis (pitch) and finally the localised x axis (roll).

While not available at the start of this thesis, Orcina has since added the functionality to calculate hydrodynamic parameters using OrcaWave and full coupled aerolesatic anlysis of FWT's in OrcaFlex itself.

3.2 Simulation Modelling Approach

The general simulation approach used in the course of this work is outlined in this section. As multiple different software are required the process is shown in a simple flow chart in Figure 3.1. A 3D CAD software (Solidworks) is used to create a 3D model of the floating platform. In Chapter 5 the generation of the 3D model will be bypassed by automated generation of a mesh in Matlab. Ansys AQWA is used to calculate the floating body hydrodynamic parameters. Additional linearised viscous damping and mooring stiffness matrix are input at this stage in order to correctly calculate the second order forces. The calculated forces are then imported into the time domain solver OrcaFlex, where Morison equation drag only elements and finite element mooring lines are added. Post processing of results is carried out in Matlab.

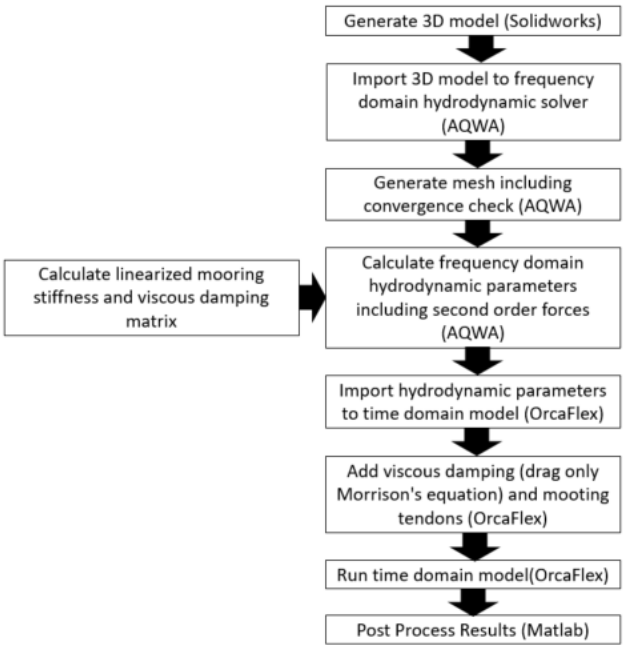


Figure 3.1: Simulation Flow Chart

3.2.1 Viscous Drag

In this work viscous drag is modelled using modified drag only Morison equation elements, where the inertia term is set to zero. In this method the added mass term in Morison equation is set to zero. Potential flow theory methods cannot account for viscous effects hence the additional requirement here. The drag term scales to the square of the relative velocity and is calculated using the following equation $F_d = \frac{1}{2}\rho C_d D v_r |v_r|$, where ρ is the density of water, D is the representative horizontal dimension of the element, and v_r is the relative velocity between the vessel and wave or current particle velocity. The forces and velocities are calculated and applied at the elements centre. Drag coefficients are generally sourced through existing literature, experimental test campaigns or from CFD models. In this section the drag coefficients are selected from still water free decay tests, with the method detailed in Section 4.3.3.

3.2.2 Tendon Stiffness

In a tension moored platform the mooring lines provide not only the station keeping forces in the horizontal DOF (surge, sway and yaw) as in typical moored floating bodies, but also the major restoring force in heave, pitch and roll. The mooring stiffness matrix is shown in Equations 3.1 to 3.6, where T is the pretension of a single tendon, L is the stretched length of the tendons, $K_1 = EA/L_0$ is the tendon optimum stiffness E is the Young's modulus, A is the cable cross sectional area, L_0 is the cable unstretched length, D_f is the vertical distance from centre of gravity to fairlead, R_f is the horizontal distance from centre of gravity to fairlead and x is the surge motion. The stiffness terms are taken from [279] with additional nonlinear coupling terms from [280]. In this work the stiffness terms are only used to calculate the first order RAO in AQWA in order to correctly produce the second order forces, and thus the nonlinear terms, which include x are neglected. The time domain OrcaFlex model includes these stiffness terms including all cross coupling through a finite element tendon model. Bending stiffness is neglected in these stiffness terms as the tendons are nearly aligned in a straight line because of the high cable pretensioning [73], especially for the small body motions assumed in potential flow theory model.

$$C_{11} = C_{22} = 6T/L + 6K_1x^2/L^2 \tag{3.1}$$

$$C_{33} = 6K_1 \tag{3.2}$$

$$C_{44} = C_{55} = 6T/D_f^2/L + 3K_1R_f^2 + 6TD_f \tag{3.3}$$

$$C_{66} = 6TR_f^2/L \tag{3.4}$$

$$C_{31} = 6x(AE - T)/2L^2 \tag{3.5}$$

$$C_{42} = C_{24} = -C_{51} = -C_{15} = 6TD_f/L \tag{3.6}$$

3.2.3 Natural Periods

Natural periods of the floating platform are calculated for the uncoupled DOF by Equation 3.7. In reality due to the highly coupled DOF and nonlinear forces, the natural periods will be non constant and instead a function of excitation amplitude. For small body assumptions where the coupling between DOF is minimal, the uncoupled natural periods will be useful. For more detailed analysis of the fully coupled non constant natural periods a backbone analysis should be performed. For the horizontal DOF, surge, sway and yaw, the hydrostatic restoring force, k, is zero.

$$T_n = 2\pi\sqrt{(M + M_a)/(k + c)} \tag{3.7}$$

3.2.4 Methods to determine RAO

Response Amplitude Operators (RAO) are commonly used by an offshore structure designer, modeller and operator in order to have an understanding of the structures responses across all frequencies the platform will have dynamic response to. After determining the hydrostatics of a platform, calculating the RAO is generally the next step in evaluating a potential design. As offshore structures must operate in complex offshore wave conditions with multiple wave frequencies present at any instant, and responses such as second order motions may come at frequencies outside the original excitation frequency, determining how to calculate RAO is not as trivial as first assumed.

The basic idea behind an RAO is to divide the response of the structure by the magnitude of the waves exciting it. Numerous methods exist to determine the RAO of floating platforms. This section compares the results of three methods. The first method termed the Energy Spectra Method involves dividing the square root of the response energy spectra by the square root of the input energy spectrum. The second method termed the Cross Correlation Auto Correlation (CSAS) method involves dividing the cross spectral density of the input and output by the auto spectral density of the input.

The third method is that produced by the commercial software MIKE21 and is black box method, with no information given on how it is generated. In the following formula H(ω) is the FRF, Sxy(ω) and Sxx(ω) are the cross-spectral and auto-spectral densities of the input x(t) and the output y(t).

$$RAO_{ES} = H(\omega) = \frac{\sqrt{Sy(\omega)}}{\sqrt{Sx(\omega)}} \tag{3.8}$$

$$RAO_{CC} = H(\omega) = \frac{Sxy(\omega)}{Sxx(\omega)} \tag{3.9}$$

As the MIKE21 method was not used for this PhD work, data from an experimental campaign on a generic FWT was used in order to make this comparison. This generic semi-semi submersible platform was part of a commercially confidential test campaign, and tbhus no further information on the platform may be provided here. All methods pick up the pitch natural frequency response at 0.0287 Hz, although the magnitudes vary significantly at 63, 6.9 and 3.3 °/m for the Energy Spectra, MIKE21 and CSAS methods respectively. In the wave frequency region (0.06 - 0.19Hz) all three methods are seen to give near exact results. The FFT method is seen to give extremely large values outside of this region, especially in the low frequency region due to the division by extremely small, near zero wave amplitudes. For the analysis of second order motions, the CSAS method gives more intuitive results to the analyst and is thus used for this work. For more information the readers are directed to this work [286].

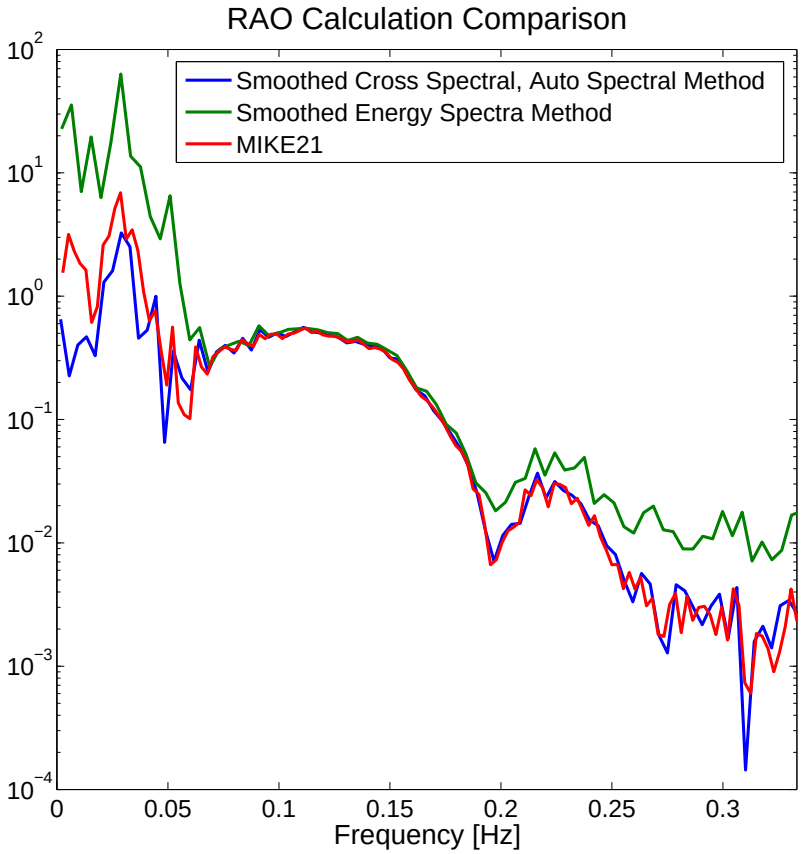


Figure 3.2: Comparison of RAO Calculation Method

Chapter 4

Numerical Modelling of FWT

In this chapter the numerical modelling approach used in the course of this work is outlined. Common methods in the design and analysis of floating offshore structures include parameter estimation from first principles, numerical modelling and physical experimental tank testing. The Technology Readiness Levels (TRLs) are generally used to state a technologies maturity along a standardised path. This research will involve TRL levels 1 to 3, and thus a full reliance on numerical modelling and physical scaled experimental tank testing is undertaken.

The numerical modelling approach is validated by a 1/30th scale model of a tension moored floating wind turbine, HEXWIND. The platform motions and tendon tension in regular wave, JONSWAP irregular waves and observed rogue waves are used for the validation. The mean thrust force on the scale prototype is modelled using a high RPM ducted fan. In this chapter the tower is modelled both experimentally and numerically as a rigid cantilevered beam, where as in a deployed FWT the tower is a flexible element.

The use of numerical modelling allows a platform developer to efficiently optimise the FWT design, de-risking the complete deployment life-cycle. The flow of the chapter is as follows: The HEXWIND platform is introduced and the general simulation procedure is outlined, methods to calculate viscous drag forces, tendon restoring stiffness, natural periods and second order forces are then detailed. Numerical convergence studies on various element discretisations are given next. The numerical model is then validated by a 1/30th wave basin test campaign, an introduction to the experimental set up is

followed by still water fitting of drag coefficients. Comparisons between the numerical and experimental results in motions and tendon tensions are given for regular, irregular and rogue waves. Comparisons between results using first order only forces and second order forces generated using Newman's approximation or full QTFs are given. Uncertainty in the experimental incident wave is accounted for by performing simulations using both a theoretical wave spectra and observed wave time series. An analysis of drag coefficient variation with sea-state is given. A numerical tendon pretension sensitivity study is performed as the experimental test campaign showed tension slippage across the test duration.

A detailed numerical and experimental test campaign led to the following conclusions about the HEXWIND FWT platform:

- A numerical model of the HEXWIND FWT has been developed and validated by 1/30th scale experimental wave basin tests.

- Slack tendon events of the HEXWIND platform have been observed by both physical tank testing and numerical modelling indicating a failure in the design

- A nonlinear increase in response to increasing wave heights was identified with greatest significance for heave motions between 8 and 10 seconds and pitch between 7 and 8 seconds.

- The effects of second order difference frequency loads are minimal on the HEXWIND platform.

- Individual tendon pretension variations from the design pretension was found to have most significance on the pitch and roll motions.

- Surge drag coefficients derived from still water free decay tests were found to be unsuitable for irregular wave tests. Fitting of drag coefficients to irregular wave motion results showed a seastate by seastate approach is required to correctly predict the platform drag effects.

4.1 HEXWIND Numerical Modelling

The HEXWIND platform as shown in Section 2.2 Figure 2.7 was numerically modelled using a combined ANSYS AQWA and OrcaFlex model. Details of the platform can be seen later in this chapter in Table 4.4. ANSYS AQWA is used to calculate the hydrodynamic and hydrostatic parameters, that is the hydrostatic stiffness, the radiated wave added mass and damping, the Froude-Krylov and diffraction forces and the second order, difference-frequency and sum-frequency forces. In order to correctly calculate the second order wave forces the tendon stiffness most be correctly accounted for in the frequency domain model. Wave periods are calculated from 2.5 s to 125 s with 46 evenly spaced periods in between. Wave directions are calculated at 30° spacing from 0° to 330°. OrcaFlex computes a time domain model, solving the Cummins equation for radiated wave effects and the tendons by a finite element model. Hydrodynamic loading on the tendons is applied by a Morison equation model.

4.1.1 Natural Periods

Natural periods of the floating platform are shown in Table 4.1. For the design of TLP platforms the horizontal DOF natural period should be below the wave period region, while the other DOF natural period should be above it. Hydrodynamic parameters are only calculated down to 2.5 s, due to mesh size limitations, and thus the heave and pitch natural frequency lie outside this range. As a frequency domain analysis of the experimental platform motions shows no significant motions at these natural periods, this limitation is deemed acceptable.

Mode	T_n [s]
Surge	50.32
Heave	1.03
Pitch	0.39

Table 4.1: Natural Periods

4.1.2 Second-Order Loads

For tension moored platforms, with some natural frequencies above the wave frequency excitation zone, it is possible that heave and pitch sum-frequency QTF's may dominate the wave loading over the first order effects [186]. For these reasons the second order forces are studied in detail in this section. Wave drift damping is modelled by use of the Aranha formula [281]. The second order forces are calculated in the frequency domain in Ansys AQWA, using the additional tendon stiffness terms described in Section 3.2.2. Additional stiffness terms are also included to shift the pitch natural frequency to account for the flecible towers effect on the combined pitch-tower bending moment.

The calculated full QTF difference frequency surge forces are presented in Figure 4.1, while the full QTF sum frequency heave and pitch forces are shown in Figure 4.2 and 4.3. the white dashed lines indicate constant sum or difference frequency pairs. Second order forces cause most issues when they excite the natural frequencies of the platforms. Along the surge natural frequency region of ~ 0.02 Hz there is no significant concentration of the slow drift force, instead it is evenly distributed across many difference frequency pairs. The surge natural frequency shows a slow drift force of <5 kN/m^2 For the heave natural frequency at $\sim$ 1 Hz, the sum frequency loads also shows no major spike, with the load around 0.5 kN/m^2. As the pitch natural frequency is even higher, at $\sim$ 2.5 Hz, it is outside the ability of AQWAs numerical modelling capabilities, due to limitations on the number of mesh elements, and thus possible wave frequencies to simulate.

Analysis of the experimental response showed no significant responses above 0.5 Hz, hence the validity of this numerical modelling approach.

Surge and pitch QTF's shown the majority of the force is concentrated in waves with one component having an extremely low frequency component of less than 0.25 Hz. As these waves are not expected to have any significant energy in reality the effects are not likely to be a design issue.

Pitch QTF's show that wave frequency pairs that could be expected to occur in irregular sea-states give up to 4500 kN.m/m^2. The lowest frequency with any significant energy that such a second order force occurs at is around 0.2 - 0.15 Hz.

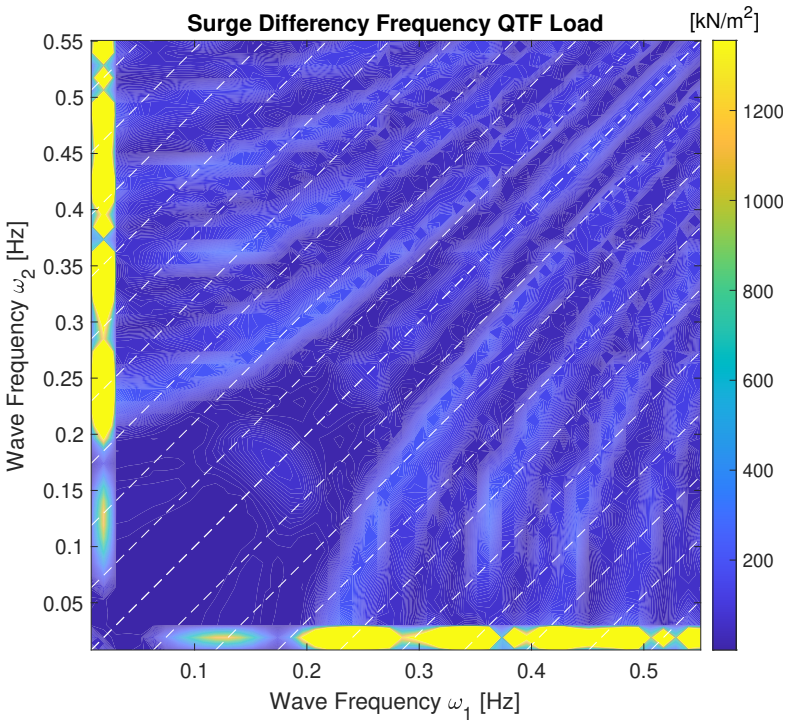


Figure 4.1: Surge Difference Frequency QTF Load

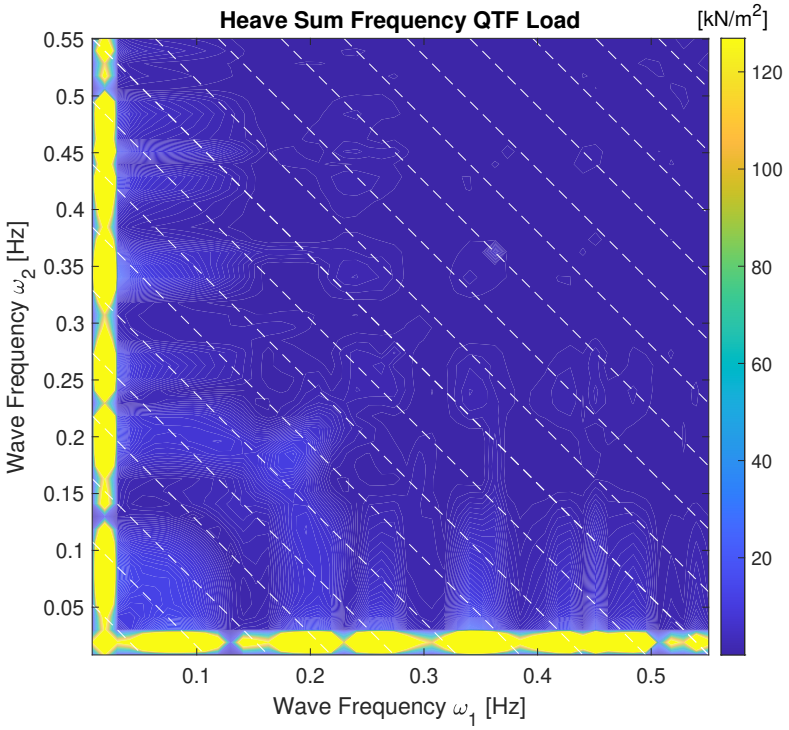


Figure 4.2: Heave Sum Frequency QTF Load

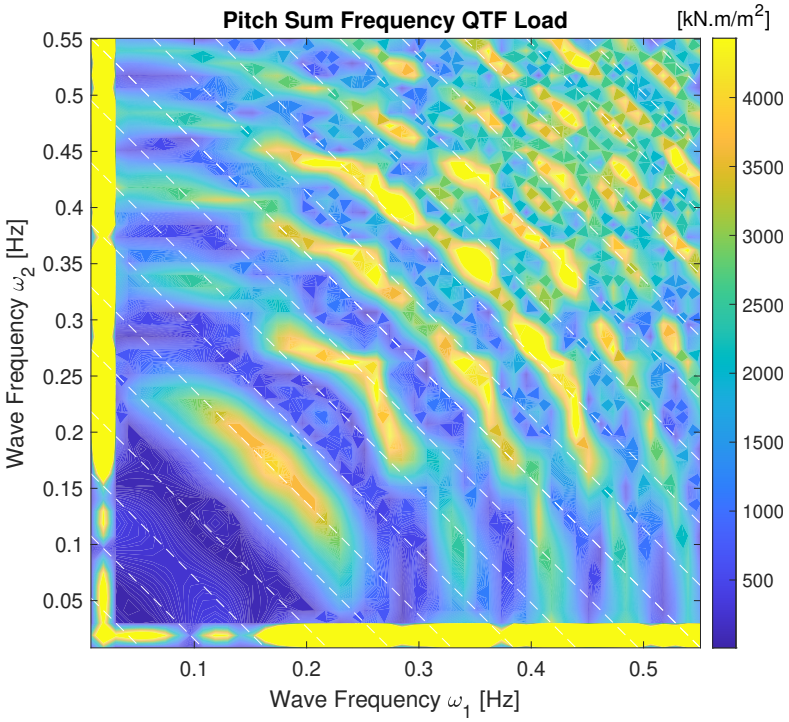


Figure 4.3: Pitch Sum Frequency QTF Load

4.2 Numerical Convergence

In order to have confidence in the numerical modelling results, a number of convergence studies are carried out. Ansys AQWA is used to solve for the hydrodynamic parameters. A convergence study on the number of mesh elements, the number of wave directions, the number of viscous drag elements, the number of tower elements and the number of mooring line elements is carried out. While convergence is required to show model stability, it is the convergence of the solution to the continuous equations that govern the physical phenomenon that will show consistency. To demonstrate this complete consistency. theoretical solutions are also given where possible and feasible in the scope of this work.

4.2.1 Mesh Convergence Study

In this section the numerical convergence on the mesh size in Ansys AQWA is performed. In Ansys AQWA the maximum number of diffracting mesh elements is 12000. The maximum frequency possible to solve is constrained by the maximum mesh element size. The maximum wave frequency wavelength is 6 times the largest mesh element. (diagonal length in panel model $< 1/6$ of smallest wave length analysed from) [282]. An example mesh is shown in Figure 4.4.Pitch was chosen to be the output marker to test the quality of the mesh convergence. Results can be seen in Figure 4.5, and show convergence between the models with 10877 and 11963 elements. AQWA uses an automatic mesher based on a selected defeaturing tolerance.

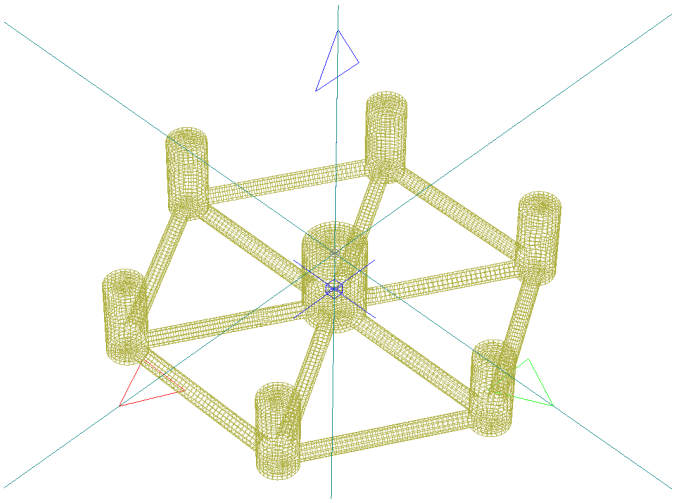


Figure 4.4: HEXWIND mesh with 10877 elements

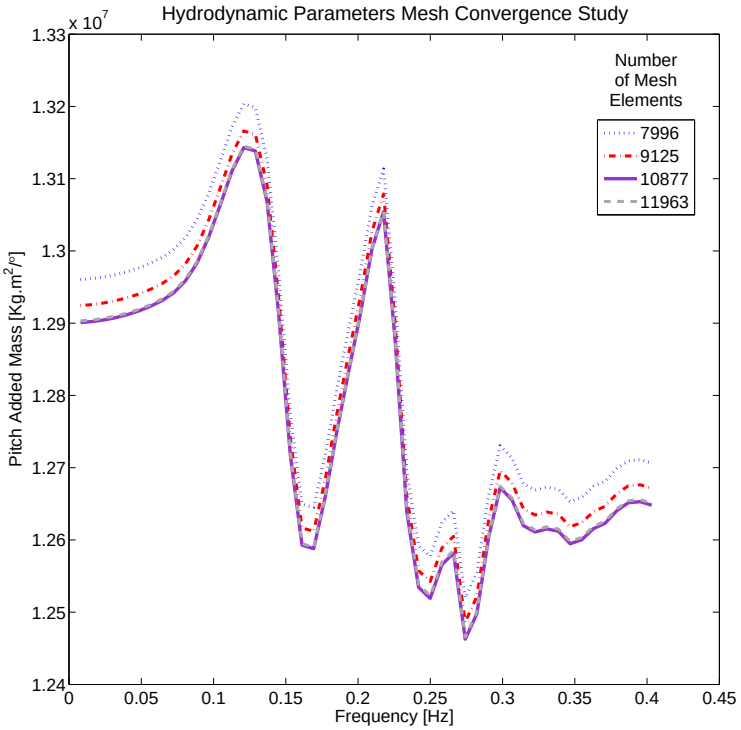


Figure 4.5: Pitch Added Mass for Mesh Convergence Study

4.2.2 OrcaFlex Mooring Convergence Study

OrcaFlex uses a finite element model for the simulation of mooring lines, composed of a number of nodes which are interconnected by elements. Thus the number of nodes is the number of segments plus one. The segments only model the axial and torsional properties of the line. The other properties (mass, weight, buoyancy etc.) are all lumped to the nodes. In this section the number of segments is varied as equal to 2^n, where n are integer values from 1 to 14.

The transverse and longitudinal tendon wave frequencies are governed by Equations 4.1 and 4.2.

$$f_{TenT} = \frac{n}{2L_u}\sqrt{\frac{T_0}{\mu}} \tag{4.1}$$

$$f_{TenL} = \frac{n}{2L_u}\sqrt{\frac{EA}{\mu}} \tag{4.2}$$

A transverse free decay test of a single tensioned tendon is carried out. This is similar to plucking a guitar string to find its resonance period. The centre of the tendon is offset slightly horizontally, before being released at the start of the simulation. A simulation of 20 s is solved at a time-step of 1000 Hz. Figure 4.6 shows the frequency response of the tendon free decay test at each segment discretization The first six transverse modes can be clearly identified, while only the 2nd, 6th and 10th longitudinal modes are excited by the initial transverse motion. The first three transverse results show an extremely close match to the theoretical calculations, with errors of less than 1%, and require, respectively, 32, 64 and 256 segments in order to converge. For the higher observed modes the error grows to just under 7% and require 8192 segments to reach convergence. The longitudinal results differ by 7.7% and for the 2nd, 6th and 10th modes require 8, 32 and 64 segments to reach convergence respectively. The computational and memory expense is also greatly different between models, and is also a deciding driver in deciding the discretization The two segment model takes approximately 1 second to solve and 6 MB to store the results, while the 16384 segments model takes approximately 2 hours

and 7 GB to store. As a trade off between the conflicting objectives of accuracy and computational expense a discretisation of 64 segments was chosen as sufficient for this work.

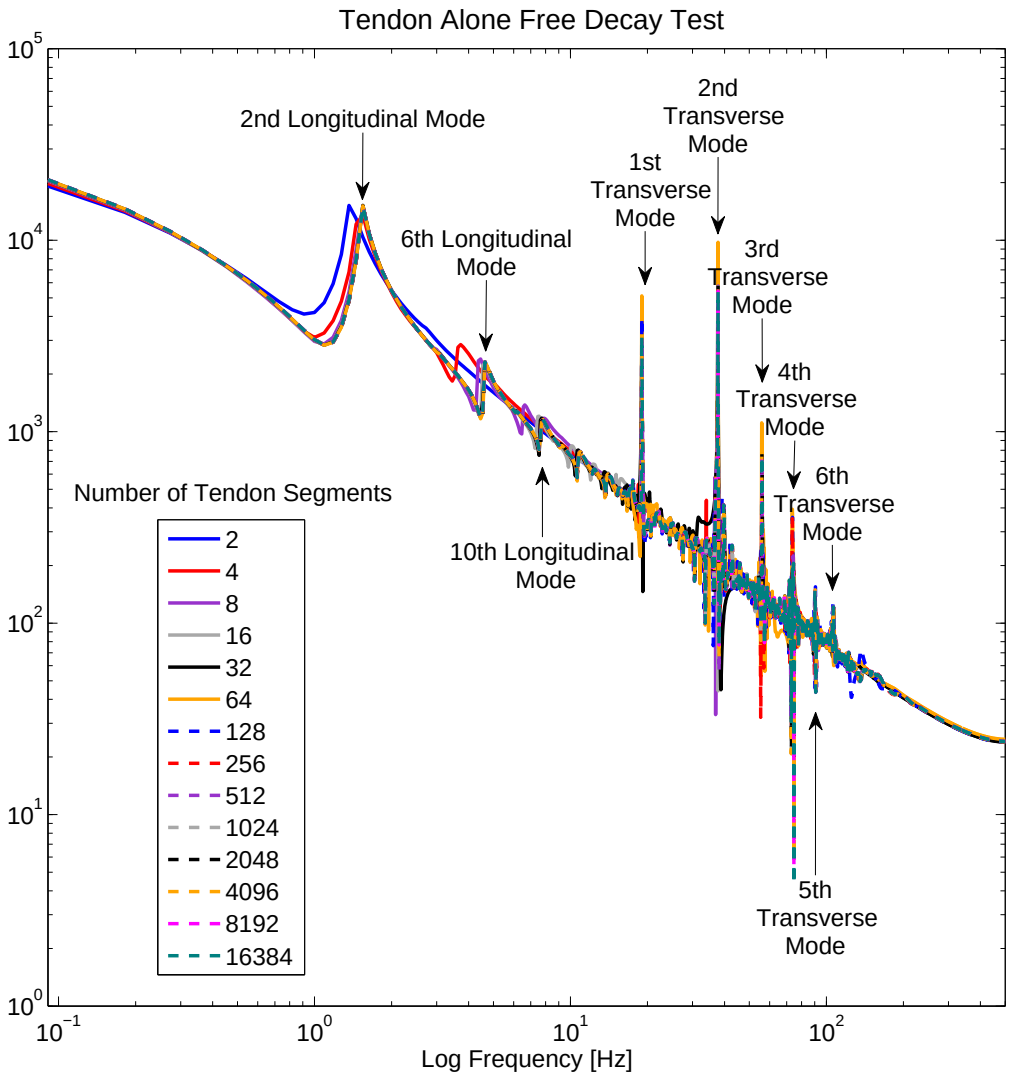


Figure 4.6: Tendon Free Decay Segment Discretization Convergence Test

While this FEM used by OrcaFlex can model tension, torsion and bending forces of a line element, a higher order model is required to include shear forces. Geometrically exact Continuum methods such as Simo-Reissner allow the calculation of line element shear forces [283]. The Simo-Reissner method allows for arbitrarily large rotations and displacements. The Timoshenko model allows for only geometrically linear shear force

Table 4.2: Tendon Free Decay Convergence Test: Transverse Results

Mode Number (#)	Theoretical Transverse (Hz)	Simulation Transverse (Hz)	Segments Required for Convergence (#)
1	19.028	18.998	32
2	38.055	37.724	64
3	57.083	56.994	256
4	76.110	74.350	8192
5	95.138	90.364	8192
6	114.166	106.535	8192

Table 4.3: Tendon Free Decay Convergence Test: Longitudinal Results

Mode Number (#)	Theoretical Longitudinal (Hz)	Simulation Longitudinal (Hz)	Segments Required for Convergence (#)
2	1.675	1.546	8
6	5.024	4.636	32
10	8.374	7.726	64

[284]. The exclusion of shear forces in this work is based on the assumption that the tendon length is much greater than its diameter meaning these will be considerably less than the effects due to the bending [285].

4.2.3 Viscous Drag Element Size Convergence Study

In the OrcaFlex model, viscous drag is modelled using a number of "6D Buoys", which are set up to only take into account the drag term from Morison equation. The discretization of the viscous drag elements is thus similar to the tendon discretization, where each 6D buoy is subdivided into a number of segments. Tendon 1 tension is used as the output marker, as this force accumulates the effects of all platform DOF, in order to compare these results. As the discretization effect is likely to be more significant in larger wave heights, a H_S of 10 m is used in this simulation.

Results from Tendon 1 tension RAO are shown in Figure 4.7. The low frequency components ($<$ 0.18 Hz) show exactly the same response regardless of the discretization and are thus omitted from the figure. Some divergence can be seen in the higher frequency response, although convergence occurs relatively quickly. In this figure the x-axis is

focused on the main tension peak which occurs at the platforms pitch natural frequency. Convergence of the results can already be observed for a segment size of 2 m. One high frequency response component at 0.62 Hz requires a segment size of 0.5 m for convergence. For this work the 2 m discretization is generally found to be acceptable, as the force error at this high frequency component are less than 2 % that of the higher number of discretisations.

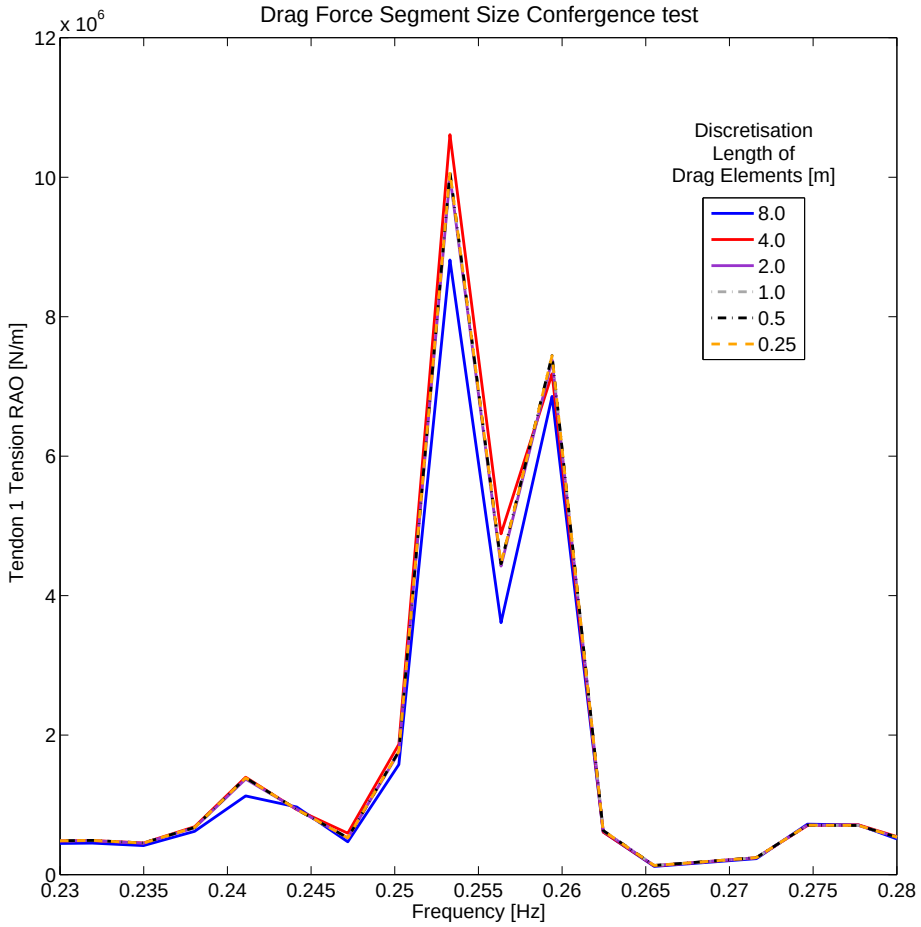


Figure 4.7: Drag Force Segment Discretization Convergence Test

4.2.4 Flexible Tower Element Size Convergence Study

In the OrcaFlex model the flexible tower is modelled by a finite element line model.

The number of line elements that are required to accurately model the flexibility

of the tower is studied here. In contrast to the homogeneous tendon described above, the tower is made from tapering steel cylindrical sections. In OrcaFlex the tower is modelled as a line element that is discretised into a number of sections. Each section has homogeneous mass and stiffness properties. The number of sections is varied from 1 to 48. Each section is further discretised into 10 segments with homogeneous properties.

A free decay test of the tower alone, rigidly fixed at its base, is carried out by offsetting the nacelle in the x direction before releasing it. Frequency domain results of the number of tower sections convergence study are presented in Figure 4.8. Only 2 sections are required to correctly predict the first fundamental frequency of the tower at 0.392 Hz, although 16 sections are required to accurately predict the amplitude of motion. 16 sections are also required to correctly identify the higher frequency modes at 4.857 Hz and 14.642 Hz. Modes at higher frequencies than this require a further discretization beyond 48 sections and are thus not discussed here. 16 sections are deemed sufficient for the purpose of this work.

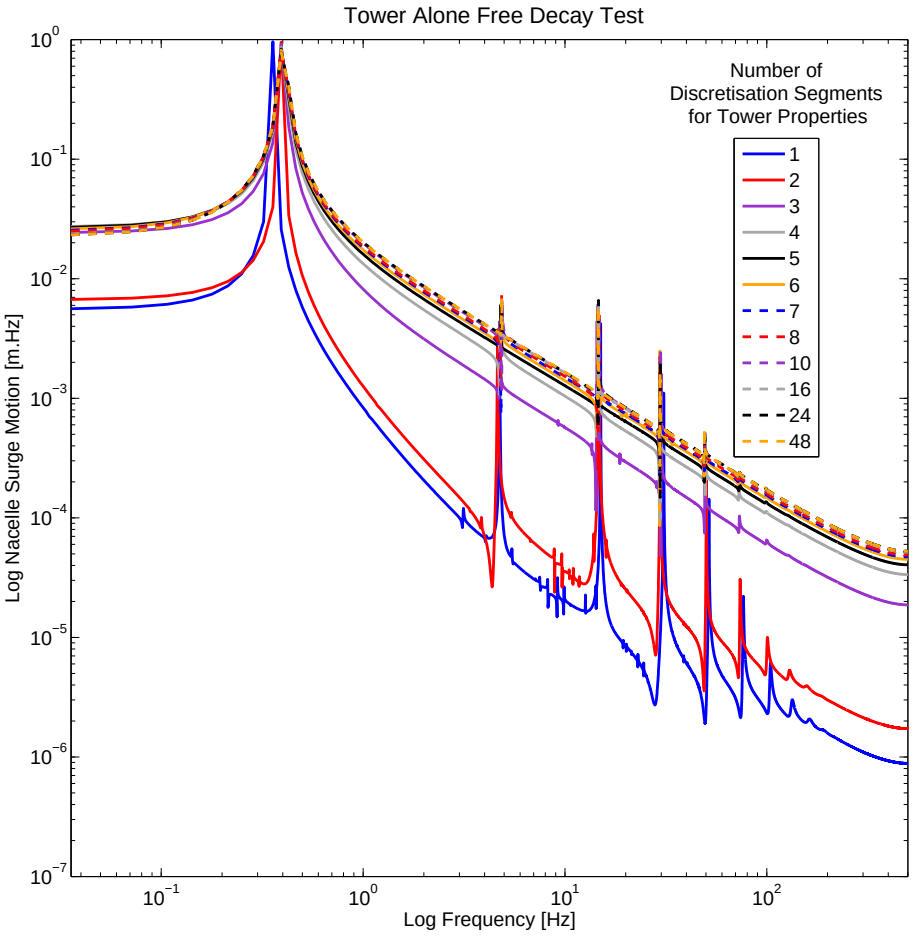


Figure 4.8: Tower Free Decay Segment Discretization Convergence Test

4.3 Numerical Model Validation

In order to validate the numerical modelling approaches developed in the section proceeding this, experimental tank testing of the HEXWIND platform was undertaken. The model was scaled according to Froude scaling laws and has scale of 1:30. Details of the HEXWIND FWT are shown in Table 4.4 at model and full scale. In order to eliminate differences between the models, it was decided to use the scaled model dimensions and mass for the full scale numerical model. An introduction to the wave basin test facility and model set up is first outlined. Still water free decay tests are used to fit the viscous drag damping terms. Comparisons between the numerical and experimental results in motions and tendon tensions are given for regular, irregular and rogue waves. Com-

Property Name	Model	Units	Full Scale	Units
Total Mass	99.69	Kg	2691.61	tons
Platform Mass	78.29	Kg	2113.81	tons
Tower Mass	8.30	Kg	224.10	tons
RNA Mass	13.10	Kg	353.70	tons
Displacment	0.15	m^3	3967.29	m^3
Total Tendon Pretension	499.53	N	13487.42	kN
Tendon Unstretched length	5.407	m	162.2	m
Tower Height	2.58	m	77.50	m
Platform Draft	0.42	m	12.50	m
Column Heights	0.83	m	25.00	m
Central Column Diameter	0.30	m	9.00	m
Outer Column Diameter	0.20	m	6.00	m
Connecting Pontoons	0.09	m	2.70	m

Table 4.4: HEXWIND properties, model and full scale

parisons between results using first order only forces and second order forces generated using Newman's approximation or full QTFs are given. Uncertainty in the experimental incident wave is accounted for by performing simulations using both a theoretical wave spectra and observed wave timeseries. An analysis of drag coefficient variation with sea-state is given. A numerical tendon pretension sensitivity study is performed as the experimental test campaign showed tension slippage across the test duration.

4.3.1 Wave Basin

The TLP was tested in the deep water basin, in IFREMER, Brest, France. The tank is 50 m long, 12.5 m wide and 10 m deep. Sinusoidal regular waves and irregular panchromatic waves of a Bretschneider (BS) spectrum were generated using a single hydraulic v-shaped wave plunger, and reflections absorbed at the opposite end by a porous parabolic beach. Waves were measured using two servo-controlled wave gauges, motions were captured using three Qualisys motion tracking captures picking up four UV markers, mooring loads were measured with six 500 N load cell located at tendon anchor positions.

Merians formula, Equation 4.3, is used to determine the main sloshing modes of the wave basin, where n is the number of nodes, L is the horizontal dimension of the basin measured in the direction of wave motion, g is the acceleration of gravity, and d is the

Mode Number	Lengthwise 50 m [s]	Widthwise 12.5 m [s]
1	78.2	19.6
2	39.1	9.8
3	26.1	6.5
4	19.6	4.9
5	15.6	3.9
6	13.0	3.3
7	11.2	2.8
8	9.8	2.4
9	8.7	2.2
10	7.8	2.0

Table 4.5: Sloshing Modes of the wave basin

depth of the water. L is taken as both the length and width of the basin, in order to get the sloshing modes in either direction. Results are shown in full scale for the first 10 modes in Table 4.5.

$$T = (1/n)(2L/\sqrt{(gd)}) \tag{4.3}$$

Wave testing consisted of regular monochromatic sinusoidal waves, Irregular JONSWAP spectral waves and created observed "Rogue" waves from the Atlantic Marine Energy Test Site (AMETS). All waves tested are long crested.

4.3.2 Model Set Up

4.3.2.1 False Bottom

As the design water depth was 150 m full scale (5 m model scale) and thus shallower than the 10 m deep tank, a false bottom was installed, raising the height of the anchor points to that desired. There is some limitation in this method, as the waves will not "feel" this water depth and will act like waves in 300 m (10 m). An underwater photograph of the false bottom can be seen in Figure 4.9. The false bottom was composed of a reinforced concrete foundation supporting a column and frame. Lifting eye bolts in the frame provided the tendon termination points. Additionally pairs of each termination points were coupled with slings and further supported through extra ballast. This false

floor was supplied and installed by the IFREMER research team.

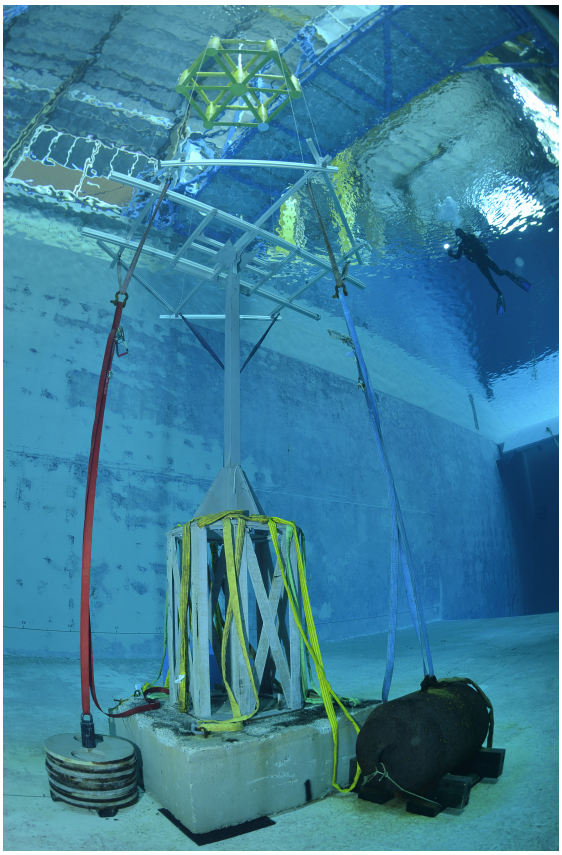


Figure 4.9: Photograph of HEXWIND as installed in the wave basin. In the foreground the false bottom can be seen. Copyright IFREMER with permission for reproduction granted

4.3.2.2 Fabrication

The floating hexagonal platform consists of six outer and one central buoyancy column(s). The outer buoyancy columns consists of six 0.2 m diameter polyvinyl chloride (PVC) pipes, joined to the central column by twelve (six top and six bottom) 0.09 m diameter PVC pipes. The outer buoyancy columns are also connected to each other by twelve (six top six bottom 0.09 m diameter PVC pipes. The central column was fabricated from 0.3 m diameter PVC pipe and provides sufficient buoyancy to counteract the weight of the tower and nacelle. The mooring tendons were composed of six mooring lines made of 3 mm diameter stainless steel wires. The wind turbine tower was 2.58 m high and was fabricated with a 0.07 m diameter stainless steel pipe (7.4 kg). As the thruster was not

heavy enough to model the turbine, additional lead weights are also placed at the top of the tower (8.5 kg). The mooring tendons are attached to the top of the column via the load cells, the tendon wire passes through a loop on the bottom of the columns in order to redirect the force away from the column base plates.

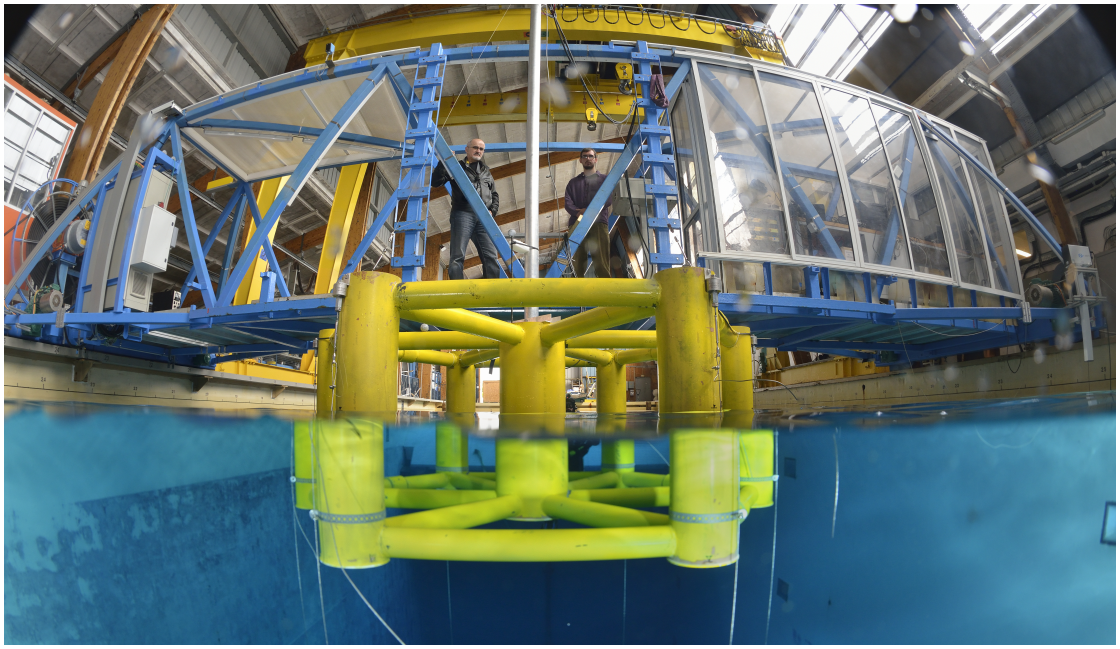


Figure 4.10: Photograph of HEXWIND from the still water level. Perspective is distorted due to the use of an underwater fish eye lens. Copyright IFREMER with permission for reproduction granted

4.3.3 Still Water

Surge free decay tests are used to determine the platform damping coefficients. Attempts to perform experimental pitch and heave free decay tests were unsuccessful due to the highly constrained nature of the tension mooring arrangement. In the numerical model the decay tests were performed using a semi-rigid winch, with stiffness of 1E6 kN. The winch is used to offset the platform by 12 m. The winch position is chosen to be 100 m away from the platform, in order for the correct platform surge set-down coupling to be seen in the static solve. The steady-state position of the model includes this offset. At a simulation time $T = 0s$ the winch is released. In the physical experiment the platform is offset horizontally by a rigid body until the Qualisys motion capture shows the required

distance. After a wait time of 10 s the platform is released.

Fitting of the required drag coefficient is done iteratively as is shown in Figure 4.11. Results show the dual effects of increasing the drag damping, firstly in reducing the amplitude of motions and secondly of increasing the decay period. When the viscous drag is neglected, i.e. $C_D = 0$, only radiation damping exists, and the experimental and numerical natural period can be seen to match. At low frequency oscillations the radiation damping effects are quite small. Increasing the drag damping increases the oscillation period and the numerical and experimental periods begin to diverge. The change in damped and undamped period can be calculated using Equation 4.4 [287], where T_0 is the undamped natural period $T_{0,D}$ is the damped natural period and ζ is the critical damping ratio. Potential solutions to this period problem involves reducing the potential theory added mass to include some viscous effects on the added mass term, or by adding additional stiffness to the numerical model. As the change in oscillation frequency is quite minor in this work, no additional corrections are made. A drag coefficient of 2.5 was selected and used throughout the numerical modelling process.

$$T_0 = T_{0,D}\sqrt{1-\zeta^2} \tag{4.4}$$

As free decay tests are carried out in a still environment (in the case of floating bodies in still water) the applicability of damping rates derived from such tests for use in non still water situations should be questioned. Furthermore as damping is proportional to the relative velocity (either linearly or squared), it is large oscillation motions that will result in the greatest damping forces. Large amplitude damping behaviour is not well described by current techniques (Polynomial fitting of drag terms) [288]. As free decay motions occur at the damped natural frequency, only the damping values at the damped natural frequency may be derived [289]. Because of these limitations the use of irregular wave motions to derive damping rates for the HEXWIND platform will be studied in the next sections.

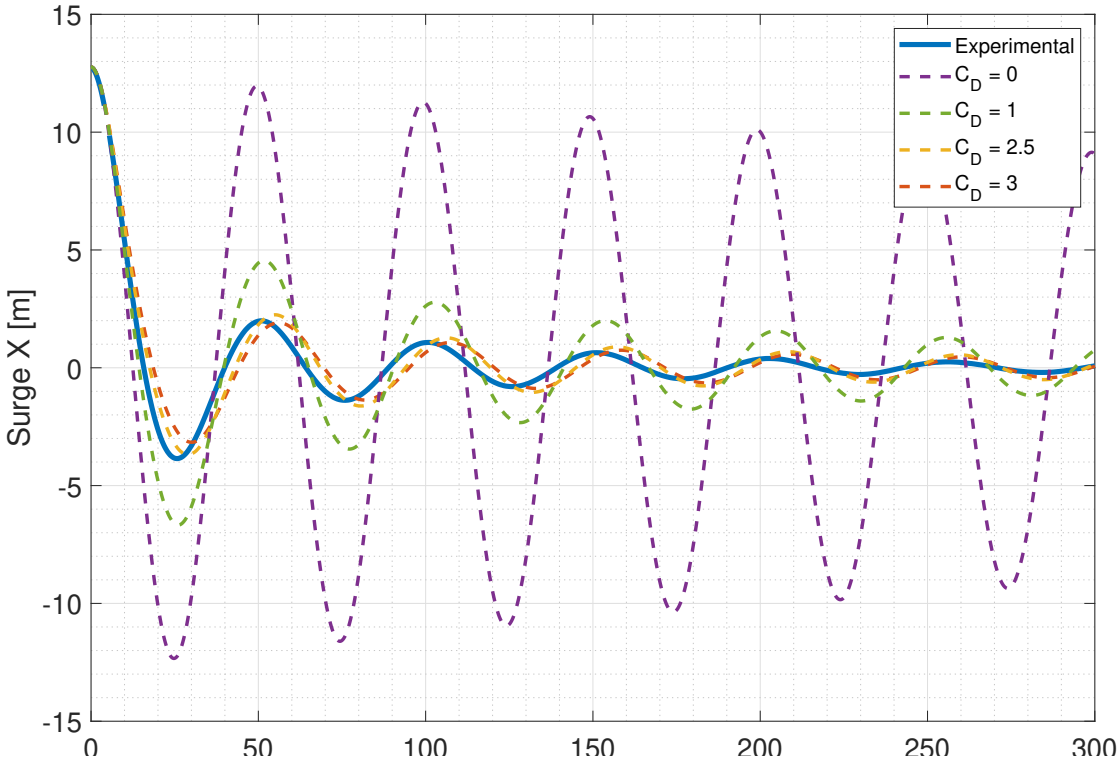


Figure 4.11: Numerical & Experimental Surge free decay tests, showing the effects of varying the drag coefficient

4.3.4 Wind load

Wind loading was modelled with a high revolutions per minute (RPM) remote control (RC) air-plane ducted propeller. This was controlled by *LABVIEW* via a micro-controller. Wind loading followed NREL's 5 MW reference turbine thrust curve [290]. Thrust was generated to match that generated at wind speeds of 8, 11.5, 16, 20 and 25 m/s using the pulse width modulation, calibrated in Figure 4.13. The fan had a mass of 0.75 kg, which equaled approximately 20 tons at full scale, much lighter than the required RNA mass. Additional weights were added above and below the propeller in order to not interfere with the air flow.

Each wind load case involved a constant wind speed which was verified by a bending load cell connecting the fan to the tower, as can be seen in Figure 4.12.

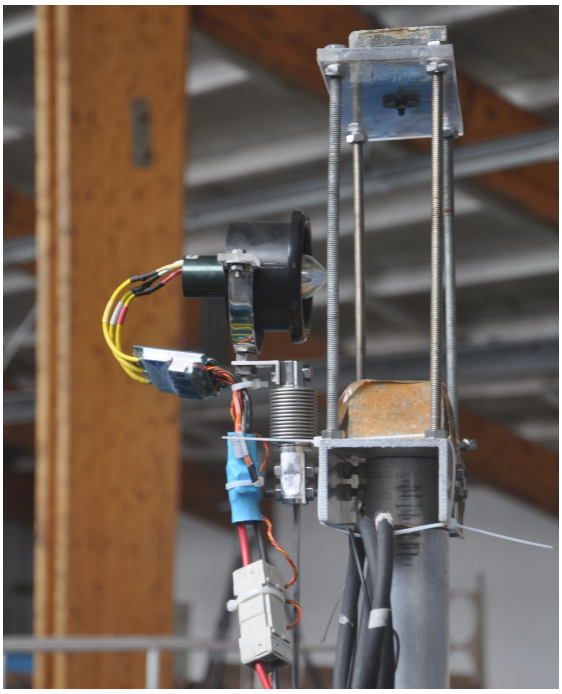


Figure 4.12: Photograph of Wind Load Thruster, mounted on Bending Load Cell.

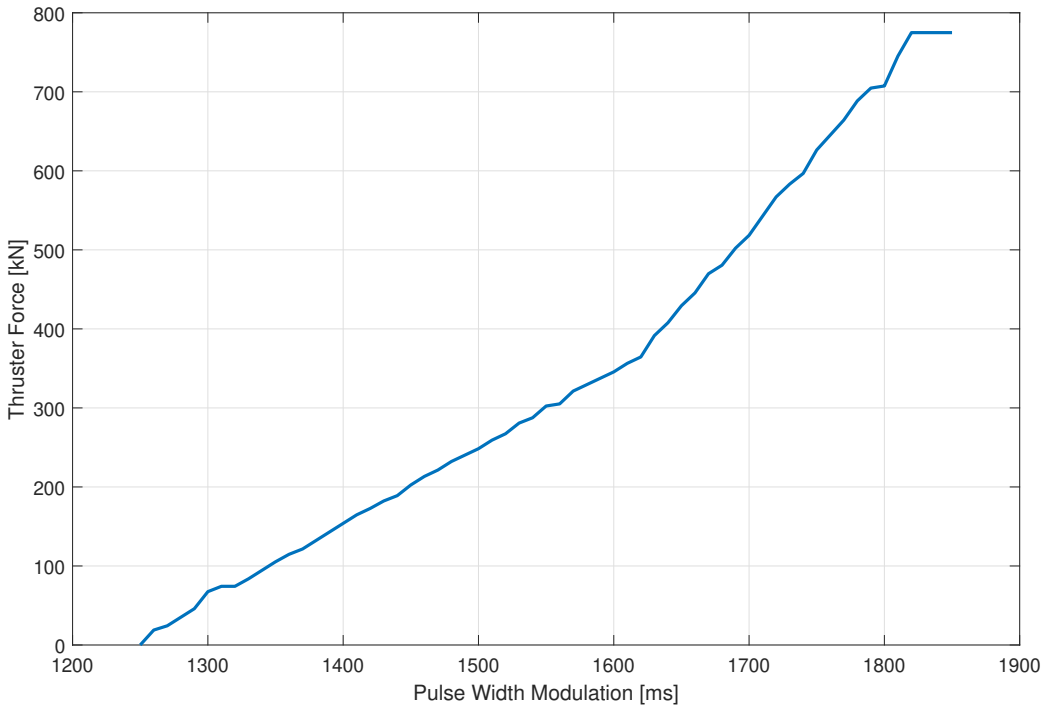


Figure 4.13: Calibration of Thrust Load generation, PWM shown at model scale, while thrust is shown at full scale

4.3.5 Tendon pretension

During testing there was difficulty in keeping the tendon pretension balanced and constant between the 6 lines. All individual tests had the still water tensions recorded before the test began, with intermittent adjustments of the tension in an attempt to balance and achieve the required pretension. With 6 lines, balancing the tension between them is a complex and difficult process. Due to time constraints in testing, it was decided to proceed with testing even when the ideal pretension was not present.

In the following table, Table 4.6, the tensions before each tests commenced are presented. Large increases in the total pretension, indicate that the load cells have lost calibration, as there is no possible physical reason for such an increase. Decreases in pretension may be due to elongation of the tendon wires, loosening of the wire connectors or slow leak water breaches of the hull. When the platform was removed from the basin the weight was checked again and matched the pre deployed value, indicating that the latter was not the reason for the gradual reductions in pretension observed. Due to the long recalibration time, model removal and model set-up, it was decided to continue with the testing even in light of this issue. The most critical changes in pretension are discussed next. Before Regular Wave no. 9, the pretension in lines 3 and 4 increase by 38 % and 18 % respectively, with the overall pretension increasing by 7 %. Before Irregular Wave no. 13, the pretension in lines 3 and 4 increase by 40 % and 18 % respectively, with the overall pretension increasing by 8 %. Before Rogue Wave no. 10, line 4 has an increase in 50 %, while lines 1 and 2 decrease by 30 %. Overall pretension increases by 10 %.

As these changes in pretension will affect the model motions a sensitivity study on the individual tendons pretension value is carried out. Pretension in individual lines is randomly varied by up to $\pm$ 2 %, $\pm$ 5 %, $\pm$ 10 % and $\pm$ 50 % compared to the original pretension. Total pretension is kept within 0.5 % $\pm$ of the design value. 50 random permeations of each level are simulated for a regular wave RAO study at 10 m wave heights. Due to the large number of simulations required, the period interval is increased from the original 0.1 s to 0.5 s. This change in pretension is most evident in the pitch and tendon tension response and these RAO's are plotted in Figures 4.14 and 4.15. For

the 2 % and 5 % pretension variation, the change in platform motion and tension RAO are negligible, the 10 % variation shows a small but noticeable effect, while at the 50 % level the changes in tendon tension RAO can be up to 18% at some periods. This sensitivity study shows that although there are large variations in the pretension across the experimental tests, the effect on the results is not as severe as was initially assumed. The absolute value of tendon tension is most likely to be effected by these variations, so comparing the numerical and experimental values should be undertaken with some caution.

The load cells were calibrated in Ireland before being transported by road and ferry to the wave test facility in France. It is recommended that for future test campaigns to recalibrate at the test site in order to avoid the issues observed in this experimental test campaign.

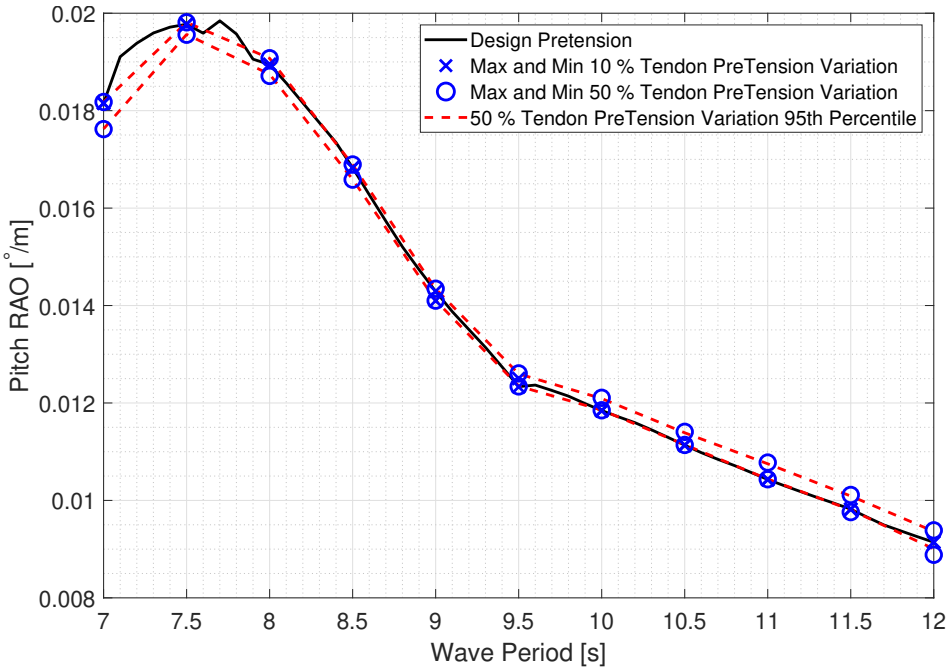


Figure 4.14: Numerical Pitch RAO for Regular Waves, Individual Pretension Variation Study

4.3.6 Regular Waves

Regular sinusoidal waves are tested according to Table 4.7. Wind thrust loads of 800 kN and 450 kN are tested referring to a peak load of 11.5 and moderate load of 16 m/s

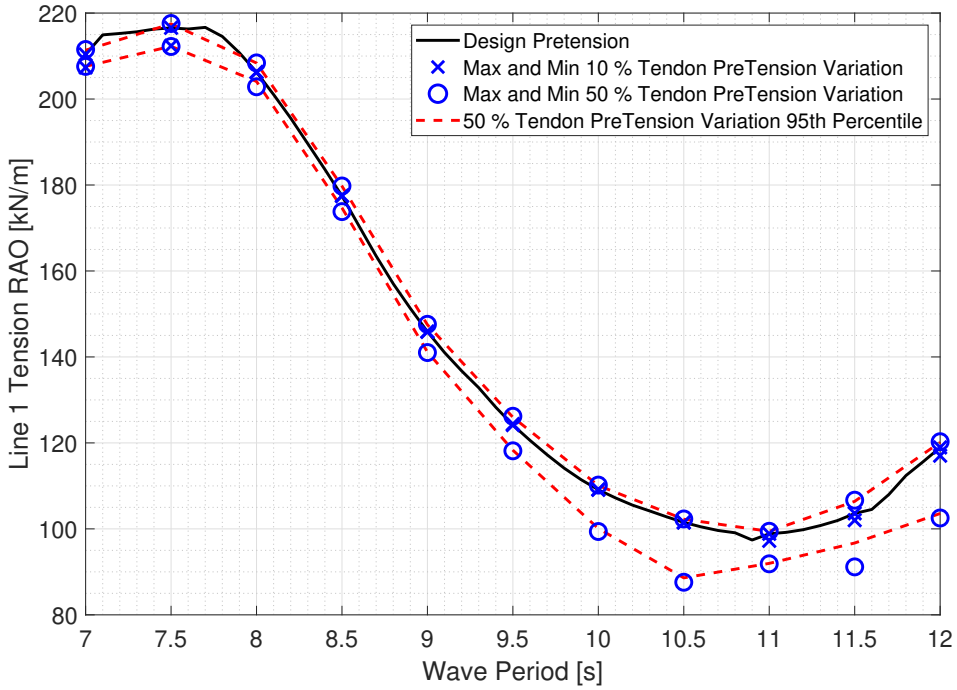


Figure 4.15: Numerical Tendon Tension RAO for Regular Waves, Individual Pretension Variation Study

respectively. The numerical model is also run for wave only cases in order to give a general overview of the RAO behaviour. These wave only RAO simulations are run for wave heights of 1 m, 2 m, 5 m and 10 m in order to show the nonlinear behaviour that arises from the stiff mooring system. Wave periods from the breaking wave length of each wave height to 12 s, with 0.1 s increments are simulated. The largest coupling effect is due to the surge set down effect, which is evident in the heave RAO. This set down can be simply calculated by Equation 4.5, where L is the tendon length and θ is the angle of rotation of the tendon base [291].

$$Z_s = L(1 - cos(\theta)) \tag{4.5}$$

In Figures 4.16 to 4.19 the motion and line tensions RAO are shown, comparing the experimental and numerical motions. For surge response, the trend in frequency dependant response is well observed, showing a peak at the lower period values and then a linear trend of increasing response with increasing wave period. For wave periods above 6 s simulations constantly slightly under predict the motions, while for the two

short wave periods below 6 s no trend can be observed. The nonlinear effects on surge show a slight increase in the region of 5 - 6 s, while showing a decrease above 7 s.

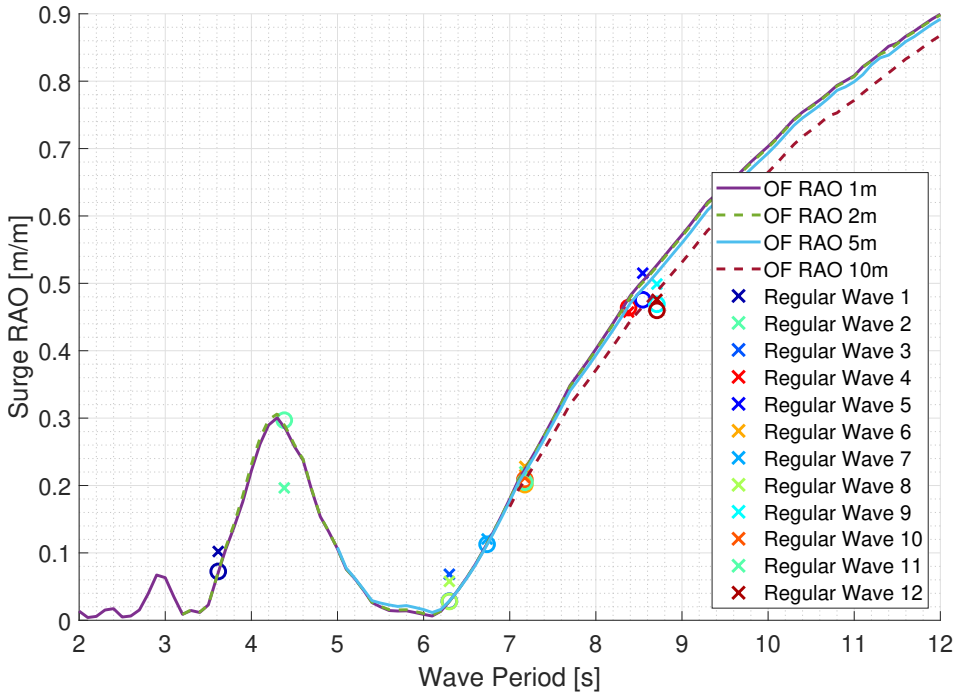


Figure 4.16: Numerical & Experimental Surge RAO's for Regular Waves, crosses indicates Experimental value, circles indicates simulated value

As the heave response is dominated by the surge set down effects the same general trend can be observed as the surge RAO. The non-linearity of increasing surge set down coupling due to increasing wave height are most pronounced for the heave response. These coupling effects are especially important around the frequencies of large amplitude surge motion, i.e. 4.5 s and at above 6 s. The regular wave no. 1 heave response is predicted extremely well. For wave periods above 7 s the simulated values over predict the experimental heave response. This over-prediction is not evident in the wave only simulations, indicating the fact that it is related to the mean wind thrust modelling induced offset.

Regarding the pitch RAO it should be noted that all responses are extremely low, below 0.06 °/m and thus a great deal of error exists in the experimental observation of such low values, meaning the motion capture markers move by less than 3 mm. The general trend is well predicted by the numerical models although the regular wave no.

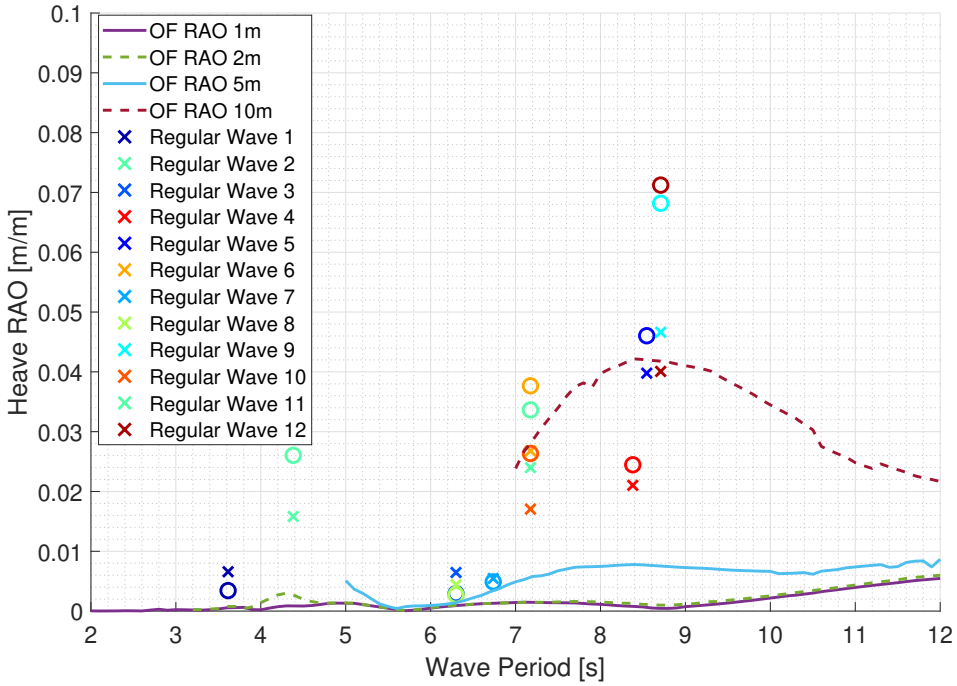


Figure 4.17: Numerical & Experimental Heave RAO's for Regular Waves, crosses indicates experimental value, circles indicates simulated value

2. mean wind thrust effects are severely under predicted. In this region the pitch RAO gradient is extremely steep, increasing from the RAO minimum response of 0.005 °/m at 3.3 s to the maximum of 0.045 °/m at 4.4 s. The nonlinear RAO to wave height relationship increases the pitch motions, with the most notable effects between 7 s and 9 s.

The mean of the two most heavily loaded mooring tendons, lines 1 and 2, are used to illustrate the comparison between numerical and experimental line tensions. Tensions follow the same shape as the pitch RAO, although the nonlinear wave height tension relationships is inversely proportional above 7.5 s. Above this wave period it is assumed that the inversely proportional nonlinear wave height surge relationship dominates the tensions reductions.

in Figures A.1 to A.11 the regular wave spectral density's are shown (moved to Appendix A). These figures show a good match between observed and numerical peak natural period, wave and sub-harmonic frequency responses. While amplitudes of motion show some mismatch. In general it can be said that the response in the numerical models is more narrow banded that the broad banded observed response. It is in the

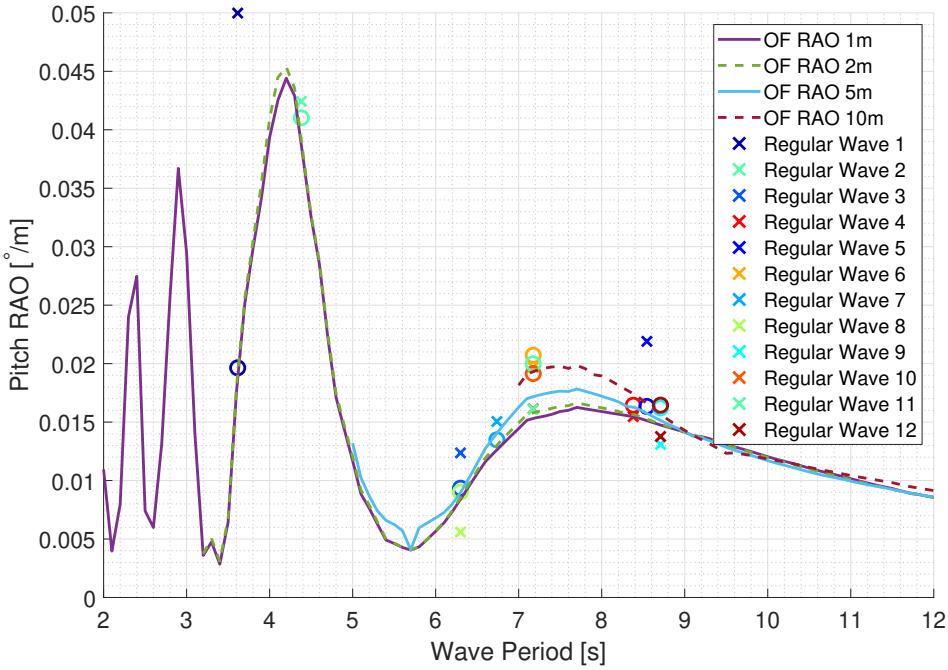


Figure 4.18: Numerical & Experimental Pitch RAO's for Regular Waves, crosses indicates experimental value, circles indicates first order simulated value

region directly above and below the main frequency response peaks that shown the largest difference between experimental and numerical responses. An exact reason for this difference in spectral peak bandwidth has not been established, some hypothesis are as follows. Nonlinear wave forcing: Viscous effects on the first order wave forces, the lack of an instantaneous wave surface elevation to calculate nonlinear radiation and diffraction wave forces. There are some frequency responses missing in the numerical model most notably at 0.22 Hz in surge and heave and at 0.36 Hz in Surge and Pitch for regular wave 1.

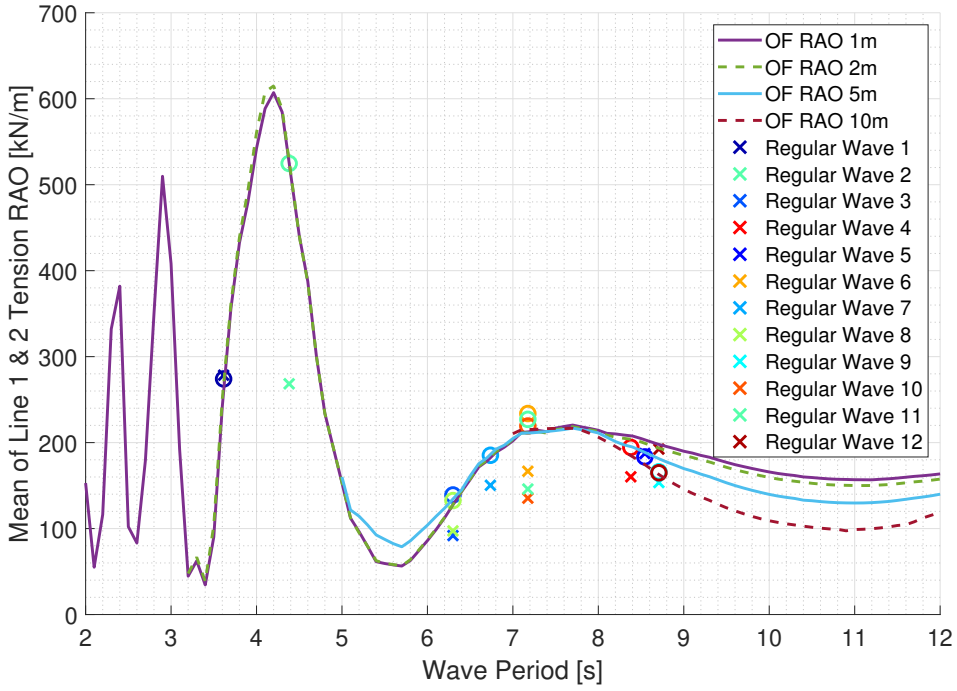


Figure 4.19: Numerical & Experimental Line 1 Tension RAO's for Regular Waves, crosses indicates experimental value, circles indicates first order simulated value

Wave Name	Tendon 1 [kN]	Tendon 2 [kN]	Tendon 3 [kN]	Tendon 4 [kN]	Tendon 5 [kN]	Tendon 6 [kN]	Average all Tendons [kN]
Reg 1	2170	2229	2325	2324	2239	2201	2248
Reg 2	2168	2221	2343	2291	2286	2177	2248
Reg 3	2179	2209	2350	2284	2292	2158	2245
Reg 4	2180	2201	2352	2281	2301	2161	2246
Reg 5	2190	2206	2350	2285	2301	2157	2248
Reg 6	2090	2042	2295	2580	2229	2150	2231
Reg 7	2088	2007	2313	2539	2206	2131	2214
Reg 8	2085	2021	2304	2542	2222	2132	2218
Reg 9	2304	2083	2362	3108	2671	1999	2421
Reg 10	2298	2065	2363	3110	2655	2008	2416
Reg 11	2273	2059	2353	3098	2635	2009	2404
Reg 12	2281	2048	2388	3099	2645	2042	2417
Irreg 1	2088	2027	2305	2551	2243	2134	2225
Irreg 2	2092	2037	2310	2562	2236	2137	2229
Irreg 3	2170	2114	2346	2341	2048	2262	2214
Irreg 4	2179	2132	2365	2313	2061	2260	2218
Irreg 5	2179	2133	2364	2310	2059	2264	2218
Irreg 6	2181	2125	2364	2314	2058	2261	2217
Irreg 7	2194	2113	2370	2316	2055	2257	2218
Irreg 8	2200	2096	2383	2311	2047	2265	2217
Irreg 9	2276	1833	2603	2259	1918	2360	2208
Irreg 10	2209	2206	2212	2398	2088	2168	2214
Irreg 11	2233	2195	2190	2429	2117	2119	2214
Irreg 12	2268	2193	2184	2411	2139	2075	2212
Irreg 13	2415	2087	2350	3136	2643	1964	2433
Irreg 14	2378	2055	2380	3144	2643	2000	2433
Irreg 15	2383	2053	2378	3153	2650	1996	2435
Rogue 1	1825	1970	2815	2770	2410	2549	2390
Rogue 2	1824	1971	2817	2777	2418	2563	2395
Rogue 3	1828	1975	2821	2782	2430	2568	2401
Rogue 4	1833	1978	2823	2792	2438	2566	2405
Rogue 5	1844	1975	2825	2811	2420	2568	2407
Rogue 6	2013	1890	2843	2820	2484	2441	2415
Rogue 7	1983	1913	2832	2812	2473	2462	2412
Rogue 8	1965	1927	2829	2813	2466	2475	2412
Rogue 9	1970	1929	2829	2823	2469	2473	2415
Rogue 10	1592	1566	2913	3377	2810	2657	2486

Table 4.6: Tendon Pretension before each test

Regular #	Wave Height [m]	Wave Period [s]	Wind Thrust [kN]
1	1.8	3.61	450
2	3.3	4.38	800
3	6	6.30	450
4	5.4	8.38	450
5	7.5	8.54	800
6	10.2	7.18	800
7	3	6.74	450
8	4.5	6.30	800
9	11.4	8.71	450
10	8.4	7.18	450
11	9.3	7.18	800
12	12.6	8.70	0

Table 4.7: Regular Wave Details

4.3.7 Irregular Waves

JONSWAP spectral waves were also physically tested, according to Table 4.8. The peak enhancement factor is set as $\gamma = 3.3$. The wave elevation from wave probe number 1, closest to the mean offset position of the model, is spectrally analysed by a FFT with the resultant spectral densities shown in Figures A.12 to A.14. The theoretical JONSWAP spectra are also shown for comparison purposes. These figures are moved to Appendix A in order to not disturb the flow of the chapter. The wave elevations are only recorded during the model tests, due to time limitations. Thus the recordings are not the undistributed incident wave elevation but instead a combination of the incident wave and radiated waves from the model. As only two wave gauges are available, an analysis of the reflected waves is not possible, and thus not included in the preceding discussion. The author is aware that with no active wave absorption capabilities in the basin, there is the strong possibility of the build up of significant reflected waves. A long settling time between experiments of around 20 minutes is used to account for this issue to some extent.

Irregular #	**Wave H_S [m]**	**Wave T_P [s]**	**Wind Thrust [kN]**
1	1.8	5.86	800
2	3.9	11.94	800
3	2.7	8.87	800
4	3.3	7.28	450
5	4.5	10.08	450
6	6.3	12.43	450
7	6.6	11.06	400
8	7.2	11.50	380
9	7.8	12.98	800
10	8.7	12.98	400
11	6	12.00	0
12	6	12.00	380
13	6	12.00	800
14	9	14.02	380
15	9	14.02	800

Table 4.8: Irregular JONSWAP Wave Details

The following points should be noted about the observed wave spectra. In most

sea-states the peak energy is reduced compared to the JONSWAP spectra. In all cases the low frequency waves are well matched to requested values, while the high frequency waves shown some divergence, with some frequencies showing larger energy and others showing lower energy. As the radiated waves from the HEXWIND platform are more likely to occur in this high frequency region, it is presumed that they are one of the main drivers behind these outcomes.

Simulations are carried out using a first order only wave model, a first order plus Newman's approximated second order force model and a first order plus full QTF second order force model. Initial modelling shows that the results are extremely sensitive to the surge drag coefficient used in the model, and indicate that the still water drag coefficient, $C_D = 2.5$, may not be suitable for the irregular wave cases. A method involving using a sea state by seastate tuning of the drag coefficients has been used with success in the literature and is applied to this problem [292, 293].

The drag coefficient tuning process is described as follows. As the response to varying the drag coefficient is non linear the selection of drag coefficients to perform the tuning is non trivial. In this work an iterative gradient based approach is used, where the subsequent drag coefficient to simulate is selected according to equation 4.6. The error between observed and simulated is calculated using the standard deviation of the surge motion and is calculated using equations 4.7 and 4.8. A fit is achieved when the error is below 2.5% of the observed value. In order to use this gradient fitting algorithm, two initial guesses into the drag coefficient must be used, here the first guess is the still water drag coefficient value, with the second guess being the still water drag coefficient plus or minus 1 ,$C_D = 2.5 \pm 1$, depending on the sign of the initial guesses error value. It is decided to tune the drag coefficients based on the low frequency surge motion, as this low frequency motion, being a resonant problem is extremely sensitive to the levels of damping. The surge radiated wave damping is also very low at the resonant period, hence the importance of the viscous damping component. With heave and pitch motions heavily coupled to surge, it is assumed that this method will also improve the results of the other degrees of freedom. In order to avoid inducing the third order viscous drift force the drag coefficient in the splash zone (Still water $\pm$ 5 m) is set to zero[294].

$$C_{d,n} = C_{d,n-1} - E_{n-1} \times \frac{C_{d,n-1} - C_{d,n-2}}{E_{n-1} - E_{n-2}} \tag{4.6}$$

$$E_n = 100 \times \frac{\sigma_o - \sigma_s}{\sigma_o} \tag{4.7}$$

$$\sigma = \sqrt{m_0} \tag{4.8}$$

Two numerical wave elevation approaches are used in this section. In Method 1, the numerical model is run with the theoretical JONSWAP wave spectra, while in Method 2 the recorded wave elevations are used. The prior method is discussed first in the next section. Both methods match the simulation duration to the experimental duration, and all results are discussed at full scale.

4.3.7.1 Method 1: Theoretical JONSWAP waves

In this method the theoretical JONSWAP waves are used for the simulations and thus the wave elevation time series does not have temporal similitude with that experimentally observed. The reason behind this is the short term variability that inherently exists in wave time series due to the superposition of linear waves, of varying frequency, by random wave phase offsets. Second order motions are well known to be highly sensitive to this short term wave variability.

The fitted drag coefficient plotted against wave height is shown in Figure 4.20 for both Method 1 and 2. These results show a possible correlation with wave height, which is expected due to limitations of the linear wave theory velocities used to calculate the drag term in the simulation. In reality the flow is accelerated around bodies and a complex vortex wake pattern develops downstream. These effects are known to increase with increasing flow velocity and thus wave heights and therefore increase the viscous drag forces on a body.

The variance of each DOF is presented, calculated spectrally using Equation 4.8. Motions are divided into low frequency (LF), above 25 s and wave frequency (WF),

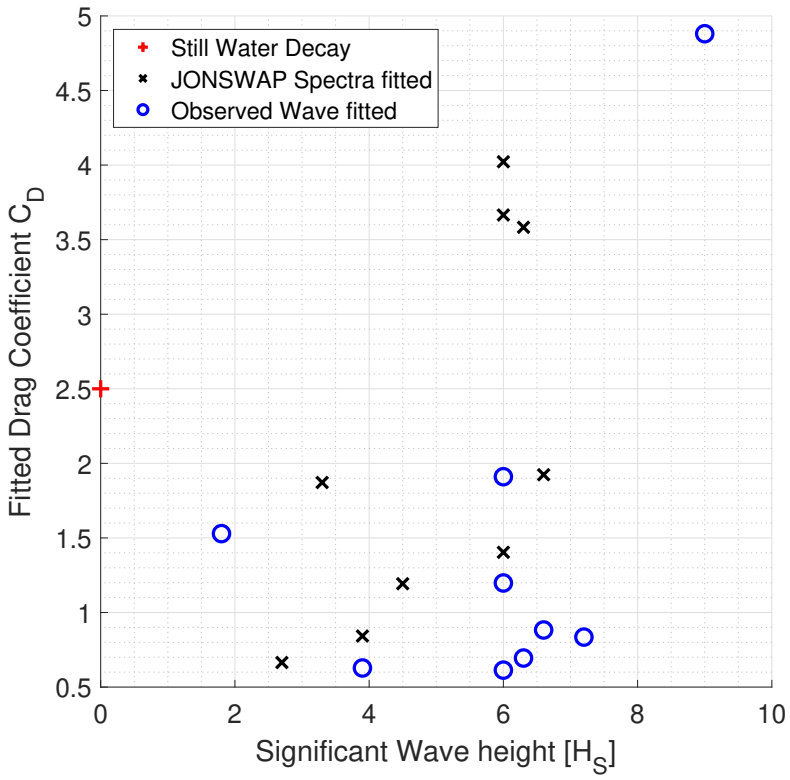


Figure 4.20: Fitted drag coefficients for the Irregular Wave Cases, Method 1 and 2. Note: for the wave cases the drag coefficient in the splash zone is set to zero in order to not induce additional third order viscous drift motions

below 25 s. The surge, heave and pitch motions standard deviations are show in Figures 4.21 to 4.23, Figures 4.24 to 4.26 and Figures 4.27 to 4.29 respectively. The mean of the two most heavily loaded tendons, line 1 and 2 are shown in Figures 4.30 to 4.32. Fitted drag coefficients are found for 9 out of the 15 irregular wave cases. Values show both an increase and a decrease over the still water value C_D values. Removing the drag force from the splash zone has shown to improve the results of the simulations, by neglecting the conflicting third order LF motion excitation and reducing the WF viscous excitation and damping. The use of full QTFs compared with Newman's approximation shows either an increase or decrease in the surge motions depending on the irregular wave case. An in depth analysis shows that the full QTF surge force spectrum is always higher than that calculated from Newman's approximation, but the force is applied at a different phase resulting in this increase or decrease in motion. The pitch motions are always increased by the use of Full QTFs over the approximate methods.

For irregular wave no. 1 and 2, both LF and WF motions and tensions are greatly over predicted by all original simulations using the still water drag coefficients. For wave no. 2, a fit is achieved with a drag coefficient of 0.8. The simulation with the fitted low frequency surge drag coefficient also shows an improvement on the LF and WF motions in the other DOF and line tensions. For wave heights above 6 m, the LF surge motions are generally well predicted, while the WF motions are greatly unpredicted. For waves no. 7 and 13, the fitted coefficients of 1.9 and 4 respectively decrease in the accuracy in the WF surge response, as opposed to all other fitted cases, where there is an increase in the accuracy of the WF response with the fitted LF drag values. The WF heave motions are generally under predicted for the higher wave cases. A LF pitch motion is evident in all experimental wave cases, with only the full QTF model for wave no. 2 showing an appropriate magnitude response. This LF pitch response is generally underpredicted and may require tuning of the QTF forces in order for the numerical model to predict it [296]. Tendon tensions are underpredicted by the numerical models in a similar trend to the pitch motion which dominates the tension response. The results are spectrally analysed for both methods 1 and 2 in parallel in Section 4.3.7.3.

4.3.7.2 Method 2: Measured JONSWAP waves

In this method the observed wave elevation from the experiments is input into the numerical model. The observed wave elevation is spectrally analysed using the Matlab FFT function, and those wave components with more than 0.01% of the peak frequencies spectral energy are inserted into the OrcaFlex model. As the computational time is directly related to the number of spectral wave components, the removal of these low energy frequencies greatly increases the computational efficiency while retaining accuracy in the results. Wave components are inserted using wave frequency, amplitude and phase data. As the phase reference system is reversed between the FFT function and OrcaFlex, the phases must be multiplied by a negative unity term.

Results of the numerical modelling are compared against the experimental observations for the motions and line tensions in Figures 4.33 to 4.44. Again 9/15 cases achieve a fitted drag coefficient, although they are not the same 9 cases as in method 1. In gen-

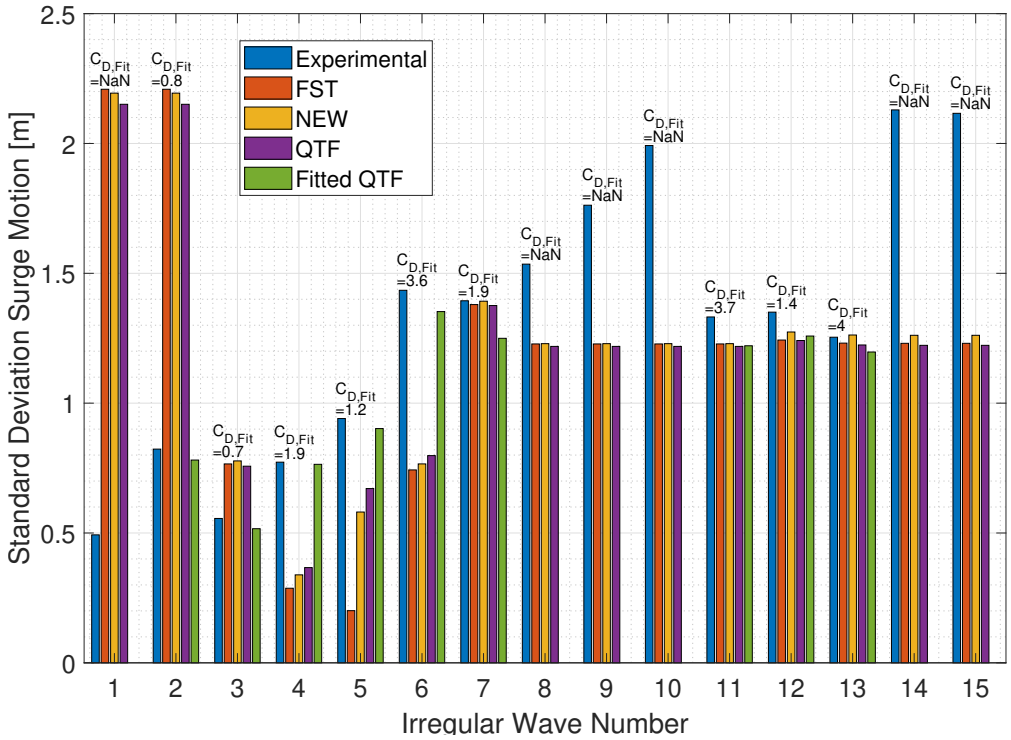


Figure 4.21: Comparison of Numerical & Experimental Surge standard deviations for Irregular Waves. Simulations with theoretical JONSWAP wave spectra

eral, the unfitted simulation results shown a much closer agreement to the experimental values, than when using the theoretical JONSWAP spectra. WF surge simulations show a dramatic improvement in the unfitted simulation accuracy compared with Method 1.

With the exception of Wave No 1 and 2, the observed wave elevation does not improve the pitch WF response compared with Method 1.

The heave standard deviations are shown in Figures 4.36 to 4.38. The low frequency surge tuning has improved the heave motions in both low and wave frequency. Most pronounced is the decrease in both low and wave frequency heave for irregular number 11, which is dramatically over predicted in the original model, but shows a good agreement in the tuned model.

The mean of Tendon 1 and 2 tension standard deviation results are shown in Figures 4.42 to 4.44. The fitted tensions are improved for all wave frequency cases, apart from in No 7, 11 and 12. Low Frequency tension predictions are generally improved, with the exceptions of No. 2, 7, 8, 9 and 15.

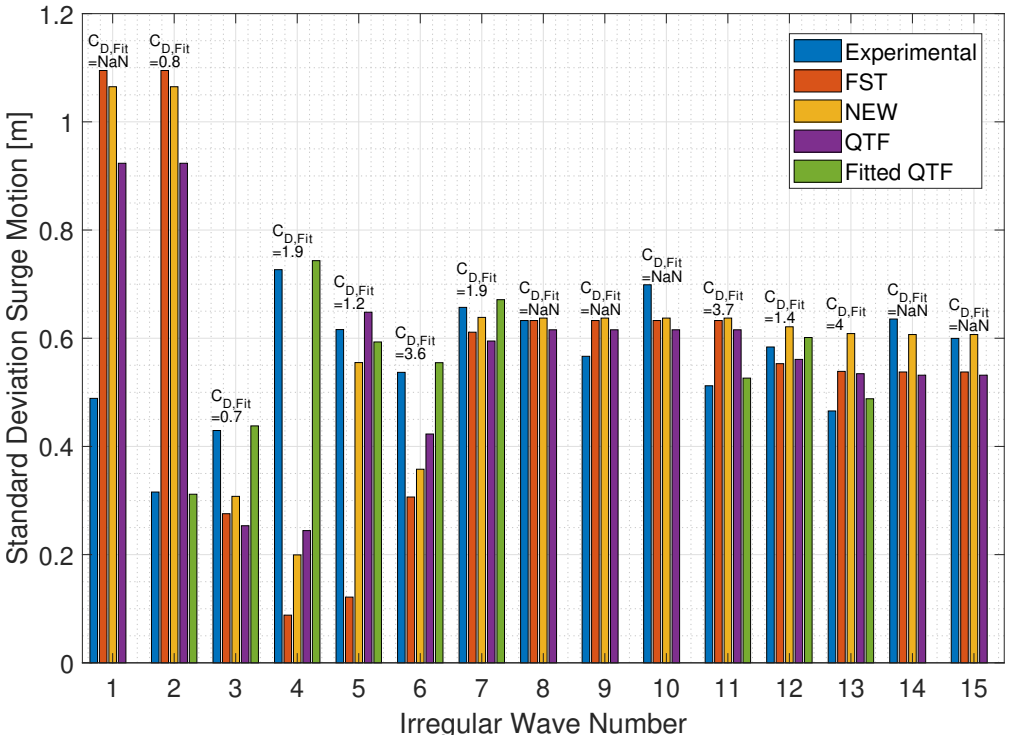


Figure 4.22: Comparison of Numerical & Experimental Surge low frequency standard deviations for Irregular Waves. Simulations with theoretical JONSWAP wave spectra

4.3.7.3 Spectral Results

The response spectral densities for the motions and tensions are shown in Figures A.15 to A.44 for both methods. The fitted drag coefficient approach is seen to also improve the accuracy of the response frequency in the wave response zone. This frequency response shift is most evident in the theoretical JONSWAP simulations, and shows a secondary positive effect of tuning the drag coefficient. Examining the data in the frequency domain, highlights how the response frequencies are much better matched when the observed wave time series is used. From these results it can be clearly seen how sensitive the response in both amplitude and frequency are to both small changes in the wave elevation time series and the drag coefficient used. Using the common still water drag coefficient and applying it to the whole body including at the splash zone significantly changes the frequency response greatly in the vicinity of the wave frequency zone.

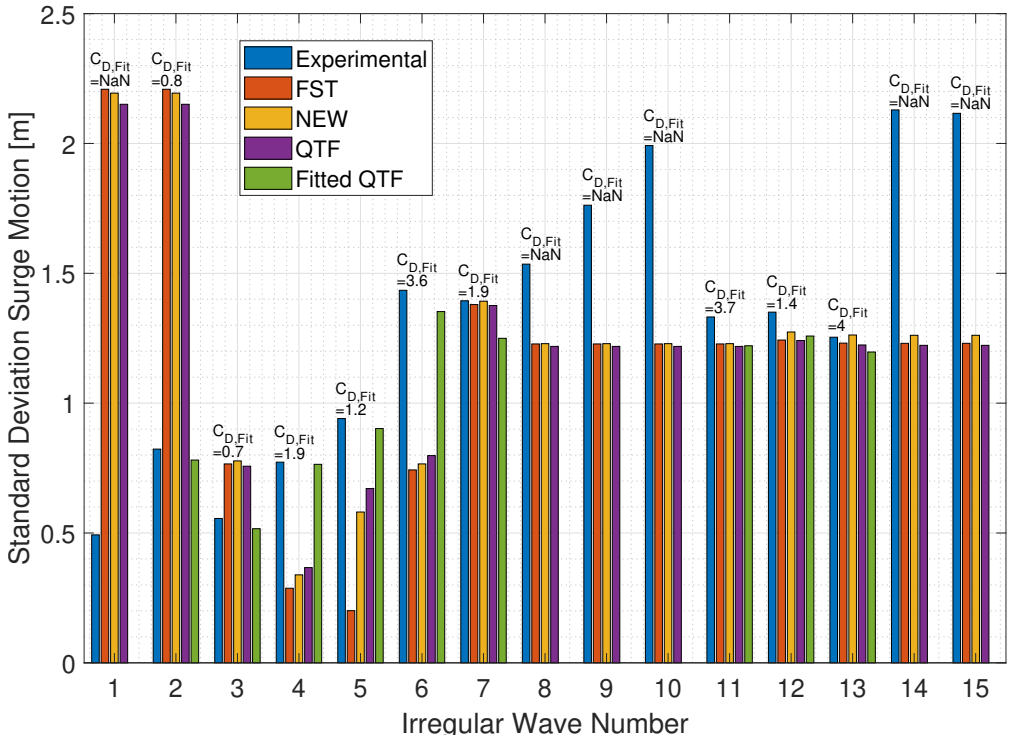


Figure 4.23: Comparison of Numerical & Experimental Surge wave frequency standard deviations for Irregular Waves. Simulations with theoretical JONSWAP wave spectra

4.3.8 Rogue Waves

In addition to the regular and JONSWAP spectral waves, rogue waves recorded from the Atlantic Marine Energy tests Site (AMETS) in Ireland were all tested. These waves came from the work of Dr. Brendan Cahill [297] and are characterised by being exceptionally large individual waves for the surrounding significant wave height. All waves have an Anomaly Index above 2.2. The observed wave elevation time history is input into the wave maker in order to generate the experimental wave elevation. The still water surge drag coefficients are used for the Rogue wave tests.

One of the most critical aspects of a TLP's response in extreme wave events is the ability to retain positive tensions in all tendons. For this reason the minimum tension of all tendons is studied in detail using the rogue waves. Simulations are performed using the varying model fidelity, similar to the previous sections. As the tendon pretension of these tests is critical for the minimum tension, and as it is quite an unknown parameter in the experimental observations due to the potential tendon slippage observed, a sensitivity

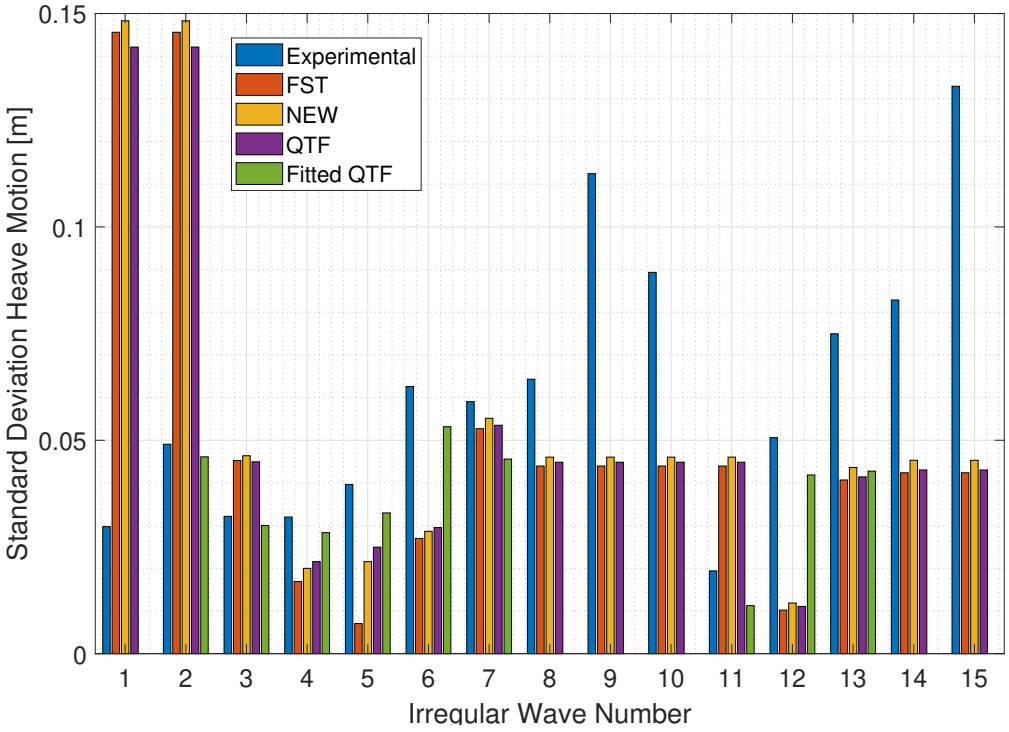


Figure 4.24: Comparison of Numerical & Experimental Heave standard deviations for Irregular Waves. Simulations with theoretical JONSWAP wave spectra

Wave Number	H_S	H_{Max}	Ai
1	3.14	7.3	2.32
2	2.95	7.14	2.42
3	2.99	7.53	2.52
4	5.49	13.71	2.50
5	6.85	15.89	2.32

Table 4.9: Rogue Wave Details

study on the individual tendons pretension is carried out similar to in Section 4.3.5. Simulations are run using 50 random permeations of the individual tendon pretension at 10% and 50% of the design pretension. Experimental rogue wave tests numbers 1- 9 had individual tendon pretension variations of up to 25%, while test number 10 had 50% variations. Due to the load cell uncertainty during the test campaign, these numbers may not be exact.

Results of the Rogue wave experiments and simulations are shown in Figure 4.45. In four cases, the experimental model has slack line events, waves number 4, 5, 9 and 10. Due to the load cell calibration issue a compression reading is observed on the load

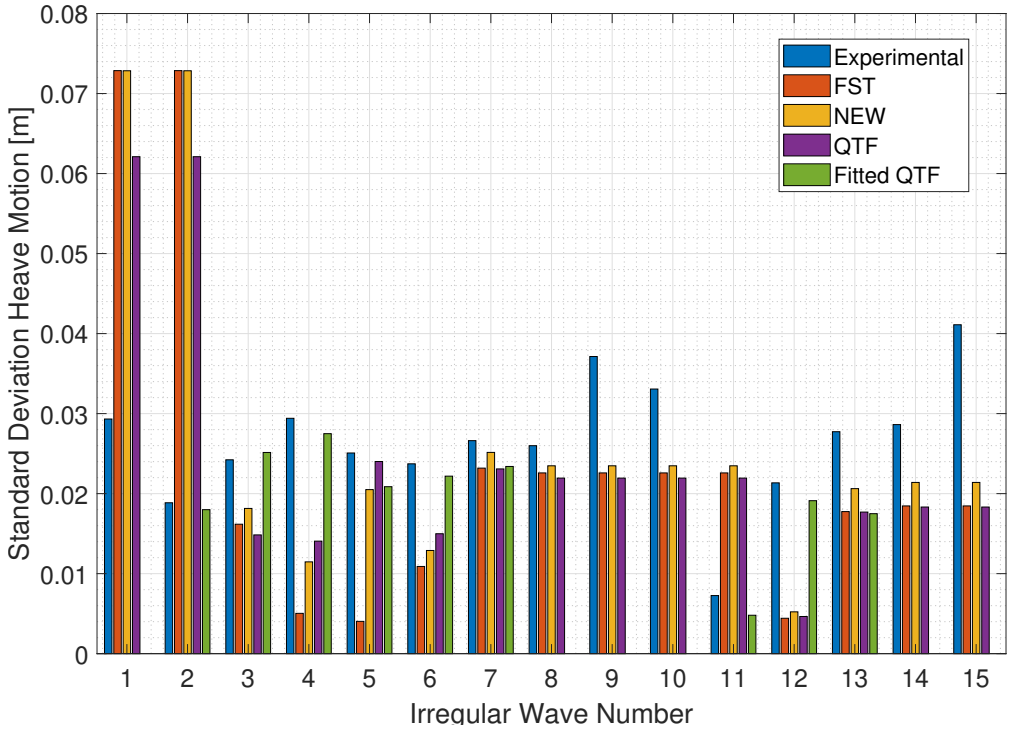


Figure 4.25: Comparison of Numerical & Experimental Heave low frequency standard deviations for Irregular Waves. Simulations with theoretical JONSWAP wave spectra

cells (negative force). Due to the tendon wires extremely low bending stiffness, it is impossible for a significant compression force to be transmitted to the load cells, hence these negative tension values further highlight the loss of load cell calibration.

In order to have some safety margin, any tensions below 5 % of the pretension are taken as slack events. The design pretension simulations, shown in the bar plots, thus predict the slack events in 3 out of the 4 observed events, that is wave numbers 5, 9 and 10. The individual pretension study shows that for cases 1 - 3, the observed values fall between those predicted by the 10 % and 50 % tension variation 50th percentile bands. While for cases 6-8, the observed values fall in the 50 % tension variation 50th percentile bands. Generally the use of second order wave forces by Newman's approximation is seen to increase the minimum tensions compared to the first order only model. Conversely the use of full QTFs lead to a decrease in the minimum tensions compared to the first order only model. The exceptions to this are wave numbers 5 and 7, where the full QTF shows an increase in the minimum tension over both other numerical methods.

For all wave numbers, with the exception of no. 4, the observed minimum tensions

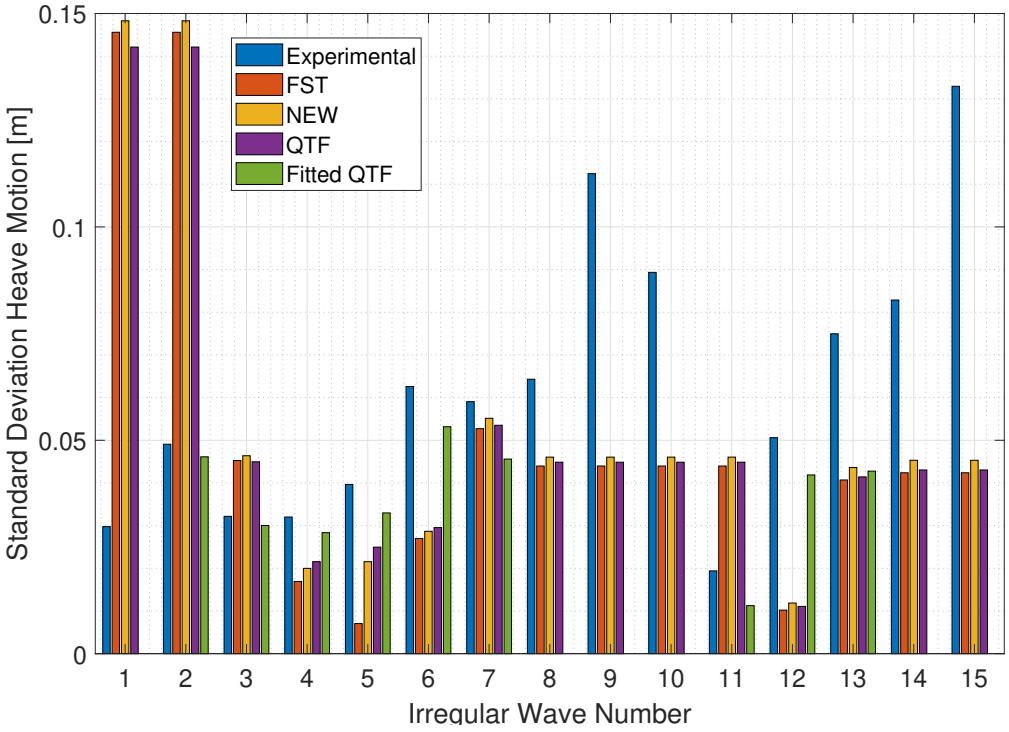


Figure 4.26: Comparison of Numerical & Experimental Heave wave frequency standard deviations for Irregular Waves. Simulations with theoretical JONSWAP wave spectra

are within the extreme range of the 50% pretension variation for simulations using the full QTF second order wave forces. For wave numbers 1 to 3, the observed results are in between the 50th percentile of numerical 10% and 50% pretension variation ranges. The tendon variations are up to $\sim 25\%$ in the experimental observations, giving some confidence to these results. For wave numbers 4 and 5, the experimental observations fall below the 50% numerical pretension variation 50th percentile range. As the observed pretension variation is of the same order as test 1 to 3 ($\sim 25\%$), this difference most likely comes from the linear superposition wave field method, which under predicts the tendon load oscillations compared to a higher order wave field [195]. For test number 4 the use of full QTF minimises the difference between the observed minimum tension, further indicating that the inclusions of higher order effects will improve predictions. For wave numbers 6 to 8, the observed minimum tensions are in the 50% numerical pretension variation range.

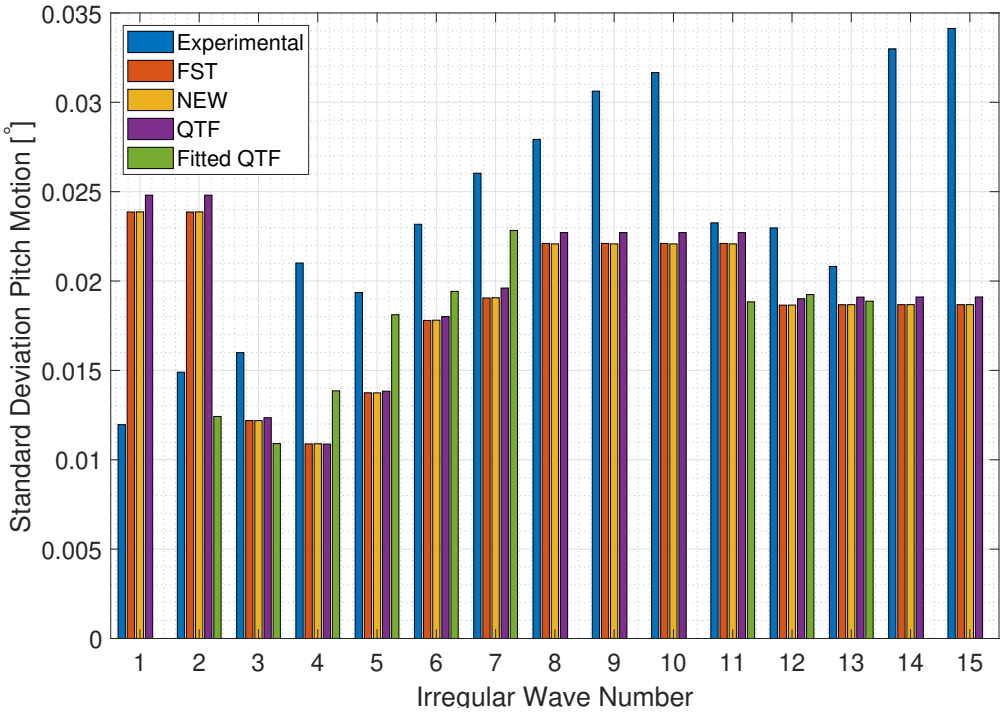


Figure 4.27: Comparison of Numerical & Experimental Pitch standard deviations for Irregular Waves. Simulations with theoretical JONSWAP wave spectra

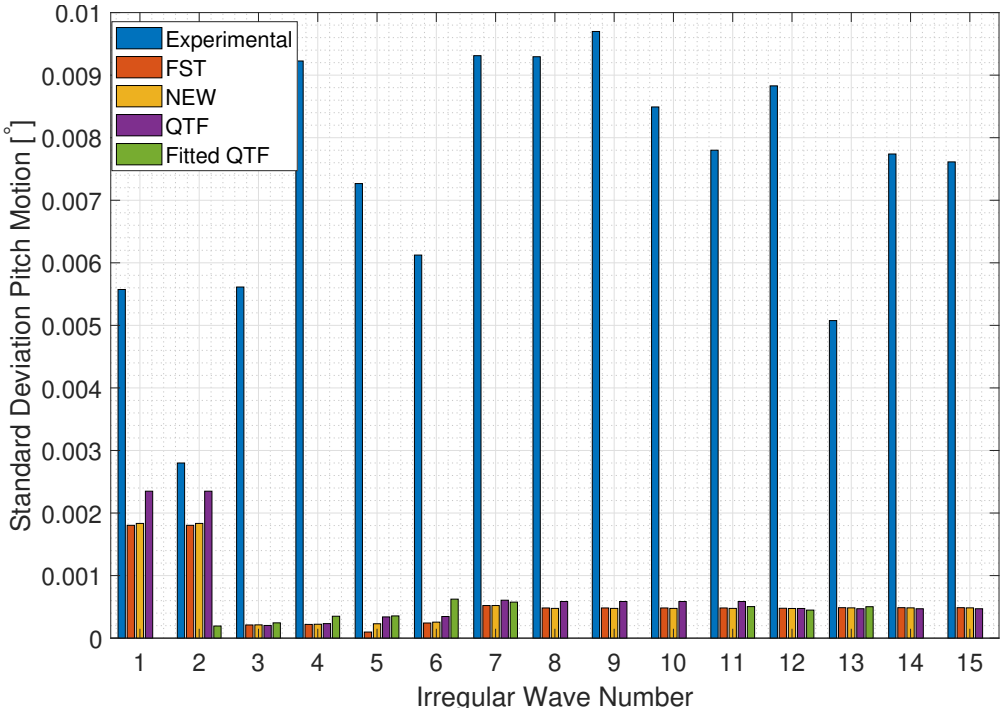


Figure 4.28: Comparison of Numerical & Experimental Pitch low frequency standard deviations for Irregular Waves. Simulations with theoretical JONSWAP wave spectra

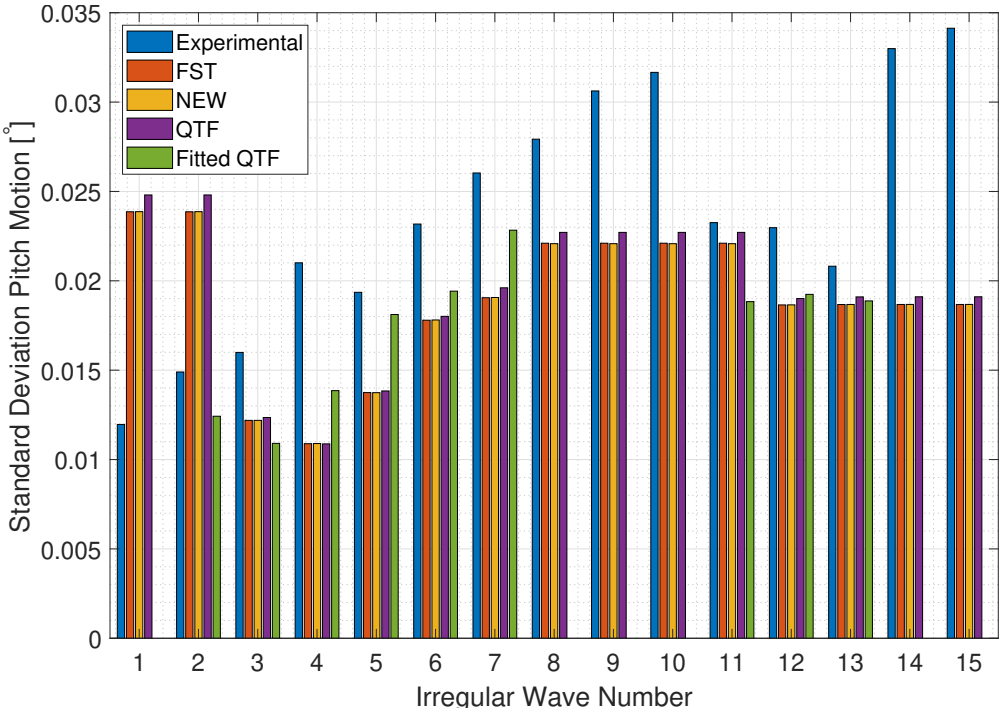


Figure 4.29: Comparison of Numerical & Experimental Pitch wave frequency standard deviations for Irregular Waves. Simulations with theoretical JONSWAP wave spectra

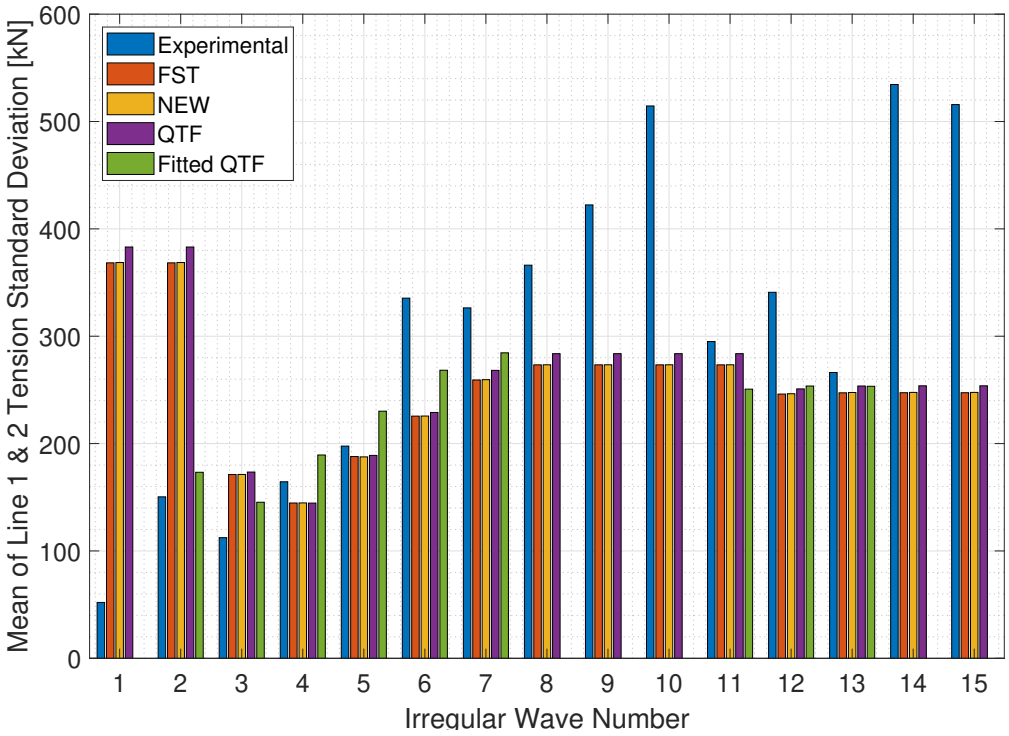


Figure 4.30: Comparison of Numerical & Experimental Tendon Tension standard deviations for Irregular Waves. Simulations with theoretical JONSWAP wave spectra

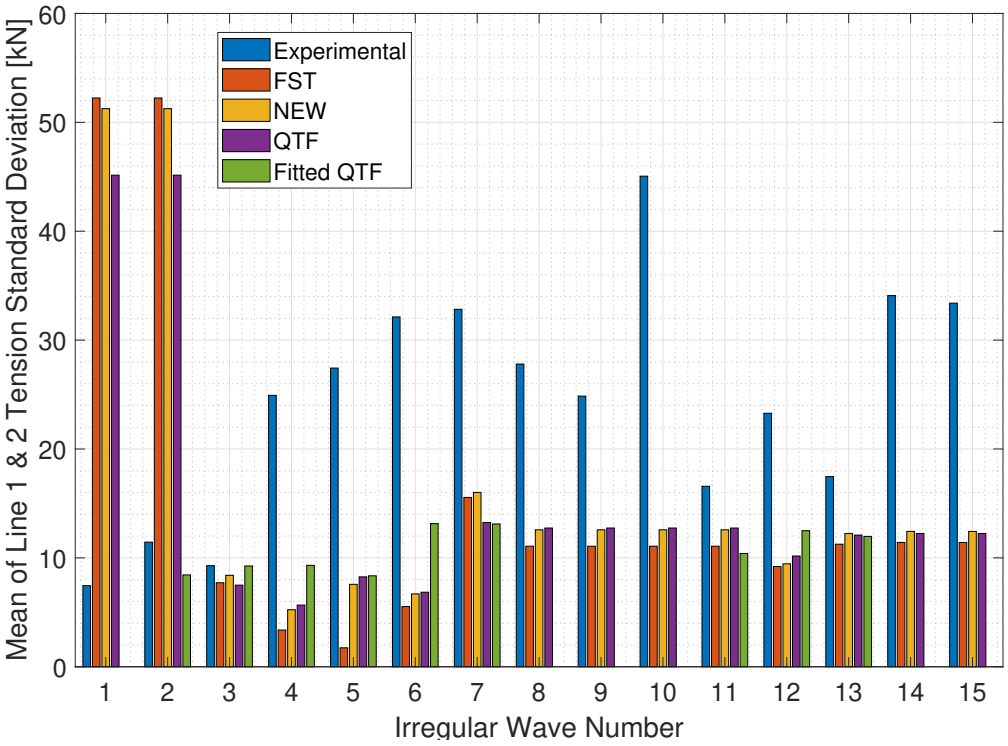


Figure 4.31: Comparison of Numerical & Experimental Tendon Tension low frequency standard deviations for Irregular Waves. Simulations with theoretical JONSWAP wave spectra

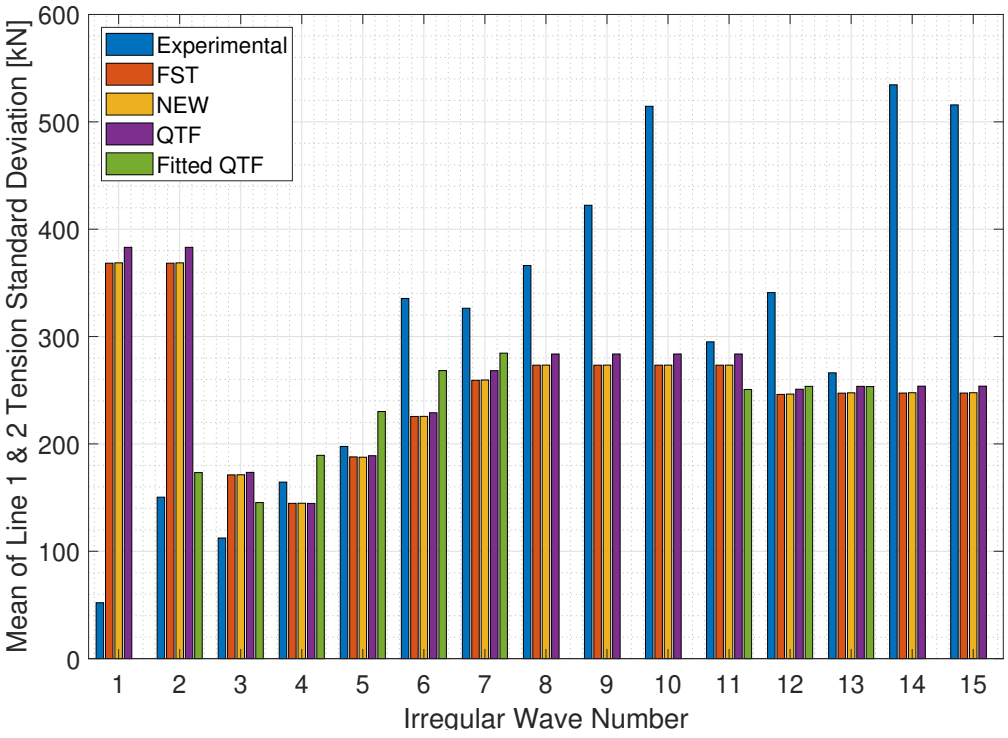


Figure 4.32: Comparison of Numerical & Experimental Tendon Tension wave frequency standard deviations for Irregular Waves. Simulations with theoretical JONSWAP wave spectra

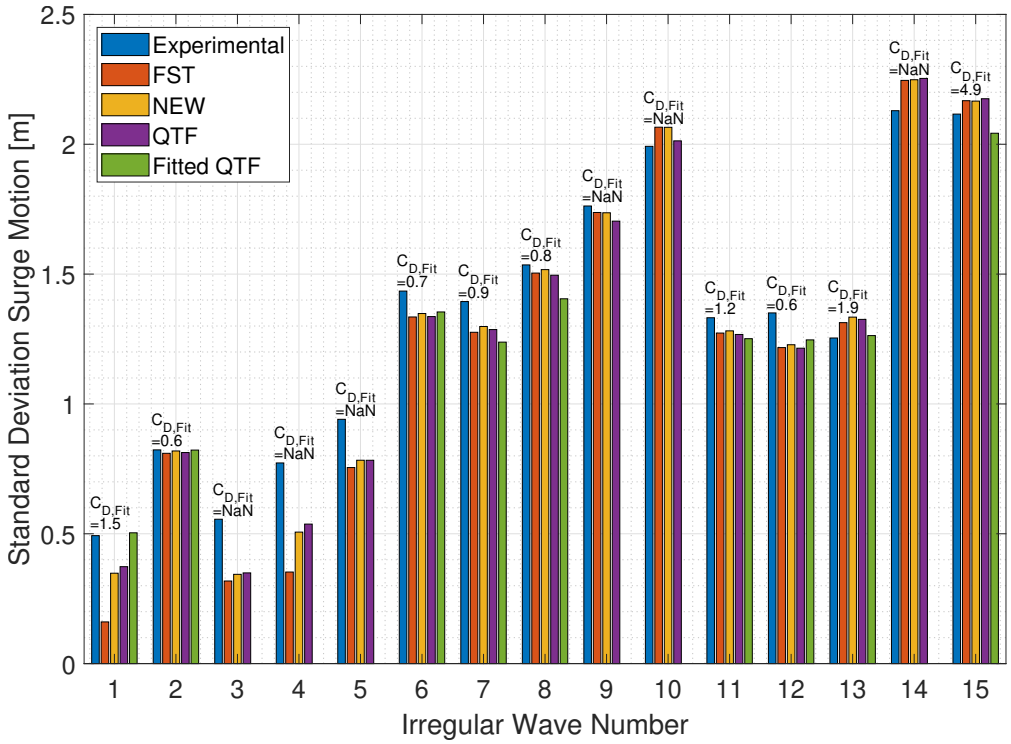


Figure 4.33: Comparison of Numerical & Experimental total frequency Surge standard deviations for Irregular Waves. Simulations with observed wave elevation. OBS, FST, NEW, QTF and Fitted QTF, indicate the observed, first order, Newman's approximation, Full QTF and drag coefficient fitted Full QTF simulations respectively

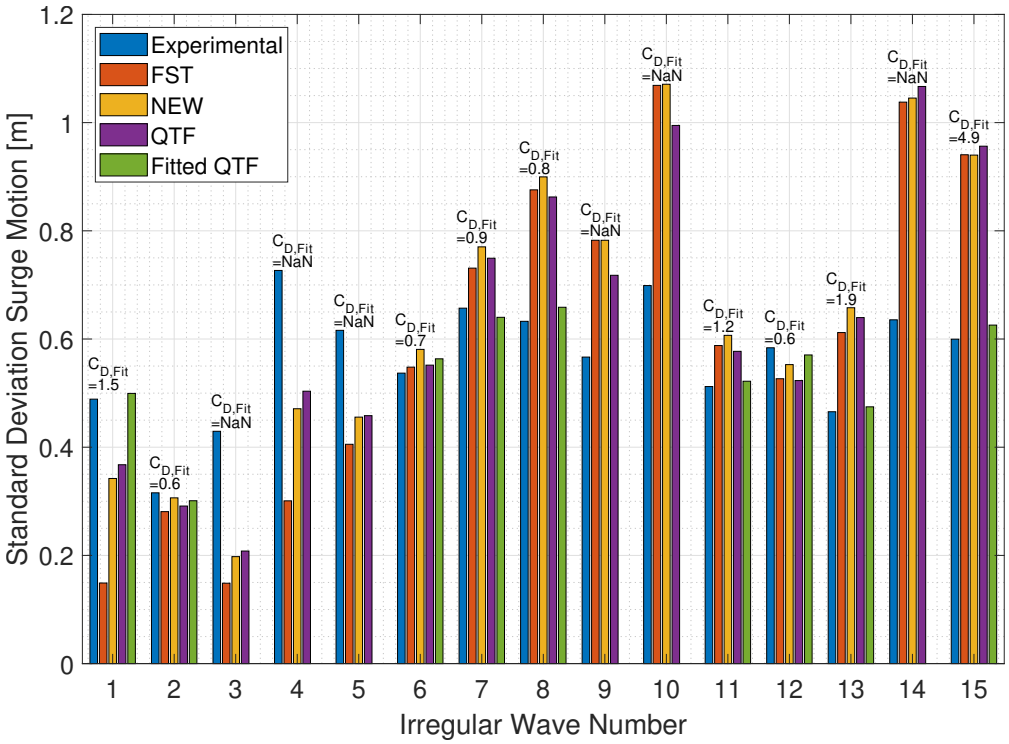


Figure 4.34: Comparison of Numerical & Experimental low frequency Surge standard deviations for Irregular Waves. Simulations with observed wave elevation. OBS, FST, NEW, QTF and Fitted QTF, indicate the observed, first order, Newman's approximation, Full QTF and drag coefficient fitted Full QTF simulations respectively

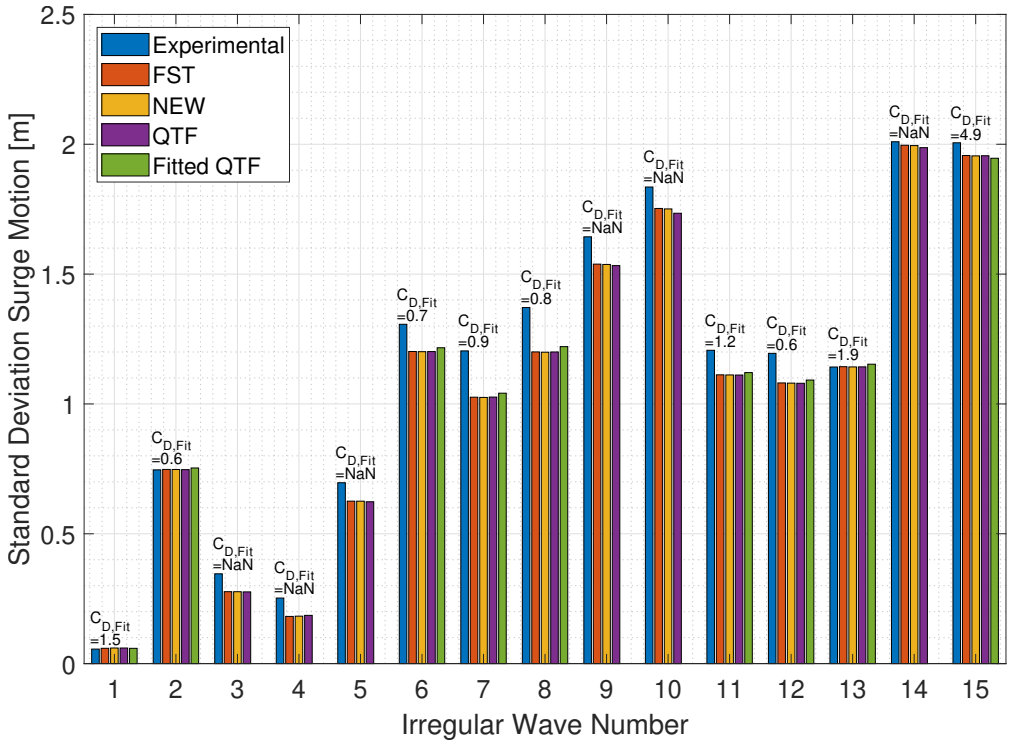


Figure 4.35: Comparison of Numerical & Experimental wave frequency Surge standard deviations for Irregular Waves. Simulations with observed wave elevation. OBS, FST, NEW, QTF and Fitted QTF, indicate the observed, first order, Newman's approximation, Full QTF and drag coefficient fitted Full QTF simulations respectively

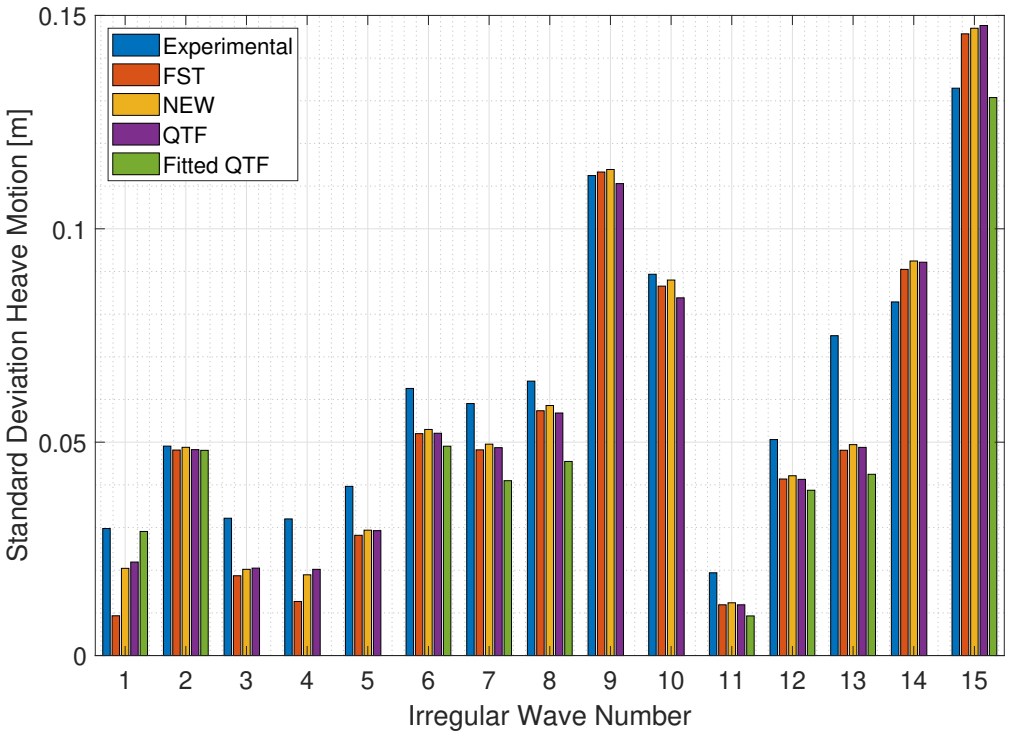


Figure 4.36: Comparison of Numerical & Experimental total frequency Heave standard deviations for Irregular Waves. Simulations with observed wave elevation. OBS, FST, NEW, QTF and Fitted QTF, indicate the observed, first order, Newman's approximation, Full QTF and drag coefficient fitted Full QTF simulations respectively

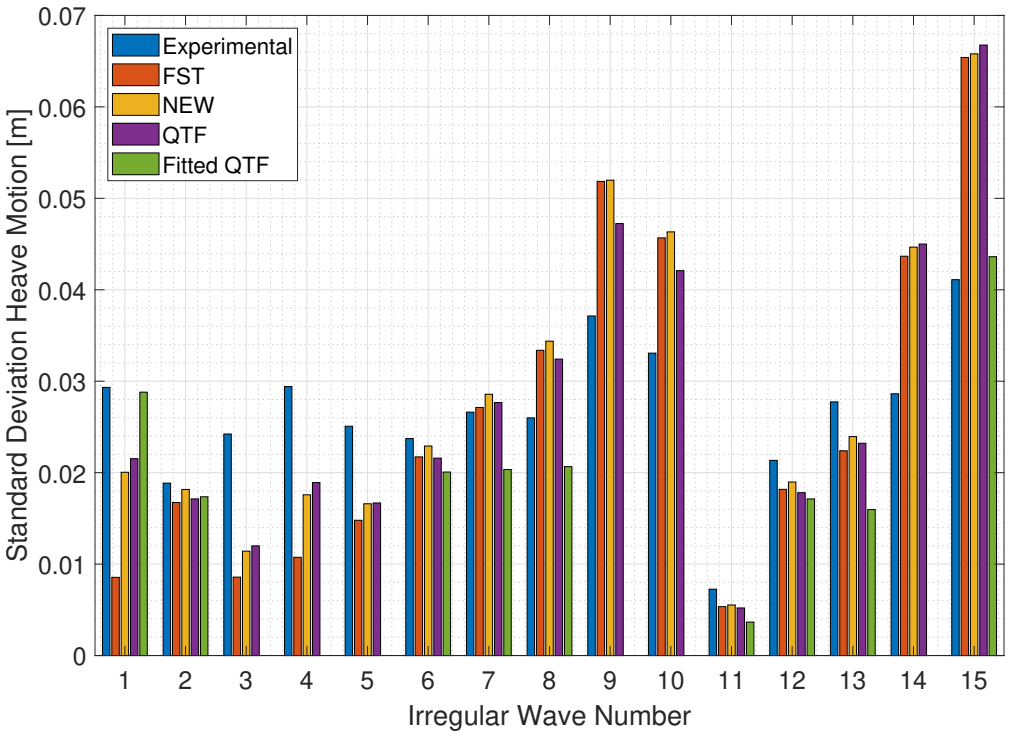


Figure 4.37: Comparison of Numerical & Experimental low frequency Heave standard deviations for Irregular Waves. Simulations with observed wave elevation. OBS, FST, NEW, QTF and Fitted QTF, indicate the observed, first order, Newman's approximation, Full QTF and drag coefficient fitted Full QTF simulations respectively

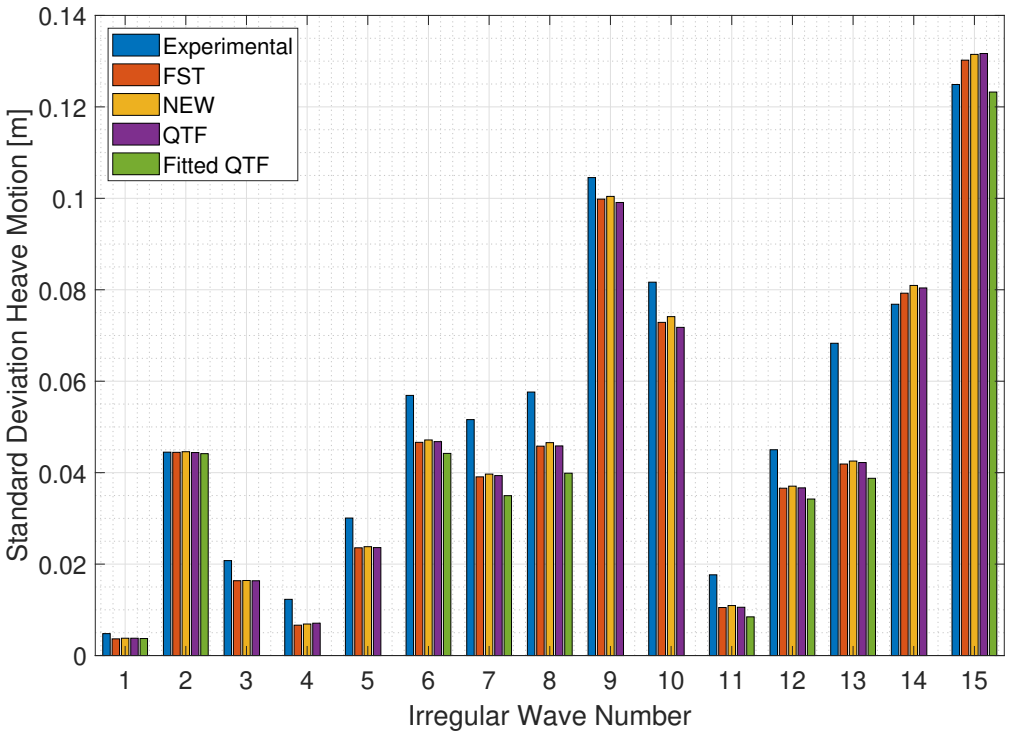


Figure 4.38: Comparison of Numerical & Experimental wave frequency Heave standard deviations for Irregular Waves. Simulations with observed wave elevation. OBS, FST, NEW, QTF and Fitted QTF, indicate the observed, first order, Newman's approximation, Full QTF and drag coefficient fitted Full QTF simulations respectively

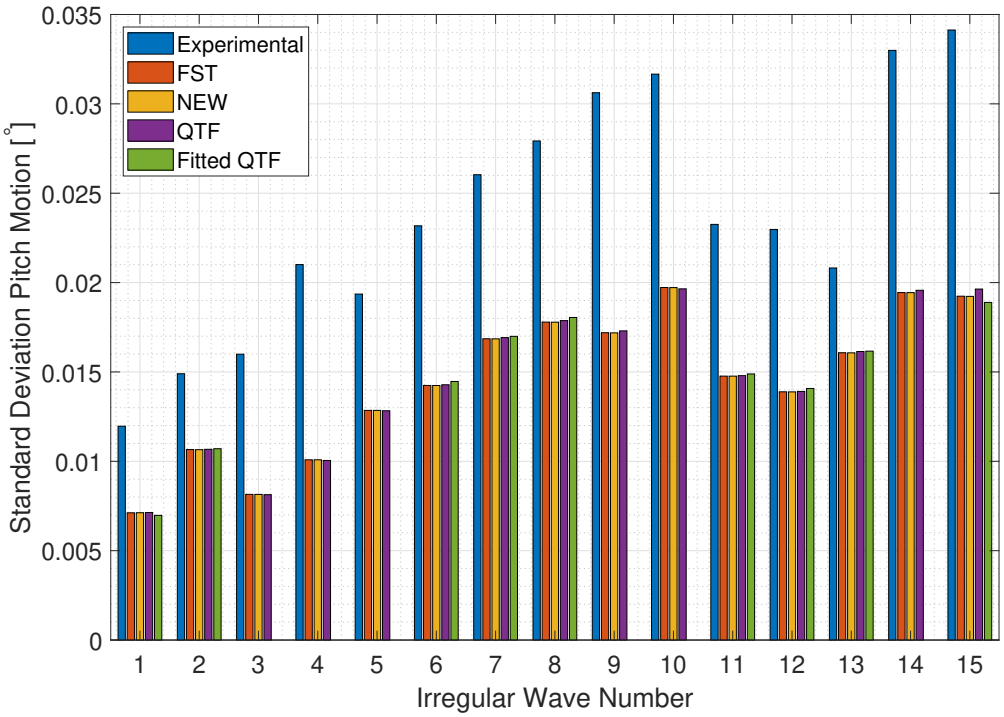


Figure 4.39: Comparison of Numerical & Experimental total frequency Pitch standard deviations for Irregular Waves. Simulations with observed wave elevation. OBS, FST, NEW, QTF and Fitted QTF, indicate the observed, first order, Newman's approximation, Full QTF and drag coefficient fitted Full QTF simulations respectively

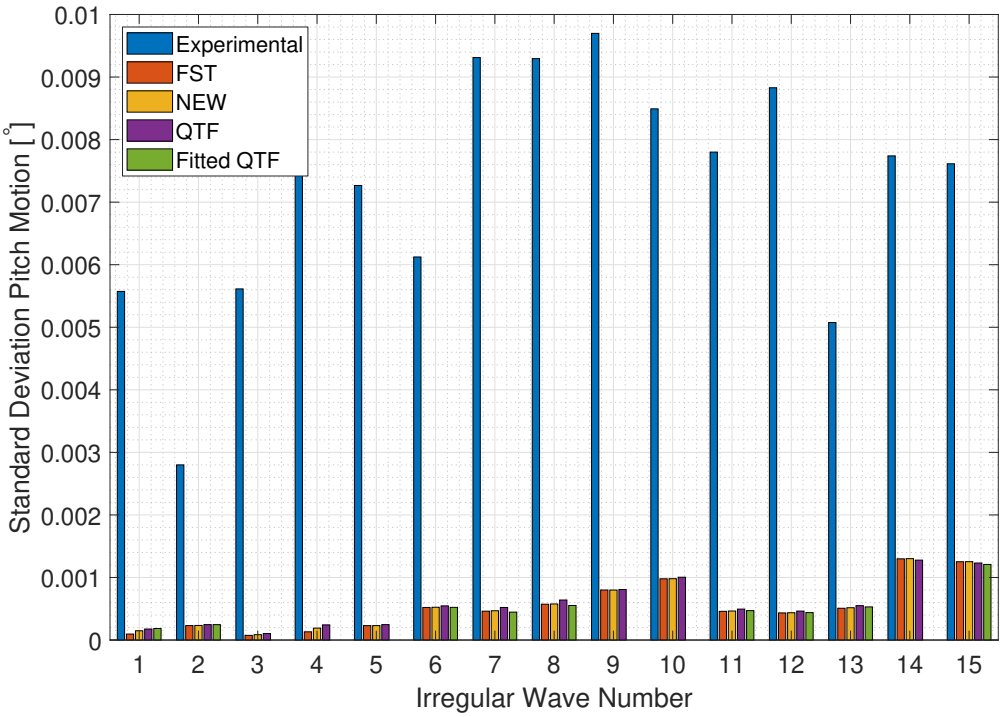


Figure 4.40: Comparison of Numerical & Experimental low frequency Pitch standard deviations for Irregular Waves. Simulations with observed wave elevation. OBS, FST, NEW, QTF and Fitted QTF, indicate the observed, first order, Newman's approximation, Full QTF and drag coefficient fitted Full QTF simulations respectively

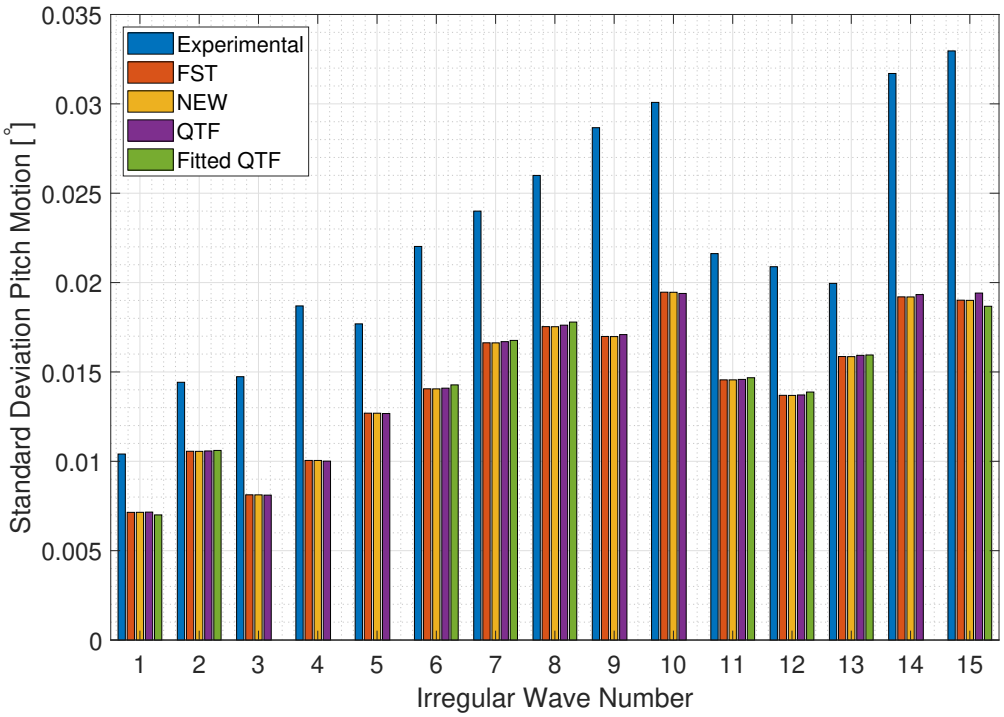


Figure 4.41: Comparison of Numerical & Experimental wave frequency Pitch standard deviations for Irregular Waves. Simulations with observed wave elevation. OBS, FST, NEW, QTF and Fitted QTF, indicate the observed, first order, Newman's approximation, Full QTF and drag coefficient fitted Full QTF simulations respectively

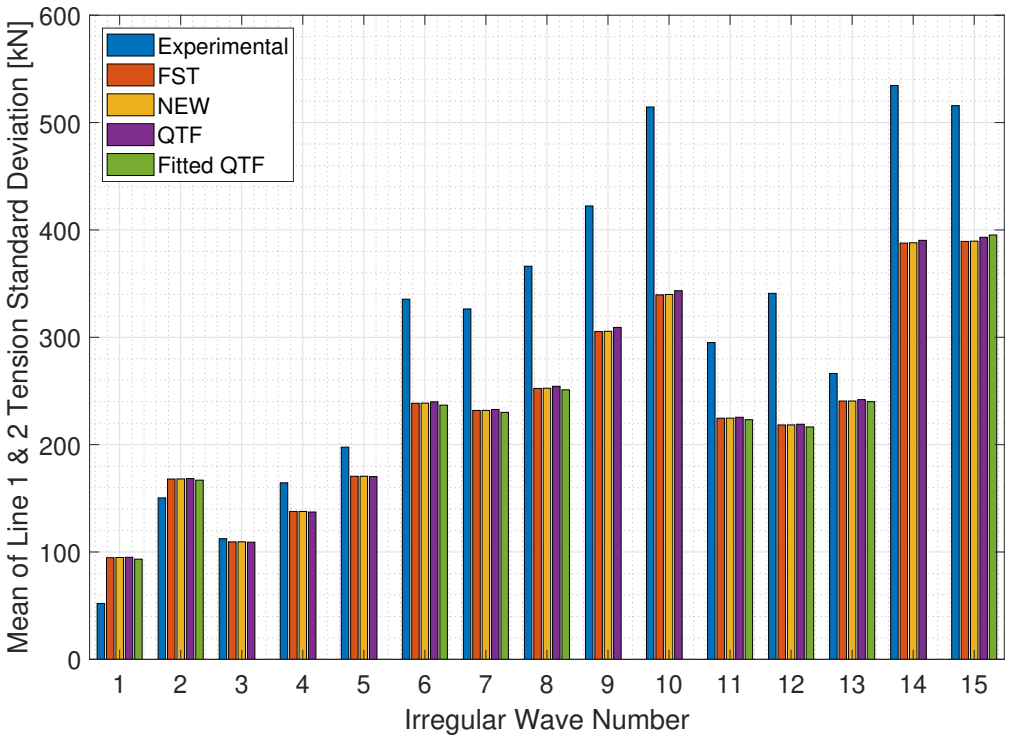


Figure 4.42: Comparison of Numerical & Experimental total frequency Tendon Tension standard deviations for Irregular Waves. Simulations with observed wave elevation. OBS, FST, NEW, QTF and Fitted QTF, indicate the observed, first order, Newman's approximation, Full QTF and drag coefficient fitted Full QTF simulations respectively

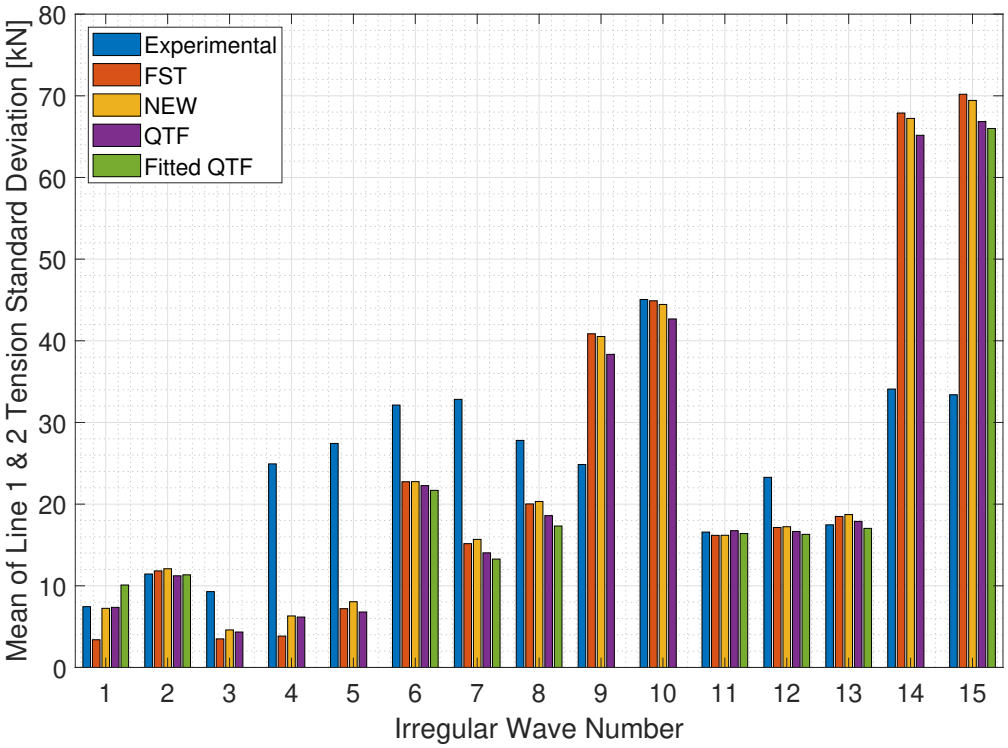


Figure 4.43: Comparison of Numerical & Experimental low frequency Tendon Tension standard deviations for Irregular Waves. Simulations with observed wave elevation. OBS, FST, NEW, QTF and Fitted QTF, indicate the observed, first order, Newman's approximation, Full QTF and drag coefficient fitted Full QTF simulations respectively

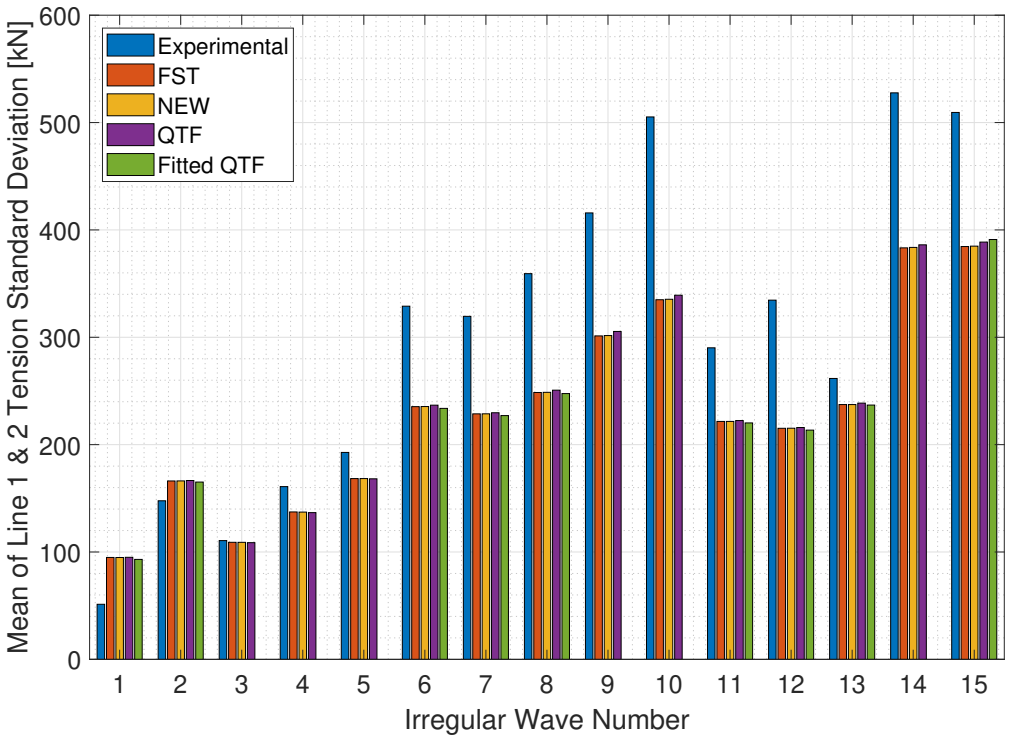


Figure 4.44: Comparison of Numerical & Experimental wave frequency Tendon Tension standard deviations for Irregular Waves. Simulations with observed wave elevation. OBS, FST, NEW, QTF and Fitted QTF, indicate the observed, first order, Newman's approximation, Full QTF and drag coefficient fitted Full QTF simulations respectively

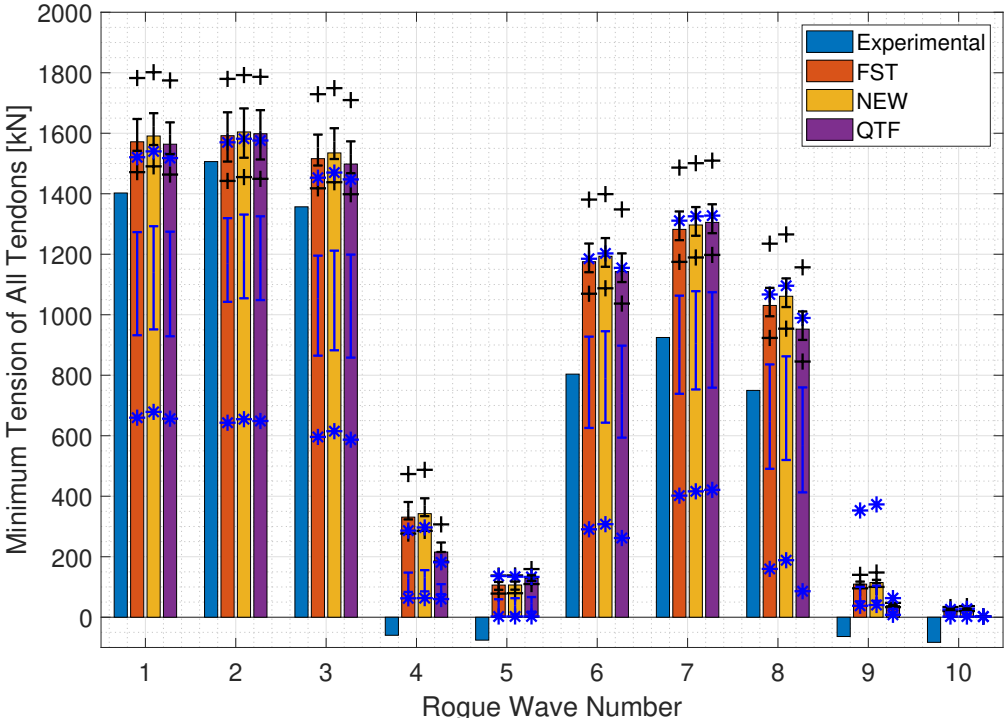


Figure 4.45: Comparison of Numerical & Experimental Minimum Tendon Tension for Rogue Waves. Black crosses and blue asterisks indicate the extreme range of the 50 random tendon tension variations at the 10% and 50% levels respectively. Black and blue error bars indicate the 50th percentile of the values at the 10% and 50% levels respectively.

4.4 Conclusions

The HEXWIND FWT platform was successfully experimentally and numerically modelled. A 1/30th scale model was used to validate the numerical modelling approach to be taken throughout this work. The importance of the nonlinear coupling on the HEXWIND RAO has been demonstrated by the regular wave responses. Of most significance is the surge heave and surge pitch coupling, leading to nonlinear RAO's. These DOF coupling effects also lead to nonlinear tendon RAO. The nonlinear coupling will also be evident in the tower bending moments and WT DOF and thus are critical for the accurate modelling of TLPFWT.

Numerical models using a range of wave force fidelity's, including first order only forces, second order forces by Newman's approximation and full QTFs have been simulated. Viscous drag forces have been applied using either the still water decay values or by fitting the required drag coefficient to the low frequency surge variance. The use of still water viscous damping coefficients has led to errors in the motion and tension amplitudes as well as frequency responses. Fitting the drag coefficient to the low frequency region, while neglecting any viscous damping in the splash zone was seen to greatly improve the numerical predictions at both low and wave frequency responses. Due to the tight coupling between motions on a TLP platform, the improvements in surge motions also led to improvements of the other degrees of freedom as well as the tendon tensions. The tuned drag coefficients were shown to have a potential wave height relationship.

Accurately predicting the low frequency surge motions is especially important for the design of tension moored FWT power umbilical. The low frequency tendon tension only amounted to around 10% of the total response and is therefore not as significant as traditionally catenary moored platforms.

The small effects of second order loads on the pitch motions and tendon tensions on the HEXWIND platform are described. First order forces dominate across all test cases. No ringing or springing phenomenon were observed. While the effects of second order forces are small, the importance of correctly predicting the second order force's phase has been demonstrated. A larger force spectrum generated using full QTFs in

comparison to Newman's approximation, may result in a reduced motion amplitude as the phase application is varied. To put these results into perspective with other TLPWT platforms, the displacement of HEXWIND is $\sim$ 4000 tons, while the displacement of a TLPWT that showed significant second order sum-frequency force effects was $\sim$ 5700 tons [298], while a TLPWT that showed negligible effects due to sum-frequency loading was $\sim$ 2800 tons [299]. These results give further evidence to the fact that the importance of second order loads on TLPWT scale with increasing displacement.

Difficulties in accurately measuring the experimental tendon tensions, due to load cell calibration failures, has been dealt with by incorporating a statistical variation of the tendon pretension into the regular and rogue wave simulations. Rogue wave tests showed the failure of the HEXWIND design under extreme wave events. Although the numerical predictions had some difficulties in predicting these extreme low tendon tensions, the general behaviour of the system was well predicted.

Due to the design failures of the HEXWIND platform in extreme wave events it was decided to design a new TLPWT. In the next chapter the numerical modelling techniques introduced and validated are built upon. The effects of tower flexibility on the design are introduced.

Chapter 5

Design of TWind

This chapter deals with the design procedures of a new tension moored floating wind turbine for Irish waters. While general design procedures for TLP WT have been previously outlined in detail, as discussed in Chapter 2, a review of existing literature for detailed design aspects identified gaps in the generalised effects of TLP tower flexibility and on the self stability in tow to site. These aspects are made the focus of this chapter.

This chapter begins with identifying the design conditions for potential Irish deployment sites. The bathymetry, wind and wave conditions are analysed. Following from this a detailed hydrodynamic analysis of the relevant platform parameters is undertaken. A study on the effects of these hydrodynamic parameters on tower flexibility and resultant responses is undertaken next. A preliminary design study on making the TLP self stable for the transportation and installation phases rounds off the chapter.

A summary of results and conclusions from this chapter are as follows:

- A bathymetry study showed that the largest exploitable area for floating wind was at 70 m water depth for areas within a distance of 40 km to shore, and at 100 m water depth for distances between 40 and 140 km from shore.
- An extreme wave extrapolation study and subsequent prediction defeating storm event demonstrated the challenges in extrapolating relatively short duration observed datasets (approximately 10 years)up to the required FWT design periods.
- An innovative shortened tower is proposed in order to increase the tower and overall

platform stiffness and thus coupled tower bending - pitch natural frequency of the platform.

- NEMOH and OpenFAST were coupled, enabling a detailed hydrodynamic parameter study to be extended into the time domain and include the WT and tower coupling effects.
- A parametric overview of pitch frequency alteration with tower flexibility is given.
- A novel tension moored floating wind turbine design is given
- A self stable tow design is presented for the new TMFWT, viable for tows in up to 3 m significant wave heights.

5.1 Design Conditions

An initial investigation into generalised design conditions for possible Irish MRE deployment sites is outlined here. Firstly bathymetry is analysed as water depth is the most important driver for the transition between fixed and floating WT's. Following from this an extreme wave analysis is carried out. A study on curtailing the produced wind energy due to large wave conditions and forced stoppage of the turbine is then investigated.

5.1.1 Bathymetry

The water depth in the Irish exclusive economic zone is analysed using bathymetry data from the European Marine Observation and Data network EMODnet [300]. This data is a collection of the best available bathymetry information at the time of writing. Where no ship track soundings are available, satellite-derived gravity data is used. A quick data verification step is done by checking against the M-buoy's water deployment depth as seen in Table 5.1 from the Marine Institute[301]. As there is some uncertainty to the buoy deployment depth and as percentage error $(100(WD_{MI} - WD_{EMO})/WD_{MI}$, where WD_{MI} and WD_{EMO} are the water depths from the Marine Institute and EMODnet respectively) is seen to be quite low, less than 5%, this data set is seen to be acceptable to be used for this purpose.

Water depths from 500 to 0 m are analysed in 10 m increments. The area at each depth is calculated using a Lambert azimuthal equal-area projection [302]. A constraint on distance to shore of 140 to 40 km is then applied. Results of the various constrains can be seen in Figure 5.2. In the unconstrained distance case, the most area corresponds to a water depth of 130 m. As the distance to shore constraint decreases so does the water depth at which the majority of the area is located. With constraints from 140 - 60 km the greatest area occurs at water depths of 100 m, at 40 km this reduces again to 70 m. From a water depth of zero to 60 m the effect of the distance to coast constraint is negligible as all water at this depth is near shore. This water depth data can be used as a basis for the design of MRE devices.

5.1.2 Extreme Wave Extrapolation

Waves with return periods of 50 and 100 years are extrapolated from the MI buoy datasets using the Average Conditional Exceedance Rate (ACER) method [303]. Advantages of the ACER method include the fact it gives a non-parametric representation of the data's exact extreme value distribution and takes into account dependence by conditioning on previous data points in the time series. The ACER k value is a parameter to be chosen reflecting the (k-1)-step memory of the data. A value of k = 1 corresponds to independent data, where as k = 2 is used for this study [304]. This k value means that independence is only checked against the previous wave height value, and will not give truly independent storm events. For the purpose of this study it is found acceptable. The dataset is assumed to be stationary, which accounting for climate change is not strictly

Table 5.1: Depth Validation

M Buoy No.	Emodnet Water Depth	MI Water Depth	Percentage Difference
1	130		
2	87	88	1,14
3	152	155	1,94
4	117	112	−4,46
5	69	70	1,43
6	3253	3100	−4,94

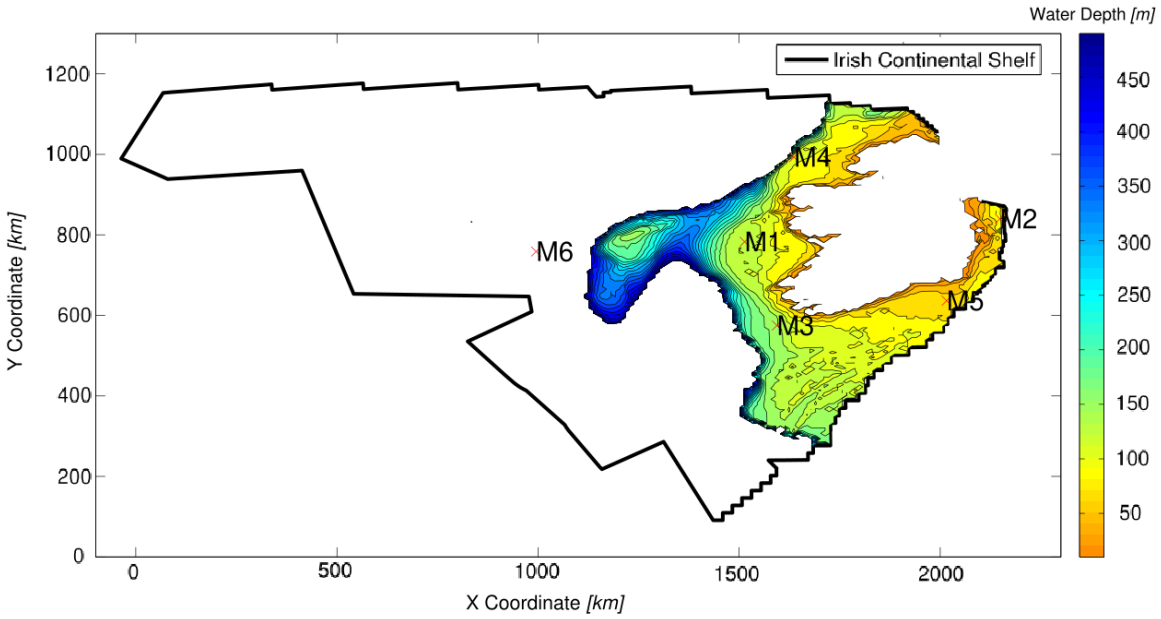


Figure 5.1: Map of Irish Continental Shelf, including contour lines of all water depth above 500 m (excluding the far offshore Rockall Bank) and the M-buoy locations. The Lambert azimuthal equal-area projection is shown here as is used for the area calculations.

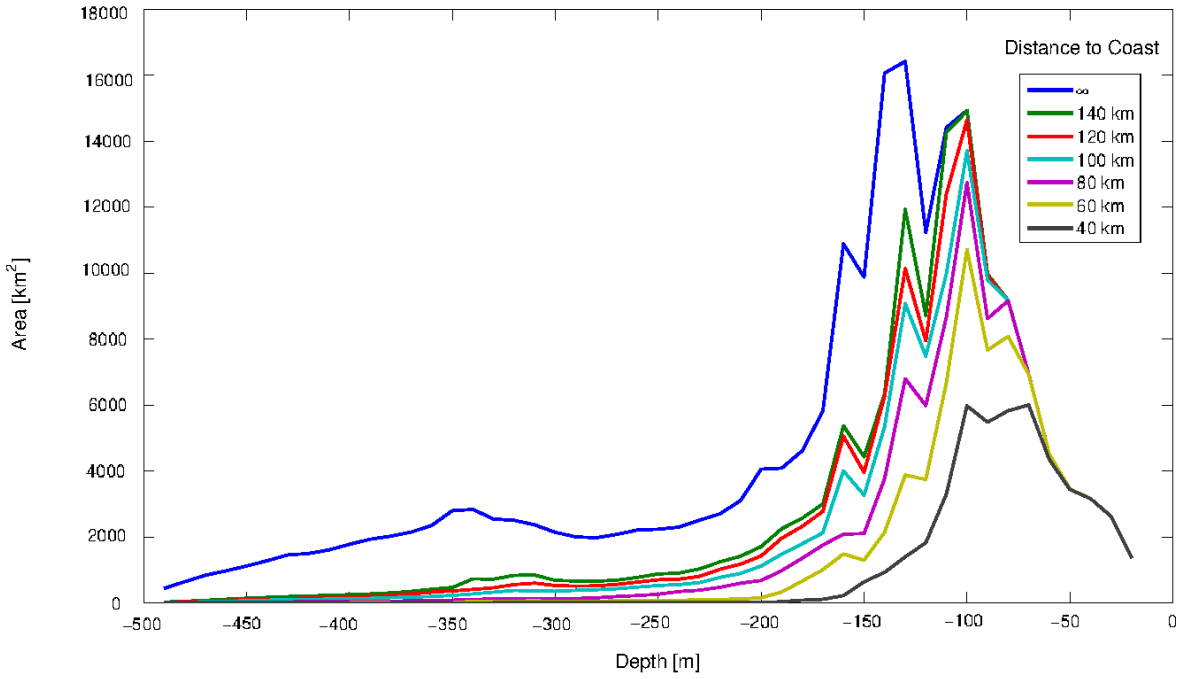


Figure 5.2: Sea Area at certain Depth and distance to Coast

correct, the changes are negligible over the limited time period available for this study. Both the significant wave height, H_s and maximum wave height, $H_{s,max}$ are extrapolated in this manner with results given in Table 5.2.

Periods are extrapolated by fitting a linear regression model to the 95 percentile highest waves and corresponding periods. Periods are given for the mean and 95 percentile confidence intervals.

Operational extreme waves are also analysed. Wave data is binned in 1m increments according to significant wave height. The H_{MAX} with a return period of 50 years for each bin is determined using the Peaks over Threshold (POT) method [304]. A minimum of 25 unique storm events, need to be taken for each bin, meaning only the lower H_S bins can be extrapolated in this way. A caveat of this analysis is the fact that H_{MAX} data is sparse from the M-Buoy dataset. As an example from deployment in May 2001 till late October 2010, the M2 buoy recorded significant wave height but no maximum wave height. Maximum wave height data is thus only available after this date. Figure 5.3 and 5.4 show the predicted H_{MAX} and A_i respectively. The A_i can be seen to decrease with increasing significant wave height. This will have an important effect on the peak loading design of MRE converters. For the design of WEC's this will lead to important considerations for the cut-out wave height $H_{S,Cut-out}$. The most severe example of this can be seen in the M4 data, where there is a sharp jump in the predicted H_{MAX} and A_i after a H_S of 7m. This would suggest it may be wise to place the cut out wave height below this jump.

The largest H_{MAX} may not appear at largest Hs, due to anomaly index decreasing as Hs increases and the increase in damping at larger sea-states. Therefore the contour method traditionally used for extreme load analysis may not be adequate.

In mid October 2017 extremely large waves were observed off the South coast of Ireland. On the 16th October 2017 a subtropical hurricane made landfall on the West Coast of Ireland. It had generally been heading for the Irish sea, before a late turn saw it head Westwards along the Western Irish coast. As the storm travelled Northwards (from the coast of Portugal) the fetch was generally being directed into the Irish Sea. Because of this, extremely large waves were recorded at the M5 buoy, a H_S of 12.97 m

T_Z of 15.82 s and H_{MAX} of 17.813 m and T_Z of 15.82 s. This event can be described as a black swan event, and invalidates the predictions made in the previous section for the M5 site. This event highlights the dangers in using relatively short historical metocean datasets to perform long term extrapolations. Further to this, Climate change is known to increase the probability and intensity of tropical cyclone events, increasing the chances of subtropical storm events in Irish waters. As the weather phenomenon behind typical winter storms and tropical cyclones differ, extrapolations based on the former will not be relevant for possible future conditions when the latter dominates the extreme environmental loads.

5.1.3 Curtailed Wind Energy based on Wave Height

Not only will the WT be forced to cease power production in winds above the cut-off speed, it may also be required to shut down in sea-states above a certain threshold, when nacelle accelerations become too large. In this section the energy generated by the NREL reference WT at the M-Buoy sites is analysed. Cut out significant wave heights, when the WT enters survival mode, from 1 m to 18 m are analysed. Figure 5.5 shows the results of this analysis. The dashed lines indicate the maximum produced energy of each site if no wave height curtailment is used, while the solid lines show the generated energy at varying wave heights. In Table 5.3 the cut out significant wave height when the curtailed generated energy is a percentage of total generated energy is shown. This table is valuable to specify what the operational requirements of the FWT should be.

Recently there has been significant growing interest in the deployment of offshore

M Buoy No.	$H_{S,50}$ [m]	$H_{S,100}$ [m]	$H_{Max,50}$ [m]	$H_{Max,100}$ [m]
1	13.5	13.8		
2	5.62	5.67	8.12	8.21
3	14.9	15.2	21.5	22.4
4	17.6	18.1	26.4	27.6
5	9.16	9.41	11.9	12.2
6	14.6	14.8		

Table 5.2: Extreme Waves Extrapolation Results

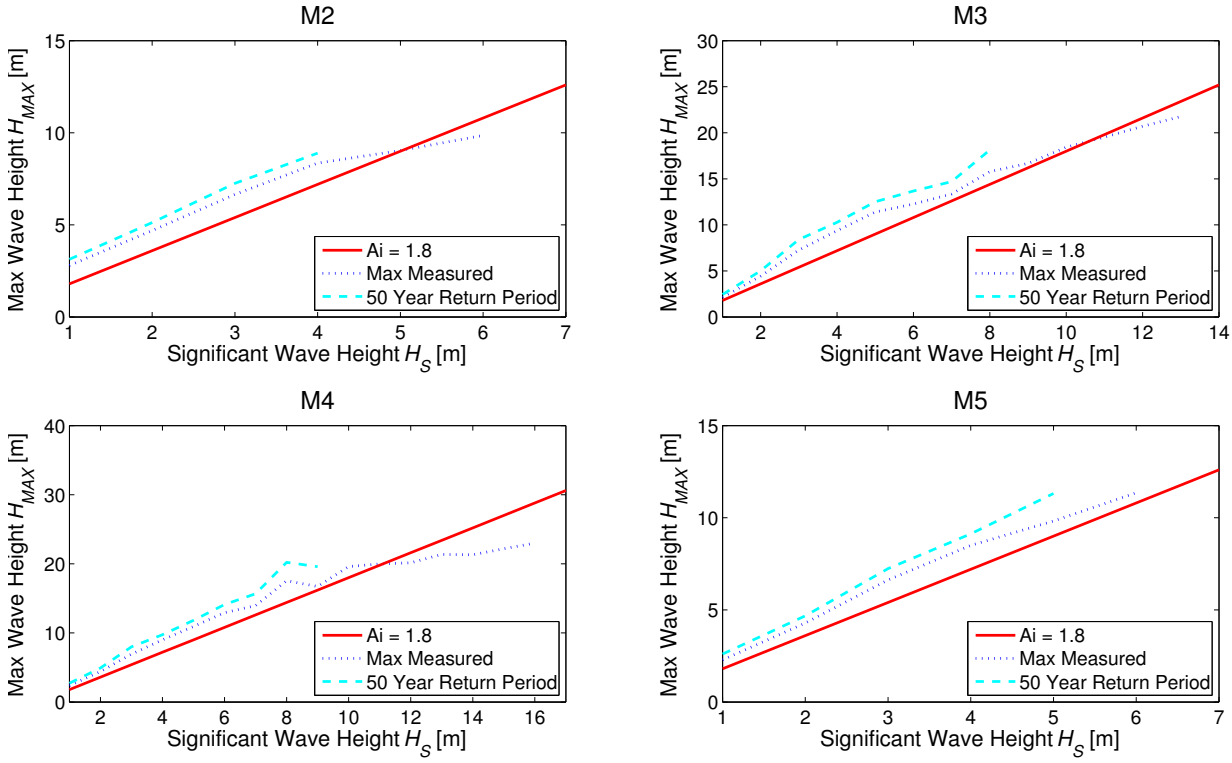


Figure 5.3: Extreme Wave Analysis for Binned Significant Wave Heights: Maximum Wave Height

floating wind turbines in Irish waters and thus the information available to potential developers has grown dramatically. As an example, the readers are directed to the EU EirWind project, for further details on Irish offshore conditions and maritime spacial planning facts[305].

	70 %	90 %	95 %	99 %	99.9 %
M Buoy No.	Wave Height H_S [m]				
1	4.2	6.1	7.3	10	13
2	1.4	2.3	2.9	4.1	5.4
3	4	6	7.2	9.8	13.9
4	4.1	5.9	7	9.5	12.6
5	2.4	3.8	4.5	6.1	8
6	4.5	6.5	7.7	10.6	14.3

Table 5.3: Cut out Significant Wave Height where Curtailed Generated Energy is a percentage of Total Generated Energy

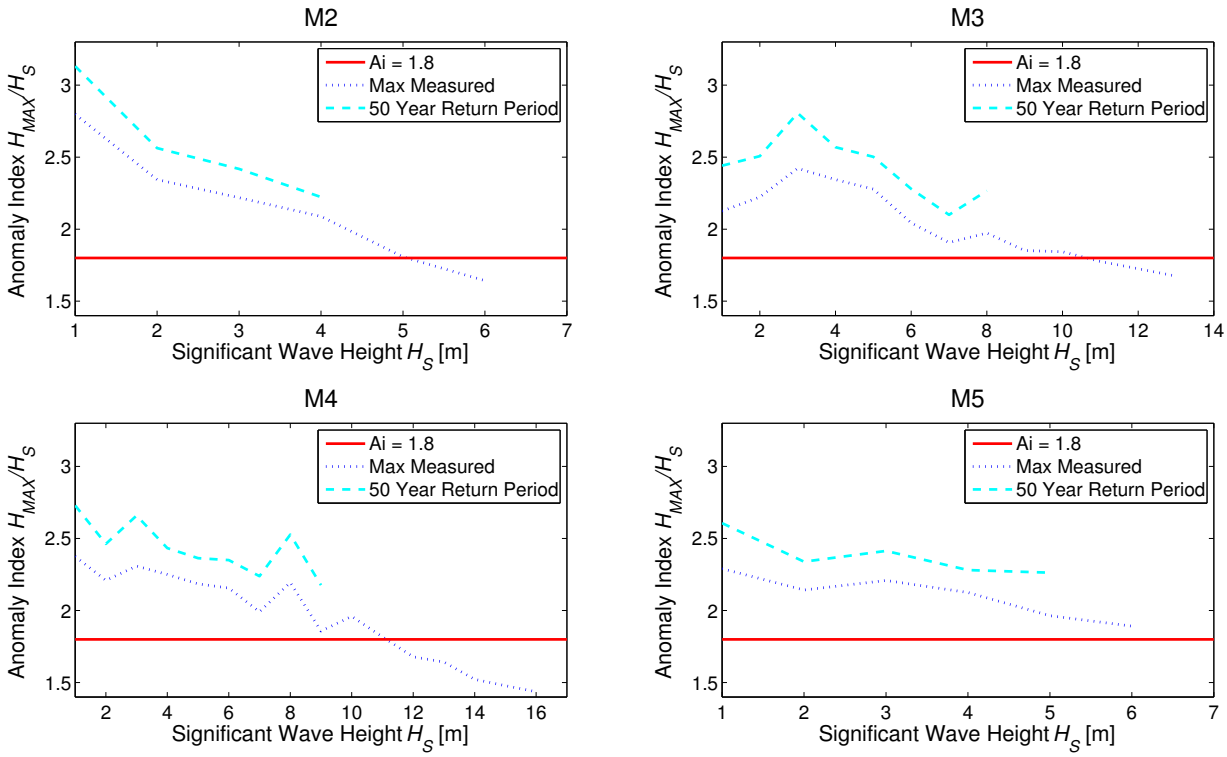


Figure 5.4: Extreme Wave Analysis for Binned Significant Wave Heights: Anomaly Index

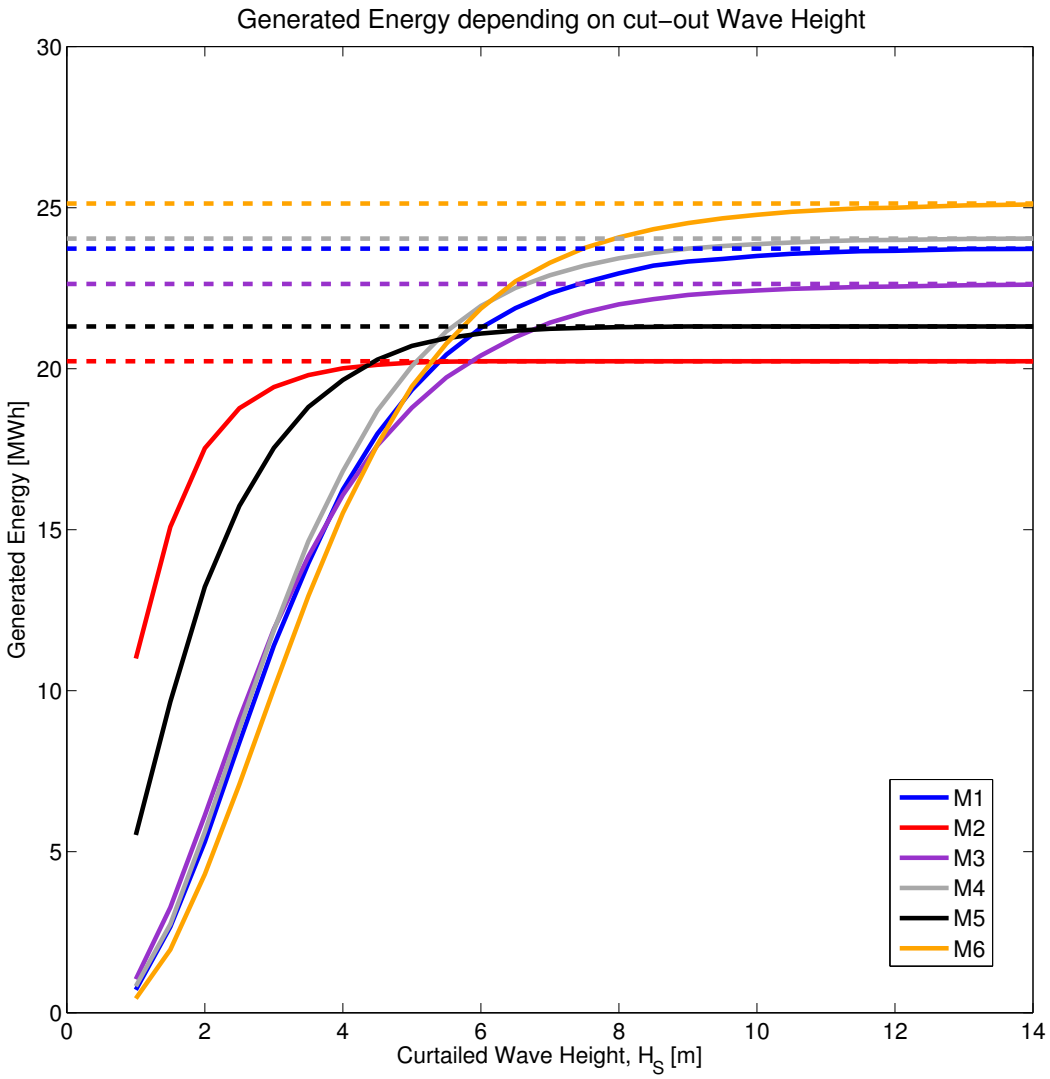


Figure 5.5: Curtailed Energy dependant on wave height at which wind turbine ceases power production. Dashed lines indicate the total available energy without imposing any wave height curtailment.

5.2 Design Turbine

5.2.1 NREL 5 MW Ref Turbine

As a standard reference turbine in the offshore industry, the NREL 5 MW reference turbine [306] is used for the design of the new TWind. Since the start of this work the size and power of WTs, particularly for offshore deployments has grown dramatically. There is now a 15 MW reference turbine developed by the CORWIND H2020 EU project [307]. While a 5 MW turbine may seem small by modern industrial standards there is still many research advancements being made by using this reference turbine these days [308]. As the purpose of this thesis is to not design a commercially viable floating WT support structure, but instead to analysis some of the challenges in the design of such, the continued use of the 5 MW WT is found acceptable. Furthermore the constant chasing of bigger WT capacities and thus resulting platform redesigns have been a significant slow down to the demonstration of viable FWT concepts.

5.3 Design of Tower

The tower is designed to be soft-stiff, i.e. its natural frequency being between the 1P and 3P regions. A 10% safety factor is generally applied to the 1P and 3P frequencies in order to avoid potential excitation's of the tower by the rotor. The natural frequency of the tower changes by its placement on a flexible structure [310] and thus any change in tower substructure must be analysed as to its effect on the tower itself. Following from this, various tower designs placed on a single TLWT platform at varying water depth are analysed. BMODES is used to determine the towers bending modes and frequencies. The platform dynamics are modelled using infinite added mass and linear hydrostatic and mooring stiffness terms.

The towers analysed are those used in the OC3-Hywind platform, the MIT-NREL TLP and modified versions of each. The modified versions have their lengths cut to the minimum required for blade clearance and below this point are made virtually "rigid" by lateral stiffeners. The shortened tower is reduced in length from 87.6 to 77.6. The

shortened "braced" towers are designed in attempt to increase the structural stiffness of the platform, and thus increase the pitch natural frequency of the platform. The properties of the reduced towers are the same as the original, apart from the lower 10 m have been removed.

In Figure 5.6 pitch free decay tests of the original tower and shortened tower mounted on a generic TLP are shown as a proof of concept. The platform mass is not altered between tower types and as the original tower has a larger mass, this model has a slightly lower pretension. The pitch NF can be seen to increase from 0.32 Hz for the standard tower to 0.34 Hz for the shortened tower. Due to the wave breaking limit, this seemingly small change in frequency means a 10.8% reduction in the maximum possible waves at the pitch natural frequency from 2.10 m to 1.87 m. Due to the wave energy being proportional to the product of the height squared and the period, this means a further 24.8% reduction in the wave energy possible at this new natural frequency.

Two additional designs are simulated, the first one having an increased platform mass, in order to match the standard towers pretension, and secondly having an increased pretension. The step change in pretension is kept as a constant between these models. From the resultant free decay tests, one can observe how the increased mass increases the low frequency pitch response while reduces the high frequency component (respectively below and above the resonance frequency).

As the coupled platform pitch and tower bending moments may be excited by second order sum-frequency waves it is recommended to perform a detailed analysis of this tower redesign in future work.

Figure 5.9 shows the change that water depth, and thus platform stiffness and tower properties has on the first tower bending frequency. Increasing the water depth reduces the tower frequency. Increasing tower stiffness increases tower frequency. All effects are more pronounced at lower water depths. If the 10% safety factor is strictly adhered to, the suitable water depth for this platform and the two original towers is between 100 and 220m, the corresponding depths for the modified tower being between 120 and 240m.

The MIT-NREL platform also suffers from a similar problem [15] as the 1st Tower S-S is located in the 3P region at 0.58 Hz. According to discussion on the NREL Forum,

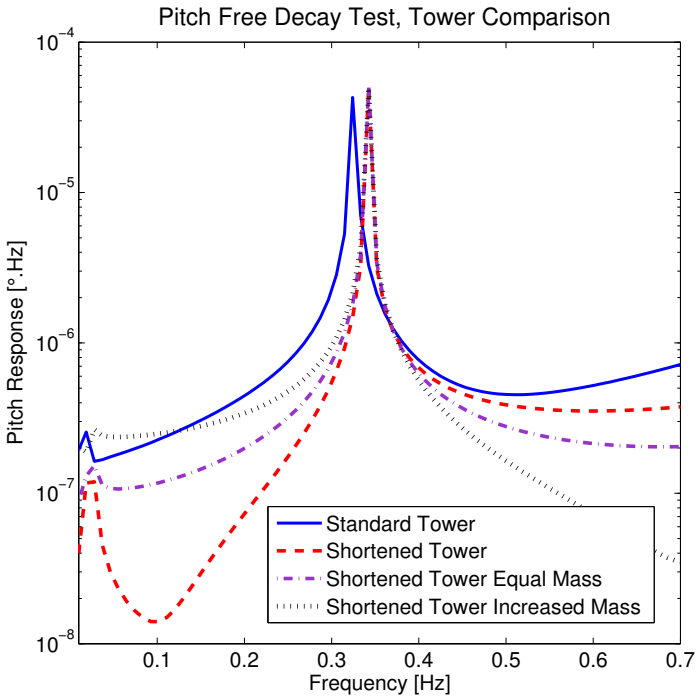


Figure 5.6: Pitch Free Decay Test spectral density, Comparison of original tower with three novel shortened tower designs. A shortened tower with reduced, equal and increased mass as compared with the original tower design.

Jonkman [311] stated that this problem was analysed, and found to be insignificant due to no tower resonance being observed. The F-A and S-S first bending frequencies for this structure are also shown on the above mentioned figure to give an insight into this problem.

5.4 Design of Floating Substructure

A braceless floating substructure is chosen to avoid the well known fatigue stress concentration zones of tubular node members.

5.4.1 Maximum size of tubular elements

The maximum size of tubular steel elements from on and offshore wind energy are compared here to give an estimate of what is practical to fabricate and transport. In conventional onshore wind turbines tower sections are generally limited by transportation

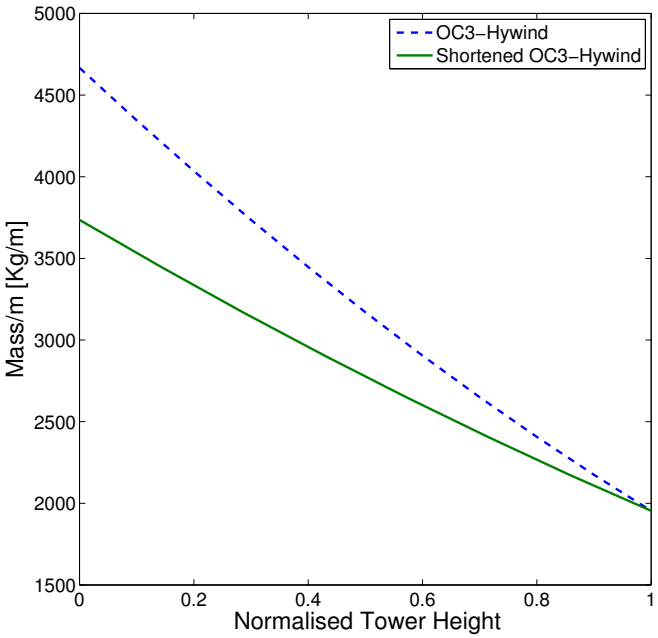


Figure 5.7: Comparison Mass properties of New Tower type with OC3-Hywind tower

to 4.3 m in diameter, or, in some cases, 4.6 m if routes permit, to fit under overhead obstructions [312]. In Ireland the process for transportation of vehicles and loads that do not exceed 27.4 m in length and 4.3 m in width is streamlined on major routes under a Permit Scheme administered by An Garda Síochána [313]. Monopile foundations have vastly grown in diameter and length for the increasing water depth at sites. As an example the XL monopile for the Veja Mate in water depths of roughly 40 m are 7.8 m in diameter [314]. In the following parameter analysis in Section 5.6, the cylindrical diameter is chosen between 4 m and 7.2 m in order to stay within the range outlined above. A detailed cost analysis, including transportation, manufacturing and constructibility amongst other factors is beyond the scope of this work, and should be performed in order to find a commercially optimal design.

5.5 Design Optimisation

This section looks at what output parameters are most important to minimise in order to design an optimised FWT. Initial spreadsheet estimations of the design space have been

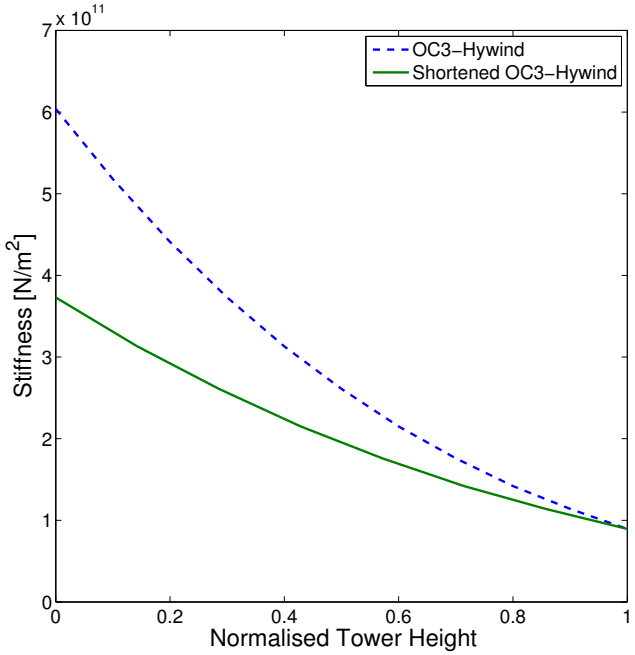


Figure 5.8: Comparison of New Tower type with OC3-Hywind tower, Stiffness properties

clearly described in the literature [315]. The general design guidelines are as follows: The surge and sway natural periods should be above 25 s to avoid coupling with the first order wave frequencies. The heave, roll/bending, and pitch/bending natural periods should be below 3.5 s for similar reasons. The rigid body natural periods may be calculated by using Equation 3.7. As it is difficult to quantify the effects of the the tower flexibility at an early design stage, a detailed study of such behaviour is carried out in subsequent sections of this chapter in order to aid future designers of TLPWT. The tendon tension should remain positive in all load cases in order to avoid snap loading events. In order to limit the angle of the tendon connections to the hull, a limit on the mean surge offset of 5% the water depth is recommended. [316]. In addition it is recommended to minimise the dynamic surge motion in order to avoid the WT operation in the high tip speed ratio regime. This will help reduce fluctuations in torque which could lead to fatigue problems [101]. It is also recommended to minimise the surge motion in order to make the design of the power umbilical cable as simple as possible.

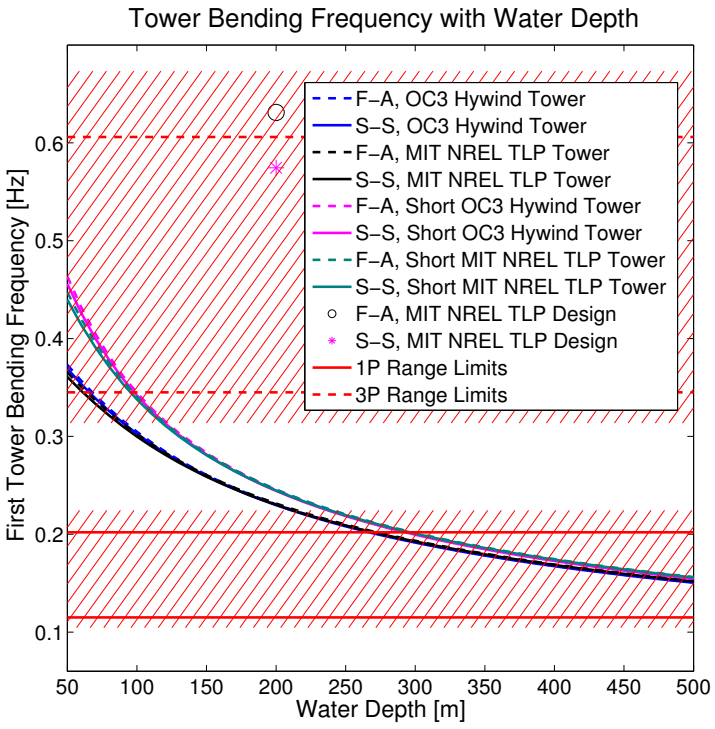


Figure 5.9: Tower Bending Mode Frequency with Water Depth

5.6 Parameter Study

Due the design requirements discussed at the beginning of this chapter, and the knowledge on multi column TLP's gained in Chapter 3, it was decided to continue the multi column design. A preliminary design showed a concept with 4 outer columns and one central column to be favourable.

The outer columns are connected to the central column at the bottom through four horizontal lower pontoons. This outer column connection follows a radial bend in order to enable the marine operation that will be discussed latter in Section 6.5. The top of the outer columns is connected to the top of central column through the use of beam elements. As the central column is higher than the outer columns these beams slope upwards towards the central connection node. The bottom of the shortened tower rests on this raised central node.

A general parameter study was carried out, varying the draft, column spacing, column and pontoon diameter and bend diameter. The parameters were chosen to give a general

overview of the platform dynamics and not necessarily on engineering performance. Each parameter combination was modelled, resulting in 250 unique models. These parameters can be seen in Table 5.4. An overview of three models from the parameter study are shown in Figure 5.10. The mesh shown in this figure are for visualisation purposes only.

A preliminary structural analysis was carried out using simplified principles derived from the NORSOK (Originally named the Norwegian shelf's competitive position) steel standards [317]. A mesh for each model was generated in Matlab and subsequently the hydrodynamic parameters calculated using the potential flow theory and boundary element method in NEMOH.

Table 5.4: Parameter Table

Parameter Name	Min [m]	Max [m]	Δ [m]
Column Spacing	20	40	5
Bend Radius	2	6	4
Column Radius	2	3.8	0.4
Draft	20	40	5

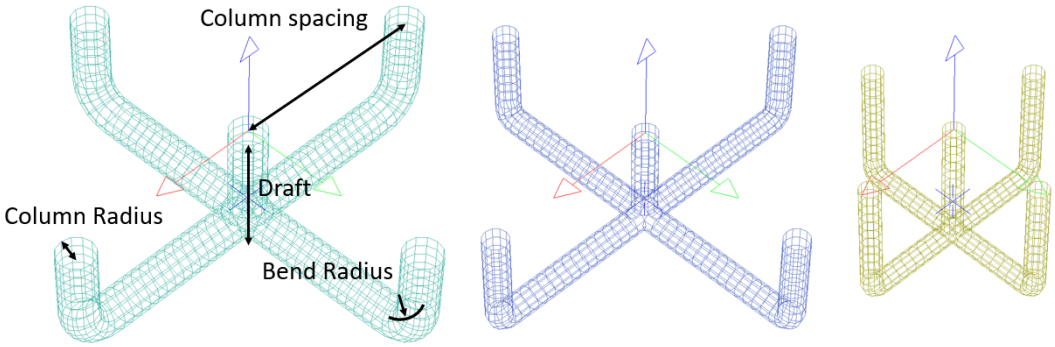


Figure 5.10: Three Models from the Parameter Study

5.6.1 Parameter Study of Hydrodynamic Parameters

The frequency domain hydrodynamic outputs from NEMOH are analysed in this section. All parameters bar two were held constant in order to determine the effect varying each

parameter has on the hydrodynamic parameters. As only two bend radii are analysed, this parameter is studied in conjunction with one other design parameters.

5.6.1.1 Parameter Study of Varying Draft

In Figure 5.11 the column spacing and radius are held constant at 20 m and 2 m respectively, while varying the draft and bend radius. Increasing the draft means the column length increases. As expected, surge added mass is seen to significantly increase with increasing draft, while reducing slightly with larger bend radius. Increasing draft shows a negligible effect on the surge radiation damping, demonstrating that the majority of the damping occurs at the water surface. Investigating the section with wave frequencies between 0.06 to 0.18 Hz, it can see that as the draft is increased, the peak of this region decreases in frequency. In Figure 5.12 it can be seen how this change effects the surge excitation force. There is a ~15% increase in the force magnitude and a reduction in the peak frequency in the area between 0.12 Hz to 0.10 Hz. Increasing the platform draft shows a slight decrease in the heave added mass at 0.1 Hz, with a slight increase for frequencies above 0.14 Hz.

Increasing the bend radius decreases the heave added mass, due to the resultant shortening of the pontoons. In Figure 5.13 increasing the draft can be seen to significantly reduce the heave radiation damping, by an order of 90 %, as the pontoons depth increases and thus its effect on the free surface diminishes. The heave excitation force is seen (Figure 5.14) to increase slightly in the frequency range up to 0.2 Hz with increasing draft, the peak frequency shifting from 0.11 Hz to 0.10 Hz. For frequencies greater than 0.2 no change in the heave excitation force is observed.

Figure 5.15 shows the effect varying the draft and bend radius has on the radiation terms. Increasing the draft increases the added mass and decreases the damping. A frequency shift in the low frequency pitch damping from 0.14 Hz to 0.12 Hz is also observed. Increasing the bend radius decreases the pitch added mass, and low frequency pitch damping, while increasing the higher frequency pitch damping. Figure 5.16 shows that increasing the draft increases the high frequency pitch excitation force (above 0.18 Hz), while reducing the low frequency component. A reduction in the pitch peak excita-

tion frequency from 0.11 Hz to 0.09 Hz is also observed.

Figure 5.17 shows how increasing the draft increases the yaw added mass, while the damping and excitation forces (Figure 5.18) remains constant. Increasing the bend radius reduces the yaw added mass.

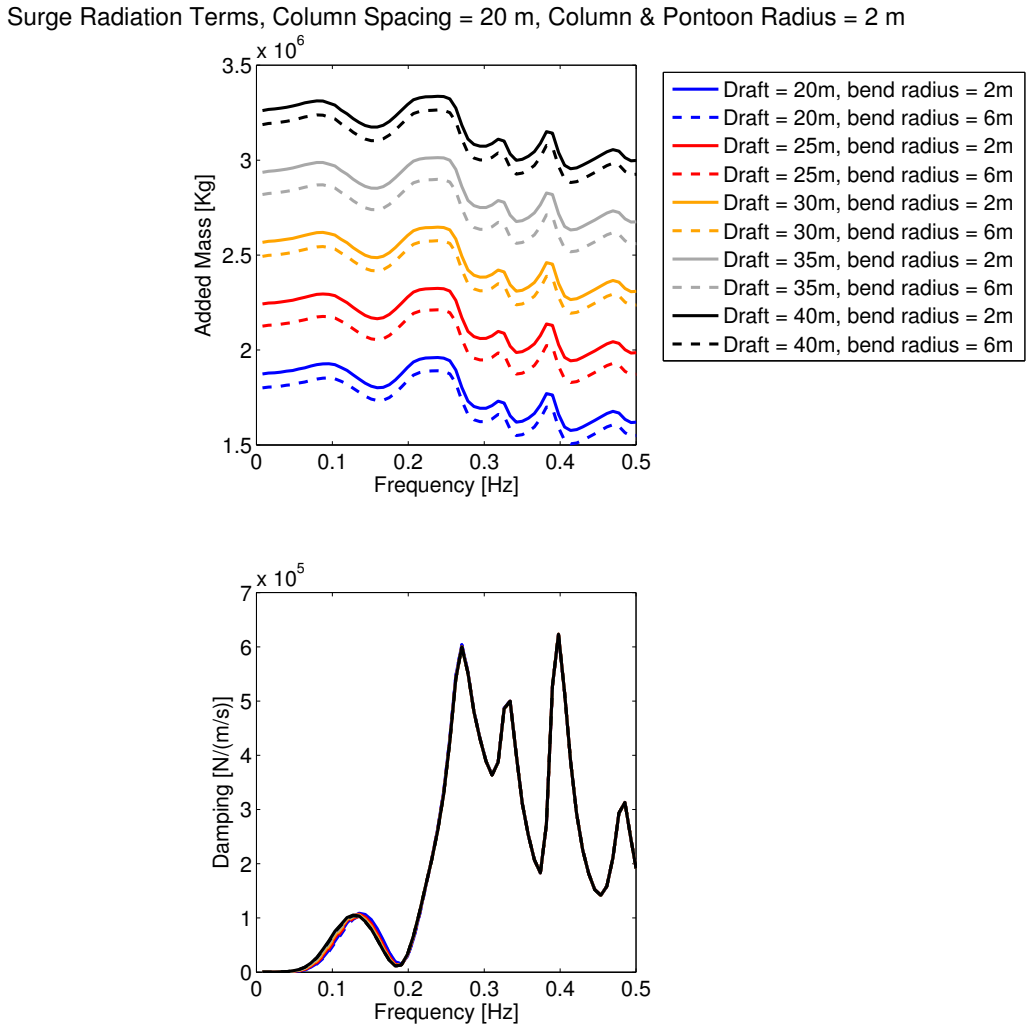


Figure 5.11: Effect of Increasing Platform Draft on the Surge Radiation Terms

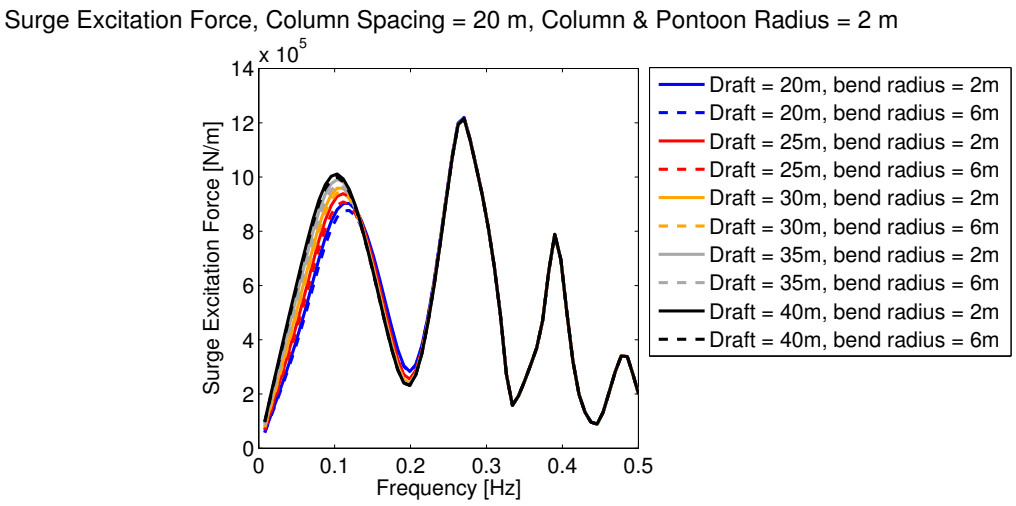


Figure 5.12: Effect of Increasing Platform Draft on the Surge Excitation Force

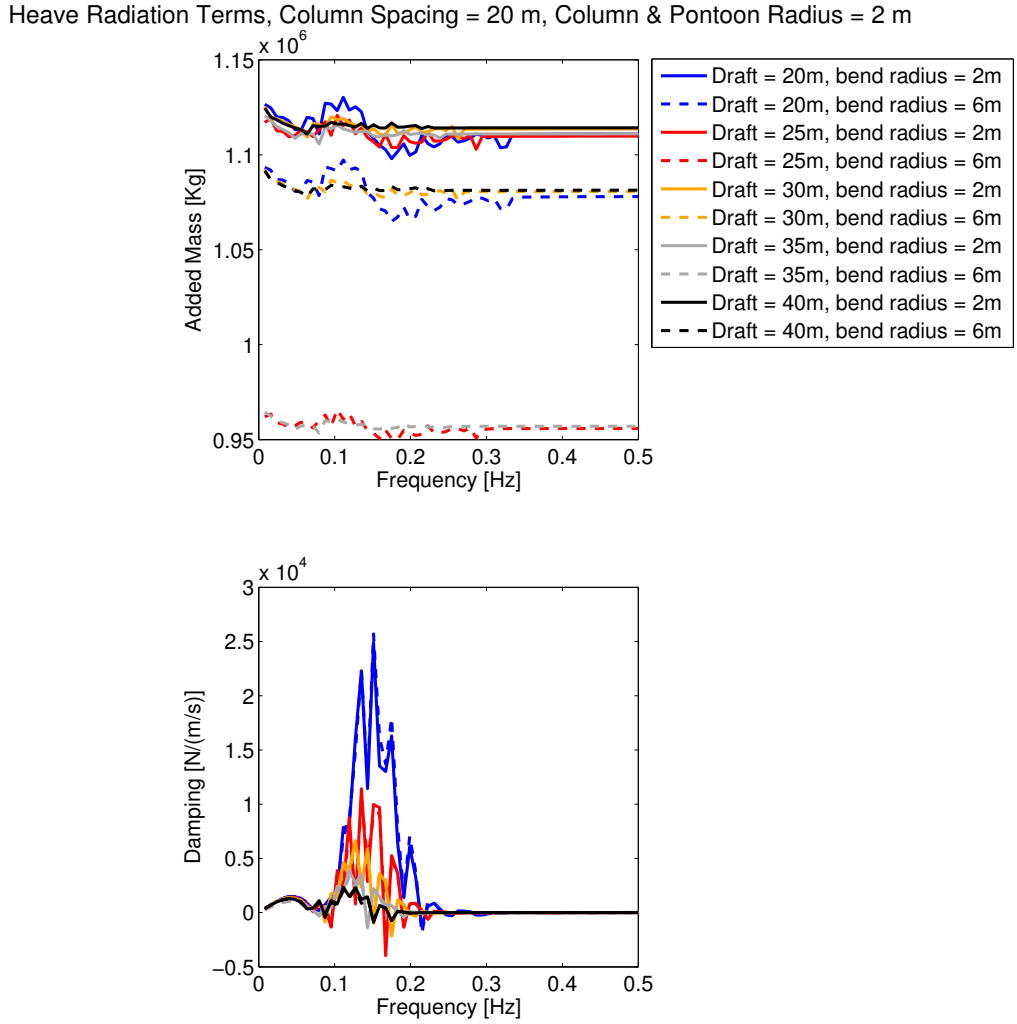


Figure 5.13: Effect of Increasing Platform Draft on the Heave Radiation Terms

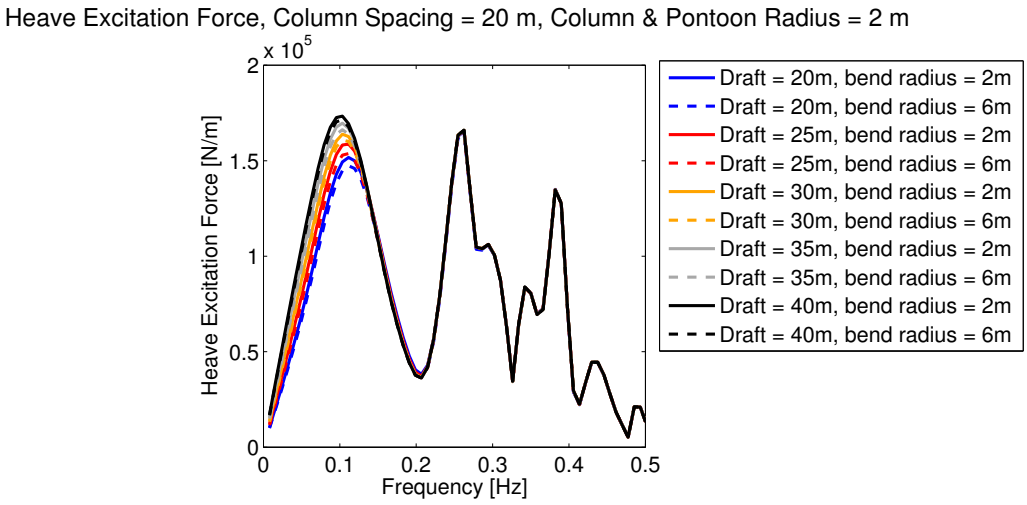


Figure 5.14: Effect of Increasing Platform Draft on the Heave Excitation Force

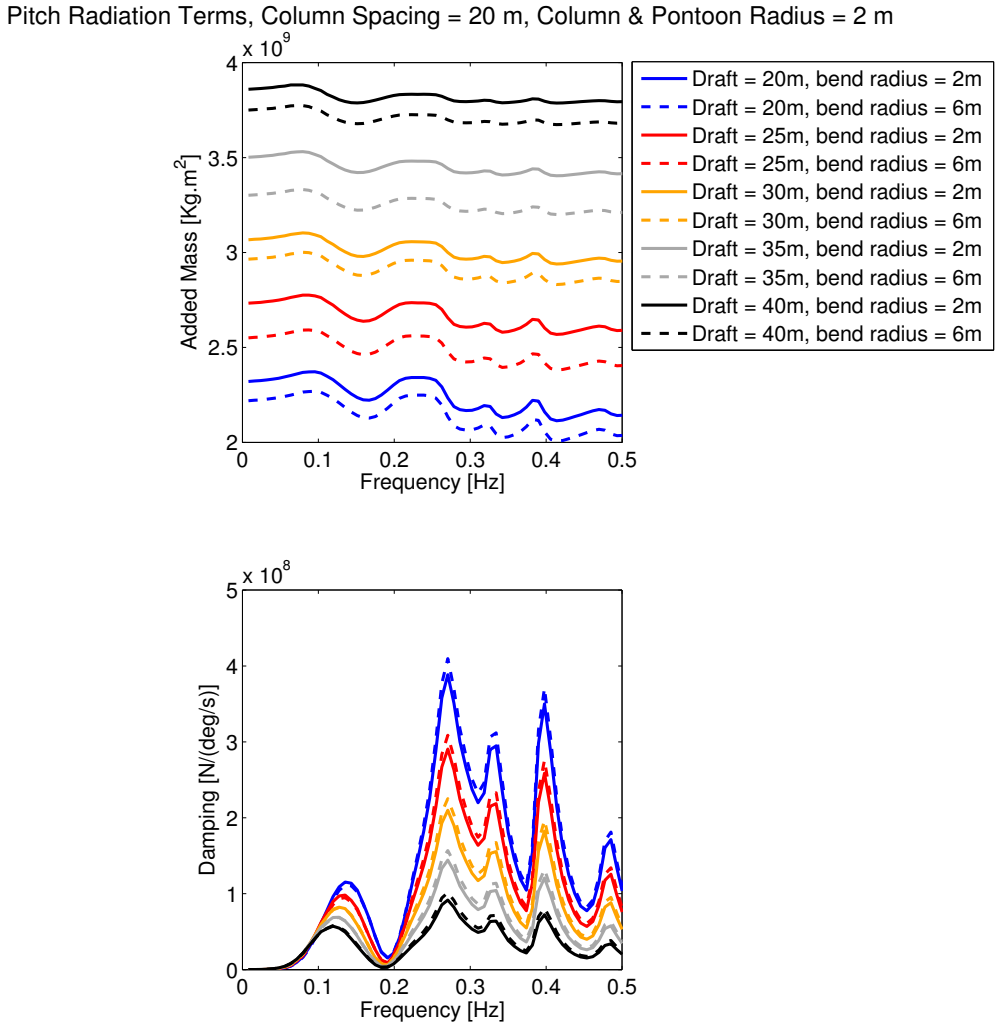


Figure 5.15: Effect of Increasing Platform Draft on the Pitch Radiation Terms

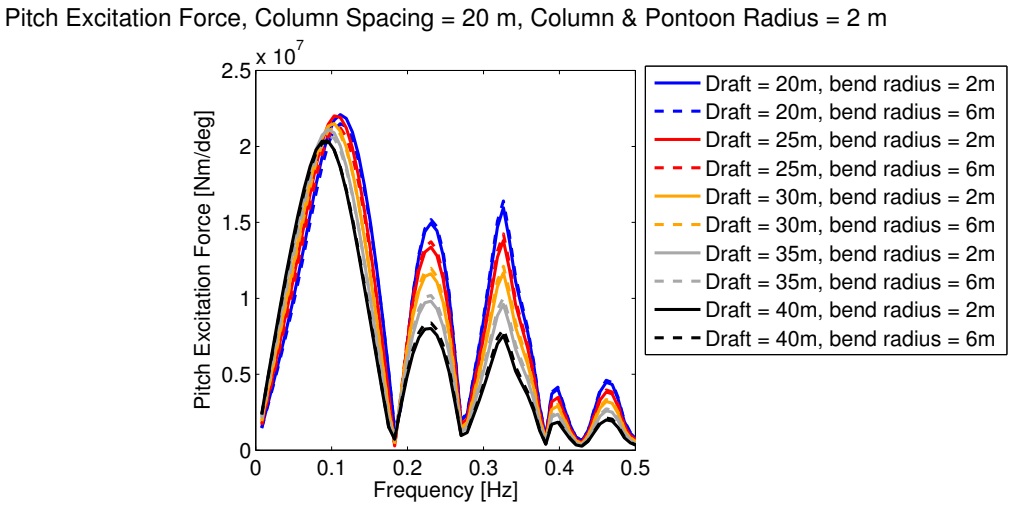


Figure 5.16: Effect of Increasing Platform Draft on the Pitch Excitation Force

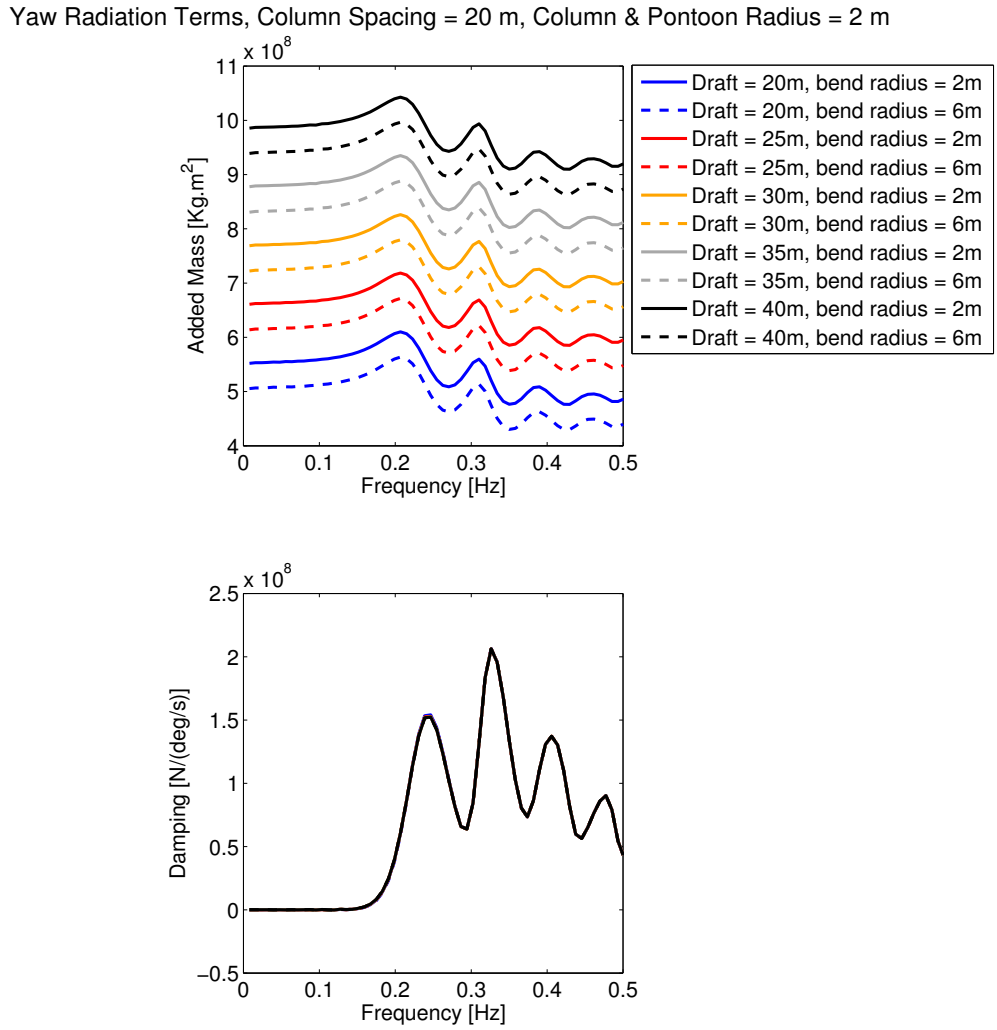


Figure 5.17: Effect of Increasing Platform Draft on the Yaw Radiation Terms

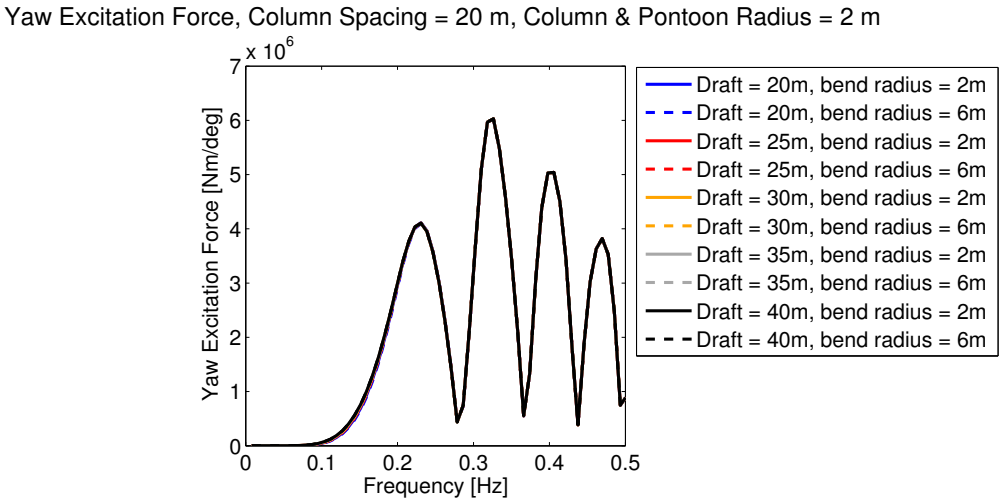


Figure 5.18: Effect of Increasing Platform Draft on the Yaw Excitation Force

5.6.1.2 Parameter Study of Column and Pontoon Radius

In Figure 5.19 the column spacing and draft are both held constant at 20 m, while the column, pontoon and bend radii are varied. Increasing the column radius is shown to significantly increase the surge added mass and damping. This increase also shifts the peak frequency in the added mass term from 0.23 Hz at a column radius of 2 m to 0.09 Hz at 3.6 m. The high frequency component of the surge damping is shifted from 0.4 Hz to 0.42 Hz with this increase in column radius. In Figure 5.20 a substantial increase in the surge excitation force can be observed with this change. This increase can be observed over a frequency range from 0 to 0.34 Hz, above this frequency an increase in surge excitation force is less notable and at high frequencies actually reduces.

In Figure 5.21 the heave added mass and damping can be seen to significantly increase with increased column radius, a slight decrease occurs with increased bend radius. Figure 5.22 shows a similar significant increase in the heave excitation force.

In Figure 5.23 the pitch added mass decreases with increasing column radius and bend radius, while the pitch damping is frequency dependant. For frequencies below 0.2 Hz, increasing the radius increases the damping, while above this frequency the inverse is true. Figure 5.24 shows how this change effects the pitch excitation force in a highly non-linear frequency dependant fashion. For frequencies below 0.19 Hz increasing the

radius leads to an increase in the pitch excitation force, while the inverse is true for frequencies above 0.19 Hz. Between 0.19 Hz and 0.19 Hz it is the middle column radii of 2.4 m and 2.8 m which show the largest excitation, with 2 m and 3.2 m showing a similar response, while 3.6 m shows the lowest excitation.

In Figures 5.25 and 5.26 we see both radiation terms and excitation forces increasing with increased column radius.

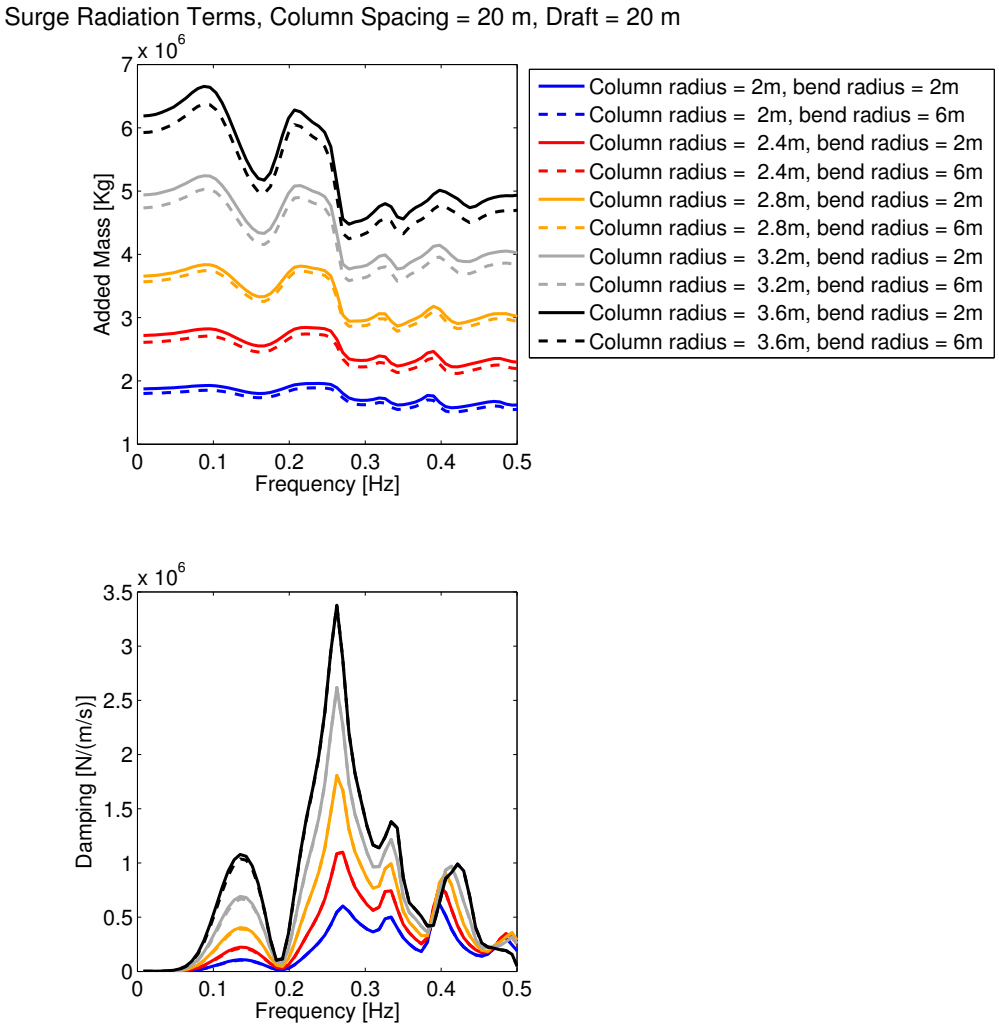


Figure 5.19: Effect of Increasing Column and Pontoon Radius on the Surge Radiation Terms

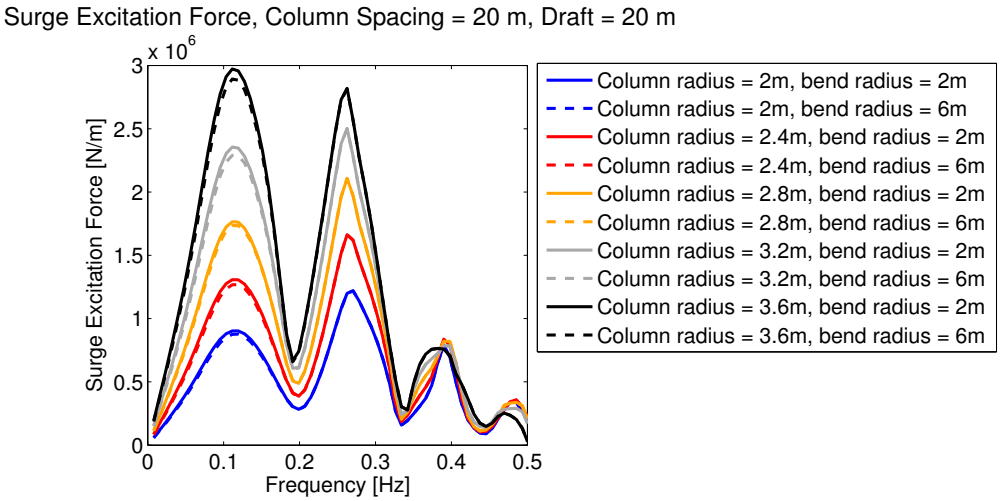


Figure 5.20: Effect of Increasing Column and Pontoon Radius on the Surge Excitation Force

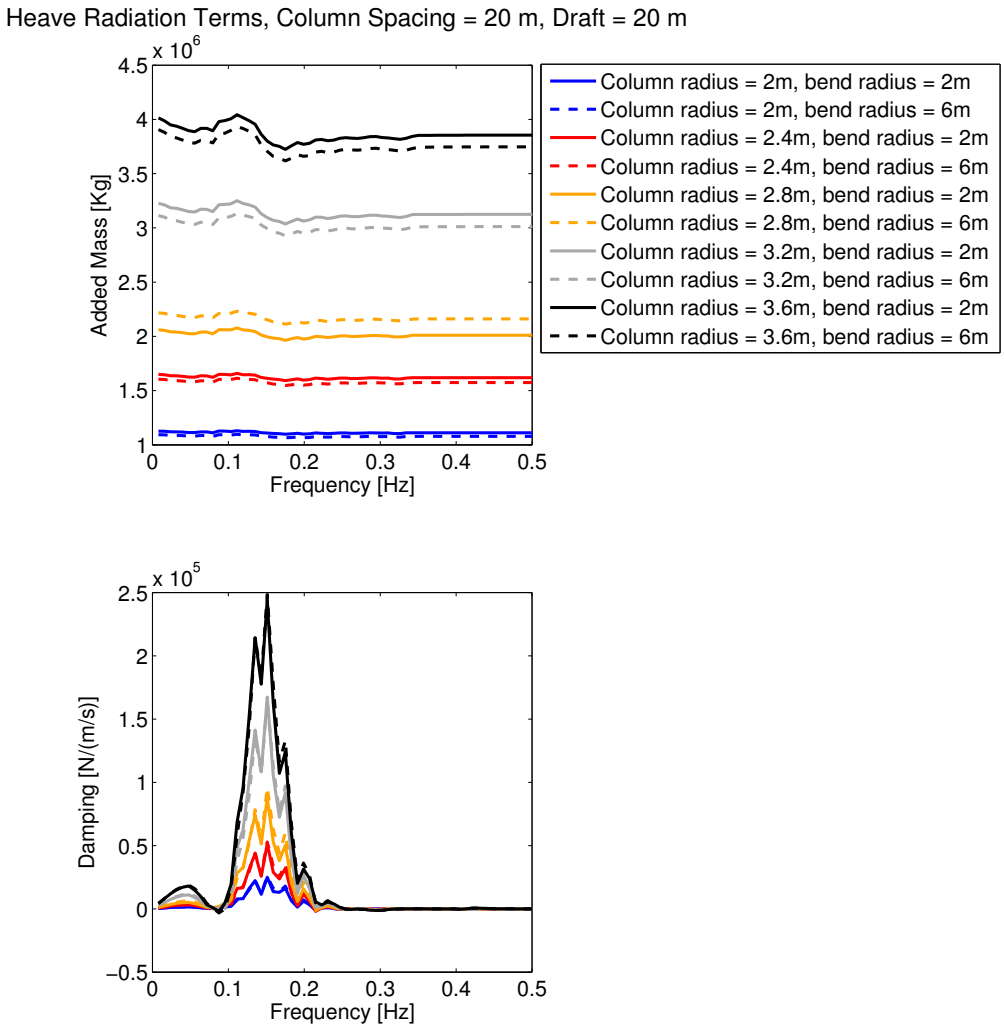


Figure 5.21: Effect of Increasing Column and Pontoon Radius on the Heave Radiation Terms

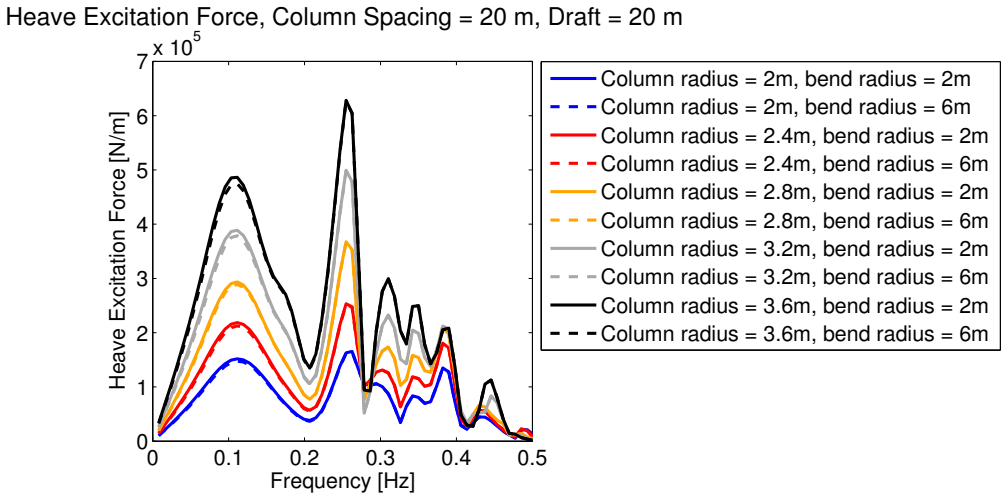


Figure 5.22: Effect of Increasing Column and Pontoon Radius on the Heave Excitation Force

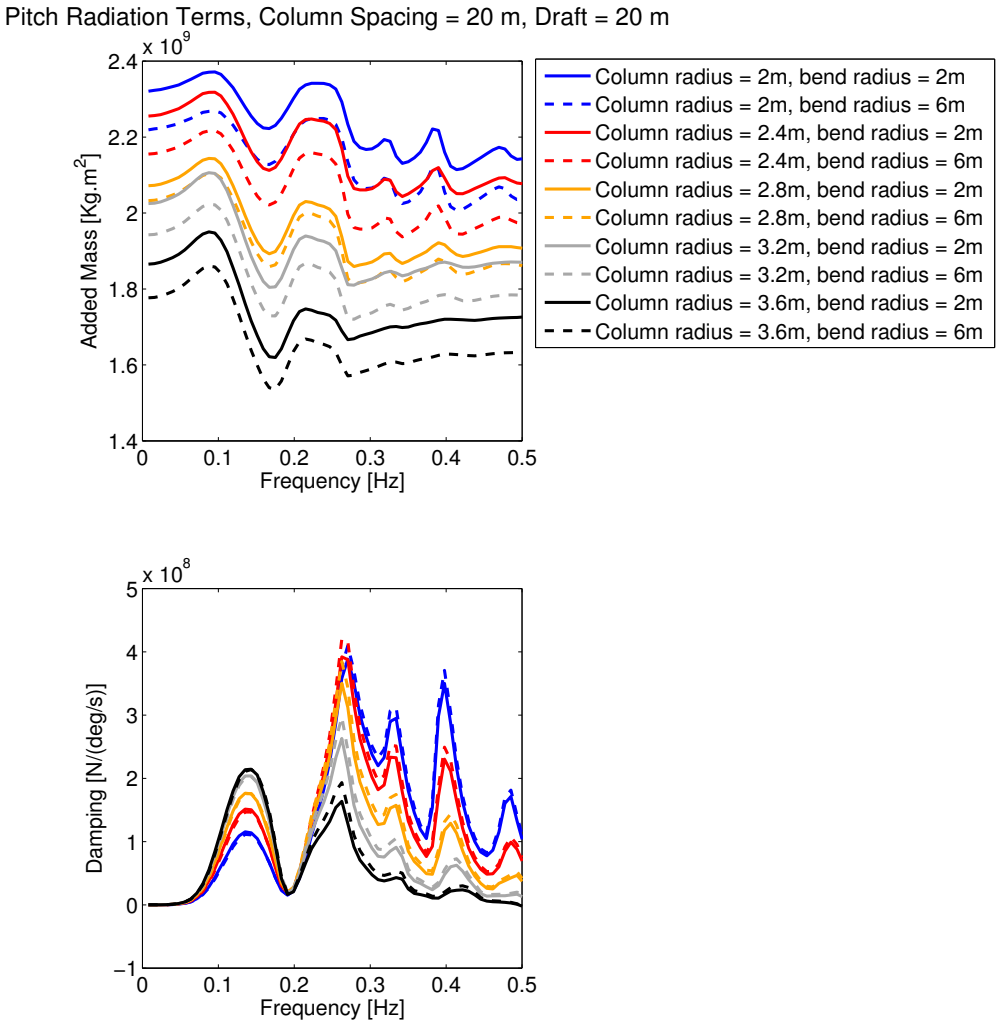


Figure 5.23: Effect of Increasing Column and Pontoon Radius on the Pitch Radiation Terms

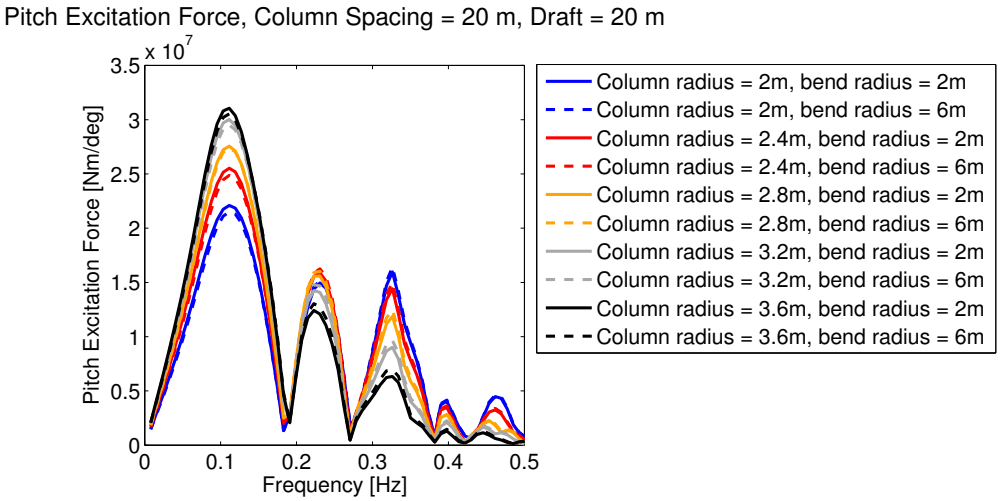


Figure 5.24: Effect of Increasing Column and Pontoon Radius on the Pitch Excitation Force

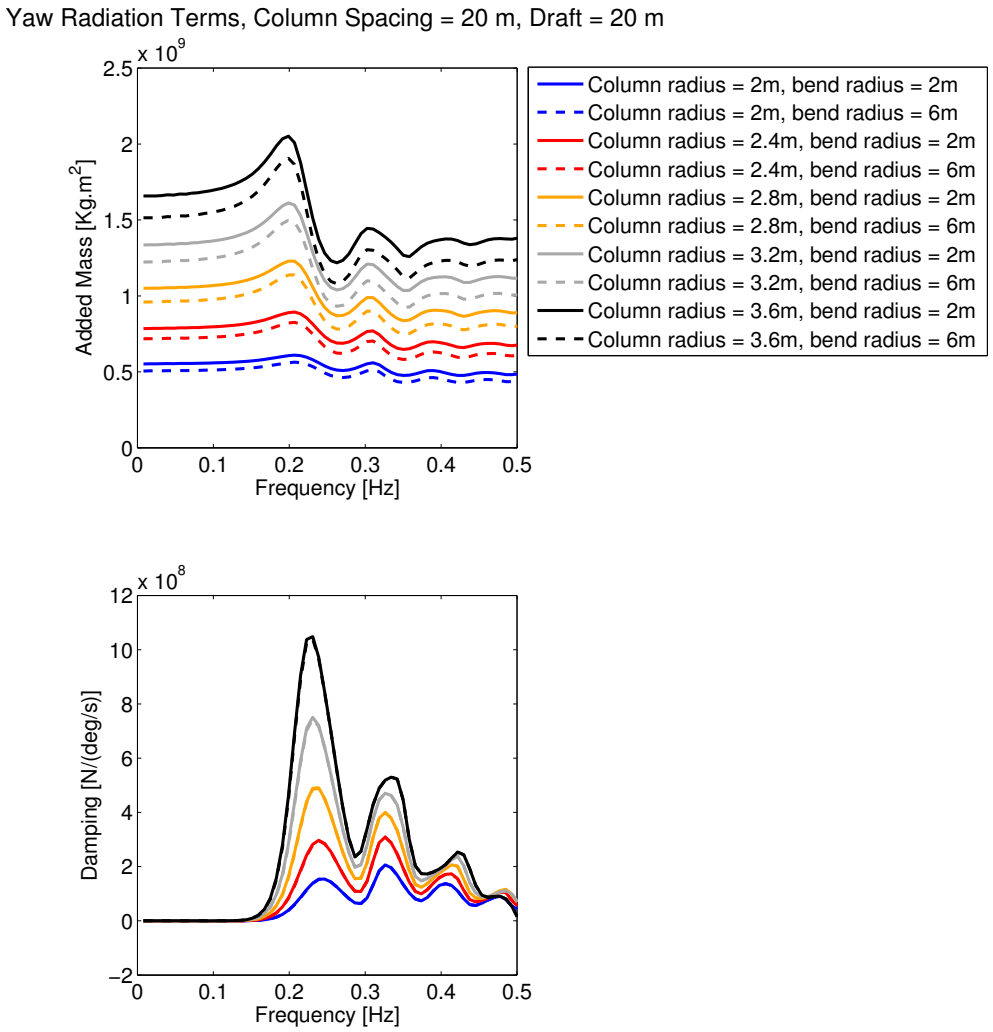


Figure 5.25: Effect of Increasing Column and Pontoon Radius on the Yaw Radiation Terms

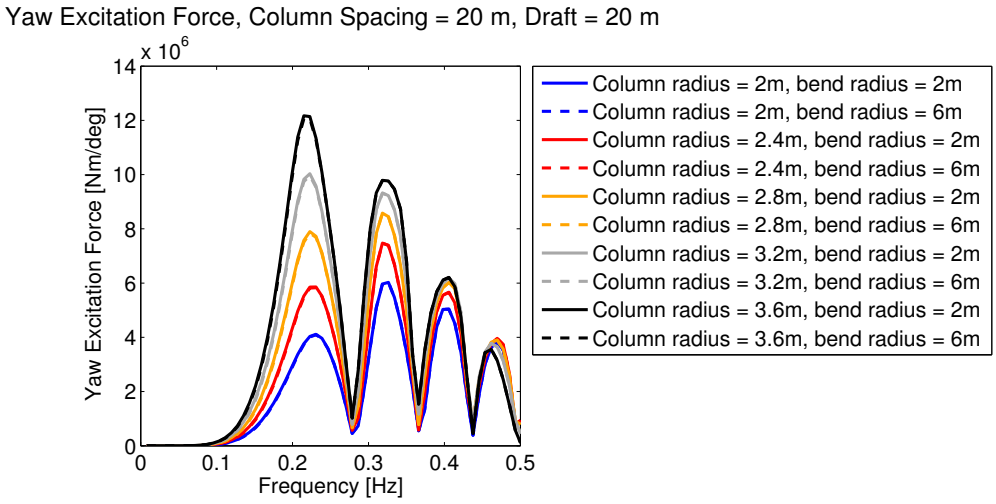


Figure 5.26: Effect of Increasing Column and Pontoon Radius on the Yaw Excitation Force

5.6.1.3 Parameter Study of Column Spacing

In Figure 5.27 the draft and column radius is kept constant at 20 m and 2 m respectively, while the column spacing and bend radius is varied. Increasing the column spacing means the pontoon lengths must increase accordingly, which results in the increased surge added mass that can be observed. The peak in the added mass spectra here moves from 0.23 Hz at a column spacing of 20 m to 0.18 Hz at 40 m. Damping in the region of 0.06 to 0.18 Hz, reduces by an order of 50% as the column spacing increases from minimum to maximum, with the peak of this region moving from 0.14 Hz to 0.12 Hz, indicating that column to column interaction significantly effects the surge damping.

In Figure 5.29 the heave added mass and radiation terms can be seen to increase with increased column spacing. The peak in the heave damping reduces from a frequency of 0.15 Hz to 1.13 Hz. Figure 5.30 the heave excitation force is seen to slightly reduce with increased column spacing.

Figure 5.31 shows how increasing the column spacing increases the pitch added mass and also reduces the peak frequency from 0.1 Hz to 0.08 Hz. Increasing the bend radius decreases the added mass. Similar to the surge damping, the pitch damping in the region of 0.06 to 0.18 Hz, reduces by an order of 50%, with the peak of this region moving from 0.14 Hz to 0.12 Hz. Figure 5.32 shows how the peak in the pitch excitation force increases

with column spacing and high frequency peak decreases from 0.33 Hz to 0.23 Hz.

In Figures 5.33 and 5.34 an increase in the excitation force is observed for both yaw radiation terms and excitation forces. The yaw added mass, radiation, and excitation forces peak frequency decreases from 0.21 Hz to 0.16 Hz, 0.33 Hz to 0.29 Hz and

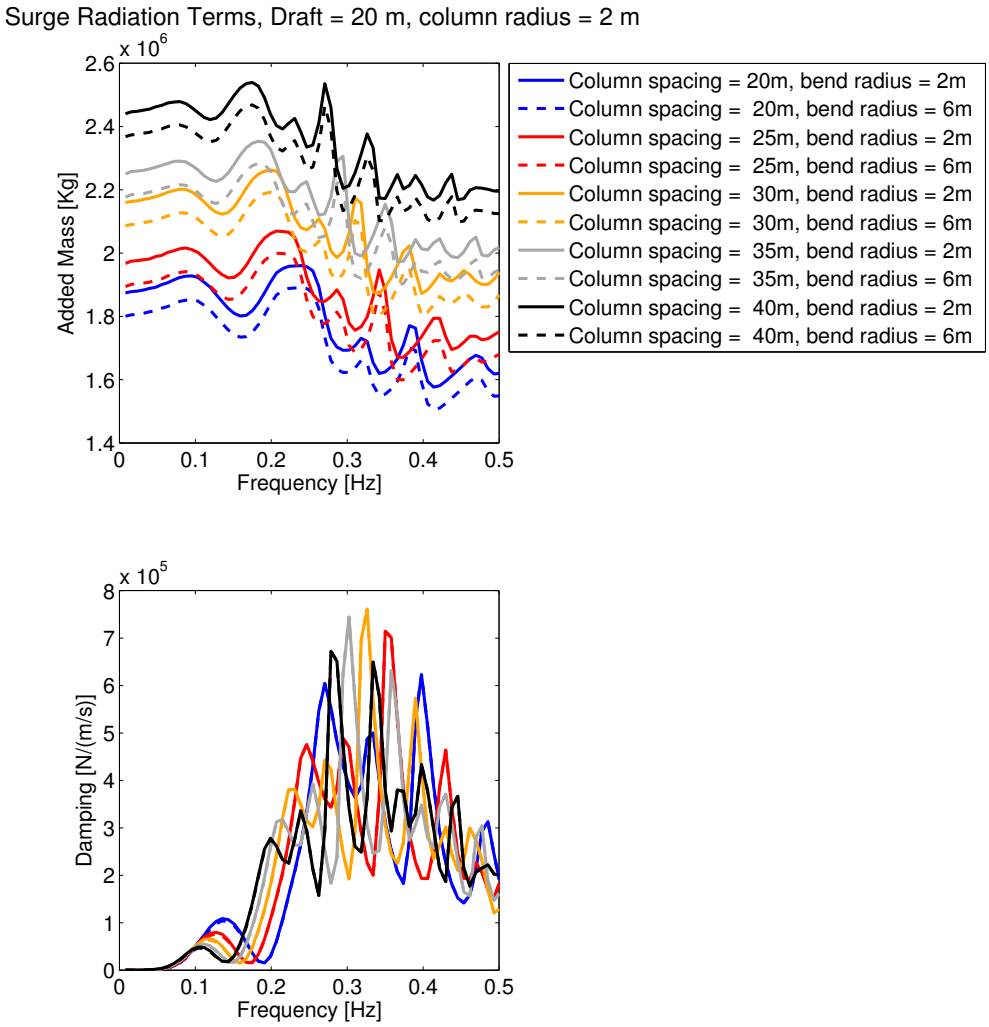


Figure 5.27: Effect of Increasing Column Spacing on the Surge Radiation Terms

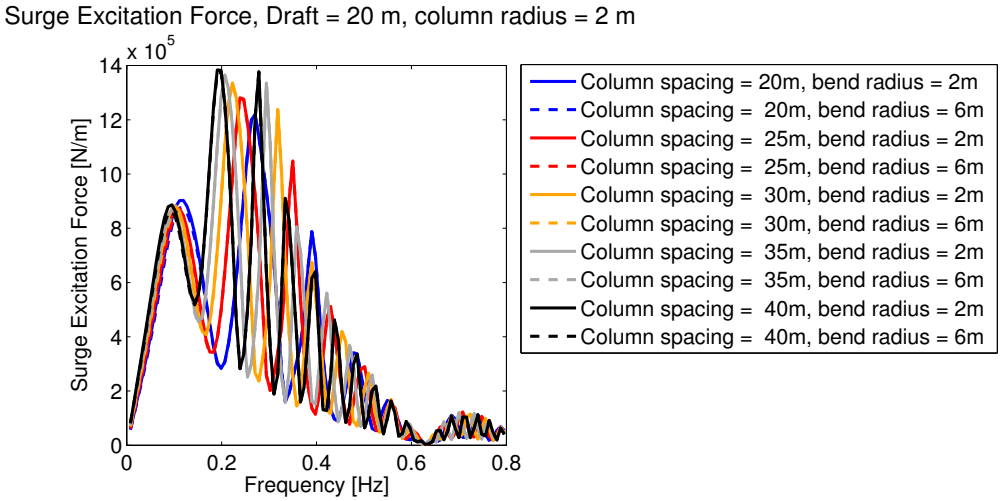


Figure 5.28: Effect of Increasing Column Spacing on the Surge Excitation Force

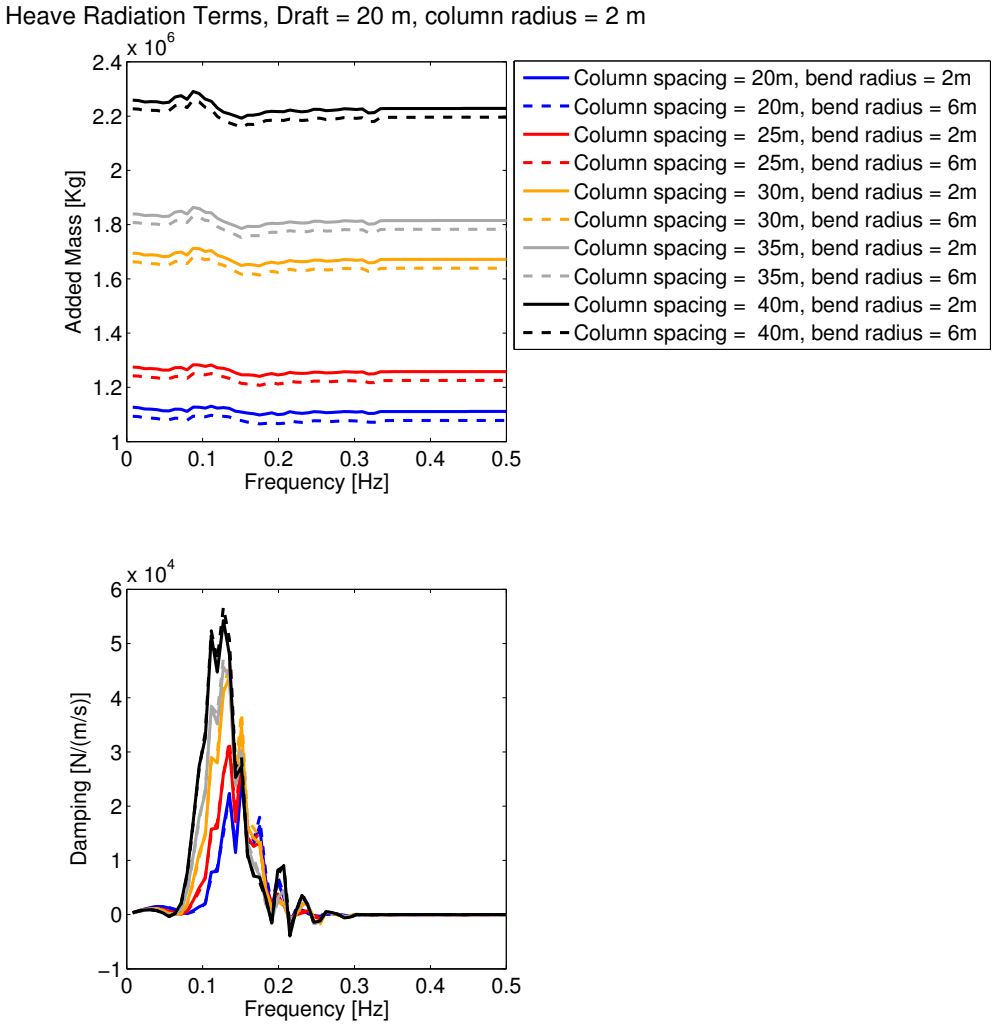


Figure 5.29: Effect of Increasing Column Spacing on the Heave Radiation Terms

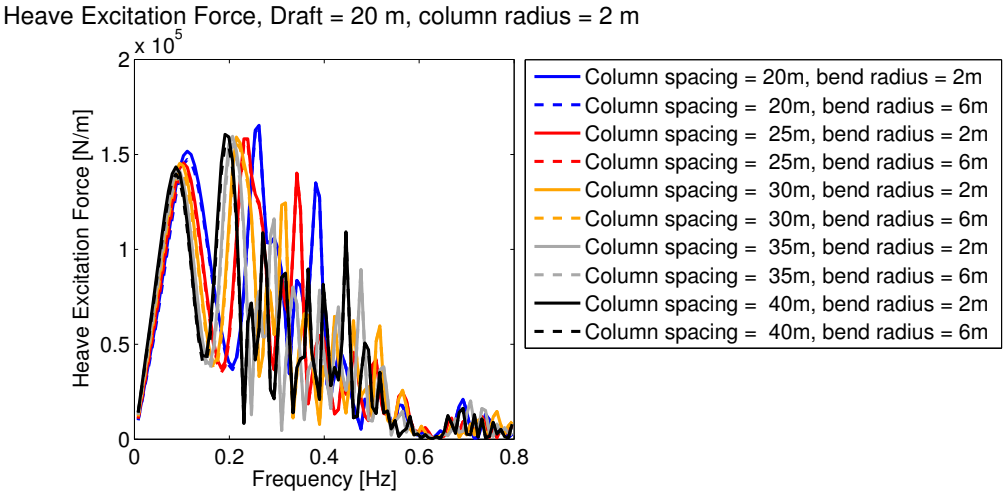


Figure 5.30: Effect of Increasing Column Spacing on the Heave Excitation Force

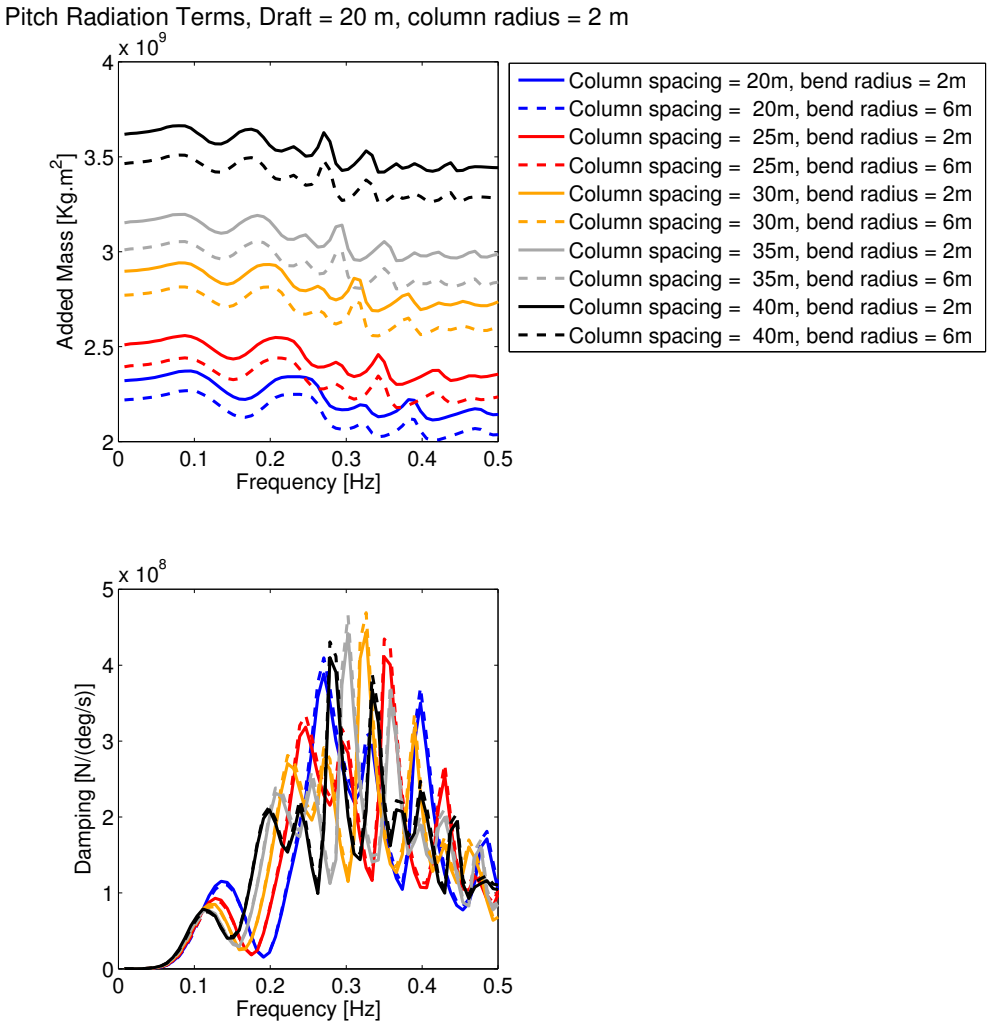


Figure 5.31: Effect of Increasing Column Spacing on the Pitch Radiation Terms

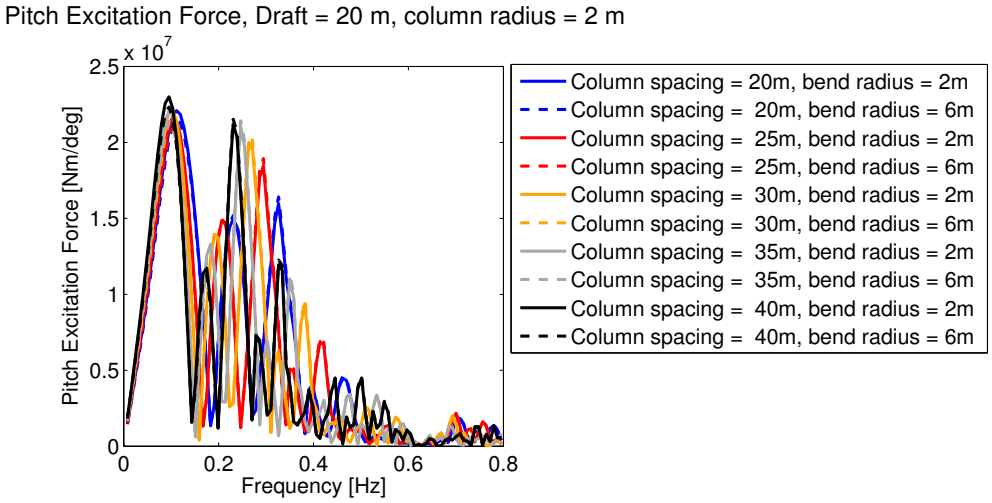


Figure 5.32: Effect of Increasing Column Spacing on the Pitch Excitation Force

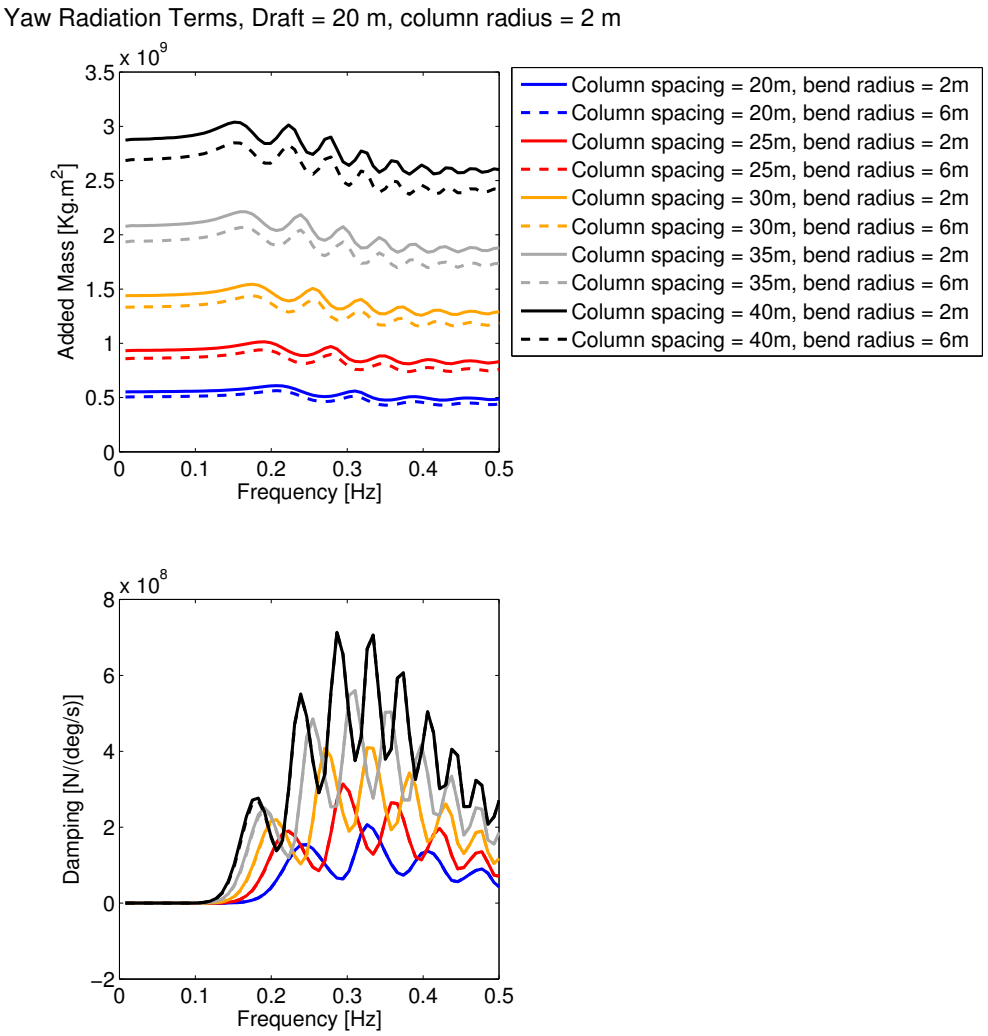


Figure 5.33: Effect of Increasing Column Spacing on the Yaw Radiation Terms

A summary of the parameter study is given as follows:

- Increasing the draft has the effect of:
  - Significantly increasing the surge, pitch and yaw added mass coefficient.
  - Significantly decreasing the heave and pitch damping.
  - Increasing surge and heave excitation forces.
  - Decreasing pitch excitation forces.
  - Negligible changes in heave added mass, surge and yaw damping and yaw excitation forces are observed.

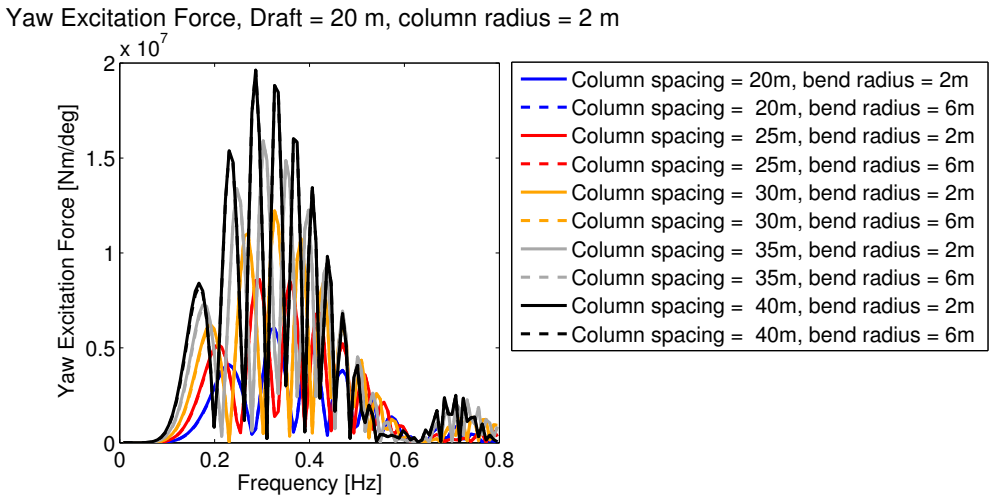


Figure 5.34: Effect of Increasing Column Spacing on the Yaw Excitation Force

- Increasing the column radius has the effect of:
  - Significantly increasing surge, heave and yaw added mass.
  - Significantly decreasing pitch added mass.
  - Significantly increasing surge, heave and yaw damping.
  - Significantly increasing low frequency pitch damping and decreasing high frequency pitch damping.
  - Significantly increasing surge, heave and yaw excitation forces
  - Significantly increasing low frequency pitch excitation forces and decreasing high frequency pitch excitation forces.
- Increasing column spacing has the effect of:
  - Significantly increasing surge, heave and pitch added mass.
  - Both increasing and shifting the peak yaw added mass towards a lower frequency region.
  - Decreasing low frequency damping.
  - Significantly decreasing heave damping
  - Both significantly decreasing pitch and yaw damping and shifting the response to a lower frequency region.

Table 5.5: Summary of Hydrodynamic Term Parameter Study

Parameter Increasing	Added Mass				Damping				Excitation Force			
	X	Z	RY	RZ	X	Z	RY	RZ	X	Z	RY	RZ
Draft	⇑	•	⇑	⇑	•	⇓	⇓	•	↑	↑	↓	•
Column Radius	⇑	⇑	⇓	⇑	⇑	⇑	⇑ ⇓	⇑	⇑	⇑	⇑ ⇓	⇑
Column Spacing	⇑	⇑	⇑	⇑ ←	⇓ •	⇓	⇓ ←	⇑ ←	←	←	⇑ ←	⇑ ←
Bend Radius	↓	⇓	↓	⇓	•	•	↑	•	↓	↓	↓ ↑	•

Where ↑ and ↓ indicate slight increases and decreases, ⇑ and ⇓ indicate large increases and decreases, • indicates no or negligible change. Where there are two arrows, the first indicates the change in a low frequency region and the second indicates a change in a high frequency region. ← indicates a frequency shift towards lower frequencies.

  - shifting the surge and heave excitation forces to a lower frequency region
  - Giving a significantly large increase in both pitch and yaw excitation forces while shifting the response to a lower frequency region.

- Increasing the pontoon-column interface bend radius has the effect of:
  - Decreasing surge and pitch added mass .
  - Significantly decreasing heave and yaw added mass.
  - Increasing pitch damping.
  - Negligible change in surge, heave and yaw damping.
  - decreasing surge and heave excitation forces
  - decreasing low frequency pitch excitation forces while increasing high frequency pitch excitation forces
  - Negligible change in yaw excitation forces.

5.6.2 FAST Model Set-up

A time-domain model is required for tension moored floating wind turbines, in order to accurately model the coupled DOF (due to high tendon restoring stiffness and WT controller) and the non-linear viscous drag forces. In order to run FAST time-domain simulations of the floating platforms generated in the previous parameter study, numerous

sub files of the main FAST file must be correctly configured. Matlab scripts are developed to automatically generate and populate these FAST input text files, creating a fully integrated hydrodynamic parameter to time domain WT coupled analysis software. In order for the hydrodynamic module HYDRODYN to read the hydrodynamic parameters, they must be first converted from the NEMOH format to the WAMIT format.

BMODES is used to generate the tower bending shapes, which in a TLPWT is dependant on not only tower structural properties, but also platform and tendon parameters. In order to generate the correct hydrodynamic coupling the following 6 x 6 terms are required as BMODES inputs: infinite frequency added mass of the platform, the hydrostatic and mooring stiffness matrices. The resultant tower fore-aft and side to side mode shapes are input to the ElastoDyn solver as coefficients of the 2nd to 6th powers.

The finite element mooring analysis code MoorDyn is used to model the dynamic tendon stiffness and wave-tendon interactions. MoorDyn validation work can be seen at [318].

5.6.3 Effect of Flexible Tower

RAO's of each platform model were generated in FAST using white noise wave excitations. For each platform model two simulations were ran, the first with a rigid WT tower and the second with a flexible WT tower. Figures 5.35 shows the increased pitch natural period which occurs when the flexible tower is modelled 5.36. In the top figure all simulations are shown. Two distinct peaks can be observed, centred on 3.5s and 4.7s for the rigid and flexible tower simulation methods respectively. The bottom figure shows the mean of each simulation method; rigid or flexible tower. here it can be observed that for periods above 5.5s the response between models is nearly identical, with the flexible tower having a slightly increased response. The flexible tower can be seen to increase the low period excitation. Figure 5.36 shows the effect of the flexible tower on tendon tension RAO's. For short period waves the platform pitch response is seen to dominate the tendon tensions, and thus the change in spectral response with tower flexibility shows the same change in period as described for the pitch response above.

Although this change in natural pitch frequency has been well documented in existing

literature, no attempt to quantify how this change is dependant on platform properties has yet been given. Comparing the change in pitch frequency against the tendon pretension and platform draft shows that the magnitude of pitch frequency change can be seen to be inversely proportional to pretension, and directly proportional to draft increases. With increasing draft the tendon length decreases and thus tendon stiffness increases In Figure 5.37 it can be clearly seen how a higher pretension means a lower rigid tower pitch frequency and smaller deviation between the fixed tower model and flexible tower model. This deviation increases as the pretension decreases and rigid tower frequency increases. Figure 5.38 is the same as 5.37 but the y axis has been replaced by the ratio between platform mass to tendon pretension. As this ratio increases, the rigid tower and change in rigid tower to flexible tower pitch frequencies also increase.

A higher pretension means the increased pitch tendon stiffness dominates the effect over the flexible tower.

Next the two tower modelling techniques effect on the magnitude of pitch motion and tendon tension is analysed. In Figure 5.39 the percentage change in the standard deviation of pitch motion from rigid tower to flexible tower is shown against total platform pretension. A log scale in the y axis was required, due to the large increases and decreases noted, greater than 1000%. An attempt was made to link this change to a large number of parameters; platform geometry, mass, pretension, hydrodynamic interactions and natural frequencies, and proved inconclusive. A statistical method to predict the effect of tower flexibility has thus been elusive. It would be of great benefit to the designers of TLFWT's and would allow greater confidence in design decisions at an earlier stage in the design process. The highly frequency dependant nature of the hydrodynamic parameters is likely to govern this unpredictability. As the pitch response governs the tendon loading at high frequency waves, and the response for both tower modelling techniques at low frequencies is identical, the percentage change in the standard deviation between techniques is extremely similar to that of pitch and is not plotted here.

A hypothesis behind this behaviour, is that the flexible tower shifts the pitch resonance modes to frequencies with higher/lower excitation and or radiated wave forces. This effect is worth further investigation as it may be crucial to the early stage TLPWT

design process.

In Figure 5.40 the pitch RAO of the model with largest increase in the standard deviation between techniques is shown as an example. It was indicated as a green circle in the previous figure. Here the flexible tower significantly increases the pitch response. Again the y-axis is shown in log scale due to the extremely large change. In contrast to this Figure 5.41 shows the largest decrease.

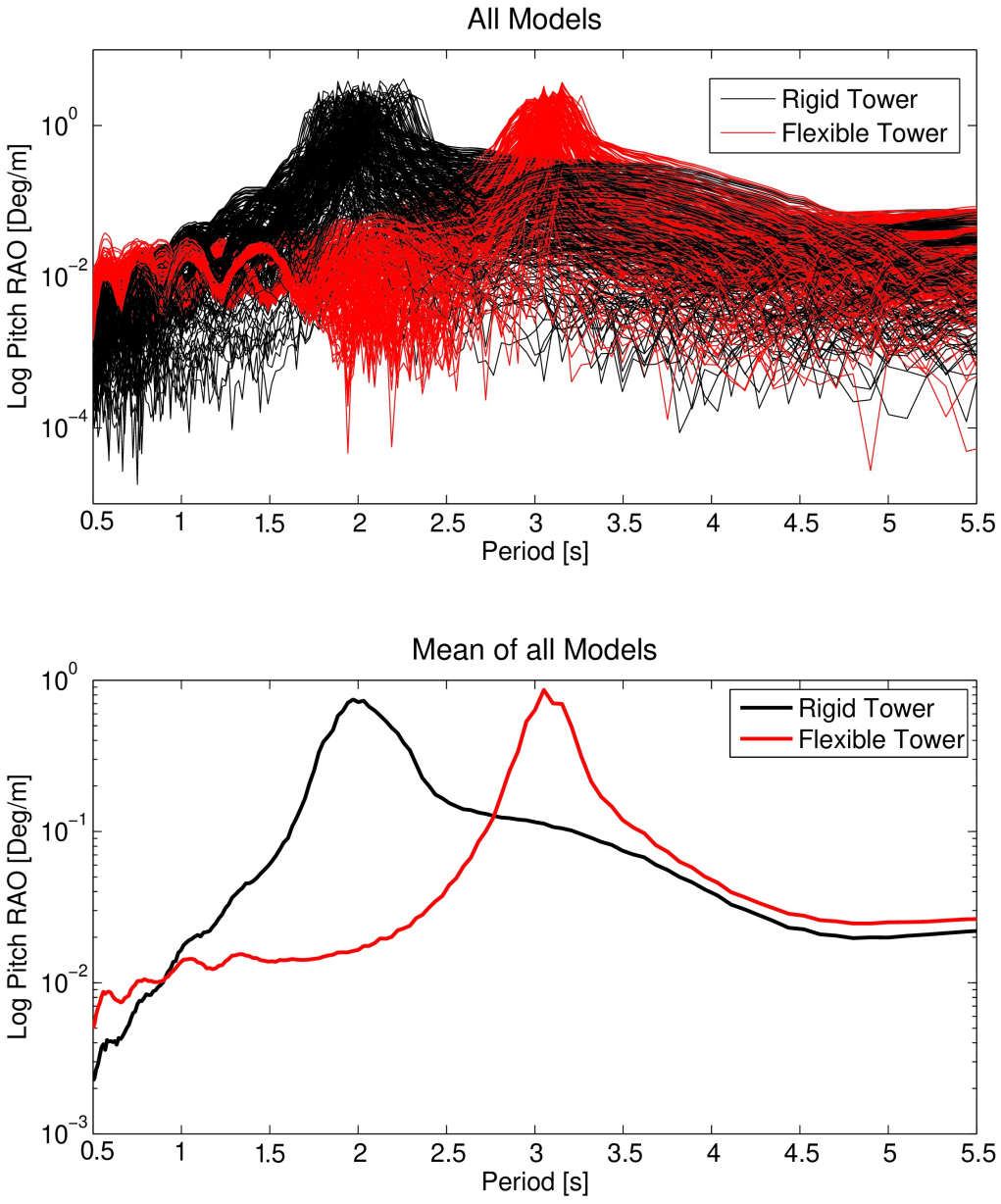


Figure 5.35: Effect of Flexible Tower on Pitch RAO

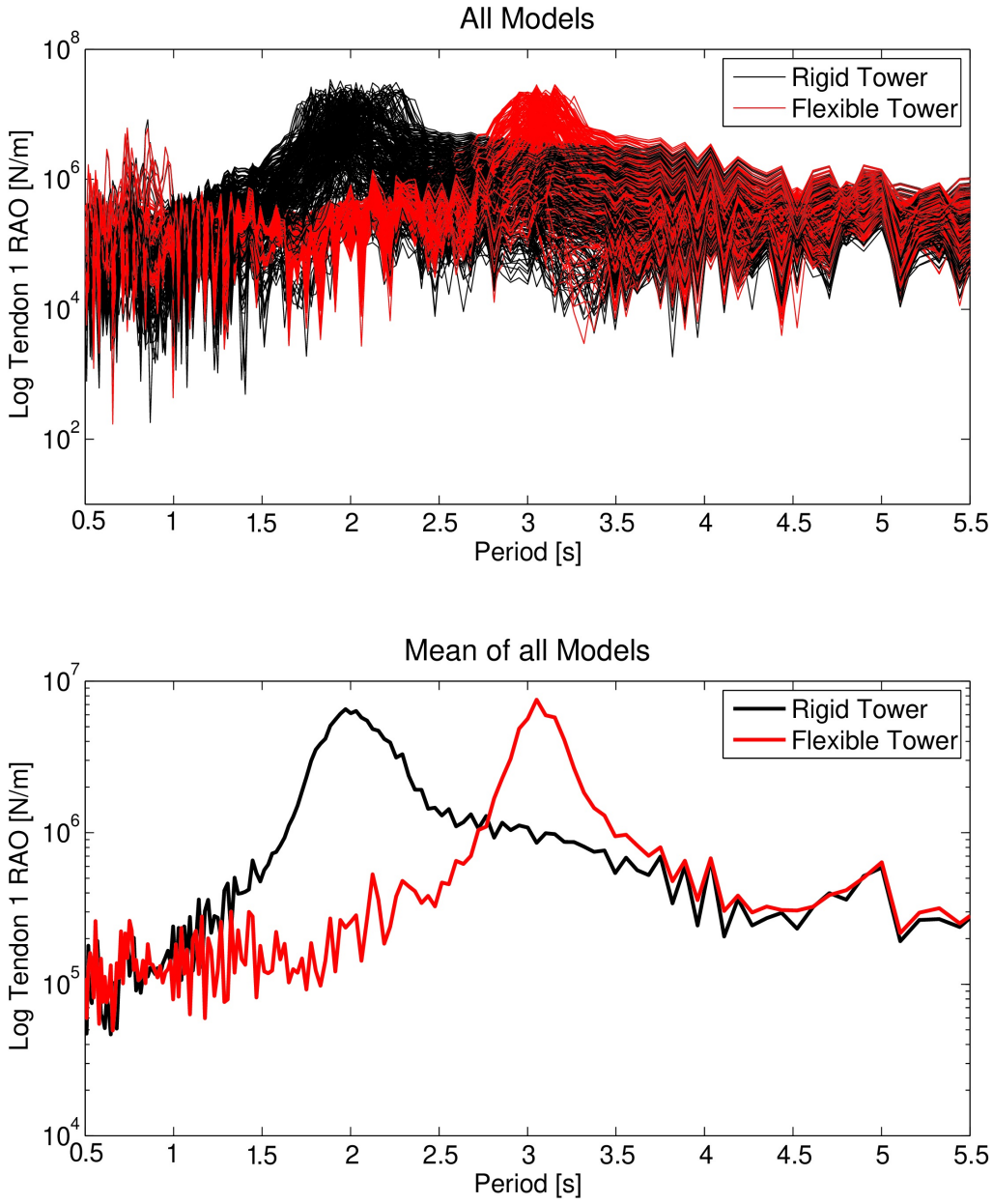


Figure 5.36: Effect of Flexible Tower on Tendon Tension RAO

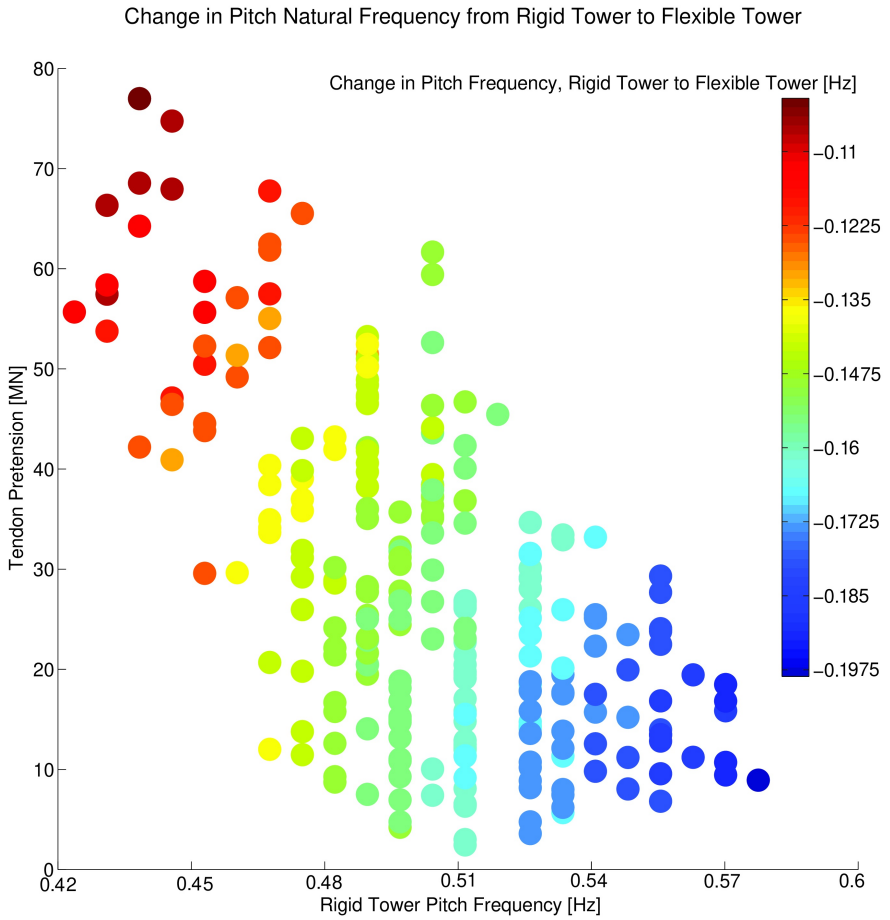


Figure 5.37: Effect of Flexible Tower and Tendon Pretension on Pitch Natural Frequency

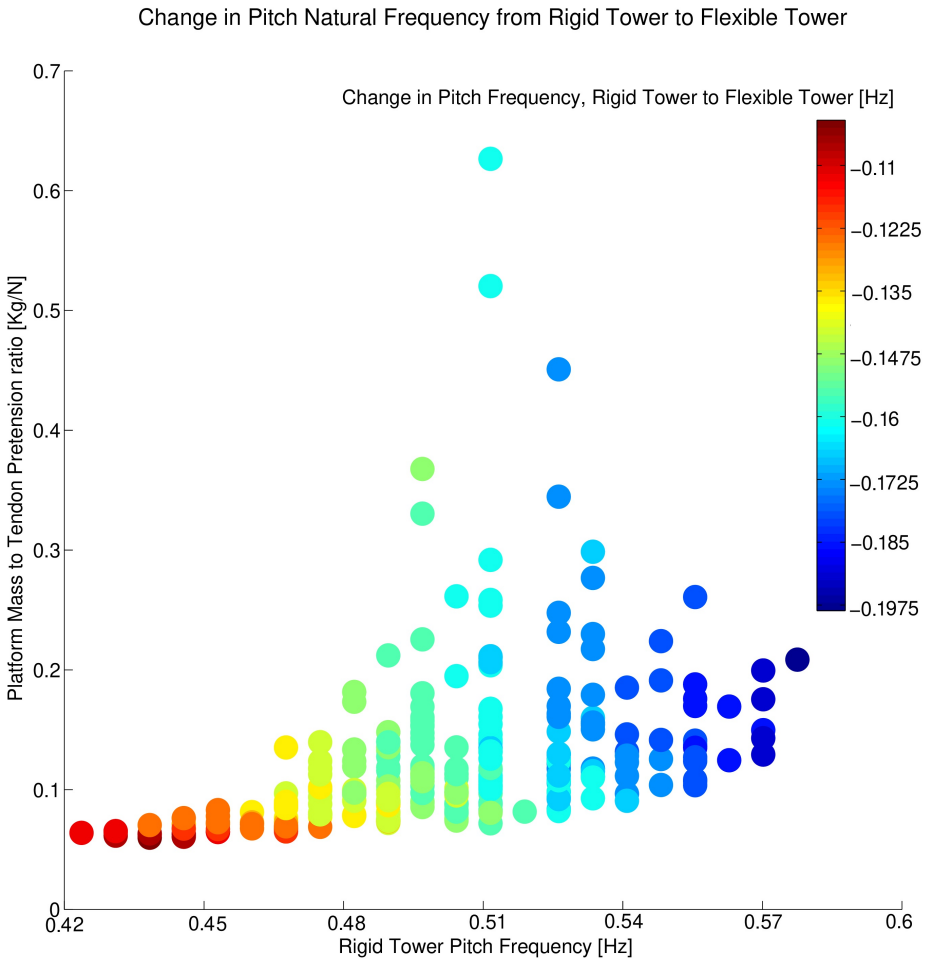


Figure 5.38: Effect of Flexible Tower and Platform Mass to Tendon Pretension Ratio on Pitch Natural Frequency

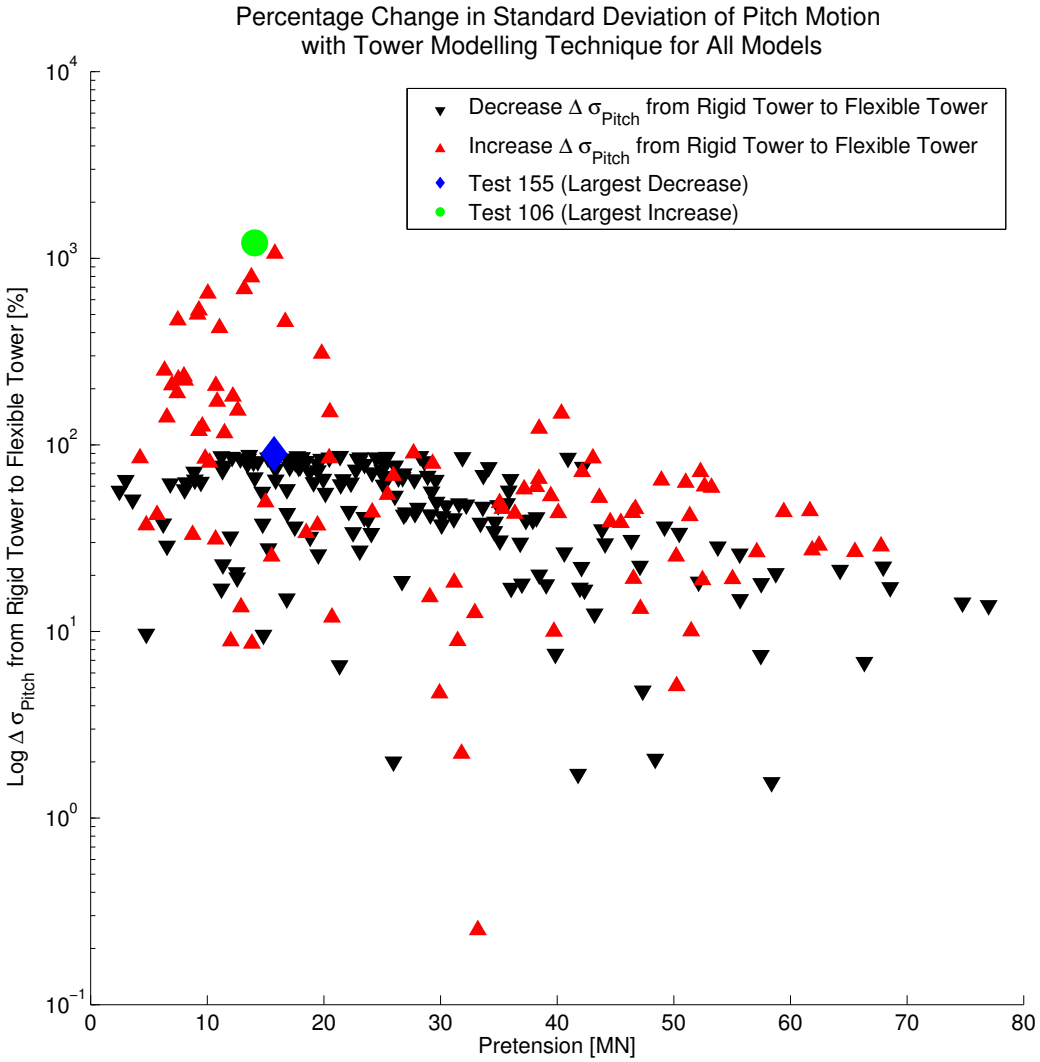


Figure 5.39: Effect of Flexible Tower and Platform Mass to Pitch Standard Deviation, All Models

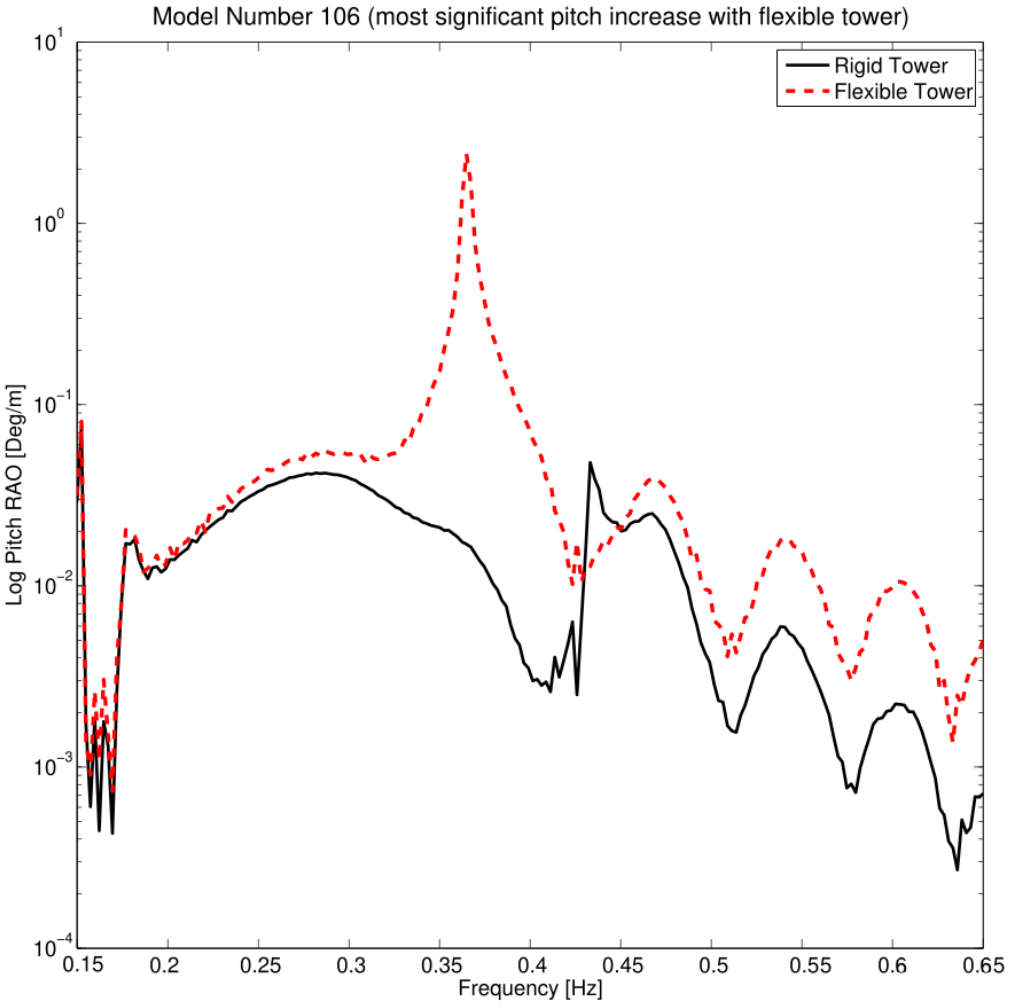


Figure 5.40: Effect Tower Modelling Technique, Model 106

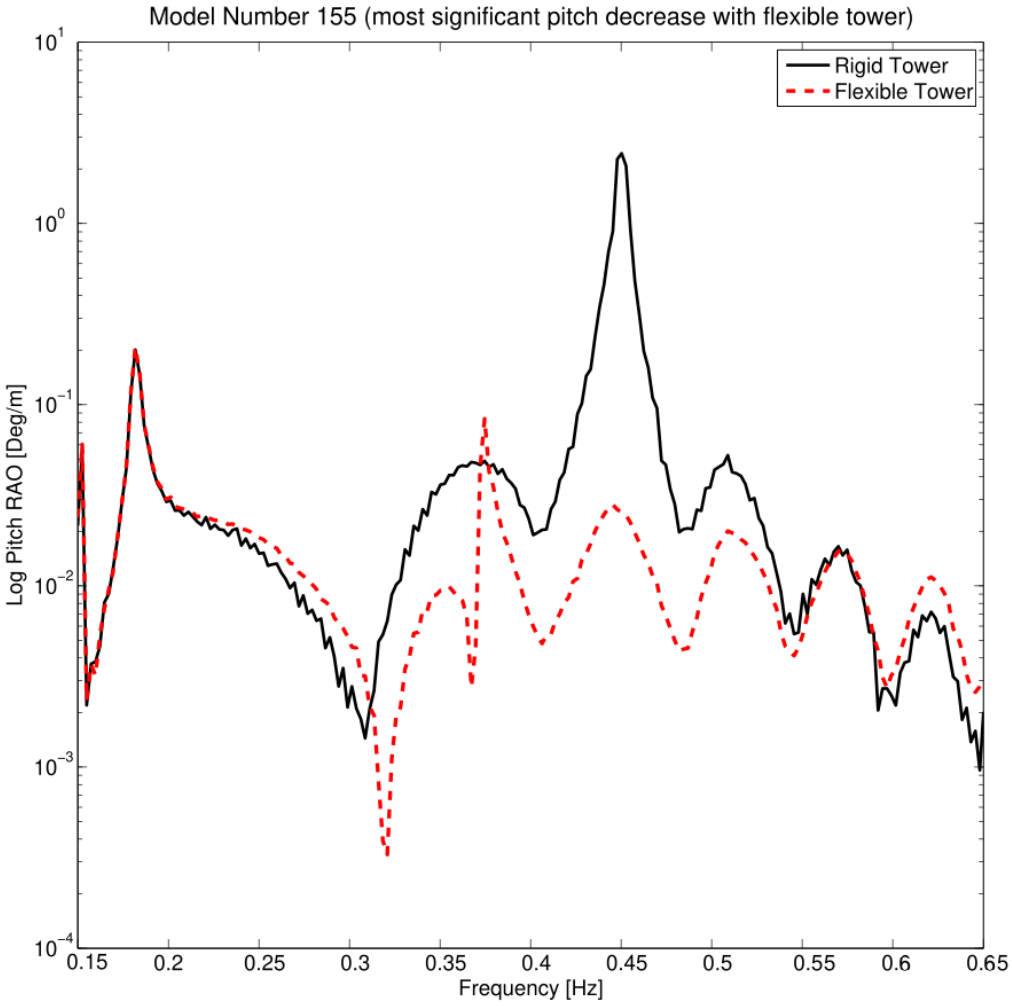


Figure 5.41: Effect Tower Modelling Technique, Model 155

5.6.4 Design Result

An initial design is selected from the parameter study with details of the selected properties listed in Table 5.6. This design case was selected for ease of scale model fabrication. A 3D image of the selected design is also shown in Figure 5.42 This design will be used as the base design for the following sections and chapters. As no detailed cost analysis is part of this work, the design is selected based on its reasonable hydrodynamic, coupled WT and low weight characteristics. Further analysis of these as well as a detailed structural and construct ability analysis should be performed in future work.

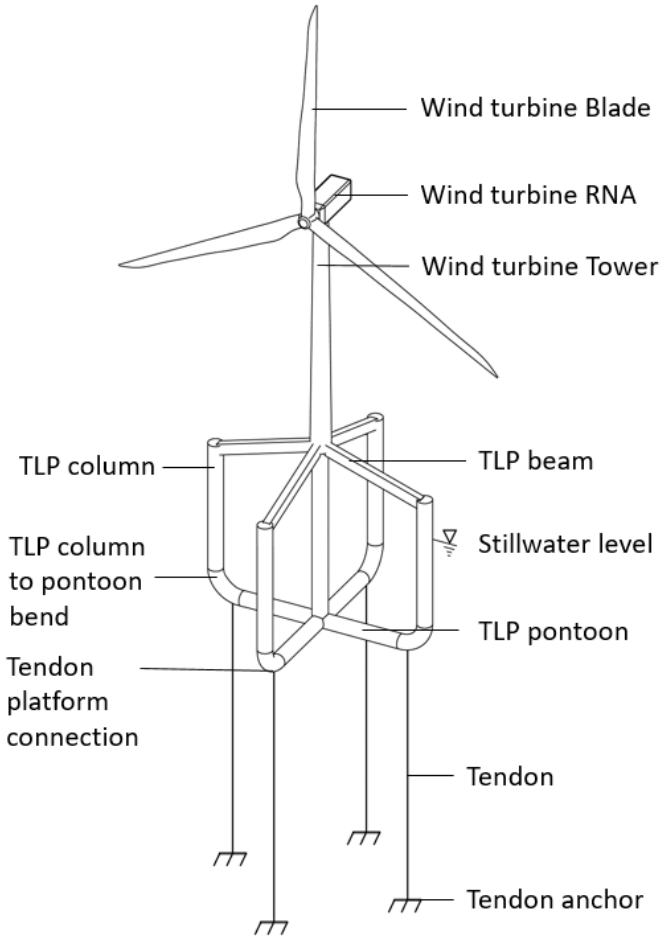


Figure 5.42: 3D Impression of Initial Design. Components are drawn to scale

Property Name	Value	Units
Water Depth	110	m
Total Mass	2079.84	tons
Platform Mass	1487	tons
Tower Mass	239.14	tons
RNA Mass	353.70	tons
Displacement	3188.04	m^3
Total Tendon Pretension	11622	kN
Tendon Unstretched length	75.857	m
Tower Length	70.00	m
Platform Draft	34.00	m
Outer Column Heights	44.00	m
Center Column Heights	54.00	m
Column Diameter	4.00	m
Connecting Pontoon Diameter	4.00	m
Bend Radius	6.00	m

Table 5.6: Initial Design properties

5.7 Installation Stability Design

In this section the stability of the platform is analysed for the transportation and instillation phase. As TLP's are not inherently stable without the addition of the restoring forces provided by the tendons, the transportation phase of the platforms from quayside to installation site poses a challenge. Cylindrical torus bodies are rigidly attached to each of the outer columns in order to provide a greater hydrostatic restoring moment. These "floats" are then water ballasted in order to provide the correct total platform draft. The correct draft is defined as being half the floats total height. These floats will become the WEC torus buoys in the following chapter.

The DNV codes define the required stabilised for a TLP in temporary free-floating conditions during construction, tow-out and installation to be the same as required for column-stabilized units such as semi-submersibles That is the area under the righting moment curve to the angle of down-flooding shall be equal to or greater than 130% of the area under the wind heeling moment curve to the same limiting angle.

The wind heeling moment is calculated as the thrust force generated by wind speeds of 1 m/s to 55 m/s on the parked WT. The buoyancy restoring force is calculated from

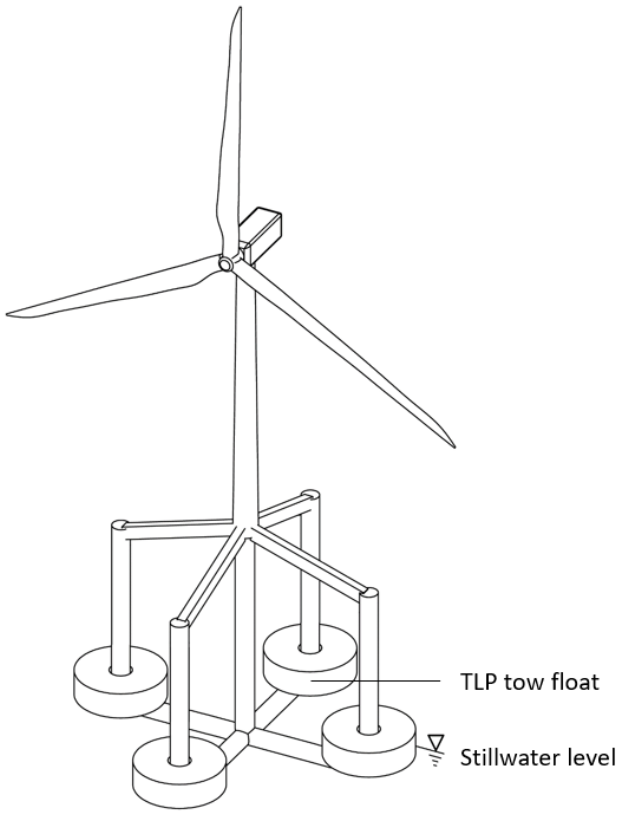


Figure 5.43: 3D Impression of Transport and Installation Condition. Components are drawn to scale

the 3D geometry in order to avoid small angle approximation errors. Figures 5.44 to 5.46 show the restoring moment (RM) and wind heeling moments (WHM). Heeling moments are shown for wind speeds of 4, 8, 16 and 32 m/s for illustrative purposes. As the wind thrust force and thus heeling moment is proportional to the square of the wind speed a cubic increase in WHM can be clearly seen. For a draft of 5m and float radius of 5m, the restoring moment turns negative after 14 °, this increases to 18 °for a radius of 6 m and beyond 20 °for larger radii. For a draft of 4m, the restoring moment turns negative after 12 °, this increases to 16 °for a radius of 6 m, 19.5 °for a radius of 7m and beyond 20 °for larger radii. For a draft of 3m, the restoring moment turns negative after 11 °, this increases to 14 °for a radius of 6 m, 17 °for a radius of 7m and beyond 20 °for larger radii.

From [319] the down-flooding angle is defined as the "minimum heel angle where an external opening without weather-tight closing appliance is submerged". The whole

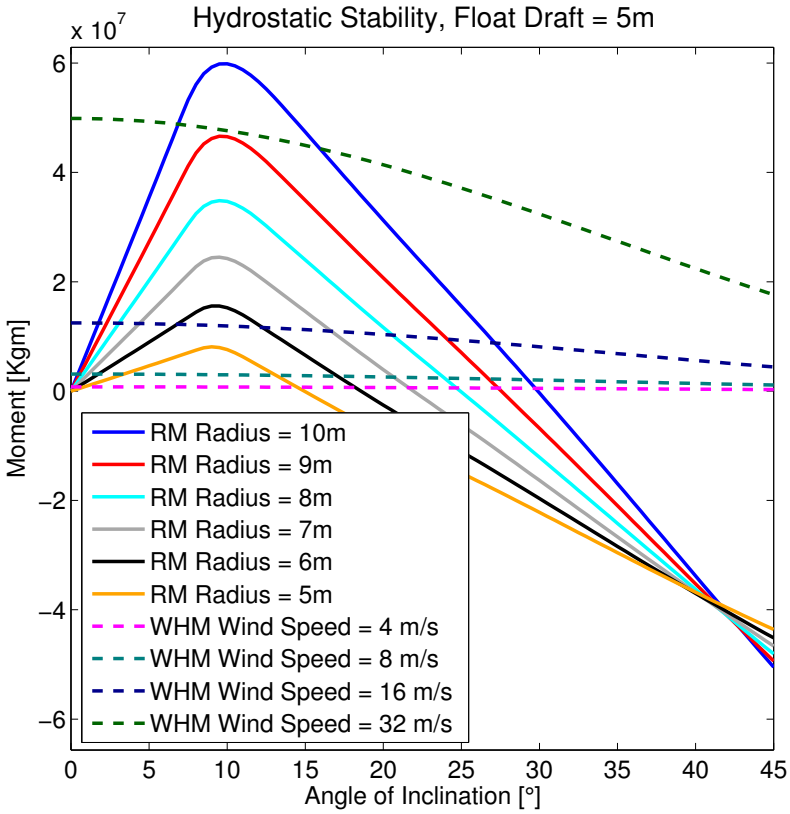


Figure 5.44: Static Stability of Floats with a Draft of 5 m

floating platform would comply to the above criteria, and an angle of inclination of 90 °(So that the tower opening is submerged) is unrealistic. Instead the points at which the top of the floats begin to take on green water are used as the angles of down-flooding.

The angle at which the floats surface begins to penetrate the SWL can be simply calculated with the equation $\phi_{Float} = tan^{-1}(FB_{Float}/(Columnspacing + R_{Float}))$. Figure 5.47 shows the maximum wind speeds that various float radii can survive, either taking the top of the float or 20°'s as the angle of down-flooding.

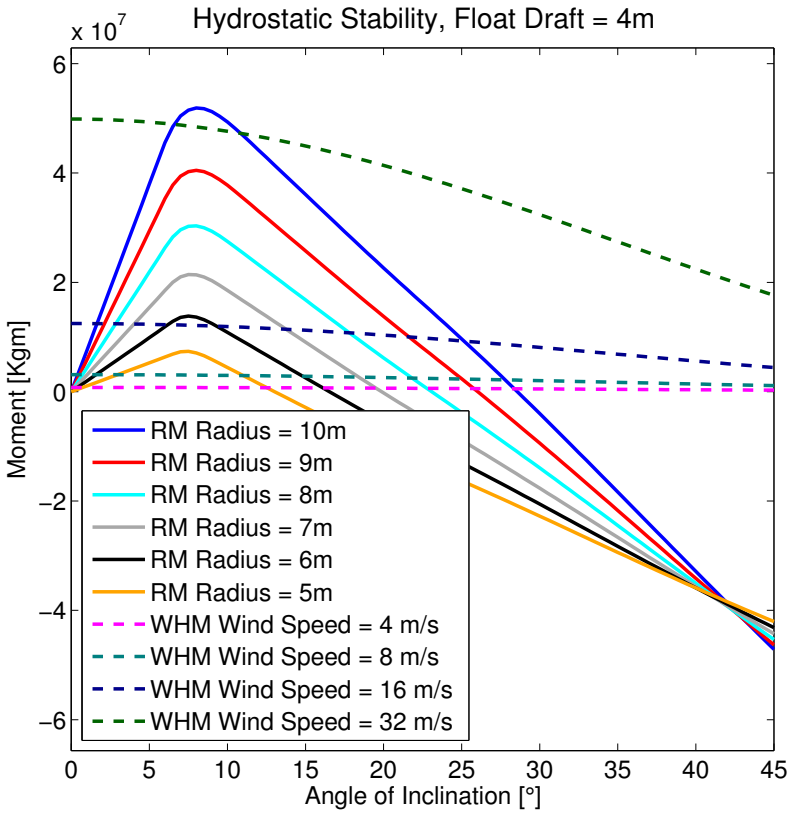


Figure 5.45: Static Stability of Floats with a Draft of 4 m

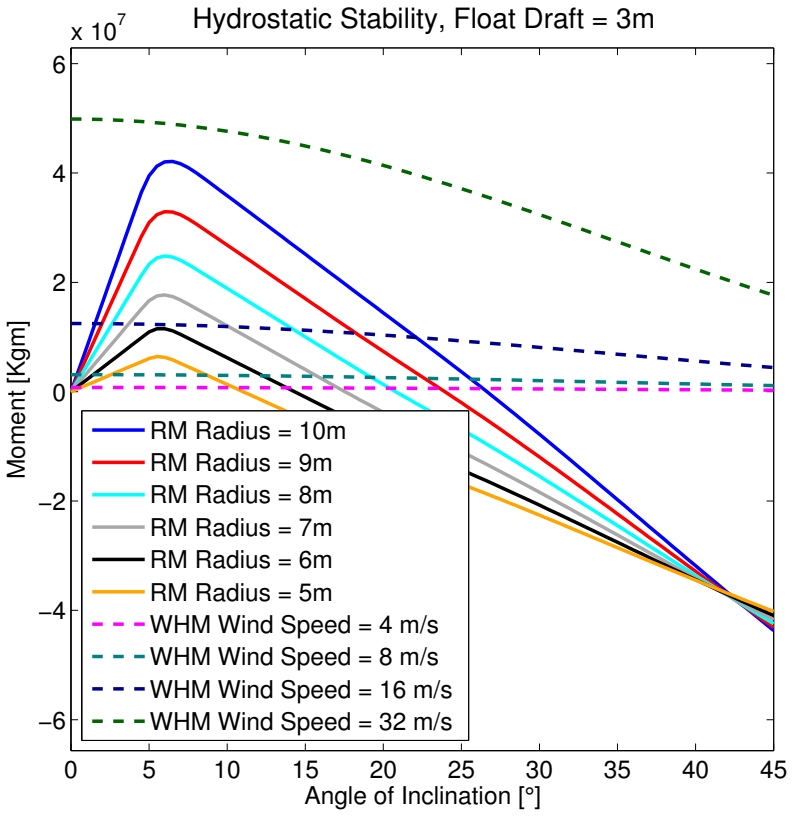


Figure 5.46: Static Stability of Floats with a Draft of 3 m

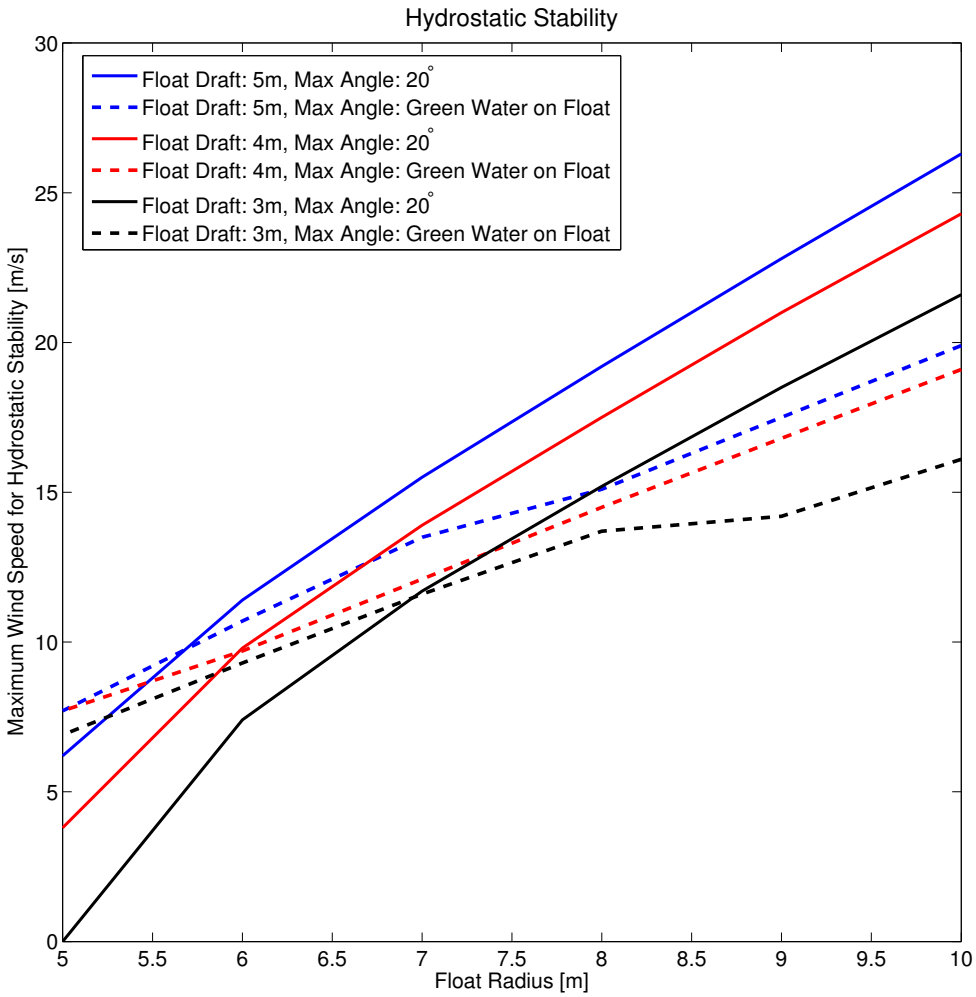


Figure 5.47: Maximum Wind Speed which comply with the DNV Stability Requirements

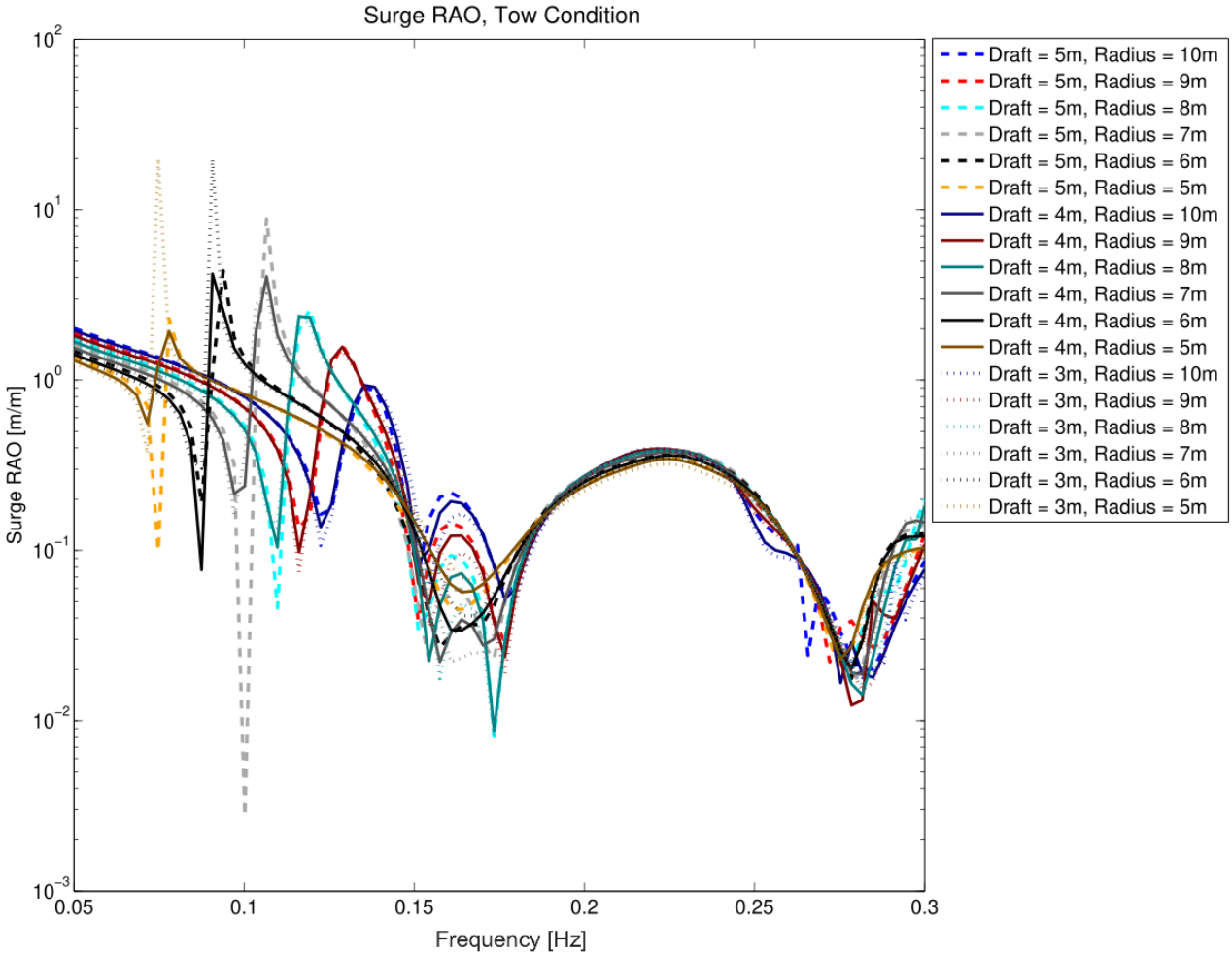


Figure 5.48: TWind Tow Condition Surge RAO

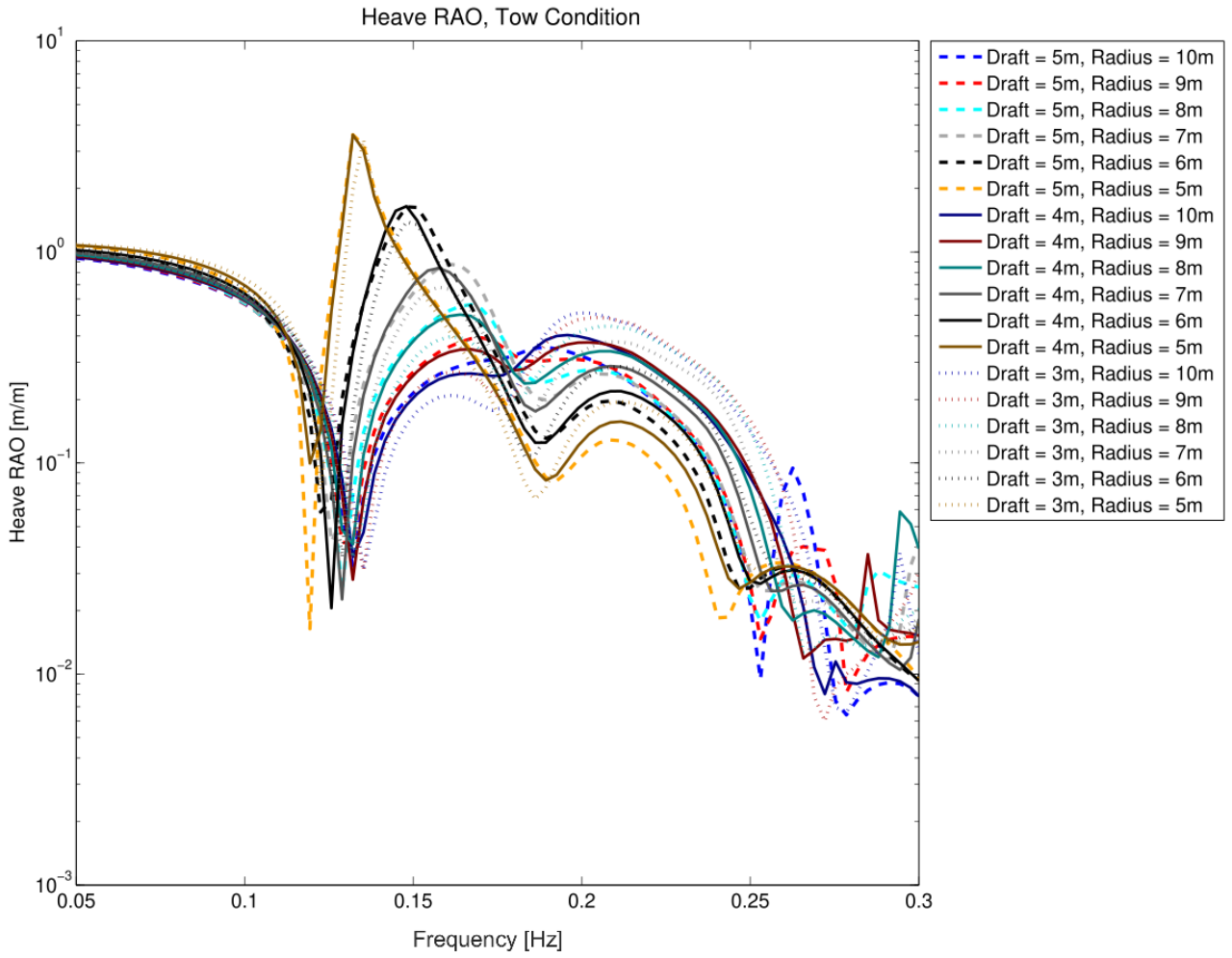


Figure 5.49: TWind Tow Condition Heave RAO

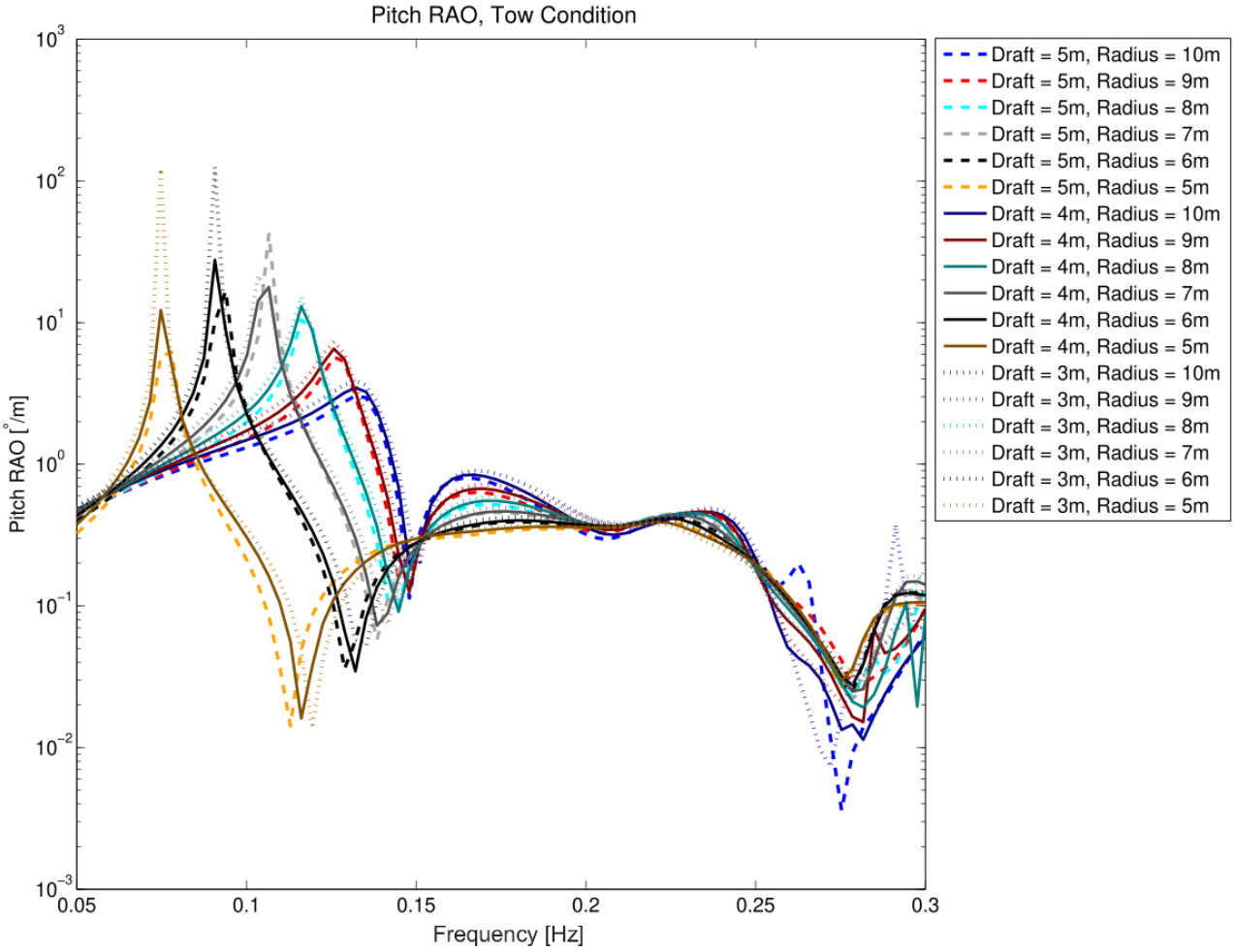


Figure 5.50: TWind Tow Condition Pitch RAO

5.8 Time Domain Modelling of Tow Conditions

The hydrodynamic stability in tow conditions was then analysed in the time-domain. The tug boat operation was synthesised by use of a static winch with a stiffness of 50 kN/m. The platform was towed for 2400 s with the length of winch wire chosen based on the simulation time and maximum tow speed. As the winch cable used in these simulations is much longer than a realistic tow cable, a greater lateral movement is present in the simulations that have a diagonal force component. This method to synthesise a vessel and FWT towing situation does not take into account the tug vessel motions, or catenary dynamics of the towing line. these simplifications will reduce the accuracy of the study, but provide a general overview of the towing behaviour. For a detailed numerical study on a FWT - vessel tow operation the readers are directed to [320].

The forward speed influences the apparent wave frequency that the platform sees. Thus wave frequencies away from the platform natural frequencies can cause resonance issues. The encounter frequency for varying tow velocities and wave directions can be calculated by Equation 5.1, where λ is the wavelength, c is the wave celerity, V is the tow velocity and μ is the angle between wave and towing direction [321]. Examples of the encounter frequency variations with wave direction and towing velocity are shown in Figures 5.51 to 5.53 for wave periods of 5 s, 7.5 s and 10 s.

$$T_{enc} = \frac{\lambda}{c - V.cos\mu} \tag{5.1}$$

The bollard pull of a standard large towing and anchor handling tug is around 300 ton (3 MN), for example, ULSTEIN's ALP Striker has a bollard pull of 310 ton (3.04 MN), while the Rolls Royce Far Samson UT 761 CD design offshore vessel has a bollard pull of 423 ton (4.15 MN). Rather than use a single large vessel a combination of smaller vessels could also be used to achieve the desired bollard pull. In the literature, examples of using multiple smaller vessels to tow FWT to installation sites are evident, and as well as reducing costs this approach also provides additional control over the FWT by the ability to apply forces in multiple directions simultaneously. In other research on towing FWTs, a smaller tug vessel with a bollard pull of 65 ton was used [320].

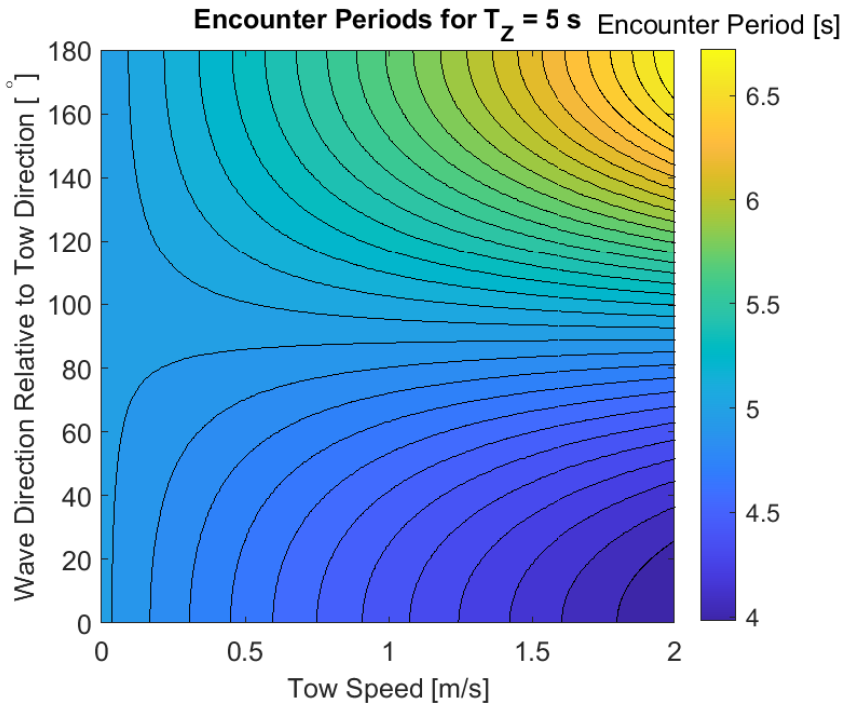


Figure 5.51: Encounter Periods for Varying Tow Speeds and Wave Directions, $T_z = 5$ s

In order to analyse the suitability of the proposed self stable tow designs to the real environmental conditions that will be encountered a time-domain towing modelling is developed. A large parameter study on the environmental and towing conditions are considered according to Table 5.7. Spectral Bretschneider waves are used. The wave or Wind direction indicates the angle between the towing direction and wind/wave direction. Current has not been modelled in the current towing study, however the effects of current will increase the required bollard pull if the forces are in opposing directions. Limits on maximum roll and pitch angles of 20 and 12.5 degrees during the transportation phase have been set [322]. Towing velocities of 0.25 - 1.5 m/s are analysed, roughly equivalent to 0.5 to 3 knots.

Table 5.7: Tow Study Parameter Table

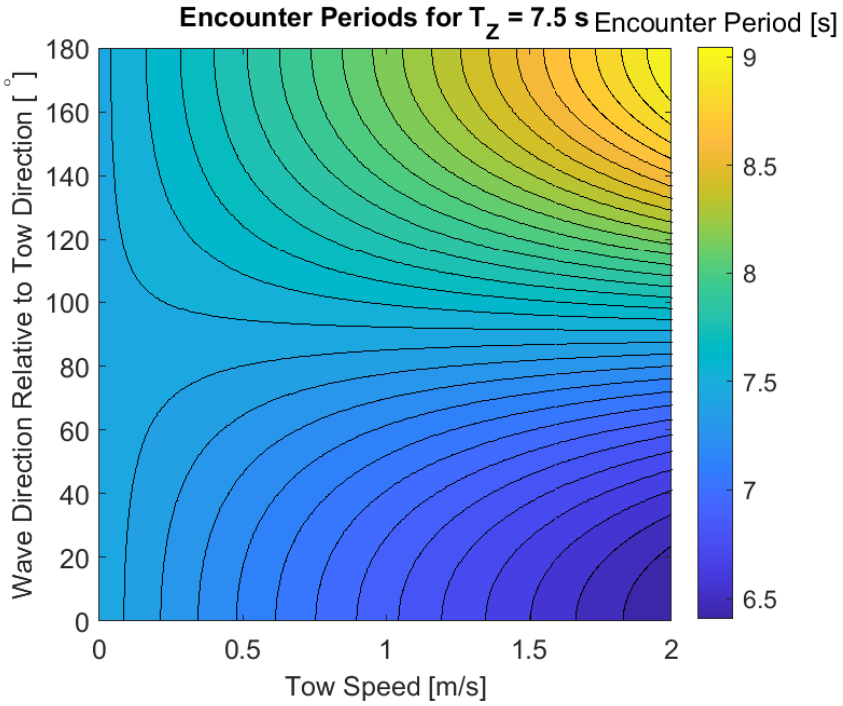


Figure 5.52: Encounter Periods for Varying Tow Speeds and Wave Directions, $T_z = 7.5$ s

Parameter Name	Min	Max	Δ	Unit
Tow Speed	0.25	1.5	0.625	m/s
Wave Height H_S	1	4	1	m
Wave Period T_p	6	10	4	s
Wave Direction D_W	0	180	90	deg
Wind Speed v	10	30	5	m/s
Wind Direction D_V	0	180	90	deg

In cases were the wave or wind forces are applied in the same direction as the towing velocity, the mean wave drift velocity or mean wind induced velocity may be greater than the towing velocity. In these cases the towing tension will be zero. Due to the large number of Figures in this section, they are moved to Appendix B in order to aid the readability. In Figures C.1 to C.4 the mean and peak tow line tension's are shown for 3m draft model in the varying conditions.

Summary results are shown in Tables 5.8 to 5.11. These results indicate that there is

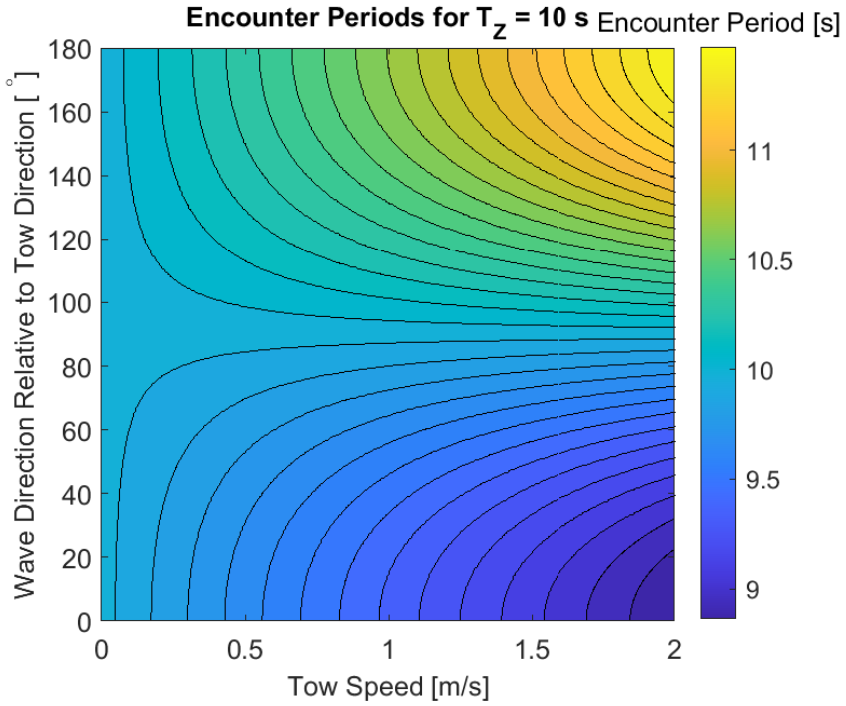


Figure 5.53: Encounter Periods for Varying Tow Speeds and Wave Directions, $T_z = 10$ s

no clear winner between the two draft designs, as each type shows a better performance over the other in some metrics. Taking a limit of 65 tons bollard pull, the 3 m draft design can be towed up to a H_S of 3 m, but for wave heights 2 - 3 m the tow speed must be reduced to 0.875 m/s. Taking this bollard pull limit for the 5 m draft design, the higher tow speed of 1.5 m/s can not be achieved at any sea-state simulated, while the 0.875 m/s tow can not be achieved for $H_S > 2$. The increased added resistance of the deeper draft design, causing the increased required bollard pull is most likely due to the increased viscous drag. The required bollard pull is dominant by environmental load cases of D_V and D_W of 180 degrees as expected, i.e. towing into the wind and wave, while the peak tow line tensions can arise with D_V of 90 degrees and D_W of 180 degrees (3 m Draft at $H_S = 4$m) or with D_V and D_W of 90 degrees (5 m Draft at $H_S = 4$ m).

The peak tow-line tensions occur at the maximum tow speed at a $H_S = 4$m $T_P = 10$ s, ~3600 kN and ~3970 kN for the 3 m and 5 m drafts respectively. Increasing the float draft decreases the RNA accelerations, while increasing the pitch and roll motions.

This towing study further identifies the complexity in the design of the TLP WT for self stability in tow and installation conditions. As the motion and acceleration limits

are generally governed by the the turbine supplier a fully integrated design approach is required to reach an optimised design and are beyond the scope of this thesis.

	Height	$H_S = 1$ m								$H_S = 2$ m							
	Period	$T_P = 6$ s				$T_P = 10$ s				$T_P = 6$ s				$T_P = 10$ s			
	Tow Speed [m/s]		V	D_V	D_W		V	D_V	D_W		V	D_V	D_W		V	D_V	D_W
Mean	0.25	198	30	180	180	216	30	180	180	298	30	180	180	335	30	180	180
Winch	0.875	338	30	180	180	360	30	180	180	447	30	180	180	527	30	180	180
Tension [kN]	1.5	622	30	180	180	638	30	180	180	736	30	180	180	804	30	180	180
Peak	0.25	367	25	180	180	489	30	180	180	742	30	180	180	917	30	180	180
Winch	0.875	411	30	180	180	647	30	180	180	661	25	180	180	1429	30	180	180
Tension [kN]	1.5	688	30	180	180	853	30	180	180	910	30	180	180	1552	30	180	180
Peak	0.25	1.05	25	0	0	2.68	30	0	180	3.47	30	0	0	5.31	30	90	0
RNA	0.875	1.05	20	180	0	2.37	10	0	180	3.47	30	0	0	4.41	30	180	180
Acc [m/s^2]	1.5	1.23	25	0	0	2.32	30	90	180	2.49	30	0	0	4.53	20	90	180
Peak	0.25	1.2	30	90	90	3.9	10	90	90	3	30	0	0	7	10	90	90
Roll	0.875	1	25	90	90	3.9	15	90	90	3	30	0	0	6.9	15	90	90
Motion[°]	1.5	1	30	90	90	3.8	20	90	90	2.3	30	90	90	7	15	180	90
Peak	0.25	1.2	30	0	0	4.4	30	0	180	3.1	25	0	0	7.5	20	180	0
Pitch	0.875	1.2	20	180	0	4	30	0	180	3.1	25	0	0	7.7	20	0	180
Motion[°]	1.5	1.6	25	0	0	3.6	20	0	0	3.3	20	90	0	7.1	10	0	180

Table 5.8: Results from 3m Draft Study, Hs = 1 and 2 m. V, D_V and D_W indicate the wind speed, wind and wave directions respectively

	Height	H_S = 3 m								H_S = 4 m							
	Period	T_P = 6 s				T_P = 10 s				T_P = 6 s				T_P = 10 s			
	Tow Speed [m/s]		V	D_V	D_W		V	D_V	D_W		V	D_V	D_W		V	D_V	D_W
Mean	0.25	472	30	180	180	511	30	180	180	713	30	180	180	737	30	180	180
Winch	0.875	637	30	180	180	775	30	180	180	915	30	180	180	1093	30	180	180
Tension [kN]	1.5	927	30	180	180	1068	30	180	180	1204	30	180	180	1406	30	180	180
Peak	0.25	1316	30	180	180	1488	30	180	180	2214	30	90	180	2156	30	90	180
Winch	0.875	1185	30	180	180	2274	30	180	180	1985	30	180	180	3206	30	180	180
Tension [kN]	1.5	1271	30	180	180	2494	30	180	180	1899	15	90	90	3595	30	180	180
Peak	0.25	5.59	20	0	0	8.09	20	0	0	9.3	20	90	0	10.01	25	0	0
RNA	0.875	5.59	20	0	0	8.09	20	0	0	9.3	20	90	0	10.01	25	0	0
Acc [m/s^2]	1.5	4.86	15	0	0	6.37	15	90	180	9.74	15	0	0	8.13	25	90	180
Peak	0.25	5.6	20	0	0	10	30	90	90	10.9	15	0	0	14.3	15	0	0
Roll	0.875	5.6	20	0	0	9.9	20	0	0	12.4	10	180	90	14.3	15	0	0
Motion[°]	1.5	4.4	30	90	90	9.1	10	90	90	11.1	10	180	0	12.7	25	90	90
Peak	0.25	5.9	20	0	0	10.5	25	0	0	12.6	20	90	0	14.2	25	0	0
Pitch	0.875	5.9	20	0	0	11	10	0	180	12.6	20	90	0	14.3	15	0	180
Motion[°]	1.5	8.7	15	0	0	10.6	20	0	180	12.3	15	0	0	13.6	25	90	180

Table 5.9: Results from 3m Draft Towing Study, Hs = 3 and 4 m. V, D_V and D_W indicate the wind speed, wind and wave directions respectively

	Height	$H_S = 1$ m								$H_S = 2$ m							
	Period	$T_P = 6$ s				$T_P = 10$ s				$T_P = 6$ s				$T_P = 10$ s			
	Tow Speed [m/s]		V	D_V	D_W		V	D_V	D_W		V	D_V	D_W		V	D_V	D_W
Mean	0.25	243	30	180	180	262	30	180	180	342	30	180	180	387	30	180	180
Winch	0.875	392	30	180	180	407	30	180	180	502	30	180	180	556	30	180	180
Tension [kN]	1.5	696	30	180	180	702	30	180	180	812	30	180	180	840	30	180	180
Peak	0.25	411	30	180	180	514	30	180	180	731	30	180	180	1268	10	0	180
Winch	0.875	471	30	180	180	701	30	180	180	715	30	180	180	1607	30	180	180
Tension [kN]	1.5	766	30	180	180	924	30	180	180	994	30	180	180	1685	30	180	180
Peak	0.25	0.56	30	0	0	2.66	20	0	90	1.67	30	0	0	4.86	10	180	180
RNA	0.875	0.56	30	0	0	2.61	10	90	90	1.67	30	0	0	4.54	25	180	180
Acc [m/s^2]	1.5	0.61	15	180	0	2.58	30	0	90	1.3	30	180	0	4.17	25	180	90
Peak	0.25	0.5	30	90	90	5.3	15	180	90	1.2	15	180	90	8.2	20	180	90
Roll	0.875	0.5	30	90	90	5.2	10	0	90	1.1	30	0	0	7.9	10	90	90
Motion[°]	1.5	0.5	20	90	90	5.2	30	0	90	1.1	15	90	90	8.1	30	180	90
Peak	0.25	0.6	30	0	0	5.4	20	180	0	1.2	30	0	0	9.8	25	0	180
Pitch	0.875	0.6	30	0	0	4.8	30	0	180	1.2	30	0	0	8.7	10	90	180
Motion[°]	1.5	0.8	30	0	0	3.7	25	0	180	2	20	90	0	7.7	10	0	180

Table 5.10: Results from 5m Draft Towing Study, Hs = 1 and 2 m. V, D_V and D_W indicate the wind speed, wind and wave directions respectively

	Height	H_S = 3 m								H_S = 4 m							
	Period	T_P = 6 s				T_P = 10 s				T_P = 6 s				T_P = 10 s			
	Tow Speed [m/s]		V	D_V	D_W		V	D_V	D_W		V	D_V	D_W		V	D_V	D_W
Mean	0.25	507	30	180	180	576	30	180	180	753	30	180	180	806	30	180	180
Winch	0.875	695	30	180	180	776	30	180	180	969	30	180	180	1049	30	180	180
Tension [kN]	1.5	1007	30	180	180	1071	30	180	180	1291	30	180	180	1368	30	180	180
Peak	0.25	1318	30	180	180	2262	30	180	180	2240	30	180	180	3209	30	90	180
Winch	0.875	1235	25	180	180	2751	30	180	180	1912	30	180	180	3917	30	180	180
Tension [kN]	1.5	1419	30	180	180	2772	30	180	180	2452	25	90	90	3972	30	180	180
Peak	0.25	3.33	30	0	0	6.62	25	90	0	8.76	25	180	90	8.17	25	0	0
RNA	0.875	3.33	30	0	0	6.16	25	180	180	8.66	10	90	0	8.26	30	90	0
Acc [m/s^2]	1.5	4.88	10	0	0	6.15	30	180	180	6.52	25	90	90	7.95	10	180	180
Peak	0.25	4.7	30	0	0	10.5	25	90	90	17.3	10	90	0	13.3	20	0	90
Roll	0.875	4.7	30	0	0	10.3	25	0	90	17.3	10	90	0	12.8	25	90	90
Motion[°]	1.5	4.2	25	0	0	9.9	20	180	90	10.3	25	180	0	12.9	20	180	90
Peak	0.25	4.1	30	0	0	13.6	30	0	180	11.7	10	90	0	16.5	30	90	180
Pitch	0.875	4.1	30	0	0	11.9	10	90	180	13	30	90	90	14.6	25	90	180
Motion[°]	1.5	10	10	0	0	11.6	10	0	180	12.9	30	180	0	15.1	10	180	180

Table 5.11: Results from 5m Draft Towing Study, Hs = 3 and 4 m. V, D_V and D_W indicate the wind speed, wind and wave directions respectively

5.9 Conclusions

In this chapter a general overview of the design of a novel TLP WT support structure is given. The chapter begins with an overview of the environmental design factor's for Irish waters. A preliminary bathymetry study is conducted which concludes that water depths of 70 to 130 m offer the largest possible Irish sea area of to exploit. A depth of 110 m is chosen as a preliminary water depth for the design. An extreme wave extrapolation is carried out at both a 50 and 100 year return period using the modern ACER approach. As an offshore WT will need to be set to idle in not only above rated wind speeds but also in severe wave conditions, a study on the wind wave correlation is undertaken. Using ten years of observed data from the Marine Institutes weather buoy network, an operational wave height limit based off the percentage of total wind energy available is given. This analysis shows that 90% of the available energy is harnessed at a cut out significant wave height of 2.3 m at the most sheltered location (M2), while at the most severe locations on the west coast this is raised to greater than 5.9 m (M1, M3, M4 and M6).

An innovative shortened tower is proposed in order to increase the tower and overall platform stiffness and coupled tower bending - pitch natural frequency of the platform. A preliminary frequency domain analysis shows that this shortened tower is viable at platform depths of 100 - 230m, in order to avoid coincidence of the tower bending and the 1P or 3P rotor frequencies.

A detailed hydrodynamic investigation of the TLP floating wind support structure member dimensions is given next. A tool is developed which combines the open source potential flow solver NEMOH and the fully coupled time-domain FWT code OpenFAST using Matlab, enabling a detailed hydrodynamic parameter study to be extended into the time domain and include the WT and tower coupling effects. As the TLP pitch natural frequencies is heavily coupled with the tower bending moment an in depth analysis of such behaviour linked to the hydrodynamic parameter study is given next. An overview of this pitch frequency alteration is given, aiding future designers of TLP WT in their early stage analysis.

A preliminary design and analysis of the TLP structure for self stability in the trans-

port and installation phases of deployment is given in the frequency and time-domain. This analysis shows the design to be viable at typical tow velocities and in the range of normally available bollard pulls. The complexity of the design process for the towing phase is outlined by the conflicting optimisation goals. Increasing the float draft decreases the RNA accelerations, while increasing the pitch and roll motions. The suitable final design in both operational, transportation and installation will depend on the limiting criteria imposed by the turbine supplier.

In the following chapter, the TLP will be designed to incorporate WEC's in both an operational and novel survivability mode. Validation of the numerical modelling analysis of the standalone TLPWT identified in this chapter and the TLPWT + WEC will also be undertaken by experimental wave basin testing.

Chapter 6

Design of Combined Wind and Wave Energy Convertor

This chapter deals with the design, testing and validation of the hybrid combined wind and wave energy convertor, TWindWave (*T*ension moored *Wind* and *Wave* energy convertor). The design evolves from the wind energy only platform TWind, with the transportation and installation stability floats becoming the WEC devices.

The chapter begins with an overview of the general design philosophy created for the addition of WECs onto an existing TLPWT structure. An analysis of the ratio of energy generated by wind and wave sources is then given. The design and analysis of a solitary WEC is described, in order to aid the understanding of the combined system. This single isolated WEC gives a preliminary overview of the forces and power generation capabilities that will be encountered in the combined system. A detailed parameter study of the single solitary WECs performance characteristics under varying draft and radius is completed.

The chapter continues into a detailed design and analysis of the combined wind and wave energy converter platform. Special attention is given to the coupling effects between the WEC and platform pitch/tendon tensions. Detailed hydrodynamic modelling of the combined system, including hydrodynamic interaction effects between the 5 rigid body's (TLPWT + 4 WECs) and the tower bending modes are performed. In above rated

sea-states a novel WEC survivability mode is suggested and analysed. In this mode, the WECs are submerged and rotated up to 90 degrees.

In order to validate the numerical modelling procedures of both the wind only, TWind and the combined wind and wave platform, TWindWave, a scaled model is tested in a deep water wave basin. Results from the 1/37 scale model are compared against the simulated data. The validation study gives confidence in the design and modelling procedure as outlined in this research work, increasing the knowledge on TLPWT and combined TLP wind and wave energy converters with potential to increase the percentage of sustainable energy generated onto the Irish grid.

A summary of results and conclusions from this chapter are as follows:

- A combined tension moored wind and wave energy convertor was designed, simulated and experimentally tested in this chapter.

- A design procedure to incorporate WECs onto an existing TLPWT design has been outlined.

- The effect of hydrodynamic interaction between the platform and WEC's has been shown and quantified, demonstrating the importance of taking these effects into account on both WEC power production and platform structural requirements. The addition of WEC generally increases tower bending moments

- Novel WEC survival modes were presented and analysed. The survival operation involved disconnecting the WEC PTO before ballasting, submerging and rotating the WEC floats along the TLP columns. Results of this survival mode demonstrate the prove of concept, showing decreased tendon loading for long period waves, but also show that a redesign is required to avoid the increase in pitch response for short period waves.

- Numerical models of the standalone TWind device and the TWindWave device under parked and operating WEC modes were validated by a 1/37th scale wave basin test campaign.

6.1 Design Philosophy

The design philosophy used here describes the basic principles for incorporating WEC onto a TLPWT system. One combined Wind and WEC design philosophy is to add WECs that will require a minimal change to the TLPWT structure. This idea involves exploiting the pretension of the TLPWT which is required for survival stability, but unused during the operational energy generation phase of the WT. This unused tension is used for the WECs power generation phase. Figure 6.1 shows this in graphical form. A maximum and conservative limit on WEC "exploitable tension" is described here as the maximum/minimum tension under maximum and no wind cases. This figure shows a simplified view where there is no cut-out sea-state applied to the wind turbine. In reality the dashed lines indicating the maximum and minimum tensions under wind load will decrease and increase as this wave height to wind turbine cut-out conditions are applied.

This approach will increase the fatigue loading and require a structural redesign of the FWT platform, but it means that a conclusive comparison to the WT with and without WECs is possible.

6.2 Preliminary Design

6.2.1 Wind to Wave Ratio

In order to preliminary design the combined wind and wave energy converter, an initial sizing method is used. Data from existing literature is used to design the ratio between wind and wave energy. A sensitivity analysis of WEC diameter, capture width ratio (CWR), wave resource and WT capacity factor (CF) is performed.

CWR for various diameters and drafts were calculated from a commonly cited benchmark study [323], as the wave resource was not given in the text, it was calculated from site data to be 64.34 kW/m. A linear fit is applied comparing CWR to WEC diameter (D), resulting in the equation $CWR = 0.0201 \times D - 0.1194$. Although this equation is not a true fit in a physical sense, as a WEC of zero diameter will not have a CWR of -0.12, It is deemed suitable for the range of WEC diameters from 8 to 24m as shown in

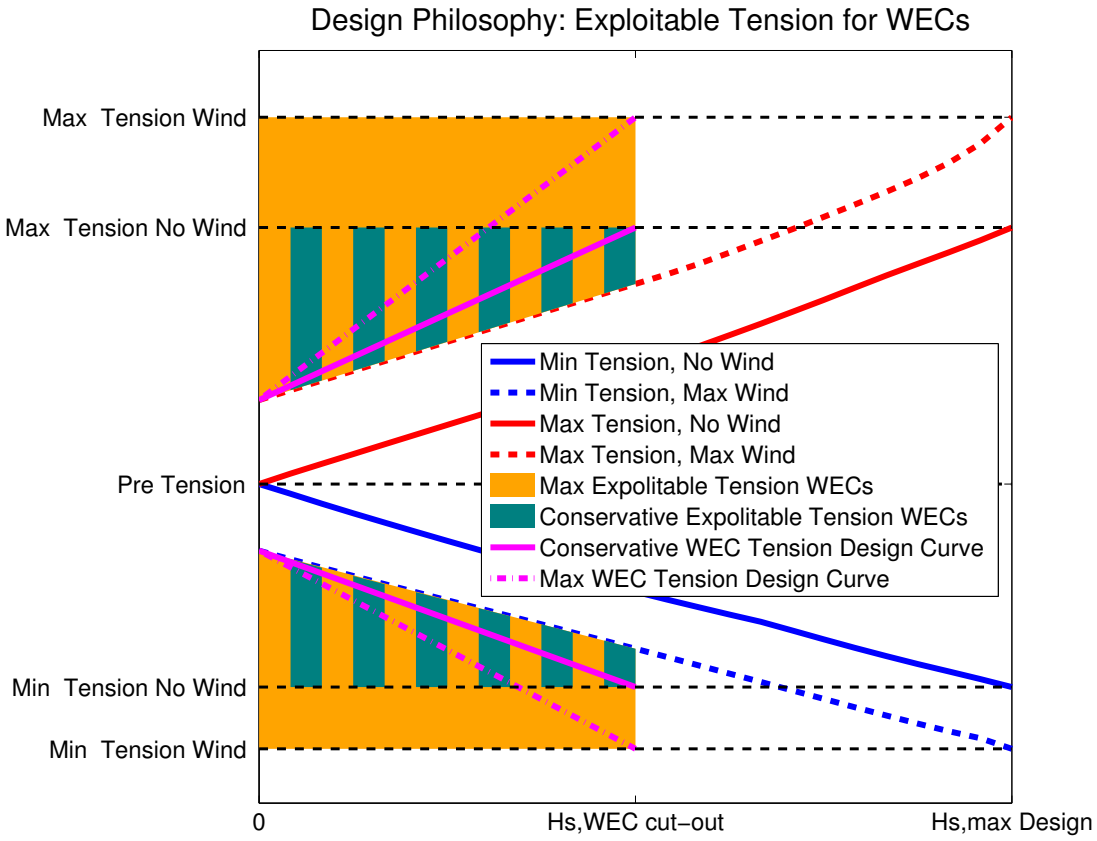


Figure 6.1: Design Philosophy for the addition of WEC to an existing TLPWT. The pretension required for TLPWT survivability is exploited for the WECs power generation phase

.

Figure 6.2.

The NREL 5 MW WT is used with a CF of 0.3 to 0.5. Recent data from the first FWT farms has shown that a CF above 0.5 is easily achievable, i.e. Hywind Scotland with a CF 0.57 [324]. The wave resource is varied as follows; low (20kW/m), medium (40kw/m) and high 60(kW/m). The number of WECs is chosen as 1, 4, 16 and 64. The ratio of wind and wave average annual energy production (WWR) is shown in Figure 6.3. This figure demonstrates the difficulty in combining the two technologies, the mature wind energy greatly overshadowing the wave energy, unless a large number of large WECs is used. For the single WEC case the WWR varies from 860 to 172 for the small WEC (10m) and 80 to 16 for the large WEC (24m). For the sixty-four WEC case the WWR varies from 14 to 3.4 for the small WEC (10m) and 1.25 to 0.25 for the large WEC (24m).

In order to successfully integrate the two technologies this balance must be reconciled with additional added value from the WEC technology. The added value may be "smoother" power production, reducing the WT motions or providing benefit to WT survivability. This section examines the design of a combined wind and wave energy system with special interest to this added value.

Using the 4 legged platform developed in Chapter 4, the logical choice is 4 WECs per platform, one on each leg. This results in a WWR of between 6 and 31, depending on the factors listed previously.

6.3 Design of standalone WEC

In order to design the combined system, a detailed understanding of the operation and design of a standalone WEC must be first undertaken. A torus shaped heave only point-absorber (PA) WEC that moves relative to a fixed column is used in this work. WECs absorb mechanical power from waves and convert it to electrical power. This conversion process depends on many detailed engineering design factors, type of power take off (PTO) etc. so in this work the absorbed mechanical power is treated as a proxy for the produced electrical power [325]. In reality the generated electrical power will always be less than the mechanical power.

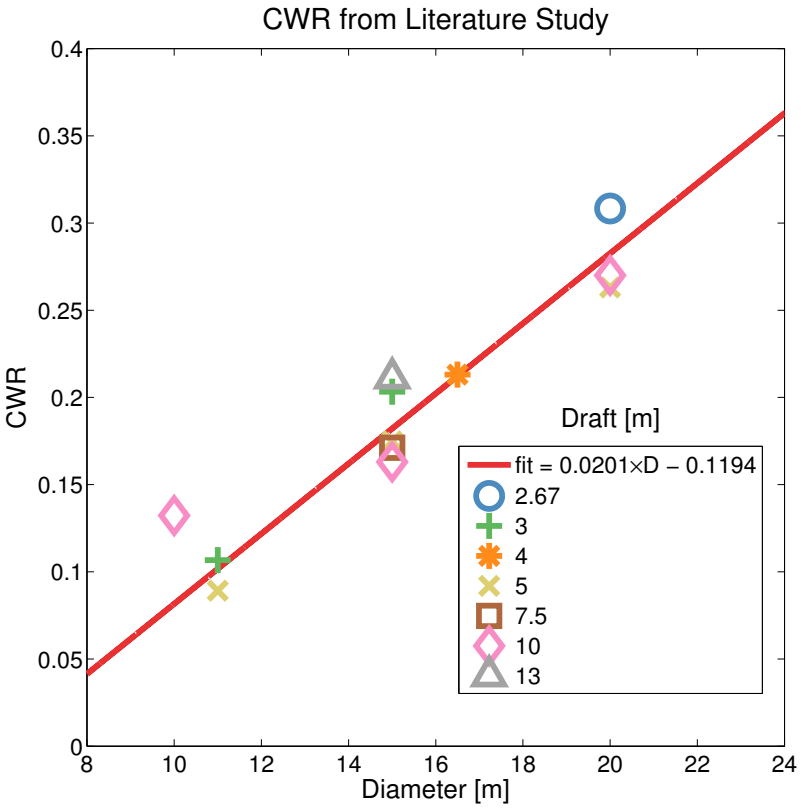


Figure 6.2: WEC capture width ratio from literature study

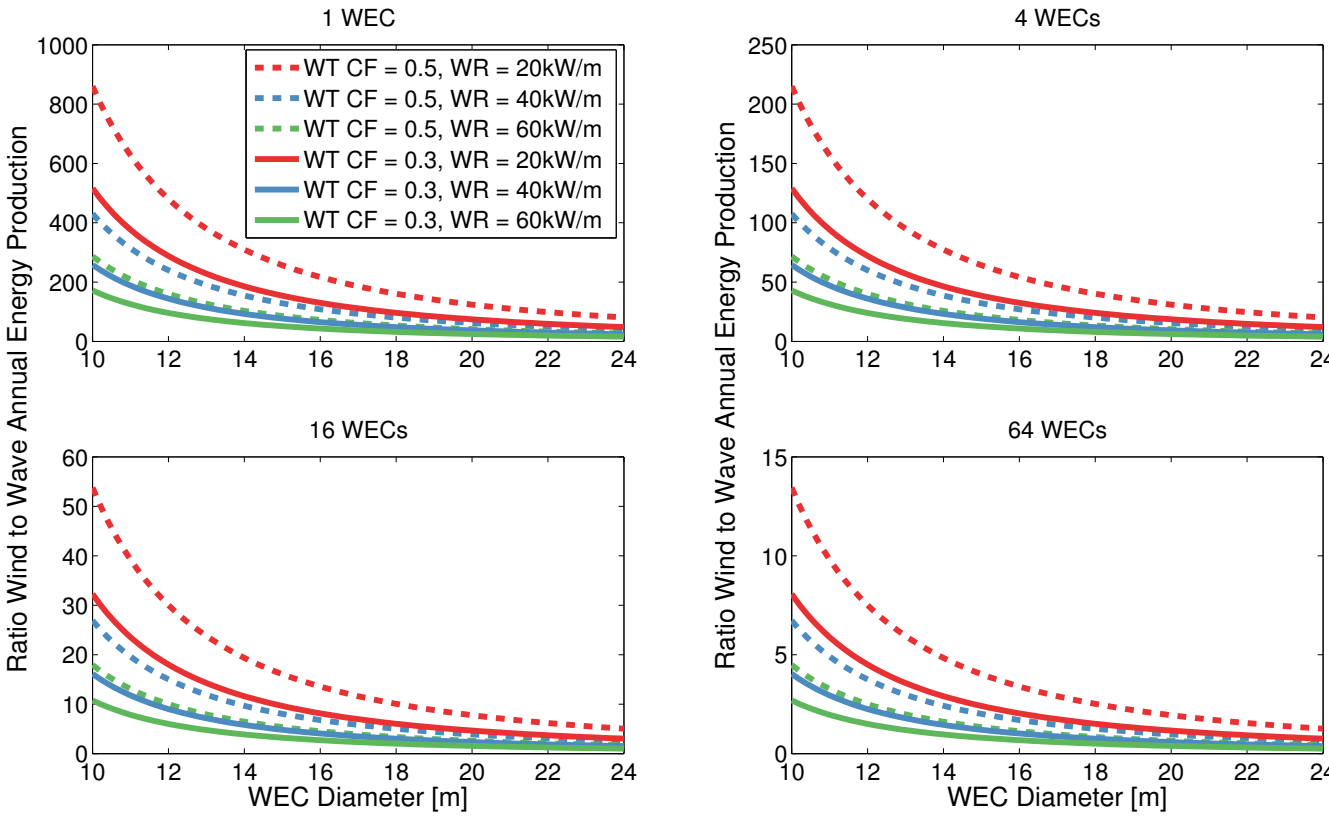


Figure 6.3: Ratio of Annual Wind Energy to Wave Energy

In this section possible WEC device designs will be analysed for performance characteristics. The performance characteristics are those used in the previously cited WEC benchmark study [323]. The additional performance metric ratio of absorbed energy to RMS pitch force has been added due to platform pitch motion being a dominant driver for platform tendon force. The simulation are performed in the frequency domain to enable an efficient preliminary study on the system.

6.4 WEC Parameter Study

A detailed study on the torus shaped WEC is carried out here. The draft and diameter of the WEC are chosen as the two most important parameters to vary. The WEC radius and draft are varied from 5 to 10 m and 3 to 6 m respectively. The mass and thus ballast of the WEC is chosen such that the required draft is obtained. Zhang found that for torus shaped WECs with a moon pool the power absorption is a maximum when the radius of the moon pool is closest to that of the reactance disk inside it [326]. Following from this inner radius of the WEC is set as the minimum which allows the WECs to travel along the columns.

Figure 6.4 shows how these performance metrics vary for various radii and draft. The shallowest draft (3m) is shown to have the best performance across all metrics bar the absorbed energy per pitch force. The diameter which shows best performance varys depending on which performance metric is analysed. CWR is shown to be proportional to diameter and inversely proportional to draft. Absorbed energy per WEC mass is seen to be inversely proportional to diameter and draft. Absorbed energy per WEC surface area is shown to be proportional to diameter and inversely proportional to draft. Absorbed energy per WEC pitch moment is shown to be inversely proportional to diameter and proportional to draft. Absorbed energy per WEC PTO force is shown to be non-linear with radius, with the peak being at 7m and inversely proportional to draft.

Table 6.1: WEC Details

WEC No.	Radius (m)	Height (m)	Draft (m)	Mass (Kg)	Kxx = Kyy (m)	Kzz (m)
1	10	12	6	$1{,}83 \cdot 10^6$	6,27	7,64
2	9	12	6	$1{,}47 \cdot 10^6$	5,88	6,94
3	8	12	6	$1{,}14 \cdot 10^6$	5,51	6,24
4	7	12	6	$8{,}49 \cdot 10^5$	5,17	5,54
5	6	12	6	$5{,}98 \cdot 10^5$	4,88	4,84
6	5	12	6	$3{,}85 \cdot 10^5$	4,64	4,14
7	10	10	5	$1{,}53 \cdot 10^6$	6,07	7,64
8	9	10	5	$1{,}22 \cdot 10^6$	5,65	6,94
9	8	10	5	$9{,}49 \cdot 10^5$	5,25	6,24
10	7	10	5	$7{,}07 \cdot 10^5$	4,88	5,54
11	6	10	5	$4{,}98 \cdot 10^5$	4,54	4,84
12	5	10	5	$3{,}21 \cdot 10^5$	4,25	4,14
13	10	8	4	$1{,}22 \cdot 10^6$	5,89	7,64
14	9	8	4	$9{,}78 \cdot 10^5$	5,45	6,94
15	8	8	4	$7{,}59 \cdot 10^5$	5,02	6,24
16	7	8	4	$5{,}66 \cdot 10^5$	4,61	5,54
17	6	8	4	$3{,}99 \cdot 10^5$	4,23	4,84
18	5	8	4	$2{,}57 \cdot 10^5$	3,89	4,14
19	10	6	3	$9{,}17 \cdot 10^5$	5,73	7,64
20	9	6	3	$7{,}34 \cdot 10^5$	5,27	6,94
21	8	6	3	$5{,}69 \cdot 10^5$	4,82	6,24
22	7	6	3	$4{,}25 \cdot 10^5$	4,38	5,54
23	6	6	3	$2{,}99 \cdot 10^5$	3,96	4,84
24	5	6	3	$1{,}93 \cdot 10^5$	3,56	4,14

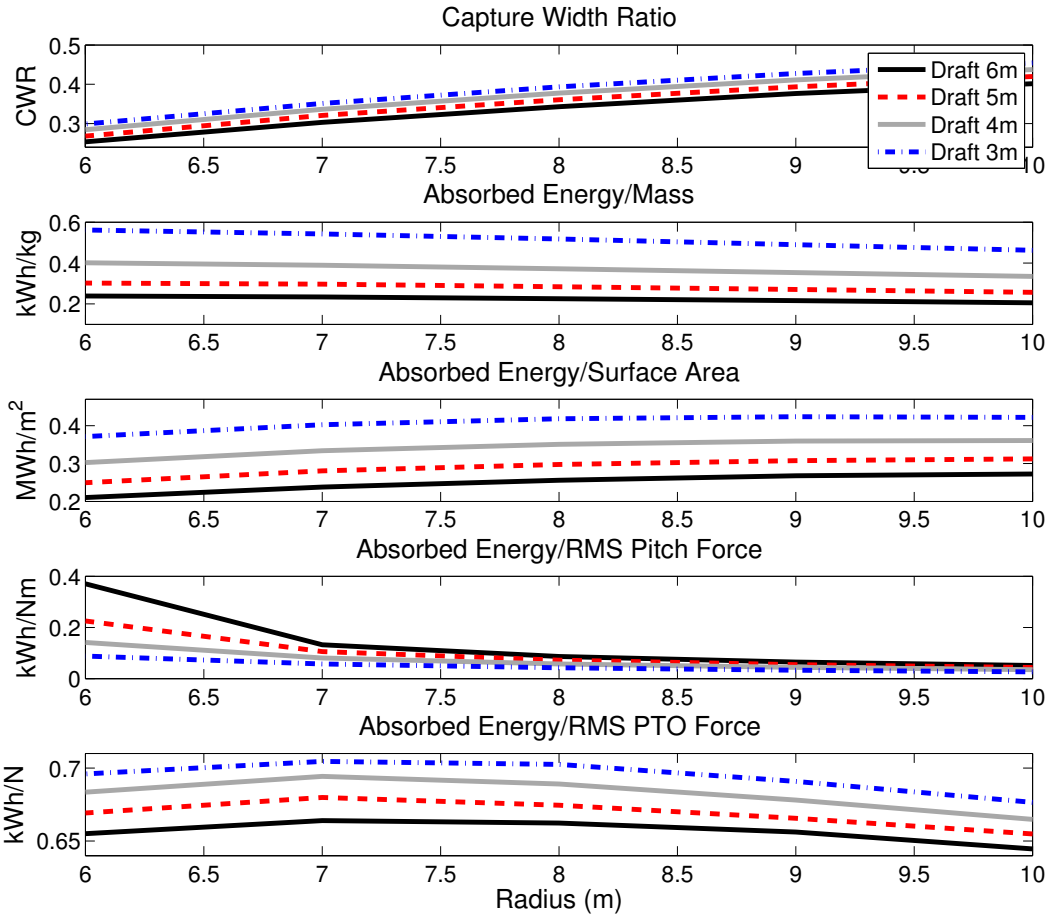


Figure 6.4: Performance Metrics for Individual WEC

6.5 WEC and TLP Survivability

The great increase of the water plane area and subsequent increase in wave loading on the TLP platform from the WEC's is detrimental to goals of a streamlined platform with low wave loading. Survival modes which relieve this issue are explored in this section.

6.5.1 Surge Plates

Water Entrapment plates are increased diameter plates which are added to platforms to increase the added mass and damping of the platform and thus reduce the motion response. They are most commonly used in the form of "Heave Plates" added to semi-submersible platforms, for example WindFloat.

In this case novel "Surge Plates" are used to reduce the horizontal motions of the platform. As the Surge Plates in this case are WEC's when in their survival state, the two uses must be designed in parallel. Thus it is important to note the effect that the draft of the WEC and thus thickness of surge plates is interlinked and vital to the design. Vortex shedding and thus damping was enhanced due to reducing thickness of the heave plate disks [327]. It has been recommended that to maximize the damping effects, the minimum thickness that satisfies structural and fatigue strength requirements should be chosen [266]. These results are related to the typical plate geometries for water entrapment devices. It has not been investigated if the results transfer to water entrapment cylinders as presented here, or to the use in surge rather than heave. The use of plates to increase the surge drag forces and reduce motions has been seen in the literature before [146].

The design of the surge plates is such that they are below the most severe wave action zone. The surge plates will have the unwanted effect of increasing current loading on the platform.

In the survivability mode the WECs are disconnected from the power take-off system (which remains at the top of the columns), ballasted and submerged along the columns. This storage concept has been studied on the Hywind-Torus WEC [47] design.

A novel idea involved storing the WECs in a rotated orientation is investigated. The

concept involved increasing the surge natural period of the system further beyond the wave periods by an increased surge added mass. The WECs were rotated in increments of 22.5°resulting in conditions of 0°, 22.5°, 45°, 67.5°and 90°. The buoyancy-mass ratio and thus tendon force were kept constant in order to normalise results. Keeping the moments of inertia constant allowed a reduction in the number of variables.

6.5.2 Submergence Operation

A common submergence mechanism is by use of a variable ballast system (VBS). The platforms buoyancy is altered by replacing air with a ballast medium, generally sea-water. Water volume may be altered with compressed air or a hydraulic pumping mechanism. Corrosion and bio-fouling of the interior of the ballast chambers must be accounted for.

The volume of seawater ballast required for the range of WEC sizes analysed will be 500m^3 to 3500m^3. Typical hydraulic marine pumps operate with flow speeds of 200 - 5000 m$^3/Hr$, resulting in ballast operation times of between 0.1 and 17.5 hours. The faster machines are generally heavier, more expensive and require a higher energy demand. On the other hand as the WECs provide a survival stability benefit in the ballasted condition as opposed to a survival liability at their operational draft, the submergence speed is crucial.

Activating the survival mode depends on both the sea-state magnitude and duration. The number of yearly activation's at various sites is calculated based on the same environmental data as used in the design section. The number of operations per year is proposed as between 10 and 50.

6.6 TWindWave

This section introduces the detailed analysis of the novel tension moored wind and wave energy converter, TWindWave. It is composed of a 5 MW WT, supported by a four legged tension moored platform, which is used as the reactant device for four pitch restrained heaving PAs, each rated as 250 kW. A preliminary analysis of float shape resulted in a decision to use a wall sided cylindrical geometry. Power production could be increased

with inverted cone or hemisphere geometry's, although these significantly increase the hydrodynamic pitch force which the platform columns must restrain in this device. This section describes the first iteration of this concepts design, where the buoyancy and mass and thus pretension of the FWT is unchanged due to the addition of the WEC components. It should be noted that this is a significant simplification of the problem, and the mass of the FWT would most likely significantly increase due to the addition of the WEC's due to an increase in both fatigue and ultimate loading and the required WEC PTO system. The WEC and mooring system details can be seen in Tables 6.2 to 6.3. The TLP characteristics are unchanged from that presented in Table 5.6.

6.6.1 Survival Mode

In contrast to a WT's reliable survival mode for high wind speeds where the blades are pitched out of the wind direction, resulting in a decrease in loading, the survival modes for WECs in above rated power production sea-states offer severe challenges. Unlike wind loading which is generally significantly uni-directional, the wave load vector rotates through a full 360 degrees over every wave period, meaning a "pitching" technique similar to a WT's blades is impossible. The fact that the wave load decreases exponentially in depth, is used for the benefit of the submerging survival mode outlined as follows here. In sea-states above operational conditions, the PTO systems are disconnected from each float, the floats are then sea-water ballasted and submerged along the platform column, after which they are "locked" in position, similar to as outlined by Wan [50]. The floats are ballasted such that the mass to buoyancy ratio of the system is unchanged. If the

Table 6.2: WEC Properties

WEC outer diameter	20 m
WEC inner diameter	5 m
WEC draft	3 m
WEC freeboard	3 m
WEC displacement	904680 Kg
WEC mass	905570 Kg
WEC mass moment of inertia Ixx, Iyy	29732480 kg.m^2
WEC mass moment of inertia Izz	52857750 kg.m^2

floats are submerged below 25m they begin to rotate along the connecting bend between the platform column and pontoon. It is envisaged that this rotation will provide significant benefit to the performance of the platform in extreme waves. In a rotated position the floats have a large surface area perpendicular to the platforms main motion degrees of freedom (DOF): surge and sway, in this way they act as "surge plates" reducing the motions of these DOF. These "surge plates" are similar to the traditional heave plates which reduce a floating platforms heave and pitch motion by acting as water entrapment plates, greatly increasing both the radiation terms and viscous damping of the platform. The increased added mass in the surge direction will beneficially decrease the platform surge natural frequency, increasing the distance between such and the wave frequency range, and thus reducing platform surge motions and tendon loads. The increased surface area perpendicular to the surge motion will increase the viscous damping. This rotational movement requires greater complexity in the float rollers and an increased internal diameter, as they are required to deal with a varying diameter along the bend. To transfer back to an operational condition, compressed air is used to expel the water from the ballast chambers and excess buoyancy returns the floats to the surface. Increasing the added mass and viscous damping of TLP WT's has been studied in the literature by adding porous outer cylinders to the platform [328], significant reductions in the low frequency resonant response were observed as a result. This section analyses various submergence depths and float angles, which can be seen in Figure 6.7. The use of such surge plates has been described in the literature as reducing the surge frequency of a SPAR FWT [146] [147]

Table 6.3: Mooring System Properties

Number of mooring lines	4
Fairlead distance from centre	25 m
Unstretched mooring line length	75.857 m
Line diameter	0.127 m
Line mass per unit length	116.03 Kg/m
Line extensional stiffness	1500000000 N

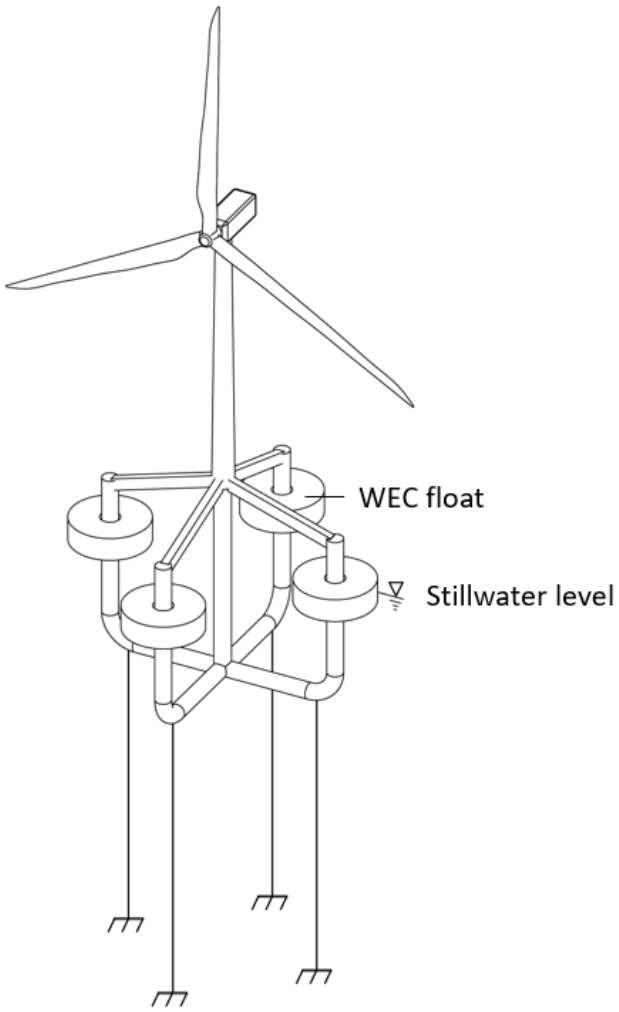


Figure 6.5: 3D Impression of TwindWave Operational mode with WECs at the mean water level. Components are drawn to scale

6.7 Numerical Modelling

Hydrodynamic parameters are calculated using ANSYS AQWA for 50 wave frequency's from 0.008Hz - 0.4Hz and 12 equally spaced wave directions. OrcaFlex is used for time domain simulations. Additional quadratic viscous damping of the platform and WEC floats is added to the model using modified Morison equation drag only elements. Drag coefficients are determined using the DNV standards. The tower is modelled as a flexible body of varying stiffness along its length. No wind load is applied. The optimum frequency dependant PTO damping is set using equation 6.1 [329].

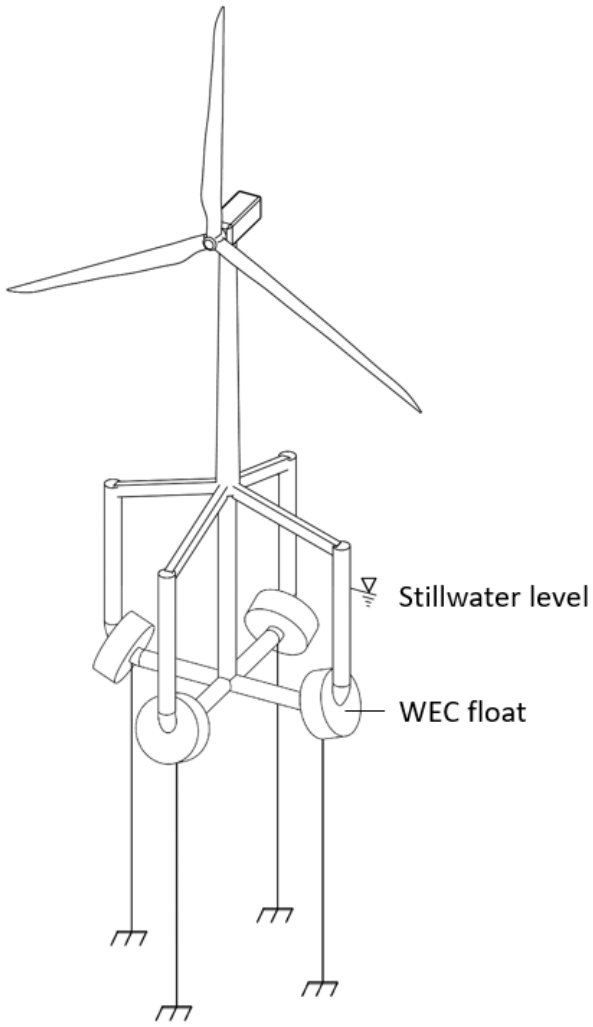


Figure 6.6: 3D Impression of TWindWave Survival mode with WEC submerged and rotated to 67.5 degrees. Components are drawn to scale

$$B_{PTO}(\omega) = \sqrt{B_{33}(\omega) + 1/\omega^2(-(m + A_{33})\omega^2 + K_{H33})^2} \tag{6.1}$$

Where $B_{PTO}(\omega)$ is the frequency dependant damping, $B_{33}(\omega)$ is the frequency-dependent heave radiation damping, m is the platform mass, A_{33} is the platform added mass in heave and K_{H33} is the platform heave hydro static stiffness. Simulations of a duration of 3600s are run. For operational conditions the sea-states in table 6.4 are used, for survival states, white noise waves which span a frequency interval of 0.01 Hz to 0.3 Hz are used. An overview of the TWindWave model setup in OrcaFlex is shown in Figure 6.8. WEC numbers are shown in Figure 6.9

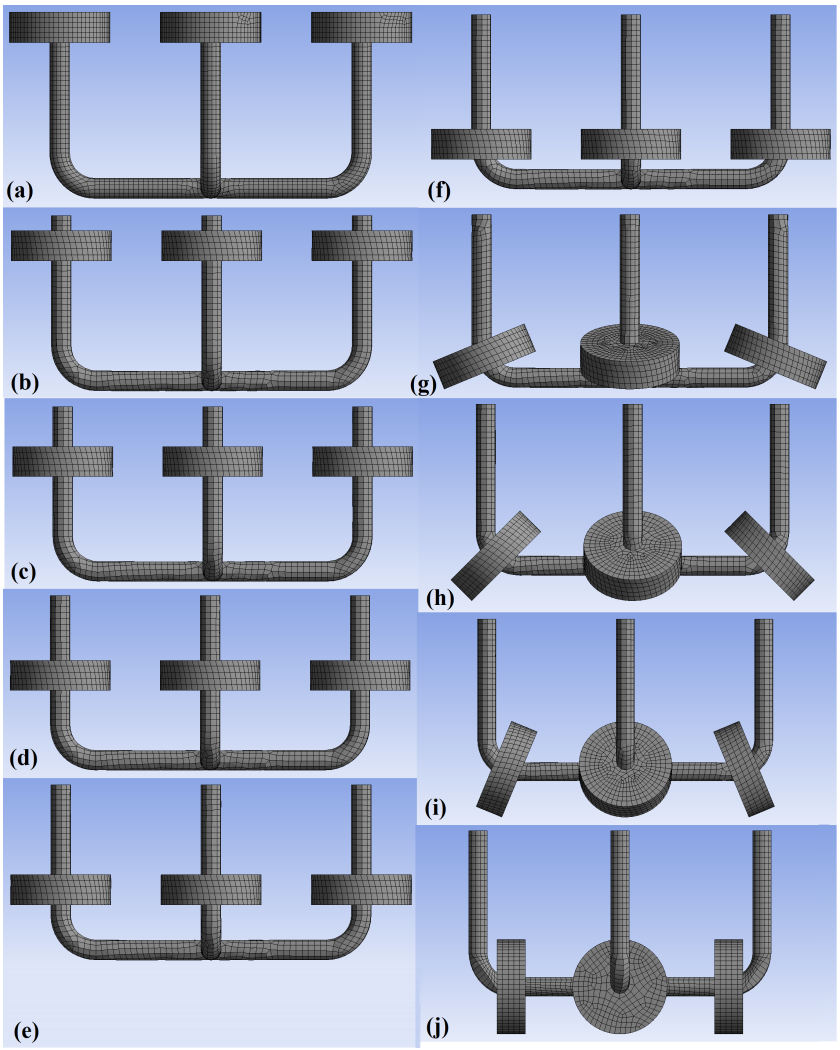


Figure 6.7: Mesh for mode cases analysed: (a) Operational, (b)-(j) Survival Submergence: (b) 5 m, (c) 10 m, (d) 15 m, (e) 20 m, (f) 25 m, (g) 22.5°, (h) 45.0°, (i) 67.5°, (j) 90.0°

6.8 Results

6.8.1 Hydrodynamic Interaction

The five body hydrodynamic interaction matrix is analysed in the frequency domain. Strong interaction is noted between the platform surge and float surge motions, the float surge and float heave motions and a floats pitch on the other floats pitch motion. This is shown in Figures 6.10 to 6.15, where the bodies main diagonal radiation terms indicates the scale of the interaction. Figures 6.10 and 6.11 shows strong coupling for both radiation terms between the platform surge and float surge for high frequency

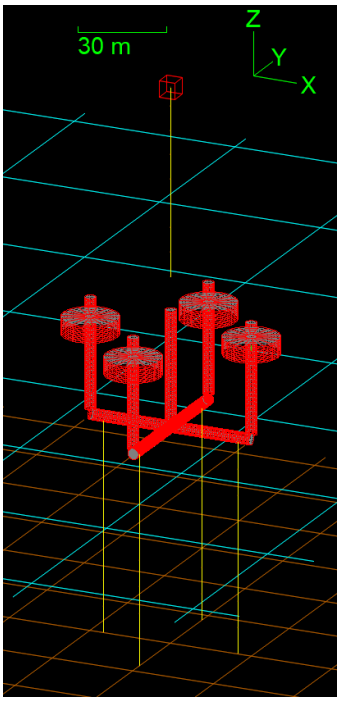


Figure 6.8: View of model setup in OrcaFlex

waves. The terms are opposite in sign and thus the floats damp the platform motion. For coupling between float surge and float heave, Figure 6.12 shows mild coupling for added mass, while Figure 6.13 shows strong coupling for the radiation damping. For coupling between the floats pitch motion the same trend can be seen. A weak interaction for added mass, refRD4, while a strong interaction can see for the radiation damping component, where the interaction effect dominates over the bodies main diagonal term.

6.8.2 Power Production

The instantaneous power of each WEC is calculated using equation 6.2, and converted to an average power for each sea state by equation 6.3. This is the mechanical power and no attempt has been made to take into account electrical and/or other losses. Figure 6.16 shows this averaged power for each sea state, for both the interacting and non-interacting cases. For the up-wave WEC 1, the power is generally slightly under predicted by the non-interacting case, apart from the short wave period sea-states 1 and 4. For the symmetric WEC's 2 and 4, the average power is further averaged between the two devices, as they are parallel to the wave front. The non-interacting case significantly over

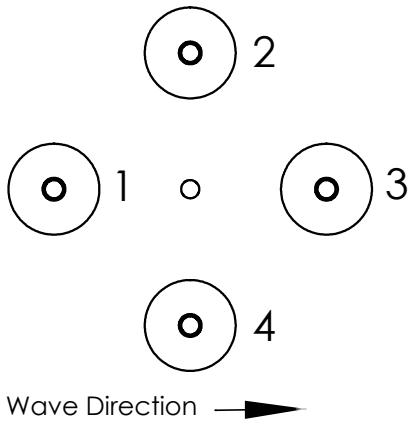


Figure 6.9: WEC and tendon numbering scheme

predicts absorbed power, of between 13.3% and 3.7%, although the effect seems to be decreasing with increased wave height. For the down-wave WEC 3, the non-interacting case vastly over predicts absorbed power, of between 27.2% and 19.3%. Total power from the complete system is over predicted by between 6.3% and 14.7%. The over prediction is due to the WEC's reacting to the undisturbed wave field.

$$P_{inst} = B_{PTO}(\omega)x'(t)^2 \tag{6.2}$$

$$P_{avg}(H_s, T_e) = (1/T)\int_{t=0}^{T} P_{inst}(t)dt \tag{6.3}$$

Where P_{inst} is the instantaneous mechanical power, $x'(t)$ is the WEC's heave velocity, P_{avg} is the averaged wave power, H_s is the significant wave height, T_E is the wave energy period and T is the simulation time.

Table 6.4: Simulated Sea-states

Wave Number	Hs (m)	Tz (s)
1	1	5,81
2	1	6,64
3	1	7,47
4	1,5	5,81
5	1,5	6,64
6	1,5	7,47
7	1,5	8,3
8	1,5	9,13
9	1,5	9,96
10	2	7,47
11	2	8,3
12	2	9,13
13	2	9,96

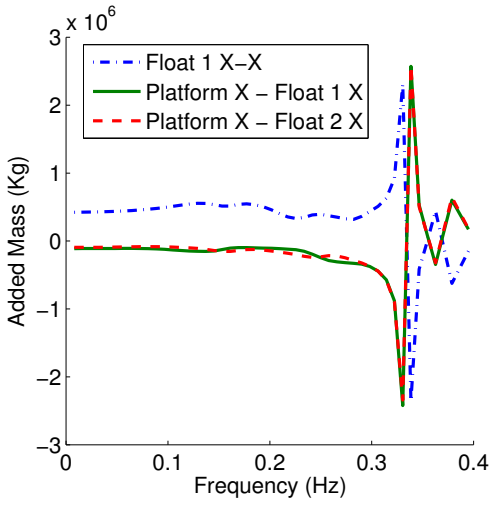


Figure 6.10: Added mass for coupled platform surge and float surge

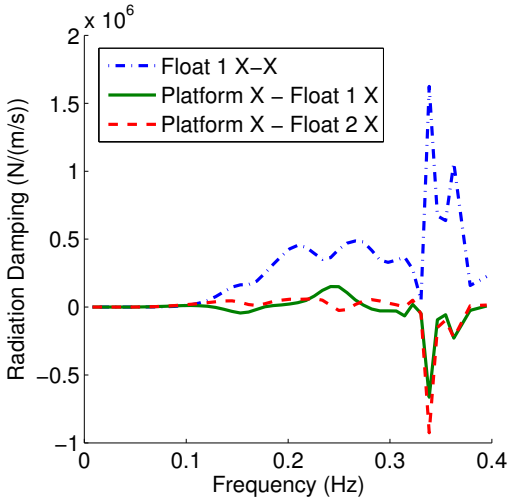


Figure 6.11: Radiation damping for coupled platform surge and float surge

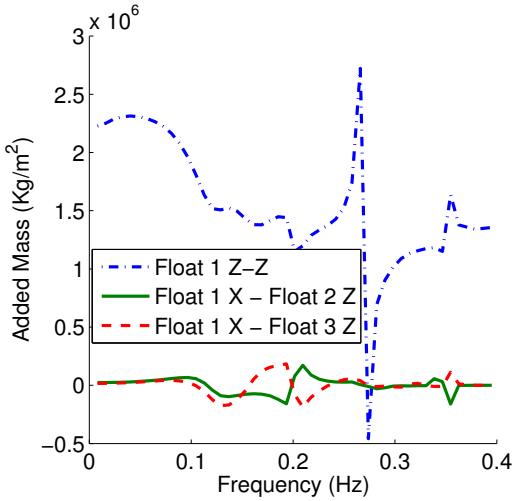


Figure 6.12: Added mass for coupled float 1 surge and float 3 & 4 surge

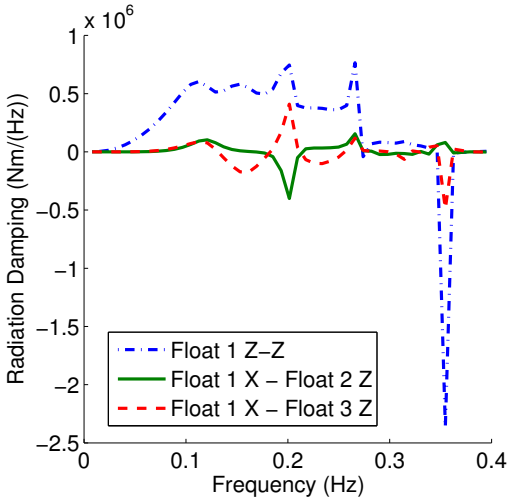


Figure 6.13: Radiation damping for coupled float 1 surge and float 3 & 4 surge

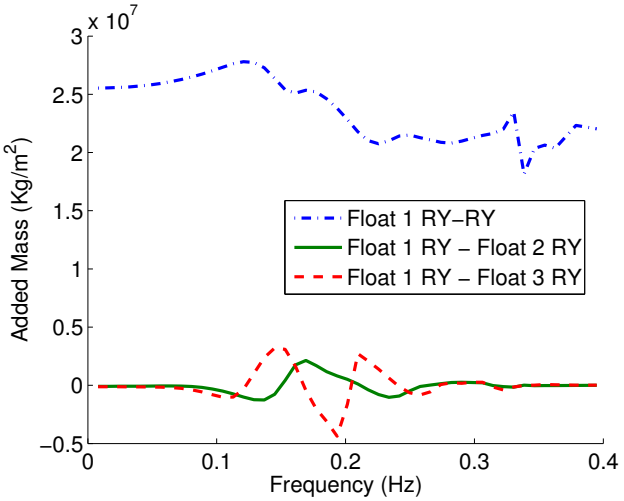


Figure 6.14: Added mass for coupled float 1 pitch and float 3 & 4 pitch

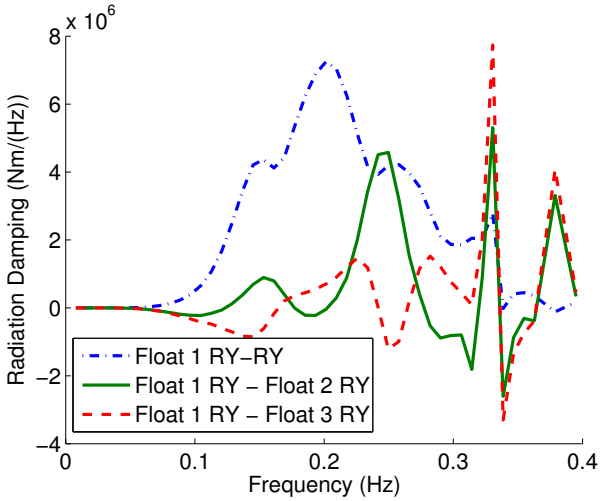


Figure 6.15: Radiation damping for coupled float 1 pitch and float 3 & 4 pitch

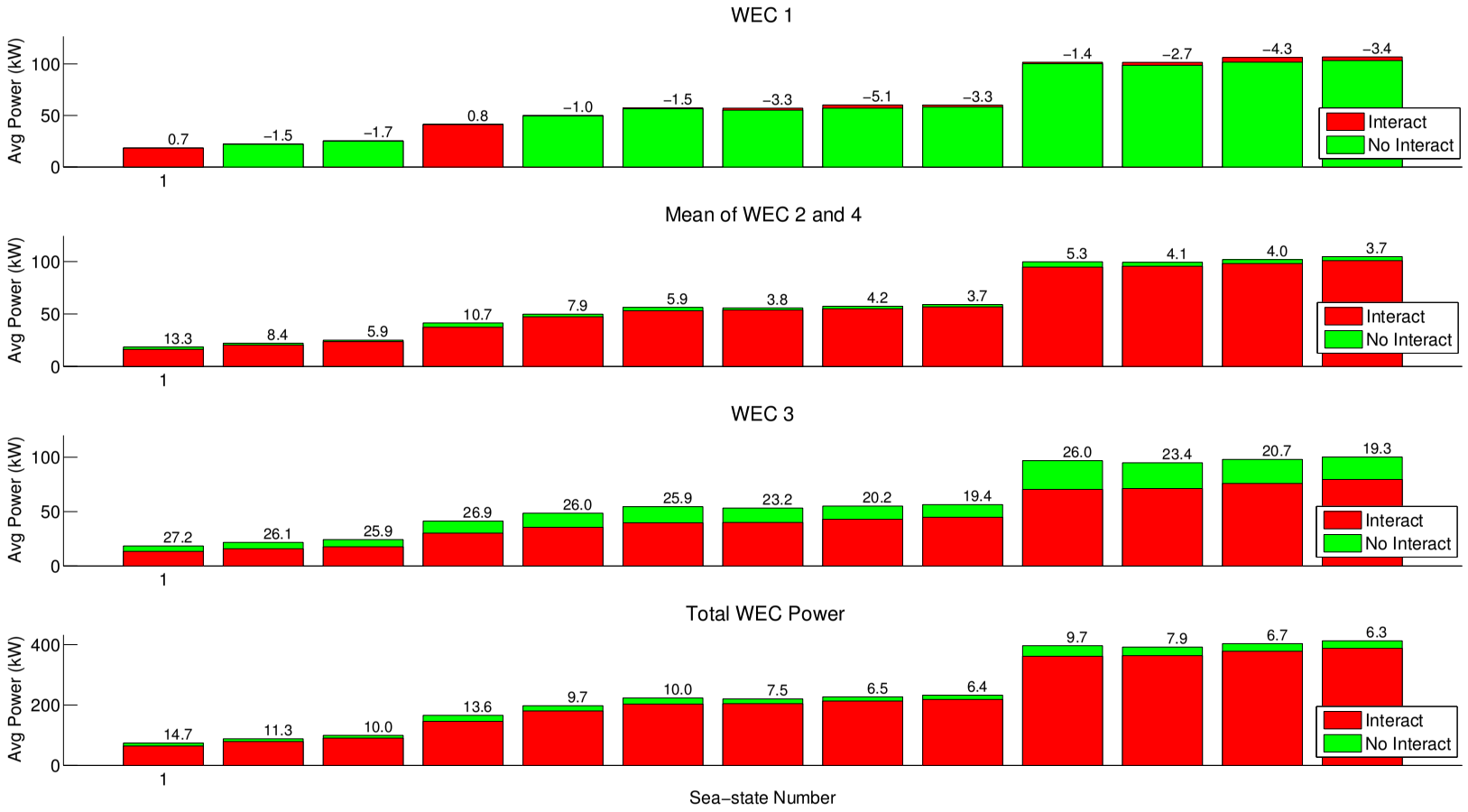


Figure 6.16: Average power for WEC's, numbers indicate percentage change from the hydrodynamic interaction to no-interaction simulations

6.8.3 Platform Performance

The floating wind turbine platform performance is compared next, between the hydrodynamic interaction, non interaction and without the WEC's completely. Figure 6.17 compares the WT towers max and RMS bending moments (BM). For nearly all sea-states the WEC's can be seen to increase these BM. Sea-states 2 and 5 are the exception to this, where it is the FWT alone which has the highest BM. Sea-state 4 shows the largest increase in tower BM of 106%. These results show that the ultimate and fatigue strengths of the WT tower would need to be increased to accommodate the WECs. Figure 6.18 shows the platform surge, heave, pitch and nacelle accelerations. The addition of the WEC's significantly increases all of these output parameters, with the hydrodynamic interaction damping these increases somewhat. The percentage increases are also similar across all parameters. Figure 6.19 shows the change in tendon tension, where the addition of the WEC's increases the maximum and decreases the minimum thus, increasing the risk of a snap loading event. Therefore the WEC's must enter survival mode when this tension fluctuation becomes too large.

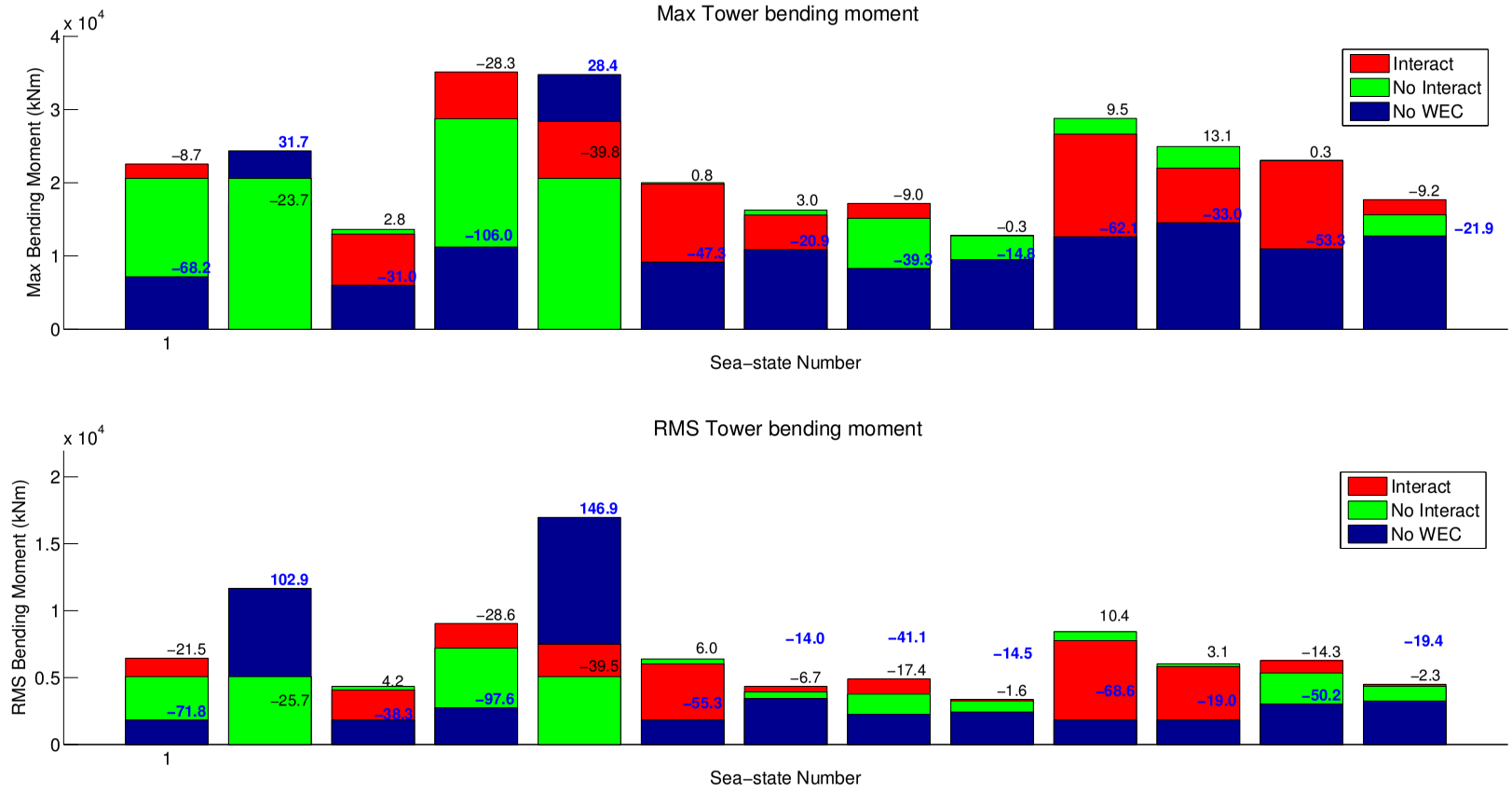


Figure 6.17: Tower bending moment, numbers in black indicate percentage change from hydrodynamic interaction to no interaction case, numbers in bold blue indicate percentage change from interaction case to no WEC case

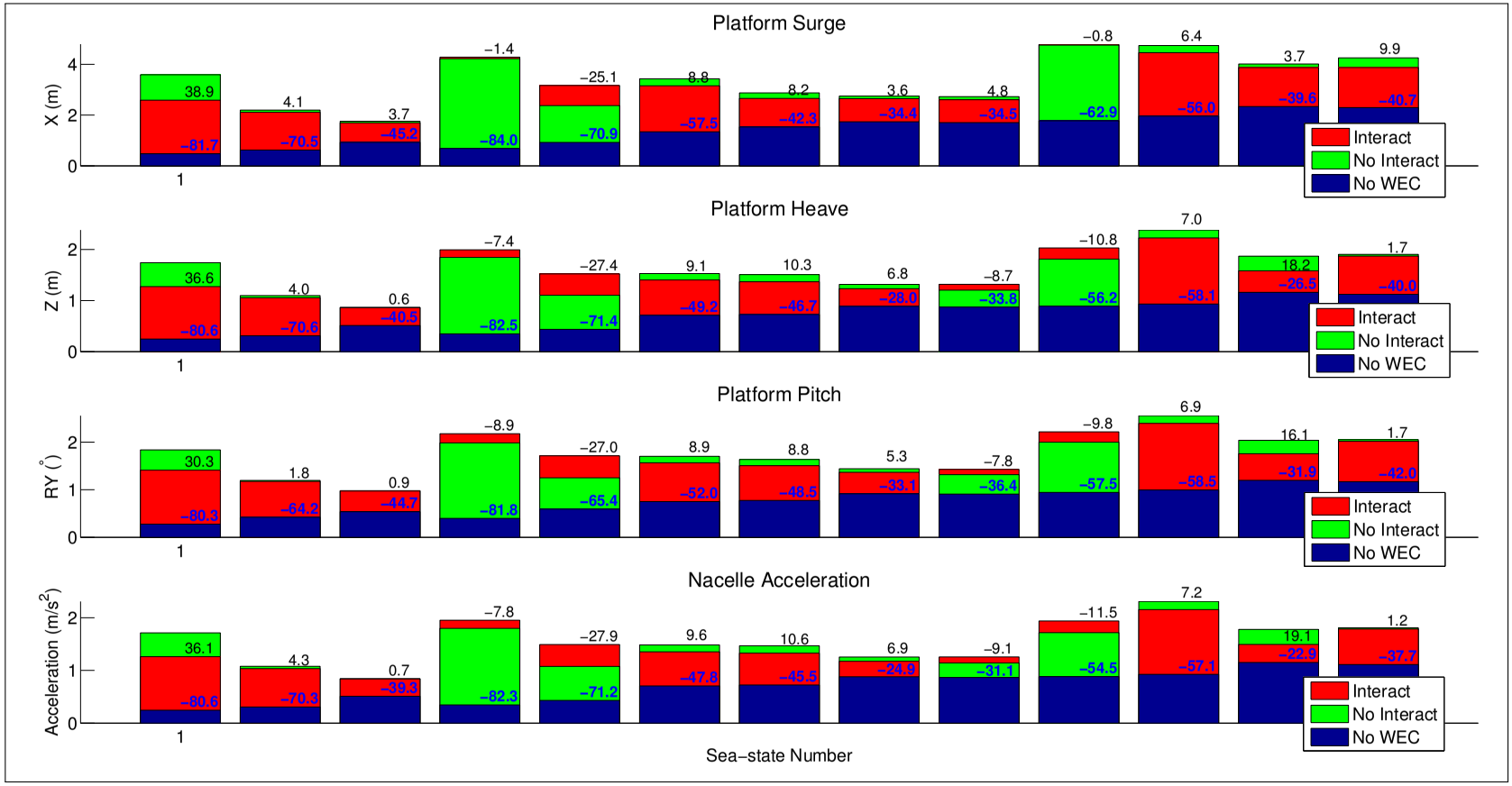


Figure 6.18: Platform Surge, Heave Pitch and Nacelle Acceleration, numbers in black indicate percentage change from hydrodynamic interaction to no interaction case, numbers in bold blue indicate percentage change from interaction case to no WEC case

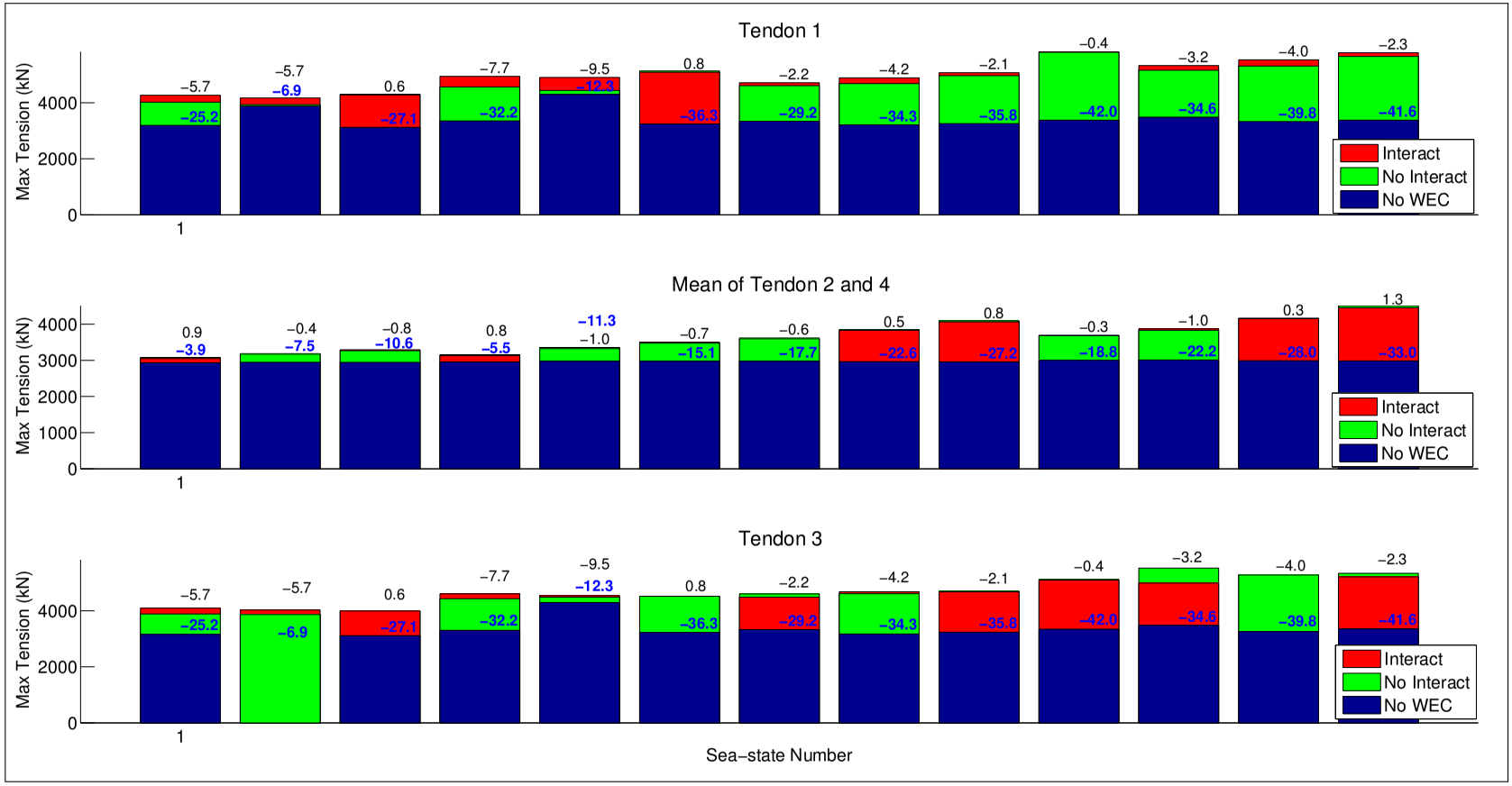


Figure 6.19: Platform tendon tension, numbers in black indicate percentage change from hydrodynamic interaction to no interaction case, numbers in bold blue indicate percentage change from interaction case to no WEC case

6.8.4 Survival Modes

An analysis of the various survival modes are given here. Figure 6.20 shows the platform surge, heave, pitch, nacelle acceleration, tendon 1 tension and tower bending moment RAO's. Of most significance is the change in pitch and tendon tension RAO. It can be seen that the survival states had the intended effect of decreasing motions and tendon tensions, but only for waves with period greater than 6s, below this period, the proposed survival modes exhibit a high pitch response at 5.3s - 5.8s, which dominates the tendon tension. Surge and heave RAO can be seen to slightly decrease as the WEC's move to a deeper draft. As some results are visually inconclusive from the figure, Table 6.5 shows the area under each of these RAO curves. The area is calculated using a trapezoidal integration method. These results are then compared to the case of -5m submergence. Taking a summed equal weighting of each of the outputted results for each case (i.e. the average of each row in the table), submergence strategies with an angle of 45° and 90° give most advantage over the base case. A final design wold involve weighting each result on the overall importance, and involve detailed limits on WT motions and structural design aspects. These results demonstrate the prove of concept of this combined systems WEC survival mode, but also show that a redesign to avoid the increase in pitch response is required.

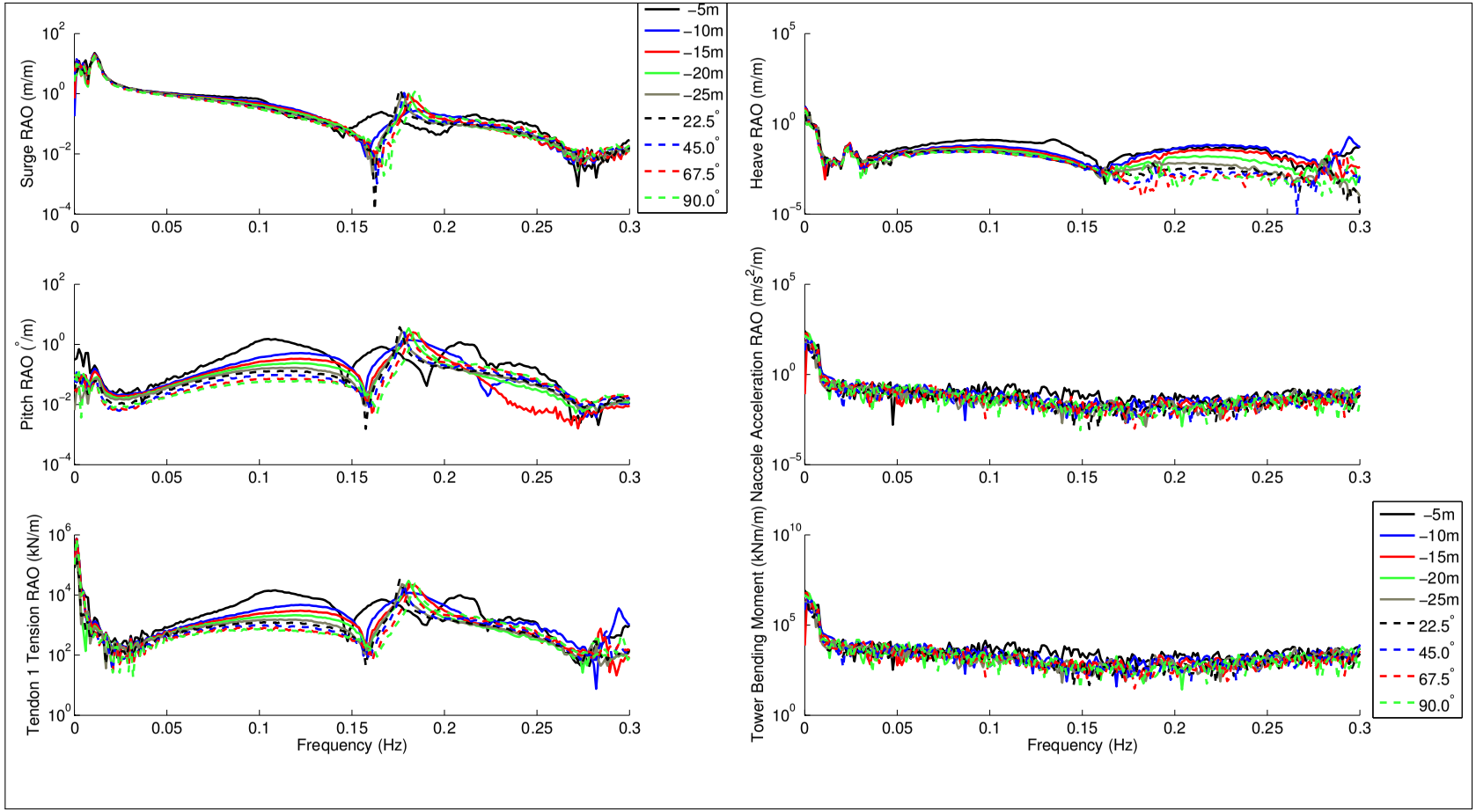


Figure 6.20: RAO's for platform surge, heave and pitch motions, nacelle acceleration, tendon 1 tension, and tower bending moment for various submergence methods

Table 6.5: Results of Submergence Method

	X	Z	RY	A	T 1	T 2	T 3	T 4	Tow BM
C	Percentage difference from -5 m submergence [%] case								
-10 m	22.4	-67.6	99.6	-48.2	-86	-18.7	-53.6	-18.7	-43.2
-15 m	43.9	-84.1	74.9	-41.3	-80.7	-27.3	-57.6	-27.3	-40.7
-20 m	-23	-52.4	81.6	-35.9	-61.6	-8.1	-67.2	-8.1	-37.3
-25 m	-22.5	-54.8	-25	-38.7	-70.9	-7.4	-64.4	-7.4	-41.4
22.5 °	-22.8	-55.1	-21.8	-38.4	-72.6	-8	-71.8	-7.9	-41.1
45.0 °	10.5	-78.6	-64.9	-37.1	-79.8	-34.6	-72.8	-34.4	-38.9
67.5 °	30.4	-79.6	-1.8	-29.2	-73.3	-31.6	-67.6	-31.7	-32.3
90.0 °	-27.5	-86.2	-52.7	-15	-82.7	-31.9	-74	-31.7	-18.5

Where C is the Case, and the first four numbers in this column refer to vertical submergence and the last four refer to vertical submergence combined with angular rotations in degrees

6.9 Numerical Model Validation

Experimental modelling of the combined wind and wave energy platform TWindWave as well as the wind energy TWind platform from Chapter 5 is undertaken in this chapter. All experimental modelling is carried out in the LIR NOTF's deep water basin. In the design and scaling of the physical model, correctly scaling the tower mass and stiffness was the most complex operation. The suitable and available aluminium cylindrical pipe sections to build the tower in combination with the basin and wave generation capabilities resulted in setting a scaling factor of 1/37. Three model cases are compared, the TWind with no WECs, TWindWave with WECs and PTO damping and TWindWave with WECs and no PTO damping. Due to the number of model test set ups and limited available tank time, tank testing was limited to regular sinusoidal wave testing only. In future this work should be extended to include spectral panchromatic waves.

The OrcaFlex-AQWA modelling technique as described and used elsewhere in this thesis is also used for this section. The numerical model used for this validation takes into account both structural and hydrodynamic coupling between the 5 rigid bodies.

6.9.1 LIR National Ocean Test Facility Deepwater Basin

The LIR National Ocean Test Facility Deepwater Basin is 35 m by 12 m with a maximum depth of 3 m. For these experiments the water depth was set to 2.98 m, just above the move-able floors maximum depth, in order to match the full-scale design conditions of 110m. Waves are generated using 16 independently controllable hinged force feedback paddles situated along the width of the basin. On the other end of the wave basin is a porous parabolic artificial beach for passive wave absorption. The wave generation paddles also act as an active wave absorption system by force control. 6 DOF motion capture recording is provided by the use of 3 Qualisys cameras with markers located on the rigid body's. 6 wave probes are used to record the water surface elevation along the basin.

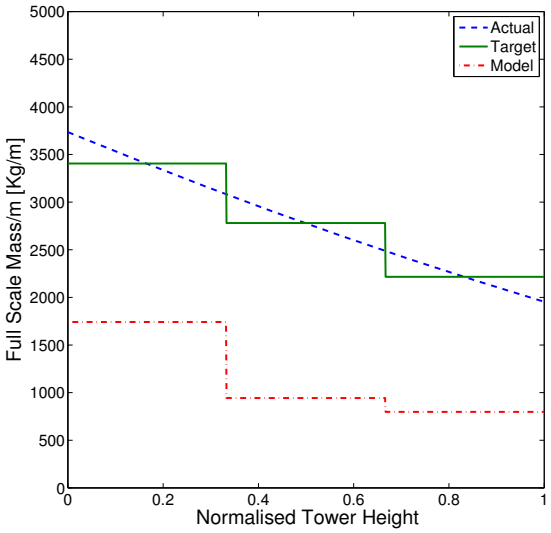
6.9.2 Design and Fabrication of Physical Model

The TWind floating section is fabricated in house from 110 mm outer diameter PVC "10 bar" pressure pipe. Due to the large pipe diameter, pipe fittings (bends and caps) had to be ordered from Germany and the model bottom central node had to be custom made. The bottom central node, a 5 Way joiner (Joining 4 orthogonal horizontal pipes and 1 vertical), is 3D printed, images of which are included in Appendix C. The diagonal braces, TLP-tower interface and tower are fabricated by external fabricators in aluminium. Four motion capture markers are placed on the TLP rigid body.

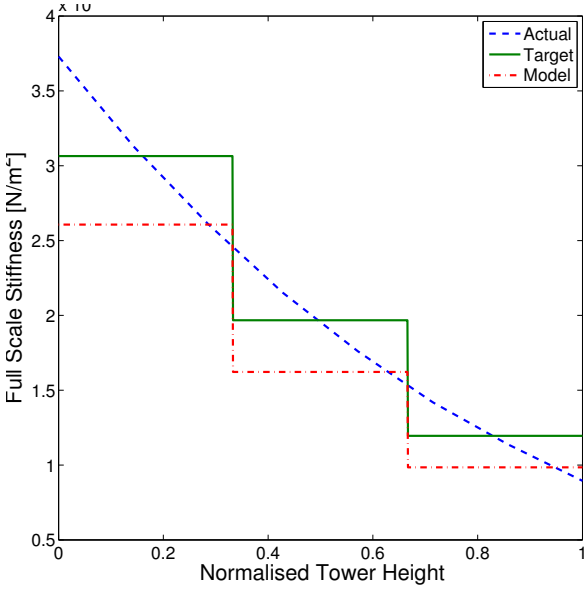
6.9.2.1 Tower

The modified OC3 Hywind tower designed in Chapter 4 is physically modelled by scaling its stiffness and mass properties in order to create the appropriate bending frequencies. The tower is divided into three sections with constant aluminium sectional area, with the stiffness of each section matching the full scale tapered stiffness as closely as possible. Correct stiffness scaling results in the mass of each section being considerably below that required at full scale (See Figure 6.21), thus additional mass must be added without significantly increasing the stiffness of the structure. Additional aluminium cylindrical

elements are evenly distributed along the length of the structure as required to match the mass properties. Seven "lumped mass's" are chosen to meet these requirements. The RNA mass is scaled as a cuboid piece of lead attached on a perspex plate on top of the tower.



(a) Mass



(b) Stiffness

Figure 6.21: Tower Mass (A) and Stiffness (B) as Designed and with available materials

In Figure 6.22 a photograph of the TWindWave platform in TWind only mode is shown as installed in the wave basin.

6.9.2.2 WEC

The two WEC support beams are fabricated in aluminium and connect two of the outer columns (One support beam connecting the bow column to the starboard column and one beam connecting the port and stern columns). These support beams are only designed to ease the experimental set up and are not considered for the full scale design. The WEC floats are made from polyester foam sheets, using a rotary mill to achieve the correct diameter. Additional steel sheets are applied to the top an bottom of the floats. These plates give the correct WEC float mass, moment of inertia, add stiffness and provide suitable robust fastening locations for the WEC PTO dampers and other auxiliary equipment.

The PTO damping force is provide by the use of adjustable dash-pot dampers. The four dampers are calibrated before testing, with results visible in Figure 6.26. Some spread can be seen between the damping curves of each dash-pot, with a range of approximately 10 %, but is taken as satisfactory for this testing. The dampers are connected to the floats by use of a ball and socket pivot joint to allow some additional relative motions between the WEC floats and the TLP and a load cell to record the applied force. The WEC support beams hold the main body of the dampers, from which the damping levels can be adjusted. The floats are constrained to travel in a pure translation mode along the length of the TLP columns by the use of heave and yaw rollers and plates. As the roller bearings are in the splash zone, they are fabricated from plastic and glass in order to offset potential water ingress and damage.

The WEC support beam and dash-pot dampers are only installed in the two WEC set ups, i.e. the WEC with PTO damping and free WEC cases. To ensure the mass distributions and tendon pretension remain equal between these cases and the TWind case, additional mass is added to the TWind model when in wind only mode. The additional mass is added to the underside of the column end caps (These caps are also removed fully for the WEC cases). As the WEC floats are constrained to single DOF (Heave), only a single motion capture marker is required on each float in order to record that motion. In Figures 6.24 to 6.26, details of the two WEC configurations are shown.

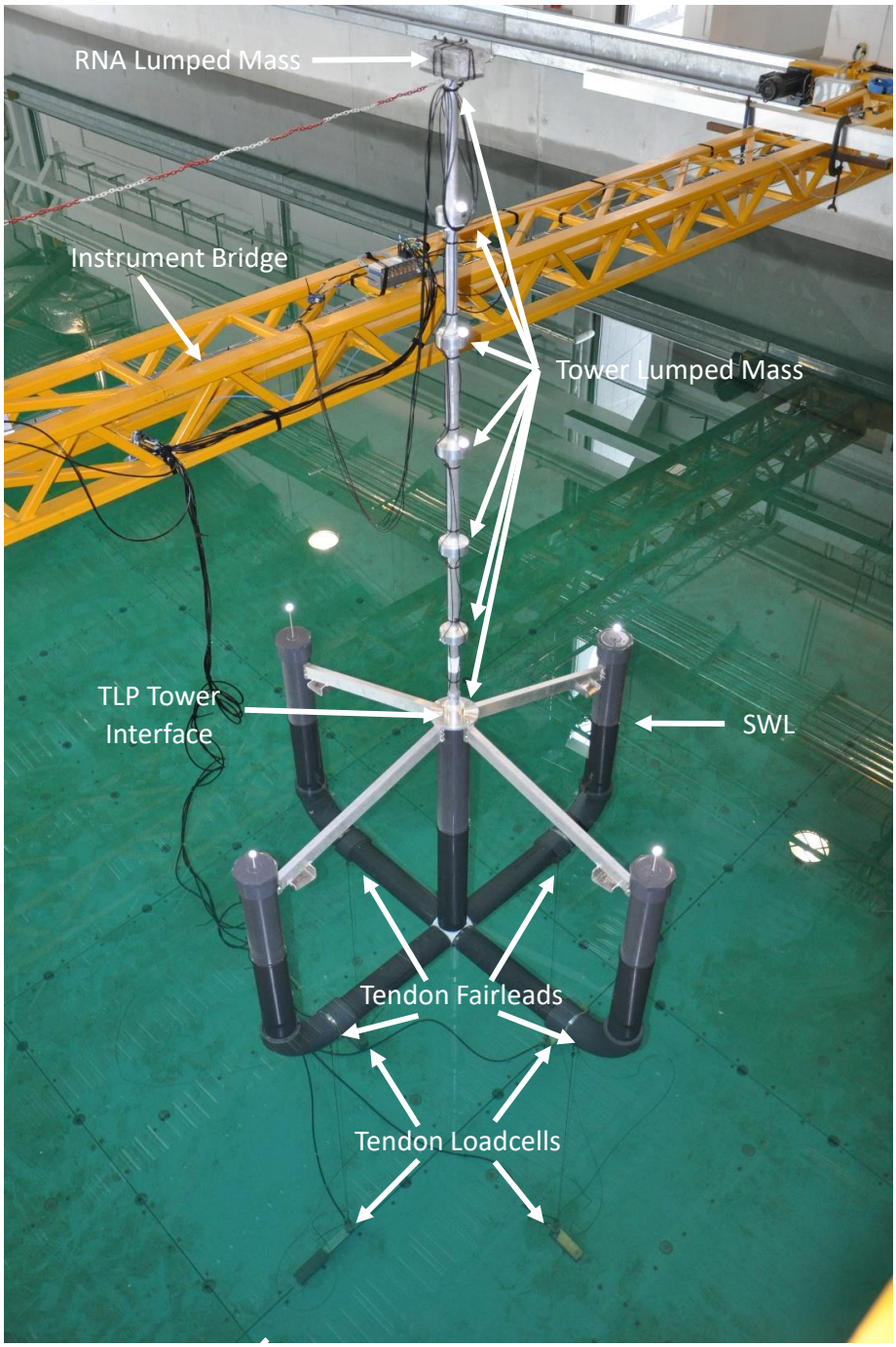


Figure 6.22: Photograph of TWindWave in Wind only mode (TWind). As installed in wave basin

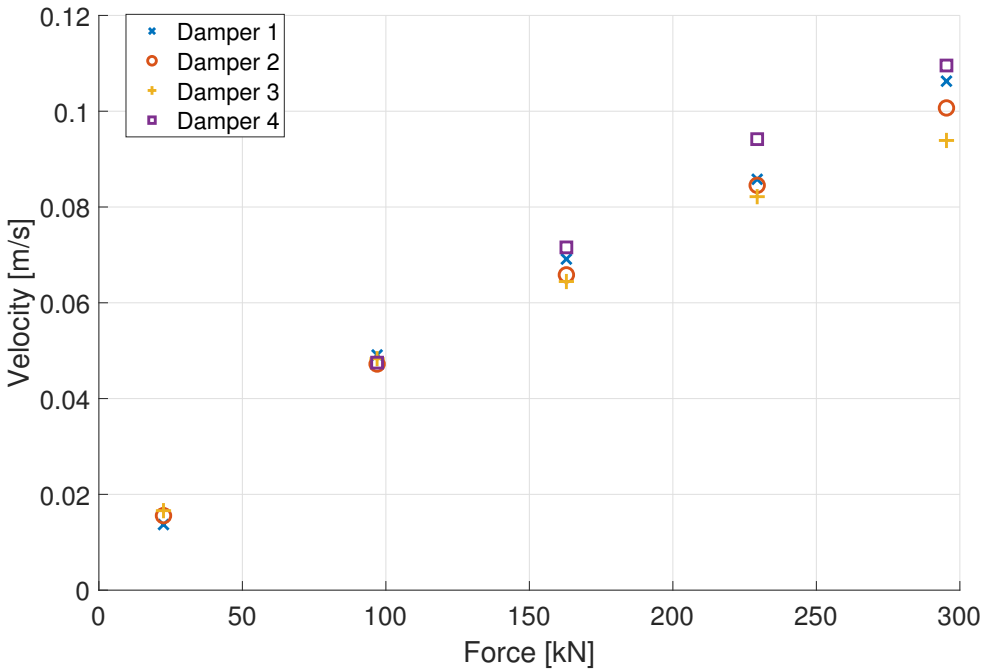


Figure 6.23: Calibration of PTO Dampers, Results shown at full scale

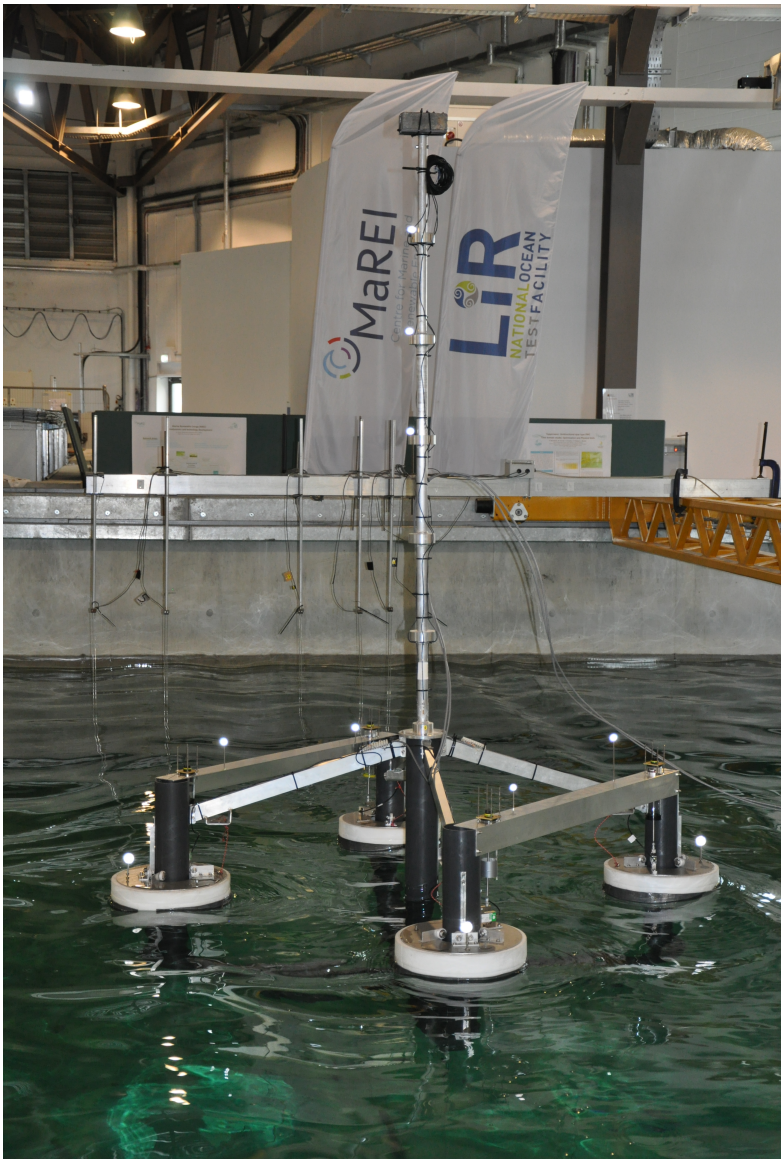


Figure 6.24: Photograph of TWindWave in WEC Operational Mode

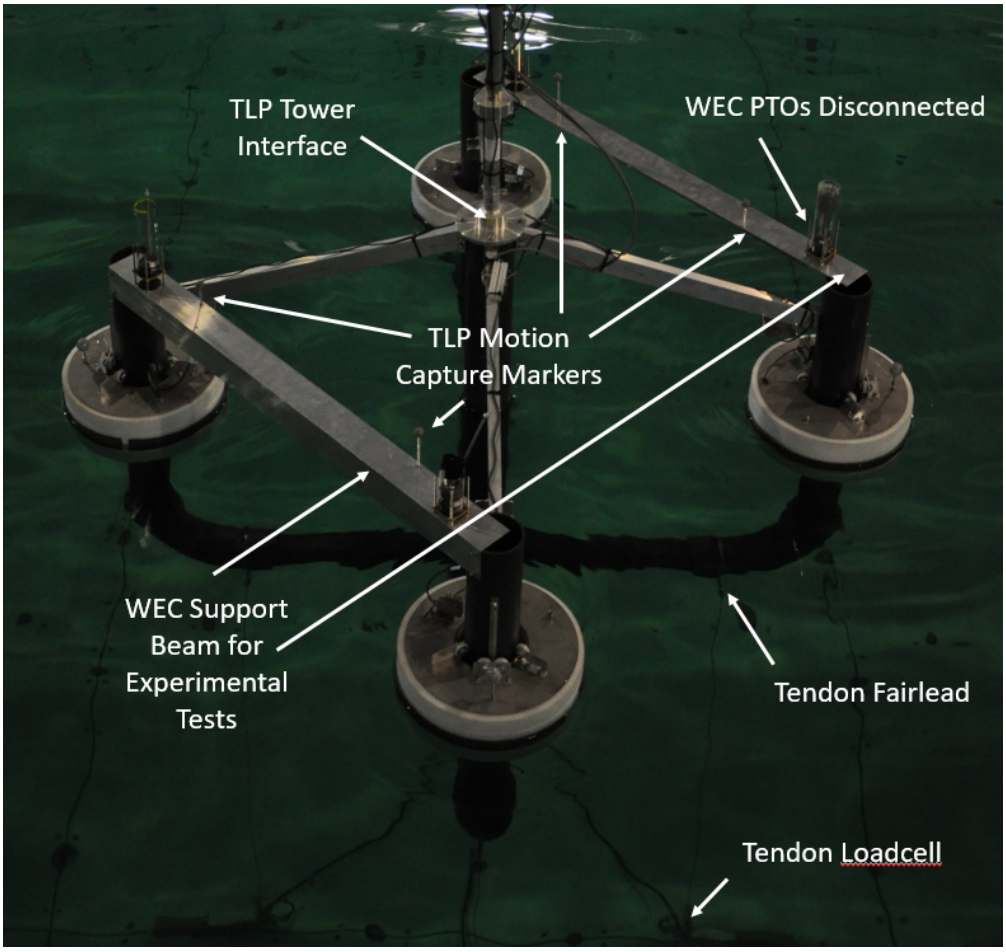


Figure 6.25: Photograph of TWindWave in WEC free mode in wave basin, showing details of the WEC - platform interface.

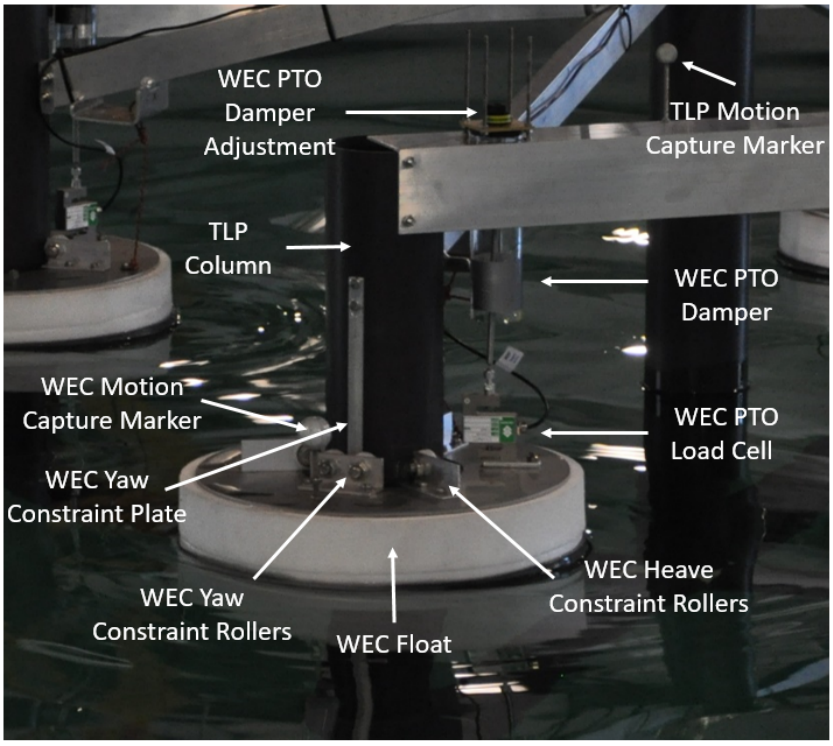


Figure 6.26: Photograph of TWindWave in WEC operational mode in wave basin , showing details of the WEC - platform, tendon and tower interfaces.

6.9.2.3 Regular Waves

Regular wave experiments with a wave height of 1 m and 2 m and periods from 6 s to 18 s in increments of 2 s were performed. Two wave heights were studied in order to analyse nonlinear wave height scaling effects.

In Figure 6.27 the platform surge RAO is compared. For the low periods of 6 s and 8 s and also 14 s the numerical and experimental results are near identical. For wave periods of 10 s and 12 s, the numerical model is seen to slightly under predict the experimental results. For a wave period of 16 s the numerical model severely under predicts the surge motion in all cases except for the TWind alone at 2m wave heights. At 18 s the numerical model slightly over predicts the experimental results.

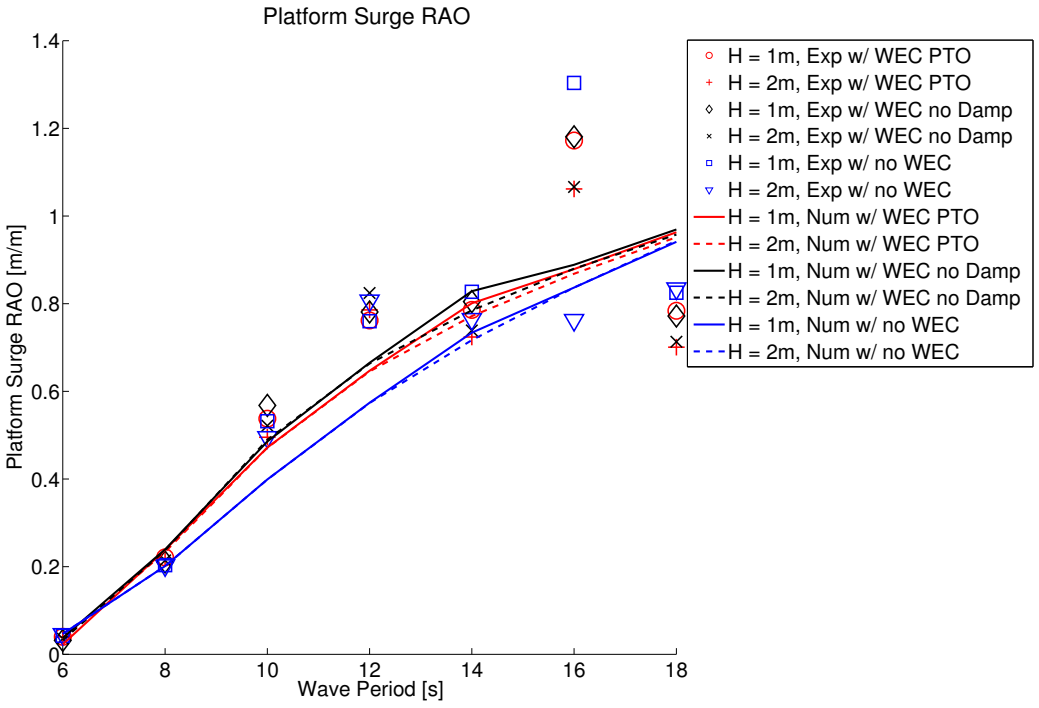


Figure 6.27: Regular wave surge comparison between the numerical and physical modelling techniques for all TWindWave configurations tested

In Figure 6.28 the platforms heave RAO is compared. Firstly it must be noted that the values of the heave RAO are extremely small, with a maximum full scale value of less than 0.03 m/m. At scale this results in a response of less than 1mm, making measurements extremely difficult. The numerical model of the TWind and TWindWave

with undamped WECs cases under predicts the heave motions at all periods, while the trend is broadly similar. The addition of WEC PTO damping means the numerical model show a slight under prediction at low period waves of 6 s and slight over prediction at longer periods. There are numerous outliers in the experimental results which follow the numerical trend indicating it may not be over predicting in actuality.

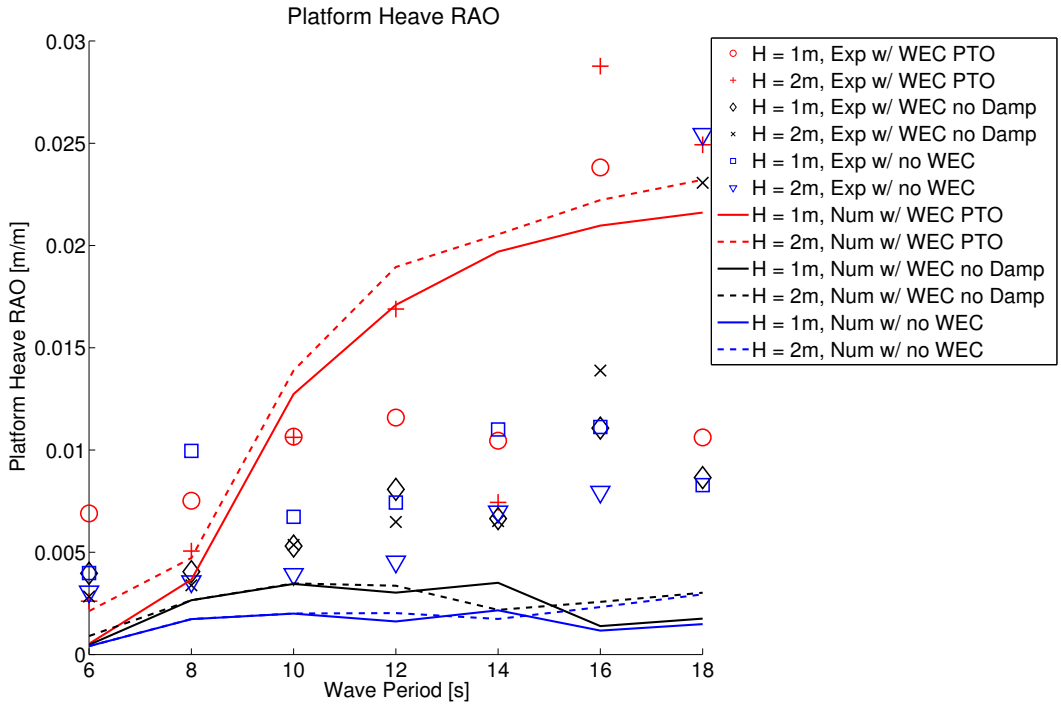


Figure 6.28: Regular wave heave comparison between the numerical and physical modelling techniques for all TWindWave configurations tested

In Figure 6.29 the platforms pitch RAO is compared. Similar to the heave RAO, the magnitude of pitch RAO is very low, less than 0.1 °/m. In spite of this the comparison between numerical and experimental results can be seen to be quite good. For the TWind alone the comparison for wave periods below 14 s is extremely close. For wave periods of 14 s and 16 s and 2 m wave height, the TWind results are again extremely accurate, for these same wave periods but wave heights of 1m, the experimental RAO are much larger than the 1m RAO, indicating that a second order wave damping force may exist here. Comparing TWindWave with undamped WECs the numerical and experimental results are similar for periods of 6 s and 8 s, while the numerical modelling under predicts

at longer periods. Including the WEC PTO damping means the numerical model over predicts while compared to the experimental results, although a similar trend is observed.

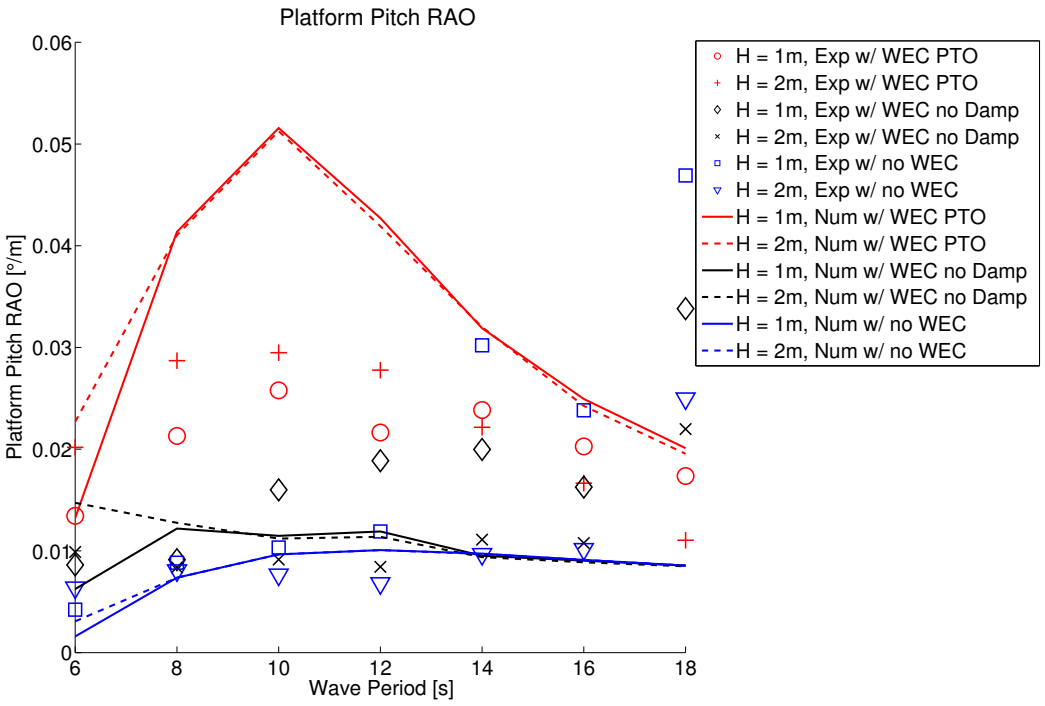


Figure 6.29: Regular wave pitch comparison between the numerical and physical modelling techniques for all TWindWave configurations tested

In Figures 6.30 to 6.32 the tendon tensions are compared. In both the TWind and free WEC set ups, the numerical models over estimate the mid platform (the port and starboard tendon) tensions compared to the experimental results. For the bow and stern tendons (No. 1 and 3) the results match quite closely for these two cases, although the numerical model tends to show a slight underestimation. The clear increase in the numerical models tension results with the addition of the free WECs compared to the TWind case are not evident in the experimental result, were both of these cases have similar tension response. The addition of the WEC PTO force dramatically increases the tendon tensions as was predicted by the numerical models. The tendon RAO with the additional WEC PTO force are an order of 5 times the Wind only and free WEC set ups. For waves above 8 s, the numerical tensions for the bow line and port + starboard lines over predict the experimental results. For the stern line, the experimental results

generally appear larger than the numerical.

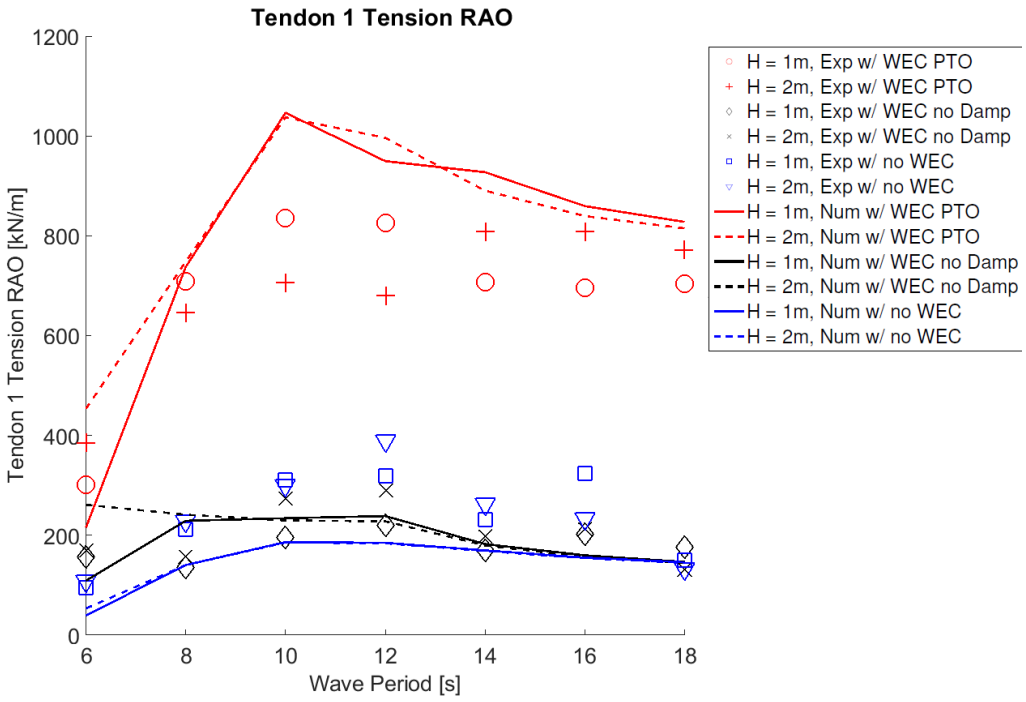


Figure 6.30: Regular wave Tendon 1 tension comparison between the numerical and physical modelling techniques for all TWindWave configurations tested

Figures 6.33 to 6.35 compare the heave response of the WECs floats themselves. The port and starboard WECs are in line and perpendicular to the wave direction. For this reason the average of these two WECs is taken as the response metric here. In general the agreement between numerical and experimental results is quite good. The WEC motions are generally smaller in both the free and damped experimental results compared to the numerical model, most likely due to additional friction from the rollers and dash-pot damper in the wave basin set up.

The WEC heave results clearly show the nonlinear RAO effects. RAO are smaller for the 2m wave height, for all WEC's and floats, indicating the importance of viscous damping effects. It is likely that WEC damping coefficient used in the numerical model should be increased.

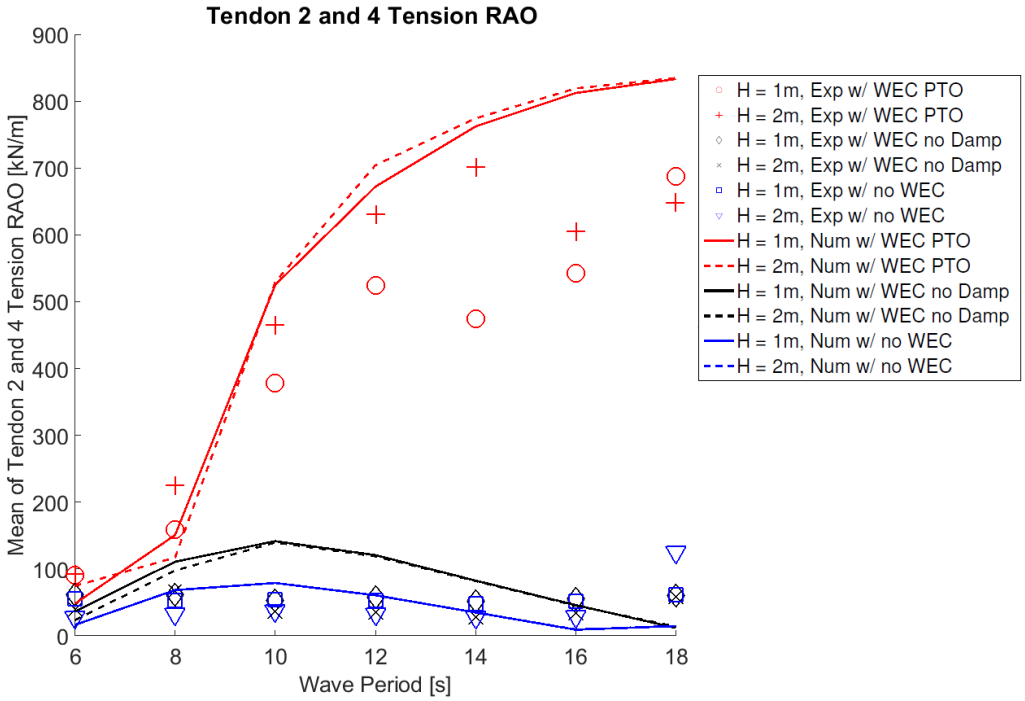


Figure 6.31: Regular wave Tendon 2 and 4 tension comparison between the numerical and physical modelling techniques for all TWindWave configurations tested

6.10 Conclusions

The novel combined tension moored wind and wave energy converter TWindWave has been introduced in this chapter. A design procedure to incorporate WECs onto an existing TLPWT design has been outlined. This procedure involves harnessing the large tendon pretensions that are required to maintain the platform integrity in survival sea-states for use in the WEC operational phase. A preliminary performance study of a standalone WEC is carried out, before the detailed design study on the combined system is undertaken.

The effect of hydrodynamic interaction between the platform and WEC's has been shown and quantified, showing the importance of taking these effects into account. Overall power production is shown to decrease when hydrodynamic interaction is taken into account, due to the shielding effect of the WECs. The structural and hydrodynamic effect of including the WEC onto the platform is then shown, increasing the platform design requirements. The addition of WEC generally increases tower bending moments,

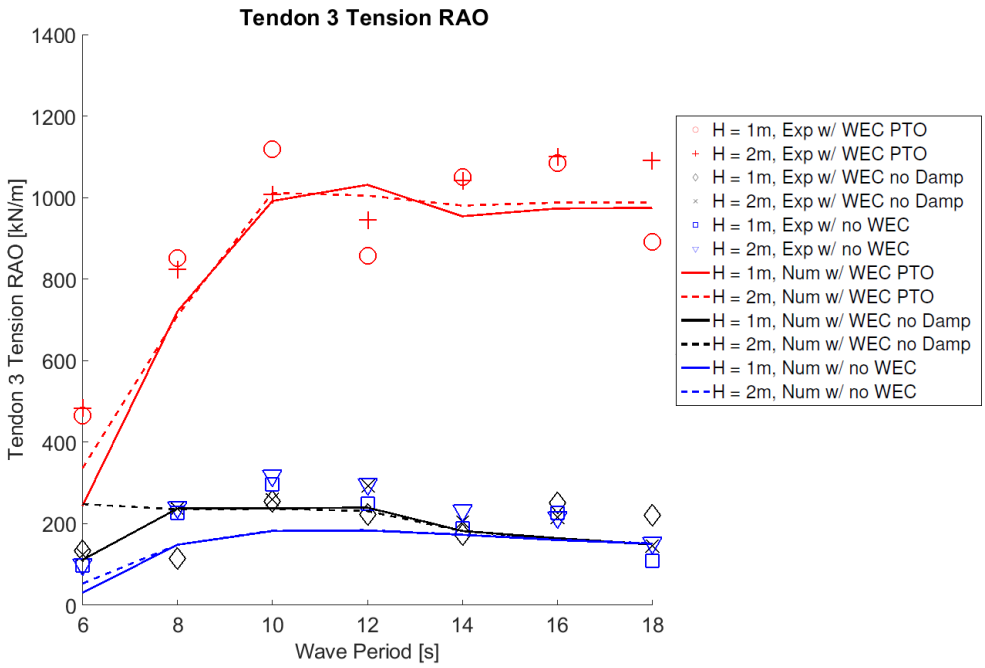


Figure 6.32: Regular wave Tendon 3 tension comparison between the numerical and physical modelling techniques for all TWindWave configurations tested

up to 106% higher than the wind only platform. Sea-states at around 6.6 s show an exception,with the WECs reducing these bending moments. This demonstrates that there is an additional potential for use as load reduction devices. This sea-state is close to the heave natural period of the WEC floats at 6.4 s, meaning that the addition of a WEC resonance mechanism such as reactive control [330] or the wave-spring [331] technology has the possibility of load reduction across a wide range of wave periods. These control technologies work by moving the WEC's response in phase with the wave frequency. It is recommended to study this potential in detail in future work.

Novel WEC survival modes are also introduced and demonstrated. These modes involve disconnecting the WEC PTO before ballasting, submerging and rotating the WEC floats along the TLP columns. Results of this survival mode demonstrate the prove of concept, showing decreased tendon loading for long period waves, but also show that a redesign is required to avoid the increase in pitch response for short period waves.

1/37th scale physical model testing of the standalone TWind device and the TWindWave device under two WEC set-ups was carried out in the LIR National Ocean Test

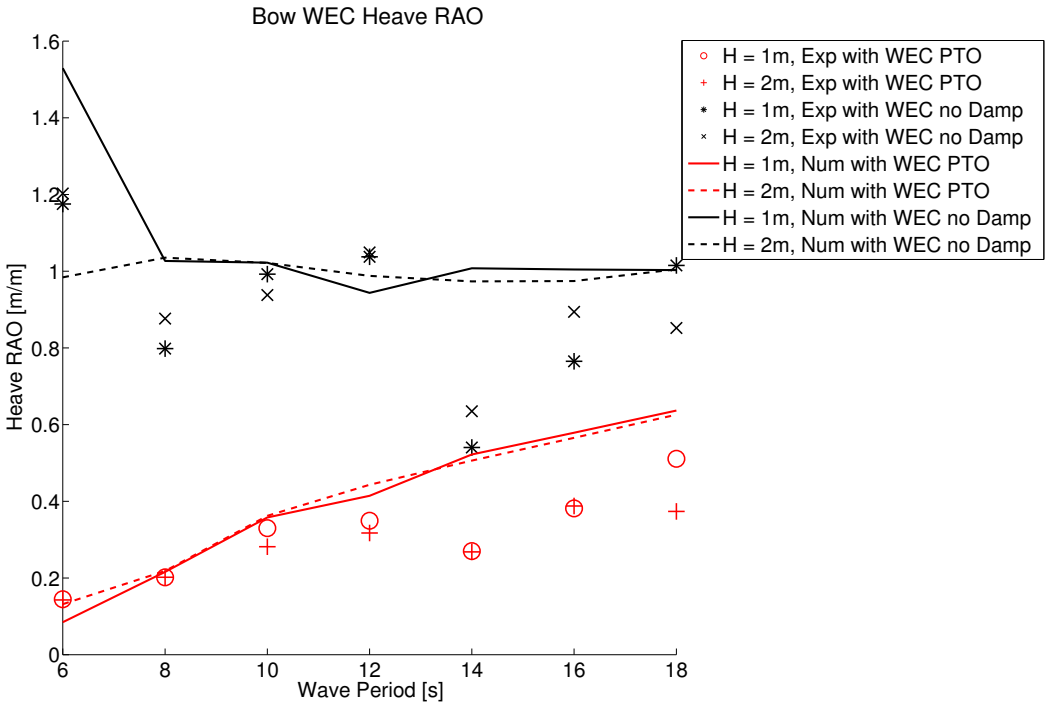


Figure 6.33: Regular wave Bow WEC comparison between the numerical and physical modelling, with and without PTO damping

Facility's deepwater basin. Comparisons between these experimental results and the simulations outlined in this chapter have validated the numerical modelling approach used here. Close fits in platform and WEC DOF have been observed.

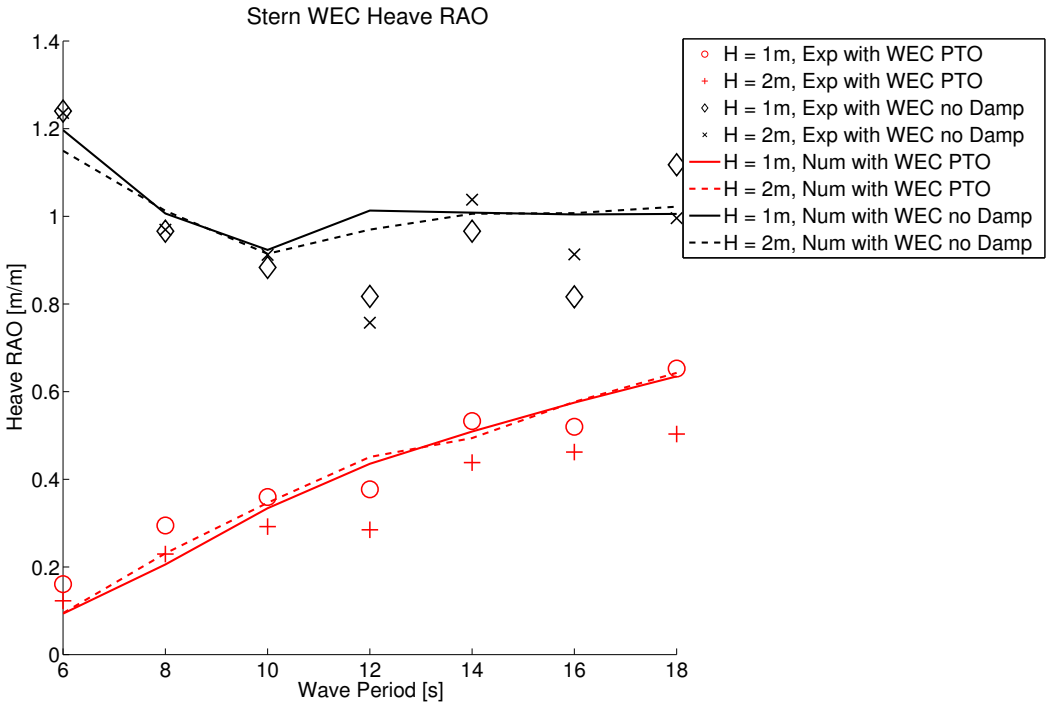


Figure 6.34: Regular wave Bow WEC comparison between the numerical and physical modelling, with and without PTO damping

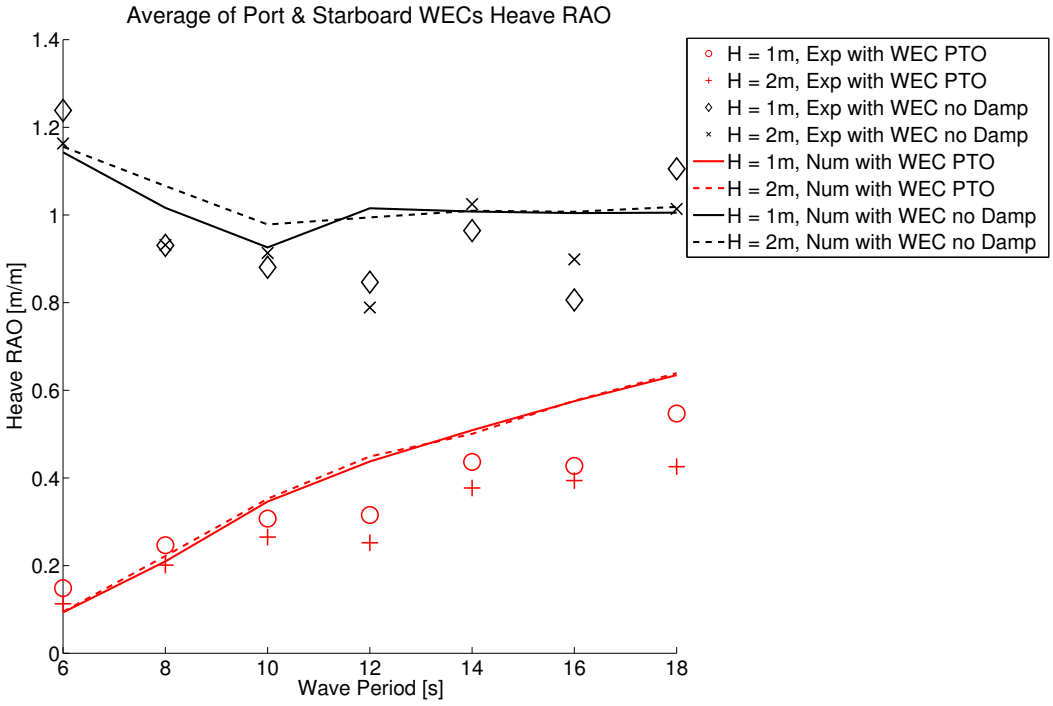


Figure 6.35: Regular wave Port and Starboard WEC comparison between the numerical and physical modelling, with and without PTO damping

Chapter 7

Design Sensitivity to Anchor Misposition

7.1 Introduction

This chapter deals with specific design sensitivities that relate the idealised design of tension moored FWTs, to variability of real-world operational conditions. As a FWT design evolves and matures it increases up the TRL stages. With the increase in TRL more detailed design considerations should be taken into account.

These details relate to the inherent design sensitivities involved in deploying and operating devices in a marine environment, specifically those with tendon pretension providing the primary stability mechanism. The design sensitivity of a TMFWT's anchor positional tolerances is selected for a detailed studied in this chapter.

TLP tendons are designed and modelled assuming the installed anchor position is exactly as is designed. With requirements to install a high number of tendon anchors (Taking the mean number of OWT units per farm in 2016, 79 [332] and assuming four tendons per unit, resulting in approximately 300 anchors) there is potential that the required positional design accuracy of individual anchors may not be met, or that marine operations may be expedited by relaxing such limits. The difficulties of balancing tendon pretension discussed earlier in Section 4.3.5 also highlight this potential issue. The dynamic effects of such anchor misplacement on platform performance metrics is analysed

here.

A summary of results and conclusions from this chapter are as follows:

- Design sensitivity to TMFWT anchor misposition has been investigated in detail for the first time in the literature.
- The worst case anchor misposition locations at a 3m tolerance increase nacelle acceleration by 53%.
- Two mitigation methods are proposed and tested in order to reduce the need for positional accuracy. One of these methods, the Furthest Neighbour Installation Method (FNIM) shows great promise for reducing platform dynamics, although at the expense of increased downwind tendon forces.

7.2 Anchor Misposition

For tension moored FWT, tendons are generally designed to be vertical. The "as installed" position of the anchors however may not be in exactly the same position as was designed. It is known that this anchor misposition leads to a change in platform motions and loads [333], however previous studies on this issue have only used linear low fidelity numerical models [334]. This section investigates the sensitivity of a tension moored FWT to anchor positional tolerances using a fully coupled model. For proposed Irish Atlantic sites, the availability of enough weather windows to carry out installation, operations and maintenance on marine energy devices has been predicted as being limited [335]. For the complex anchor tendon system type discussed in here this is obviously of great concern. Thus any method to decrease the temporal or sea state conditions required is vital for deployments in these harsher environments. Even in the case of exactly positionally correct anchor installation, the long life of FWT (30 years) means that soil creep may mean the anchors end up offset from the original installation and design locations [336][337][338]. Geotechnical issues with the sea floor may also necessitate anchor relocation from the design position. In the case of piles positioned using piling templates and rigid monolithic gravity based anchors anchor misposition will not be in issue. For

other types of anchors the positional tolerance will be of a concern to the designer.

7.2.1 Anchor Type and Positional Tolerance

A number of different types of anchor systems have been proposed for tension moored floating wind turbines etc. These include; pile, gravity, suction, drag and grouted rock anchors. Drag anchors with vertical load capabilities are likely to have the greatest positional offset from the target as the installation process is quite primitive and involves a great deal of uncertainty as to the final positioning of the anchor. The DNV codes [339] state that the permissible installation tolerances shall be determined taking into account the increased difficulty in accurate seabed positioning caused by large water depth and environmental conditions. Position tolerances can be an absolute, for example 1m, or depth dependant, for example 1% of water depth. Anchor positioning may also be modified from the design conditions by unexpected ground conditions, for example boulders in the sand or clay, which make installation at that location impossible. Installation of anchors requires special anchor handling vessels with dynamic positioning (DP) systems. DP systems can keep a vessel “on location" by applying an active thrust, thus making it easier to achieve the required positional accuracy. In order to apply the appropriate reactive thrust, DP systems measure wind speed but calculate wave and drift loads and thus the positional control systems used integrate a feedback feature and require some time to become positionally stable. It is assumed that increasing the anchor positional tolerance will allow the anchors to be installed in shorter weather windows, more severe sea states, or by less expensive vessels that have less capable DP systems. This section investigates what the effect of increasing these positioning tolerances will have on the platform dynamics (motions and tendon forces). A literature review of the topic found a surprising lack of publications. In 1993, Hamilton [334] presented a method to calculate the linear effects of anchor misposition by using linear pitch and roll motion but keeping quadratic terms in yaw motion, although no results using this method were presented.

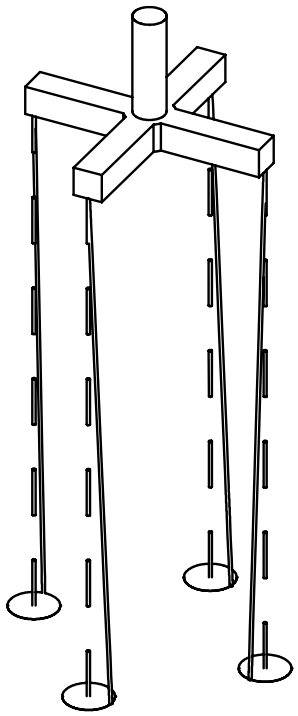


Figure 7.1: View of platform and anchor misposition. Dashed tendon line is the design case with no misposition, solid tendon line is the misposition case. Seabed circles indicate the anchor target area. Horizontal distances of the misposition length are exaggerated to retain clarity.

7.2.2 Methods

The tension moored floating NREL 5 MW reference [306] wind turbine platform; TLPWT 4 [340] was used for this study. The water depth is taken as 150m. Hydrodynamic parameters are computed from ANSYS AQWA for 8 wave directions and 50 frequencies from 0.008Hz- 0.4Hz. Time domain modelling is required due to the highly non-linear nature of the tendon stiffness and platform dynamical coupling and is carried out using the coupled OrcaFlex and Fast package FASTlink v8 [341]. Additional quadratic viscous damping of the platform is added to the model using modified Morison equation drag only elements. Mooring tendon stiffness is not mentioned in the cited paper and are modelled with an axial stiffness of $1.5 * 10^9$N using Morison equation elements. Eight anchor angular offset positions are chosen for each anchor ($360\ ^\circ/8 = 45\ ^\circ$) and with four

anchors this allows for 4096 possible combinations. Figure 7.2 shows the possible anchor positions. These combinations result in a number of duplicate simulations, where the effective spacing of the anchors is equal and all are offset in the same direction. Four of these duplicates are included in the study as the wave elevation will be non-exact at the varied position (different frequencies that make up the wave spectrum having different velocities). As the waves are long-crested and do not include a y component, the four positions, which are mirror positions about the x-axis to those four mentioned previously, are not included in the study. This results in a total number of 4092 simulations. The anchor position tolerances are chosen as absolute values of 1, 2 and 3 m (Tolerance/depth ratio of 0.0067, 0.0133 and 0.02). This study assumes the worst case scenario, where anchors are positioned along the limits of these tolerances. Survival state is modelled using a JONSWAP spectrum with Hs of 12.7 m, Tp of 14.1 s and wind speed 50 m/s for 1300 s (Ignoring the first 100s to give a usable time of 20 minutes or 1200s). Wave and wind were modelled as being directionally aligned. For comparability all simulations use the same random phase seed number. Figure 7.1 shows a 3D view of the platform with and without anchor misposition.

7.2.3 Misposition Results

Displacements and rotations are calculated at the platform's centre of gravity, accelerations are measured at the centre of the nacelle. Nacelle acceleration is used as this metric is a limiter given by WT suppliers. Anchor misposition is weighted by the perimeter distance added to the square of the in wave positions and then normalised by the base case of 0 m misposition. The perimeter distance is calculated as the path length around the as installed position of all anchors. The in wave position is calculated as the anchor position parallel to the wave direction. In this case the wave direction has no y component and thus this value purely relates to the anchors x position. It should be noted that this normalisation process does not represent any physical quantity and is solely used in order to visually represent the results in Figure 7.5. Equation 7.1 shows the normalisation function, where $\bar{P}$ is the normalised position, p is the perimeter length, i is the anchor number, n is the number of anchors, xw is the in wave position, j is the misposition

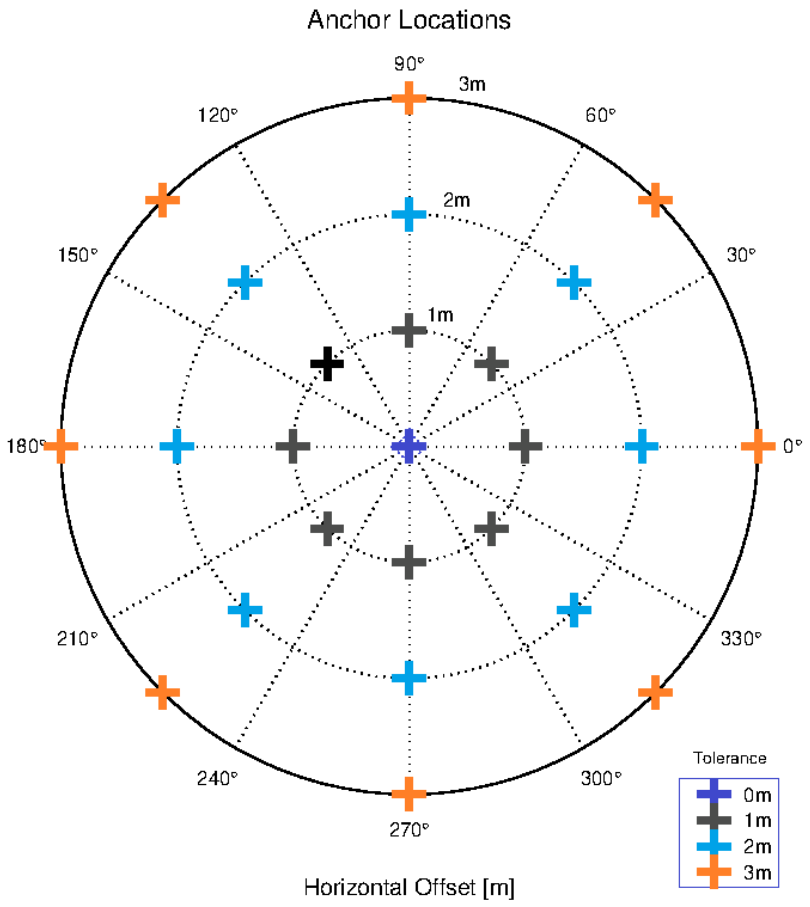


Figure 7.2: Possible Anchor Positional Locations

number and 0 is the zero misposition baseline case. The results of the normalisation process are values between 0.69 and 1.41, where unity represents the design case.

$$\bar{P}_j = \frac{p_j + \sum_{i=1}^{n} xw_i^2}{p_0 + \sum_{i=1}^{n} xw_0^2} \tag{7.1}$$

Figure 7.3 a shows the mooring misalignment which results in the most severe accelerations from the simulation study, where the anchors parallel (Tendons 1 & 3) and the anchors perpendicular (Tendons 2 & 4) to the wave direction are shifted to the maximum relative distances. Figure 7.3 a shows this relative anchor position, the reader should note that the X and Y axis dimensions are distorted for the inter anchor cases to retain clarity. Figure 7.4 b shows the surge displacement, Figure 7.4c the nacelle acceleration and Figure 7.4d the tension in Tendon 1. A segment of the simulation time series (from 168s - 182s) which shows the largest deviation between the 0 m and 3 m case across all the dynamics is shown to retain reader clarity. The most significant result is a 53% increase in maximum nacelle acceleration. Figures 7.5 to 7.6 shows all the cases. Figure 7.5 b-d shows the maximum surge, heave and pitch displacement and maximum nacelle acceleration, Figure 7.6 e-h shows the maximum tendon forces. Of particular note are the large motions and forces that are located in the range of 0.95 - 1.1 normalised anchor position. X is surge, Z is heave, RY is pitch, A is acceleration and T1-4 are the tensions in tendon 1-4

7.2.4 Mitigation Methods

Two novel mitigation methods are proposed for the misposition issues presented previously. Both methods involve changing the target anchor position based on the position of previously installed anchors. This is in contrast to a traditional method, where anchor targets are identified before installation and are rigid as they do not evolve as anchors are installed. First a nearest neighbour installation method is proposed, followed by a furthest neighbour installation method. If the distances between the anchors are equal, the first one anticlockwise of those already installed is chosen. The ten anchor offsets, at 3m tolerance, that show the most severe results are used as test comparison cases to

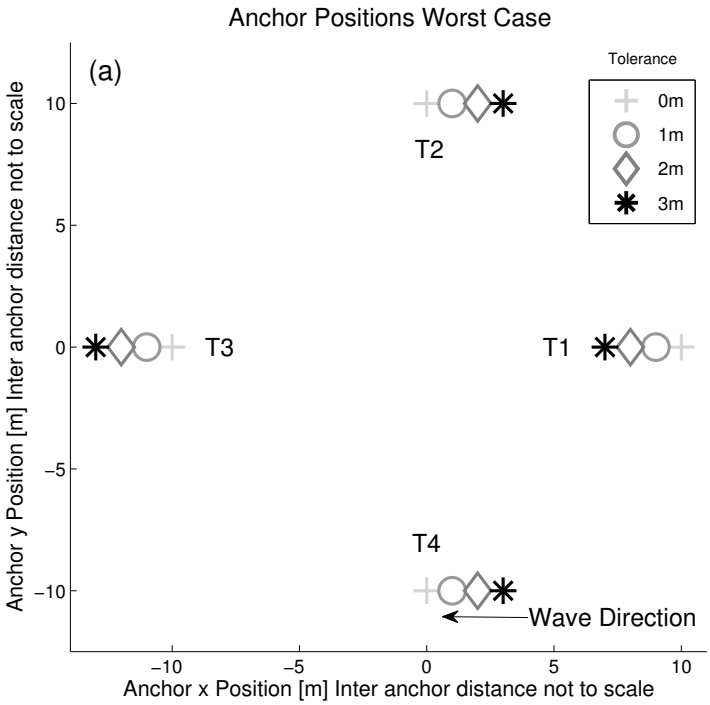


Figure 7.3: Anchor misposition worst case

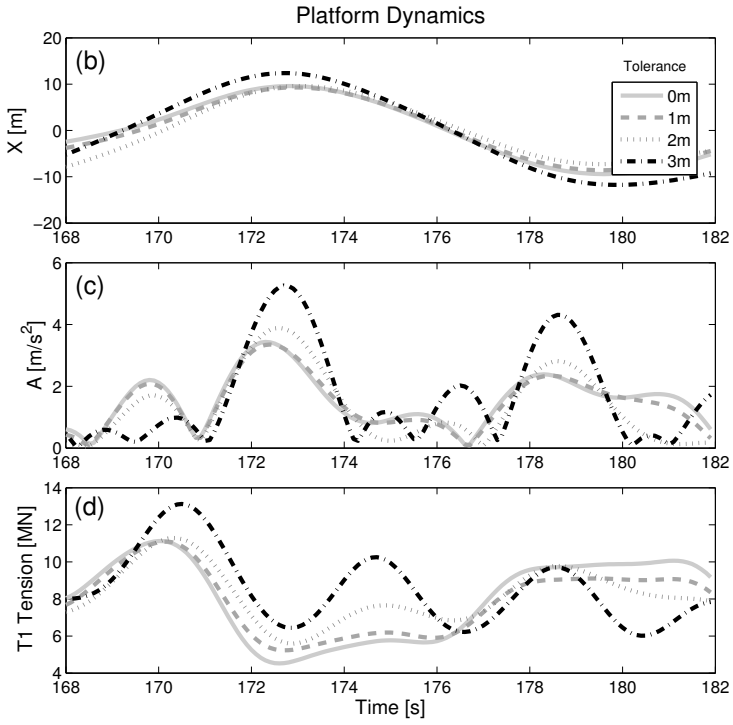


Figure 7.4: Anchor misposition effects on Dynamics: Worst Case, where X is the platform surge, A is the nacelle acceleration and T1 is Tendon 1

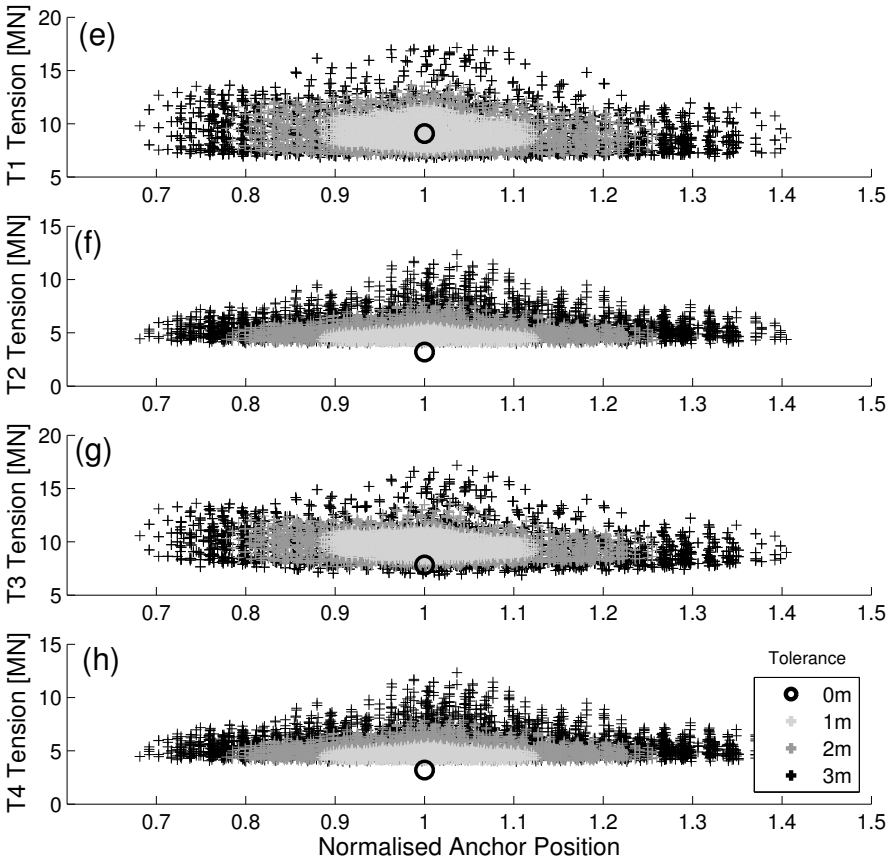


Figure 7.5: Anchor Misposition effects on Dynamics: All Cases, where T 1-4 is Tendon 1 - 4

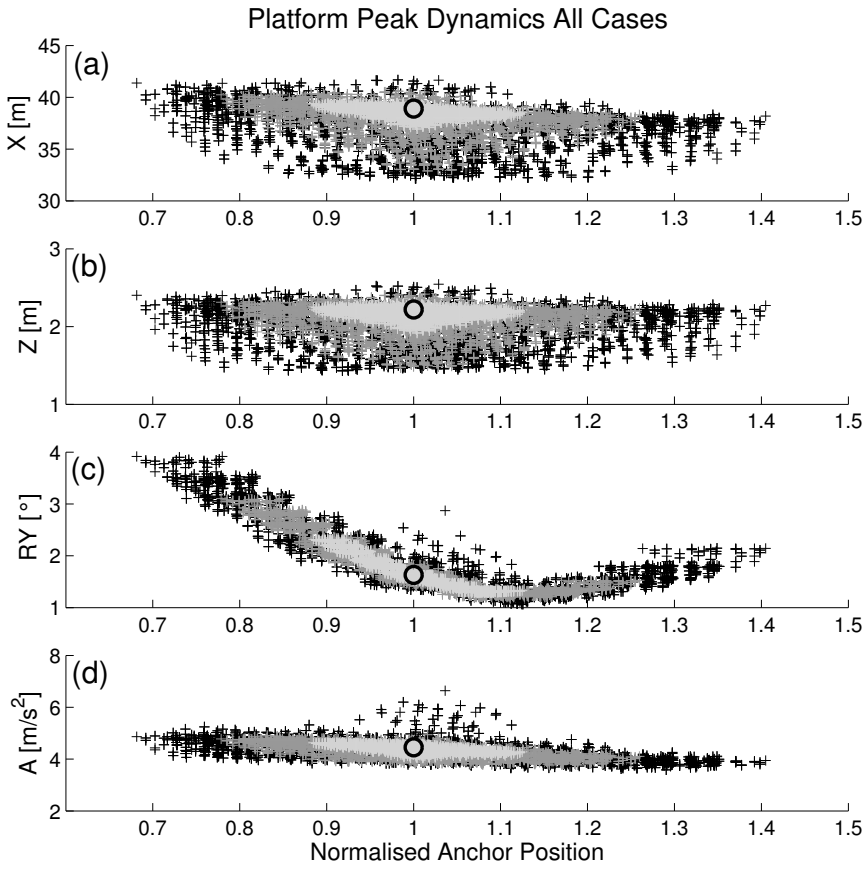


Figure 7.6: Anchor Misposition effects on Dynamics: All Cases, where X, Z, RY is the platform surge, heave, pitch, A is the nacelle acceleration

compare each method. An example for the same offset positions of both of these methods is shown in Figure 7.7, where x and y are the two horizontal positional coordinates, a) shows the nearest neighbour installation method and b) shows the furthest neighbour installation method. Anchor names are the same as Figure 7.3a

7.2.4.1 Nearest Neighbour Installation Method

The nearest neighbour installation method (NNIM) installs the anchors in order of which is closest to those already installed. The offset of each previous anchor is used to determine the location of subsequent anchors. The first anchor is installed in the original target area. The as installed position of the anchor is recorded. The order of subsequent anchors are chosen based on which minimises the distance to the already installed anchor(s). If the distance between two possible anchors are equal, the one in an anticlockwise to those already installed is chosen. A new target area for this next anchor is identified based on position of previous anchor(s). This procedure is continued for each subsequent anchor using the average offset of the previous anchors. The methodology is described for the four anchor case in Equations 7.2 to 7.5 with the governing formula in Equation 7.6. Here the x and y positions are a subset of P (P = [x,y]) P_I, P_D and ΔP_O denotes the installed, design and offset positions respectively. The possible values for ΔP_O are shown in Figure 7.2.

$$P_{I,1} = P_{D,1} + \Delta P_{O,1} \tag{7.2}$$

$$P_{I,2} = P_{D,2} + \Delta P_{O,2} + \Delta P_{O,1} \tag{7.3}$$

$$P_{I,3} = P_{D,3} + \Delta P_{O,3} + (\Delta P_{O,2} + \Delta P_{O,1})/2 \tag{7.4}$$

$$P_{I,4} = P_{D,4} + \Delta P_{O,4} + (\Delta P_{O,3} + \Delta P_{O,2} + \Delta P_{O,1})/3 \tag{7.5}$$

$$P_{I,i} = P_{D,i} + \Delta P_{O,i} + \frac{\sum_{n=1}^{i-1} \Delta P_{O,n}}{(i-1)} \tag{7.6}$$

7.2.4.2 Furthest Neighbour Installation Method

The furthest neighbour installation method (FNIM) follows the NNIM, except in the order of anchor installation. In this method the order of subsequent anchors are chosen based on which are furthest apart from those already installed. The first anchor is installed in the original target area. The anchor that is furthest from this first anchor is then installed using the first anchors offset position. Subsequent anchors are installed in order of which are furthest from their nearest neighbour first. The results presented here weight all previous installations equally, that is the average of all previous offsets are used to determine the new anchor positions. Equations 7.2 to 7.6 also describe this method, although the anchor order will be different.

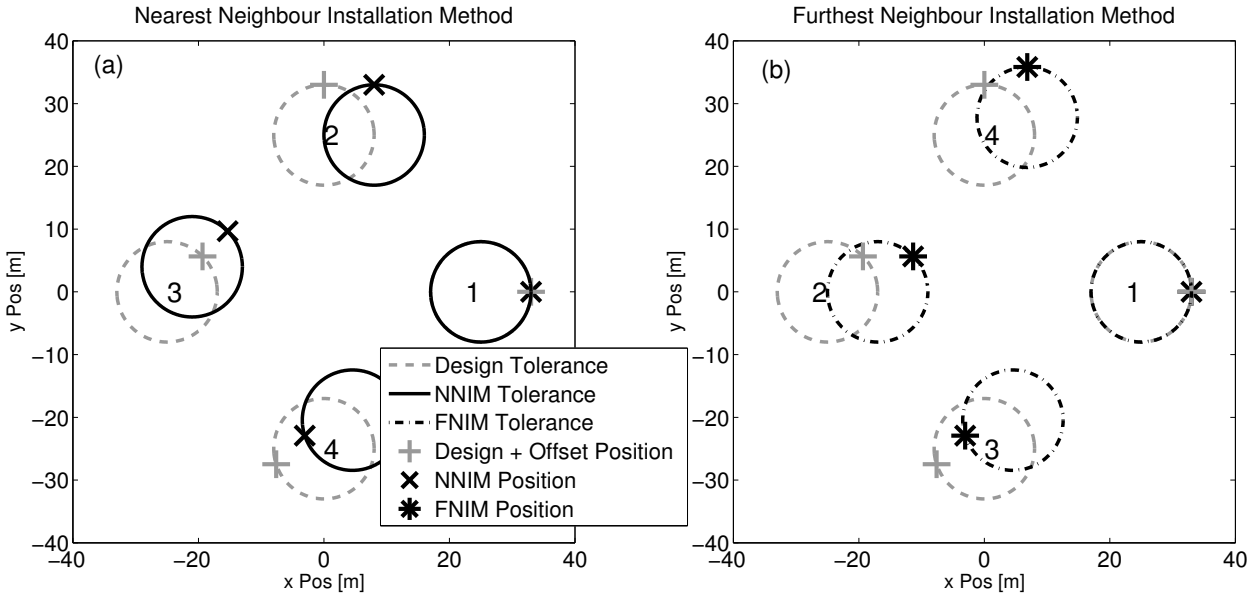


Figure 7.7: Examples of NNIM and FNIM positional results. Horizontal offset distance has been distorted to retain clarity. Numbers indicate installation order

7.2.5 Mitigation Results

Figure 7.8 compares the results of the two proposed mitigation methods against the “as designed" plus offset case for the ten simulations cases. Negative and positive results

indicate reductions and increases respectively for the relevant dynamics. Results for the NNIM are inconclusive, with some offset cases showing reduced and some showing increased peak dynamics. Results for the FNIM are conclusive, as all simulations show the same trend and are shown in Table 7.1. The percentage change in results compared to the design case are shown here. All ten cases show decreased platform motions and nacelle accelerations over the design case. The upwind T1 tendon shows decreased peak loadings but these positive results come at the expense of increased peak loadings in all other tendons. Results for root mean square (RMS) motions and loading follow the same trend as the peak values presented here and are thus not shown.

Table 7.1: Results of the FNIM [% Change to design case], where X, Z and RY is the platform surge, heave, and pitch, A is the nacelle acceleration, and $T1-4$ is the tendon tension in line 1 - 4

	X	Z	RY	A	T1	T2	T3	T4
Mean	-9.8	-18.8	-22.3	-9.5	-5.0	4.3	6.0	20.7
Standard Deviation	1.3	3.1	12.1	5.3	1.4	206	1.6	3.9

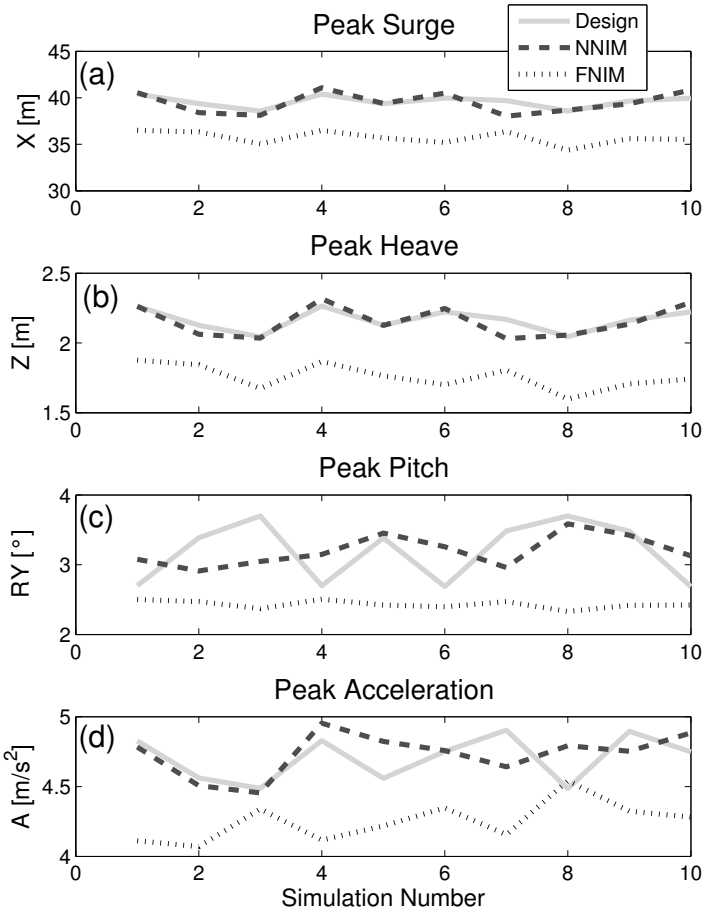


Figure 7.8: Results of NNIM and FNIM compared to the design offset for ten worst case simulations, where X, Z, RY is the platform surge, heave, pitch, A is the nacelle acceleration.

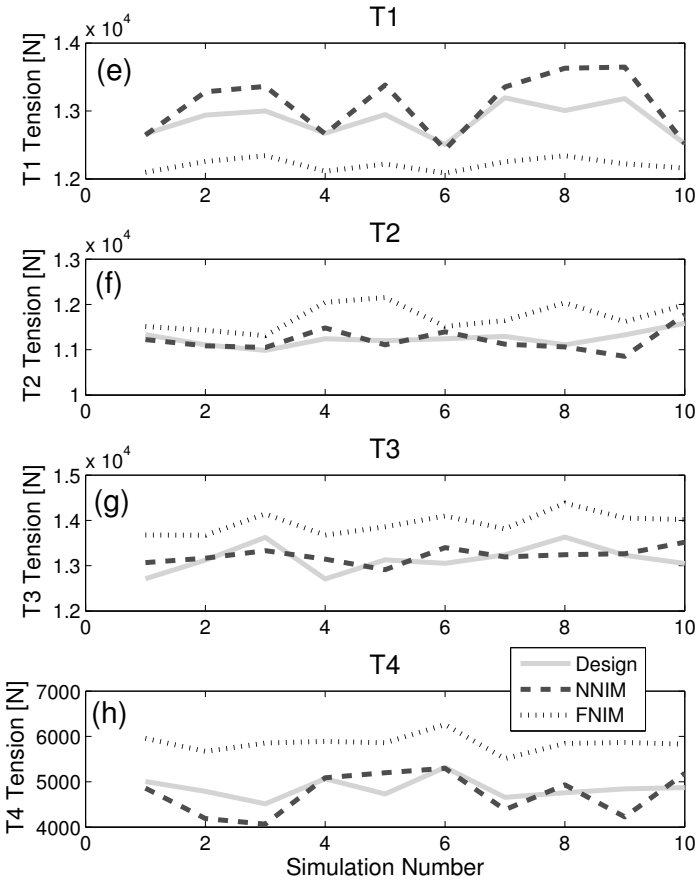


Figure 7.9: Results of NNIM and FNIM compared to the design offset for ten worst case simulations, where T1-4 is Tendon 1 - 4

Chapter 8

Discussion and Conclusions

8.1 Discussion

The results and methods presented in this thesis will be beneficial for future designers of TMFWT as well as the wider offshore floating wind community.

The detailed TLPWind parameter study presented in this thesis will aid platform developers to locally tailor their platform offerings to specific offshore windfarm meteocean and supply chain conditions. The challenges faced by a platform original equipment manufacturer (OEM) in developing multiple global farms in diverse operating, certification and insurance conditions will require the use of automated analysis tools in order to be competitive. The use of such automated technology development tools should be integrated between all possible interfaces, be it the WT OEM or the fabrication and port facility. Automating the simulation creation, running and post processing will allow greater optimisation of future FWT concepts, especially where the WT will be further modified from a standard offshore WT. As classification standards and guidelines are rapidly being improved and updated for this nascent industry, and inflation eats into existing project margins, a projects flexibility to design decisions will be of an increasing benefit. WT capacities are predicted to increase beyond the currently available 15 MW, into 20 MW and beyond. Platform concept developers must thus now be developing innovations for quite a broad design envelope of unknown WT parameters, RNA mass, blade flexibility, controllers etc. With each country or region defining their own local

requirements and lease award criteria this design process automation has even further benefits.

The parameter study on flexible towers has demonstrated how platform concept developers should strive to find platform dimensions where the addition of the tower flexibility significantly reduce the platform dynamics by shifting hydrodynamics to more favourable regions. With increasing WT capacity this will become a greater issue as the longer towers shift the natural frequencies further into excitation zones.

Challenges in the addition of WEC to a TLP are identified in this work. The conflicting stability requirements for the WT and required dynamic behaviour of the WEC floats are one such area to overcome. The capacity divergence between the calculated outputs in wind and wave energy presented in this work further call into question the benefits of such an arrangement.

The possibility of using the floats only for the tow stability and survival modes should be highlighted. With this alternative suggested design, the floats will not be used to extract wave energy, hence no additional PTO costs or complexity to the platform. Furthermore the dynamic instability problems identified and described will no longer be an issue in this case. In this proposed design the floats would remain submerged for significant durations, between being installed on site and requiring either decommissioning or major operations involving large component replacement and O&M activities with tow to port. The mechanism for float submergence and resurfacing would need to be extremely resilient to long periods without use, avoiding seizure of components etc. The increased complexity of multiple moving bodies must be heavily considered for the harsh marine environment were simplicity has traditionally been the winning formula. The balance between innovations and practicality must be at the forefront of the industry. The high cost of tow to port for major component replacement may also mean that an offshore alternative may need to be found. In this case the tow floats may only be used for initial installation and decommissioning, remaining in the survival mode for the complete operational project phase.

As increased design tolerances mean increased fabrication, installation time and costs, the ability of a concept to have relaxed tolerances will greatly improve its competitive-

ness. In this work the design sensitivity of TMFWT to anchor positional tolerances is highlighted as one such issue. It is advised to include such an analysis in early stage concept development work, as the optimum design will not be simply the cheapest platform, but also including metrics on which is quickest and or easiest to install. The design sensitivity to anchor positional tolerances is expected to be reduced as mooring systems become more slack, but such effects should still be consider. The typically used drag embedment anchors for catenary mooring systems will require either extensive geotechnical sampling or involve a great deal of uncertainty over holding capacity and final installation location. The risk of anchor or mooring line failure and subsequent catastrophic cascading failure of a multiple floating units will require sufficient capacity to avoid such failures, be it through redundancy or increased component sizing. For TMFWT failure of a full tendon leg will most likely result in overturning and sinking of the unit. In this case there is no potential for a cascading failure mechanism to develop and thus may be beneficial compared to other worst case situations with self stable type floating units..

Challenges in balancing the tendon pretension from the experimental wave basin test campaign discussed in Chapter 4 will also be a potential issue at full scale deployments. The use of accurate tension adjustments during the platform-tendon on site installation will be critical.

8.2 Limitations

The limitations of the various techniques used in this thesis are discussed next here.

8.2.1 Chapter 3. Numerical Modelling of FWT

In this chapter, the effects of a flexible tower are neglected in both numerical and experimental models. As the first tower bending frequency is highly coupled to the platforms pitch response, this leads to a slight inaccuracy in the pitch response frequency and amplitude. In Chapter 4 the tower flexibility is fully accounted for, with the modification of pitch frequency and amplitude parametrised by platform geometry and pretension. The effects of the WT on platform motions are also simplified to only a constant thrust

force in both simulations and physical model tests. This simplification neglects the effects of the WT controller, rotor torque, gyroscopic moment, varying wind speed, the relative wind speed velocity caused by the difference between incoming wind velocity and RNA velocity. In Chapter 5 all these WT effects are accounted for in the design of a novel TMFWT by use of the fully coupled software OpenFAST. Linear wave theory with superposition of wave frequencies was assumed for the wave field and motions and loads were calculated assuming linear potential theory forces. This theory is based on the assumption that the flow is irrotional and non-viscous. Nonlinear terms in viscous forces and mooring stiffness (resulting in coupled DOF) are included in the model. a These limitations mean that the numerical and physical modelling process used is non conservative, however was adequate for the purpose of this chapter, as the limitations and failures of the HEXWIND platform design were successfully identified.

8.2.2 Chapter 4. Design of TWind

The second order forces were not calculated for the new TWind designs presented in this chapter. As the new designs are of a similar displacement to the HEXWIND platform, the second order force effects are assumed to be minor. A detailed structural assessment was not including in the design of the platform. The tow model did not include the tug vessel, instead the problem was simplified to an extremely long winch which pulled the TWind device. This simplification neglects the coupling that may exist between the vessel and platform and the catenary dynamics of the tug line.

8.2.3 Chapter 5. Design of Combined Wind and Wave Energy Convertor

A detailed structural assessment was not including in the design of the combined wind and wave energy platform. The response in the various survival mode's was not tested experimentally.

8.2.4 Chapter 6. Design Sensitivity to Anchor Misposition

The anchor misposition study did not take into account any vertical or rotational variation in tendon termination location, instead only a horizontal offset was studied.

8.3 Future Work

It is recommended to carry out the following research work that was beyond the scope and available time and resources of this thesis. These are areas identified throughout the course of the research work that would help carry the research forward.

8.3.1 Chapter 3. Numerical Modelling of FWT

- Extend the drag coefficient fitting study to include the potential Reynolds and KC number effects, and for non-linear wave-current interactions.

8.3.2 Chapter 4. Design of TWind

- Extend the Environmental resource assessment to include an extreme wind analysis for Irish offshore locations.
- Extend the TWind hull parameter study to include the effects of second order sum frequency wave loading.
- Carry out a structural analysis of the TWind device proposed in this thesis.
- Integrate an economic lifetime cost assessment model into the platform parameter study.

8.3.3 Chapter 5. Design of Combined Wind and Wave Energy Convertor

- Model the effects of second order wave forces on the TWindWave device. As the WEC's absorb energy from the wave field the slow drift difference frequency QTF loads will increase in magnitude, compared to a rigid device.

- Experimentally tank test the TWindWave device in the two most promising WEC survival modes as identified in this work.
- Investigate the potential to use WECs as motion and load reduction devices by use of advanced WEC floater resonance modification technologies such as control theories or the wave spring technology.
- Carry out a structural analysis of the TWindWave device proposed in this thesis.

8.3.4 Chapter 6. Design Sensitivity to Anchor Misposition

- Experimentally test the effects of tendon anchor misposition.
- Refine the anchor misposition mitigation method proposed in this work to include the effects of wind and wave misalignment and multi-directional wave spectra.

8.4 Recommendations

The following recommendations are the accumulation of knowledge gained through applying engineering design and simulation models to an existing tension moored wind turbine platform, HEXWIND, and from the design of both a novel tension moored wind and a combined tension moored wind and wave energy device, TWindWave. From an initial metocean assessment through to details of the platform lifecyle, the platform technology designer or project developer will encounter a broad range of challenges with decisions often based on complex interactions between datasets. At each step in the design process the required model fidelity is scaled according to the needs and safety factors governing that design stage. General recommendations to aid the designer are given in this chapter.

8.4.1 Design Conditions

Offshore site conditions will dominate the majority of floating wind farm developments design decisions. From initial concept stage all the way though to site decommissioning, achieving an accurate local characterisation should be a major priority for all project developers. As timelines for offshore floating wind planning stages are in the order of 5

– 10 years or more before deployment will take place, and operational lifetimes of 25 - 30 years, the available local data is likely to grow throughout the project developments lifetime. As the information levels increase, there should be sufficient flexibility provided throughout the project to deal with design factors and load cases being modified. As a case study, during the duration of this design study, a storm event with a significantly larger wave height than all previous measurements of the site (M5 Buoy) was observed. This significant wave height of 12.8 m, was 40 % larger than the previous high in that location of 9.2 m. Recordings at this buoy had begun in 2004, giving 14 years of data to the date of that event. As recommendations on extreme wave extrapolations generally define a prediction confidence limit of five times the data set duration, conventional wisdom would allow this data set to predict an up to 70 year return period. In reality this observed wave height was larger than both the 50 and 100 year return period predictions based on the available data preceding the event, and thus could result in damages or failures of any deployments made based on the initial design loads. With climate change alternating ocean behaviors, for example modifying tropical cyclone tracks and intensity's or oceanic current changes such abrupt changes in observation patterns may become more common.

Due to the complex mechanisms involved in many design decisions throughout the project development, (for examples the platform technology type, mooring arrangement, anchor type, turbine selection etc.) changes in the design values may dramatically alter the decision process and result in a fundamental alteration to the original design choices. Conventional design approaches based on segregated design tools or spreadsheets will most likely miss or cause delays during this detailed reanalysis. For this reason it is recommended to integrate all design decisions into a single tool or work flow. In doing so, updates to data at any stage of the design will be accounted for. Clear design decision outputs should be made as often as possible, so that the existing design momentum will not overweight new information.

8.4.2 Recommendations for Design Approaches

Numerical modelling and physical tank testing are vital tools in the successful and optimised designs of novel structures. For the design of complex novel structures such as floating wind turbines with high numbers of DOF and highly coupled motions, involving interactions across a broad ranch of physics, the use of an equally sophisticated design analysis is required. The use of a full range of numerical model and simulation fidelity's are recommended. As model accuracy is directly related to computational expense and thus solver time, approximate models with quick simulation time should be used in a combination with detailed higher order models. As the higher order modelling methods (including physical model testing here) will provide governance to the successful implementation of the lower fidelity design tools, the use of such should be given an immediate priority in the project development timeline. In the case of complex fully coupled models, the consequences of specific parameter changes may be convoluted or difficult to interpret. In these cases the use of simpler but validated models may give the designer clarity over the interactions.

In the design process the required fidelity of one or more physical phenomenon (Aerodynamic, Hydrodynamic, Elastodynamic etc.) is likely to require a more thorough understanding and implementation than an "off the shelf " simulation tool is cable of providing. Details such as viscous effects on second order wave forced motions and structural flexibility or a complicated wave and wind - structural interaction have the potential to make or completely ruin a potential design. Software used in the design process should therefore be as flexible and modular as possible in order to fully integrate these novel uncertainties and model approximations. By pushing the limits of current scientific understanding into such phenomenon, the optimized designs of future novel offshore structures is likely to emerge.

A successful design approach requires a truly multidisciplinary design team, with experts across the fields and in communication with not only the turbine suppliers, but also the relevant certification authority amongst many others.

In this work various details of the overall tension mooring wind turbine design are

highlighted and analysed in detail. These details arose from the authors own identification of the particulars of the presented design's. As the designers understanding of the unique challenges and opportunities inherent in the technology grow, they will be incorporated into the simulation tools, resulting in multiple design iterations. With floating wind turbines this design iteration should be repeated as often as is feasible until the convergence between technology and full understanding of it's unique behaviour.

The modification of the coupled pitch and tower bending frequencies due to a TLPs flexible tower has been parameterised for the first time that the author is aware of. These results will be extremely useful to the early design stage of future TLP WT technologies. The use of drag coefficient's derived from still water decay tests for use in wave conditions was shown to give inaccurate results. It is thus recommended to use sea state by sea state tuning of drag coefficients.

Due to limitations of any approximate method for second order sum frequency forces it is recommended to perform simulations using full QTF as soon as possible in the design process. Calculation of QTF loads are non-trivial for a TMFWT due to the modification of the pitch frequency by the flexible tower which must be accounted for in the calculation. Current modelling approaches for this issue involve applying additional pitch stiffness to a rigid body in order to match the flexible bodys pitch-tower coupled natural frequency.

8.4.3 Recommendations for Experimental Tank Testing

The purpose of experimental tank testing is to identify inaccuracies in the assumptions that govern the design tools and simulation physics and thus give greater confidence in a novel designs reliability and robustness. During a physical model test campaign there should be sufficient skilled personal availability in order to run numerical models with as high a fidelity as is solve-able in a near one test time to one simulation solve duration. Integration of both experiment and simulations signals into a real time result system is of a great benefit to the design team and would allow a more optimised use of the most likely expensive wave basin time. Having access to both physical and numerical results in parallel allows more flexibility in the experiment scheduling with a greater focus applied

to those areas of divergence. It is ideal if any unplanned or unknown events in set-up, basin characteristics, wave generation behaviour, wave reflections, model or mooring properties can be quickly and easily applied to the simulation model and these new unknowns accounted for. This allows any unrecognised or unpredicted behaviours to be given a high experimental priority. At a TRL level of 3, the assumptions used for TRL levels 1 and 2 are tested and validated. Accurately characterising the behaviour of novel floating platforms at an early TRL level, allows the project to confidently increase up the TRL levels at greater speeds.

8.4.4 Pathway to Standardization

The IEC 61400-3 (design standard for offshore floating wind turbines), states that an integrated load analysis has to be carried out before a turbine is certified. Not only a requirement for certification, these simulations are also required in order to develop a cost-effective, high-performance floating offshore wind turbine concept [174]. Testing and simulation methods have not reached a standard level across the industry, with each technology developer applying independent methods. As such it is a challenge for a project developer to correctly identify the risk profile of any potential deployed technology.

To deliver the lowest LCOE and investor risk profiles, FWT designers and project developers should be looking at standardisation as a way of simplifying the processes of design, construction, installation, maintenance and decommissioning. Rather than only relying on certification for commercial deployment, it is recommended to apply industry wide certification throughout the TRL levels. Recently the industry has been moving towards such, with guidelines for experimental tank testing of FWT such as the ITTC recommended procedures and guidelines for model tests of offshore wind turbines, although these have yet to become standard across different wave tank facilities [342]. The adoption and independent verification of such procedures by all participants in the development of FWT technologies is thus recommended.

Appendix A

HEXWIND Experimental Validation of Numerical Model

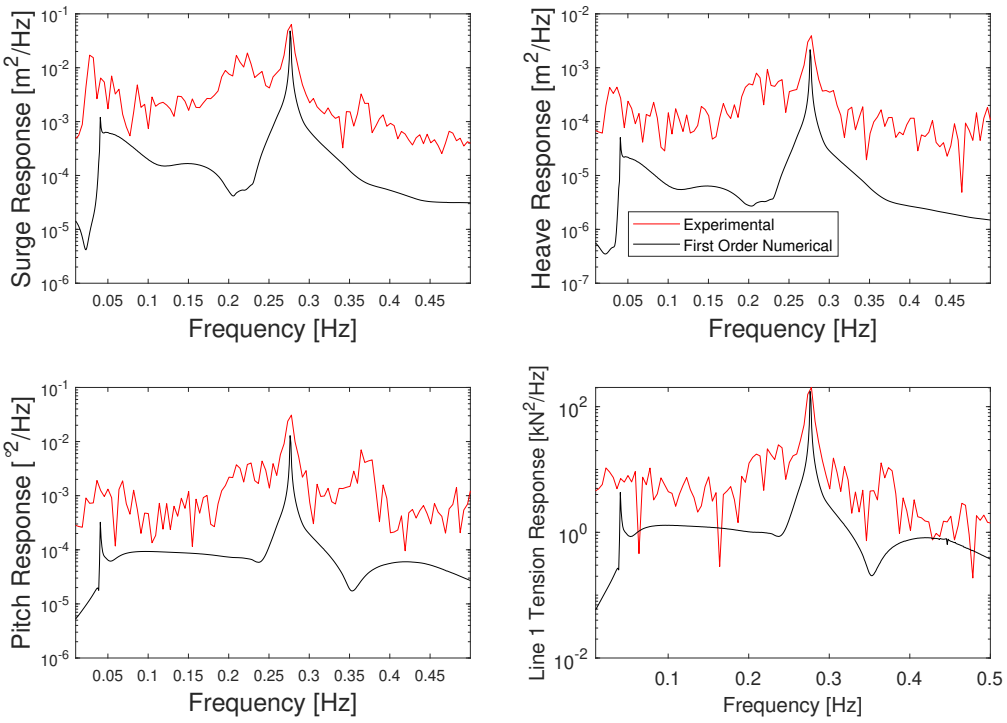


Figure A.1: Regular Wave 1, Numerical & Experimental Spectral Density Responses

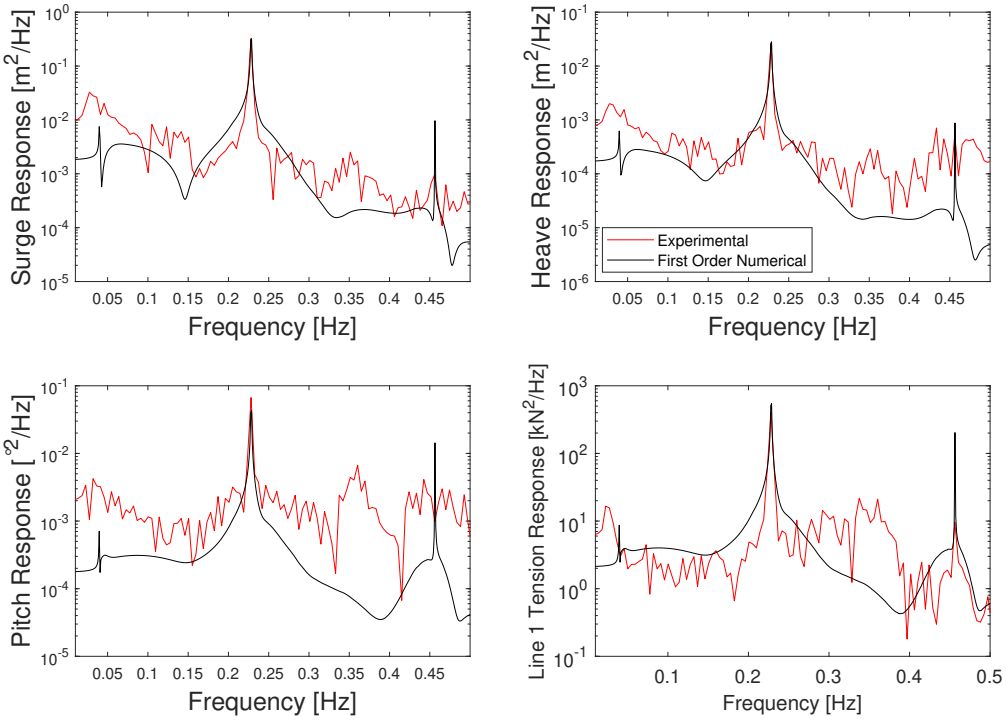


Figure A.2: Regular Wave 2, Numerical & Experimental Spectral Density Responses

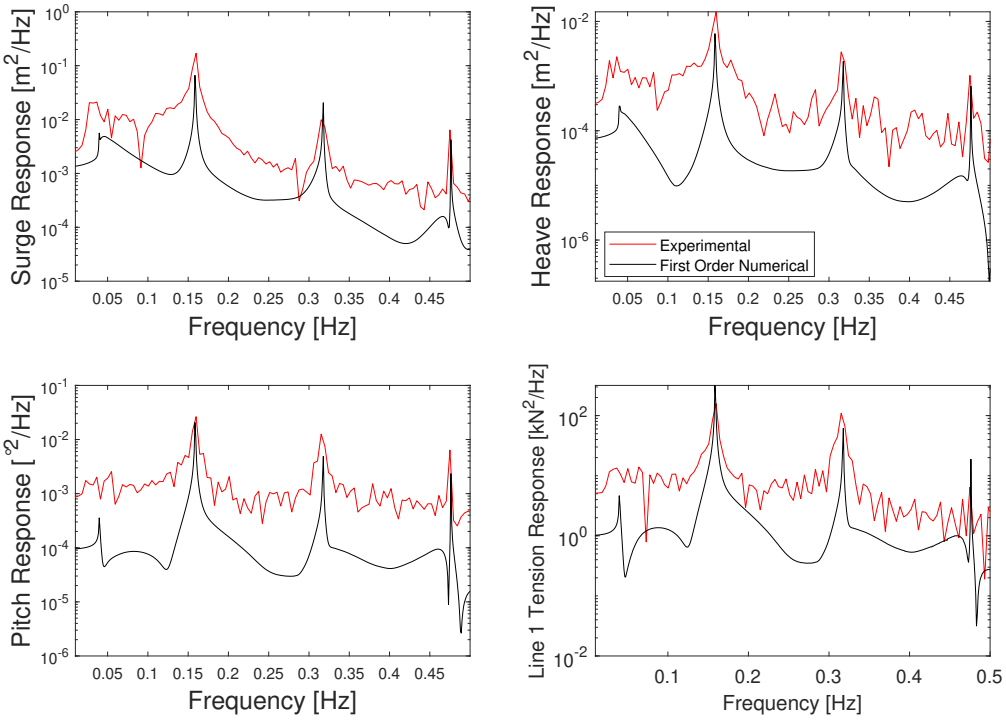


Figure A.3: Regular Wave 3, Numerical & Experimental Spectral Density Responses

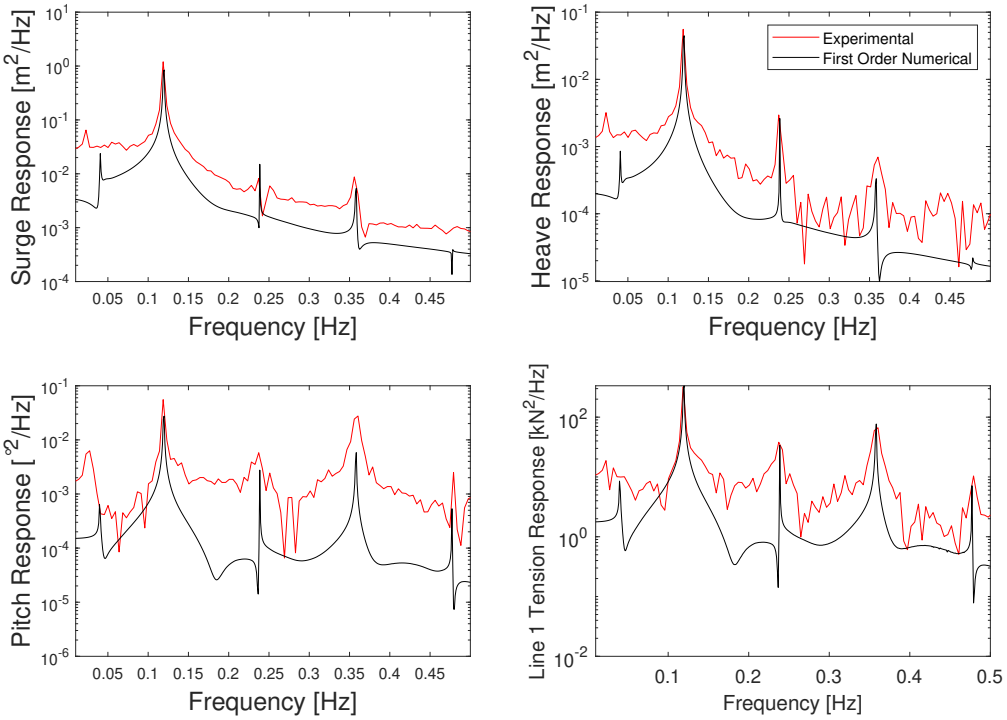


Figure A.4: Regular Wave 4, Numerical & Experimental Spectral Density Responses

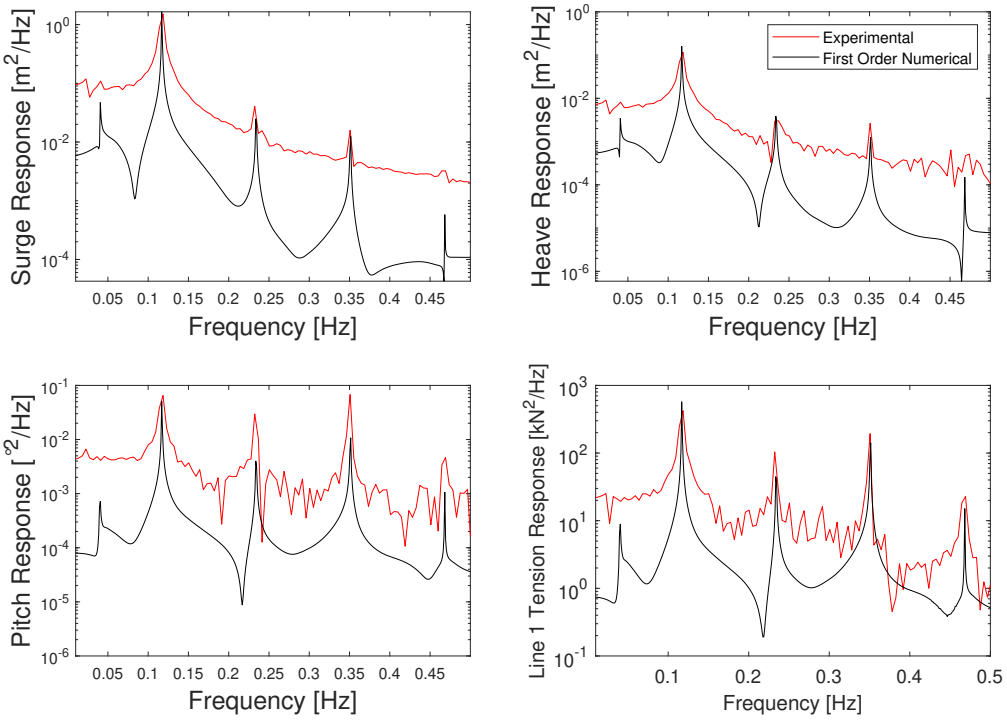


Figure A.5: Regular Wave 5, Numerical & Experimental Spectral Density Responses

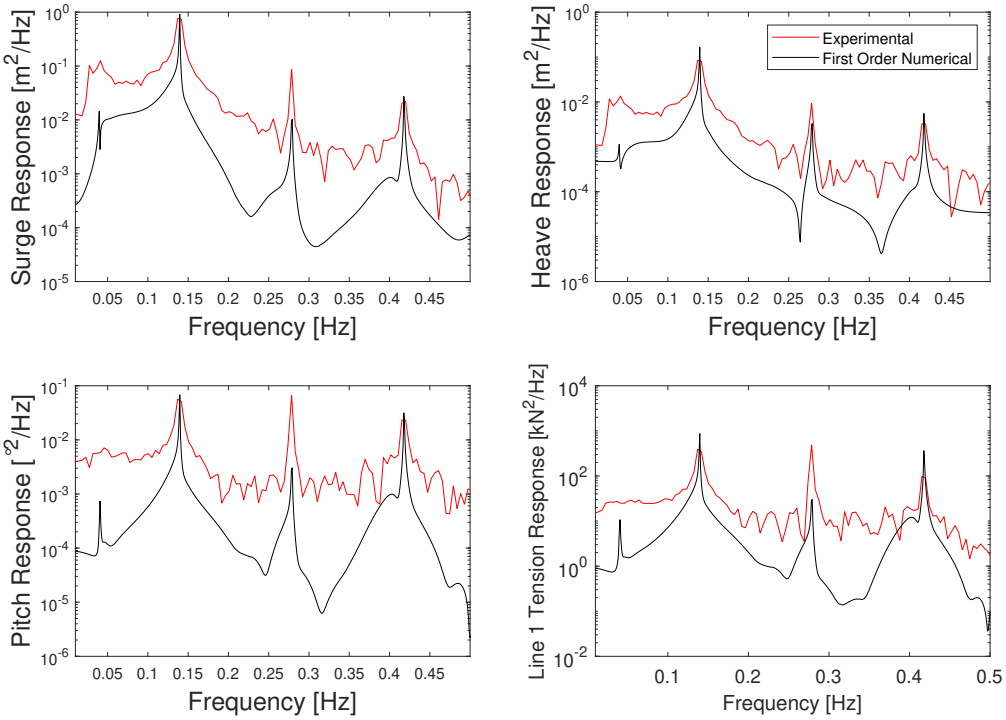


Figure A.6: Regular Wave 6, Numerical & Experimental Spectral Density Responses

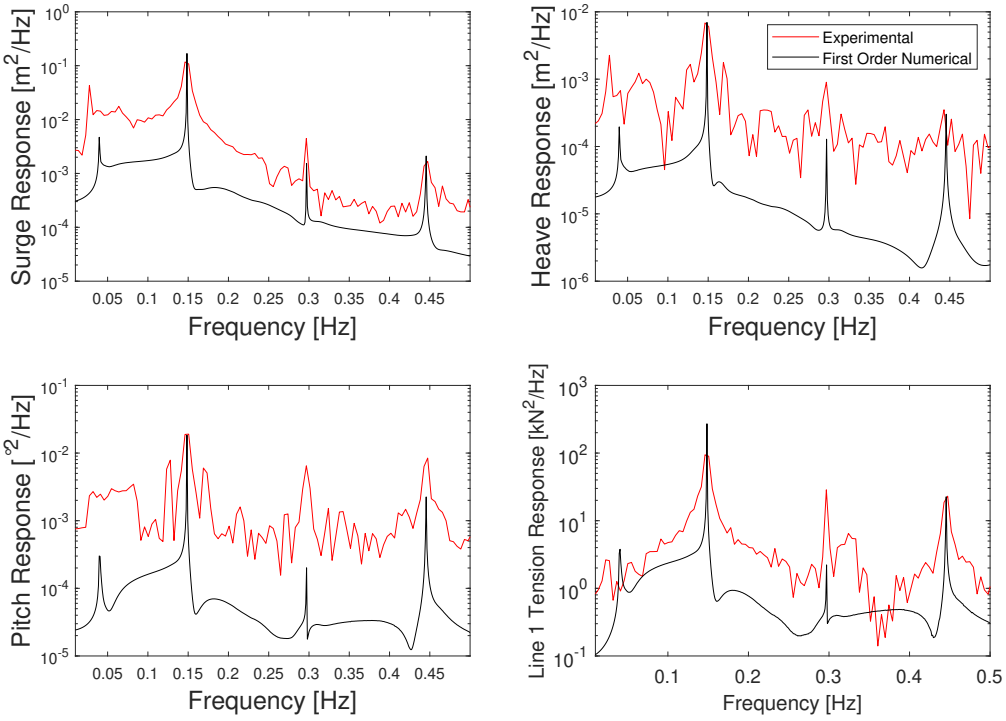


Figure A.7: Regular Wave 7, Numerical & Experimental Spectral Density Responses

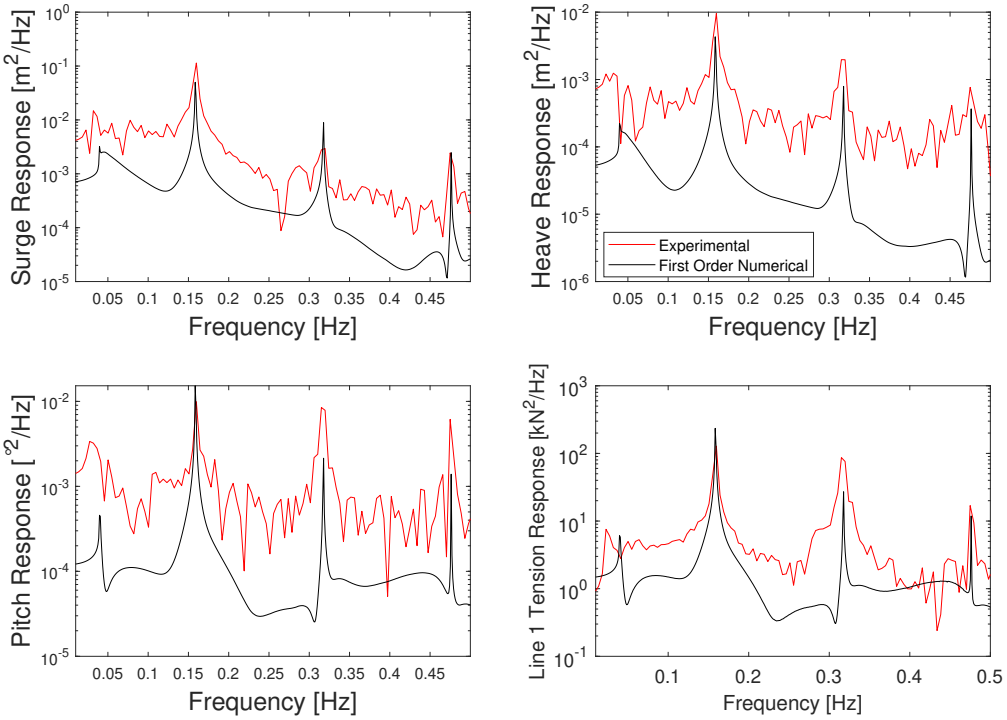


Figure A.8: Regular Wave 8, Numerical & Experimental Spectral Density Responses

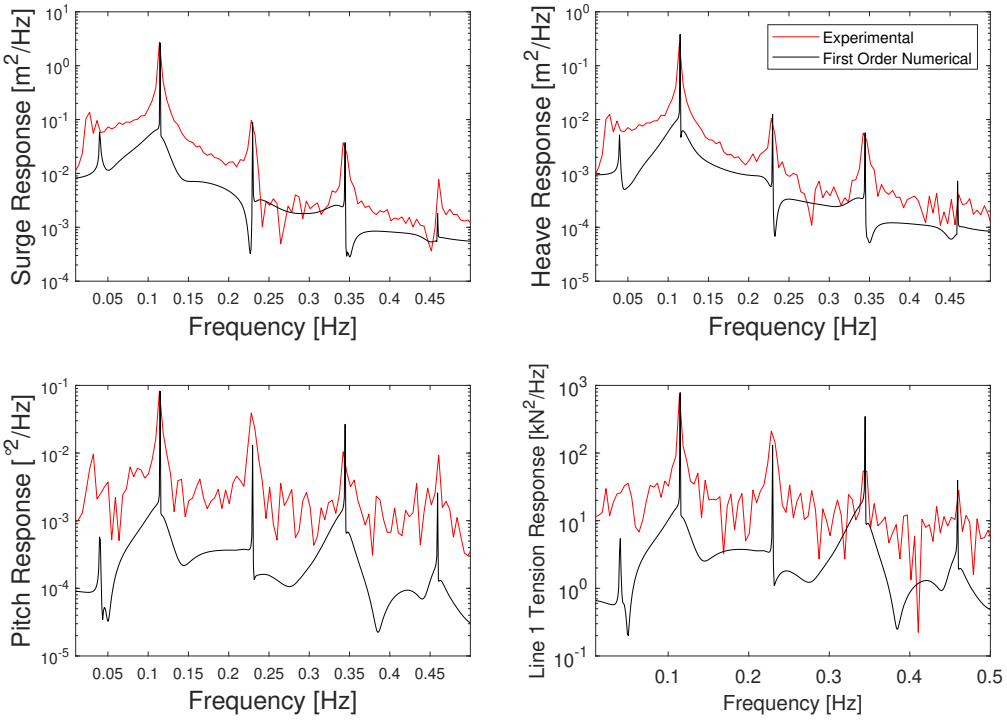


Figure A.9: Regular Wave 9, Numerical & Experimental Spectral Density Responses

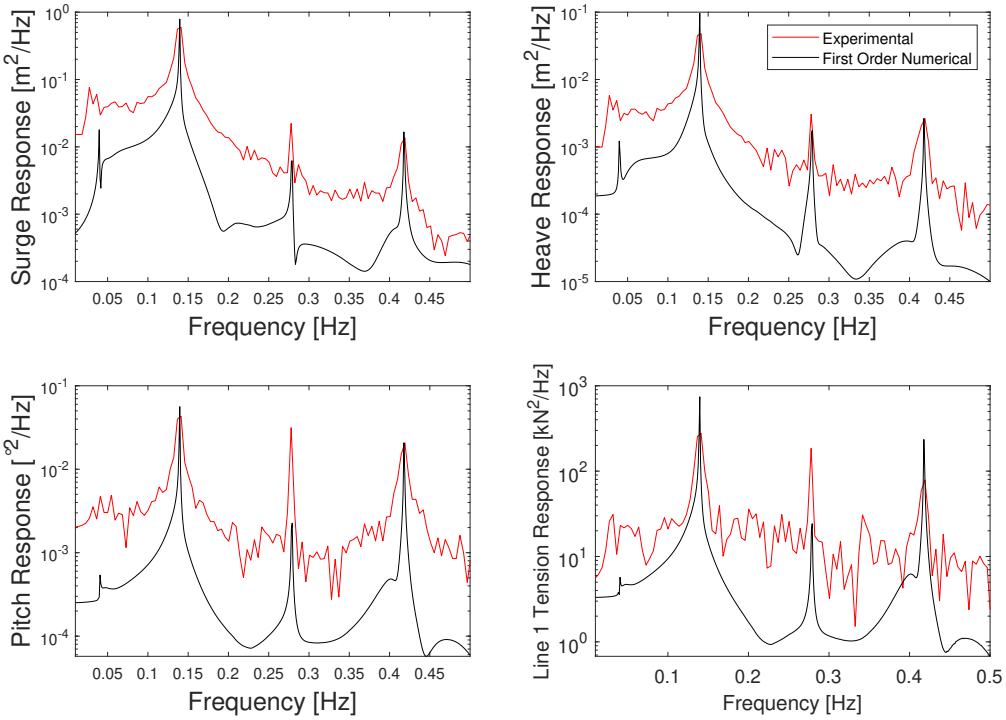


Figure A.10: Regular Wave 10, Numerical & Experimental Spectral Density Responses

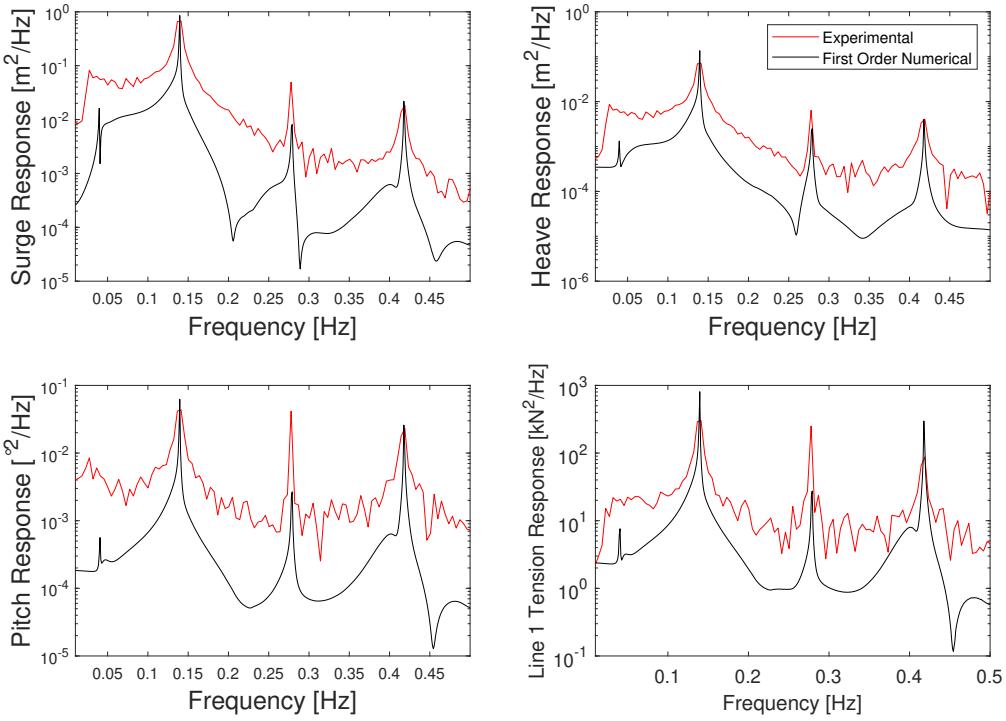


Figure A.11: Regular Wave 11, Numerical & Experimental Spectral Density Responses

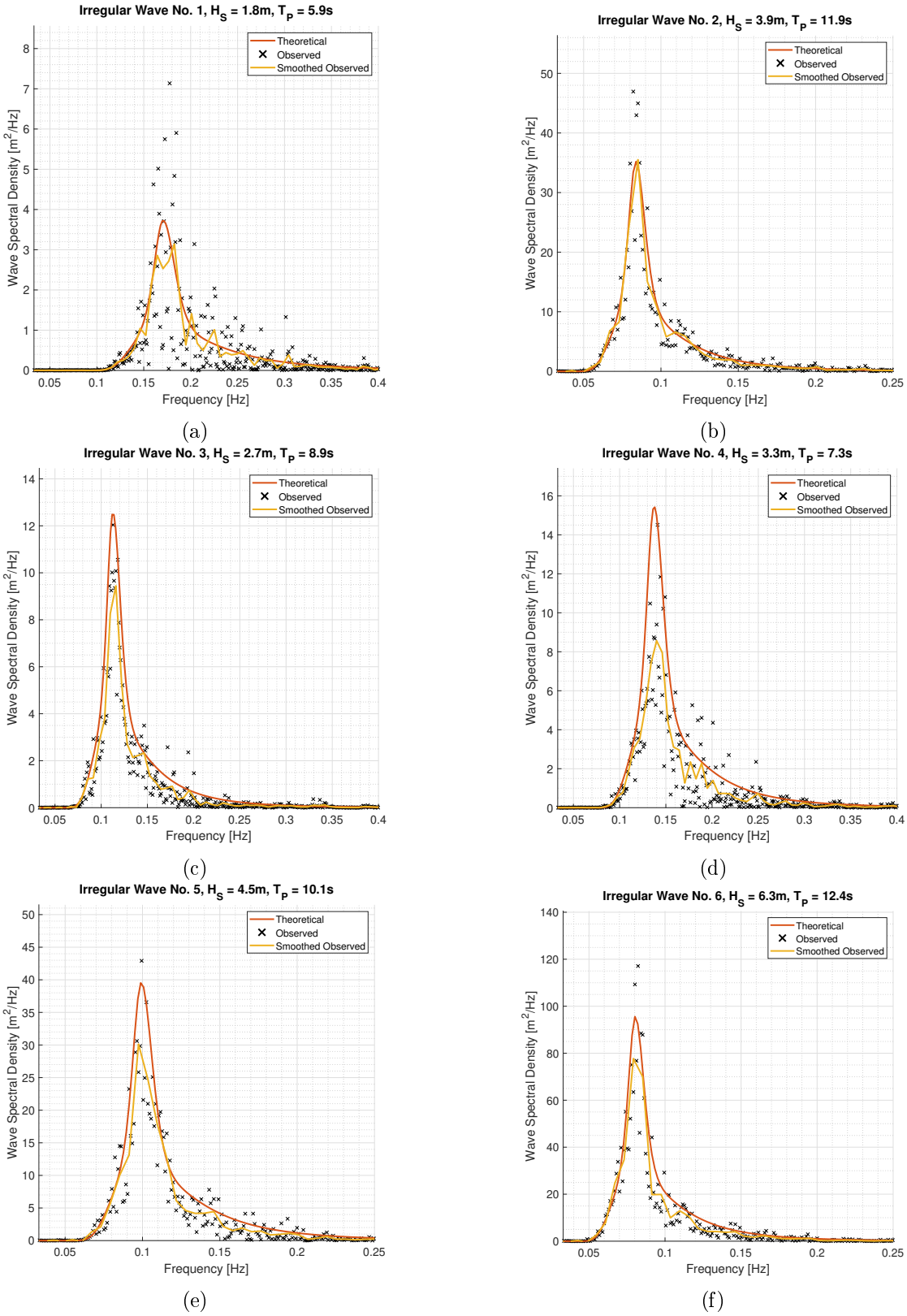
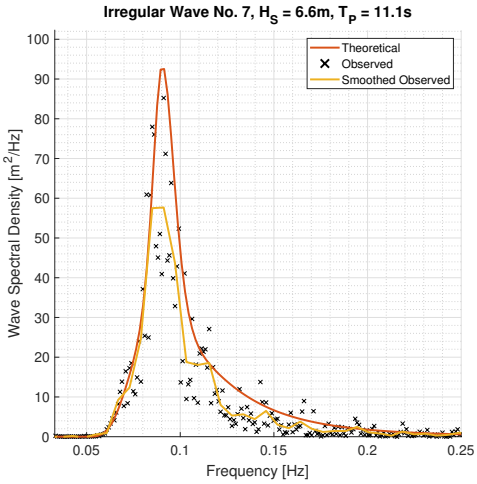
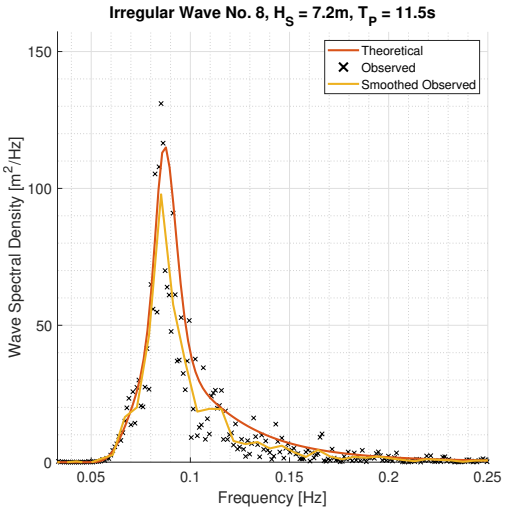


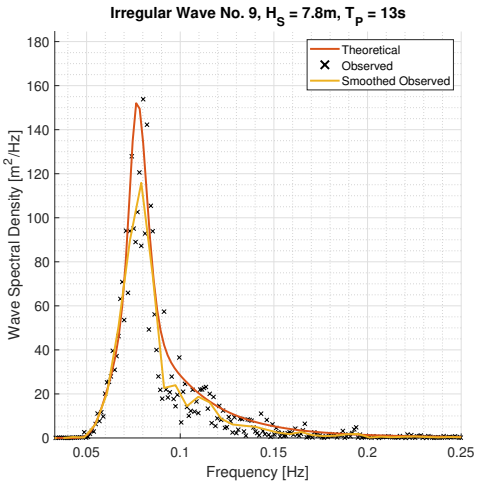
Figure A.12: Comparison Between Theoretical JONSWAP and Observed Spectral Density, Irregular Wave No. 1 - 6



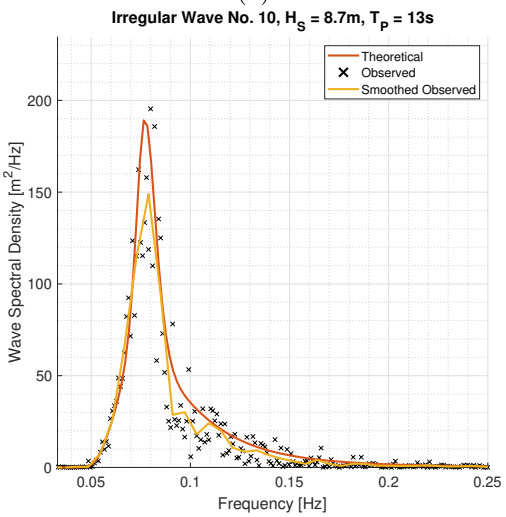
(a)



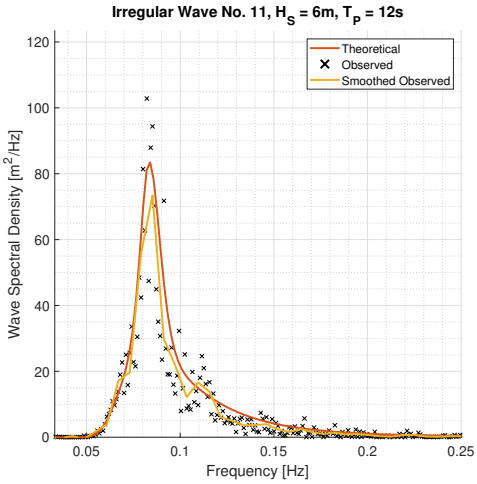
(b)



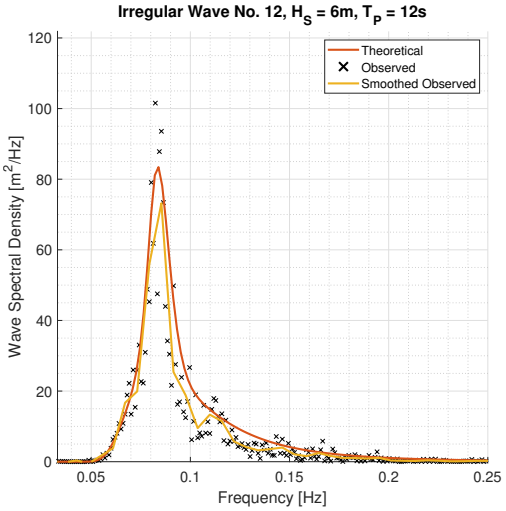
(c)



(d)



(e)



(f)

Figure A.13: Comparison Between Theoretical JONSWAP and Observed Spectral Density, Irregular Wave No. 7 - 12

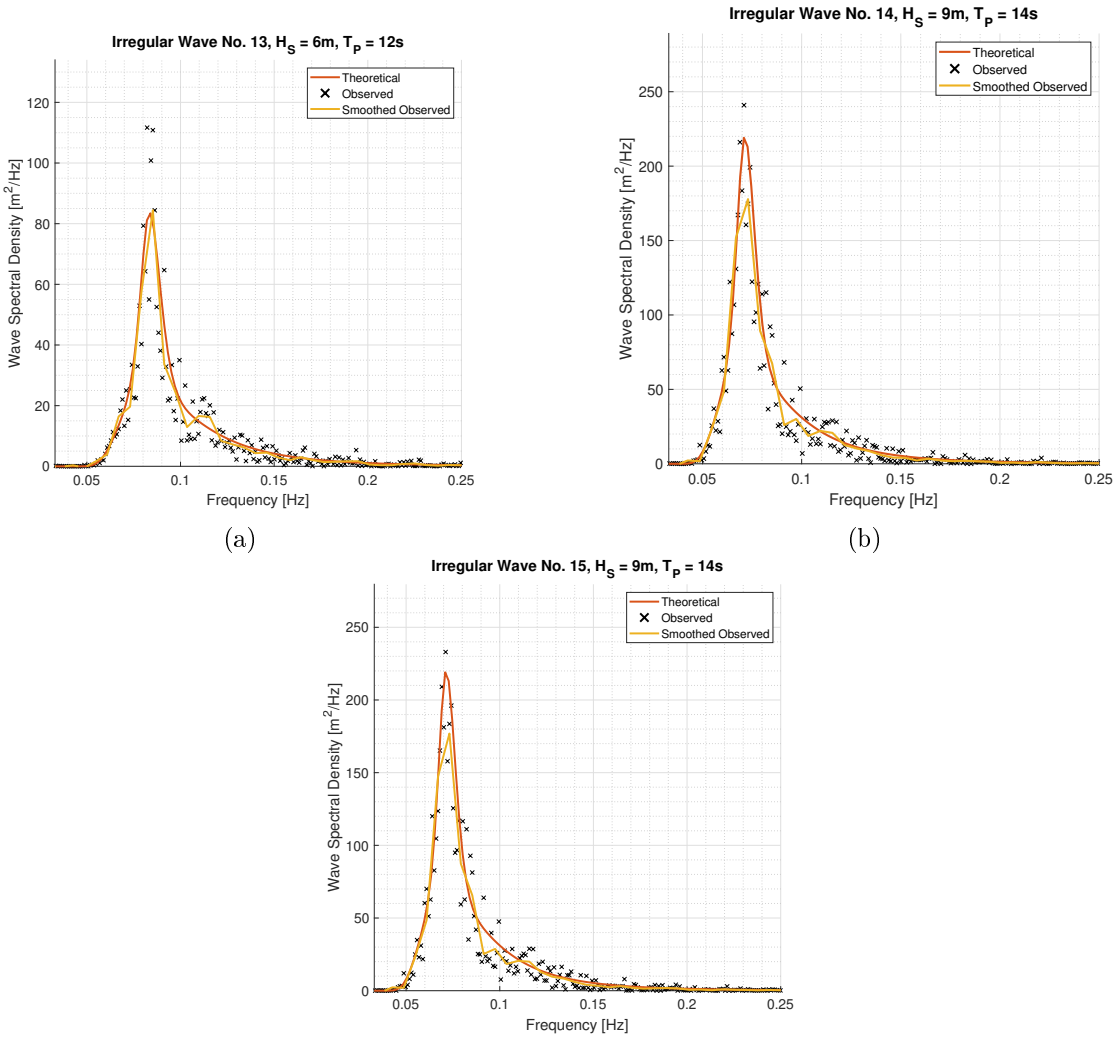


Figure A.14: Comparison Between Theoretical JONSWAP and Observed Spectral Density, Irregular Wave No. 13 - 15

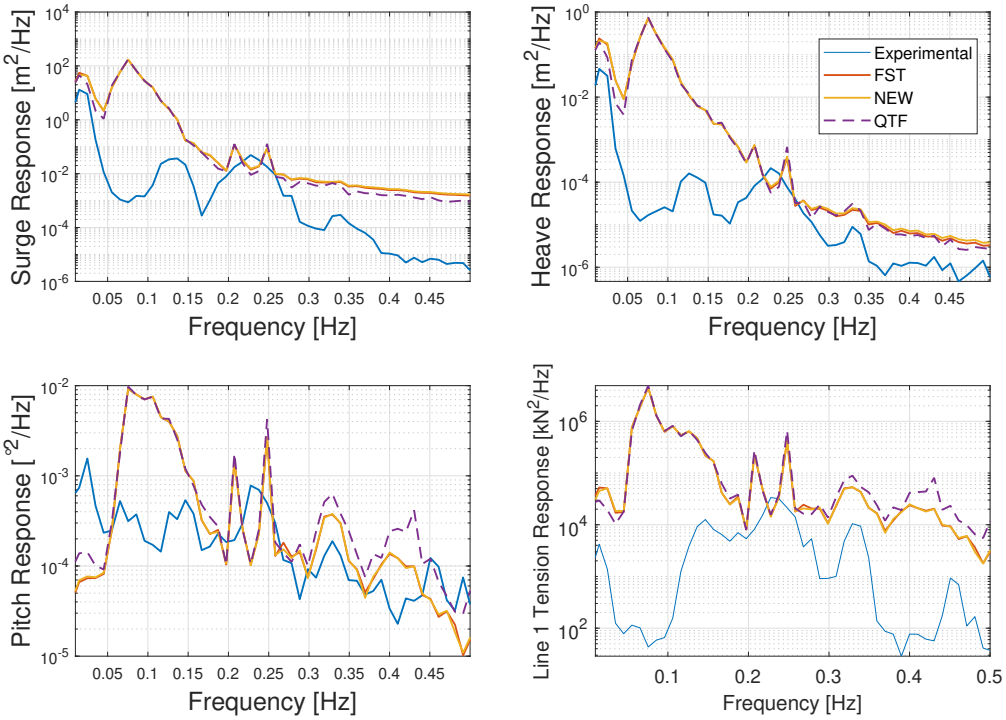


Figure A.15: Numerical & Experimental Surge, Heave, Pitch and line 1 Tension Spectral Response Density for Irregular Wave 1. Simulations with theoretical JONSWAP wave spectra

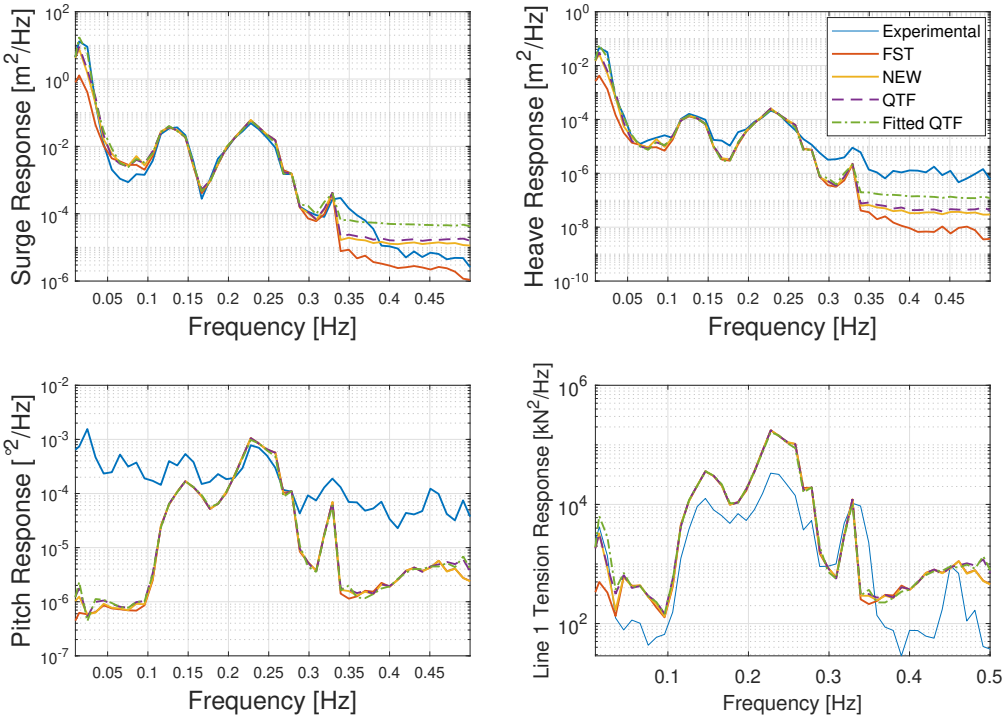


Figure A.16: Numerical & Experimental Surge, Heave, Pitch and line 1 Tension Spectral Response Density for Irregular Wave 1. Simulations with observed wave time series

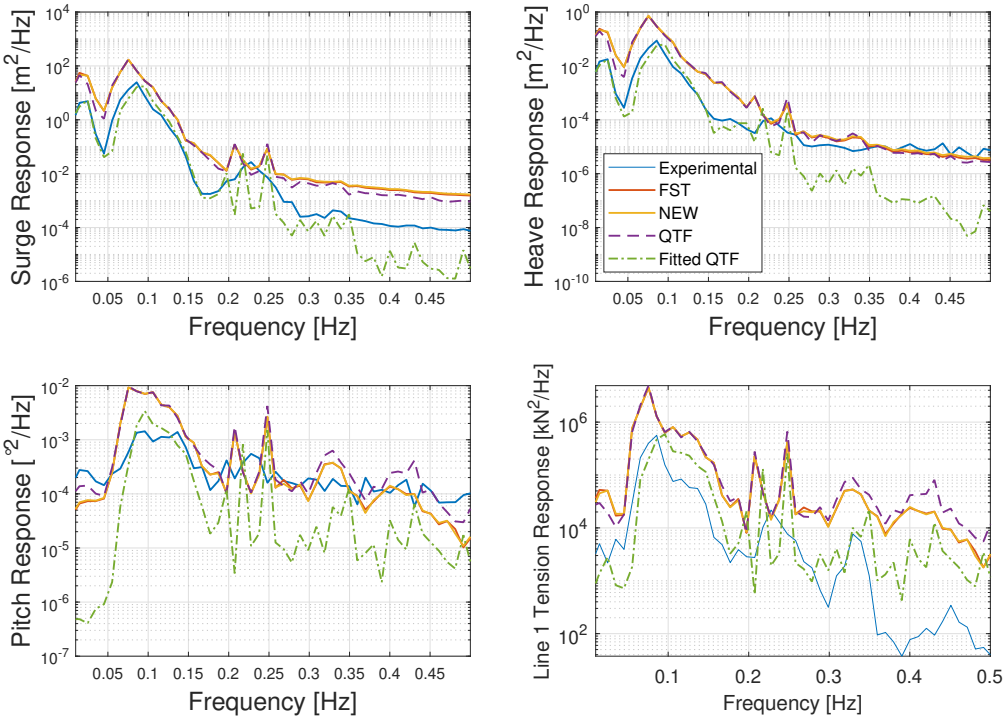


Figure A.17: Numerical & Experimental Surge, Heave, Pitch and line 1 Tension Spectral Response Density for Irregular Wave 2. Simulations with theoretical JONSWAP wave spectra

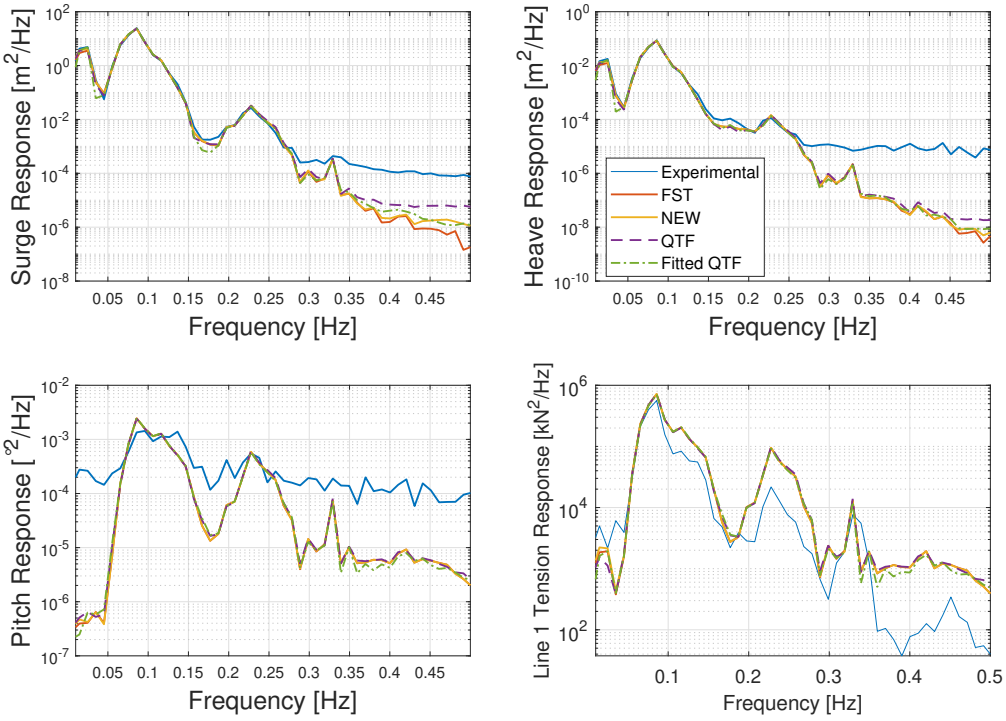


Figure A.18: Numerical & Experimental Surge, Heave, Pitch and line 1 Tension Spectral Response Density for Irregular Wave 2. Simulations with observed wave time series

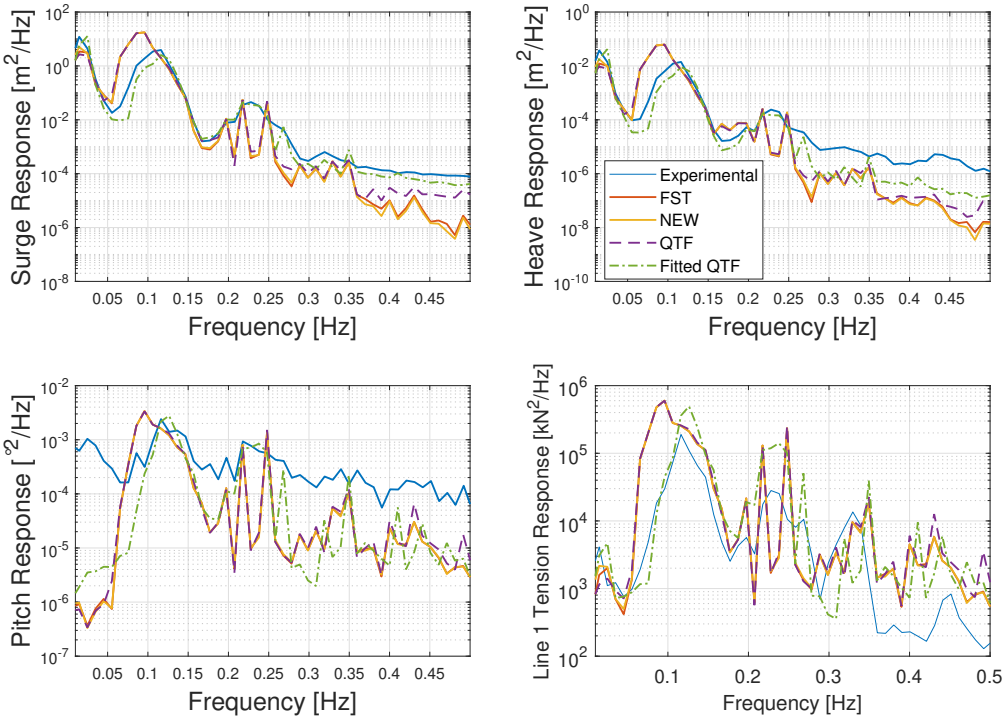


Figure A.19: Numerical & Experimental Surge, Heave, Pitch and line 1 Tension Spectral Response Density for Irregular Wave 3. Simulations with theoretical JONSWAP wave spectra

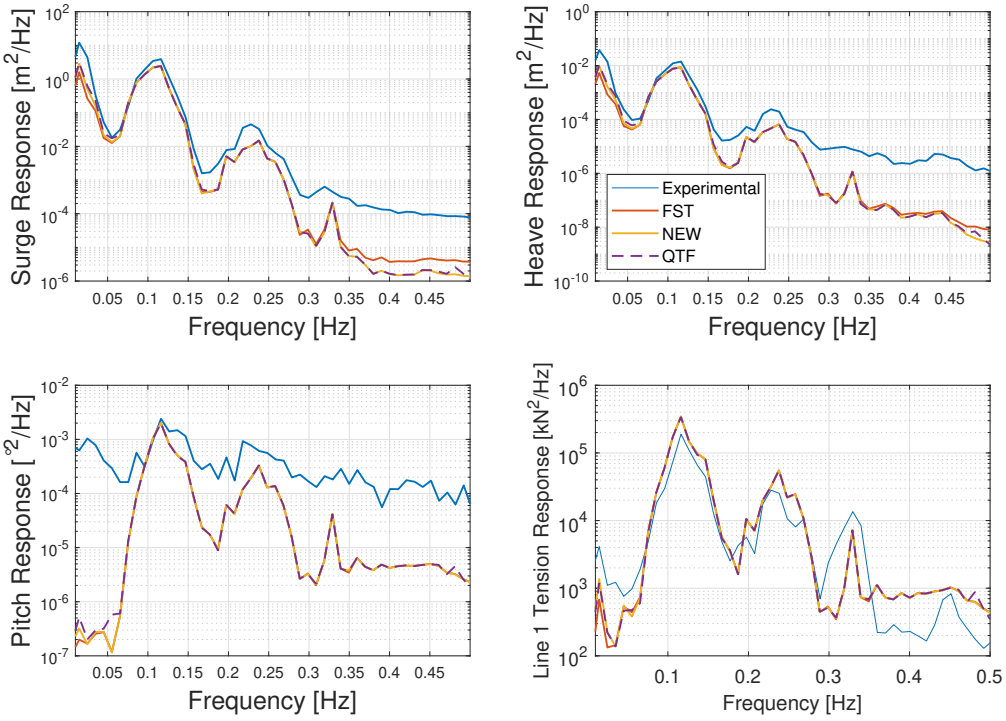


Figure A.20: Numerical & Experimental Surge, Heave, Pitch and line 1 Tension Spectral Response Density for Irregular Wave 3. Simulations with observed wave time series

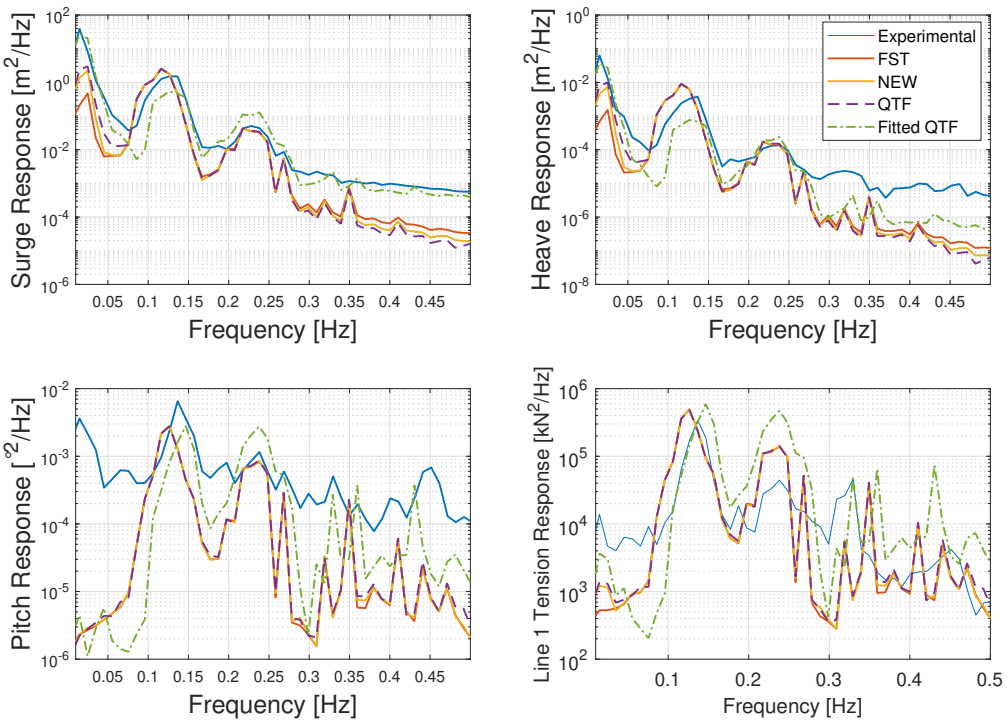


Figure A.21: Numerical & Experimental Surge, Heave, Pitch and line 1 Tension Spectral Response Density for Irregular Wave 4. Simulations with theoretical JONSWAP wave spectra

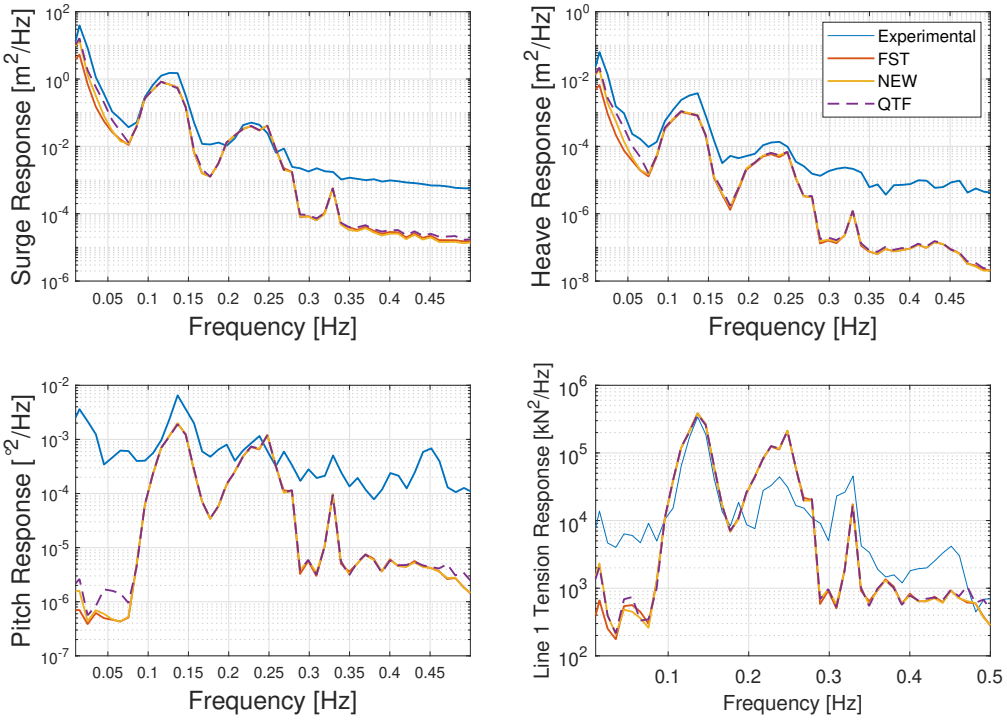


Figure A.22: Numerical & Experimental Surge, Heave, Pitch and line 1 Tension Spectral Response Density for Irregular Wave 4. Simulations with observed wave time series

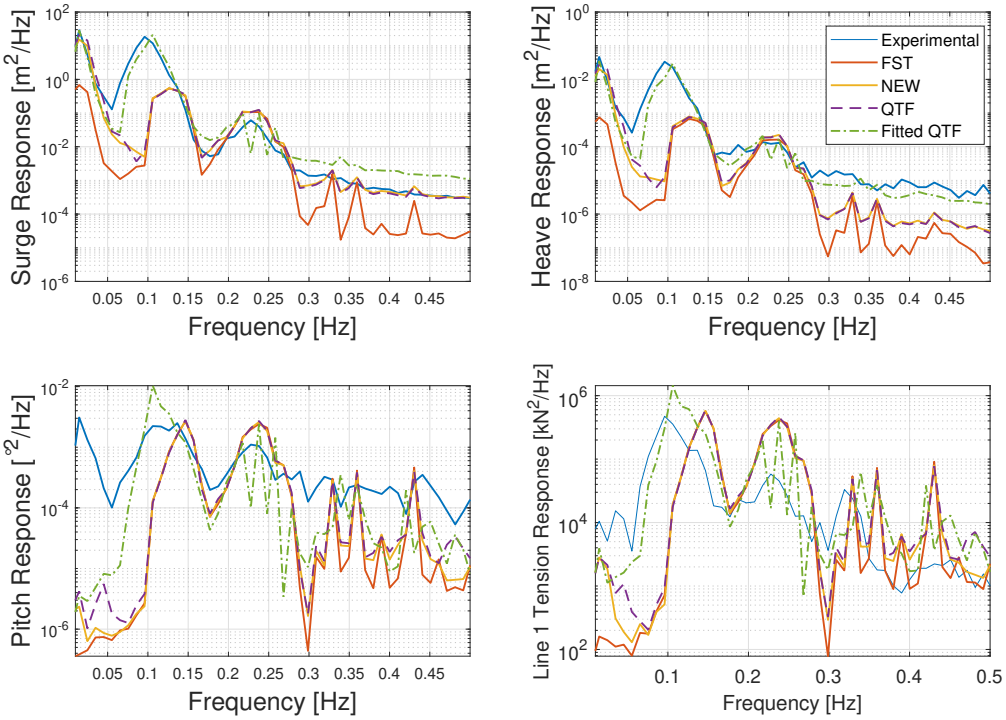


Figure A.23: Numerical & Experimental Surge, Heave, Pitch and line 1 Tension Spectral Response Density for Irregular Wave 5. Simulations with theoretical JONSWAP wave spectra

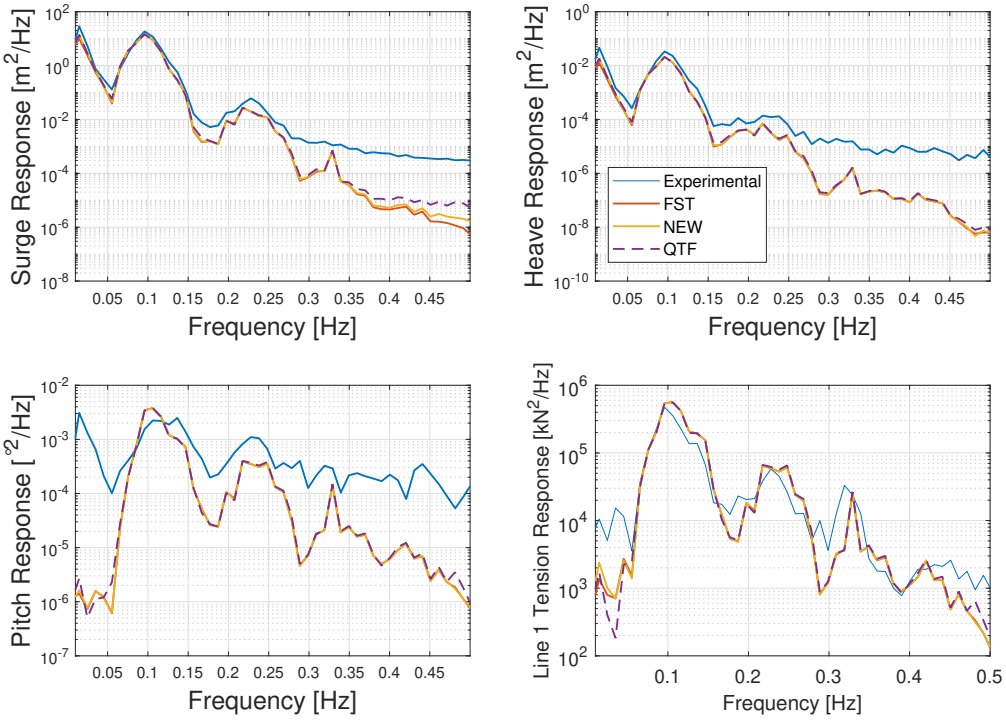


Figure A.24: Numerical & Experimental Surge, Heave, Pitch and line 1 Tension Spectral Response Density for Irregular Wave 5. Simulations with observed wave time series

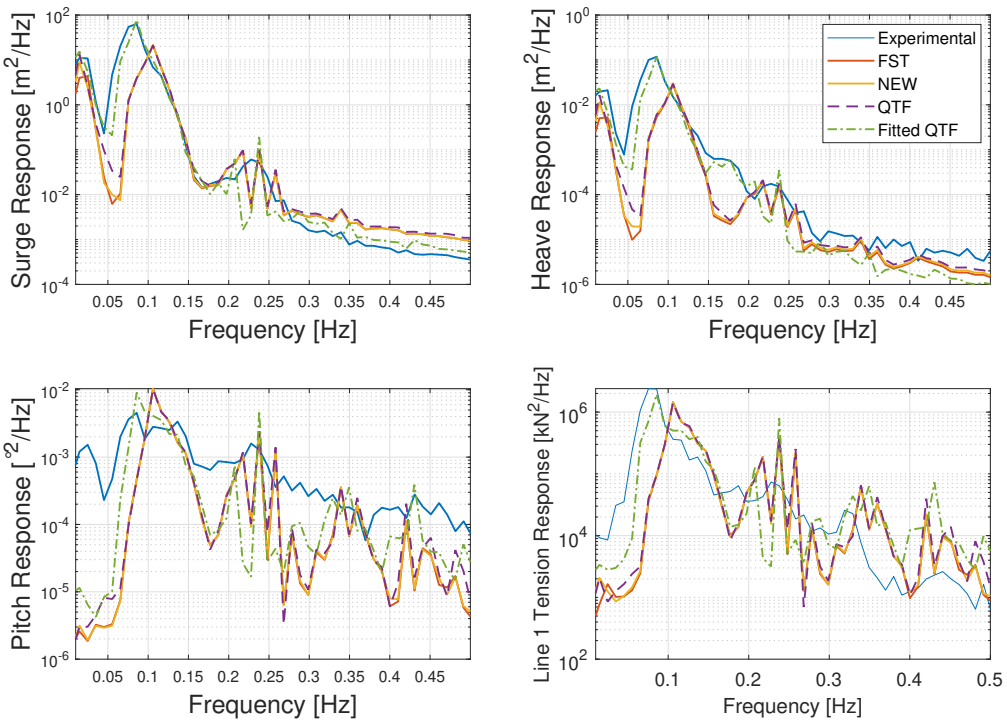


Figure A.25: Numerical & Experimental Surge, Heave, Pitch and line 1 Tension Spectral Response Density for Irregular Wave 6. Simulations with theoretical JONSWAP wave spectra

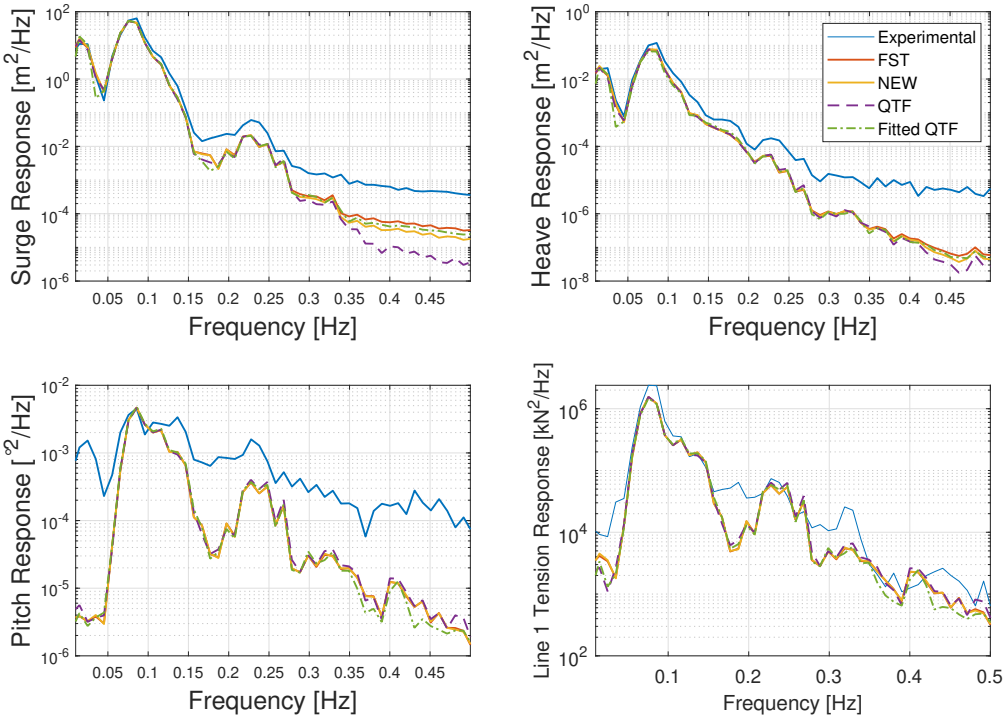


Figure A.26: Numerical & Experimental Surge, Heave, Pitch and line 1 Tension Spectral Response Density for Irregular Wave 6. Simulations with observed wave time series

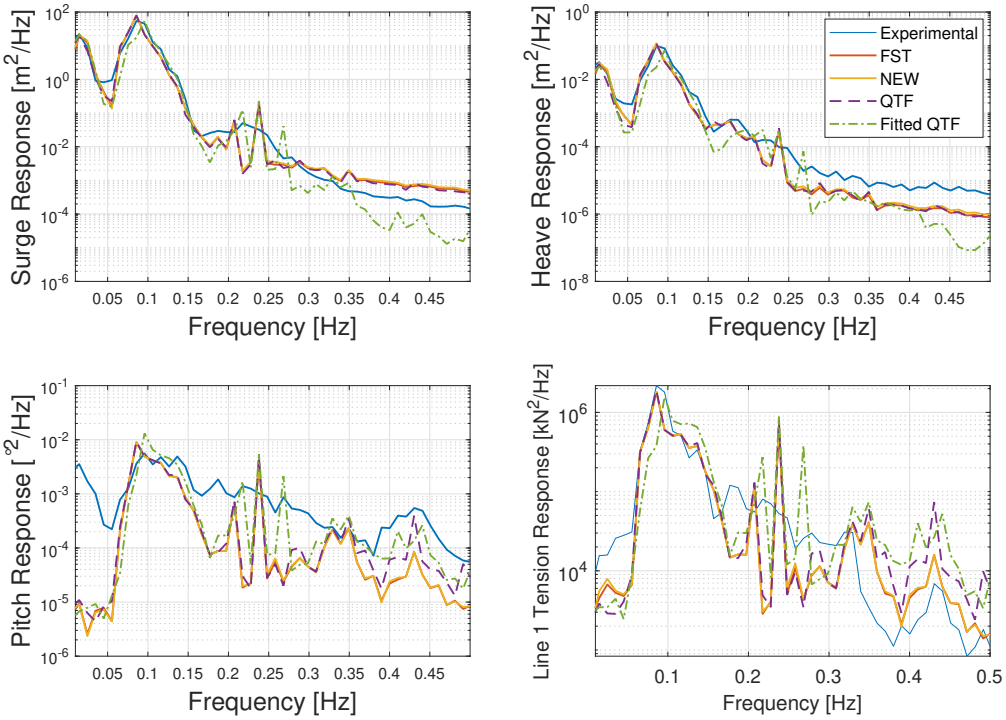


Figure A.27: Numerical & Experimental Surge, Heave, Pitch and line 1 Tension Spectral Response Density for Irregular Wave 7. Simulations with theoretical JONSWAP wave spectra

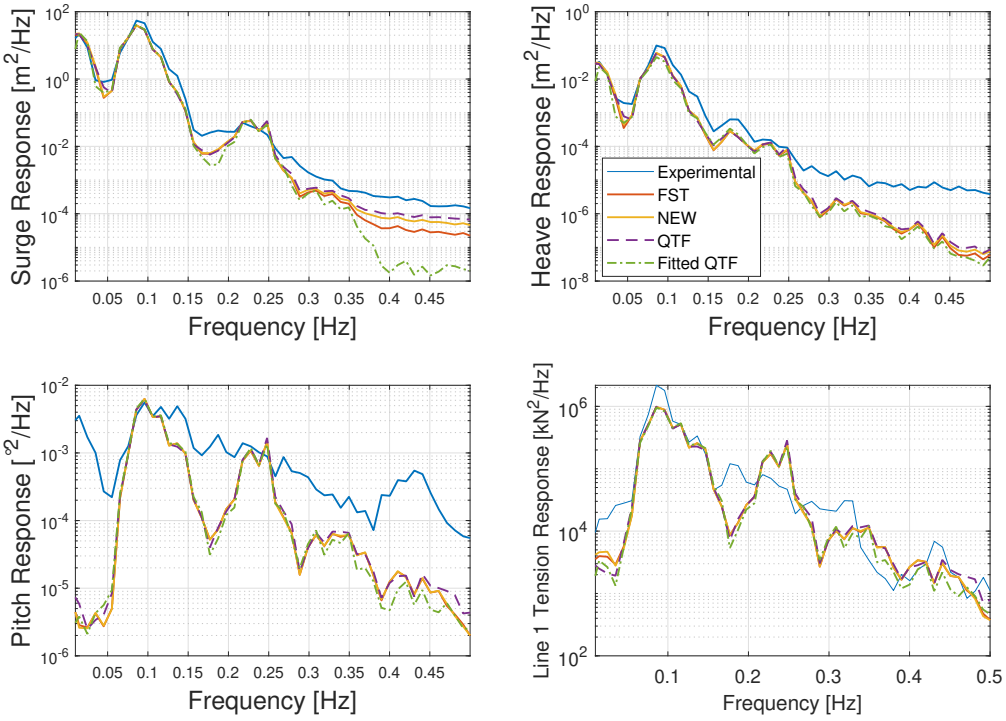


Figure A.28: Numerical & Experimental Surge, Heave, Pitch and line 1 Tension Spectral Response Density for Irregular Wave 7. Simulations with observed wave time series

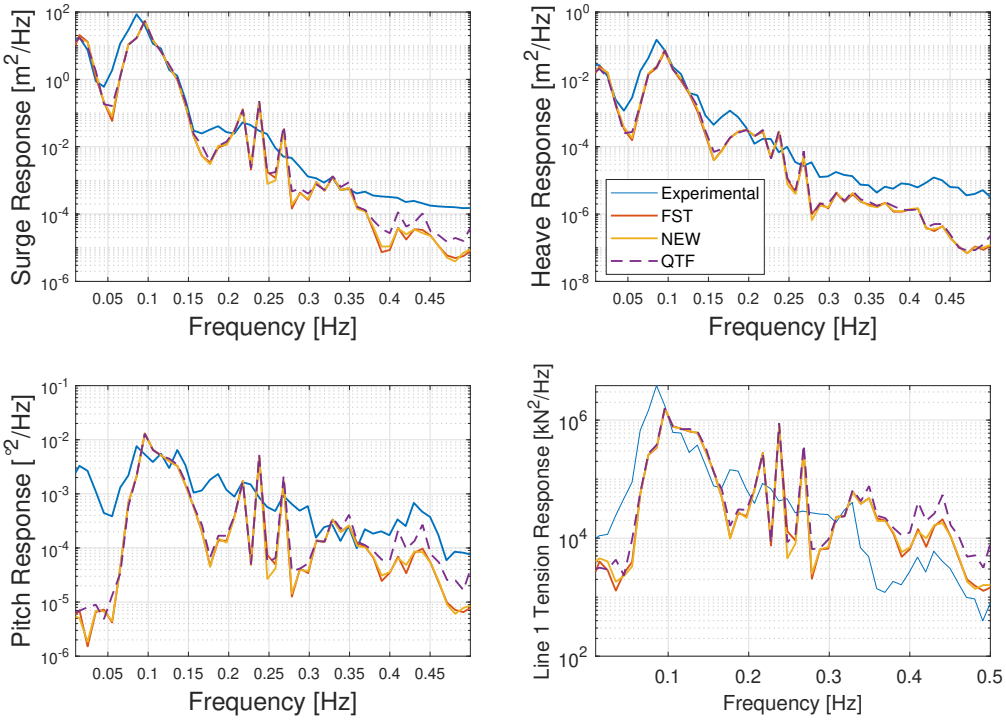


Figure A.29: Numerical & Experimental Surge, Heave, Pitch and line 1 Tension Spectral Response Density for Irregular Wave 8. Simulations with theoretical JONSWAP wave spectra

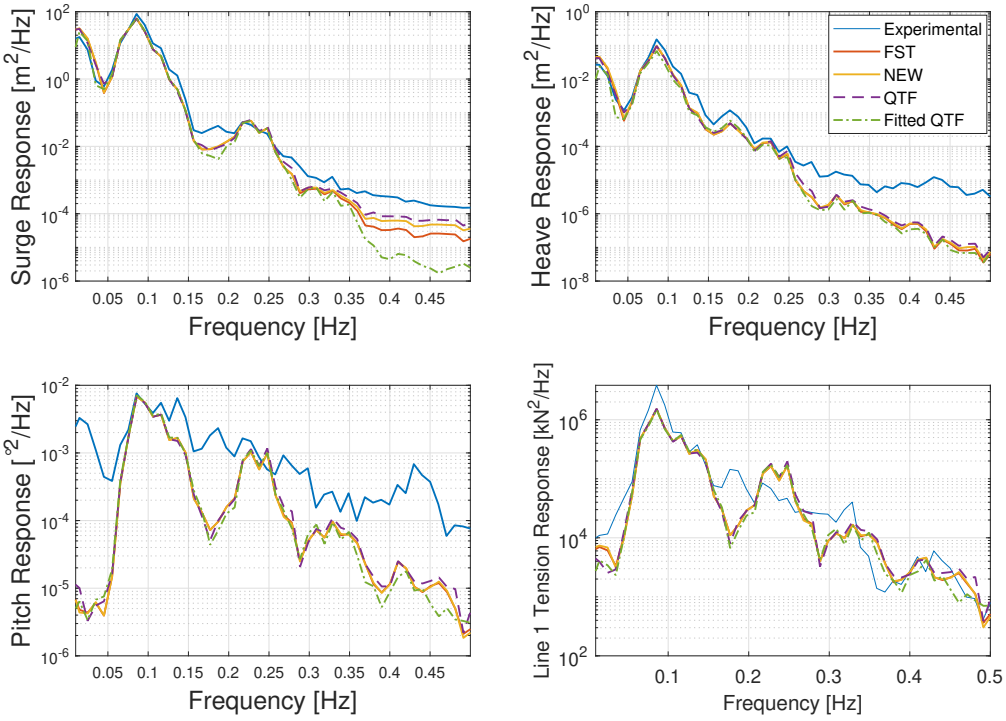


Figure A.30: Numerical & Experimental Surge, Heave, Pitch and line 1 Tension Spectral Response Density for Irregular Wave 8. Simulations with observed wave time series

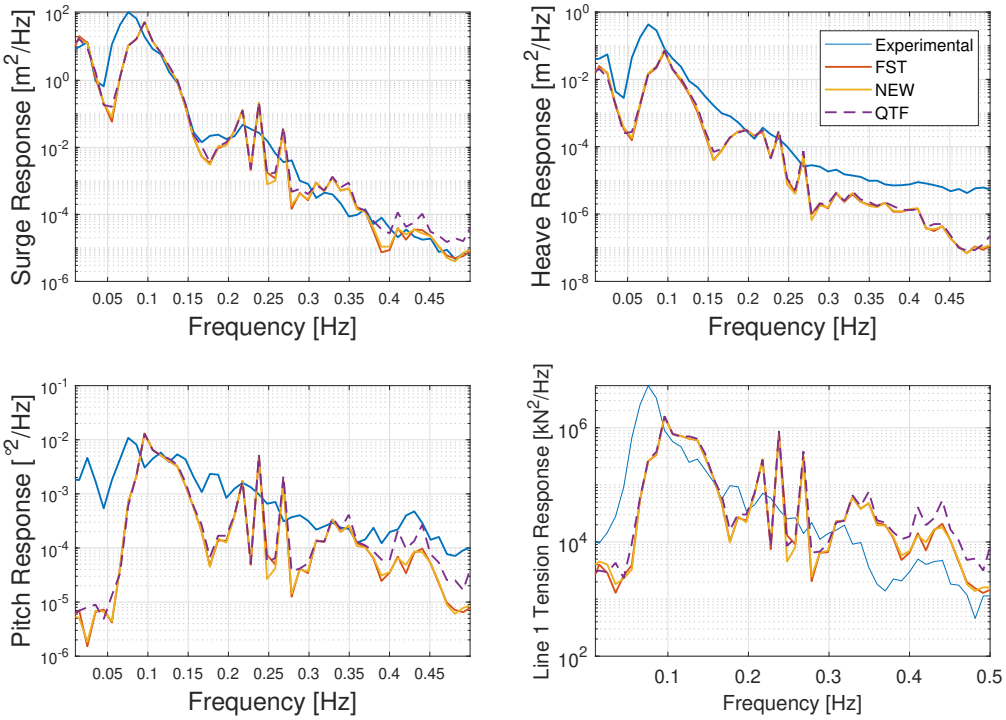


Figure A.31: Numerical & Experimental Surge, Heave, Pitch and line 1 Tension Spectral Response Density for Irregular Wave 9. Simulations with theoretical JONSWAP wave spectra

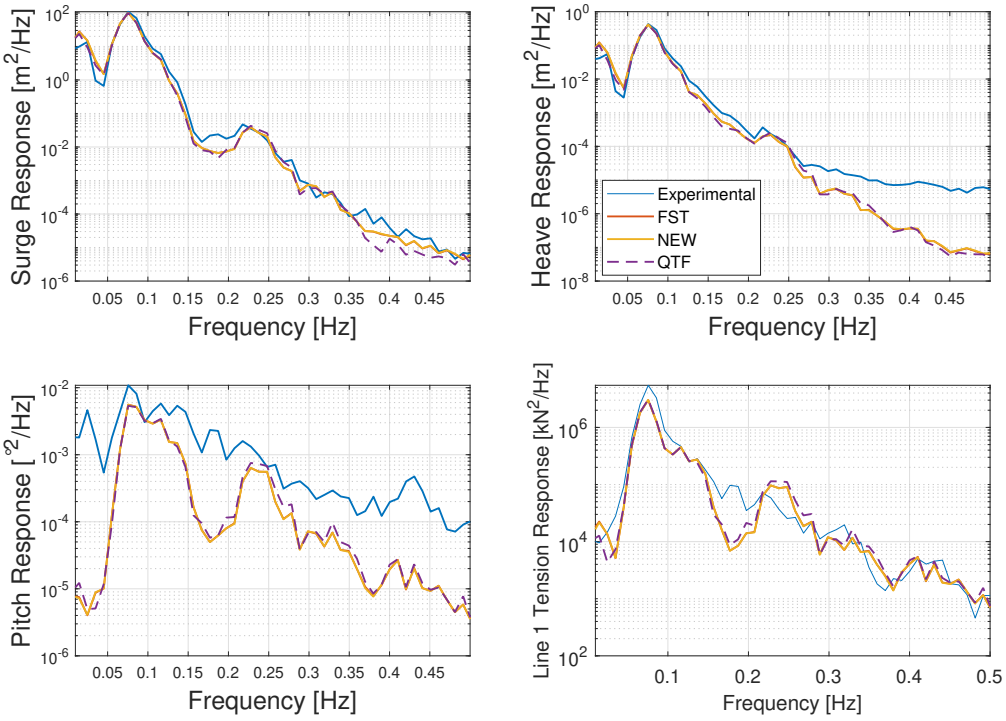


Figure A.32: Numerical & Experimental Surge, Heave, Pitch and line 1 Tension Spectral Response Density for Irregular Wave 9. Simulations with observed wave time series

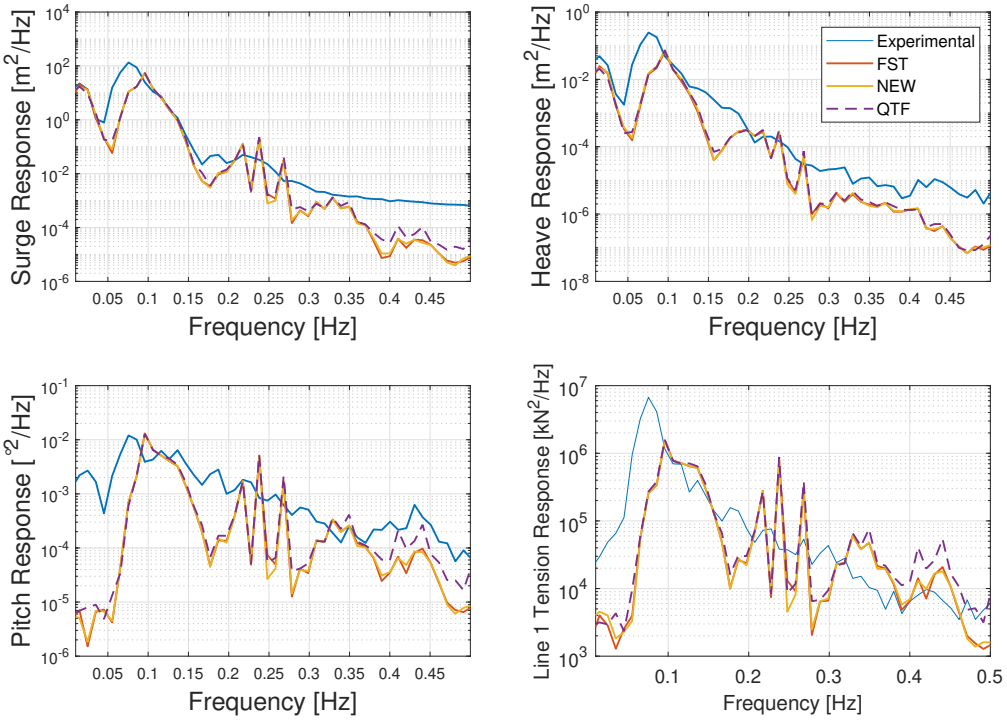


Figure A.33: Numerical & Experimental Surge, Heave, Pitch and line 1 Tension Spectral Response Density for Irregular Wave 10. Simulations with theoretical JONSWAP wave spectra

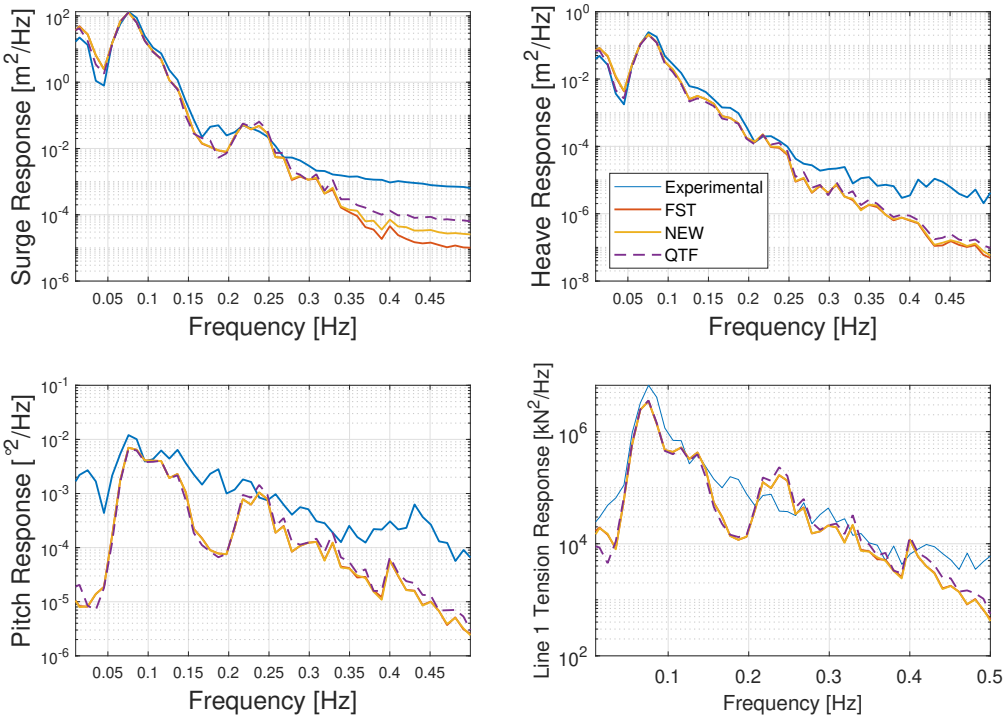


Figure A.34: Numerical & Experimental Surge, Heave, Pitch and line 1 Tension Spectral Response Density for Irregular Wave 10. Simulations with observed wave time series

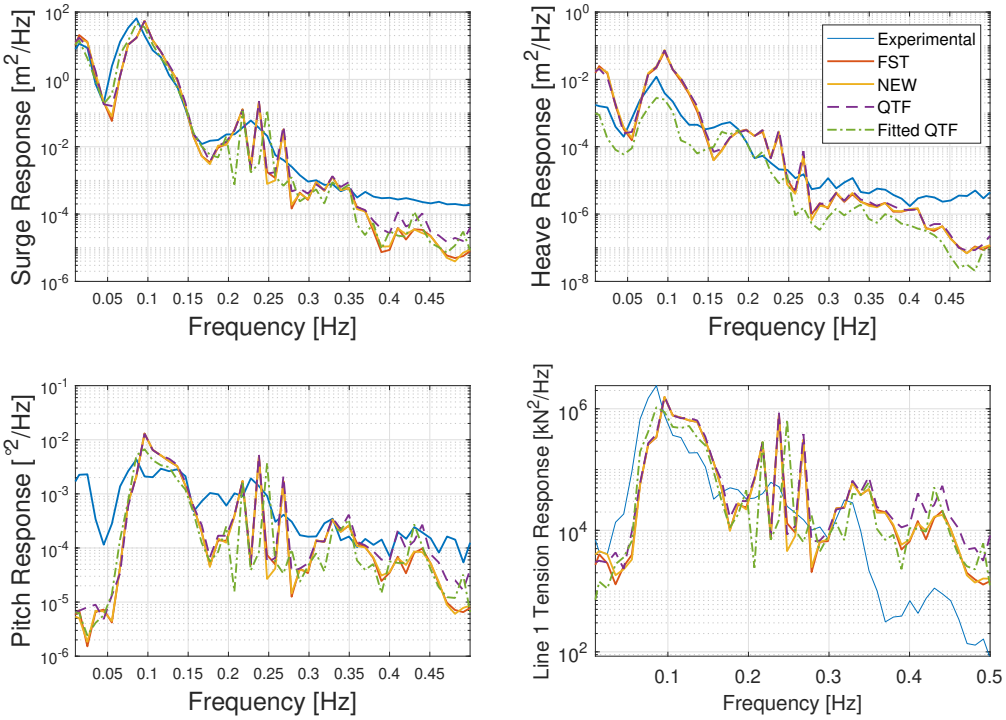


Figure A.35: Numerical & Experimental Surge, Heave, Pitch and line 1 Tension Spectral Response Density for Irregular Wave 11. Simulations with theoretical JONSWAP wave spectra

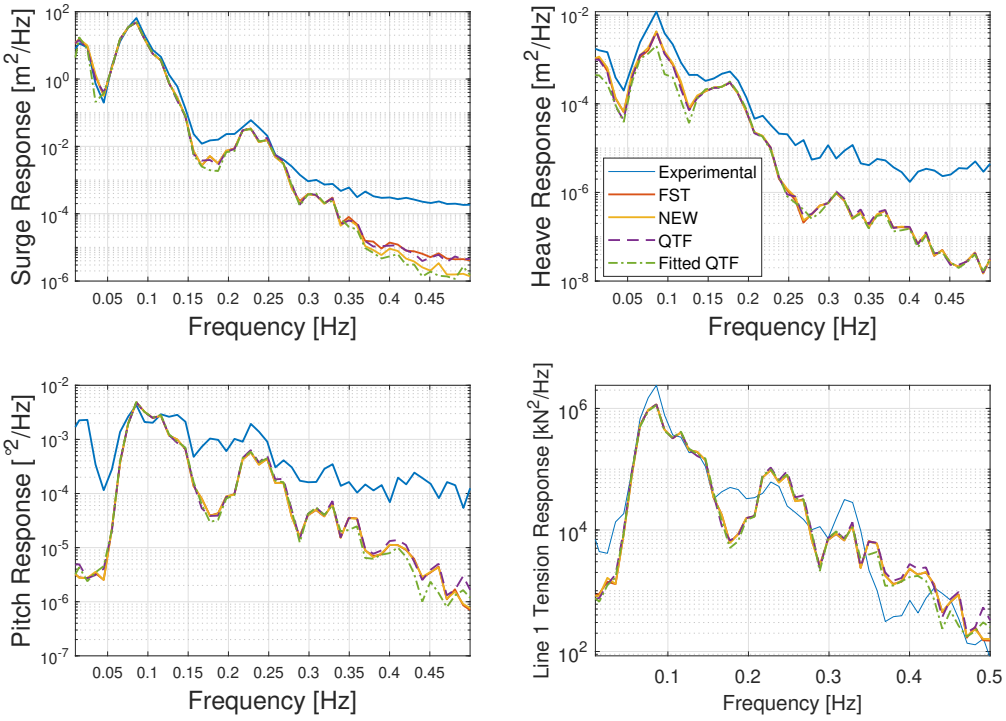


Figure A.36: Numerical & Experimental Surge, Heave, Pitch and line 1 Tension Spectral Response Density for Irregular Wave 11. Simulations with observed wave time series

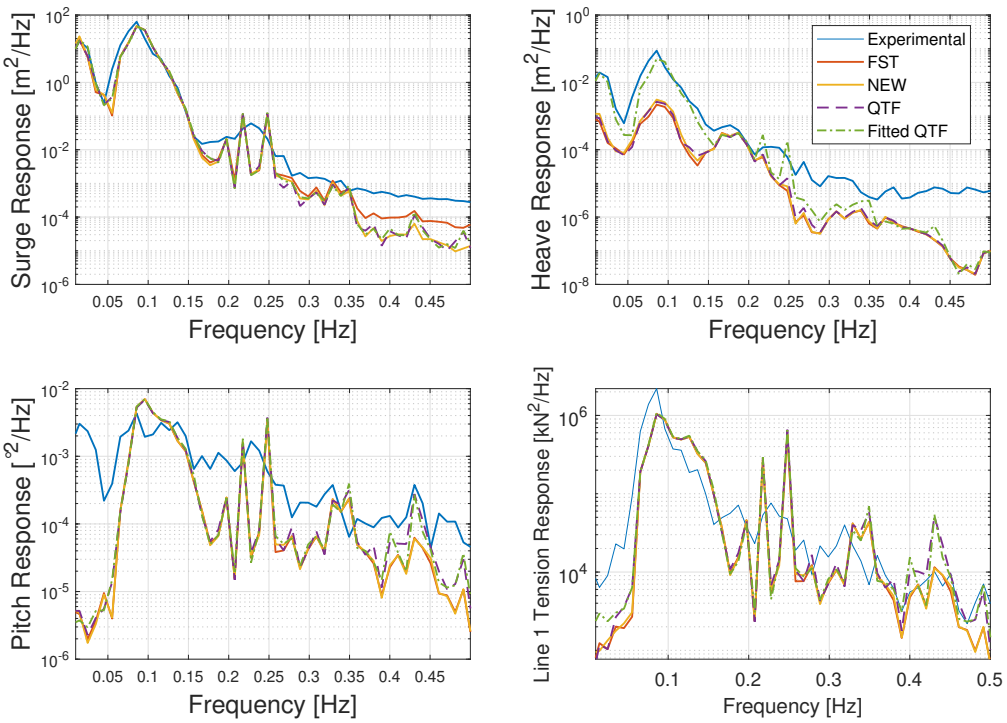


Figure A.37: Numerical & Experimental Surge, Heave, Pitch and line 1 Tension Spectral Response Density for Irregular Wave 12. Simulations with theoretical JONSWAP wave spectra

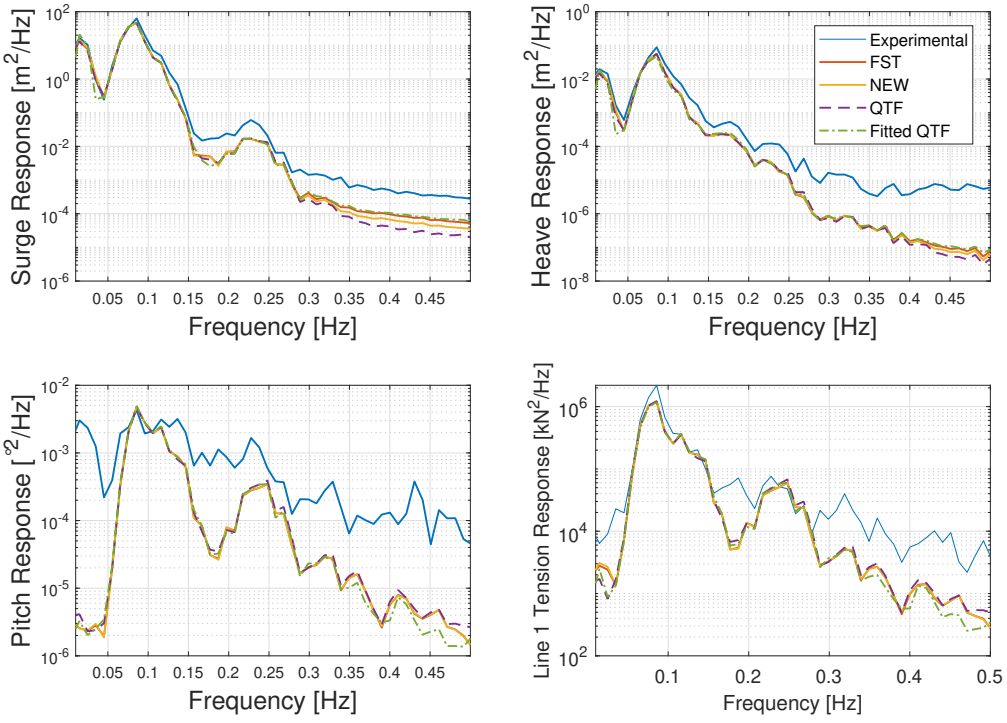


Figure A.38: Numerical & Experimental Surge, Heave, Pitch and line 1 Tension Spectral Response Density for Irregular Wave 12. Simulations with observed wave time series

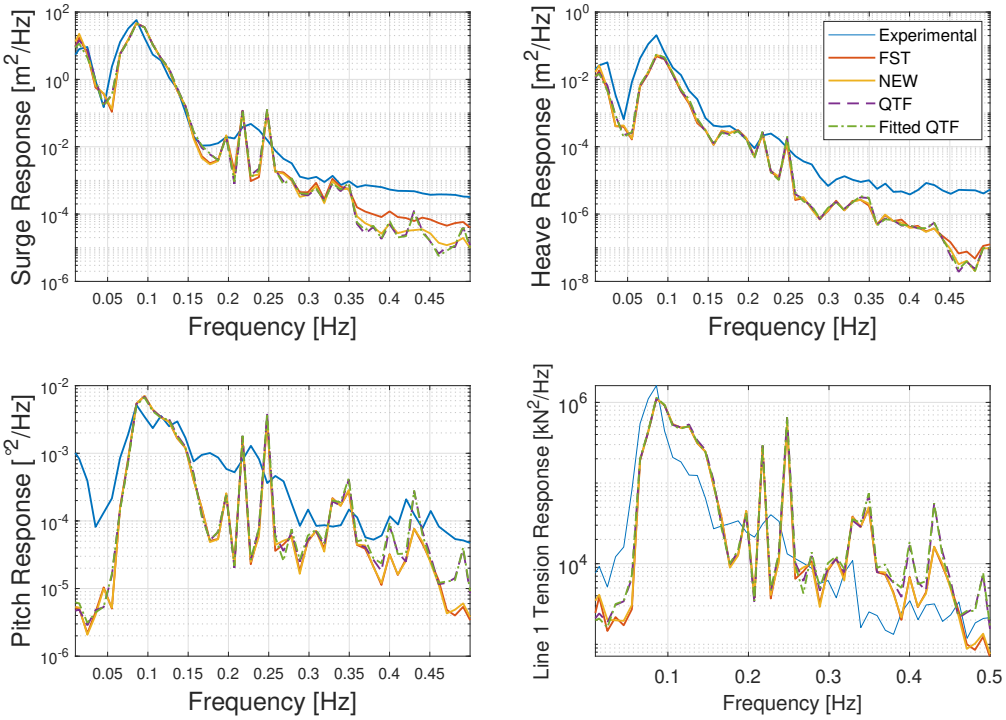


Figure A.39: Numerical & Experimental Surge, Heave, Pitch and line 1 Tension Spectral Response Density for Irregular Wave 13. Simulations with theoretical JONSWAP wave spectra

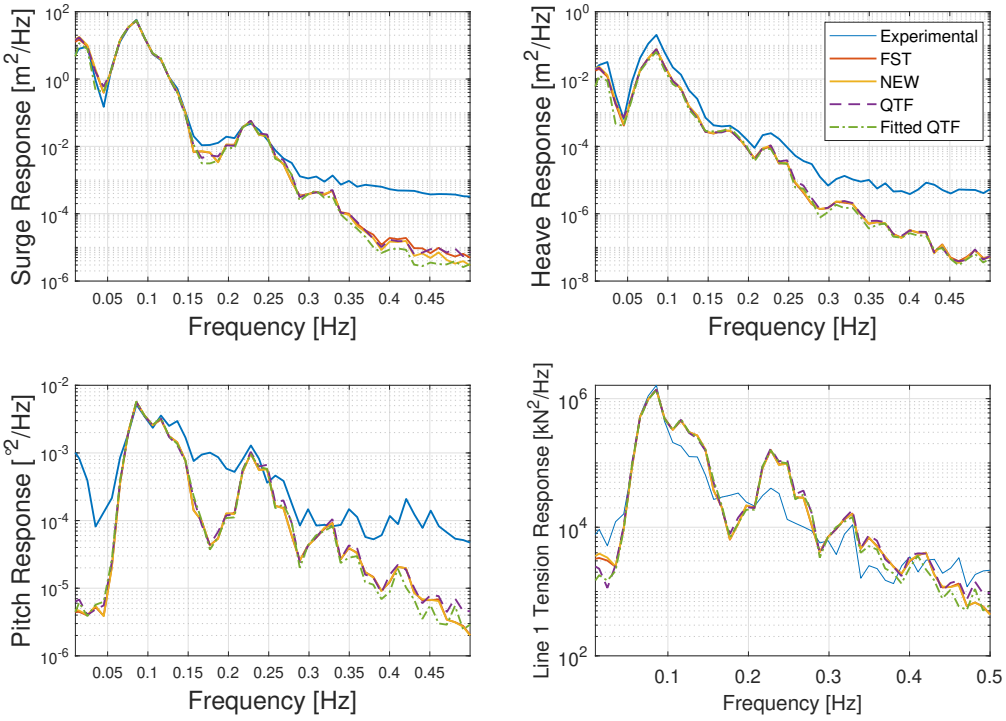


Figure A.40: Numerical & Experimental Surge, Heave, Pitch and line 1 Tension Spectral Response Density for Irregular Wave 13. Simulations with observed wave time series

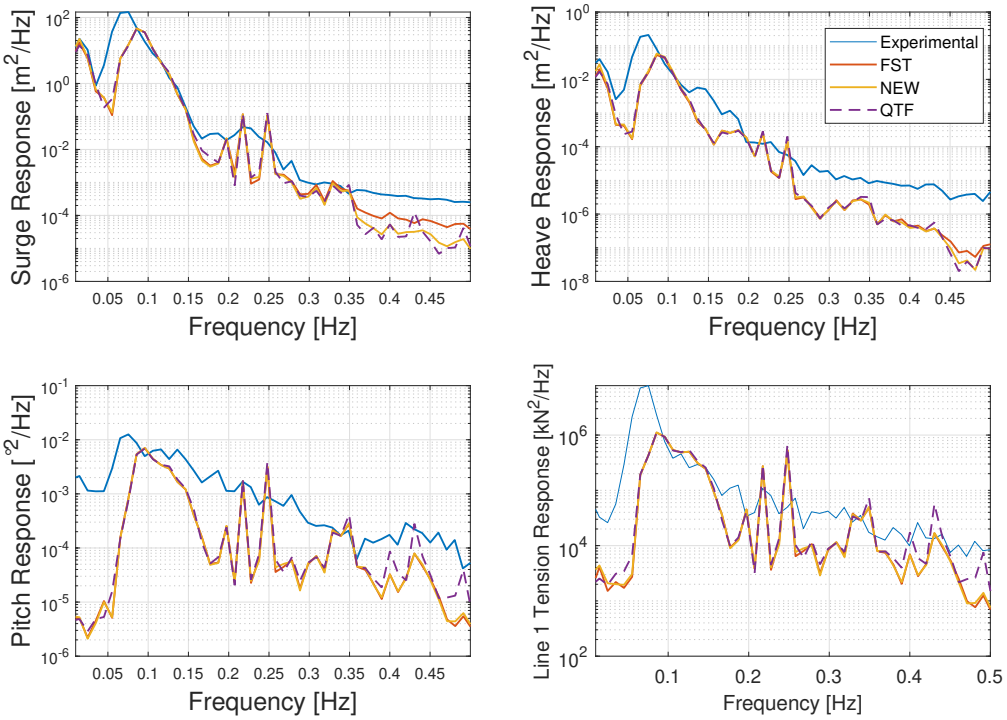


Figure A.41: Numerical & Experimental Surge, Heave, Pitch and line 1 Tension Spectral Response Density for Irregular Wave 14. Simulations with theoretical JONSWAP wave spectra

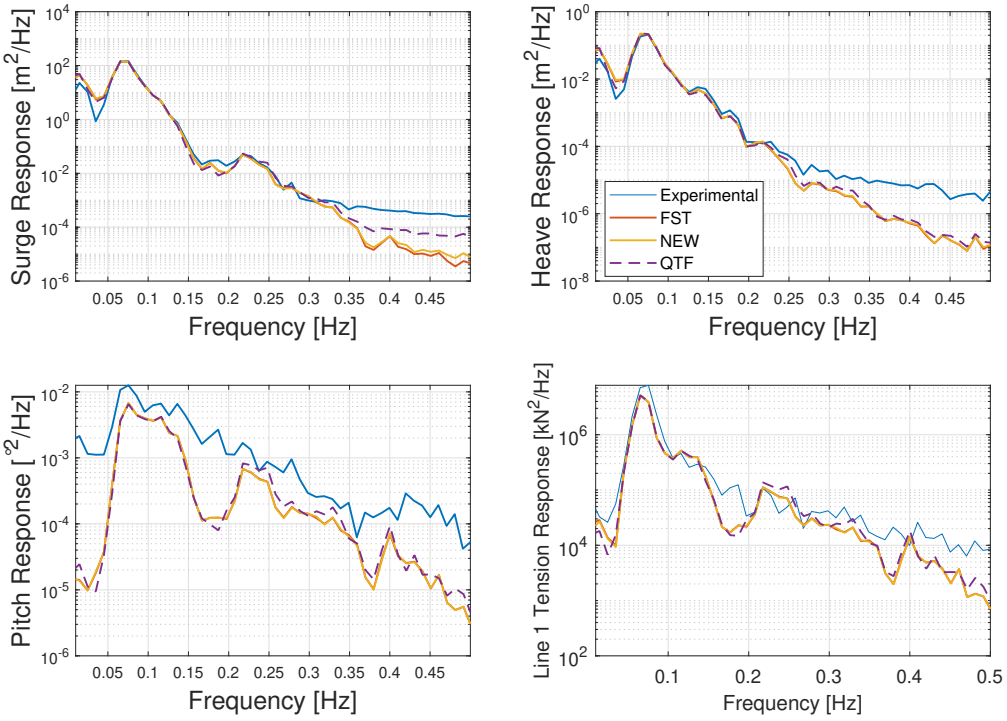


Figure A.42: Numerical & Experimental Surge, Heave, Pitch and line 1 Tension Spectral Response Density for Irregular Wave 14. Simulations with observed wave time series

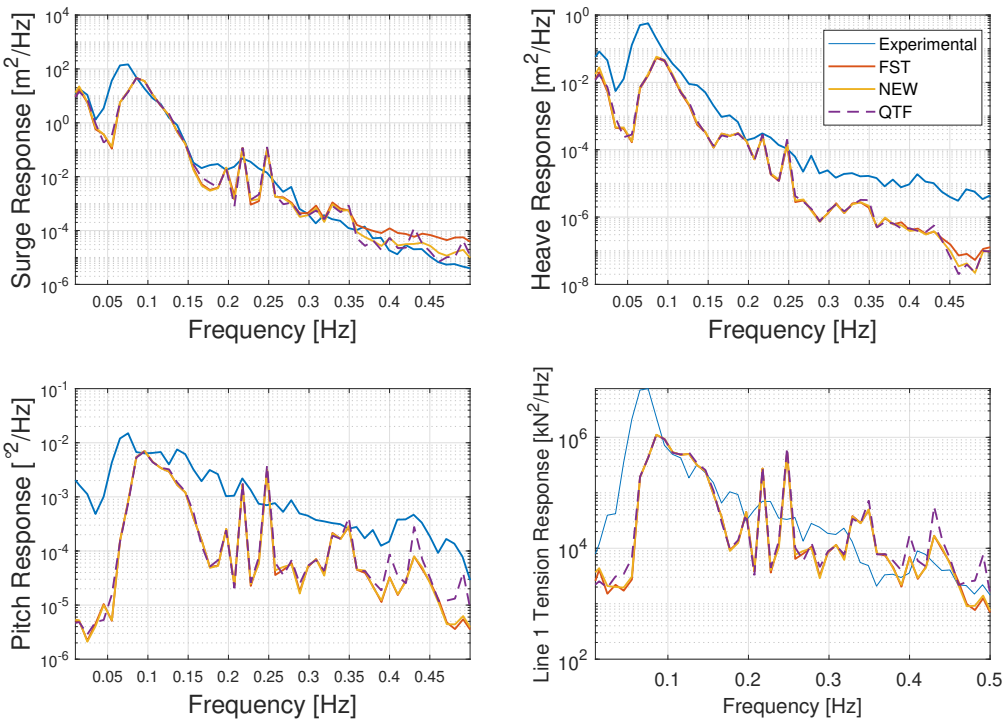


Figure A.43: Numerical & Experimental Surge, Heave, Pitch and line 1 Tension Spectral Response Density for Irregular Wave 15. Simulations with theoretical JONSWAP wave spectra

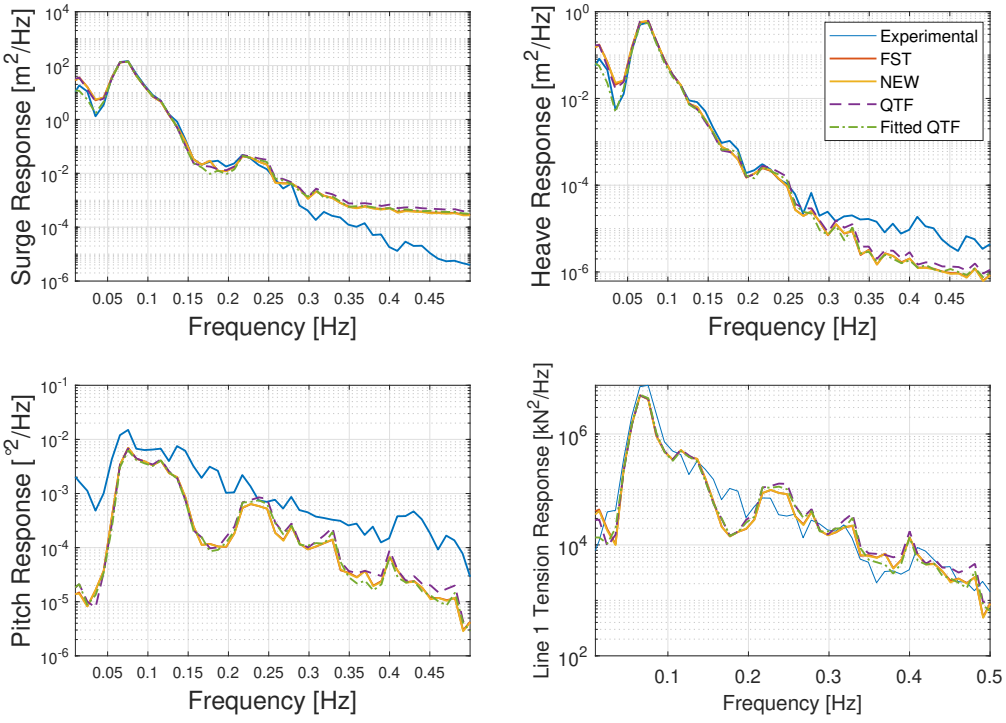


Figure A.44: Numerical & Experimental Surge, Heave, Pitch and line 1 Tension Spectral Response Density for Irregular Wave 15. Simulations with observed wave time series

Appendix B

Acer Method

The Average Conditional Exceedance Rate (ACER) method is an approach to estimate the extreme value distribution from sampled process [343]. This method reduces the estimation of extreme value distribution to calculations of a set of ACER functions at high thresholds with different degrees of conditioning. The ACER method models the conditional exceedances with a prescribed analytical function whose parameters are determined by optimization of curve-fitting, which is a more generalized case as compared to POT method. This method has the capability to capture sub-asymptotical behavior of the data, thus is less restrictive and more flexible than that based on asymptotical extreme value theory, and yields better prediction of extreme value distribution.

The concept of ACER of order k is presented in Equations B.1 to B.3, where X are the observations, N is the number of datapoints.

$$\varepsilon_k(\eta) = \frac{1}{N-k+1}\sum_{j=k}^{N}\alpha_{k,j}(\eta), k = 1, 2, ... \tag{B.1}$$

$$\alpha_{1,j}(\eta) = Prob\{X_j > \eta\}, j = 1, ..., N \tag{B.2}$$

$$P(\eta) = Prob(M_n \leq \eta) \tag{B.3}$$

Appendix C

Results of TWind Time-domain Tow Simulations

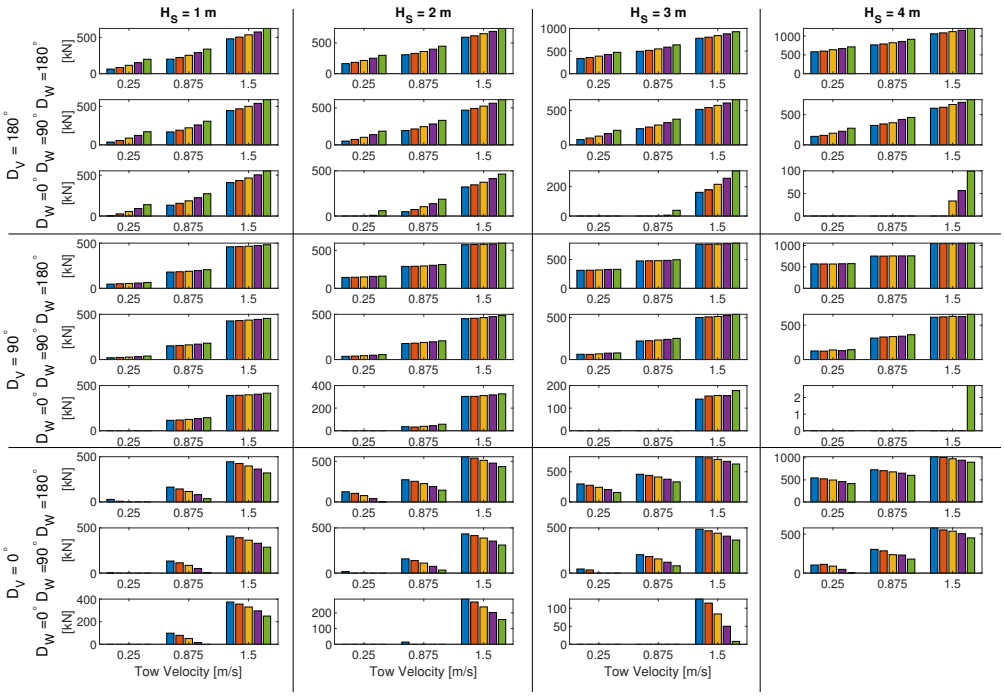


Figure C.1: Winch Mean Tension Float Draft 3 m, Peak Wave period of 6 s. Barplot colours indicate wind speeds, blue (10 m/s), red (15 m/s), orange (20 m/s), purple (25 m/s), green (30 m/s). D_V and D_W indicate the wind and wave direction respectively.

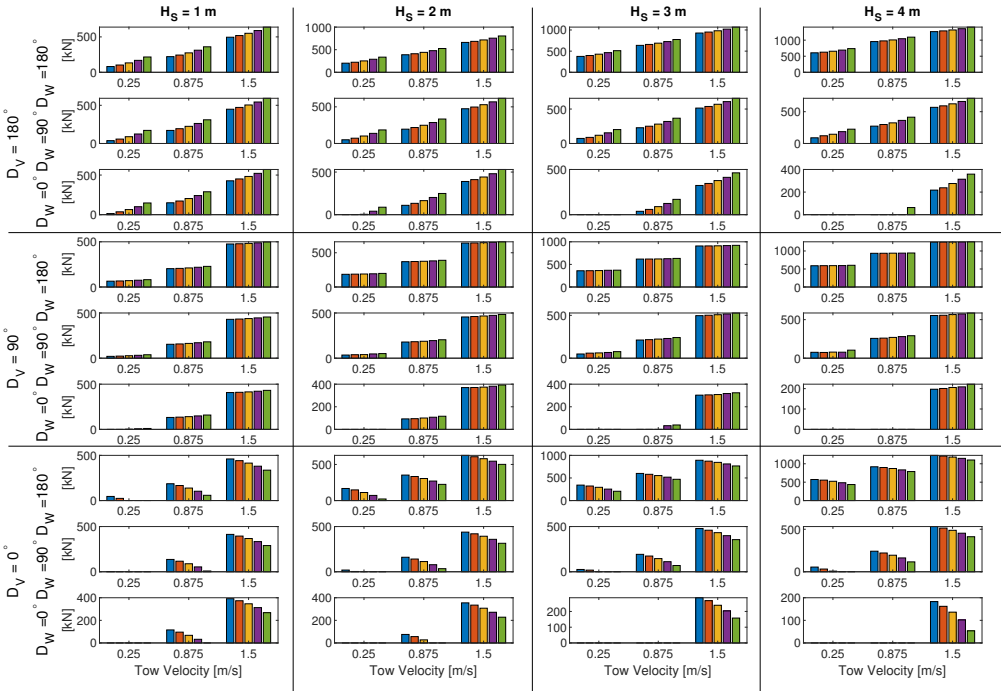


Figure C.2: Winch Mean Tension Float Draft 3 m, Peak Wave period of 10 s. Barplot colours indicate wind speeds, blue (10 m/s), red (15 m/s), orange (20 m/s), purple (25 m/s), green (30 m/s). D_V and D_W indicate the wind and wave direction respectively.

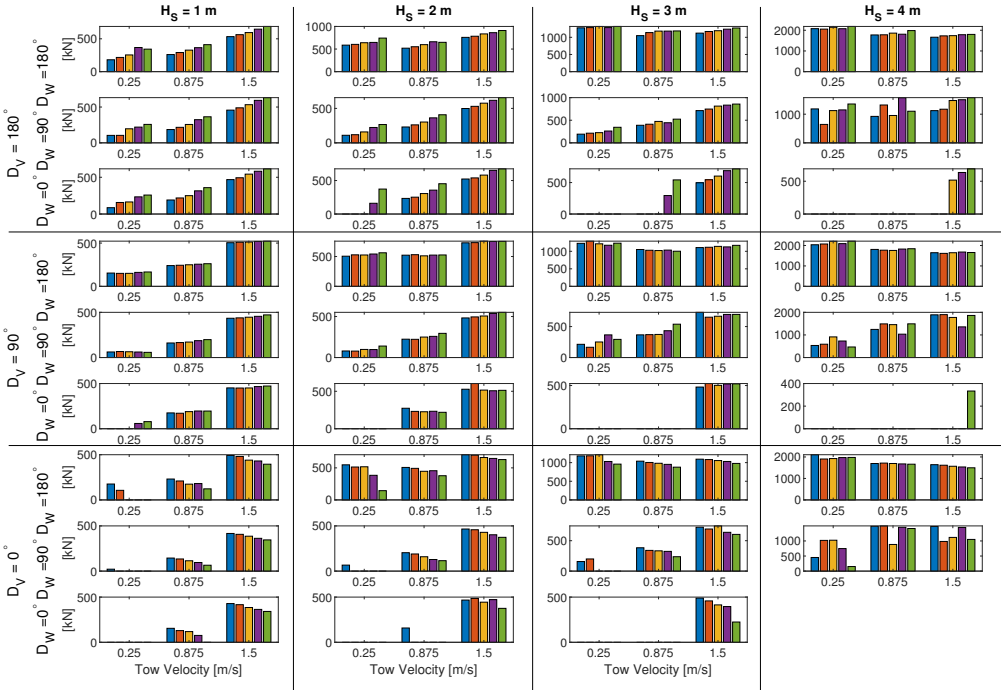


Figure C.3: Winch Peak Tension Float Draft 3 m, Peak Wave period of 6 s. Barplot colours indicate wind speeds, blue (10 m/s), red (15 m/s), orange (20 m/s), purple (25 m/s), green (30 m/s). D_V and D_W indicate the wind and wave direction respectively.

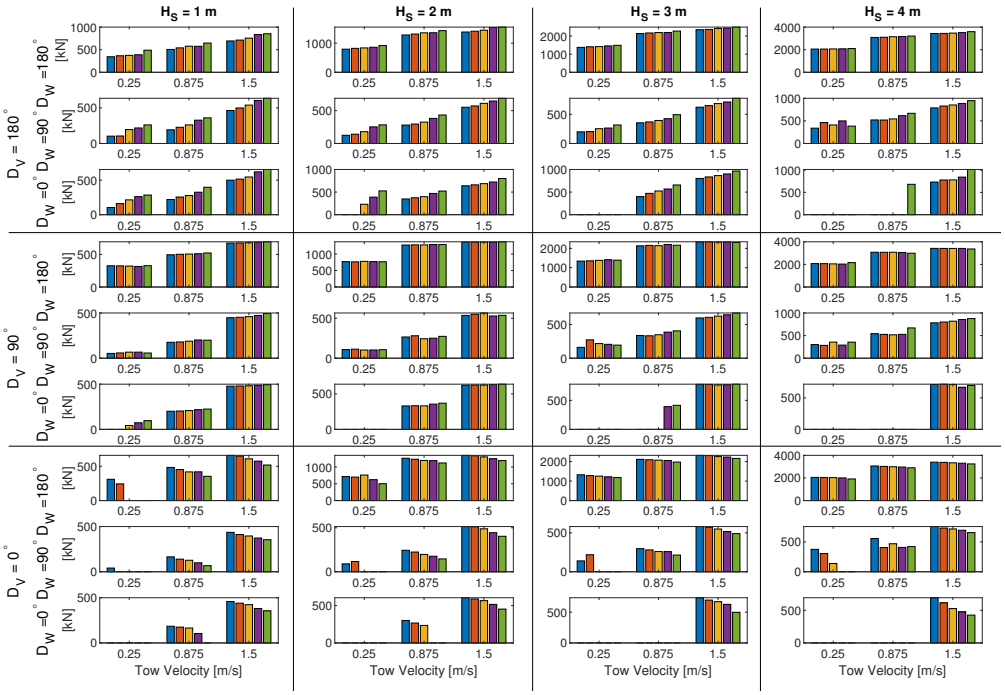


Figure C.4: Winch Peak Tension Float Draft 3 m, Peak Wave period of 10 s. Barplot colours indicate wind speeds, blue (10 m/s), red (15 m/s), orange (20 m/s), purple (25 m/s), green (30 m/s). D_V and D_W indicate the wind and wave direction respectively.

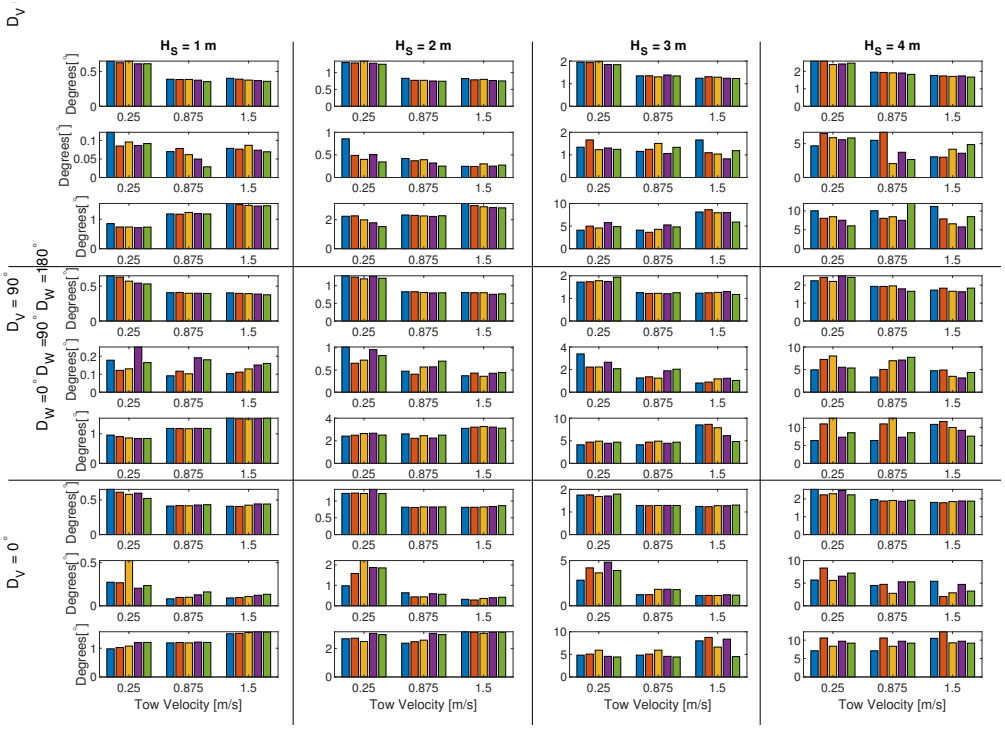


Figure C.5: Peak Pitch Motion Float Draft 3 m, Peak Wave period of 6 s. Barplot colours indicate wind speeds, blue (10 m/s), red (15 m/s), orange (20 m/s), purple (25 m/s), green (30 m/s). D_V and D_W indicate the wind and wave direction respectively.

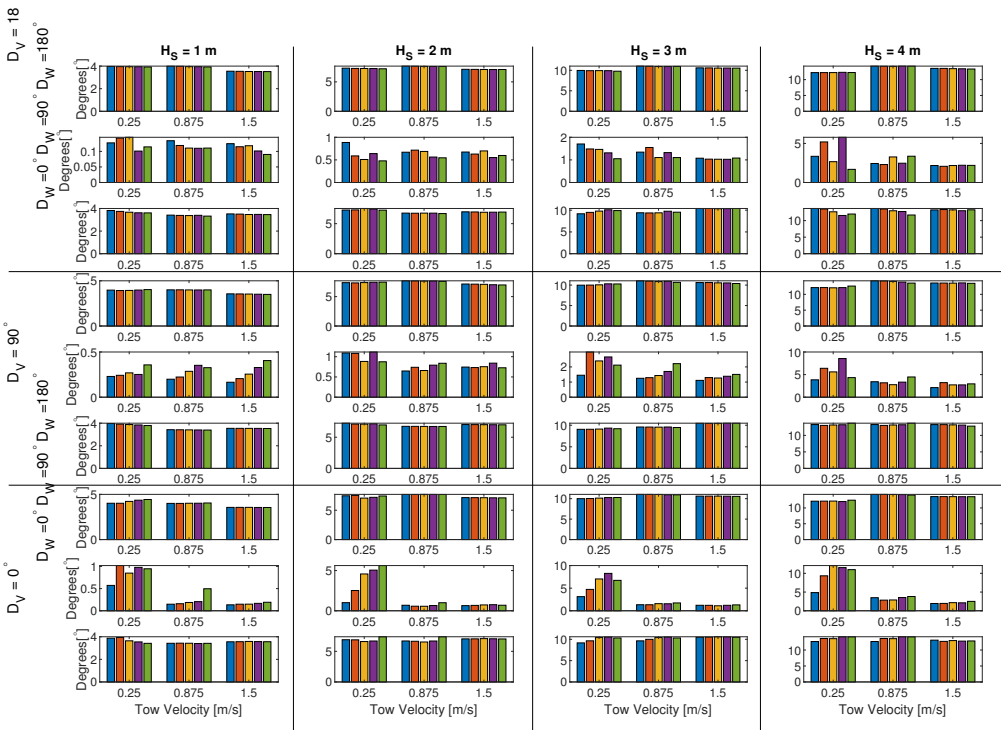


Figure C.6: Peak Pitch Motion Float Draft 3 m, Peak Wave period of 10 s. Barplot colours indicate wind speeds, blue (10 m/s), red (15 m/s), orange (20 m/s), purple (25 m/s), green (30 m/s). D_V and D_W indicate the wind and wave direction respectively.

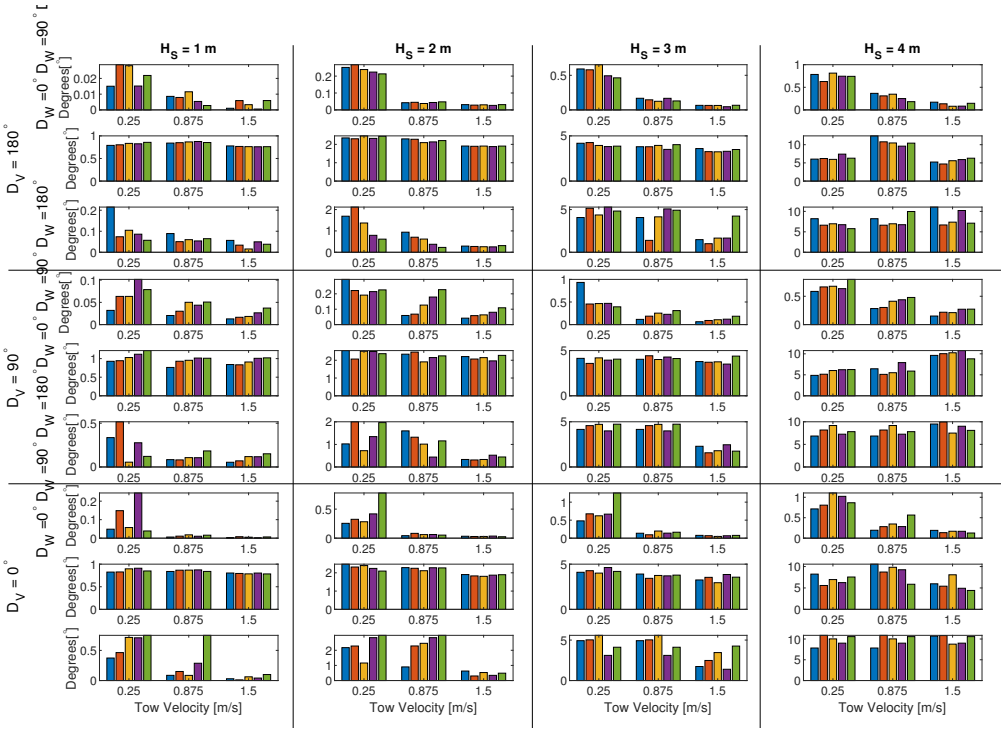


Figure C.7: Peak Roll Motion Float Draft 3 m, Peak Wave period of 6 s. Barplot colours indicate wind speeds, blue (10 m/s), red (15 m/s), orange (20 m/s), purple (25 m/s), green (30 m/s). D_V and D_W indicate the wind and wave direction respectively.

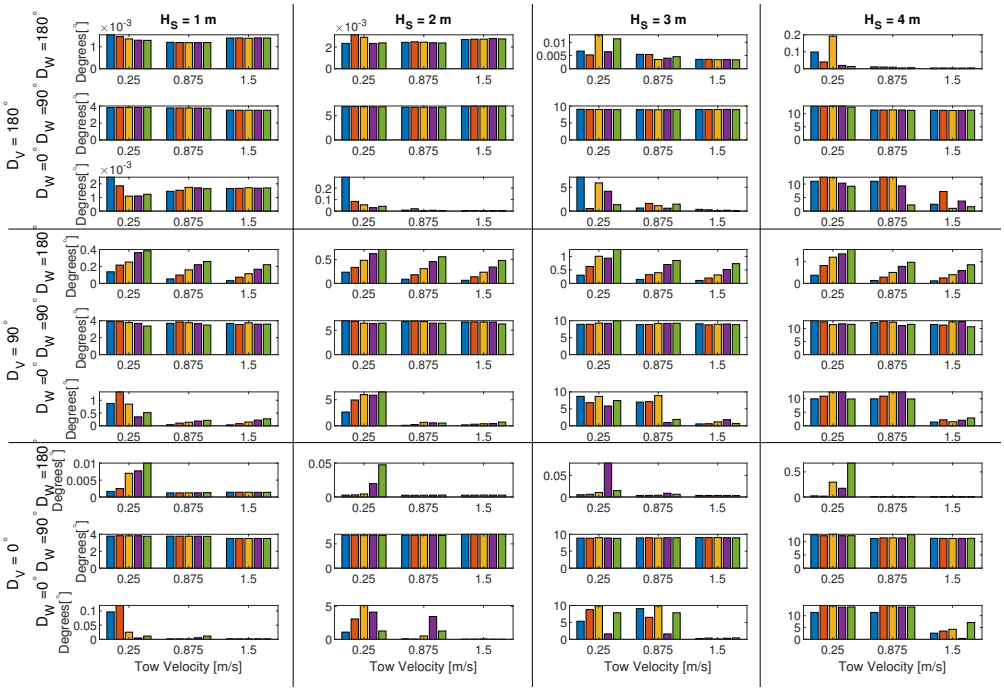


Figure C.8: Peak Roll Motion Float Draft 3 m, Peak Wave period of 10 s. Barplot colours indicate wind speeds, blue (10 m/s), red (15 m/s), orange (20 m/s), purple (25 m/s), green (30 m/s). D_V and D_W indicate the wind and wave direction respectively.

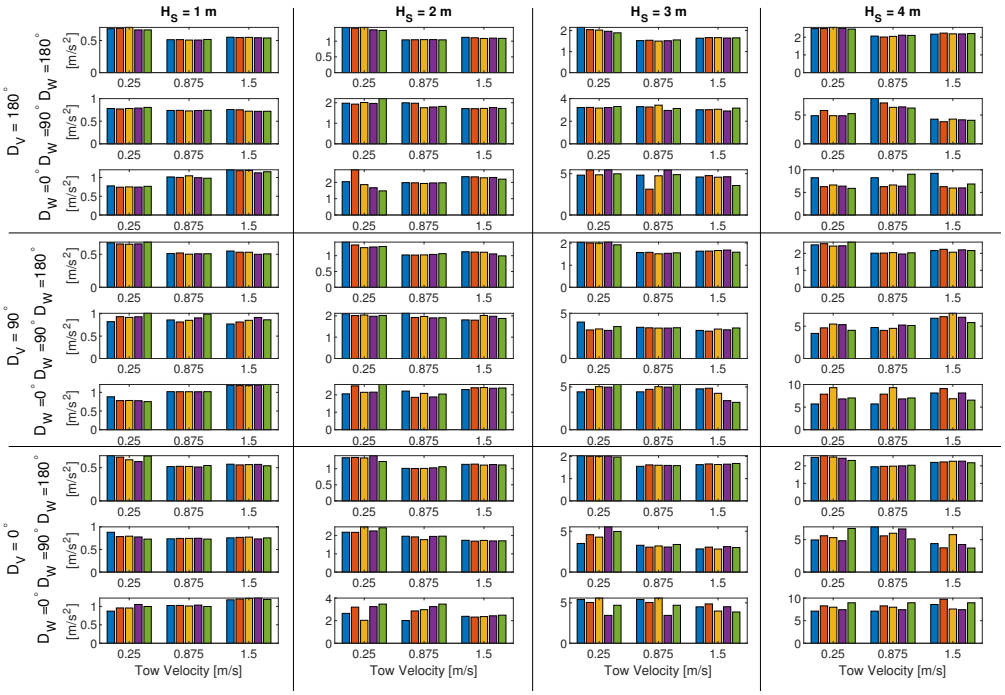


Figure C.9: RNA Peak Acceleration Float Draft 3 m, Peak Wave period of 6 s. Barplot colours indicate wind speeds: blue (10 m/s), red (15 m/s), orange (20 m/s), purple (25 m/s), green (30 m/s). D_V and D_W indicate the wind and wave direction respectively.

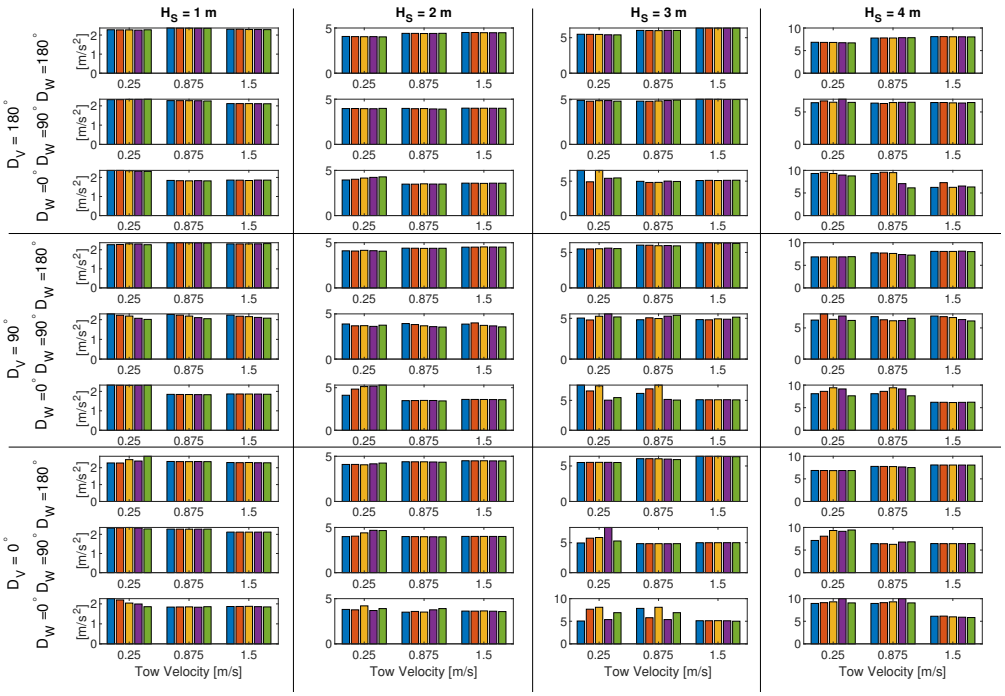


Figure C.10: RNA Peak Acceleration Float Draft 3 m, Peak Wave period of 10 s. Barplot colours indicate wind speeds: blue (10 m/s), red (15 m/s), orange (20 m/s), purple (25 m/s), green (30 m/s). D_V and D_W indicate the wind and wave direction respectively.

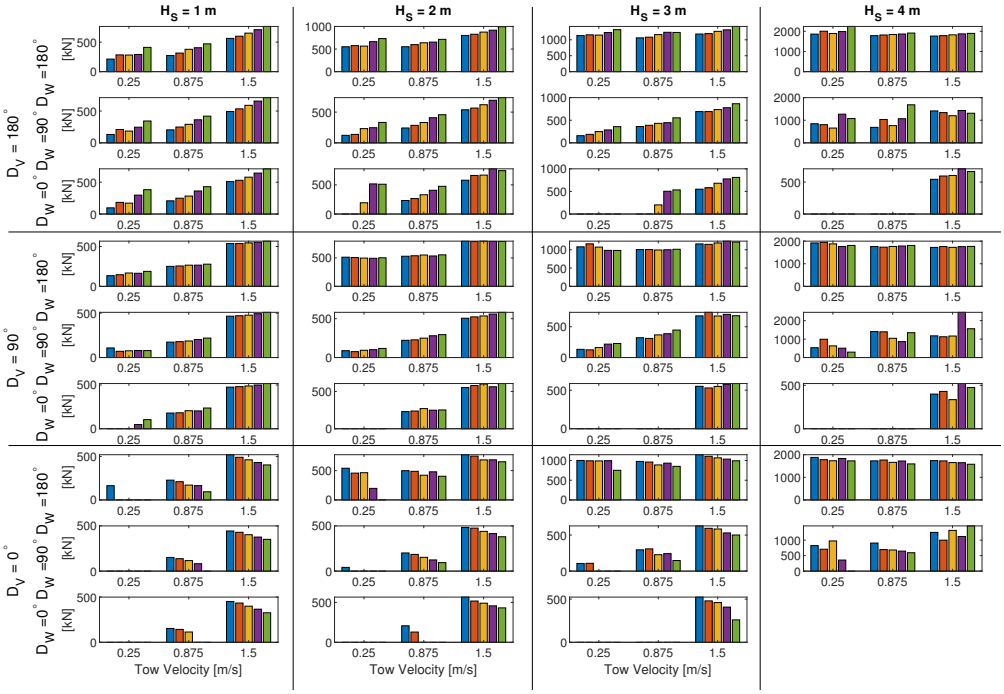


Figure C.11: Winch Peak Tension Float Draft 5 m, Peak Wave period of 6 s. Barplot colours indicate wind speeds, blue (10 m/s), red (15 m/s), orange (20 m/s), purple (25 m/s), green (30 m/s). D_V and D_W indicate the wind and wave direction respectively.

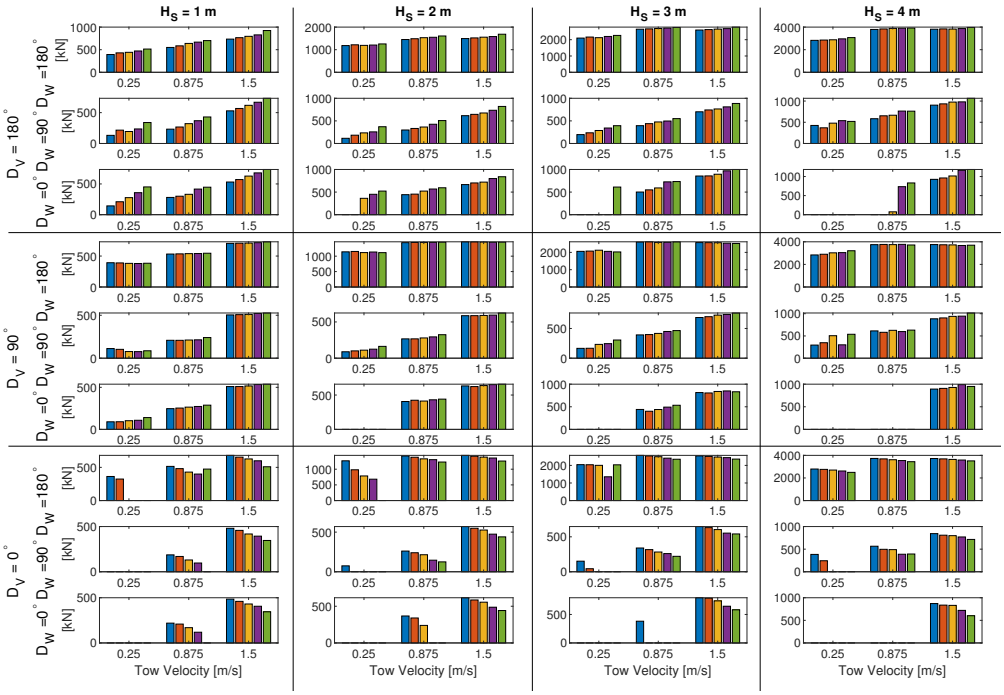


Figure C.12: Winch Peak Tension Float Draft 5 m, Peak Wave period of 10 s. Barplot colours indicate wind speeds, blue (10 m/s), red (15 m/s), orange (20 m/s), purple (25 m/s), green (30 m/s). D_V and D_W indicate the wind and wave direction respectively.

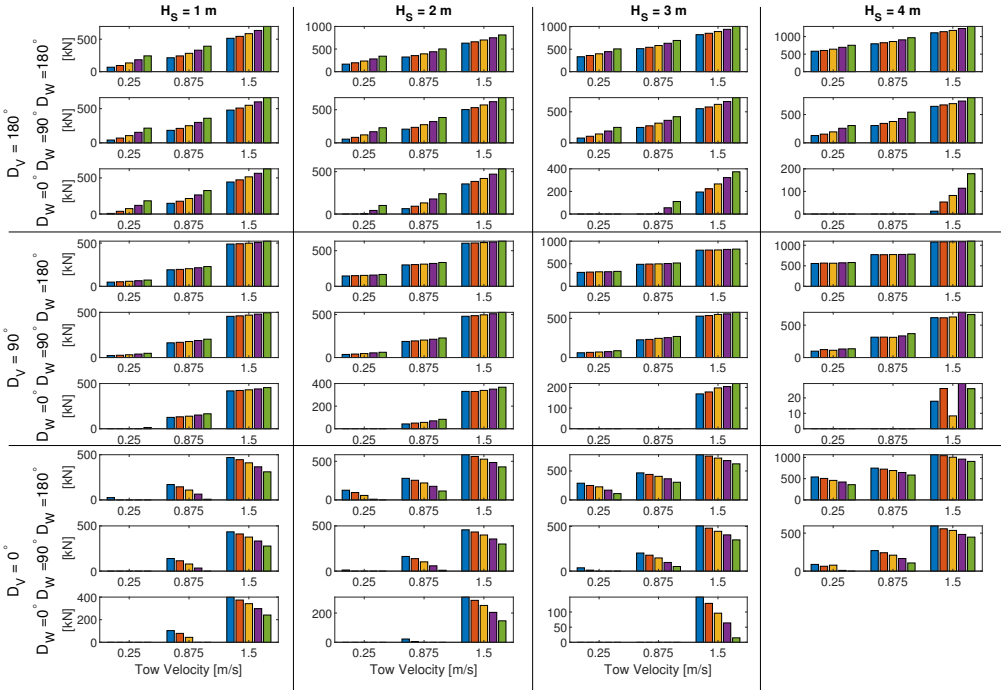


Figure C.13: Winch Mean Tension Float Draft 5 m, Peak Wave period of 6 s. Barplot colours indicate wind speeds, blue (10 m/s), red (15 m/s), orange (20 m/s), purple (25 m/s), green (30 m/s). D_V and D_W indicate the wind and wave direction respectively.

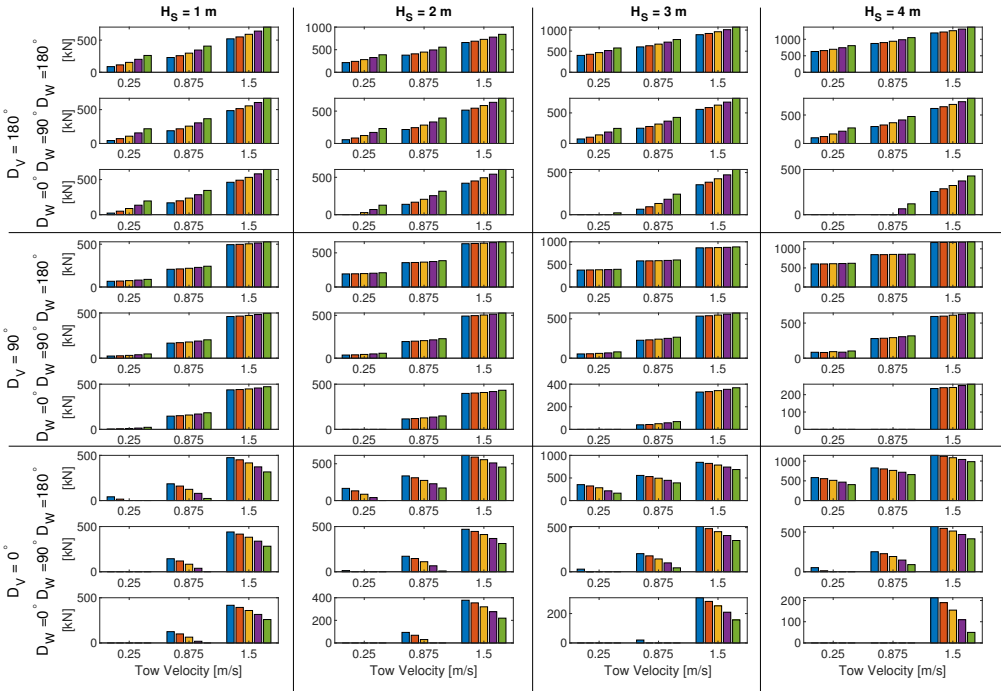


Figure C.14: Winch Mean Tension Float Draft 5 m, Peak Wave period of 10 s. Barplot colours indicate wind speeds, blue (10 m/s), red (15 m/s), orange (20 m/s), purple (25 m/s), green (30 m/s). D_V and D_W indicate the wind and wave direction respectively.

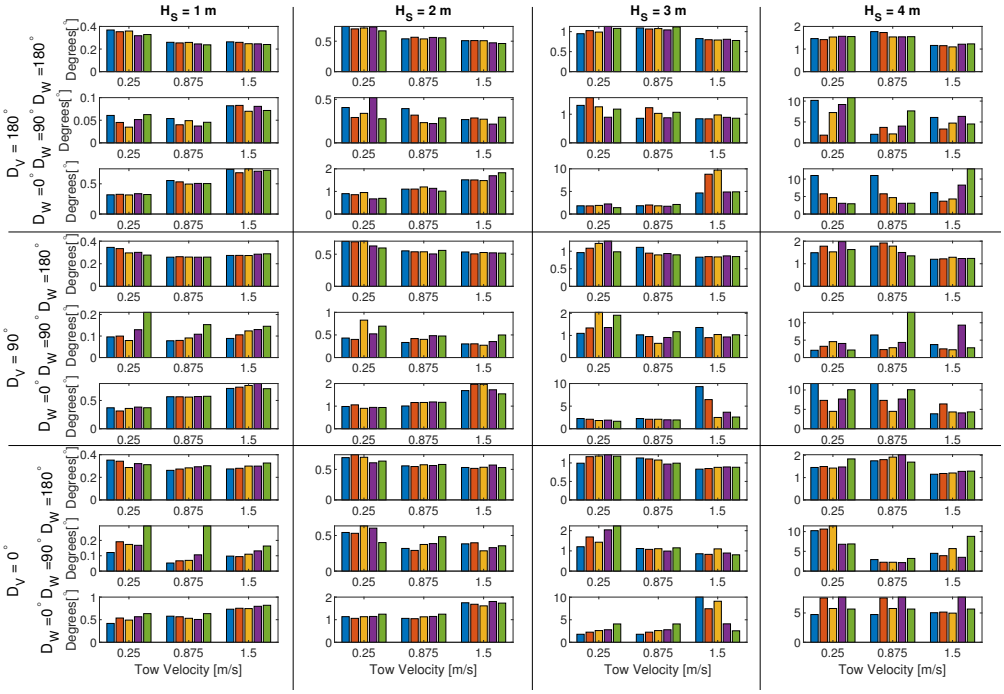


Figure C.15: Peak Pitch Motion Float Draft 5 m, Peak Wave period of 6 s. Barplot colours indicate wind speeds, blue (10 m/s), red (15 m/s), orange (20 m/s), purple (25 m/s), green (30 m/s). D_V and D_W indicate the wind and wave direction respectively.

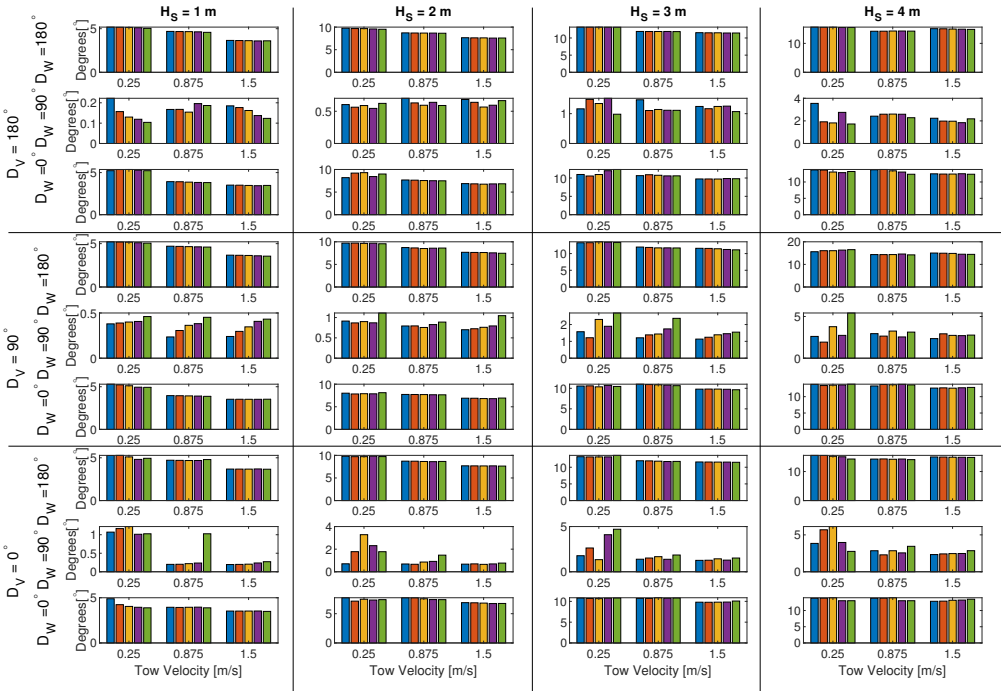


Figure C.16: Peak Pitch Motion Float Draft 5 m, Peak Wave period of 10 s. Barplot colours indicate wind speeds, blue (10 m/s), red (15 m/s), orange (20 m/s), purple (25 m/s), green (30 m/s). D_V and D_W indicate the wind and wave direction respectively.

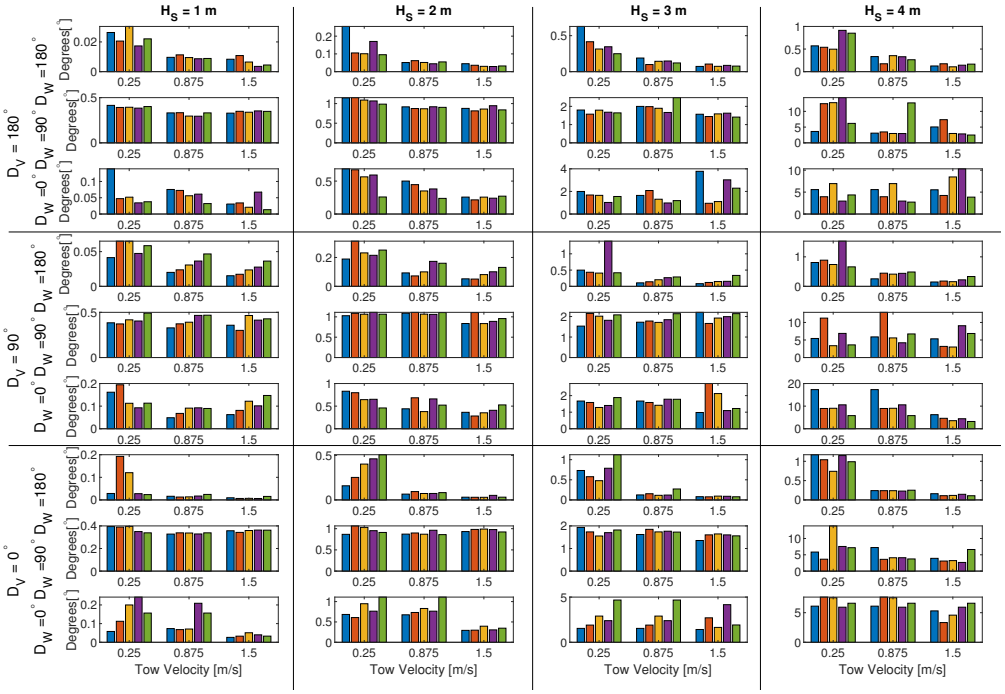


Figure C.17: Peak Roll Motion Float Draft 5 m, Peak Wave period of 6 s. Barplot colours indicate wind speeds, blue (10 m/s), red (15 m/s), orange (20 m/s), purple (25 m/s), green (30 m/s). D_V and D_W indicate the wind and wave direction respectively.

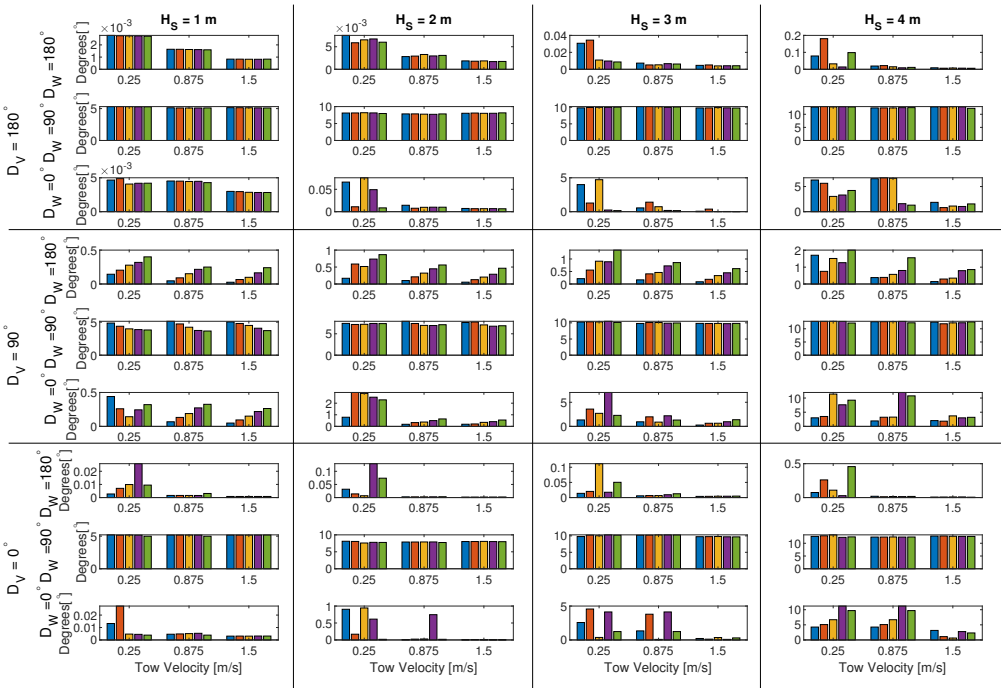


Figure C.18: Peak Roll Motion Float Draft 5 m, Peak Wave period of 10 s. Barplot colours indicate wind speeds, blue (10 m/s), red (15 m/s), orange (20 m/s), purple (25 m/s), green (30 m/s). D_V and D_W indicate the wind and wave direction respectively.

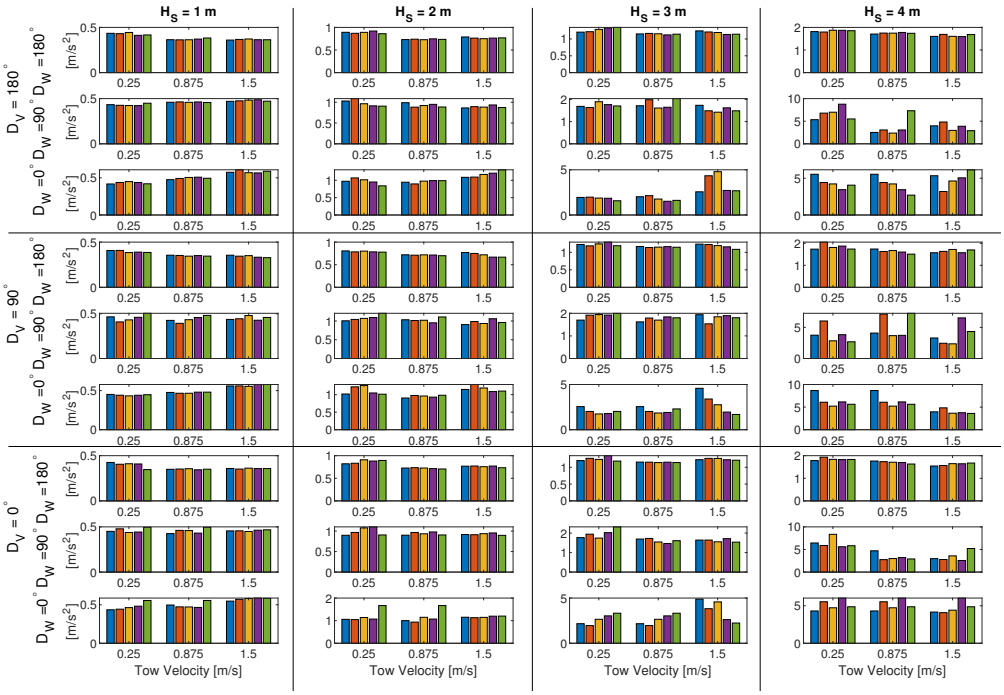


Figure C.19: RNA Peak Acceleration Float Draft 5 m, Peak Wave period of 6 s. Barplot colours indicate wind speeds, blue (10 m/s), red (15 m/s), orange (20 m/s), purple (25 m/s), green (30 m/s). D_V and D_W indicate the wind and wave direction respectively.

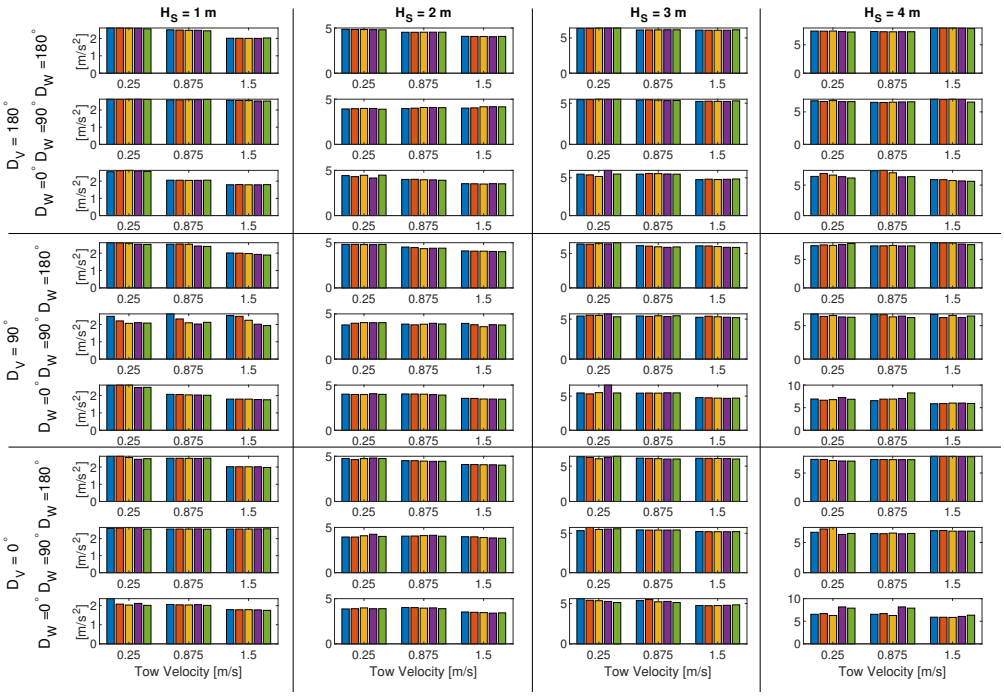


Figure C.20: RNA Peak Acceleration Float Draft 5 m, Peak Wave period of 10 s. Barplot colours indicate wind speeds, blue (10 m/s), red (15 m/s), orange (20 m/s), purple (25 m/s), green (30 m/s). D_V and D_W indicate the wind and wave direction respectively.

Appendix D

TWind and TWINDWAVE Scale Model Five Way Joiner Fabrication Process

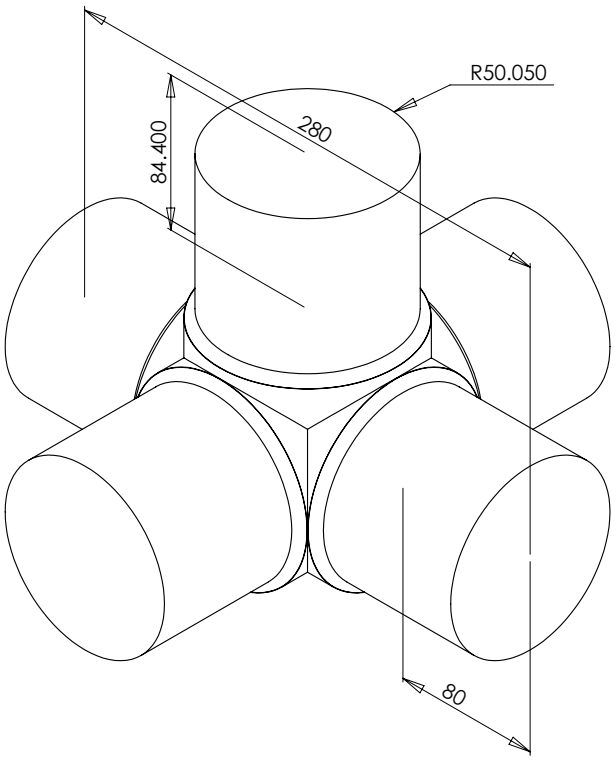


Figure D.1: 3D Model of 5 Way Joiner

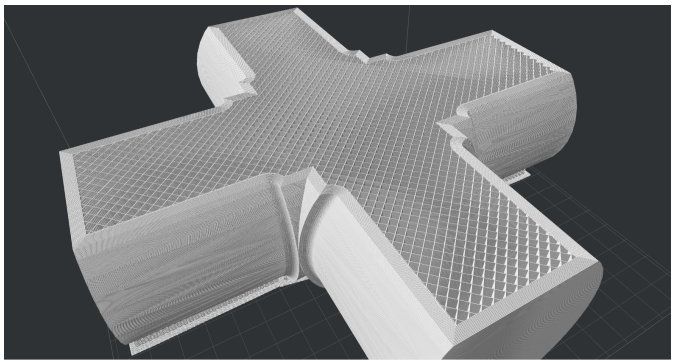


Figure D.2: 3D Model of 5 Way Joiner in 3D Printing Software including Internal Mesh Stiffner

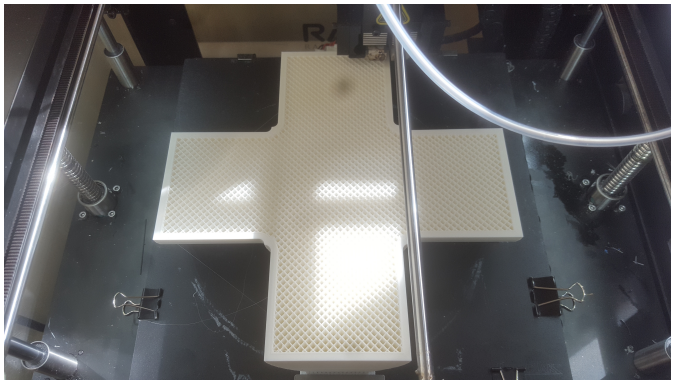


Figure D.3: Photograph of 5 Way Joiner During the 3D Printing Process

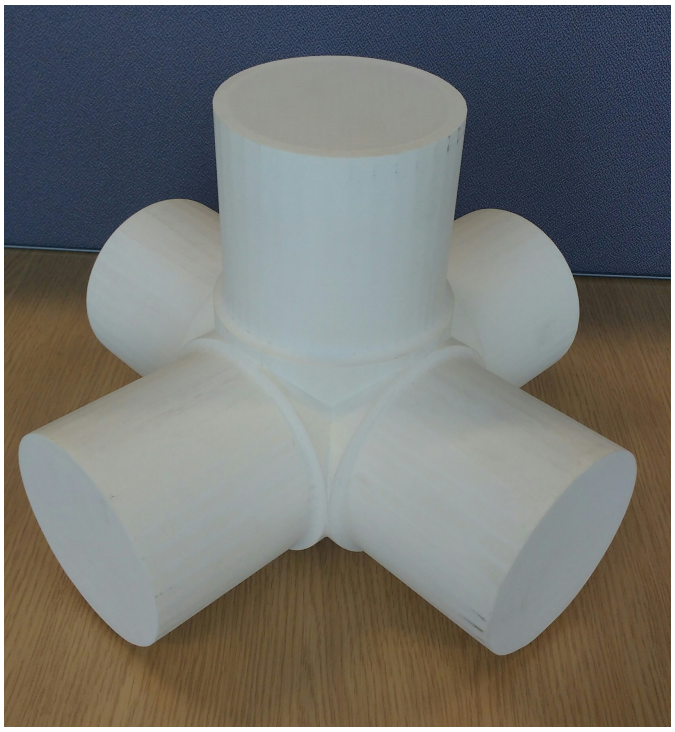


Figure D.4: Photograph of Completed 5 Way Joiner

Bibliography

[1] GWEC. Global wind report 2021. Technical report, Brussels, 2021.

[2] DNVGL. Floating wind:the power to commercialize. Technical report, OSLO, 2020.

[3] IEA. Offshore wind outlook 2019. Technical report, Paris, 2019.

[4] William E Heronemus. *Pollution-Free energy from the offshore winds.* Marine Technology Society, 1972.

[5] Walt Musial, Sandy Butterfield, and Andrew Boone. Feasibility of floating platform systems for wind turbines. In *23rd ASME Wind Energy Symposium, Reno, NV*, 2004.

[6] KC Tong. Technical and economic aspects of a floating offshore wind farm. *Journal of Wind Engineering and Industrial Aerodynamics*, 74:399–410, 1998.

[7] Sciencedirect.com. .sciencedirect.com/. Accessed: 2021-01-30.

[8] Offshore Renewable Energy Catapult. Floating wind: technology assessment – interim findings. Technical report, 2015.

[9] Denis Matha, Germán Pérez Morán, Kolja Müller, and Frank Lemmer. Comparative analysis of industrial design methodologies for fixed-bottom and floating wind turbines. In *ASME 2016 35th International Conference on Ocean, Offshore and Arctic Engineering*, pages V006T09A055–V006T09A055. American Society of Mechanical Engineers, 2016.

[10] Mareike Strach-Sonsalla, Michael Muskulus, et al. Prospects of floating wind energy. *International Journal of Offshore and Polar Engineering*, 26(02):81–87, 2016.

[11] Laura Castro-Santos, Almudena Filgueira-Vizoso, Luis Carral-Couce, and José Ángel Fraguela Formoso. Economic feasibility of floating offshore wind farms. *Energy*, 112:868–882, 2016.

[12] Andrew R Henderson and David Witcher. Floating offshore wind energy—a review of the current status and an assessment of the prospects. *Wind Engineering*, 34(1):1–16, 2010.

[13] Sandy Butterfield, Walt Musial, Jason Jonkman, Paul Sclavounos, and Libby Wayman. Engineering challenges for floating offshore wind turbines. In *Copenhagen Offshore Wind Conference, Copenhagen, Denmark*, pages 377–382. Citeseer, 2005.

[14] Christopher Christopher Henry Tracy. *Parametric design of floating wind turbines*. PhD thesis, Massachusetts Institute of Technology, 2007.

[15] Denis Matha. Model development and loads analysis of an offshore wind turbine on a tension leg platform with a comparison to other floating turbine concepts: April 2009. Technical report, National Renewable Energy Laboratory (NREL), Golden, CO., 2010.

[16] Jr. William L. Hurley and Charles J. Nordstrom. Pelastar cost of energy: A cost study of the pelastar floating foundation system in uk waters. Offshore Wind Floating Platform Demonstration Project FEED Study.

[17] Yongsheng Zhao, Jianmin Yang, and Yanping He. Preliminary design of a multi-column tlp foundation for a 5-mw offshore wind turbine. *Energies*, 5(10):3874–3891, 2012.

[18] C Casale, Ettore Lembo, Laura Serri, and Silvano Viani. Preliminary design of a floating wind turbine support structure and relevant system cost assessment. *Wind Engineering*, 34(1):29–50, 2010.

[19] Andrew R Henderson, Kimon Argyriadis, J Nichos, and David Langston. Offshore wind turbines on tlps-assessment of floating support structures for offshore wind farms in german waters. In *10th German wind energy conference, Bremen, Germany*, pages 1–5, 2010.

[20] J Amate, P Gómez, V De Diego, P Trigo, G Sánchez, G González, A Llana, and L Giner. How to install a tlp substructure for offshore wind? tlpwind® case study. *EWEA Offshore 2015*, 2015.

[21] F Adam, T Myland, F Dahlhaus, and J Großmann. Gicon®-tlp for wind turbines-the path of development. *Proc. RENEW*, 2014.

[22] François Caillé, Pauline Bozonnet, Timothée Perdrizet, Yann Poirette, and Cécile Melis. Model test and simulation comparison for an inclined-leg tlp dedicated to floating wind. In *International Conference on Offshore Mechanics and Arctic Engineering*, volume 57786, page V010T09A070. American Society of Mechanical Engineers, 2017.

[23] F.M. Johnson and A.M. Filak. Construction and installation process to deploy a wind turbine "wtg" on a tension leg platform/spar in medium to deep water, September 4 2014. US Patent App. 13/998,626.

[24] Kazuhiro Iijima, Yuiko Kuroda, Yasunori Nihei, and Motohiko Murai. Comparison of weathervane performance between two types of fowt systems moored to spm. In *ASME 2015 34th International Conference on Ocean, Offshore and Arctic*

Engineering, pages V006T05A010–V006T05A010. American Society of Mechanical Engineers, 2015.

[25] Michael Borg, Morten Walkusch Jensen, Scott Urquhart, Morten Thøtt Andersen, Jonas Bjerg Thomsen, and Henrik Stiesdal. Technical definition of the tetraspar demonstrator floating wind turbine foundation. *Energies*, 13(18):4911, 2020.

[26] Shengwen Xu, Motohiko Murai, Xuefeng Wang, and Kensaku Takahashi. A novel conceptual design of a dynamically positioned floating wind turbine. *Ocean Engineering*, 221:108528.

[27] Shengwen Xu, Motohiko Murai, Xuefeng Wang, and Kensaku Takahashi. A novel conceptual design of a dynamically positioned floating wind turbine. *Ocean Engineering*, 221:108528, 2021.

[28] S Astariz and G Iglesias. Output power smoothing and reduced downtime period by combined wind and wave energy farms. *Energy*, 97:69–81, 2016.

[29] Francesco Fusco, Gary Nolan, and John V Ringwood. Variability reduction through optimal combination of wind/wave resources–an irish case study. *Energy*, 35(1):314–325, 2010.

[30] Lucy Cradden, Hakim Mouslim, Olivier Duperray, and David Ingram. Joint exploitation of wave and offshore wind power. In *Proceedings of the ninth European wave and tidal energy conference. Southampton, UK*, pages 1–10, 2011.

[31] Julia Fernandez Chozas, HC Sørensen, and NE Helstrup Jensen. Economic benefit of combining wave and wind power productions in day-ahead electricity markets. In *4th International Conference on Ocean Energy*, 2012.

[32] Arianna Azzellino, Vincenzo Ferrante, Jens Peter Kofoed, Caterina Lanfredi, and Diego Vicinanza. Optimal siting of offshore wind-power combined with wave energy through a marine spatial planning approach. *International Journal of Marine Energy*, 3:e11–e25, 2013.

[33] Carlos Pérez-Collazo, D Greaves, and G Iglesias. A review of combined wave and offshore wind energy. *Renewable and Sustainable Energy Reviews*, 42:141–153, 2015.

[34] Barbara Zanuttigh, Elisa Angelelli, Andreas Kortenhaus, Kaan Koca, Yukiko Krontira, and Phoebe Koundouri. A methodology for multi-criteria design of multi-use offshore platforms for marine renewable energy harvesting. *Renewable Energy*, 85:1271–1289, 2016.

[35] V Baudry and A Babarit. Assessment of the annual energy production of a heaving wave energy converter sliding on the mast of a fixed offshore wind turbine. In *Renewable Energy Congress XI (WREC XI)*, 2010.

[36] V Pakrashi, J Murphy, K O'Sullivan, C Long, and PO Kelly-Lynch. Structural design implications when a combined wind and wave energy platform is applied in differing site scenarios.

[37] Bjarne S Kallesøe, TJ Larsen, US Paulsen, A Køhler, FH Dixen, CB Mørch, J Kringelum, and HF Hansen. Aero-hydro-elastic simulation platform for wave energy systems and floating wind turbines. *Roskilde: Danmarks Tekniske Universitet, Risø Nationallaboratoriet for Bæredygtig Energi.(Denmark. Forskningscenter Risoe. Risoe-R*, (1767), 2011.

[38] Antoine Peiffer, Dominique Roddier, and Alexia Aubault. Design of a point absorber inside the windfloat structure. In *ASME 2011 30th International Conference on Ocean, Offshore and Arctic Engineering*, pages 247–255. American Society of Mechanical Engineers, 2011.

[39] Alexia Aubault, Marco Alves, António Sarmento, Dominique Roddier, and Antoine Peiffer. Modeling of an oscillating water column on the floating foundation windfloat. In *ASME 2011 30th International Conference on Ocean, Offshore and Arctic Engineering*, pages 235–246. American Society of Mechanical Engineers, 2011.

[40] Antoine Peiffer and Dominique Roddier. Design of an oscillating wave surge converter on the windfloat structure. In *Proceedings of the 4th International Conference on Ocean Energy*, 2012.

[41] Keith Patrick O'Sullivan. Feasibility of combined wind-wave energy platforms. 2014.

[42] Madjid Karimirad and Kourosh Koushan. Windwec: Combining wind and wave energy inspired by hywind and wavestar.

[43] Michael Borg, Maurizio Collu, and Feargal P Brennan. Use of a wave energy converter as a motion suppression device for floating wind turbines. *Energy Procedia*, 35:223–233, 2013.

[44] Constantine Michailides, Chenyu Luan, Zhen Gao, and Torgeir Moan. Effect of flap type wave energy converters on the response of a semi-submersible wind turbine in operational conditions. In *ASME 2014 33rd International Conference on Ocean, Offshore and Arctic Engineering*, pages V09BT09A014–V09BT09A014. American Society of Mechanical Engineers, 2014.

[45] Constantine Michailides, Zhen Gao, and Torgeir Moan. Experimental study of the functionality of a semisubmersible wind turbine combined with flap-type wave energy converters. *Renewable Energy*, 93:675–690, 2016.

[46] Chenyu Luan, Constantine Michailides, Zhen Gao, and Torgeir Moan. Modeling and analysis of a 5 mw semi-submersible wind turbine combined with three flap-type wave energy converters. In *ASME 2014 33rd International Conference on Ocean, Offshore and Arctic Engineering*, pages V09BT09A028–V09BT09A028. American Society of Mechanical Engineers, 2014.

[47] Made Jaya Muliawan, Madjid Karimirad, Torgeir Moan, and Zhen Gao. Stc (spar-torus combination): a combined spar-type floating wind turbine and large point absorber floating wave energy converter—promising and challenging. In *ASME*

2012 31st International Conference on Ocean, Offshore and Arctic Engineering, pages 667–676. American Society of Mechanical Engineers, 2012.

[48] Nianxin Ren, Zhen Gao, and Torgeir Moan. Long-term stochastic dynamic analysis of a combined floating spar-type wind turbine and wave energy converter (stc) system for mooring fatigue damage and power prediction. In *ASME 2014 33rd International Conference on Ocean, Offshore and Arctic Engineering*, pages V09AT09A026–V09AT09A026. American Society of Mechanical Engineers, 2014.

[49] Made Jaya Muliawan, Madjid Karimirad, Zhen Gao, and Torgeir Moan. Extreme responses of a combined spar-type floating wind turbine and floating wave energy converter (stc) system with survival modes. *Ocean Engineering*, 65:71–82, 2013.

[50] Ling Wan, Zhen Gao, and Torgeir Moan. Model test of the stc concept in survival modes. In *ASME 2014 33rd International Conference on Ocean, Offshore and Arctic Engineering*, pages V09AT09A010–V09AT09A010. American Society of Mechanical Engineers, 2014.

[51] Arka Mitra, Saptarshi Sarkar, Arunasis Chakraborty, and Sourav Das. Sway vibration control of floating horizontal axis wind turbine by modified spar-torus combination. *Ocean Engineering*, 219:108232, 2021.

[52] Chenyu Zhao, Philipp R Thies, Qi Ye, and Johanning Lars. System integration and coupled effects of an owt/wec device. *Ocean Engineering*, 220:108405, 2021.

[53] Erin E Bachynski and Torgeir Moan. Point absorber design for a combined wind and wave energy converter on a tension-leg support structure. In *ASME 2013 32nd International Conference on Ocean, Offshore and Arctic Engineering*, pages V008T09A025–V008T09A025. American Society of Mechanical Engineers, 2013.

[54] Ling Wan, Marilena Greco, Claudio Lugni, Zhen Gao, and Torgeir Moan. Nonlinear motion simulations of a combined wind and wave energy converter con-cept in survival conditions considering water-entry and exit phenomena.

[55] Nianxin Ren, Zhe Ma, Baohua Shan, Dezhi Ning, and Jinping Ou. Experimental and numerical study of dynamic responses of a new combined tlp type floating wind turbine and a wave energy converter under operational conditions. *Renewable Energy*, 151:966 – 974, 2020.

[56] Thomas Soulard, Aurélien Babarit, Bruno Borgarino, Mickael Wyns, and Migel Harismendy. C-hyp: A combined wave and wind energy platform with balanced contributions. In *32nd International Conference on Ocean, Offshore and Arctic Engineering, no. OMAE2013-10778, Nantes, France*, 2013.

[57] Thomas Soulard, Aurélien Babarit, and Bruno Borgarino. Preliminary assessment of a semi-submersible floating wind turbine combined with pitching wave energy converters. In *10th European Wave and Tidal Energy Conference (EWTEC2013)*, 2013.

[58] A. Iturrioz, J. Sarmiento, V. Ayllón, J.A. Armesto, A. Jurado, R. Guanche, C. Vidal, and I.J. Losada. Experimental and numerical design of a combined wind-wave concept. In *Progress in Renewable Energies Offshore: Proceedings of the 2nd International Conference on Renewable Energies Offshore (RENEW2016), Lisbon, Portugal, 24-26 October 2016*, 2016.

[59] T.P. Mazarakos, D.N. Konispoliatis, and S.A. Mavrakos. Design of a tlp floating structure concept for combined wind and wave energy exploitation. In *Progress in Renewable Energies Offshore: Proceedings of the 2nd International Conference on Renewable Energies Offshore (RENEW2016), Lisbon, Portugal, 24-26 October 2016*, 2016.

[60] Beatrice Fenu, Valentino Attanasio, Pietro Casalone, Riccardo Novo, Giulia Cervelli, Mauro Bonfanti, Sergej Antonello Sirigu, Giovanni Bracco, and Giuliana Mattiazzo. Analysis of a gyroscopic-stabilized floating offshore hybrid wind-wave platform. *Journal of Marine Science and Engineering*, 8(6):439, 2020.

[61] Laura Castro-Santos, Elson Martins, and C Guedes Soares. Cost assessment methodology for combined wind and wave floating offshore renewable energy systems. *Renewable Energy*, 97:866–880, 2016.

[62] Josip Bašić and Joško Parunov. Analytical and numerical computation of added mass in ship vibration analysis. *Brodogradnja*, 64(2):0–0, 2013.

[63] Baolei Geng, Bin Teng, Huaqing Zhang, and Baoyou Zheng. Viscous damping effect on the first order motion response of a truss spar. *Journal of Shipping and Ocean Engineering*, 2(2), 2012.

[64] CL Siow, Jaswar Koto, and Hassan Abyn. Semi-submersible heave response study using diffraction potential theory with viscous damping correction. *Journal of Ocean, Mechanical and Aerospace Science and Engineering*, 5, 2014.

[65] CL Siow, Jaswar Koto, Hassan Abyn, and NM Khairuddin. Linearized morison drag for improvement semi-submersible heave response prediction by diffraction potential. *Science and Engineering*, 6, 2014.

[66] Godine Kok Yan Chan, Paul D Sclavounos, Jason Jonkman, and Gregory Hayman. Computation of nonlinear hydrodynamic loads on floating wind turbines using fluid-impulse theory. In *ASME 2015 34th International Conference on Ocean, Offshore and Arctic Engineering*, pages V009T09A038–V009T09A038. American Society of Mechanical Engineers, 2015.

[67] Michael Borg, Anders Melchior Hansen, and Henrik Bredmose. Floating substructure flexibility of large-volume 10mw offshore wind turbine platforms in dynamic calculations. In *Journal of Physics: Conference Series*, volume 753, page 082024. IOP Publishing, 2016.

[68] Kazuhiro Iijima, Sharath Srinivasamurthy, and Masahiko Fujikubo. Structural modeling for flexible floating offshore wind turbine – flexible model vs rigid model. In *IEEE/OES International Convention - Return to the Oceans, At Kobe, Japan*, pages 280–283. Techno-Ocean 2016, 2016.

[69] Chenyu Luan, Zhen Gao, and Torgeir Moan. Development and verification of a time-domain approach for determining forces and moments in structural components of floaters with an application to floating wind turbines. *Marine Structures*, 51:87–109, 2017.

[70] Lene Eliassen, Jasna B Jakobsen, Andreas Knauer, and Finn Gunnar Nielsen. Cascade analysis of a floating wind turbine rotor. In *Journal of Physics: Conference Series*, volume 555, page 012053. IOP Publishing, 2014.

[71] Minu Jeon, Seungmin Lee, and Soogab Lee. Unsteady aerodynamics of offshore floating wind turbines in platform pitching motion using vortex lattice method. *Renewable Energy*, 65:207–212, 2014.

[72] D Manolas, V Riziotis, and S Voutsinas. Assessment of 3d aerodynamic effects on the behaviour of floating wind turbines. In *Journal of Physics: Conference Series*, volume 555, page 012067. IOP Publishing, 2014.

[73] Marco D Masciola. *Dynamic Analysis of a Coupled and an Uncoupled Tension Leg Platform*, volume 73. 2011.

[74] Marco Masciola, Meyer Nahon, and Frederick Driscoll. Preliminary assessment of the importance of platform–tendon coupling in a tension leg platform. *Journal of Offshore Mechanics and Arctic Engineering*, 135(3):031901, 2013.

[75] Ivo Senjanović, Neven Hadžić, and Marko Tomić. On the linear stiffness of tension leg platforms. In *International Maritime Association of the Mediterranean*, 2011.

[76] Ivo Senjanović, Marko Tomić, and Smiljko Rudan. Investigation of nonlinear restoring stiffness in dynamic analysis of tension leg platforms. *Engineering structures*, 56:117–125, 2013.

[77] Marco Masciola, Amy Robertson, Jason Jonkman, Alexander Coulling, Andrew Goupee, et al. Assessment of the importance of mooring dynamics on the global response of the deepcwind floating semisubmersible offshore wind turbine. In *The*

Twenty-third International Offshore and Polar Engineering Conference. International Society of Offshore and Polar Engineers, 2013.

[78] Dongsheng Qiao and Jinping Ou. Mooring line damping estimation for a floating wind turbine. *The Scientific World Journal*, 2014, 2014.

[79] Zi Lin and P Sayer. An enhanced stiffness model for elastic lines and its application to the analysis of a moored floating offshore wind turbine. *Ocean Engineering*, 109:444–453, 2015.

[80] Qing'an Li, Yasunari Kamada, Takao Maeda, Junsuke Murata, Kohei Iida, and Yuta Okumura. Fundamental study on aerodynamic force of floating offshore wind turbine with cyclic pitch mechanism. *Energy*, 99:20–31, 2016.

[81] Elizabeth N Wayman, PD Sclavounos, S Butterfield, J Jonkman, W Musial, et al. Coupled dynamic modeling of floating wind turbine systems. In *Offshore Technology Conference*. Offshore Technology Conference, 2006.

[82] Jason Mark Jonkman. *Dynamics modeling and loads analysis of an offshore floating wind turbine*. ProQuest, 2007.

[83] YH Bae and MH Kim. Rotor-floater-mooring coupled dynamic analysis of mono-column-tlp-type fowt (floating offshore wind turbine). *Ocean Systems Engineering*, 1(1):95–111, 2011.

[84] Madjid Karimirad, Quentin Meissonnier, Zhen Gao, and Torgeir Moan. Hydroelastic code-to-code comparison for a tension leg spar-type floating wind turbine. *Marine Structures*, 24(4):412–435, 2011.

[85] Ruoyu Zhang, Yougang Tang, Jun Hu, Shengfu Ruan, and Chaohe Chen. Dynamic response in frequency and time domains of a floating foundation for offshore wind turbines. *Ocean Engineering*, 60:115–123, 2013.

[86] Madjid Karimirad and Constantine Michailides. Dynamic analysis of a braceless semisubmersible offshore wind turbine in operational conditions. *Energy Procedia*, 80:21–29, 2015.

[87] MA Yu, Zhi-qiang HU, and Long-fei XIAO. Wind-wave induced dynamic response analysis for motions and mooring loads of a spar-type offshore floating wind turbine. *Journal of Hydrodynamics, Ser. B*, 26(6):865–874, 2015.

[88] Evaggelos G Karageorgopoulos and Athanassios A Dimas. Coupled hydrodynamic and structural behavior of spar buoy floating wind turbines using fast.

[89] Frederick Driscoll, Jason Jonkman, Amy Robertson, Senu Sirnivas, Bjørn Skaare, and Finn Gunnar Nielsen. Validation of a fast model of the statoil-hywind demo floating wind turbine. *Energy Procedia*, 94:3–19, 2016.

[90] Tor Anders Nygaard, Jacobus De Vaal, Fabio Pierella, Luca Oggiano, and Roy Stenbro. Development, verification and validation of 3dfloat; aero-servo-hydro-elastic computations of offshore structures. *Energy Procedia*, 94:425–433, 2016.

[91] Hyunseong Min, Cheng Peng, Fei Duan, Zhiqiang Hu, and Jun Zhang. Numerical simulation of dynamics of a spar type floating wind turbine and comparison with laboratory measurements. In *ASME 2016 35th International Conference on Ocean, Offshore and Arctic Engineering*, pages V006T09A034–V006T09A034. American Society of Mechanical Engineers, 2016.

[92] Antonio Pegalajar-Jurado, Henrik Bredmose, Michael Borg, Jonas G Straume, Trond Landbø, Håkon S Andersen, Wei Yu, Kolja Müller, and Frank Lemmer. State-of-the-art model for the lifes50+ oo-star wind floater semi 10mw floating wind turbine. In *Journal of Physics: Conference Series*, volume 1104, page 012024. IOP Publishing, 2018.

[93] Lei Wang and Bert Sweetman. Conceptual design of floating wind turbines with large-amplitude motion. *Proceedings of Society of Naval Architects and Marine Engineers*, 2011.

[94] Frank Sandner, David Schlipf, Denis Matha, Robert Seifried, and Po Wen Cheng. Reduced nonlinear model of a spar-mounted floating wind turbine. 2012.

[95] Madjid Karimirad and Torgeir Moan. A simplified method for coupled analysis of floating offshore wind turbines. *Marine Structures*, 27(1):45–63, 2012.

[96] RC Lupton. Characterising dynamic non-linearity in floating wind turbines. In *Journal of Physics: Conference Series*, volume 555, page 012064. IOP Publishing, 2014.

[97] Denis Matha, Frank Sandner, and David Schlipf. Efficient critical design load case identification for floating offshore wind turbines with a reduced nonlinear model. In *Journal of Physics: Conference Series*, volume 555, page 012069. IOP Publishing, 2014.

[98] Richard Lupton. *Frequency-domain modelling of floating wind turbines*. PhD thesis, University of Cambridge, 2015.

[99] Sara Salehyar and Qiang Zhu. Aerodynamic dissipation effects on the rotating blades of floating wind turbines. *Renewable Energy*, 78:119–127, 2015.

[100] Yingguang Wang. Robust frequency-domain identification of parametric radiation force models for a floating wind turbine. *Ocean Engineering*, 109:580–594, 2015.

[101] R Farrugia, T Sant, and D Micallef. A study on the aerodynamics of a floating wind turbine rotor. *Renewable Energy*, 86:770–784, 2016.

[102] Geliang Liu, Zhiqiang Hu, and Fei Duan. Preliminary analysis about coupled response of offshore floating wind turbine system in time domain. In *ASME 2015 34th International Conference on Ocean, Offshore and Arctic Engineering*, pages V009T09A042–V009T09A042. American Society of Mechanical Engineers, 2015.

[103] Neeraj Aggarwal, R Manikandan, and Nilanjan Saha. Nonlinear short term extreme response of spar type floating offshore wind turbines. *Ocean Engineering*, 130:199–209, 2017.

[104] Frank Lemmer, Steffen Raach, David Schlipf, and Po Wen Cheng. Parametric wave excitation model for floating wind turbines. *Energy Procedia*, 94:290–305, 2016.

[105] Madjid Karimirad and Torgeir Moan. Effect of aerodynamic and hydrodynamic damping on dynamic response of spar type floating wind turbine. In *EWEC2010*, 2010.

[106] Sébastien Gueydon. Aerodynamic damping on a semisubmersible floating foundation for wind turbines. *Energy Procedia*, 94:367–378, 2016.

[107] Paula Doubrawa, Matthew J Churchfield, Marte Godvik, and Senu Sirnivas. Load response of a floating wind turbine to turbulent atmospheric flow. *Applied Energy*, 242:1588–1599, 2019.

[108] Macheng Shen, Zhiqiang Hu, and Geliang Liu. Dynamic response and viscous effect analysis of a tlp-type floating wind turbine using a coupled aero-hydro-mooring dynamic code. *Renewable Energy*, 99:800–812, 2016.

[109] YH Bae, MH Kim, SW Im, et al. Effects of tower elasticity and aero-loading in aero-elastic-control-floater-mooring coupled dynamic analysis for a tlp-type fowt. In *The Twenty-second International Offshore and Polar Engineering Conference*. International Society of Offshore and Polar Engineers, 2012.

[110] Tobias Finn. Hydroelasticity of a large floating windturbine platform. 2014.

[111] Christof Wehmeyer, Francesco Ferri, Morten Thøtt Andersen, and Ronnie Refstrup Pedersen. Hybrid model representation of a tlp including flexible topsides in non-linear regular waves. *Energies*, 7(8):5047–5064, 2014.

[112] Chong Ma, Kazuhiro Iijima, and Yasunori Nihei. Strongly coupled method for predicting the response of flexible fowt with mooring and its experimental validation. In *ASME 2014 33rd International Conference on Ocean, Offshore and Arctic Engineering*, pages V007T05A023–V007T05A023. American Society of Mechanical Engineers, 2014.

[113] A Campos, M Molins, P Trubat, and D Alarcón. Analysis of structural second order effects on a floating concrete platform for fowt's. *Energy Procedia*, 94:155–163, 2016.

[114] Y Xing, M Karimirad, and T Moan. Modelling and analysis of floating spar-type wind turbine drivetrain. *Wind Energy*, 17(4):565–587, 2014.

[115] Christof Wehmeyer, , and JH Rasmussen. Mooring response of a floating offshore wind turbine in nonlinear irregular waves. *Journal of Ocean andWind Energy*, 2(1):37–44, 2015.

[116] Atsede G Endegnanew, Kristian Satertro, Sverre Gjerde, Harald Svendsen, Olimpo Anaya-Lara, John O Tande, Kjetil Uhlen, and Svein Gjolmesli. Integrated modelling platform for dynamic performance assessment of floating wind turbines. *Energy Procedia*, 80:376–391, 2015.

[117] Feike Savenije and Johan Peeringa. Control development for floating wind. In *Journal of Physics: Conference Series*, volume 524, page 012090. IOP Publishing, 2014.

[118] Paul A Fleming, Antoine Peiffer, and David Schlipf. Wind turbine controller to mitigate structural loads on a floating wind turbine platform. In *ASME 2016 35th International Conference on Ocean, Offshore and Arctic Engineering*, pages V006T09A044–V006T09A044. American Society of Mechanical Engineers, 2016.

[119] Andrew J Goupee, Richard W Kimball, and Habib J Dagher. Experimental observations of active blade pitch and generator control influence on floating wind turbine response. *Renewable Energy*, 104:9–19, 2017.

[120] Cheng Zhang and Franck Plestan. Individual/collective blade pitch control of floating wind turbine based on adaptive second order sliding mode. *Ocean Engineering*, 228:108897, 2021.

[121] Eivind Lindeberg, Harald G Svendsen, and Kjetil Uhlen. Smooth transition between controllers for floating wind turbines. *Energy Procedia*, 24:83–98, 2012.

[122] Steffen Raach, David Schlipf, Frank Sandner, Denis Matha, and Po Wen Cheng. Nonlinear model predictive control of floating wind turbines with individual pitch control. In *2014 American Control Conference*, pages 4434–4439. IEEE, 2014.

[123] Feng Yang, Qing-wang Song, Lei Wang, Shan Zuo, and Sheng-shan Li. Wind and wave disturbances compensation to floating offshore wind turbine using improved individual pitch control based on fuzzy control strategy. In *Abstract and Applied Analysis*, volume 2014. Hindawi Publishing Corporation, 2014.

[124] Søren Christiansen, Thomas Bak, and Torben Knudsen. Damping wind and wave loads on a floating wind turbine. *Energies*, 6(8):4097–4116, 2013.

[125] S Christiansen, T Knudsen, and Thomas Bak. Extended onshore control of a floating wind turbine with wave disturbance reduction. In *Journal of Physics: Conference Series*, volume 555, page 012018. IOP Publishing, 2014.

[126] Frank Lemmer, David Schlipf, and Po Wen Cheng. Control design methods for floating wind turbines for optimal disturbance rejection. In *Journal of Physics: Conference Series*, volume 753, page 092006. IOP Publishing, 2016.

[127] Yu Ma, Paul D. Sclavounos, John Cross-Whiter, and Dhiraj Arora. Wave forecast and its application to the optimal control of offshore floating wind turbine for load mitigation. *Renewable Energy*, 128:163–176, 2018.

[128] Pedro A Galvani, Fei Sun, and Kamran Turkoglu. Aerodynamic modelling of nrel 5-mw wind turbine for nonlinear control system design: A case study based on real-time nonlinear receding horizon control. *Aerospace*, 3(3):27, 2016.

[129] Axelle Viré, Jiansheng Xiang, Matthew Piggott, Colin Cotter, and Christopher Pain. Towards the fully-coupled numerical modelling of floating wind turbines. *Energy Procedia*, 35:43–51, 2013.

[130] Ali Nematbakhsh, Erin E Bachynski, Zhen Gao, and Torgeir Moan. Comparison of wave load effects on a tlp wind turbine by using computational fluid dynamics and potential flow theory approaches. *Applied Ocean Research*, 53:142–154, 2015.

[131] Thanh-Toan Tran and Dong-Hyun Kim. The platform pitching motion of floating offshore wind turbine: A preliminary unsteady aerodynamic analysis. *Journal of Wind Engineering and Industrial Aerodynamics*, 142:65–81, 2015.

[132] Thanh Toan Tran and Dong-Hyun Kim. The coupled dynamic response computation for a semi-submersible platform of floating offshore wind turbine. *Journal of Wind Engineering and Industrial Aerodynamics*, 147:104–119, 2015.

[133] Ali Nematbakhsh, Zhen Gao, and Torgeir Moan. Benchmarking of a cfd based numerical wave tank for studying wave load effects on fixed and floating offshore structures. *Journal of Offshore Mechanics and Arctic Engineering*, 2016.

[134] Luca Oggiano, Fabio Pierella, Tor Anders Nygaard, Jacobus De Vaal, and Emile Arens. Comparison of experiments and cfd simulations of a braceless concrete semi-submersible platform. *Energy Procedia*, 94:278–289, 2016.

[135] V Leble and GN Barakos. A coupled floating offshore wind turbine analysis with high-fidelity methods. *Energy Procedia*, 94:523–530, 2016.

[136] Nicolai F Heilskov and Ole Svenstrup Petersen. Non-linear 3d hydrodynamics of floating wind turbine compared against wave tank tests. In *ASME 2016 35th International Conference on Ocean, Offshore and Arctic Engineering*, pages V002T08A066–V002T08A066. American Society of Mechanical Engineers, 2016.

[137] J Yan, A Korobenko, X Deng, and Y Bazilevs. Computational free-surface fluid–structure interaction with application to floating offshore wind turbines. *Computers & Fluids*, 141:155–174, 2016.

[138] Vladimir Leble and George Barakos. Demonstration of a coupled floating offshore wind turbine analysis with high-fidelity methods. *Journal of Fluids and Structures*, 62:272–293, 2016.

[139] LIU Yuanchuan, XIAO Qing, Atilla Incecik, and De-Cheng Wan. Investigation of the effects of platform motion on the aerodynamics of a floating offshore wind turbine. *Journal of Hydrodynamics, Ser. B*, 28(1):95–101, 2016.

[140] Simon Burmester, Guilherme Vaz, and Ould el Moctar. Towards credible cfd simulations for floating offshore wind turbines. *Ocean Engineering*, 209:107237, 2020.

[141] C Wright, K O'Sullivan, J Murphy, and V Pakrashi. Experimental comparison of dynamic responses of a tension moored floating wind turbine platform with and without spring dampers. In *Journal of Physics: Conference Series*, volume 628, page 012056. IOP Publishing, 2015.

[142] Denis Matha, Frank Sandner, Climent Molins, Alexis Campos, and Po Wen Cheng. Efficient preliminary floating offshore wind turbine design and testing methodologies and application to a concrete spar design. *Philosophical Transactions of the Royal Society of London A: Mathematical, Physical and Engineering Sciences*, 373(2035):20140350, 2015.

[143] A Otter, J Murphy, and CJ Desmond. Emulating aerodynamic forces and moments for hybrid testing of floating wind turbine models. In *Journal of Physics: Conference Series*, volume 1618, page 032022. IOP Publishing, 2020.

[144] José Azcona, Faisal Bouchotrouch, and Felipe Vittori. Low-frequency dynamics of a floating wind turbine in wave tank–scaled experiments with sil hybrid method. *Wind Energy*, 22(10):1402–1413, 2019.

[145] Yasunori Nihei and Hiroyuki Fujioka. Aerodynamic effects on tlp type wind turbines and predictions of the electricity they generate. *Journal of Marine Science and Application*, 10(2):139–149, 2011.

[146] Hyunkyoung Shin, Pham Thanh Dam, et al. Model test of a floating offshore wind turbine moored by a spring-tensioned-leg. In *The Twenty-second International Offshore and Polar Engineering Conference*. International Society of Offshore and Polar Engineers, 2012.

[147] Hyunkyoung Shin, Sangrai Cho, and Kwangjin Jung. Model test of an inverted conical cylinder floating offshore wind turbine moored by a spring-tensioned-leg. *International Journal of Naval Architecture and Ocean Engineering*, 6(1):1–13, 2014.

[148] Giuseppe Roberto Tomasicchio, Elvira Armenio, Felice D'Alessandro, Nuno Fonseca, Spyros A Mavrakos, Valery Penchev, Holger Schuttrumpf, Spyridon Voutsi-

nas, Jens Kirkegaard, and Palle M Jensen. Design of a 3d physical and numerical experiment on floating off-shore wind turbines. *Coastal Engineering Proceedings*, 1(33):67, 2012.

[149] A Courbois, O Flamand, JL Toularastel, P Ferrant, and JM Rousset. Applying relevant wind generation techniques to the case of floating wind turbines. In *6th European and African Wind Engineering Conference*, pages 1–8, 2013.

[150] Christof Wehmeyer, Francesco Ferri, Peter Bak Frigaard, Jesper Skourup, et al. Experimental study of an offshore wind turbine tlp in uls conditions. In *The Twenty-third International Offshore and Polar Engineering Conference*. International Society of Offshore and Polar Engineers, 2013.

[151] Marc Le Boulluec, Jérémy Ohana, Alexis Martin, and Anne Houmard. Tank testing of a new concept of floating offshore wind turbine. In *ASME 2013 32nd International Conference on Ocean, Offshore and Arctic Engineering*, pages V008T09A100–V008T09A100. American Society of Mechanical Engineers, 2013.

[152] Frank Adam, Thomas Myland, Burkhard Schuldt, Jochen Großmann, and Frank Dahlhaus. Evaluation of internal force superposition on a tlp for wind turbines. *Renewable Energy*, 71:271–275, 2014.

[153] Fons Huijs, Erik-Jan de Ridder, and Feike Savenije. Comparison of model tests and coupled simulations for a semi-submersible floating wind turbine. In *ASME 2014 33rd International Conference on Ocean, Offshore and Arctic Engineering*, pages V09AT09A012–V09AT09A012. American Society of Mechanical Engineers, 2014.

[154] Sinpyo Hong, Inwon Lee, Seong Hyeon Park, Cheolmin Lee, Ho-Hwan Chun, and Hee Chang Lim. An experimental study of the effect of mooring systems on the dynamics of a spar buoy-type floating offshore wind turbine. *International Journal of Naval Architecture and Ocean Engineering*, 7(3):559–579, 2015.

[155] Michel Make and Guilherme Vaz. Analyzing scaling effects on offshore wind turbines using cfd. *Renewable Energy*, 83:1326–1340, 2015.

[156] Fei Duan, Zhiqiang Hu, and Jin Wang. Model tests of a spar-type floating wind turbine under wind/wave loads. In *ASME 2015 34th International Conference on Ocean, Offshore and Arctic Engineering*, pages V009T09A044–V009T09A044. American Society of Mechanical Engineers, 2015.

[157] Fei Duan, Zhiqiang Hu, Geliang Liu, and Jin Wang. Experimental comparisons of dynamic properties of floating wind turbine systems based on two different rotor concepts. *Applied Ocean Research*, 58:266–280, 2016.

[158] Alexis Campos, Climent Molins, Xavier Gironella, Pau Trubat, and Daniel Alarcón. Experimental rao's analysis of a monolithic concrete spar structure for offshore floating wind turbines. In *ASME 2015 34th International Conference on Ocean, Offshore and Arctic Engineering*, pages V001T01A016–V001T01A016. American Society of Mechanical Engineers, 2015.

[159] Michel Make, Guilherme Vaz, Gerson Fernandes, Simon Burmester, and Sebastien Gueydon. Analysis of aerodynamic performance of floating wind turbines using cfd and bemt methods. In *ASME 2015 34th International Conference on Ocean, Offshore and Arctic Engineering*, pages V009T09A052–V009T09A052. American Society of Mechanical Engineers, 2015.

[160] Steven Martin, Sandy Day, and Conor B Gilmour. Rotor scaling methodologies for small scale testing of floating wind turbine systems. In *ASME 2015 34th International Conference on Ocean, Offshore and Arctic Engineering*, pages V009T09A045–V009T09A045. American Society of Mechanical Engineers, 2015.

[161] Sébastien Gueydon, Guillaume Venet, and Gerson Fernandes. Influence of the rotor characterization on the motion of a floating wind turbine. In *ASME 2015 34th International Conference on Ocean, Offshore and Arctic Engineering*, pages V009T09A053–V009T09A053. American Society of Mechanical Engineers, 2015.

[162] Antonio Pegalajar-Jurado, Anders M Hansen, Robert Laugesen, Robert F Mikkelsen, Michael Borg, Taeseong Kim, Nicolai F Heilskov, and Henrik Bredmose. Experimental and numerical study of a 10mw tlp wind turbine in waves and

wind. In *Journal of Physics: Conference Series*, volume 753, page 092007. IOP Publishing, 2016.

[163] Gordon Stewart and Michael Muskulus. A review and comparison of floating offshore wind turbine model experiments. *Energy Procedia*, 94:227–231, 2016.

[164] Sarah McElman, Arjen Koop, Erik-Jan de Ridder, and Andrew Goupee. Simulation and development of a wind-wave facility for scale testing of offshore floating wind turbines. In *ASME 2016 35th International Conference on Ocean, Offshore and Arctic Engineering*, pages V006T09A035–V006T09A035. American Society of Mechanical Engineers, 2016.

[165] V Gevorgian. Grid simulator for testing a wind turbine on offshorefloating platform. *Contract*, 303:275–3000, 2012.

[166] Anthony M Viselli, Andrew J Goupee, and Habib J Dagher. Model test of a 1: 8-scale floating wind turbine offshore in the gulf of maine. *Journal of Offshore Mechanics and Arctic Engineering*, 137(4):041901, 2015.

[167] Anthony M Viselli, Andrew J Goupee, Habib J Dagher, and Christopher K Allen. Volturnus 1: 8: Conclusion of 18-months of operation of the first grid-connected floating wind turbine prototype in the americas. In *ASME 2015 34th International Conference on Ocean, Offshore and Arctic Engineering*, pages V009T09A055–V009T09A055. American Society of Mechanical Engineers, 2015.

[168] Bjørn Skaare, Finn Gunnar Nielsen, Tor David Hanson, Rune Yttervik, Ole Havmøller, and Arne Rekdal. Analysis of measurements and simulations from the hywind demo floating wind turbine. *Wind Energy*, 18(6):1105–1122, 2015.

[169] M. Belloli, I. Bayati, A. Facchinetti, A. Fontanella, H. Giberti, F. La Mura, F. Taruffi, and A. Zasso. A hybrid methodology for wind tunnel testing of floating offshore wind turbines. *Ocean Engineering*, 210:107592, 2020.

[170] Stanislav Rockel, Joachim Peinke, Michael Hölling, and Raúl Bayoán Cal. Wake to wake interaction of floating wind turbine models in free pitch motion: An eddy viscosity and mixing length approach. *Renewable Energy*, 85:666–676, 2016.

[171] Erin E Bachynski, Valentin Chabaud, and Thomas Sauder. Real-time hybrid model testing of floating wind turbines: sensitivity to limited actuation. *Energy Procedia*, 80:2–12, 2015.

[172] I Bayati, M Belloli, D Ferrari, F Fossati, and H Giberti. Design of a 6-dof robotic platform for wind tunnel tests of floating wind turbines. *Energy Procedia*, 53:313–323, 2014.

[173] Gordon Stewart and Michael Muskulus. Aerodynamic simulation of the marintek braceless semisubmersible wave tank tests. In *Journal of Physics: Conference Series*, volume 749, page 012012. IOP Publishing, 2016.

[174] Elif Oguz, David Clelland, Alexander H Day, Atilla Incecik, Juan Amate López, Gustavo Sánchez, and Gonzalo González Almeria. Experimental and numerical analysis of a tlp floating offshore wind turbine. *Ocean Engineering*, 147:591–605, 2018.

[175] Josh Davidson, Simone Giorgi, and John V Ringwood. Identification of wave energy device models from numerical wave tank data—part 1: Numerical wave tank identification tests.

[176] Amir Rasekhi Nejad, Erin E Bachynski, Marit I Kvittem, Chenyu Luan, Zhen Gao, and Torgeir Moan. Stochastic dynamic load effect and fatigue damage analysis of drivetrains in land-based and tlp, spar and semi-submersible floating wind turbines. *Marine Structures*, 42:137–153, 2015.

[177] JM Jonkman and Denis Matha. Dynamics of offshore floating wind turbines—analysis of three concepts. *Wind Energy*, 14(4):557–569, 2011.

[178] Amy N Robertson, Jason M Jonkman, et al. Loads analysis of several offshore floating wind turbine concepts. In *The Twenty-first International Offshore and*

Polar Engineering Conference. International Society of Offshore and Polar Engineers, 2011.

[179] Bonjun J Koo, Andrew J Goupee, Richard W Kimball, and Kostas F Lambrakos. Model tests for a floating wind turbine on three different floaters. *Journal of Offshore Mechanics and Arctic Engineering*, 136(2):020907, 2014.

[180] Andrew J Goupee, Bonjun J Koo, Richard W Kimball, Kostas F Lambrakos, and Habib J Dagher. Experimental comparison of three floating wind turbine concepts. *Journal of Offshore Mechanics and Arctic Engineering*, 136(2):020906, 2014.

[181] Yasunori Nihei, Kazuhiro Iijima, Motohiko Murai, and Tomoki Ikoma. A comparative study of motion performance of four different fowt designs in combined wind and wave loads. In *ASME 2014 33rd International Conference on Ocean, Offshore and Arctic Engineering*, pages V007T05A025–V007T05A025. American Society of Mechanical Engineers, 2014.

[182] Ali Nematbakhsh, Erin E Bachynski, Zhen Gao, Torgeir Moan, et al. Comparison of wave-induced response of a tlp wind turbine obtained by cfd method and potential theory. In *The Twenty-fourth International Ocean and Polar Engineering Conference*. International Society of Offshore and Polar Engineers, 2014.

[183] Zheng-Shou Chen, Wu-Joan Kim, and Jae-Hoon Yoo. Fsi analysis of tlp tether system for floating wind turbine. *Journal of Ocean Engineering and Technology*, 24(1):10–19, 2010.

[184] Wang YH F, Fan Y H, and Yang L. The analysis of vibrations induced by variation section vortex in tension leg platform for a floating wind turbine. *Computer Modelling and new Technologies*, 18(11):1160–66, 2014.

[185] Hyun-Sung Kim, Byoung Wan Kim, Seok Won Hong, Sa Young Hong, et al. Numerical study for the effect of viv on tendon of tlp. In *The 26th International Ocean and Polar Engineering Conference*. International Society of Offshore and Polar Engineers, 2016.

[186] YH Liu, MH Kim, CH Kim, et al. The computation of second-order mean and double-frequency wave loads on a compliant tlp by hodem. *International Journal of Offshore and Polar Engineering*, 5(02), 1995.

[187] Line Roald, Jason Jonkman, Amy Robertson, and Ndaona Chokani. The effect of second-order hydrodynamics on floating offshore wind turbines. *Energy Procedia*, 35:253–264, 2013.

[188] PeiWen Cong, Ying Gou, and Bin Teng. Effect of pontoons on free surface elevation around a tlp platform. *Science China Technological Sciences*, 57(1):163–180, 2014.

[189] Sébastien Gueydon, Pierre-Yves Wuillaume, Jason Jonkman, Amy Robertson, Andrew Platt, et al. Comparison of second-order loads on a tension-leg platform for wind turbines. In *The Twenty-fifth International Offshore and Polar Engineering Conference*. International Society of Offshore and Polar Engineers, 2015.

[190] Antonio Pegalajar-Jurado, Henrik Bredmose, and Michael Borg. Multi-level hydrodynamic modelling of a scaled 10mw tlp wind turbine. *Energy Procedia*, 94:124–132, 2016.

[191] AM Hansen and R Laugesen. *Experimental study of the dynamic response of the DTU 10MW wind turbine on a tension leg platform*. PhD thesis, MSc thesis, DTU Wind Energy. Kgs. Lyngby, Denmark, 2015.

[192] Jia-yang Gu, Jie Wu, et al. Study on the transient dynamic characteristics of tlp under impact load. In *The Twenty-fourth International Ocean and Polar Engineering Conference*. International Society of Offshore and Polar Engineers, 2014.

[193] J Zou, Y Xu, CH Kim, CT Zhao, et al. Ringing of issc tlp due to laboratory storm seas. *International Journal of Offshore and Polar Engineering*, 8(02), 1998.

[194] Taeyoung Kim, Yonghwan Kim, et al. Study on prediction method for the springing-induced tension responses of tlp. In *The Twenty-fifth International Offshore and Polar Engineering Conference*. International Society of Offshore and Polar Engineers, 2015.

[195] Kun Xu, Min Zhang, Yanlin Shao, Zhen Gao, and Torgeir Moan. Effect of wave nonlinearity on fatigue damage and extreme responses of a semi-submersible floating wind turbine. *Applied Ocean Research*, 91:101879, 2019.

[196] Min Luo, Chan Ghee Koh, Wei Xian Lee, Pengzhi Lin, and Dominic E Reeve. Experimental study of freak wave impacts on a tension-leg platform. *Marine Structures*, 74:102821, 2020.

[197] Raffaello Antonutti, Christophe Peyrard, Lars Johanning, Atilla Incecik, and David Ingram. An investigation of the effects of wind-induced inclination on floating wind turbine dynamics: heave plate excursion. *Ocean Engineering*, 91:208–217, 2014.

[198] Raffaello Antonutti, Christophe Peyrard, Lars Johanning, Atilla Incecik, and David Ingram. The effects of wind-induced inclination on the dynamics of semi-submersible floating wind turbines in the time domain. *Renewable Energy*, 88:83–94, 2016.

[199] Zahid Ullah, Naik Muhammad, and Dong-Ho Choi. Effect of hydrostatic nonlinearity on the large amplitude response of a spar type floating wind turbine. *Ocean Engineering*, 172:803 – 816, 2019.

[200] RC Lupton and RS Langley. Scaling of slow-drift motion with platform size and its importance for floating wind turbines. *Renewable Energy*, 101:1013–1020, 2017.

[201] Alexandre N. Simos, Felipe Ruggeri, Rafael A. Watai, Antonio Souto-Iglesias, and Carlos Lopez-Pavon. Slow-drift of a floating wind turbine: An assessment of frequency-domain methods based on model tests. *Renewable Energy*, 116:133 – 154, 2018.

[202] Jie Yang, Yan-Ping He, Yong-Sheng Zhao, Yan-Lin Shao, and Zhao-Long Han. Experimental and numerical studies on the low-frequency responses of a spar-type floating offshore wind turbine. *Ocean Engineering*, 222:108571, 2021.

[203] Zhixin Zhao, Wenhua Wang, Wei Shi, and Xin Li. Effects of second-order hydrodynamics on an ultra-large semi-submersible floating offshore wind turbine. *Structures*, 28:2260 – 2275, 2020.

[204] M Philippe, A Babarit, and P Ferrand. Effect of wave direction relative to wind on the motions of offshore floating wind turbine systems. In *International conference and exhibition on ocean energy*, 2010.

[205] TB Johannessen, S Haver, T Bunnik, and B Buchner. Extreme wave effects on deep water tlps lessons learned from the snorre a model tests. *Proc. Deep Offshore Technology 2006*, pages 28–30, 2006.

[206] Madjid Karimirad, Zhen Gao, and Torgeir Moan. Dynamic motion analysis of catenary moored spar wind turbine in extreme environmental condition. In *EOW2009*, 2009.

[207] Wei-ting Hsu, Krish P Thiagarajan, Michael MacNicoll, and Richard Akers. Prediction of extreme tensions in mooring lines of a floating offshore wind turbine in a 100-year storm. In *ASME 2015 34th International Conference on Ocean, Offshore and Arctic Engineering*, pages V009T09A050–V009T09A050. American Society of Mechanical Engineers, 2015.

[208] Aysan Jamalkia, Mir Mohammad Ettefagh, and Alireza Mojtahedi. Damage detection of tlp and spar floating wind turbine using dynamic response of the structure. *Ocean Engineering*, 125:191–202, 2016.

[209] Katsunari Fujioka, Yasunori Nihei, and Kazuhiro Iijima. Seaquake loads acting on offshore wind turbine. In *ASME 2016 35th International Conference on Ocean, Offshore and Arctic Engineering*, pages V006T05A010–V006T05A010. American Society of Mechanical Engineers, 2016.

[210] Yingguang Wang. Optimal threshold selection in the pot method for extreme value prediction of the dynamic responses of a spar-type floating wind turbine. *Ocean Engineering*, 134:119–128, 2017.

[211] Yichao Liu, Riccardo Ferrari, Ping Wu, Xiaoli Jiang, Sunwei Li, and Jan-Willem van Wingerden. Fault diagnosis of the 10mw floating offshore wind turbine benchmark: A mixed model and signal-based approach. *Renewable Energy*, 164:391 – 406, 2021.

[212] Salem Okpokparoro and Srinivas Sriramula. Uncertainty modeling in reliability analysis of floating wind turbine support structures. *Renewable Energy*, 165:88 – 108, 2021.

[213] Yuki Mizukami, Yasunori Nihei, Kazuhiro Iijima, and Naoyuki Hara. A study on motion characteristics of wind turbine on a floating platform in blade pitch control malfunction. In *ASME 2016 35th International Conference on Ocean, Offshore and Arctic Engineering*, pages V006T05A015–V006T05A015. American Society of Mechanical Engineers, 2016.

[214] Sharath Srinivasamurthy, Kazuhiro Iijima, Yasunori Nihei, and Naoyuki Hara. Coupled simulation between fast and hydro-structural code for a flexible fowt considering blade pitch control malfunction. In *ASME 2016 35th International Conference on Ocean, Offshore and Arctic Engineering*, pages V006T05A009–V006T05A009. American Society of Mechanical Engineers, 2016.

[215] Sharath Srinivasamurthy, Kazuhiro Iijima, Masahiko Fujikubo, and Yasunori Nihei. Elastic-plastic behavior analysis for a flexible fowt subjected to blade pitch control malfunction. *Journal of the Japan Society of Naval Architects and Ocean Engineers*, 23:179–187, 2016.

[216] YH Bae, MH Kim, and HC Kim. Performance changes of a floating offshore wind turbine with broken mooring line. *Renewable Energy*, 101:364–375, 2017.

[217] Michele Martini, Alfonso Jurado, Raúl Guanche, and Iñigo Losada. Probabilistic assessment of floating wind turbine access by catamaran vessel. *Energy Procedia*, 94:249–260, 2016.

[218] Michele Martini, Alfonso Jurado, Raúl Guanche, and Iñigo J Losada. Evaluation of walk-to-work accessibility for a floating wind turbine. In *ASME 2016 35th International Conference on Ocean, Offshore and Arctic Engineering*, pages V006T09A038–V006T09A038. American Society of Mechanical Engineers, 2016.

[219] K Raed, D Karmakar, and C Guedes Soares. Uncertainty modelling of wave loads acting on semi-submersible floating support structure for offshore wind turbine. 2015.

[220] Roberts Proskovics, Gail Hutton, Ralph Torr, and Matti Niclas Scheu. Methodology for risk assessment of substructures for floating wind turbines. *Energy Procedia*, 94:45–52, 2016.

[221] Jonas Skaare Amundsen. Consequences of introducing a cut-out wave height on a floating wind turbine concept. Master's thesis, Norwegian University of Life Sciences, Ås, 2013.

[222] Michele Martini, Raúl Guanche, José A Armesto, and Iñigo J Losada. Met-ocean conditions influence over floating wind turbine energy production. In *ASME 2015 34th International Conference on Ocean, Offshore and Arctic Engineering*, pages V009T09A056–V009T09A056. American Society of Mechanical Engineers, 2015.

[223] EI Zountouridou, GC Kiokes, S Chakalis, PS Georgilakis, and ND Hatziargyriou. Offshore floating wind parks in the deep waters of mediterranean sea. *Renewable and Sustainable Energy Reviews*, 51:433–448, 2015.

[224] Sung Hyun Hwang and Hong Jin Kim. Assessment of floating offshore wind farm in korea.

[225] Anja Eide Onstad, Marit Stokke, and Lars Sætran. Site assessment of the floating wind turbine hywind demo. *Energy Procedia*, 94:409–416, 2016.

[226] Zi Lin, Xiaolei Liu, and Saeid Lotfian. Impacts of water depth increase on offshore floating wind turbine dynamics. *Ocean Engineering*, 224:108697, 2021.

[227] Giovanni Rinaldi, Anna Garcia-Teruel, Henry Jeffrey, Philipp R Thies, and Lars Johanning. Incorporating stochastic operation and maintenance models into the techno-economic analysis of floating offshore wind farms. *Applied Energy*, 301:117420, 2021.

[228] Emre Uzunoglu and Carlos Guedes Soares. *An integrated design approach for a self-float capable tension leg platform for wind energy.* 11 2021.

[229] Paul Sclavounos, Christopher Tracy, and Sungho Lee. Floating offshore wind turbines: Responses in a seastate pareto optimal designs and economic assessment. In *ASME 2008 27th International Conference on Offshore Mechanics and Arctic Engineering*, pages 31–41. American Society of Mechanical Engineers, 2008.

[230] Sungho Lee et al. Dynamic response analysis of spar buoy floating wind turbine systems. 2008.

[231] Kenji Shimada, Masahiro Miyakawa, Takumi Ohyama, Takeshi Ishihara, Yukinari Fukumoto, Kouichirou Anno, Hideaki Okada, and Yoichi Moriya. Preliminal study on optimum design of a tension leg platform for the offshore wind generated energy system. *Renewable Energy*, 27, 2010.

[232] Koji Suzuki, Hiroshi Yamaguchi, Masayuki Akase, Akihiko Imakita, Takeshi Ishihara, Yukinari Fukumoto, and Takumi Oyama. Initial design of tlp for offshore wind farm. In *Proc. of Renewable Energy 2010 International Conference*, 2010.

[233] Anders Myhr, Tor Anders Nygaard, et al. Load reductions and optimizations on tension-leg-buoy offshore wind turbine platforms. In *The Twenty-second International Offshore and Polar Engineering Conference.* International Society of Offshore and Polar Engineers, 2012.

[234] Ørjan Fredheim. Fatigue analysis of column-brace connection in a semi-submersible wind turbine, 2012.

[235] Matthew Hall, Brad Buckham, and Curran Crawford. Evolving offshore wind: A genetic algorithm-based support structure optimization framework for floating wind turbines. In *OCEANS-Bergen, 2013 MTS/IEEE*, pages 1–10. IEEE, 2013.

[236] Latha Sethuraman. Hydrodynamics and drive-train dynamics of a direct-drive floating wind turbine. 2014.

[237] Xun Meng, Qi Lou, Ruifeng Shi, et al. Multi-criteria-decision-making of a tlp support with large-capacity owt at deep water. In *The Twenty-fourth International Ocean and Polar Engineering Conference*. International Society of Offshore and Polar Engineers, 2014.

[238] Yeshwant Prabhu Chodnekar, Sukomal Mandal, et al. Hydrodynamic analysis of floating offshore wind turbine. *Procedia Engineering*, 116:4–11, 2015.

[239] Xun Meng, Xiaohan Liu, Huiyuan Tian, Meng Liu, Changzhi Wu, et al. Optimal design and experimental evaluation of a tlp for fowt at moderate water depth. In *The 26th International Ocean and Polar Engineering Conference*. International Society of Offshore and Polar Engineers, 2016.

[240] HF Wang and YH Fan. Spoke dimension on the motion performance of a floating wind turbine with tension-leg platform. *Shock and Vibration*, 2016, 2016.

[241] Mareike Leimeister, Erin E Bachynski, Michael Muskulus, and Philipp Thomas. Rational upscaling of a semi-submersible floating platform supporting a wind turbine. *Energy Procedia*, 94:434–442, 2016.

[242] Ali C. Kheirabadi and Ryozo Nagamune. Real-time relocation of floating offshore wind turbine platforms for wind farm efficiency maximization: An assessment of feasibility and steady-state potential. *Ocean Engineering*, 208:107445, 2020.

[243] John Marius Hegseth, Erin E. Bachynski, and Joaquim R.R.A. Martins. Integrated design optimization of spar floating wind turbines. *Marine Structures*, 72:102771, 2020.

[244] Alonso J Juvinao Carbono, Ivan FM Menezes, and Luiz Fernando Martha. Mooring pattern optimization using genetic algorithms. *6th World Congresses of Structural and Multidisciplinary Optimization*, pages 1–9, 2005.

[245] Tore Hordvik. Design analysis and optimisation of mooring system for floating wind turbines. 2011.

[246] Marek Goldschmidt and Michael Muskulus. Coupled mooring systems for floating wind farms. *Energy Procedia*, 80:255–262, 2015.

[247] SF Rodrigues, R Teixeira Pinto, M Soleimanzadeh, Peter AN Bosman, and P Bauer. Wake losses optimization of offshore wind farms with moveable floating wind turbines. *Energy Conversion and Management*, 89:933–941, 2015.

[248] SD Weller, Lars Johanning, Peter Davies, and SJ Banfield. Synthetic mooring ropes for marine renewable energy applications. *Renewable Energy*, 83:1268–1278, 2015.

[249] Yuan Ma, Chaohe Chen, Tianhui Fan, Xinkuan Yan, and Hongchao Lu. Research on motion inhibition method using an innovative type of mooring system for spar floating offshore wind turbine. *Ocean Engineering*, 223:108644, 2021.

[250] Kun Xu, Kjell Larsen, Yanlin Shao, Min Zhang, Zhen Gao, and Torgeir Moan. Design and comparative analysis of alternative mooring systems for floating wind turbines in shallow water with emphasis on ultimate limit state design. *Ocean Engineering*, 219:108377, 2021.

[251] Hong-Duc Pham, Franck Schoefs, Patrice Cartraud, Thomas Soulard, Hien-Hau Pham, and Christian Berhault. Methodology for modeling and service life monitoring of mooring lines of floating wind turbines. *Ocean Engineering*, 193:106603, 2019.

[252] Magnus J Harrold, Philipp R Thies, Lars Johanning, David Newsam, Michael Checkley, and Claudio Bittencourt Ferreira. Dynamic load reduction and station keeping mooring system for floating offshore wind. In *International Conference on*

Offshore Mechanics and Arctic Engineering, volume 51975, page V001T01A018. American Society of Mechanical Engineers, 2018.

[253] Frank Sandner and Po Wen Cheng. Conceptual design of floating wind turbines. 2013.

[254] Frank Lemmer, Steffen Raach, David Schlipf, and Po Wen Cheng. Prospects of linear model predictive control on a 10 mw floating wind turbine. In *ASME 2015 34th International Conference on Ocean, Offshore and Arctic Engineering*, pages V009T09A071–V009T09A071. American Society of Mechanical Engineers, 2015.

[255] AD Arnott, CA Greated, A Incecik, A McLeary, et al. An investigation of extreme wave behaviour around a model tlp. *International Journal of Offshore and Polar Engineering*, 8(01), 1998.

[256] W Bai, X Feng, R Eatock Taylor, and KK Ang. Fully nonlinear analysis of near-trapping phenomenon around an array of cylinders. *Applied Ocean Research*, 44:71–81, 2014.

[257] HA Wolgamot, R Eatock Taylor, and PH Taylor. Radiation, trapping and near-trapping in arrays of floating truncated cylinders. *Journal of Engineering Mathematics*, 91(1):17–35, 2015.

[258] Ian GC Ashton, Lars Johanning, and Brian Linfoot. Measurement of the effect of power absorption in the lee of a wave energy converter. In *ASME 2009 28th International Conference on Ocean, Offshore and Arctic Engineering*, pages 1021–1030. American Society of Mechanical Engineers, 2009.

[259] Merrick C Haller, Aaron Porter, Pukha Lenee-Bluhm, Ken Rhinefrank, Erik Hammagren, Tuba Ozkan-Haller, and David Newborn. Laboratory observation of waves in the vicinity of wec-arrays. Technical report, Oregon Wave Energy Trust, 2011.

[260] Vicky Stratigaki, Peter Troch, Tim Stallard, David Forehand, Matt Folley, J Peter Kofoed, Michel Benoit, Aurélien Babarit, Marc Vantorre, and J Kirkegaard. Sea-state modification and heaving float interaction factors from physical modelling of

arrays of wave energy converters. *Journal of Renewable and Sustainable Energy*, 7(6):061705, 2015.

[261] Michael O'Cathain, Bernt J Leira, and John Ringwood. Modelling of multibody marine systems with application to wave-energy devices. 2007.

[262] Uwe S Paulsen, Michael Borg, Helge Aa Madsen, Troels Friis Pedersen, Jesper Hattel, Ewen Ritchie, Carlos S Ferreira, Harald Svendsen, Petter A Berthelsen, and Charles Smadja. Outcomes of the deepwind conceptual design. *Energy Procedia*, 80:329–341, 2015.

[263] Abdullah Mobin Chowdhury, Hiromichi Akimoto, and Yutaka Hara. Comparative cfd analysis of vertical axis wind turbine in upright and tilted configuration. *Renewable Energy*, 85:327–337, 2016.

[264] Zhengshun Cheng, Helge Aagaard Madsen, Wei Chai, Zhen Gao, and Torgeir Moan. A comparison of extreme structural responses and fatigue damage of semi-submersible type floating horizontal and vertical axis wind turbines. *Renewable Energy*, 2017.

[265] Zhengshun Cheng, Kai Wang, Zhen Gao, and Torgeir Moan. A comparative study on dynamic responses of spar-type floating horizontal and vertical axis wind turbines. *Wind Energy*, 20(2):305–323, 2017.

[266] Longbin Tao and Shunqing Cai. Heave motion suppression of a spar with a heave plate. *Ocean Engineering*, 31(5):669–692, 2004.

[267] Carlos Lopez-Pavon and Antonio Souto-Iglesias. Hydrodynamic coefficients and pressure loads on heave plates for semi-submersible floating offshore wind turbines: A comparative analysis using large scale models. *Renewable Energy*, 81:864–881, 2015.

[268] Hang Zhu, Jinping Ou, and Gangjun Zhai. Conceptual design of a deep draft semi-submersible platform with a moveable heave-plate. *Journal of Ocean University of China*, 11(1):7–12, 2012.

[269] Minnan Yue, Qingsong Liu, Chun Li, Qinwei Ding, Shanshan Cheng, and Haitian Zhu. Effects of heave plate on dynamic response of floating wind turbine spar platform under the coupling effect of wind and wave. *Ocean Engineering*, 201:107103, 2020.

[270] Xiaoqiang Sean Bian, Steven J Leverette, and Oriol R Rijken. A tlp solution for 8000 ft water depth. In *ASME 2010 29th International Conference on Ocean, Offshore and Arctic Engineering*, pages 255–262. American Society of Mechanical Engineers, 2010.

[271] Yulin Si, Hamid Reza Karimi, and Huijun Gao. Modeling and parameter analysis of the oc3-hywind floating wind turbine with a tuned mass damper in nacelle. *Journal of Applied Mathematics*, 2013, 2013.

[272] Minho Ha and Cheolung Cheong. Pitch motion mitigation of spar-type floating substructure for offshore wind turbine using multilayer tuned liquid damper. *Ocean Engineering*, 116:157–164, 2016.

[273] Hsien Hua Lee and HH Juang. Experimental study on the vibration mitigation of offshore tension leg platform system with uwtlcd. *Smart Structures and Systems*, 9(1):71–104, 2012.

[274] Xiaohui Zeng, Yang Yu, Liang Zhang, Qingquan Liu, and Han Wu. A new energy-absorbing device for motion suppression in deep-sea floating platforms. *Energies*, 8(1):111–132, 2014.

[275] Amy N Robertson, Fabian Wendt, Jason M Jonkman, Wojciech Popko, Habib Dagher, Sebastien Gueydon, Jacob Qvist, Felipe Vittori, José Azcona, Emre Uzunoglu, et al. Oc5 project phase ii: validation of global loads of the deepcwind floating semisubmersible wind turbine. *Energy Procedia*, 137:38–57, 2017.

[276] Dewey H Hodges. *Nonlinear composite beam theory*. American Institute of Aeronautics and Astronautics, 2006.

[277] Anthony T Patera. A spectral element method for fluid dynamics: laminar flow in a channel expansion. *Journal of computational Physics*, 54(3):468–488, 1984.

[278] Jintai Chung and GM Hulbert. A time integration algorithm for structural dynamics with improved numerical dissipation: the generalized-alpha method. *Journal of applied mechanics*, 60(2):371–375, 1993.

[279] Mohammed Khair Al-Solihat and Meyer Nahon. Mooring and hydrostatic restoring of offshore floating wind turbine platforms. In *Oceans-St. John's, 2014*, pages 1–5. IEEE, 2014.

[280] Mohammad Reza Tabeshpour and Reza Hedayatpour. Analytical investigation of nonlinear heave-coupled response of tension leg platform. *Proceedings of the Institution of Mechanical Engineers, Part M: Journal of Engineering for the Maritime Environment*, 233(3):699–713, 2019.

[281] JAP Aranha. A formula for 'wave damping'in the drift of a floating body. *Journal of Fluid Mechanics*, 275:147–155, 1994.

[282] Det Norske Veritas. Global performance analysis of deepwater floating structures. *Høvik: Det Norske Veritas*, 2010.

[283] Christoph Meier, Alexander Popp, and Wolfgang A Wall. Geometrically exact finite element formulations for slender beams: Kirchhoff–love theory versus simo–reissner theory. *Archives of Computational Methods in Engineering*, 26(1):163–243, 2019.

[284] Stephen P Timoshenko. Lxvi. on the correction for shear of the differential equation for transverse vibrations of prismatic bars. *The London, Edinburgh, and Dublin Philosophical Magazine and Journal of Science*, 41(245):744–746, 1921.

[285] Ron Adrezin and Haym Benaroya. Response of a tension leg platform to stochastic wave forces. *Probabilistic Engineering Mechanics*, 14(1-2):3–17, 1999.

[286] Deirdre O'Donnell, Jimmy Murphy, and Vikram Pakrashi. Comparison of response amplitude operator curve generation methods for scaled floating renewable energy

platforms in ocean wave basin. *ASME Letters in Dynamic Systems and Control*, 1(2):021012, 2021.

[287] Jong-Shyong Wu and Mang Hsieh. An experimental method for determining the frequency-dependent added mass and added mass moment of inertia for a floating body in heave and pitch motions. *Ocean Engineering*, 28(4):417–438, 2001.

[288] Antonio C Fernandes and Allan C Oliveira. The roll damping assessment via decay model testing (new ideas about an old subject). *Journal of Marine science and application*, 8(2):144–150, 2009.

[289] Kelley Ruehl, Dominic D Forbush, Yi-Hsiang Yu, and Nathan Tom. Experimental and numerical comparisons of a dual-flap floating oscillating surge wave energy converter in regular waves. *Ocean Engineering*, 196:106575, 2020.

[290] Jason Jonkman, Sandy Butterfield, Walter Musial, and George Scott. Definition of a 5-mw reference wind turbine for offshore system development. Technical report, National Renewable Energy Laboratory (NREL), Golden, CO., 2009.

[291] YM Low. Influence of the setdown of a tension leg platform on the extreme airgap response. *Applied Ocean Research*, 32(1):11–19, 2010.

[292] MY Mahfouz, R Faerron-Guzmán, K Müller, F Lemmer, and PW Cheng. Validation of drift motions for a semi-submersible floating wind turbine and associated challenges. In *Journal of Physics: Conference Series*, volume 1669, page 012011. IOP Publishing, 2020.

[293] Madsen, F.J. and Pegalajar-Jurado, A. and Bredmose, H. and Faerron-Guzman, R. and Müller, K. and Lemmer, F. Lifes50+ deliverable d4.6 model validation against experiments and map of model accuracy across load cases. `https://lifes50plus.eu/wp-content/uploads/2018/11/GA_640741_LIFES50_D4.6.pdf`, 2018. [Online; accessed 8-December-2020].

[294] Shan Ma, De-kang Xu, Wen-yang Duan, Ji-kang Chen, Kang-ping Liao, and Hui Wang. The numerical study of viscous drag force influence on low-frequency surge

motion of a semi-submersible in storm sea states. *Ocean Engineering*, 213:107511, 2020.

[295] Masami Sato and Takaya Kobayashi. A fundamental study of the flow past a circular cylinder using abaqus/cfd. In *2012 SIMULIA Community Conference*, 2012.

[296] Carl Trygve Stansberg, Karl Erik Kaasen, Bjørn Christian Abrahamsen, Arne Nestegård, Yanlin Shao, Kjell Larsen, et al. Challenges in wave force modelling for mooring design in high seas. In *Offshore Technology Conference*. Offshore Technology Conference, 2015.

[297] Brendan Cahill. *Characteristics of the wave energy resource at the Atlantic marine energy test site*. PhD thesis, University College Cork, 2013.

[298] YH Bae and MH Kim. Turbine floater-tether coupled dynamic analysis including second-order sum-frequency wave loads for a tlp-type fowt (floating offshore wind turbine). In *ASME 2013 32nd International Conference on Ocean, Offshore and Arctic Engineering*. American Society of Mechanical Engineers Digital Collection, 2013.

[299] Sébastien Gueydon, Jason Jonkman, et al. Update on the comparison of second-order loads on a tension leg platform for wind turbines. In *The 26th International Ocean and Polar Engineering Conference*. International Society of Offshore and Polar Engineers, 2016.

[300] Emodnet. `https://www.emodnet-bathymetry.eu/`. Accessed: 2015-09-30.

[301] Guy Westbrook. email communication, 2016.

[302] John P Snyder. An equal-area map projection for polyhedral globes. *Cartographica: The International Journal for Geographic Information and Geovisualization*, 29(1):10–21, 1992.

[303] O Karpa and A Naess. Extreme value statistics of wind speed data by the acer method. *Journal of Wind Engineering and Industrial Aerodynamics*, 112:1–10, 2013.

[304] Erik Vanem. Uncertainties in extreme value modelling of wave data in a climate change perspective. *Journal of Ocean Engineering and Marine Energy*, 1(4):339–359, 2015.

[305] V Cummins and E McKeogh. Blueprint for offshore wind in ireland 2020-2050: A research synthesis. In *EirWind project, MaREI Centre, ERI, University College Cork, Ireland*, 2020.

[306] J. Jonkman, S. Butterfield, W. Musial, and G. Scott. Definition of a 5mw reference wind turbine for offshore system development. In NREL, editor, *Technical Report NREL*, volume 1 of *1*. NREL, www.nrel.gov, 2009.

[307] Evan Gaertner, Jennifer Rinker, Latha Sethuraman, Frederik Zahle, Benjamin Anderson, Garrett Barter, Nikhar Abbas, Fanzhong Meng, Pietro Bortolotti, Witold Skrzypinski, et al. Definition of the iea 15-megawatt offshore reference wind turbine. 2020.

[308] Amu N Robertson, Sébastien Gueydon, E Bachynski, Lu Wang, Jason Jonkman, D Alarcón, Erkek Amet, Alec Beardsell, Paul Bonnet, B Boudet, et al. Oc6 phase i: Investigating the underprediction of low-frequency hydrodynamic loads and responses of a floating wind turbine. In *Journal of Physics: Conference Series*, volume 1618, page 032033. IOP Publishing, 2020.

[309] Yuka Kikuchi and Takeshi Ishihara. Upscaling and levelized cost of energy for offshore wind turbines supported by semi-submersible floating platforms. In *Journal of Physics: Conference Series*, volume 1356, page 012033. IOP Publishing, 2019.

[310] Heather Rae Martin. Development of a scale model wind turbine for testing of offshore floating wind turbine systems. 2011.

[311] Jason Jonkman. Nwtc nrel's national wind technology center message board. https://wind.nrel.gov/forum/wind/viewtopic.php?f=3&t=1665&p=7784&hilit=tower+resonance+tlp#p7784, 2016. Accessed: 14-03-2017.

[312] J Cotrell, T Stehly, J Johnson, JO Roberts, Z Parker, G Scott, and D Heimiller. *Analysis of transportation and logistics challenges affecting the deployment of larger wind turbines: summary of results.* National Renewable Energy Laboratory, 2014.

[313] Noel Ahern. S.i. no. 147/2009 - road traffic (specialised vehicle permits) regulations 2009. http://www.irishstatutebook.ie/eli/2009/si/147/made/en/print, 2009. Accessed: 21-03-2017.

[314] Vicente Negro, José-Santos López-Gutiérrez, M Dolores Esteban, Pablo Alberdi, Mario Imaz, and José-María Serraclara. Monopiles in offshore wind: Preliminary estimate of main dimensions. *Ocean Engineering*, 133:253–261, 2017.

[315] Erin E Bachynski and Torgeir Moan. Design considerations for tension leg platform wind turbines. *Marine Structures*, 29(1):89–114, 2012.

[316] Subrata Chakrabarti. *Handbook of Offshore Engineering (2-volume set)*. Elsevier, 2005.

[317] NORSOK Standard. Design of steel structures. *N-004. Rev*, 1, 1998.

[318] Fabian F Wendt, Morten T Andersen, Amy N Robertson, Jason M Jonkman, et al. Verification and validation of the new dynamic mooring modules available in fast v8. In *The 26th International Ocean and Polar Engineering Conference*. International Society of Offshore and Polar Engineers, 2016.

[319] Norske Veritas. *Stability and watertight integrity*. Det Norske Veritas, 2001.

[320] Hongyan Ding, Yanqing Han, Conghuan Le, and Puyang Zhang. Dynamic analysis of a floating wind turbine in wet tows based on multi-body dynamics. *Journal of renewable and sustainable energy*, 9(3):033301, 2017.

[321] Grant E Hearn and Andrew V Metcalfe. 7 - some typical applications. In Grant E Hearn and Andrew V Metcalfe, editors, *Spectral Analysis in Engineering*, pages 161–183. Butterworth-Heinemann, Oxford, 1995.

[322] Kabir Sadeghi. Significant guidance for design and construction of marine and offshore structures. *GAU Journal of Social & Applied Sciences*, 4(7):65–92, 2008.

[323] Aurélien Babarit, Jorgen Hals, Made Jaya Muliawan, Adi Kurniawan, Torgeir Moan, and Jorgen Krokstad. Numerical benchmarking study of a selection of wave energy converters. *Renewable energy*, 41:44–63, 2012.

[324] Hywind scotland remains the uk's best performing offshore wind farm. `https://www.equinor.com/en/news/20210323-hywind-scotland-uk-best-performing-offshore-wind-farm.html`. Accessed: 2021-06-14.

[325] M. Mohsen Moarefdoost, Lawrence V. Snyder, and Basel Alnajjab. Layouts for ocean wave energy farms: Models, properties, and optimization. *Omega*, 66:185–194, 2017. New Research Frontiers in Sustainability.

[326] WC Zhang, HX Liu, XW Zhang, and L Zhang. Semi-analytical solution of optimization on moon-pool shaped wec. *Polish Maritime Research*, 23:25–31, 2016.

[327] Krish P Thiagarajan, Indra Datta, Alex Z Ran, Longbin Tao, and John E Halkyard. Influence of heave plate geometry on the heave response of classic spars. In *International Conference on Offshore Mechanics and Arctic Engineering*, volume 36118, pages 621–627, 2002.

[328] Ed Mackay, Lars Johanning, Wei Shi, and Dezhi Ning. Model tests of a tlp floating offshore wind turbine with a porous outer column. 2020.

[329] Christopher J Cargo, Andrew R Plummer, Andrew J Hillis, and Michael Schlotter. Determination of optimal parameters for a hydraulic power take-off unit of a wave energy converter in regular waves. *Proceedings of the Institution of Mechanical Engineers, Part A: Journal of Power and Energy*, 226(1):98–111, 2012.

[330] Jonas Sjolte, Christian McLisky Sandvik, Elisabetta Tedeschi, and Marta Molinas. Exploring the potential for increased production from the wave energy converter lifesaver by reactive control. *Energies*, 6(8):3706–3733, 2013.

[331] Jørgen Hals Todalshaug, Gunnar Steinn Ásgeirsson, Eysteinn Hjálmarsson, Jéromine Maillet, Patrik Möller, Pedro Pires, Matthieu Guérinel, and Miguel Lopes. Tank testing of an inherently phase-controlled wave energy converter. *International Journal of Marine Energy*, 15:68–84, 2016.

[332] Laura Castro-Santos, Almudena Filgueira-Vizoso, Carlos Álvarez-Feal, and Luis Carral. Influence of size on the economic feasibility of floating offshore wind farms. *Sustainability*, 10(12):4484, 2018.

[333] Det Norske Veritas. Guideline for offshore structural reliability analysis—applications to tension leg platforms. *Joint Industry Project, Report*, (95-3197), 2001.

[334] J. Hamilton. *Platform & Tether Structural Dynamics*. Number 1 in Proceedings of the Seminar on Tensioned Buoyant Platforms Analysis Design and Field Experience. Bentham Press, London, 1 edition, 1993.

[335] M. O'Connor, T. Lewis, and G. Dalton. *Renewable Energy*, 52:57, 2013.

[336] Ayman Eltaher, Jason Sun, and Paul Jukes. Design of suction piles for deepwater hpht subsea pipelines. In *ASME 2008 27th International Conference on Offshore Mechanics and Arctic Engineering*, pages 361–368. American Society of Mechanical Engineers, 2008.

[337] RJ Taylor and HJ Lee. Direct embedment anchor holding capacity. Technical report, NAVAL CIVIL ENGINEERING LAB PORT HUENEME CA, 1972.

[338] Huacan Fang and Menglan Duan. *Offshore Operation Facilities: Equipment and Procedures*. Gulf Professional Publishing, 2014.

[339] DNV. *OFFSHORE STANDARD DNV-OS-H206*, page 1, 2014.

[340] E. E. Bachynski and T. Moan. *Marine Structures*, 29:89, 2012.

[341] M. Masciola, A. Robertson, J. Jonkman, and F. Driscoll. *International Conference on Offshore Wind Energy and Ocean Energy*, volume 1. NREL, Beijing, China, 2011.

[342] Noble D, Draycott S, Ordonez Sanchez S, Porter K, Johnstone C, Finch S, Judge F, Desmond C, Santos Varela B, Lopez Mendia J, Darbinyan D, Khalid F, Johanning L, Le Boulluec M, and Schaap A. Test recommendations and gap analysis report. Technical report, MaRINET2, 2018.

[343] Jie Ding, Kuangmin Gong, and Xinzhong Chen. Comparison of statistical extrapolation methods for the evaluation of long-term extreme response of wind turbine. *Engineering structures*, 57:100–115, 2013.